Thèse

Présentée et soutenue publiquement pour l'obtention du titre de

DOCTEUR DE l'UNIVERSITE DE LORRAINE

Mention : Sciences des Matériaux

Par **Mathias Lamari**

In situ characterization and modelling of retained austenite thermomechanical stability in Medium Manganese Duplex TRIP-aided steels

Soutenue publiquement le 12 avril 2023 à Nancy

Membres du jury :

Président du jury :	**Delphine RETRAINT**	**Professeur, Université de technologie de Troyes, Troyes, France**
Rapporteurs :	**Patricia VERLEYSEN**	**Professeur, Université de Gand, Gand, Belgique**
	Matthieu MAZIERE	**Maître de conférences HDR, Mines-Paris PSL, Paris, France**
Examinateurs :	**Mingxin HUANG**	**Professeur, Université de Hong Kong, Hong Kong, Chine**
	Roxane MASSION	**Maître de conférences HDR, Université de Lorraine, Metz, France**
Directeur de thèse :	**Sébastien ALLAIN**	**Professeur, Université de Lorraine, Nancy, France**
Codirecteur de thèse :	**Guillaume GEANDIER**	**Chargé de recherche, CNRS, Nancy, France**
Membre invitée :	**Kangying ZHU**	**Ingénieur de Recherche, ArcelorMittal Maizières SA, Maizières-lès-Metz, France**

Remerciements

Je tiens tout d'abord à remercier Patricia Verleysen et Matthieu Mazière pour avoir accepté d'être rapporteurs de ce long manuscrit, ainsi que Delphine Retraint, Roxane Massion et Mingxin Huang, les membres du jury pour avoir accepté d'évaluer mon travail de thèse. J'ai énormément apprécié la qualité des discussions scientifiques qui eurent lieu lors de ma soutenance.

J'exprime ma profonde gratitude envers Sébastien Allain, mon directeur de thèse, et Guillaume Geandier, mon codirecteur de thèse, pour m'avoir transmis leur passion de la métallurgie, de la mécanique et de la diffraction des rayons X haute énergie. Je les remercie pour leurs nombreux conseils et retours sur mon travail, la transmission de leur savoir, et leur amitié. Je remercie spécialement Sébastien sans qui je ne me serais pas orienté vers la métallurgie au cours de mes études aux Mines de Nancy.

Je remercie aussi Sabine Denis et Benoît Appolaire, dont les enseignements au sein du Master Métallurgie de la FST de Nancy ont été l'une des clefs du bon accomplissement de cette thèse.

Je voudrais adresser un remerciement particulier à Kangying Zhu, qui m'a encadré à ArcelorMittal et m'a guidé tout au long de ma thèse. Je remercie aussi sincèrement Astrid Perlade, Michel Soler et Jean-Christophe Hell pour m'avoir conseillé et apporté un regard complémentaire sur mon travail tout au long de la thèse. Je remercie chaleureusement Matthieu Salib qui m'a aidé à m'intégrer au sein de l'entreprise et m'en a fait découvrir différentes facettes.

Ce travail de thèse n'aurait pas été possible sans l'aide directe de techniciens, d'ingénieurs et de chercheurs. Je remercie particulièrement Coralie Jung pour les magnifiques microscopies MEB qu'elle a réalisées à ArcelorMittal sur mes échantillons medium Mn, Michaël Stoltz d'avoir assuré les traitements thermiques au bain de sel, Blandine Rémy pour la réalisation des mesures WDS. Je remercie aussi Benoît Denand, pour l'aide et l'expertise qu'il m'a fournies lors des essais mécaniques à l'IJL. Je remercie Marc Ponçot de m'avoir formé à la corrélation d'image numérique.

Je remercie aussi Jean-Philippe Tinnes et Jean-Philippe Chateau-Cornu d'avoir accepté de faire partie de mon comité de suivi de thèse. Leurs retours m'auront été précieux.

Cette longue liste de remerciements ne serait pas complète sans l'expression de ma profonde reconnaissance envers tous les amis que j'ai pu me faire durant ma thèse. Un grand merci à Nazim Abdedou et Ivan Cazic, qui auront partagé mon bureau et m'auront supporté durant la thèse ; à Marc Moreno, qui aura été comme un mentor durant le début de ma thèse ; à Imed Benrabah, qui m'aura canalisé durant la rédaction ; à Juan Macchi et Clélia Couchet, dont les discussions scientifiques et l'amitié m'auront été précieuses ; à Julien Banos et Thomas Huchard, qui, finissant en même temps que moi, auront partagé mes états d'âme finaux ; à Ilia Ushakov, Ítalo Oyarzabal et Gatien Rolland ; ainsi qu'à tous les autres, qui se reconnaîtront.

Enfin, j'ai une pensée émue pour ma famille. Merci à ma mère et à mon père pour leur amour et leur éducation, à mes frères Alexandre et Francis de me supporter et me soutenir depuis l'enfance. Merci enfin à toi Litan, qui m'a supporté et m'a accompagné dans les moments doux comme tristes de l'existence.

A ma Mère,
Diana Ruth Langier,
Toutes nos Pensées
Tout mon Amour de Fils

Table of contents

Résumé étendu en français

Ce résumé vise à souligner les aspects importants de chaque chapitre de la thèse pour les lecteurs francophones. Tous les résultats ne sont pas présentés et discutés, et les explications détaillées sont à trouver dans le texte principal (en anglais).

1. Contexte et problématique scientifique

Les aciers à très haute résistance mécanique (THR) de 3ème génération sont une classe d'acier qui comprend différents concepts microstructuraux innovants, comme les aciers trempés (*quenching*) et partitionnés (Q&P), les aciers bainitiques sans carbures (BSC) ou encore les aciers dits moyen manganèse. Les propriétés mécaniques exceptionnelles de tous ces aciers s'expliquent par leurs microstructures particulières, présentant une matrice « ferritique » nano-structurée et une quantité importante d'austénite résiduelle à température ambiante. Dans ces aciers, le bon équilibre entre résistance mécanique et ductilité est assuré par la finesse des microstructures et par un effet TRIP (plasticité induite par la transformation) efficace. L'effet TRIP est un mécanisme d'écrouissage dynamique lié à la transformation de l'austénite résiduelle en martensite lors d'une sollicitation mécanique [1]. La transformation graduelle de l'austénite ductile en martensite, plus dure que l'austénite, conduit à une augmentation rapide de l'écrouissage macroscopique de l'acier, et retarde donc l'apparition de la striction. Le développement de cette nouvelle génération d'aciers THR est vu par les constructeurs automobiles comme la meilleure opportunité pour allier réduction du poids des châssis avec une augmentation de la sécurité pour les véhicules légers [2].

La thèse vise à mieux comprendre la stabilité thermomécanique de l'austénite résiduelle des aciers THR de 3ème génération. Si dans la littérature, l'évolution de cette dernière est qualitativement comprise en fonction des caractéristiques de l'austénite (chimie, taille, morphologie, environnement, contrainte résiduelle) et de la nature de la sollicitation mécanique (triaxialité, vitesse et température de l'essai), il manque une compréhension quantitative de tous ces phénomènes et de leurs possible interactions. A cette fin, huit microstructures d'acier à effet TRIP moyen Mn ont été étudiées, ces derniers contenant plus d'austénite résiduelle comparativement aux aciers Q&P et BSC.

La présente thèse CIFRE s'inscrit dans un long projet de collaboration débuté en 2011 entre ArcelorMittal et l'Institut Jean Lamour (IJL) sur la compréhension des mécanismes de formation des microstructures THR de 3ème génération et la modélisation de leur comportement mécanique. La thèse, qui a débuté en novembre 2019, a été précédé d'un stage de fin d'étude de six mois, visant à établir certains aspects de la méthodologie employée ensuite lors de la thèse. Les résultats obtenus dans la thèse s'inscrivent aussi dans le projet européen RFCS Dynaustab, qui vise à expliquer l'évolution de la stabilité mécanique de l'austénite en condition dynamique (c'est-à-dire à haute vitesse de déformation).

Le Chapitre I est une revue bibliographique sur la formation des microstructures moyen Mn, les aspects métallurgiques et mécaniques influençant l'effet TRIP et les aspects théoriques liées à la modélisation de cet effet. Les explications sur les techniques expérimentales et des méthodes d'analyses utilisées sont données dans chacun des chapitres suivants. Le Chapitre II est dédié à l'étude

expérimentale in situ de la formation des huit microstructures choisies, à l'aide d'expériences de diffraction des rayons X de haute énergie (DRXHE) sur ligne de lumière synchrotron. Dans le Chapitre III, l'évolution de la stabilité de l'austénite résiduelle est étudiée pendant des tractions simples par DRXHE, tout en quantifiant le partitionnement des contraintes entre les phases. Le manuscrit s'achève par le Chapitre IV, dans lequel est détaillé le modèle micromécanique explicatif et quantitatif de l'effet TRIP dans les aciers étudiés. C'est un modèle à champ moyen, sensible à la taille de grain et à la chimie, qui explique les comportements mécaniques de chacune des phases (ferrite, austénite et martensite) constitutives de la microstructure de ces aciers et la transformation martensitique induite par la déformation à l'aide de lois à bases physiques.

2. Chapitre 1 : Revue bibliographique

La revue bibliographique se décompose en 5 axes pour l'interprétation des travaux présentés dans les 3 autres chapitres du mémoire. Le premier axe concerne la formation des microstructures duplex étudiées dans la thèse. Le deuxième axe revient sur des aspects plus fondamentaux de la transformation martensitique. La troisième section détaille différents modèles permettant de comprendre la transformation martensitique induite par la déformation. La quatrième partie revient sur les schémas possibles pour construire un modèle micromécanique et sur la prédiction de l'effet TRIP dans tels modèles. La dernière section concerne la description des instabilités mécaniques qui apparaissent dans les aciers moyen Mn.

Le nom « moyen Mn » des aciers étudiés dans la thèse vient de la quantité relativement importante de manganèse qu'ils contiennent, entre 3% et 12%, tout en restant inférieur aux aciers dits « Haut Mn », entièrement austénitique, et souvent sujet à un effet TWIP (plasticité induite par le maclage (*twinning* en anglais)) [3]. Avec cette composition et l'addition d'une quantité raisonnable de carbone (limité pour des raisons de soudage), il est possible d'obtenir des aciers contenant une quantité importante d'austénite à température ambiante après un traitement thermique approprié. Le traitement le plus commun consiste à appliquer un recuit intercritique pour obtenir une microstructure duplex ferrite-austénite avec des grains submicrométriques. Un tel traitement thermique est schématisé Figure 14 (a) et une micrographie MEB (microscopie électronique à balayage) d'une microstructure moyen Mn typique est proposée en Figure 14 (b) [4], [5]. Un recuit est dit intercritique quand il se fait entre les températures Ae_1 et Ae_3 [4], [5]. Ae_1 est la température au-dessus de laquelle l'austénite commence à se former à l'équilibre thermodynamique. Ae_3 est la température au-dessus de laquelle la microstructure stable est austénitique. En général, la microstructure initiale, avant recuit, est soit principalement « ferritique » laminée à froid, soit martensitique trempée.

Durant le maintien intercritique d'un acier « ferritique » laminé à froid, l'austénite va germer et croître dans la microstructure à partir de la cémentite présente dans la microstructure. Il va aussi y avoir un partitionnement en éléments d'alliage entre la matrice et l'austénite. L'austénite va s'enrichir en C et Mn et donc se stabiliser, ce qui va permettre après trempe d'en conserver une grande quantité à température ambiante. Si elle n'est pas assez stable, elle se transformera partiellement en martensite au refroidissement. Pendant le recuit, la matrice laminée à froid va recristalliser et restaurer. La microstructure finale aura une morphologie dite globulaire.

Si la matrice est martensitique avant le maintien intercritique, l'austénite va croître durant la traitement suivant un mécanisme particulier, appelé ART (transformation inverse (reverse en anglais) de l'austénite) [6]. Les films d'austénite présents dans la microstructure vont croître en épousant la morphologie aciculaire de la martensite-mère. Une relation d'orientation cristallographique, de type Kolmogorov-Sacks (K-S) est observée entre la matrice et l'austénite [7]. Pendant le traitement, la matrice martensitique restaure et s'appauvrit en C et Mn, devenant une martensite restaurée de retour à température ambiante. Par abus de langage, la matrice sera simplement appelée « ferrite » dans la littérature. Nous adopterons aussi cette appellation dans le manuscrit. La microstructure finale aura dans le cas de l'ART une morphologie aciculaire, dite fibreuse.

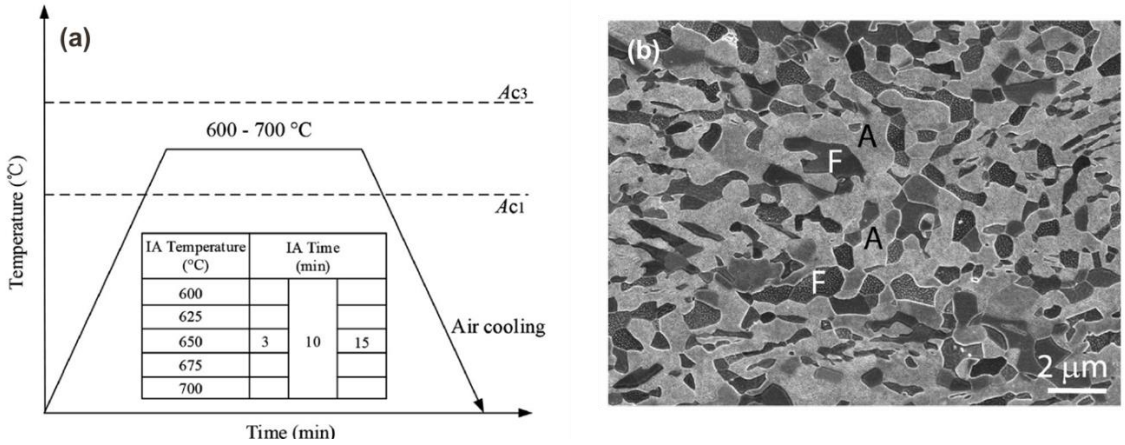

Figure 1: (a) Schéma d'un recuit intercritique pour produire des microstructures duplex moyen Mn. (b) Observation métallographique MEB d'une microstructure globulaire duplex austénite/ferrite produite après un recuit à 700°C d'un acier Fe/0.6C/6.6Mn/3Al laminé à froid [4], [5].

La transformation martensitique correspond à la transformation de l'austénite, cubique à faces centrées (CFC), en martensite quadratique centrée (QC). C'est une transformation displacive et sans diffusion. La martensite a donc une composition identique à celle de l'austénite mère. La martensite qui apparait lors du refroidissement est qualifié « d'athermique ». La température M_S est la température en-dessous de laquelle l'austénite se transforme en martensite lors d'un refroidissement. C'est aussi une mesure de la stabilité de l'austénite. L'austénite retenue à température ambiante T_A a sa température M_S en dessous de T_A.

Quand une contrainte est appliquée sur un acier contenant de l'austénite, la transformation martensitique peut être déclenchée à une température supérieure à M_S [8]. L'évolution schématique de la contrainte σ minimale à appliquer pour provoquer la transformation martensitique en fonction de la température est représentée Figure 26 (a). Deux régimes de germination sont à considérer quand on étudie la transformation induite mécaniquement [8], [9]. Dans le premier régime, la contrainte appliquée est inférieure à la limite d'élasticité de l'austénite σ_γ^γ, et la transformation est dite « assistée par la contrainte » (*stress-assisted*). Dans ce régime, la différence d'énergie de Gibbs entre l'austénite et la martensite augmente à cause de l'énergie élastique, comme schématisée Figure 26 (b), provoquant la nucléation de la martensite. Dans le second régime, la contrainte appliquée est supérieure à la limite d'élasticité de l'austénite. Cette dernière plastifie donc d'abord, créant de nouveaux sites de nucléation pour la transformation martensitique. Ce second régime est dit « induit par la déformation » (*strain-induced*). Au-delà d'une certaine température de déformation M_d, la transformation martensite ne peut plus être induite par l'application d'une contrainte.

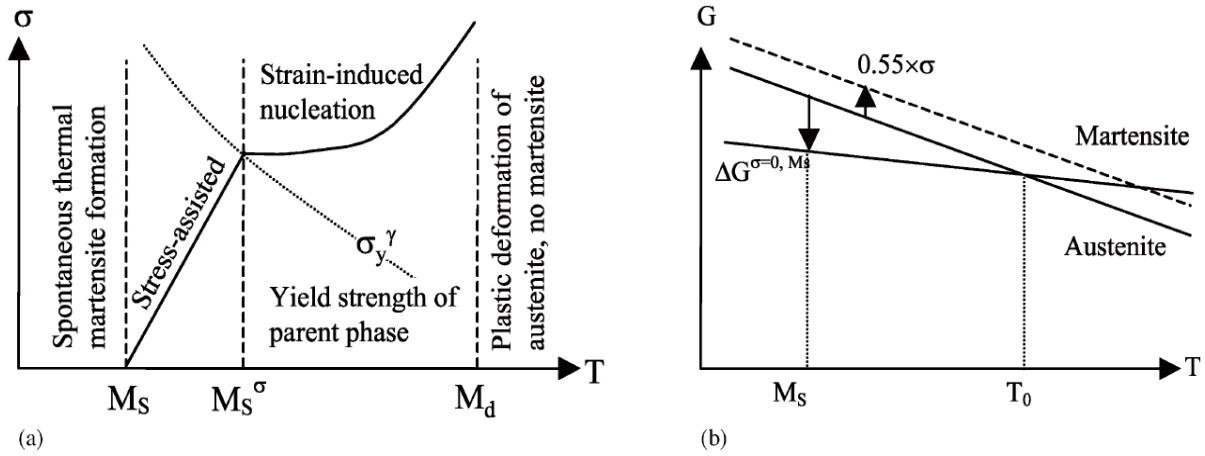

Figure 2 : (a) Evolution de la contrainte σ à appliquer à l'austénite pour déclencher la transformation martensitique, en fonction de la température. Les différents régimes de transformation sont indiqués. (b) Evolution schématique de l'énergie de Gibbs de l'austénite G^γ et de la martensite $G^{\alpha'}$ en fonction de la température. L'effet d'une contrainte appliquée sur G^γ est indiqué en ligne pointillée [8].

La transformation martensitique induite par la déformation est sensible à la stabilité de l'austénite et aux conditions de déformations. La stabilité de l'austénite est influencée par sa chimie, sa taille de grain, sa contrainte résiduelle, sa morphologie et son environnement. Les conditions de déformation correspondent à la vitesse et la température de déformation et la triaxialité du tenseur de contraintes. Des gradients de chimie et tailles peuvent exister dans la microstructure, créant une grande diversité de stabilité d'austénite et favorisant l'efficacité de l'effet TRIP.

Différentes approches pour modéliser la transformation martensite induite par la déformation existent dans la littérature. La plus influente est celle d'Olson et Cohen (OC) [10], [11]. Ces derniers ont proposé de rendre proportionnelle le flux de germination de la martensite induite avec la densité des intersections des bandes de cisaillements, cette dernière étant proportionnelle à la déformation plastique. Suivant cette méthodologie, des approches à base thermodynamique ont été développées, sensibles à la stabilité thermodynamique de l'austénite, la vitesse de déformation ou encore la triaxialité des contraintes [8], [12].

Les aciers moyen Mn sont souvent sujets à des instabilités mécaniques. Lors d'une déformation uniaxiale, la courbe de traction montre souvent un plateau de Lüders et des serrations durant le domaine plastique, aussi appelé effet Portevin-Le Chatelier. Alors que les vieillissements statiques et dynamiques sont souvent utilisés pour expliquer ces phénomènes dans la majorité des alliages métalliques, le cas des aciers moyen Mn reste à éclaircir car qu'il existe une corrélation entre instabilité mécanique (Lüders et PLC) et la transformation martensitique induite mécaniquement.

3. Chapitre 2 : Formation des microstructures moyen Mn

Huit microstructures moyen Mn sont étudiés dans la thèse : 4 microstructures globulaires et 4 microstructures fibreuses. Les microstructures fibreuses sont produites par le recuit intercritique d'une microstructure martensitique alors que les microstructures globulaires sont obtenues par le

recuit d'une microstructure principalement ferritique laminée à froid. La composition de tous les aciers est la même (Fe/0.2C/4Mn/1.5Si/0.8Al). Quatre températures de recuit intercritique T_{IA} ont été choisies : 680°C, 700°C, 720°C et 750°C. Ces choix se basent sur une étude MEB (Microscopie Electronique à Balayage) préliminaire et des calculs thermodynamiques à l'orthoéquilibre.

Les recuits intercritiques ont été réalisés dans un dilatomètre Bähr au synchrotron Petra III à DESY (Hambourg) pour obtenir les huit microstructures tout en conduisant des expériences de DRXHE. En utilisant les méthodes d'affinements Rietveld et celle dite du ratio d'intensité avec une référence (RIR), il est possible d'obtenir l'évolution des microstructures (fractions de phase en ferrite, austénite, martensite et cémentite) et les paramètres de maille de l'austénite et de la ferrite in situ lors de ces recuits.

L'évolution de la fraction d'austénite lors des traitements thermiques est représentée Figure 3 pour les huit expériences (noté (a) fibreux et (b) globulaires ; 680°C en bleu, 700°C en vert, 720°C en jaune et 750°C en rouge). La fraction transformée augmente significativement avec la température de recuit T_{IA} comme attendu par les équilibres thermodynamiques Pour les aciers fibreux, la transformation n'est clairement pas finie à la fin du traitement pour les températures inférieures à 700°C. L'analyse démontre que les cinétiques sont initialement plus lentes dans les aciers fibreux que dans les globulaires, et cette tendance s'inverse à un certain point de la transformation. Les travaux de la thèse ont relié ce phénomène à la plus grande difficulté des carbures qui apparaissent à la chauffe, à se dissoudre dans les microstructures fibreuses que dans les microstructures globulaires pour une température de recuit donnée.

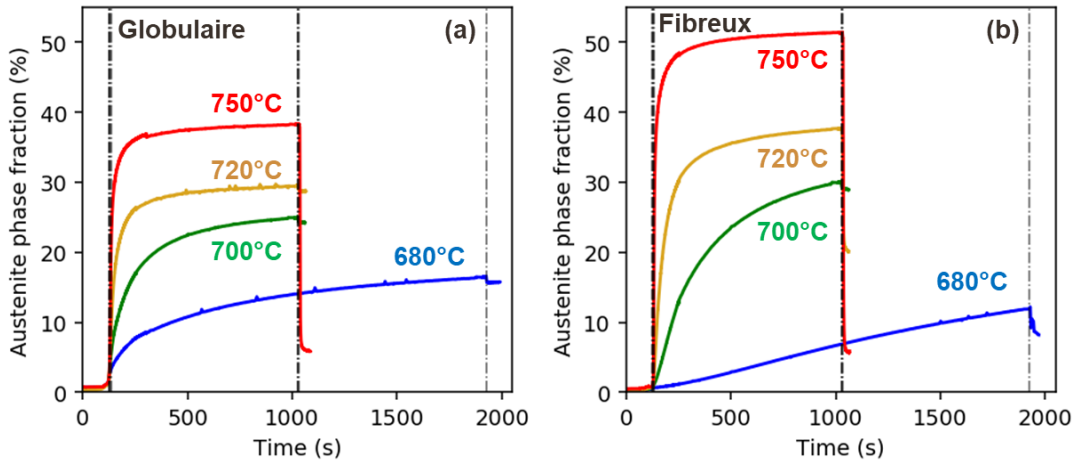

Figure 3: Evolution temporelle de la fraction de phase en austénite au cours des traitements thermiques pour les microstructures globulaires (a) et fibreuses (b). La température de recuit est indiquée sur chaque courbe. La première ligne verticale noire représente le début de la chauffe, la deuxième ligne correspond au début du refroidissement dans les aciers recuits au-dessus de 700°C (15 min) et la troisième ligne à celle du recuit à 680°C (30 min).

Des analyses MEB ont été réalisées post mortem sur chaque microstructure (i.e. après le traitement thermique de recuit). Un algorithme a été mis en place, basé sur la méthode de segmentation par montée des lignes d'eau, pour obtenir les fractions de phase de ferrite de manière automatisée, ainsi que pour quantifier les distributions de taille de grains. Des analyses par microsonde de Castaing ont aussi mis en place dans le cadre de la thèse afin d'obtenir les concentrations en éléments substitutionnels (Mn, Si et Al) de chaque phase.

L'analyse complète des images de diffraction intégrées permet d'obtenir l'évolution en carbone de l'austénite au cours de sa formation. Elle permet aussi d'obtenir l'évolution des contraintes hydrostatiques lors du refroidissement, qui joue sur la stabilité de l'austénite. Deux mécanismes explicatifs ont été identifiés : l'incompatibilité des coefficients de dilatation thermique entre l'austénite et la ferrite, et la transformation martensitique athermique. Un modèle original a été proposé et validé pour expliquer quantitativement la première contribution.

4. Chapitre 3 : Stabilité mécanique de l'austénite

En novembre 2020, des expériences de DRXHE ont aussi été réalisées au synchrotron Petra III à DESY (Hambourg) tout en conduisant des expériences de traction. Les huit microstructures ont été déformées à deux vitesses de déformation de 8×10^{-2} s^{-1} (vitesse rapide) et de 5×10^{-3} s^{-1} (vitesse moyenne). La microstructure globulaire recuite à 720°C a aussi été déformée à une vitesse lente de 5×10^{-4} s^{-1}. La corrélation d'image numérique (DIC, pour digital image correlation) a été utilisée pour mesurer les déformations locales et moyennes le long des éprouvettes de traction (en l'absence d'extensomètre sur la machine de traction).

Les courbes macroscopiques de traction en contraintes vraies sont présentées Figure 4 en parallèle des cinétiques de transformation pour les 4 échantillons globulaires. Les courbes sont tronquées à la striction. L'augmentation de la température de recuit augmente donc clairement la résistance mécanique et l'écrouissage des alliages. Cependant, elle a aussi tendance à diminuer l'allongement uniforme, avec un maximum observé pour un recuit de 700°C, en accord avec la littérature [13]. Les paliers présents sur les courbes bleues, vertes et jaunes sont révélateurs de l'effet Lüders. Les courbes jaunes et vertes sont aussi dentelées, révélant l'effet PLC caractéristiques de ces microstructures. En regardant les cinétiques de transformation, il apparait que la fraction d'austénite résiduelle présent initialement avant déformation augmente entre T_{IA} = 680°C et 720°C. Il y a après une diminution entre T_{IA} = 720°C et 750°C. La fraction d'austénite résiduelle à la striction est de l'ordre de de 3% à 5%. La stabilité mécanique de l'austénite diminue quand la température de recuit augmente, en accord avec les calculs thermodynamiques et les partitions d'éléments attendus d'éléments d'alliages.

Les courbes correspondantes pour les microstructures fibreuses ne sont pas représentées dans ce résumé, mais sont très similaires dans leurs évolutions. Une différence notable est que les performances mécaniques des microstructures fibreuses sont inférieures à celles globulaires.

A l'aide des expériences au synchrotron, il est possible d'obtenir aussi et de façon simultanée l'état de contraintes dans l'austénite et la ferrite à l'aide de la méthode des $\sin^2\psi$ (évolution des contraintes hydrostatiques et de von Mises). Un calcul micromécanique permet de retrouver la contrainte de von Mises de la martensite. Les contraintes von Mises de la ferrite et l'austénite sont représentées pour certaines expériences choisies sur la Figure 5. L'étude actuelle démontre que la contrainte d'écoulement de la ferrite n'est pas affectée par la différence de température de recuit intercritique entre 680°C et 720°C (Figure 5 (a)), contrairement à l'austénite qui voit sa contrainte diminuer (Figure 5 (b)). Après un recuit à 750°C, la ferrite et l'austénite montrent des contraintes d'écoulement supérieures à celles observées à 720°C. Si l'on compare la ferrite fibreuse à celle globulaire recuite à 720°C (Figure 5 (c)), il apparaît que la contrainte d'écoulement est supérieure dans

les microstructures globulaires, contrairement à l'austénite où elle est similaire (Figure 5 (d)). Enfin, la ferrite montre une dépendance négligeable à la vitesse de déformation, alors que l'austénite a une sensibilité négative à la vitesse de déformation. Les comportements de la martensite sont présentés et discutés dans la version complète du texte.

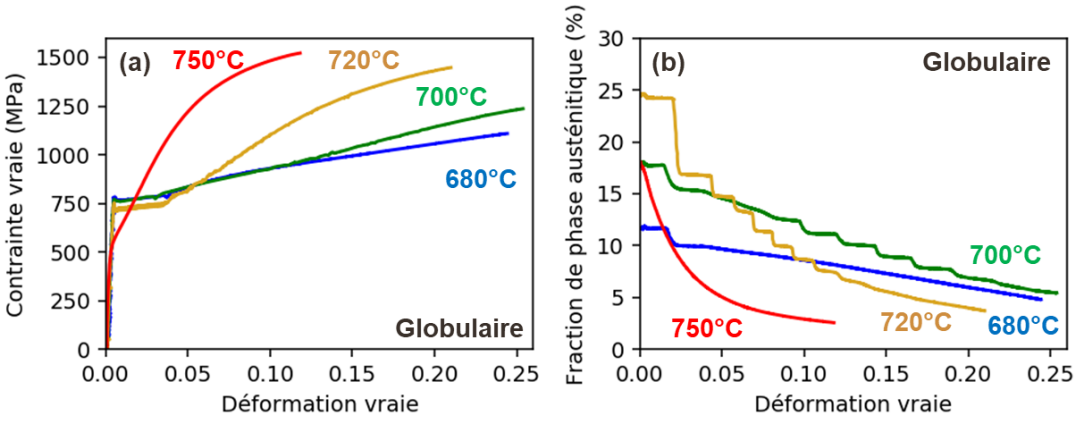

Figure 4: Evolution de la contrainte vraie (a) et de la fraction en austénite (b) au cours des tractions en fonction de la déformation vraie pour les microstructures globulaires déformées à vitesse moyenne. La température de recuit des aciers est indiquée sur chaque courbe.

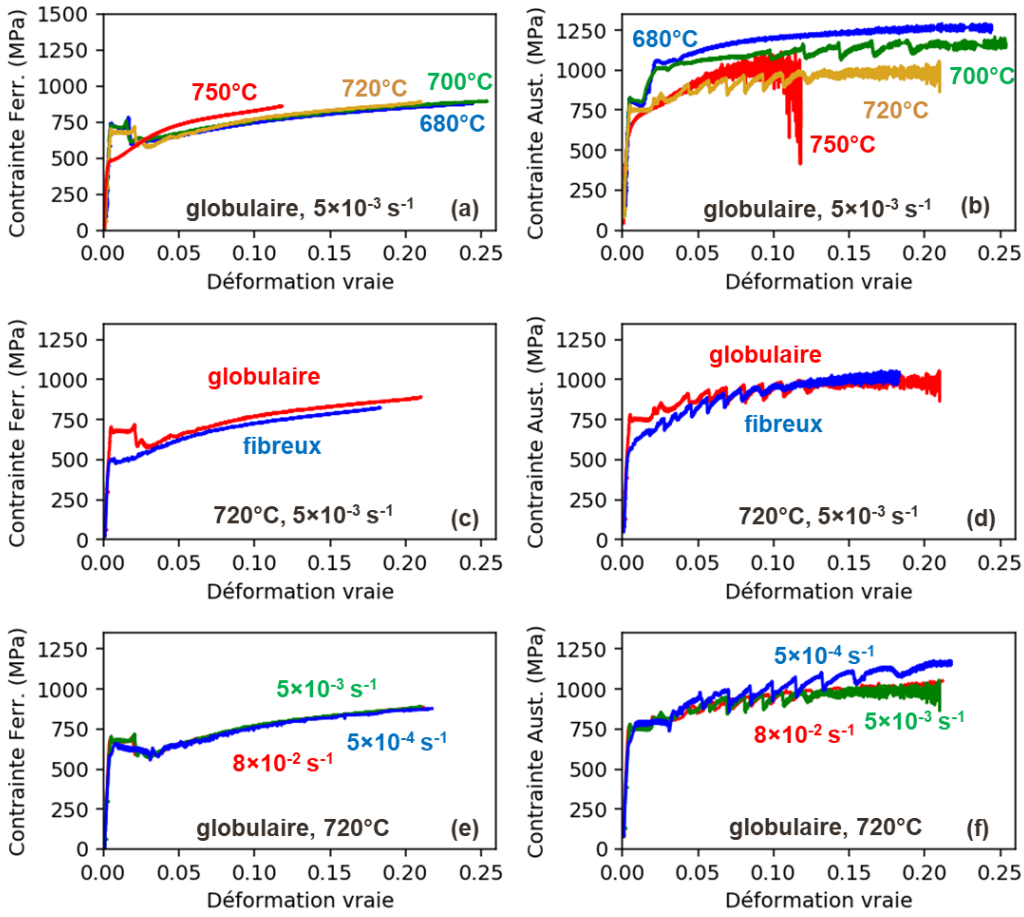

Figure 5: Contrainte de von Mises déterminée par la méthode des sin²ψ dans la ferrite (a), (c), (e) et dans l'austénite (b), (d), (f) pour différentes températures de recuit (a), (b), morphologies (c), (d) et vitesses de déformation (e), (f).

5. Chapitre 4 : Modèle micromécanique des aciers TRIP

Un modèle micromécanique à champ moyen a été développé pour expliquer les comportements observés expérimentalement dans le Chapitre III. Le modèle prend comme paramètre d'entrée les fractions de phases (ferrite, austénite et martensite), les compositions de l'austénite et de la ferrite ainsi que leurs tailles de grains moyennes (diamètre équivalent). La martensite est supposée avoir la même composition que l'austénite. Le calcul du comportement macroscopique se fait en modélisant la contrainte d'écoulement des 3 phases en présence (approche réductionniste) en fonction de leur déformation propre.

A chaque pas de temps, un pas de déformation macroscopique est appliqué. La déformation de chacune des phases est ensuite calculée à l'aide d'une loi de mélange et de l'hypothèse d'iso-travail entre les phases. Les contraintes des phases sont calculées à l'aide des équations constitutives, puis la contrainte macroscopique est retrouvée à l'aide d'une loi de mélange. Enfin, l'évolution des fractions d'austénite et martensite est calculée à l'aide d'un modèle de transformation martensitique induite mécaniquement.

Les lois de comportements entre la ferrite et l'austénite sont assez similaires. La contrainte de chacune des phases est décrite comme la somme de termes de frottement, d'écrouissage isotrope et d'écrouissage cinématique. Pour la ferrite, ces termes ont été calibrés sur des aciers IF (Interstitial Free) 100% ferritiques [14]. Pour l'austénite, les mêmes termes ont été calibrés sur des aciers 100% austénitiques [15]. Pour la ferrite, un terme lié au vieillissement statique de type KEMC (Kubin-Estrin-McCormick) simplifié [16] a été ajouté, en lien avec les résultats expérimentaux. La taille micrométrique de ferrite et austénite impose un terme additionnel permettant de limiter la sensibilité à la taille de grains, , comme expliqué dans [17].

Le modèle pour la martensite est plus innovant. Les modèles existant dans la littérature sont développés pour les aciers martensitiques bruts de trempe ou revenu, mais n'expliquent pas les comportements de la martensite induite mécaniquement. En effet dans les modèles classiques, la relation entre déformation et contrainte de la martensite est définie a priori, quand bien-même la majorité de la martensite n'existe pas initialement. Cette difficulté conceptuelle est résolue dans notre étude par le lien qui est fait entre contrainte dans la martensite et l'avancement de la transformation induite mécaniquement. L'approche utilisée ici reste conceptuellement similaire à l'approche composite continue [18], expliquant le comportement de martensite brutes de trempe. Le nouveau modèle est dénommé MIM (martensite induite mécaniquement).

Enfin, le modèle de transformation martensitique induite mécaniquement est une extension du travail de Perlade et al. [8], lui-même inspiré du modèle OC discuté préalablement. Les flux de germinations sont calculés à chaque étape de calcul en fonction de la déformation plastique de l'austénite. L'innovation principale de cette thèse est d'avoir pris en compte l'aspect autocatalytique de la transformation ainsi que les effets stabilisateurs de la taille de grain austénitique. Le modèle fourni est sensible à la température et la triaxialité.

Les résultats du modèle sont comparés aux déterminations expérimentales dans le cas de l'acier globulaire recuite à 720°C sur la Figure 6. Le modèle explique très bien le comportement de l'austénite (bleu) et de la ferrite (rouge). Le comportement de la martensite varie énormément entre

les expériences (très dures pour les basses températures de recuit, plus molle initialement pour les microstructures formées à haute température). Le modèle de martensite reproduit assez fidèlement ces différentes formes d'écrouissage. Concernant la transformation martensitique induite mécaniquement, le modèle est sensible à la taille de grain et la chimie, et toutes les cinétiques sont bien expliquées. Ces résultats sont particulièrement encourageant car la majorité des paramètres utilisés dans les lois constitutives a été calibré sur des études précédentes.

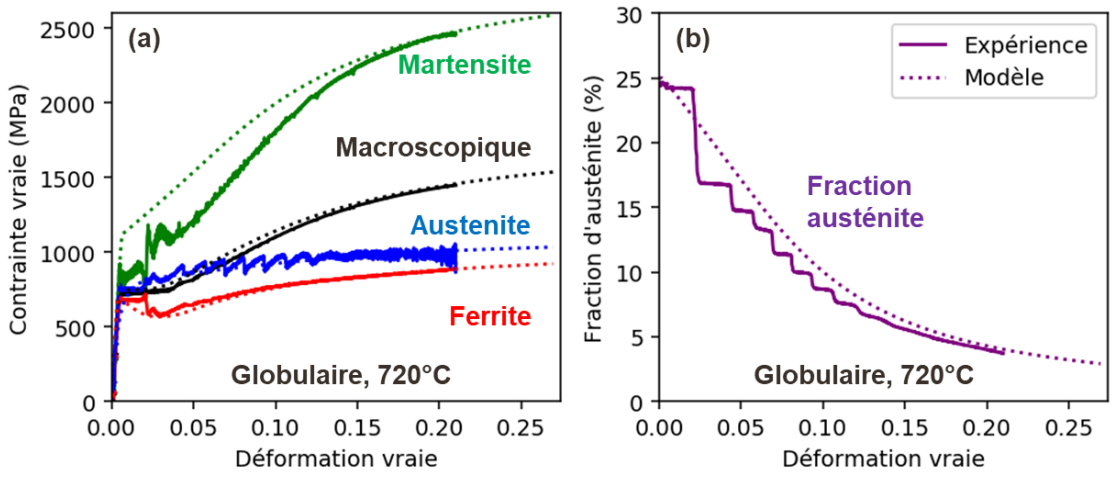

Figure 6: (a) Comparaison des contraintes d'écoulement mesurées expérimentalement (ligne continue) et calculées par le modèle (ligne en pointillé) dans la ferrite (rouge), l'austénite (bleu), la martensite (vert) et de la contrainte macroscopique (noir) de la microstructure globulaire recuite à 720°C. (b) Evolution de la fraction d'austénite dans la même expérience.

General scientific context

The current PhD project is part of a long-term partnership between the Institut Jean Lamour (IJL) and ArcelorMittal Maizières Research (AMMR) in the frame of the development of 3rd generation AHSS (Advanced High Strength Steels). The collaboration between AMMR and IJL in this field has been initiated by the PhD of Dr J.C. Hell, defended in 2011. His works, in collaboration with the LEM3 (Metz), was dedicated to quench and austempered (Q&A) steels, and has paved the way to the methodology used in the current work to investigate in situ the phase transformations of these new generations of steels by high energy X-Ray diffraction (HEXRD). The PhD of Dr J.C. Hell was followed by the CAPNANO project funded by the ANR (Agence National de la Recherche). Coordinated by IJL and involving AMMR, GPM (Rouen) and ICMB (Bordeaux), the project was dedicated to the phase transformation processes in quenching and partitioning (Q&P) steels. During the course of previous projects, the link between microstructures and mechanical properties of these new steels has not been investigated in detail. The goal of the current thesis is thus to bridge the latter gap, from an experimental and theoretical point of view, with an ambitious application to medium Mn steels. One important objective of the present PhD project is the development of a toolbox of physical-based models able to predict the mechanical properties of 3rd generation AHSS which will allow to design innovative and high-performance steels in the future.

Started in November 2019, the current PhD thesis is under a CIFRE convention of the ANRT (Association Nationale Recherche Technologie) and funded by AMMR Product Research centre, by the CNRS and the Université de Lorraine. It was preceded by a 6-month internship of the candidate, started in March 2019 and also funded by AMMR, with a goal to set the HEXRD methodology used in the current thesis. In July 2020, the European RFCS project Dynaustab started, with the aim of studying the austenite stability under dynamic loading condition in TRIP aided steels. The project is coordinated by ASBL-CRM (Belgium) and involves AMMR (France), CENIM (Spain), Gent University (Belgium), IJL (France) and TATA steel (Netherlands). The results obtained in the current PhD project fall in part within the frame of the Dynaustab project. This project also permits to hire a post-doctoral research fellow at IJL, Dr Í. Oyarzabal, dedicated to the microstructural analysis of medium Mn steels by TEM (no results of this latter work will be discussed in this manuscript). The present study also allowed to start a collaboration between IJL and LEM3 in the frame of Labex DAMAS, to better understand the physical origin of the mechanical instability in medium Mn steels.

This thesis has therefore benefited from the expertise of the IJL and AMMR teams on this new generation of steels and is in a scientific context rich in international interactions and with high expectations of industrial benefits.

Chapter I begins with a general introduction to the new 3rd generation advanced high strength (AHS) family of steels and their industrial expectations. It continues on a more dedicated bibliographic state of the art on medium Mn steels and their main characteristics. This chapter is important because it allows to explain the problematic of this thesis work, the scientific roadblocks to which it tackles and the proposed methodology. Chapter II is dedicated to the investigations of the formation of the microstructures of the studied model steels and, Chapter III to the experimental characterization of their mechanical behaviour. The last Chapter IV finally present a mean-field micromechanical model exploring the link between the microstructure and the mechanical properties of these steels.

Chapter I

I. Literature Review

1. General overview

Third generation advanced high-strength steels (AHSS) are a family of new cold-rolled and annealed steels which present very high balance between strength and ductility for light-duty vehicle production. They are in consequence the subject of intense studies by major steelmakers. Under this name, several metallurgical concepts can be found, like duplex medium manganese steels [19]–[21], carbide-free bainitic (CFB) steels [22]–[24], and quenching and partitioning (Q&P) steels [25]–[27].

The development of 3rd generation AHSS aims to substitute the 1st generation AHSS, like dual-phase (DP) steels and conventional Transformation Induced Plasticity (TRIP) aided steels [28]. The comparison between the mechanical properties of both families is shown in Figure 7. 3rd generation AHSS have the same formability as 1st generation AHSS so they can be cold stamped in a similar way to produce vehicle parts. However, 3rd generation AHSS have superior strength than 1st generation AHSS, and thus they can be used to lighten structures, especially in automotive industries. According to ArcelorMittal S-in motion project [29], the potential lightening is between 15% and 30%. Contrary to 2nd generation AHSS (austenitic Twinning Induced Plasticity (TWIP) steels), the production of the 3rd generation steels do not require technological breakthrough in the industrial manufacturing process. Thus, despite their less good ductility, 3rd generation AHSS are more appealing for automotive industry than 2nd generation AHSS and could serve to reduce car consumption in the future and their environmental fingerprint.

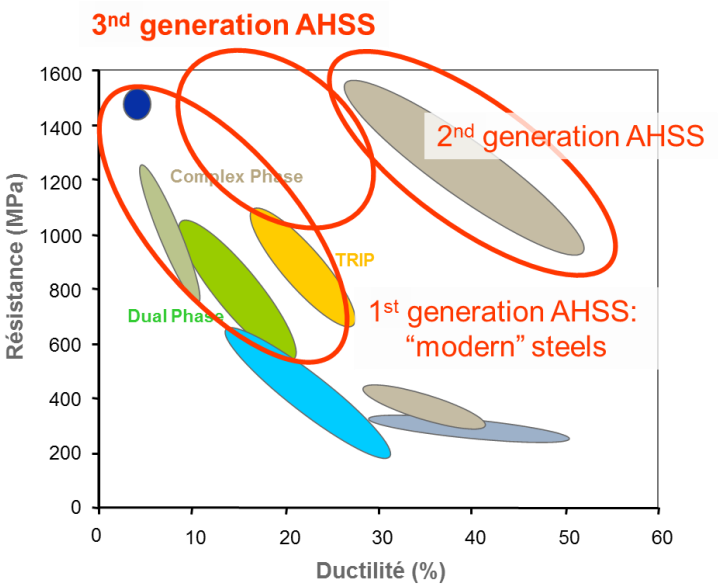

Figure 7: Comparison of the strength and ductility of different generations of AHSS [28]. The domain for 3rd generation AHSS is still a target as few products have really been put into production so far.

The very good balance between ductility and strength of those new AHSS steels is obtained thanks to complex and entangled microstructures. Despite having different chemical compositions and different thermal processing routes, the microstructures of all those steels are relatively similar, consisting of a "ferritic" matrix and a large quantity of retained austenite. The matrix can be ferrite (like in medium Mn steels), bainite (like in CFB steels) or martensite (like in Q&P steels or medium Mn). In 3rd generation AHSS, retained austenite is metastable and leads to an additional work-hardening called TRIP effect.

The thermal treatments to obtain CFB and Q&P steels are respectively represented in Figure 8 (a) and (b) [30], [31]. Both thermal treatments start similarly, with the full austenitization of the steel. For CFB steels [30], the austenitization soaking is followed by an isothermal holding at a temperature BT between B_S and M_S, which are respectively the bainite and martensite start temperatures. CFB steels are chemically designed to prevent the formation of carbide during the bainitic holding (usually, by the addition of Si and Al). Thus, concurrently to bainitic transformation, carbon partition occurs between austenite γ_1 and bainite B_1, which stabilizes austenite. After the final quench, a significant amount of austenite is retained despite the formation of fresh martensite M_2 during the final cooling. The final microstructure is very acicular.

On the contrary, in Q&P steels [31], the initial quenching is stopped at a temperature T_Q below M_S to obtain a mixture of primary martensite α_p and of austenite γ. Then, the steel is reheated at a temperature T_p, followed by an isothermal holding during which partitioning occurs between the primary martensite α_p and austenite γ. The holding is followed by a final quenching to room temperature during which secondary martensite α_s forms. At the end, Q&P microstructure consists of annealed martensite α_p, fresh martensite α_s and a significant amount of retained austenite γ. The final microstructure is also very acicular.

It must be emphasized that the name is medium Mn comes from the nominal chemistry of the steel (C between 0.05% and 0.5%, Mn between 3% and 12% [3]) without any consideration about the process. While most medium Mn steels are produced through intercritical annealing and called duplex steels (see after), medium Mn Q&P steels remain common in the literature. It is also possible to find some medium Mn CFB in the literature, as medium Mn compositions are suitable for both precited thermal treatments.

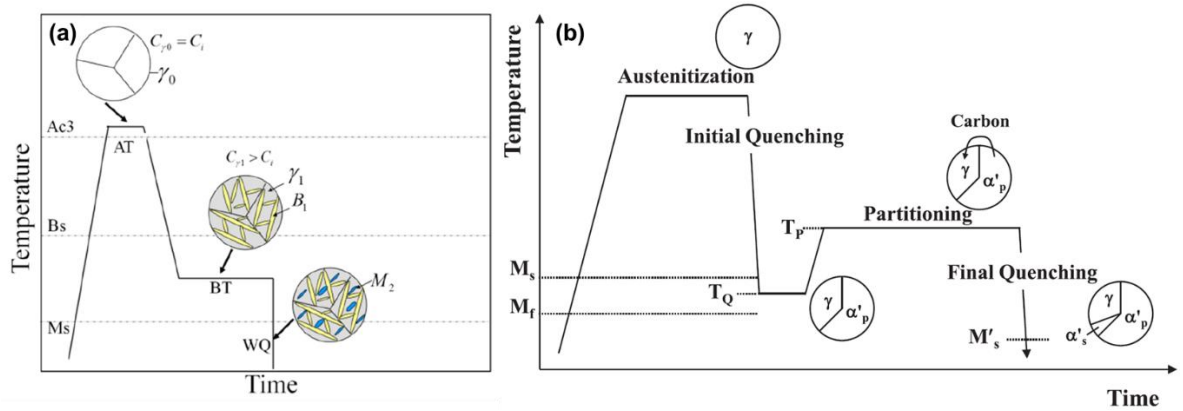

Figure 8: Typical thermal treatments to obtain (a) CFB steels [30] and (b) Q&P steels [31]. For both thermal treatments, the evolution of phases inside the microstructure is indicated (γ = austenite, B = bainite, M = α' = martensite).

Among all these 3rd generation AHSS, the present PhD thesis focuses on the understanding of medium Mn steels produced through intercritical annealing (IA) of either cold-rolled ferrite/cementite microstructures or as-quenched martensitic microstructures.

When the initial microstructure prior to IA is cold-rolled, the austenite forms according to nucleation-growth mechanisms during annealing, and the resulting microstructure consists of globular ultrafine grains (UFG) of ferrite and austenite. When the microstructure prior to IA is martensitic, the austenite forms between martensite laths according to a so-called "austenite reverted transformation" (ART), inheriting the martensite acicular morphology. The resulting microstructure will be denoted fibrous ART steels in the PhD manuscript, and consists of fibrous "ferritic" and austenitic sub-micrometric grains. In ART steels, the "ferritic" matrix is actually recovered martensite, but will still be referred as ferrite as in the literature because it has similar mechanical and thermodynamical properties. These two mechanisms of formation of medium Mn duplex microstructures will of course be detailed, discussed and compared in the following. Contrary to CFB and Q&P steels, the microstructure is mainly formed during the soaking stage of the IA and the stabilization of austenite is achieved by both carbon and substitutional elements (mainly manganese) partition between the ferritic matrix and austenite.

The globular UFG and fibrous ART medium Mn steels thus belong to 3rd generation AHSS thanks to their very fine matrix, giving the steels its high strength and toughness, while a high amount of retained austenite grants them with a high formability thanks to an efficient TRIP (Transformed Induced Plasticity) effect.

TRIP effect is a mechanism of dynamic work-hardening induced by the martensitic transformation of retained austenite during a mechanical loading. The progressive transformation of relatively soft austenite into martensite with a high yield strength leads to a quick increase in the macroscopic work-hardening rate and thus delays the apparition of necking [32], [33]. In this manner, by the increase of uniform elongation and by the transformation plasticity, mechanically induced martensitic transformation contributes to the increase of the formability of those alloys (improvement of the Forming Limit Diagram for cold-stamping operations). As it should be highlighted, the martensitic transformation is a displacive transformation. Therefore, it contributes also to the macroscopic plastic strain during a mechanical loading. However, this softening effect of the transformation is generally small compared to the hardening effect of the transformation itself.

In steels, mainly two kinds of martensitic transformation are observed, namely the martensite α' with a body-centred cubic (BCC) or slightly tetragonal (BCT) structure and the martensite ε with a hexagonal close packed (HCP) structure. The latter is often observed as an intermediate product in the transformation $\gamma \longrightarrow \varepsilon \longrightarrow \alpha'$ and is often detected in the austenitic alloys stabilized by nickel or manganese as FeNiCr or FeMnC steels [34], [35]. In the case of 3rd generation AHSS with a Mn content inferior to 7%, mainly stabilized by carbon and manganese partitioning, only the martensitic transformation α' is reported [36], [37]. Thus, in this bibliographic chapter, we will exclude the study of the TRIP effect in 100% austenitic steels, especially the ones in which mainly ε martensitic transformation occurs.

The TRIP effect and the mechanically induced martensitic transformation depend on the considered mechanical loading (strain rate and stress state, including stress triaxiality state), on the thermomechanical stability of retained austenite (chemical composition, internal stresses, grain size,

morphology) and on its environment (strength of the matrix, microtexture). The main issue is that those mechanisms are often entangled, and it is complex to experimentally decorrelate their respective contribution. This chapter aims thus to highlight the underlying mechanisms that explain the stabilization of austenite and show how to predict the associated strain-induced transformation kinetics. The prediction of the mechanical behaviour of a given TRIP-aided steel is also of the first importance for steelmakers. In this chapter, micromechanical model that predicts the macroscopic behaviours of AHSS steels including the TRIP effect will also be discussed.

This bibliographic chapter is divided into five other major parts. First, the phase transformation mechanisms of medium Mn duplex steels will be presented. The morphogenesis of both globular UFG and fibrous ART microstructures will be detailed, giving insight on the microstructural, chemical, morphological and crystallographic features of the duplex steels studied in the thesis. Secondly, the strain-induced martensitic transformation (SIMT) is detailed from a crystallographic and thermodynamical point of view. The mechanisms influencing the TRIP effect efficiency are discussed. The phenomenology of the thermal, the stress-aided and the strain-induced martensitic transformations are reminded. The third part of this chapter focuses on the modelling of the SIMT. Several models have been developed in the literature, among which Olson-Cohen pioneering model. The fourth part of this chapter is dedicated to the macroscopic mechanical behaviour of medium Mn steels, on the basis of the respective microscopic mechanical behaviours of ferrite, austenite and martensite. The advantages and drawbacks of the different possible homogenization methods are discussed to explain our own modelling strategy developed in Chapter IV.

Finally, medium Mn steels, especially globular ones, endure undermining presence of mechanical instabilities, such as Lüders banding and Portevin Le-Chatelier effect. Those phenomena are discussed at the light of dedicated literature review in the specific case of medium Mn steels in the fifth and last section of this chapter

2. Phase transformation mechanisms and morphogenesis of microstructures

The name of “medium manganese” steels comes from their significant nominal composition in manganese, between 3% and 12%, which still remains below the Mn level found in fully austenitic “high manganese” twinning-induced plasticity (TWIP) steels [3].

With such Mn composition, a reasonable amount of carbon (limited for weldability issue) and a suitable heat treatment schedule, it is possible to design duplex microstructures, with a significant amount of metastable retained austenite at room temperature. The most common thermal treatments consist in an intercritical annealing to obtain a duplex ferrite-austenite with sub-micron grains.

For the present PhD thesis, the main focus is set on duplex microstructures produced through such intercritical annealing of a cold-rolled ferrite-cementite steel or an as-quenched martensitic steel. In the following, both thermal treatments will be detailed, and the metallurgical mechanisms permitting to explain the formation of final microstructures will be highlighted. The role of other alloying elements such as Aluminium, Chromium or silicon will be evoked.

It should be mentioned that two other processes have also been considered in the literature. It is possible to apply a quenching and partitioning treatment to stabilize austenite in such steels [31], [38], [39] but with a limited help of manganese diffusion. By adding significant amount of aluminium (6% to 8%) which permits to reduce the density, it is also possible to obtain bimodal microstructures by hot-rolling with fine-grained duplex ferrite-austenite bands alternating with large δ ferritic bands [40], [41]. These concepts will not be discussed further in this chapter.

A. Design of globular duplex microstructures by intercritical annealing

a) Basic mechanisms during intercritical annealing

The ultra-fine grained (UFG) microstructures with globular morphology are produced through intercritical annealing of a cold-rolled (at least highly deformed) ferritic steel containing cementite. Intercritical annealing is defined as an annealing between A_{e1} and A_{e3} [4], [5]. For a given composition, the equilibrium transformation temperature A_{e1} is defined as the temperature above which austenite starts to form at equilibrium, while A_{e3} is the lowest temperature at which the single-phase austenitic structure is thermodynamically stable. During the intercritical annealing between A_{e1} and A_{e3}, the deformed ferritic matrix will first recrystallize during heating and the austenite will nucleates mainly on carbides (cementite) and grow depending on the intercritical annealing temperature T_{IA} [42]–[45]. At the end of the intercritical annealing, a duplex austenite-ferrite microstructure is formed, with equiaxed recrystallized grains having sub-micron size [40]. The basic thermal treatments to obtain such microstructure are presented in Figure 9, alongside with a scanning electron microscope (SEM) micrograph after etching of a typical UFG microstructure obtained at 700°C [4], [5]. In the micrograph, ferrite appears in dark contrast and austenite in light contrast. The grains of both phases are morphologically globular, meaning they are closer to an equiaxed morphology than to an acicular shape. The thermal treatment to produce globular medium Mn steels, sketched in Figure 9 (a), consists in a heating step, followed by an isothermal holding and an air-cooling/quenching (a rapid cooling) to room temperature. During intercritical annealing, cementite first and then ferrite transform into austenite. The annealing temperature is always chosen for the steel to be in the intercritical (biphasic) region. Therefore, a significant amount of ferrite is still present during the isothermal holding. The austenite stabilizers elements (carbon and manganese) will partition during the holding, from the ferritic matrix to the forming austenite. Ferrite stabilizer elements such as aluminium, silicon or chromium will on the contrary diffuse into the ferrite [46].

After the air-cooling, a significant amount of austenite is retained at room temperature, mainly stabilized by the chemical (C and Mn) enrichment [19], [20], [47], [48] and by the small grain size [9], [49], [50]. As chemical partitioning is a fundamental aspect of medium Mn steels, the gradients of composition existing in globular microstructures are discussed extensively in the subsequent section I.2.C, alongside the one of ART fibrous microstructures.

The goal in such steel is to design an austenite having a martensite start temperature M_S, i.e. a temperature below which athermal austenite to martensite transformation occurs during quenching, as close as possible to the room temperature (RT). If M_S is far lower than RT, austenite will be too stable and mechanically induced martensitic transformation will be impossible. If M_S is far higher than RT, all

austenite will transform into fresh martensite during the final cooling. The resulting microstructure will consist in ferrite and martensite (i.e. a dual-phase steel), which is not the purpose with this process. In general, medium Mn steels consist only of ferrite and austenite, but it is also common that a small fraction of austenite is transformed into fresh martensite during the final cooling. In this last case, it is more appropriate to speak about martensite austenite (MA) islands rather than austenite grains when describing the microstructure, even though it is difficult to distinguish both kinds of constituents by SEM observations.

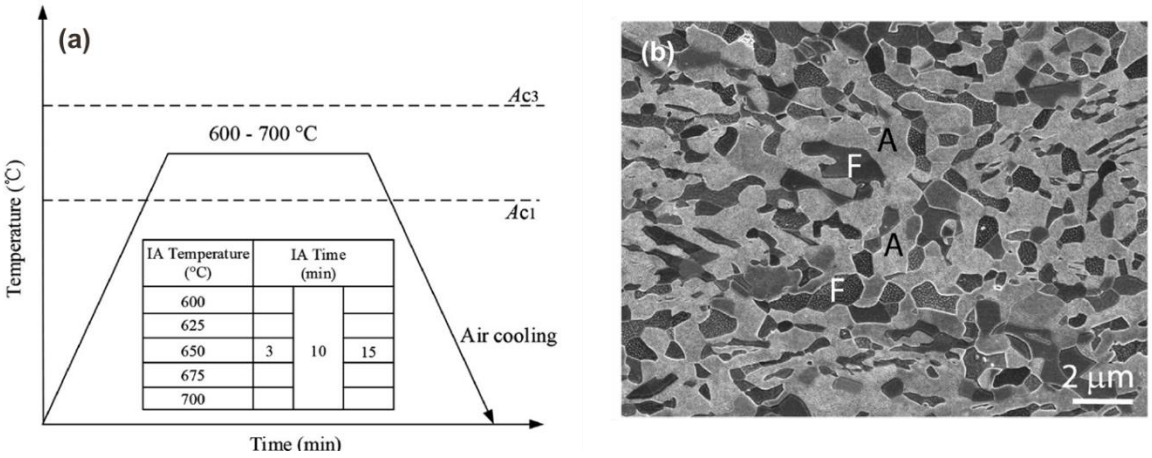

Figure 9: (a) Typical intercritical annealing to produce UFG medium Mn steels and (b) globular dual phase UFG microstructure observed by SEM resulting from an intercritical annealing at 700°C of a cold rolled Fe/0.6C/6.6Mn/3Al steel. A stands for Austenite and F for Ferrite, taken from [4], [5].

b) Effect of alloying composition on phase diagram

As previously stated, intercritical annealing is defined as an annealing between A_{e1} and A_{e3}. The pseudo-binary diagrams of medium Mn steels containing 1.7% to 4.7% Mn (wt%) are presented in Figure 10 [51]. The results presented in this subsection are also valid for fibrous ART microstructures, (discussed later in section I.2.B). The temperature A_{e1} is the temperature of the boundary between the three-phase α-γ-θ and two-phase α-θ domains (black line). The temperature A_{e3} is the temperature of the boundary between the two-phase α-γ or γ-θ and monophasic γ domains (indicated by the highest curve between red and blue line). The specificity of medium Mn steels is the addition of a significant amount of manganese, which is a gammagene element. Compared to classical binary Fe-C binary diagram, Mn makes the three-phase α-γ-θ domain appear. Increasing Mn shifts the austenite domain to lower temperature. The two-phase α-γ domain also shifts to lower temperature with increasing Mn content. Finally, the slope of the solvus α-γ/γ decreases, meaning that a given uncertainty on temperature will lead to a greater uncertainty on austenite phase fraction. Other austenite stabilizer elements that can be found in medium Mn steels are nickel, cobalt and copper [46].

In many medium Mn steels, aluminium and silicon are also added, as these elements are helpful to suppress the nucleation of cementite [6], [52]. The effects of the two elements are illustrated in the pseudo-binary diagrams reproduced in Figure 11. Increasing Si content expands the austenite and two-phase α-γ domains to upper temperatures. Si addition does not enlarge nor reduce the α-γ-θ domain. Adding Al in the steel expands the austenite and α-γ domains to upper temperatures. The

slope of the solvus α+γ/γ increases significantly. Aluminium addition also reduces the α-γ-θ domain. Silicon is also known to slow down kinetics of formation of cementite, making the amount of carbon available for austenite higher in the steel [52]. Other ferrite stabilizer elements such as chromium, molybdenum and vanadium can be found in small quantities in medium Mn steels [46].

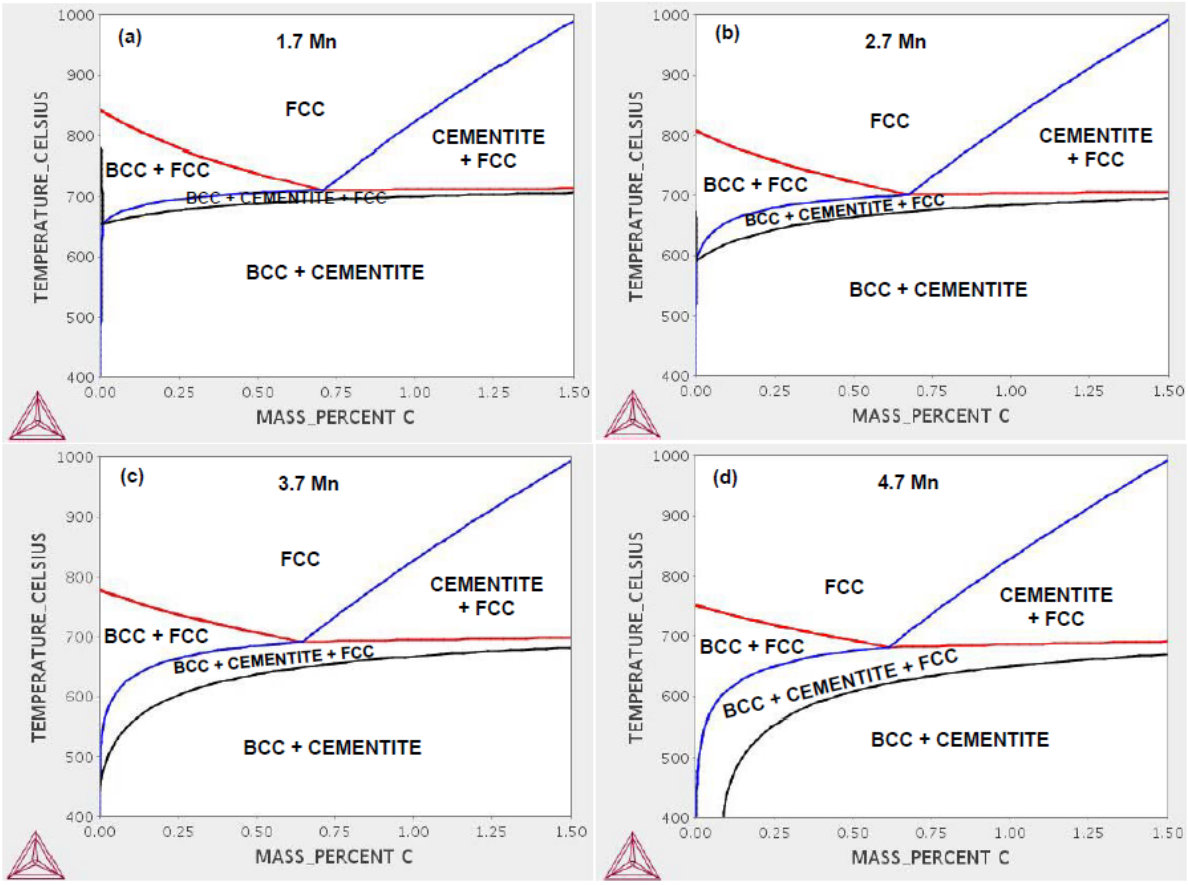

Figure 10: Pseudo-binary diagrams calculated with Thermo-Calc software for ternary steels with four Mn contents: (a) 1.7%; (b) 2.7%; (c) 3.7%; (d) 4.7% respectively. The A_{e1} temperature is indicated by the black line. The A_{e3} temperature is indicated by the red curve in the hypo-eutectoid range [51].

These pseudo-binary diagrams, while giving some insight on the effect of Mn, Si and Al elements on the medium Mn metallurgy, have some limitations. They are only valid for equilibrium conditions. During intercritical annealing, heating should be slow enough and isothermal holding long enough to be close to equilibrium conditions. During IA, carbon is not the only element that is partitioned. Mn, Si and Al are also migrating between austenite and ferrite. Hence, a quinary diagram should be rather used for Fe-C-Mn-Si-Al steel, if possible.

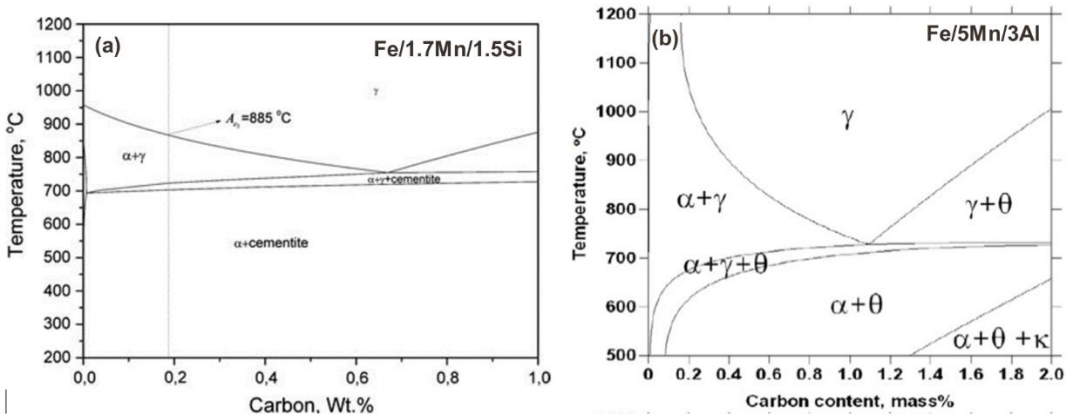

Figure 11: Pseudo-binary diagrams calculated with Thermo-Calc software for the steels: (a) Fe/1.7Mn/1.5Si [53]; (b) Fe/5Mn/3Al [54].

c) Role of cementite

In the production of UFG globular microstructures, cementite plays a fundamental role in the nucleation of austenite [55], [56] and thus on the final morphology of the microstructure. Indeed, in the cold-rolled ferritic state, before annealing, cementite serves as carbon "reservoir". SEM micrographs of various UFG medium Mn steels are shown in Figure 12 taken from [57]. These micrographs are interesting as they show intermediate stages before reaching the fully duplex microstructures, with remaining carbides. For the Fe/0.2C/5Mn steel, at T_i = 660°C, many cementite precipitates remain in the microstructure, while they are totally dissolved at T_i = 820°C. In the Fe/0.4C/2Mn steel at T_i = 720°C, the carbides are still present.

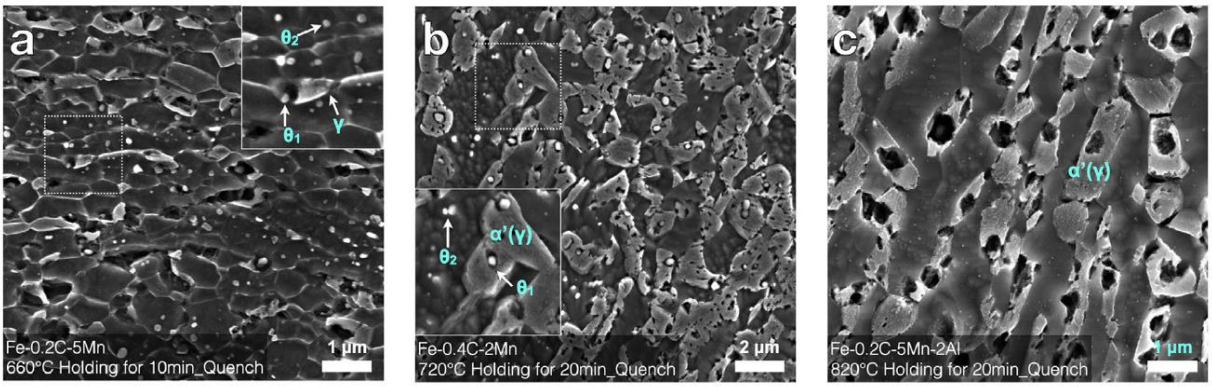

Figure 12: SEM micrographs of globular UFG microstructures obtained after intercritical annealing and quench (dilatometer study). θ corresponds to cementite (clearest particles), α'(γ) corresponds to martensite/austenite island (clear grains) and the darker phase corresponds to ferritic matrix. The nominal contents of the studied steels and intercritical annealing temperatures are given at the bottom of each image [57].

There are two kinds of cementite in the final microstructure: θ_1 cementite which is in contact with austenite islands, and θ_2 which is located inside ferritic matrix. They both participate differently to austenite nucleation and growth. From a chemical and kinematical standpoint, multiple stages succeed during the formation of austenite [55], [57], [58]. First, the rapid growth of austenite is controlled by carbon diffusion. Then, the growth is more gradual and controlled by Mn diffusion in

ferrite. Finally, a slow equilibration of Mn occurs controlled by its diffusion in austenite. In the first stage, the interface is under a negligible partitioning local equilibrium (NPLE), while there is a partitioning local equilibrium (PLE) during the second stage. The cementite enrichment in manganese may modify those steps, even suppressing the first one. Moreover, two mechanisms of nucleation coexist, as schemed in Figure 13 [57]. In the first θ_1-γ-α mechanism, austenite nucleates at the boundary between cementite and austenite. In the second γ-α-θ_2 mechanism, cementite dissolves into ferrite and carbon diffuses inside the ferritic matrix to contribute to the austenite growth elsewhere. The proportion $\phi = \theta_1/(\theta_1+\theta_2)$ of θ_1-type cementite initially presents in the microstructure can lead to significant difference in austenite formation kinetics, as implied by some simulation results of the literature shown in Figure 13 (c). The austenite phase fraction can exceed equilibrium value if enough θ_2 is present in the microstructure. Wu et al. [57] demonstrate that ϕ is a function of the intercritical annealing temperature. It is also expected that the chemistry distribution of austenite will be a function of ϕ. For instance, authors show that the θ_1 surrounding austenite is richer in alloying elements than farther austenite.

The preceding results are specific to medium Mn metallurgy and are not necessarily true for general α+θ⟶γ transformations. Finally, no specific crystalline orientation relationship between austenite and ferrite is expected from those diffusive mechanisms.

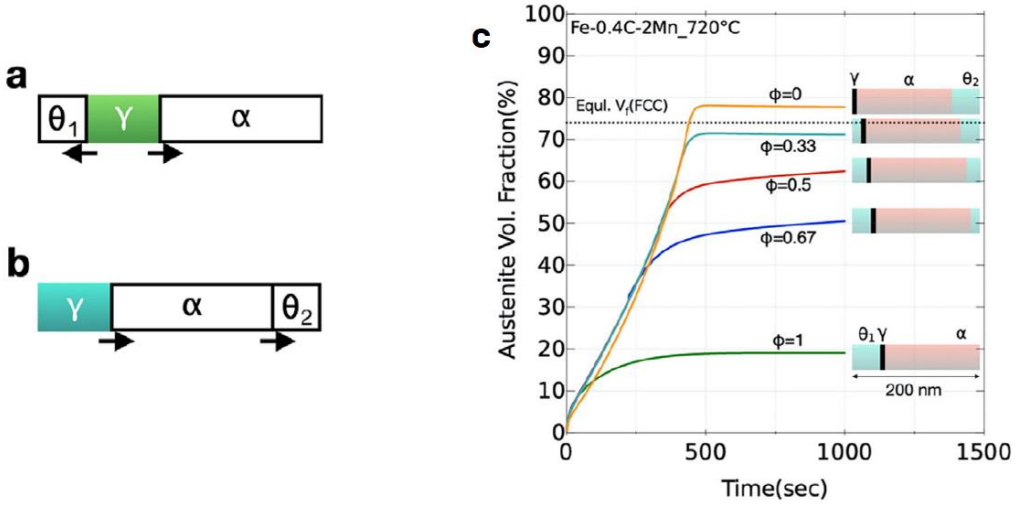

Figure 13: (a) - (b) Schematic representations of the two encountered nucleation mechanisms for austenite in cold-rolled ferritic steels during intercritical annealing. The arrows indicate the directions of interface displacements. (c) Effect of the proportion ϕ of θ_1 cementite initially presents in the microstructure on the simulation of austenite formation kinetics [57].

B. Design of fibrous duplex steels by austenite reverted transformation (ART)

a) Nucleation/growth mechanisms during IA

Another possible way to produce a duplex ferrite/austenite microstructure with a medium Mn steel is the so-called ART processing. Pioneers of this specific thermal treatment are Thomas and Koo in 1976 [6], [47] but their work has only recently been rediscovered and exploited.. ART steels are

produced through the intercritical annealing (IA) of a fully martensitic steel. To obtain this martensitic steel, a cold-rolled ferritic steel can be fully austenitized and then quenched to room temperature. The thermal treatment typically used to obtain fibrous ART microstructures starting from cold-rolled ferritic steel is sketched in Figure 14 (a) [59]. It consists of an austenitization in the monophasic γ domain, followed by a first quench, an IA and a final air cooling/quench (This is why this cycle is often referred to as 2-step annealing). The austenite formed during the first austenitization step is usually referred as primary austenite or prior austenite grain microstructure. ART stands for austenite reverted transformation, which is a specific mechanism of austenite formation from a martensitic microstructure [51], [60]. Austenite will "nucleate" at martensitic laths boundaries, and inherits the fibrous morphology from its mother martensite [59]. The term "nucleate" will be clarified later. During the intercritical annealing, remaining martensite will recover (but will not recrystallize) and will be depleted from carbon and manganese, in favour of austenite according to the phase diagrams discussed above. At room temperature, recovered martensite mechanically behaves like ferrite, and thus it is called ferrite in the following. This abusive name is the norm in literature and it is for this reason that we will also follow it. The resulting microstructure is a duplex austenite/ferrite steel, with sub-micron sized grains, as shown in Figure 14 (b) [59]. In the SEM micrography of the fibrous ART microstructure after 4% Nital etching, ferrite appears in dark contrast and austenite in light contrast. Like in the globular case, part of austenite can transform into fresh martensite during the final cooling. This latter martensite is difficult to distinguish by SEM from austenite grains since both phases are intertwined and appear in light contrast.

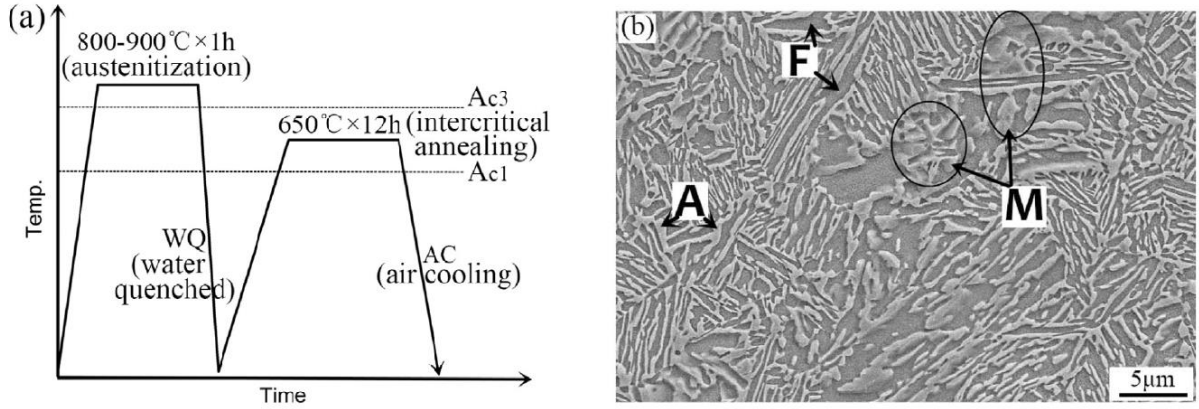

Figure 14: (a) Typical ART annealing schedule. (b) SEM micrograph of an ART-annealed steel at 650°C for 12h after austenitization at 850°C for 1h. Ferrite (F) appears as the darkest phase, while austenite (A) and fresh martensite (M) appear in lighter contrast [59].

During ART annealing of a martensitic steel, multiple nucleation mechanisms can lead to austenite formation, as summarized in Figure 16. Austenite can either forms at martensite lath boundary, at primary austenite former grain boundary, or around cementite particles. Even though no cementite is present in as-quenched martensitic microstructure prior to IA, it can precipitate during the heating stage of IA. The different mechanisms of formation lead to different austenite morphologies: acicular and globular.

Acicular austenite γ_A can nucleate at martensite packet, block or lath boundaries. The term nucleation in that case could be inadequate as austenite could in fact grow from the residual films of retained austenite located on these boundaries. Thomas has demonstrated that even in low alloyed steels, small fraction of austenite is always retained after quenching from fully-austenitic state [6]. In

Figure 15, retained austenite (white contrast) in Fe/0.3C/4Cr and Fe/0.3C/4Cr/2Mn as-quenched martensitic steels is detected between martensite laths (dark contrast) using transmission electron microscopy (TEM) in dark field mode. Thomas emphasizes that this low amount of austenite (<0.5%) is difficult to reveal even by TEM, and impossible to detect with X-ray diffraction or magnetic measurements techniques. Author proves that the amount of retained austenite increases with Mn and Ni contents, as highlighted with the comparison between Figure 15 (a) (no Mn) and Figure 15 (b) (2Mn). The growth of these residual films of retained austenite could explain straightforwardly why specific orientation relationship (OR) are observed between acicular austenite and surrounding ferrite laths.

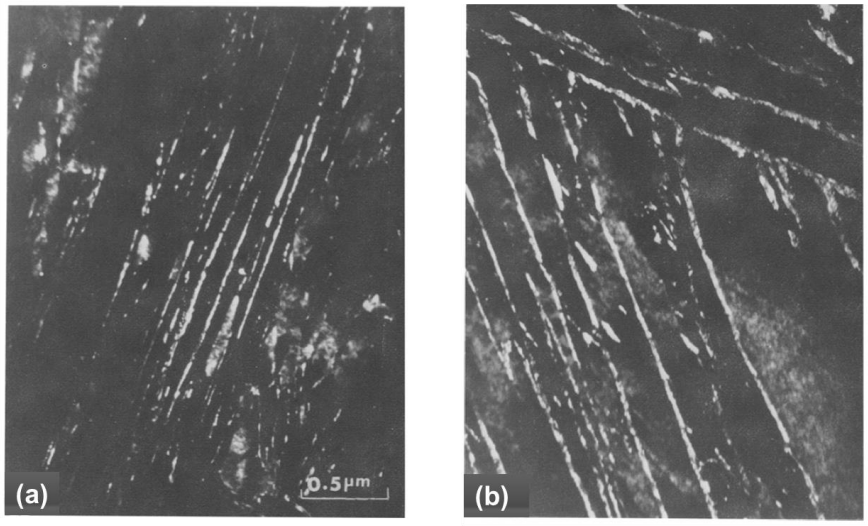

Figure 15: Dark field TEM observations of retained austenite (white phase) in two as-quenched martensitic steels. In (a), a Fe/0.3C/4Cr steel. In (b), a Fe/0.3C/4Cr/2Mn steel. Austenite appears in white contrast, while martensite appears in dark contrast [6].

This mechanism is still controversial in the literature and alternative mechanisms have been proposed for the formation mechanism of acicular austenite γ_A [61], [62]. Yang et al. [61] note that for acicular austenite, transformation occurs in two stages. In the first step (300°C to 500°C), the martensite to austenite transformation is purely displacive, while it becomes reconstructive above 500°C. They develop a thermodynamical model inspired by austenite to martensite transformation model, and calculate an austenite start temperature A_s, similar to the M_s temperature used for austenite quenching. Luo et al. [62] developed an austenite formation model rather considering a bainite-like transformation. Carbon is rapidly partitioned and the overall transformation kinetics is determined by the diffusion of Mn in γ and α.

Globular austenite γ_G rather nucleates at prior austenite (austenite formed during the first austenitization annealing) grain boundary, but also at martensite packet and block boundaries. It is rather well admitted that cementite forms during heating on these boundaries and can serve as nucleation sites for austenite [7], [62]–[64]. Adding Cr or Mn facilitates the nucleation and growth of cementite from retained austenite films by increasing the carbon diffusivity [6]. On the contrary, adding Si, Al or Ni postpone cementite appearance to higher temperature. It must be emphasized that usually, most austenite in ART medium Mn steel presents acicular morphology [7], [62]–[64].

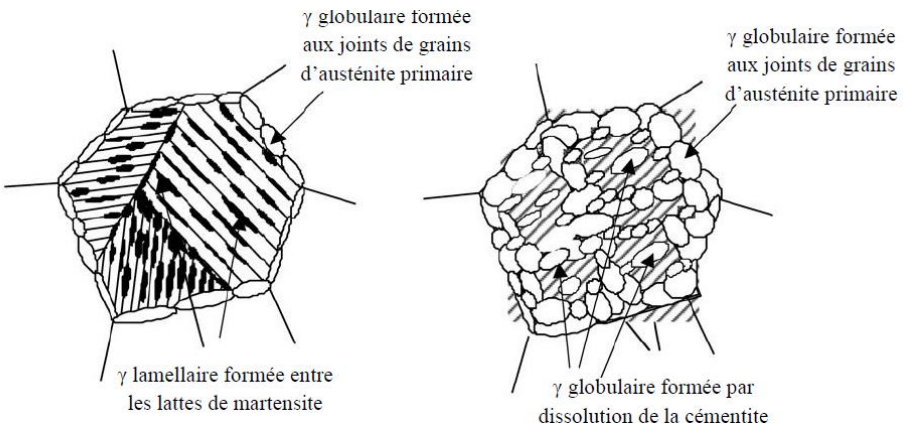

Figure 16: Schematic representation of the mechanisms and possible nucleation sites for the two morphologies of austenite in fibrous ART steels [40].

From the thermokinetics point of view, Zhang et al. [7] have quantitatively analysed and modelled the mechanism of austenite formation in a Fe/0.3C/2.02Mn/1.46Si steel. An optical micrograph and a SEM image of their steel after ART annealing is shown in Figure 17. In both images, globular austenite γ_G is clearly observable at prior austenite grain boundary (PAGB), while acicular austenite γ_A is intertwined with the ferritic matrix. DICTRA simulations are carried out at different intercritical annealing temperatures. The measured evolution of both populations of austenite, for an annealing at 775°C, is reported in Figure 17 (c) and compared with the fraction obtained through ortho-equilibrium and NPLE (non-partitioning local equilibrium) calculations. For longer annealing time, measured phase fraction exceeds the NPLE predictions and comes close to ortho-equilibrium. Zhang et al. [65] also analysed the effect of cementite precipitates θ in the matrix. They conclude that the partitioning of Mn and Si between θ and the matrix will retard reversion kinetics and leads to a transition from partitionless to partitioning growth.

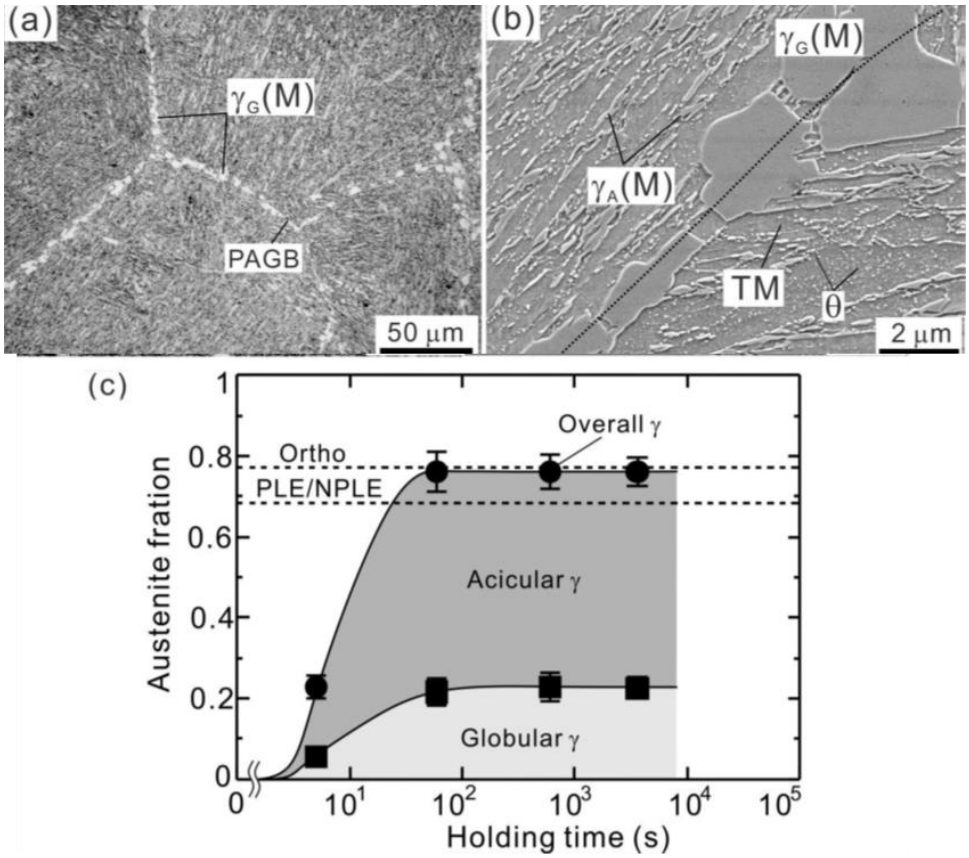

Figure 17: (a) Optical micrograph of an ART steel presenting both acicular austenite γ_A(M) and globular austenite γ_G(M) at prior austenite grain boundaries (PAGB). (b) SEM micrograph of the same microstructure. Tempered martensite (TM) can be distinguished from acicular austenite γ_A(M). Some cementite θ can be observed. (c) Evolution of acicular and globular austenite γ fractions as a function of time. Figures are extracted from [65].

b) Orientation relationship between ferritic matrix and austenite

Contrary to UFG globular steels, in ART fibrous steels, austenite and adjacent ferrite are not randomly oriented because of the specific "nucleation" mechanisms discussed above. Between them, a Kurdjumov-Sachs (K-S) orientation relationship (OR) is observed. New austenite grains will have the same crystallographic orientation as the prior austenite. This inheritance effect is referred as the austenite memory phenomenon [61]. This austenite memory relies on the presence of austenite films, and possibly the absence of residual stresses. Indeed, some authors have observed that transforming under external stress leads to a deviation from the strict austenite memory effect [63]. Zhang et al. [7] have detailed the specific OR between austenite and annealed martensite as a function of austenite morphology. This dependency on morphology is logical as γ_G and γ_A do not nucleate following the same mechanism. Their EBSD (electron back-scattered diffraction) map at a PAGB in a 0.3C/2.02Mn/1.46Si ART steel is reproduced in Figure 18, alongside a diagram detailing the crystallographic OR of acicular and globular austenite laths with respect to the neighbouring annealed martensite laths, adjacent blocks and adjacent packets. Most of acicular austenite has the same orientation as the prior austenite, but few of them have a twin-related orientation with it. Globular austenite nucleating at a PAGB or a packet boundary holds a near K-S OR with one of the adjacent blocks and grows into the other one. Intra-granular globular γ_G nucleates more when more cementite is present in the microstructure.

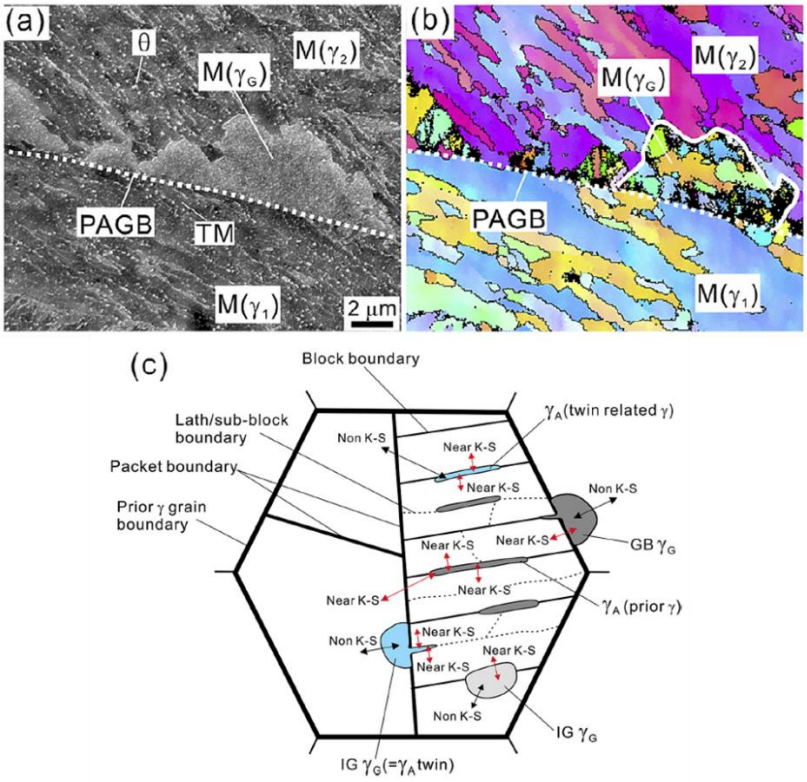

Figure 18: (a) SEM micrograph and (b) corresponding ESBD orientation map of an ART steel with a tempered martensitic matrix containing acicular austenite M(γ_1) and globular austenite M(γ_G) (c) Schematic representation of the multiple encountered nucleation mechanisms for austenite in martensitic steels during ART intercritical annealing. Orientation relationships between austenite and martensitic matrix are detailed depending on the nucleation mode (K-S = Kurdjumov-Sachs). Figures are extracted from [7].

While K-S OR is the most often reported orientation relationship between ferrite and austenite in medium Mn ART steels, some other OR have also been reported, like the Nishiyama-Wassermann OR [66], which could be a consequence of different chemical content and processing conditions.

The microtextural aspects of martensite, alongside its hierarchical organisation in lath, packets and blocks, are further discussed in section I.3.A.b). The physical reason of the existence of OR between austenite and martensite is explained in section I.3.A.a). The next section is dedicated to the partitioning of alloying content between austenite and ferrite during intercritical annealing.

C. Phases' chemical composition in medium Mn steels (UFG and ART)

One last major aspect of microstructures that has not been discussed yet concerns the chemical composition of the phases resulting from the phase transformation processes described above. As explained, these microstructures, even if they are designed at high temperature, are far from the thermodynamic equilibrium and possibly present marked intraphase chemical gradients.

In medium Mn steels produced through IA, the stability of austenite at RT is notably allowed due to the chemical partitioning between retained austenite and the ferritic matrix and subsequent enrichment in Mn and C of retained austenite. This partitioning of Mn and C is usually also accompanied by a partition of others alloying elements, such as Al, Si, Cu, Mo or Ni. The profile of

composition of austenite grain at RT is complex, its shape depending on the nucleation mechanism (classical α+θ⟶γ vs ART), the temperature and time of intercritical annealing, the morphology of austenite and the alloying element of the steels. Knowing the expected composition profiles after a thermal treatment is thus crucial to tailor the mechanical behaviour of innovative TRIP steels.

The main methods used in the literature to measure local composition of the phases are atom probe tomography (APT), energy-dispersive spectroscopy (EDS) wavelength-dispersive spectroscopy (WDS) and electron energy loss spectroscopy (EELS). The technique present different spatial and elemental resolutions and are used post-mortem (assuming in general no diffusion during the final cooling). The best resolutions are obtained with APT and scanning transmission electron microscopy (STEM).

The expected carbon profiles in austenite as a function of its morphology are represented by Sugimoto et al. (reproduced in Figure 19) [67]. For blocky retained austenite, as found in conventional TRIP steels with polygonal ferritic matrix (TPF), it is expected that there is a spike in C concentration near austenite grain boundaries (GB). This is an inheritance of the transient diffusion profile of C appearing during the formation mechanism and fixed after fast cooling. For filmy retained austenite, as found in TRIP steels with bainitic ferritic matrix (TBF) or with annealed martensitic matrix (TAM, equivalent to previously denoted fibrous ART steels), the maximum C content inside austenite grain is found at its centre, while its boundaries are poorer than the surrounding ferrite. However, Sugimoto do not explain those profile difference with morphological consideration, but rather with size consideration. Indeed, in TPF steels, interparticle path tends to be larger than for TAM or TBF steels.

A summary of the different types of profiles measured in the recent literature for medium Mn steels is given in Table 1. For each reference, the presence or absence of concentration peaks of Mn and C near the γ/α interface is indicated, alongside with the morphology of the microstructure (fibrous ART vs globular UFG), the temperature and the time of the intercritical annealing. Concerning globular ferrite, the profile of carbon shows always a peak of concentration near austenite GB in the three reviewed papers [68]–[70], as represented in Figure 19 (a). Concerning fibrous ART microstructures, the two types of possible carbon profiles are found (with C peaks: [71], without: [65], [72], [73]). As shown in Table 1, this difference cannot be interpreted in terms of temperature or time of annealing, as the two parameters T_{IA} and t_{IA} overlap between the two sets of experiments. Under further scrutiny, it appears that the medium Mn steels studied in [71] contains lot of aluminium and silicon (Fe/0.2C/10Mn/3Al/3Si and Fe/0.3C/11.5Mn/5.8Al for the steels annealed at 850°C and 700°C respectively in [71]). On the contrary, the steels that show a profile without higher C content near GB (like in Figure 19 (b)) are low in Si (0 to 1.5%) and have no Al [65], [72], [73]. The different profiles in fibrous steels can thus be understood as Al and Si differ between microstructures, changing the diffusivity of C [6] and thus its diffusion length. This remains an assumption based on few results.

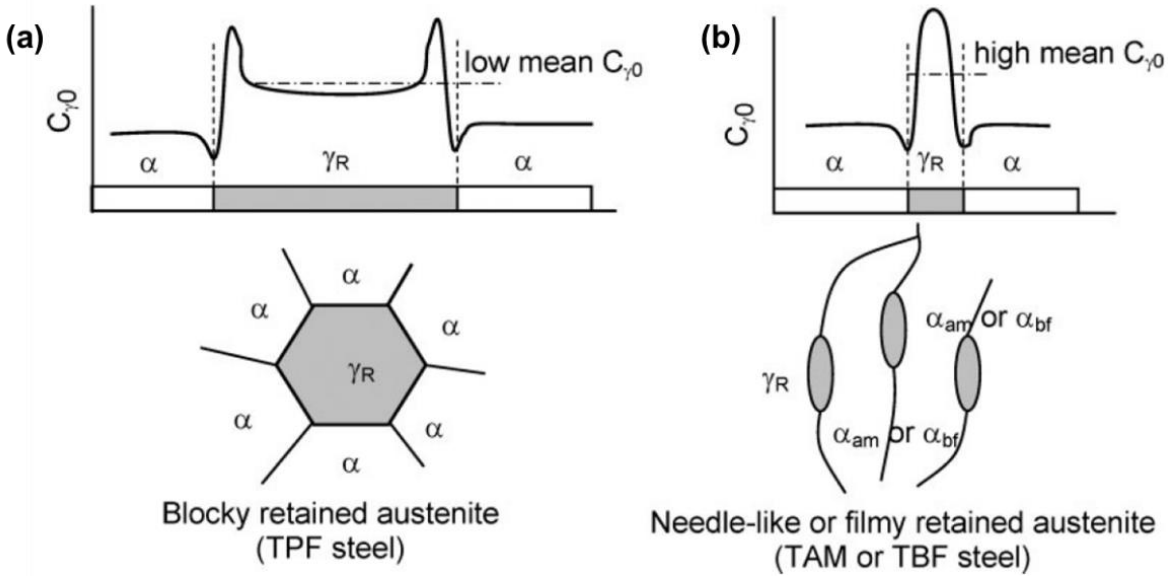

Figure 19: Illustration of the carbon concentration distribution expected in retained austenite of three kinds of TRIP aided steels. Carbon profile across retained austenite γ_R of TRIP steel with polygonal ferrite (TPF) is represented in (a). The one of TRIP steels with either annealed martensite (TAM) or bainitic ferrite (TBF) matrix is represented in (b) [67].

Microstructure morphology	Temperature of IA (°C)	Time of IA (min)	Composition of the steel	Interfacial enrichment in Mn/C	Ref.
Fibrous	700	120	Fe/0.15C/7.9Mn/0.89Si /0.13Al/0.21Mo/1.99Ni	Yes/Yes	[71]
Fibrous	850	5		Yes/Yes	[71]
Fibrous	600	30	Fe/0.15C/10Mn/2Al/(2Cu)	Yes/-	[66]
Fibrous	700	10	Fe/0.21C/4.53Mn	Yes/-	[74]
Fibrous	740/680	30/30	Fe/0.08C/2.4Mn/0.5Si/0.5Ni /0.42Mo	Yes/No	[72]
Fibrous	700/500	2/180	Fe/0.05C/7Mn/1.5Al/1.5Si /0.5Mo/1.5Cu/1.5Ni	Yes/-	[75]
Fibrous	700	2		No/-	[75]
Fibrous	600	30	Fe/0.15C/10Mn/2Cu	No/-	[66]
Fibrous	650	5	Fe/0.2C/4.72Mn/0.2Si/0.1Al	No/No	[73]
Fibrous	750	1	Fe/0.3C/2Mn/1.5Si	No/No	[65]
Globular	725	10	Fe/0.11C/4.9Mn/2Al	Yes/Yes	[68]
Globular	640	30	Fe/0.28C/6.7Mn/0.46Al	Yes/Yes	[69]
Globular	500	240	Fe/0.12C/0.3Si/7Mn	No/Yes	[70]

Table 1: Summary of the presence or absence higher level of carbon/manganese content at grain boundary (GB), between ferrite and austenite grains, as reported in the literature. For each reference, the temperature and time of intercritical annealing and the morphology of the steel is given. The composition of the steel is also given (in wt%). Systematically, Mn and C enriched austenite. When two temperatures and times are given, it means that two consecutive annealing were conducted.

The profile of C, Mn, Si across a γ/α interface is given in Figure 20 (a) for a fibrous ART Fe/0.3C/2Mn/1.5Si steel [65]. The steel was annealed at 750°C for 1 min. C and Mn partitioned in austenite, while Si partitioned in ferrite. As previously stated, the carbon profile inside austenite is homogeneous, with small variation which may be due to segregations. No accumulation of C is measured near the interface. The same goes for substitutional elements (Mn and Si). In ferrite, value of Mn and Si are close to orthoequilibrium, while the Mn and Si contents are respectively higher and lower in austenite than expected at equilibrium. Figure 20 (b) illustrates the kind of profiles that are

found in fibrous ART steels upon reheating below the first T_{IA} [72], [75], or during longer annealing at lower temperature [71]. In both cases, the diffusivity of substitutional elements is low. The fibrous steel in Figure 20 (b) is a Fe/0.08C/2.4Mn/0.5Si/0.5Ni/0.42Mo intercritically annealed at 720°C for 30 min and then reheated at 680°C for 30 min. Mn, C and Ni partitioned in austenite, and Si and Mo partitioned in ferrite. It can be observed that a segregation of Mn, Si, Ni and Mo is found in the interface.

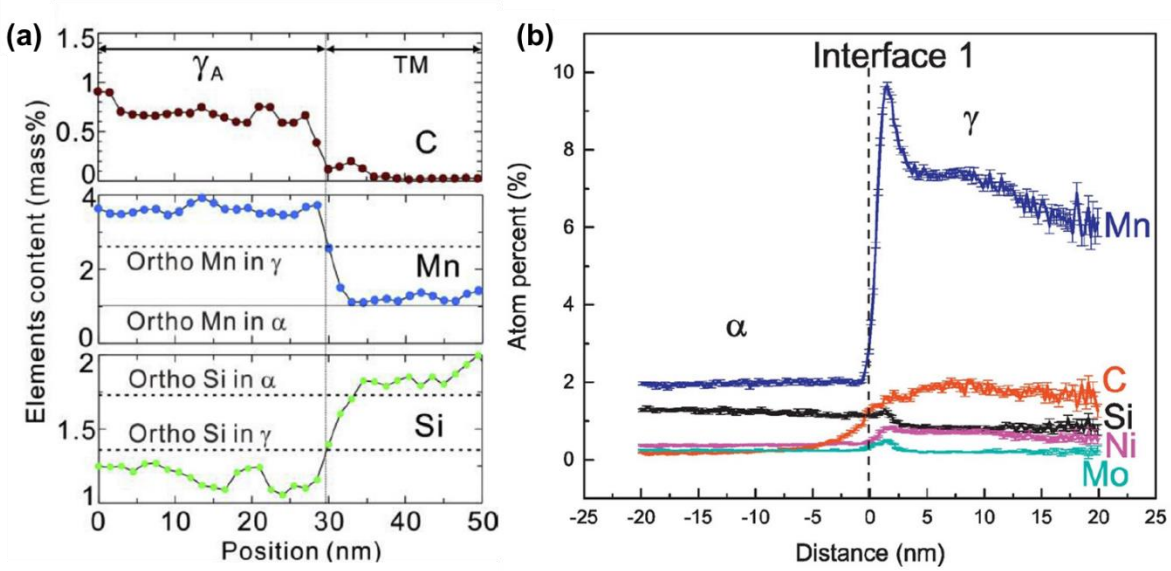

Figure 20: (a) Profiles measured by APT of C, Mn and Si across acicular austenite γ_A and thermal martensite TM interface [65]. (b) Profiles measured by APT of C, Mn, Si, Ni and Mo across acicular austenite γ and ferrite α interface [72]. From a thermal processing viewpoint, only one IA has been conducted in (a), while there have been two consecutive IA in (b).

An illustration of the typical repartition of C, Mn and Al among phases is given in Figure 21 for globular UFG medium Mn steel [68]. The 3D Mn map obtained by APT is given in (a), and the chemical profiles across ROI 1 and ROI 2 of the 3D APT are given in (b) and (c). The Fe/0.11C/4.9Mn/2Al globular medium Mn steel has been annealed at 725°C during 10 min. This steel is in reality triplex, consisting of ferrite, austenite and fresh martensite obtained from final air-cooling. The martensite and austenite have similar chemistry since martensitic transformation is diffusionless. The profiles of Mn, C and Al across α/α' interface shown in Figure 21 (b) are thus representative of an α/γ interface. For this globular steel, again, austenite is more enriched in C and Mn, while ferrite is more enriched in Al. For all alloying elements, there is a spike near the interface. Interestingly, when comparing γ/α' interface in Figure 21 (c), the amount of C and Al is similar between the two phases. However, there is more Mn in austenite (13%) when compared with martensite (10%). Therefore, these experiments reveal a gradient of Mn content in austenite at the end of isothermal holding of IA, which in turns create a gradient of austenite stability.

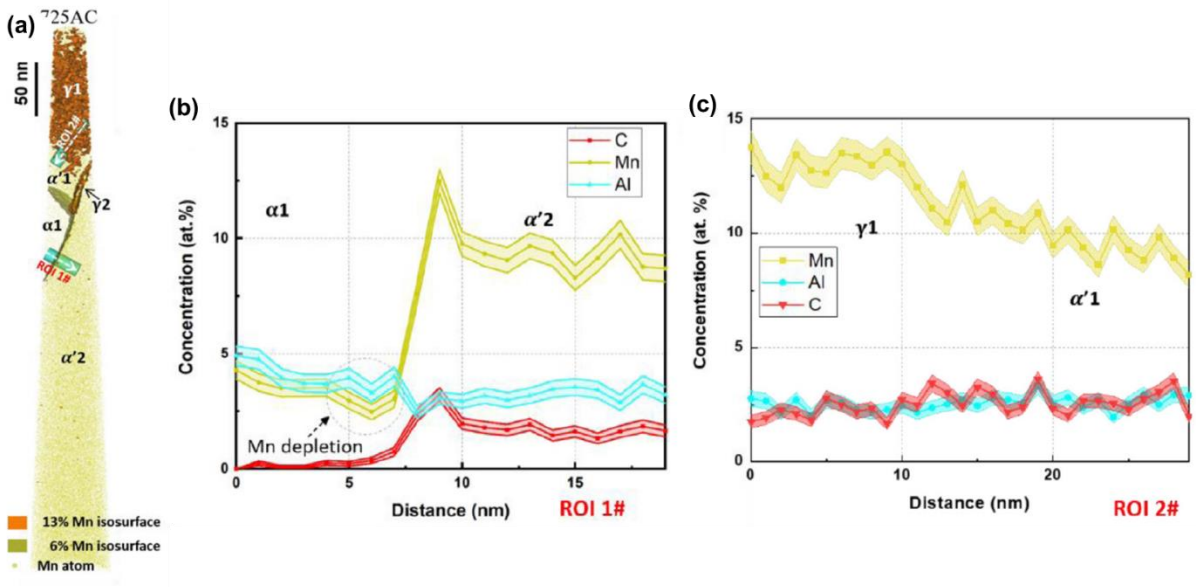

Figure 21: (a) 3D atom probe tomography maps of Mn in a medium Mn steel with a globular morphology annealed at 725°C and air-cooled. (b) and (c) C/Mn/Al concentration profiles relative to the position of the phase boundaries taken from the selected region of interest (ROI) marked in (a) and (d) [68].

In steels with fibrous ART microstructure, some measurements also show that gradient of Mn and C inside austenite grains. An atom probe measurement of the α/γ interface of a fibrous Fe/0.2C/4.72Mn/0.2Si/0.1Al steel annealed at 650°C for 5 min is shown in Figure 22 [73]. The profiles shown in (c) and (d) are taken orthogonal to the interface seen in (b). In (c) and (d), coloured dots correspond to APT measurements, while black curves correspond to a DICTRA simulation. Some clear oscillations of Mn content in austenite are visible in Figure 22 (c), which are far larger than measurement uncertainty. The same oscillations are seen for C, despite being closer to measurements uncertainty. By modifying the interface mobility in DICTRA simulations, authors successfully reproduce the experimental trend [73]. The same kind of oscillation in Mn content inside fibrous austenite grains are found by Zhu et al. using Auger nanoprobe after doing multiple consecutive intercritical annealings [74].

The profiles of C and Mn contents across α/γ interfaces are highly sensitive to other alloying elements. In their study on interfaces in medium Mn fibrous steels, Ye et al. have measured gradient of Mn and Al across α/γ interfaces of a Fe/0.15C/10Mn/2Cu, a Fe/0.15C/10Mn/2Cu/2Al and a Fe/0.15C/10Mn/2Al steels, as shown in Figure 23 (a), (b) and (c) respectively [66]. Only the amount of Cu and Al are modified between experiments. When there is only copper (Figure 23 (a)), no interfacial segregation is measured. When aluminium is added, independently of the presence or absence of Cu, the boundaries of austenite grains are richer in Mn. The authors emphasizes that ferrite stabilizer elements have a synergetic effect with Mn by reducing the interface velocity, allowing for a core-shell austenitic structure which is more stable than austenite without chemical gradient [66]. According to the authors, this allows for a gradual and sustained TRIP effect with deformation and improves the overall mechanical response of medium Mn steels.

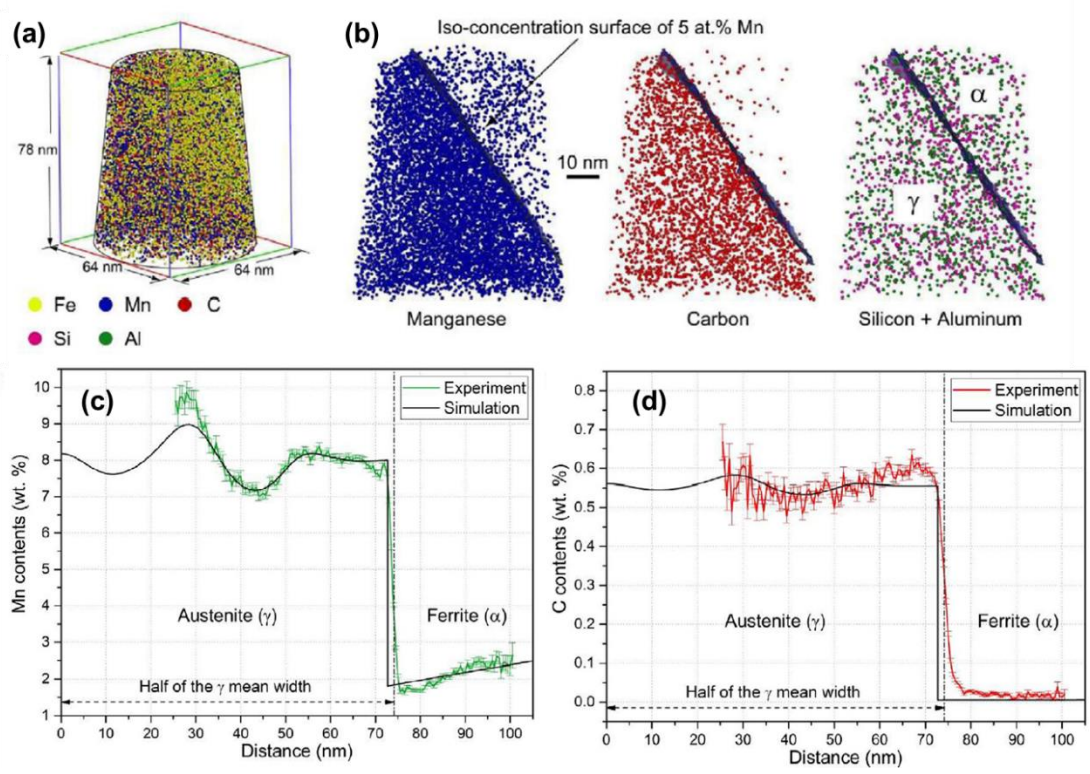

Figure 22: APT analysis of a volume containing a ferrite /austenite interface after the IA at 650 °C for 5 min: (a) 3A atom probe map showing the solute-rich γ (bottom/left) and solute-lean α (upper/right). (b) composition profiles normal to the α/γ interface for Mn, C and Si + Al. (c) and (d) Concentration profiles across the α/γ interface respectively for Mn (green) and C (blue). The 95% confidence interval is recorded on each profile. In (c) and (d), the results of a DICTRA simulation are indicated with a black line [73].

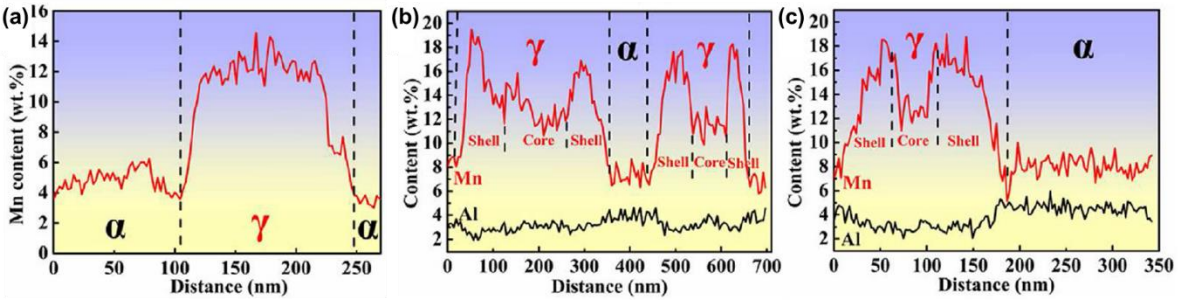

Figure 23: Composition profiles in Mn (red) and Al (black) measured by STEM-EDS of steels with a fibrous morphology. Base composition of the steels is Fe/0.15C/10Mn. In addition,: (a) +2% of Cu; (b) +2% Cu and Al; (c) +2% of Al [66].

Overall, important morphological and orientation characteristic of duplex ferrite-austenite medium Mn steels have been highlighted in the two last sections. The mechanisms of nucleation of austenite during intercritical annealing of cold-rolled and martensitic microstructures have been detailed. While no orientation relationship between the ferritic matrix and retained austenite is expected in globular UFG steels, K-S orientation relationship is expected in fibrous ART steels. The partitioning and resulting gradients of composition inside austenite and ferrite grains were extensively discussed, since their understanding is necessary to comprehend the mechanical behaviour of medium Mn steels. The next part of the chapter will be dedicated to the explanation of austenite stability at a more fundamental level, detailing the effect of chemistry, grain size, stress and environment from a thermodynamics standpoint. Austenite stability is intimately linked with martensitic transformation,

since its occurrence during quenching or deformation defines when austenite becomes unstable in those situations. Therefore, the phenomenology of thermal and mechanically-induced martensitic transformation will first be detailed.

3. Factors influencing TRIP effect efficiency

A. The martensitic transformation

a) Nature of the martensitic transformation

The martensitic transformation is a first order, displacive, diffusionless transformation of face-centred cubic (FCC) austenite into martensite. The martensite structure can be either hexagonal close packed HCP (ε-martensite) or body-centred tetragonal BCT (α'-martensite) [36], [37]. If the carbon content of α'-martensite is low enough, martensite can be considered body-centred cubic BCC. This transformation is driven by thermomechanical forces. The transformation being diffusionless, the composition of martensite is identical to its mother austenite.

In Figure 24 are detailed the conditions of existence of each kind of martensite in fully austenitic steel after quenching and deformation at room temperature as a function of the C and Mn content [36], [37] (empirical maps established by Schuman). Depending on the austenite enrichment, the microstructure after deformation can either be fully austenitic γ, γ+α', γ+ε or γ+ε+α'. Below a Mn-content of 10 wt%, no ε-martensite is reported. The nominal content of the steel of the PhD is 0.2C and 4Mn. Experiments conducted in Chapter II (see section II.5.B) will prove that austenite Mn content remains below 10% after IA. Therefore, the detailed description of ε-martensite is omitted afterwards.

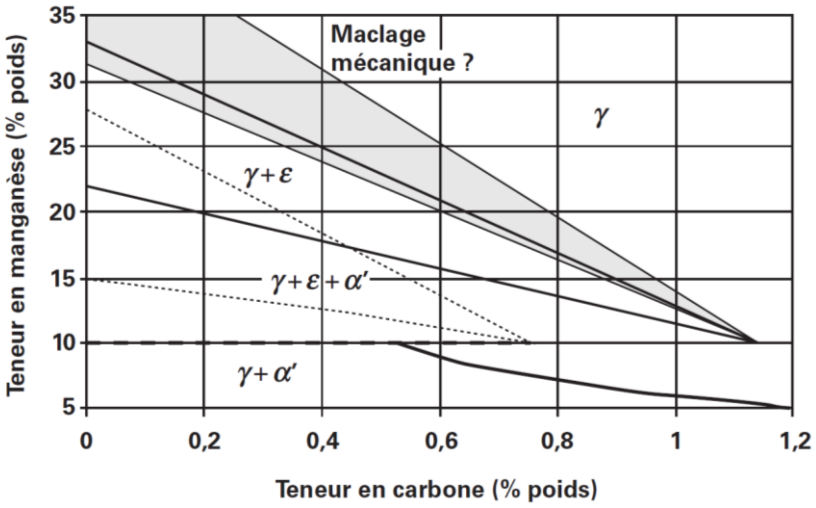

Figure 24: Microstructure of austenitic steels after quenching and deformation at room temperature as a function of carbon and manganese alloying content (wt%) [36], [37].

Considering their respective crystallographic structure, austenite is a compact phase, while martensite is not. Thus, martensitic transformation is always accompanied by a volume change at a macroscopic level [34]. Empirically, the deformation of a volume of matter during the austenite to

martensite transformation, the so-called transformation strain, is described as an invariant-plane strain ε_{emp} which is the sum of a dilatational strain ε_0 and a shear strain γ_0 [76]. The dilatational strain ε_0 equals 0.03 and γ_0 ranges from 0.22 to 0.26 [76], [77]. At a macroscopic scale, the interface between austenite and martensite is the habit plane, which is not necessarily an invariant plane due to plastic accommodation [78]. More details about the phenomenology of the martensitic transformation are given in Appendix A. The Bain transformation is introduced [79], alongside some theories like Phenomenological Theory of Martensite Crystallography (PTMC) [76], [80] and the recent Minimization of atomic Displacement (MD) theory [81].

Due to the displacive nature of the martensitic transformation, there must be an orientation relationship (OR) between austenite and martensite. The main relationships reported in literature are the Kurdjumov-Sachs (K-S) OR $\{110\}_{\alpha'}$ // $\{111\}_{\gamma}$ and $<1\text{-}11>_{\alpha'}$ // $<0\text{-}11>_{\gamma}$ and the Nishiyama-Wasserman (N-W) OR $\{111\}_{\alpha'}$ // $\{101\}_{\gamma}$ and $<10\text{-}1>_{\alpha'}$ // $<12\text{-}1>_{\gamma}$ [34], [35], [79]. Knowing the orientation of austenite, it is thus possible to predict the possible orientations of the different variants of martensite. Due to the symmetry of austenitic cubic crystallography, there are only 24 possible variants of martensite upon transformation. However, depending on the orientation relationship, some variants can be identical. As such, there are 24 distinct K-S OR, but only 12 distinct N-W OR.

b) Morphology of the martensite

At a mesoscopic scale, martensite can reveal varied morphologies, depending on its mother phase composition and deformation as well as the transformation temperature. Even though numerous nomenclatures exist to describe the possible morphologies of the martensite, authors in literature mainly describe two forms of α' martensite: plate and lath [82]. For plate martensite one dimension of martensite "grain" is negligible compared with the others two while for lath martensite, two dimensions are negligible to the last one. More details concerning the difference in morphology (plate or lath) of martensite as a function of its nature (alloying elements, M_S temperature) are given in Appendix B.

In the literature, for both globular and fibrous ART medium Mn steels, martensite has been reported to be lath-like [65], [68], [73] (as previously discussed in sections I.2.A and I.2.B). Therefore, only the microtextural aspect of lath martensite is discussed afterwards, as the nanostructured aspect of lath martensite explains also the fibrous nature of austenite found in ART medium Mn steels.

Martensite laths are organized in sets named blocks and packets. Such microtextures are shown in Figure 25 [7]. The studied steel is a medium Mn steel (Fe/0.3C/2Mn/1.5Si) in its as-quenched state from an austenitic annealing. Blocks consist of laths sharing almost the same orientation relationship with the mother austenite, while packets consist of blocks that share the same habit plane. The prior austenite grain boundary (PAGB) is indicated by a dotted-white line in Figure 25 (a) and (b), while a packet boundary (PB) is indicated in black. At a higher magnification, in Figure 25 (c), block boundaries are indicated in black, while the white lines (low angle misorientation) reveal boundaries between laths. The X-ray diffractogram (Figure 25 (d)) highlights a very small amount of retained austenite in this steel, estimated to be around 2% by Zhang et al. [7].

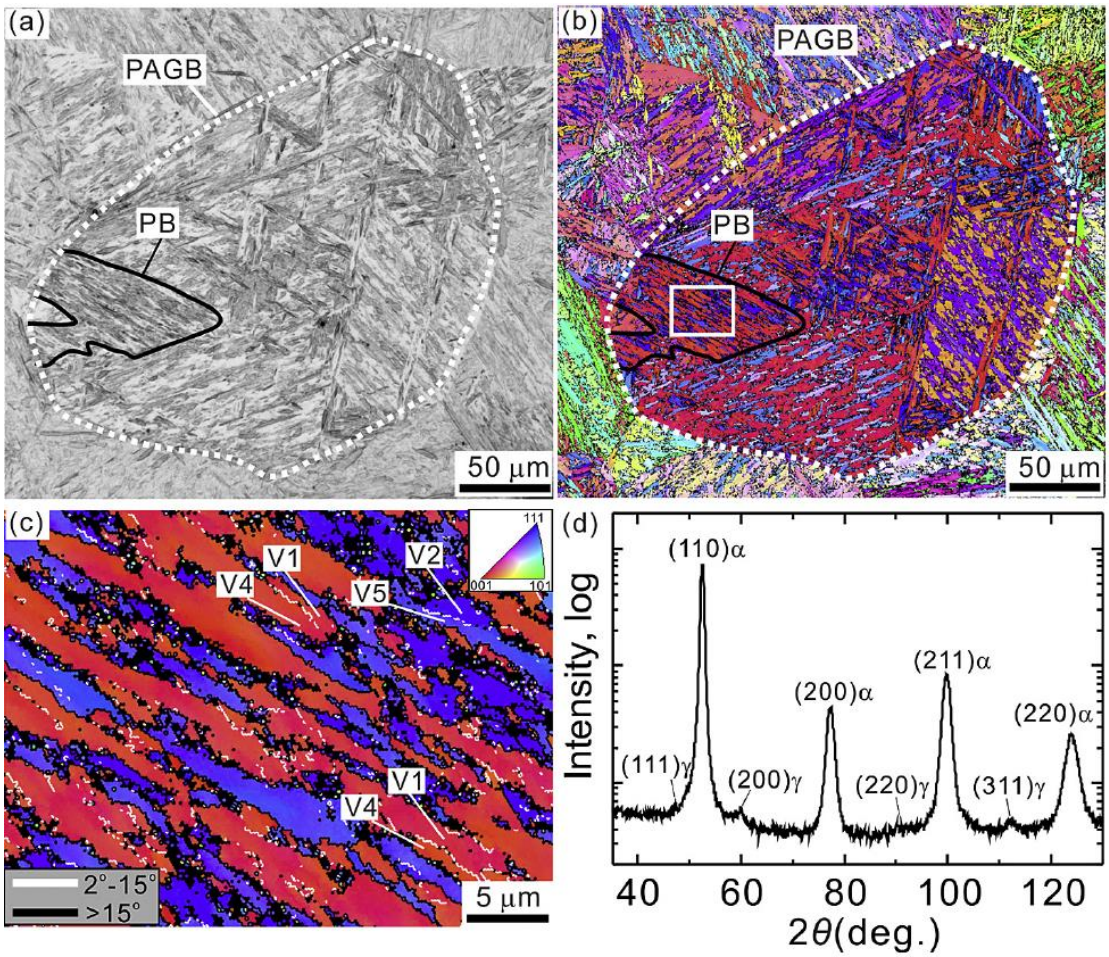

Figure 25: Martensite laths found in an as-quenched steel (Fe/0.3C/2Mn/1.5Si) observed in (a) an OM micrography and (b) an EBSD orientation map. PAGB corresponds to the prior austenite grain boundary, PB corresponds to a packet boundary. (c) is a zoom from the white rectangle in the (b) map, where low and high angle boundaries are indicated. (d) is the X-ray diffraction profile of the specimen [7].

This hierarchical organisation of martensite allows for a refinement of the microstructure. When it is heated during intercritical annealing, ART mechanism will occur, as discussed previously in section I.2.B. The austenite formed during IA bears an OR with surrounding annealed martensite and inherits the lath-like morphology and the refined structure of martensite.

c) Strain and stress induced martensitic transformation

The martensitic transformation induced from thermal treatment (quench) and the mechanically induced martensitic transformation are similar and can be understood in the same thermodynamic framework. Contrary to diffusive transformations, martensitic transformation occurs without diffusion. Thus, the chemical driving force for the transformation equals the difference $\Delta G^{\gamma\rightarrow\alpha'}$ between the Gibbs energy of austenite G^{γ} and the one of martensite $G^{\alpha'}$ at the given composition. However, the transformation never occurs spontaneously when this difference $\Delta G^{\gamma\rightarrow\alpha'}$ is equal to zero, but when a certain enthalpic barrier $\Delta G_{barrier}$ is overcome (nucleation process). For a given austenite state, in the absence of external stress, the temperature T_0 is the temperature at which $\Delta G^{\gamma\rightarrow\alpha'}$ is equal to zero. Most importantly, the martensite start temperature M_s is the temperature below which $\Delta G^{\gamma\rightarrow\alpha'}$

is higher than $\Delta G_{barrier}$. Thus, M_s is the temperature below which the considered austenite starts to transform spontaneously into martensite.

When an external stress is applied on a steel containing austenite, martensitic transformation can be triggered even at a temperature above M_S. In fact, applied stress can either destabilize austenite, or create new sites for the nucleation of martensite through plastic deformation. The schematic evolution of the minimum stress σ_γ to trigger the martensitic transformation, as a function of the temperature, is shown in Figure 26 (a) [8]. Two regimes of nucleation are to be considered when studying the mechanically induced martensitic transformation [8], [9]. In the first regime, the transformation is said to be stress-induced, or stress-aided. In this regime, the minimum stress σ_γ to apply is lower than the yield strength σ_γ^γ of austenite. Before the transformation occurs, the austenite is in its elastic domain. The minimum stress σ_γ varies linearly with the temperature, until a temperature called M_s^σ for which the minimum stress σ_γ is equal to the yield stress of austenite σ_γ^γ. Above this temperature M_s^σ, the martensitic transformation is described as strain-induced. In this second regime, the minimum applied stress σ_γ is higher than the yield strength of austenite, meaning that austenite deforms plastically before the martensitic transformation occurs. In this regime, the evolution of the minimum stress σ_γ is far from being linear. Above a certain temperature M_d, the austenite is thermodynamically so stable that no applied stress/strain on the steel can trigger the martensitic transformation.

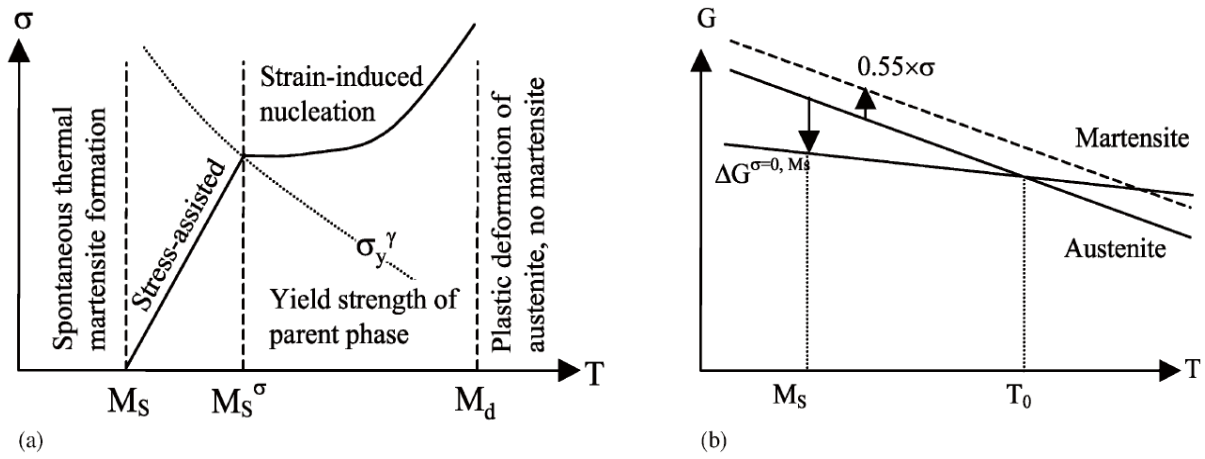

Figure 26 : (a) Evolution of the stress σ_γ to apply to austenite (denoted σ on the graph) to induce the martensitic transformation, as a function of the temperature. The different regimes of transformation are indicated. (b) Gibbs energies of austenite G^γ and martensite $G^{\alpha'}$ as a function of temperature. The effect of an applied stress on G^γ is indicated by a dotted line [8].

In the stress-induced regime, nucleation of martensite become possible due to the elastic energy stored in austenite. The Gibbs energy of austenite G^γ increases due to the applied stress, as represented in Figure 26 (b) by the dotted line in the case of a tensile state. The sites of nucleation for the stress-induced martensite will be the same as the ones for the thermal martensite. The elastic energy of austenite can be taken into account in the usual difference in Gibbs energy $\Delta G^{\gamma\rightarrow\alpha'}$ by adding a mechanical term $\sigma_\gamma \times \partial\Delta G^{\gamma\rightarrow\alpha'}/\partial\sigma_\gamma$, proportional to the applied stress σ_γ, to the purely chemical difference in Gibbs energy $\Delta G^{\gamma\rightarrow\alpha',\sigma=0}$ (for a stress-free austenite) [8], [83]:

$$\Delta G^{\gamma\rightarrow\alpha'} = \Delta G^{\gamma\rightarrow\alpha',\sigma_\gamma=0} + \frac{\partial \Delta G^{\gamma\rightarrow\alpha'}}{\partial \sigma_\gamma}\sigma_\gamma \qquad (I—1)$$

The term $\partial\Delta G^{\gamma\rightarrow\alpha'}/\partial\sigma_\gamma$ depends on the considered stress state. For a uniaxial test, Patel and Cohen have calculated this term as [83]:

$$\frac{\partial \Delta G^{\gamma\rightarrow\alpha'}}{\partial \sigma_\gamma} = \frac{1}{2}\left[\gamma_0 sin(2\theta) + \delta\,.\,\varepsilon_0\left(1 + cos(2\theta)\right)\right] \qquad (I—2)$$

where γ_0 is the shear strain of martensitic transformation, ε_0 is the normal strain of martensitic transformation, θ is the angle between the normal to the gliding plane and the applied stress direction, and δ = 1 for a tensile test or δ = -1 for a compression test. For hydrostatic stress states, applied stress can either destabilize austenite if it is positive (tensile hydrostatic stress) or stabilize austenite if it is negative (compressive hydrostatic stress) [25], [82], [83].

In the strain-induced regime, before the martensitic transformation occurs, the austenite will plastically accommodate the deformation by dislocation gliding. Numerous shear bands will appear, and martensite will nucleate at their intersections [10], [11]. Thus, in this second regime, the nucleation sites are different from the ones for thermal martensite. There will be a competition for the accommodation of elastic strain between the plastic gliding and the strain-induced martensitic transformation. The mechanisms permitting the nucleation of martensite in this regime will be further discussed in a next section.

d) Effect of applied stress

The 3D stress state of the mechanical loading affects the destabilization kinetics of austenite through the term $\partial\Delta G^{\gamma\rightarrow\alpha'}/\partial\sigma_\gamma$. The 3D stress state, notably by its effect on volume change, influences the mechanical driving force for the martensitic transformation [9]. Jacques and Lani have developed a micro-macro mechanical model which highlights the dependence of the TRIP effect to the triaxiality of the stress tensor [84], [85]. The authors state that both the hydrostatic and deviatoric components of stress tensors have an impact on the TRIP effect. To quantify this effect, the triaxiality index T^{3D} is defined as the ratio between the hydrostatic stress σ_h and the von Mises stress σ_{vM} [85]:

$$T^{3D} = \frac{\sigma_h}{\sigma_{vM}} \qquad (I—3)$$

Both σ_h and σ_{vM} refers to the macroscopic stresses of the steel [85]. It must be emphasized that for multiphase steels, like conventional TRIP-steel which the study focuses on, the mean stress state at phase scale may differ from the one macroscopically observed. The result of their experiments and model on the evolution of austenite phase fraction for different stress states are shown in Figure 27. The austenite destabilization strongly depends on the loading configuration. The value of T^{3D} for the different kinds of tests are: T^{3D} = 0 for shear test; T^{3D} = 0,33 for uniaxial tensile test; T = 0,42 for Marciniak test; T = 0.52 for Notch test; T = 0,6 for DENT test; T^{3D} = 0,66 for equibiaxial test. The kinetics of destabilization is the slowest for the lowest T^{3D} (shear stress). Then, at first, the kinetics of transformation is quicker when T^{3D} increases, until the value of T^{3D} = 0.6 (DENT test), above which the kinetics become slower. The maximum transformation rate is thus obtained at an intermediate level of the triaxiality index.

Polatidis et al. [86] emphasize that to reproduce accurately the triaxiality effect, models must account for the Lode angle θ_L. If the triaxiality index T^{3D} is proportional to the ratio of the 1st invariant of the stress tensor over the 2nd invariant of the deviatoric stress tensor, θ_L is defined as proportional to the ratio of the 3rd invariant of the deviatoric stress tensor (its determinant) over its 2nd invariant [86].

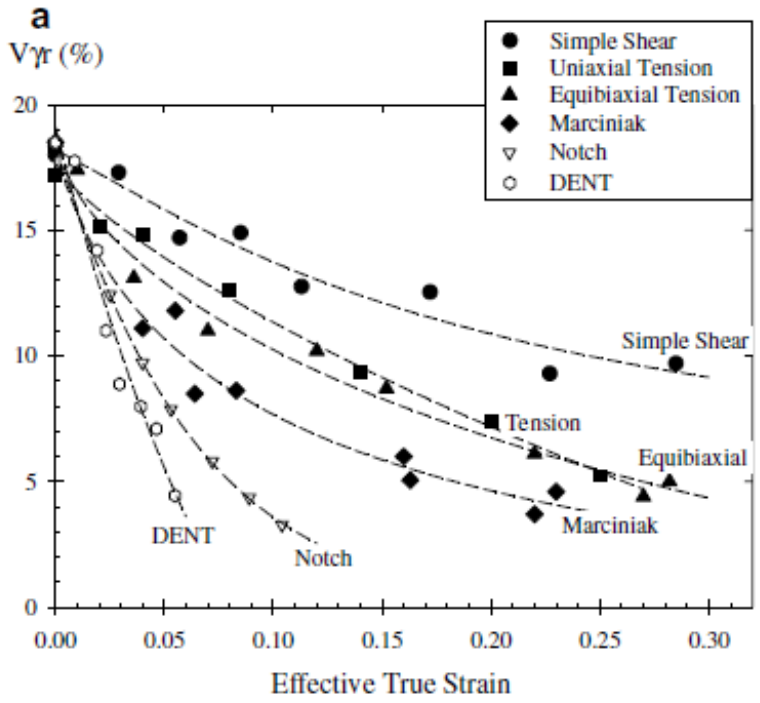

Figure 27: Evolution of the austenite volume fraction as a function of effective true strain for different stress states, in a Fe/0.3C/1.4Mn/1.4Si conventional TRIP steel [85].

The preceding remarks emphasized the necessity to use a full-field scheme to capture the effect of triaxiality on the strain-induced martensitic transformation. The effect of the 3D stress and strain tensors on the mechanical part of the driving force $\Delta G^{\gamma\rightarrow\alpha'}{}_{mech}$ is given by Prüger et al. [87]. They divide the macroscopic stress tensor Σ into its hydrostatic part P (P = 1/3 × tr(Σ)) and its deviatoric part S (S = Σ-P), and the transformation strain tensor into its volumetric part Δ_v and its deviatoric part R. Then, for any mechanical loading, $\Delta G^{\gamma\rightarrow\alpha'}{}_{mech}$ is computed as [87]:

$$\Delta G_{mech}^{\gamma\rightarrow\alpha'} = C(\Delta_v P + \|R\|.\|S\|) \qquad (I—4)$$

with C a constant. The authors emphasize that only using the triaxiality for calculating the austenite evolution during non-monotonic loadings leads to unrealistic results [88].

e) Effect of surrounding matrix

The distribution of stresses inside retained austenite is greatly influenced by the elastoplastic properties of the matrix [89]. The hardness of matrix has a direct influence on the mechanical driving force necessary to induce the martensitic transformation. The harder the matrix is, the more difficult is the martensitic transformation (increase in the enthalpic barrier $\Delta G_{barrier}$) [9]. In their work on

medium Mn steels, Chen et al. [90] have reported that when the martensitic matrix is annealed, the annihilation of dislocations, and the polygonization or coalescence of martensite laths lead to a softening of the matrix, which is then less able to suppress the martensitic transformation.

In this section, the basic mechanisms concerning martensitic transformation were explained. It was shown how the martensitic transformation can have a thermal or a mechanical origin. The driving force triggering the transformation has a chemical and a mechanical component. This mechanical component highly depends on the stress state of the applied stress, i.e. on the triaxiality of the stress tensor. If the austenite is deformed plastically, new sites of nucleation can also appear at the intersection of shear bands. An important factor for the study of martensitic transformation is the stability of the mother austenite, stability that will be the subject of the next section.

B. Factors influencing the austenite intrinsic stability

As explained in the previous section, M_s is the temperature below which the austenite transforms spontaneously into martensite. Above this temperature M_s, until a temperature called M_d, it is still possible to trigger the martensitic transformation by applying a stress on the steel. Depending on the level of the stress, the martensite will either be stress-induced or strain-induced. At room temperature RT, the TRIP effect will be all the more efficient if the M_s temperature is just below RT. Thus, it is important to control precisely the M_s temperature when designing TRIP steels. The next sections highlight the respective effects of chemical composition, internal stress, grain size, morphology and the surrounding matrix on the austenite stability (thus on the Ms temperature).

a) Effect of chemical composition

The chemical composition of retained austenite controls at the first order the driving force $\Delta G^{\gamma\rightarrow\alpha'}$ for the martensitic transformation, but also the enthalpic barrier $\Delta G_{barrier}$ for the transformation, defined in section I.3.A.c). In fact this last value is associated to the creation of new interfaces and defaults [9] whose energy are themselves composition-dependent. In 3rd generation AHSS, austenite is retained at room temperature mainly thanks to the partitioning of carbon in carbide-free bainitic steels [22]–[24] and Q&P steels [25], [27], [91], but also from manganese partitioning in medium Mn steels [19], [20], [47], [48]. From a thermodynamic standpoint, the effect of Mn, Al and Si on Fe-C pseudo-binary phase diagram has already been detailed in section I.2.A and will not be detailed again.

The stabilizing effect of alloying elements is obvious when considering the dependence of M_s to the austenite chemical composition. Several empirical formulae exist to describe this relationship. Kung has compared eight different formulae from the literature [92]. From his study, the most reliable equation seems to be the Andrews' linear equation for low alloyed steels [93] (in wt%):

$$M_s(°C) = 539 - 423C - 30,4Mn - 12,1Cr - 17,7Ni - 7,5Mo - 7,5Si + 10Co \qquad (I—5)$$

In their study on conventional TRIP steel, Blondé et al. also use an adapted Andrews' law to take into account the effect of carbon on M_s [94]. The measured coefficient in front of the carbon

weight content is 425 K/wt% for the studied TRIP-aided steel, which is very close to the value found in equation (I—5). In their modelling work on TRIP-steels, Wang and van der Zwaag use an exponential equation to take into account the dependence of M_s to austenite carbon content [95]:

$$M_s(°C) = 546 \times exp(-1.362C) \quad \text{(I—6)}$$

A very similar formula to Equation (I—6) is used by von Bohemen in his work on 3rd generation AHSS, replacing the factor 1.362 by 0.96.

b) Effect of residual stresses

The stabilizing effect of several chemical elements are extensively discussed in the literature. On the contrary, not many papers exist about the effect of residual stresses on austenite stability. Residual stresses are not to be confused with applied stresses related to the external loading, which were already discussed in section I.3.A.c). Indeed, residual stresses are internal stresses at part or at microstructure scale remaining even when the material do not endure any external load. They appear due to heterogeneities in the thermomechanical history of the part [96]. Their sums at the scale of the part are equal to 0.

Residual stress can built up at phase scale during processing route due to gradient of temperature which induces thermal stresses between part of the material [96]. Gradient of thermal treatment, alongside gradient of chemical composition can induces heterogeneous phase transformations. Those phase transformation creates internal stresses through volumetric change, transformation plasticity and variation of mechanical properties (typically in the case of martensitic transformation) [96]. For multiphase composite, the difference in coefficient of thermal expansion (CTE) between phases can create thermal stresses, even without a macroscopic thermal gradient [25], [97].

As these residual stresses are added to the applied stresses, the same framework developed by Patel and Cohen detailed in section I.3.A.c) can also be used to treat residual stresses. If we only consider hydrostatic stress inside austenite, the contribution of stress $\sigma_\gamma \times \partial \Delta G^{\gamma \rightarrow \alpha'} / \partial \sigma_\gamma$ to the driving force found in Equation (I—1) becomes [25], [83]:

$$\frac{\partial \Delta G^{\gamma \rightarrow \alpha'}}{\partial \sigma_\gamma} \sigma_\gamma = -P_\gamma \, \varepsilon_0 \, V_m \quad \text{(I—7)}$$

where P_γ is the hydrostatic pressure of austenite, ε_0 is the volume dilatation due to the martensitic transformation strain and V_m is the molar volume of martensite. The term $-P_\gamma \varepsilon_0 V_m$ is equal to 175 J/mol for the Q&P steel studied by Allain et al. [25]. As a consequence, a compressive hydrostatic pressure stabilizes the retained austenite. An apparent martensitic start temperature M_s' can be defined under the pressure P_γ. This apparent temperature M_s' is then linked with the purely chemical M_s by the difference in entropy $\Delta S^{\gamma \rightarrow \alpha'}$ between austenite and martensite [8]:

$$M_s - M_{s'} = \frac{-P_\gamma \, \varepsilon_0 \, V_m}{\Delta S^{\gamma \rightarrow \alpha'}} \quad \text{(I—8)}$$

The sensibility of M_s' to the stress is estimated to be -0.037°C/MPa for a compressive hydrostatic stress [25]. For a pressure of 670 MPa, the corresponding decrease in M_s is about 25°C. Thus, internal stresses have a measurable impact on the apparent M_s temperature.

c) Size and morphology effects

In low alloyed TRIP steels, austenite can present two morphologies: either films of austenite (film-type austenite), for example between bainitic laths in carbide-free bainitic steels or austenite laths in fibrous ART medium Mn steels, or large grains (blocky-type austenite) between bainitic blocks in carbide-free bainitic steels [50] or ferrite grains in globular medium Mn steels. The effect of morphology and size are difficult to separate since for a given microstructure, austenite films tend to be systematically smaller than austenite blocks.

A TEM micrography extracted from Sun and Yu work illustrates the respective dimensions of film-type and blocky-type austenite islands in Figure 28 (a) and (b) found in Q&P steels [26]. Austenite appears in dark contrast in the two images. The typical width of films is 100 nm, and they are situated between martensite laths. In contrast, the blocks are 5 times wider and surrounded by a softer ferritic matrix. They also highlighted a third type of austenite, which consists of ultra-fine retained austenite films. The latter were 20-30 nm thick and situated between bainitic plates.

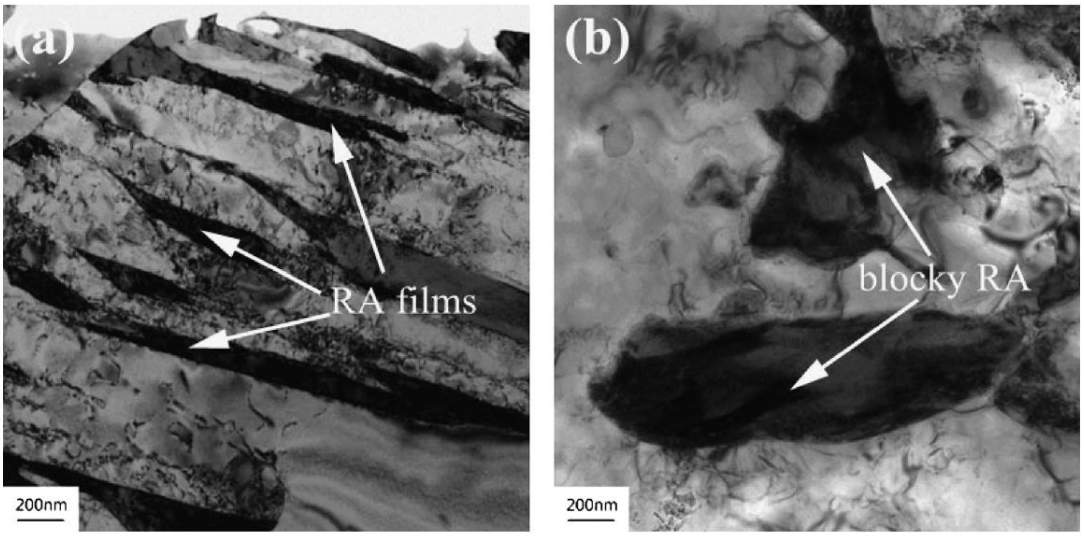

Figure 28: TEM micrographs of a Q&P steel highlighting the two observed morphologies of austenite islands encountered in these steels [26].

The effect of size of austenite grains on its stability can be understood as it affects the probability of finding some nucleation sites for martensite. The smaller the grain is, the more stable the austenite is [9]. Some studies try to correlate the austenite grain size directly with the M_s temperature. In their study on conventional TRIP steels, Melero et al. have shown for instance that M_s depends linearly to the inverse of the size of austenite [49]. More precisely, if we denote V_γ the mean volume of austenite grains, M_s^0 the martensite start temperature calculated with Andrew's law (Equation (I—5)) and M_s the apparent martensitic start temperature, they empirically establish the following equation [49]:

$$M_s = M_s^0 - B\,V_\gamma^{-\frac{1}{3}} \qquad (I—9)$$

In this equation, B is a constant equal to 475 K/µm^{-1}. Moreover, the authors have suggested that there is a minimal volume under which austenite grains stop transforming into martensite, even at necking. Thus, those grains cannot play any role in the TRIP effect. They have measured for the studied composition a minimal volume of 5 µm^3. The importance of size effect has also been reported by Wang and van der Zwaag [95] in their study on TRIP-steels, especially when the grain size reaches the value of 0.1 µm, as it was the case in their work.

The main issue comes from the possible "hidden" correlation between the grain size and the carbon content of austenite islands. Indeed, Xiong et al. have measured that film-like austenite was poorer in carbon than blocky austenite in their Q&P steels by combining XRD data with TEM [88]. Contrary to what is usually found in the literature [67], they measured a higher content of carbon in blocky austenite (1.14%) than in filmy austenite (0.64%) [98]. However, after 12% strain, all blocky-type austenite has transformed, while filmy austenite remained. Despite having less carbon, filmy austenite was still more stable, which was explained by size consideration, more compressive hydrostatic stresses and by neighbourhood effects.

The previous results highlight the difficulty to decorrelate the chemical, stress, size, shape and environmental contributions to austenite stability. Therefore, to be able to predict the mechanical austenite stability in a given microstructure, it is necessary to have a good understanding of the formation of the microstructure before loading.

4. Modelling of the mechanically induced martensitic transformation

In the previous sections, the stability of austenite at room temperature in multiphase steels has been discussed at the light of the thermodynamic. In this part, we will analyse how the kinetics of strain-induced martensitic transformation is modelled in the literature. The analysis is focused on strain-induced martensitic transformation (SIMT), rather than stress-assisted transformation since in medium Mn steels, it is the most commonly observed mechanism [99], [100]. It is also the case in our own experiments detailed in Chapter III.

A. Empirical approaches

Historically, strain-induced martensitic transformation (SIMT) was first studied in Fe-Ni-C and Fe-Ni-Cr-C metastable austenitic stainless steels [10]. In those fully austenitic steels, SIMT kinetics is easily measured with magnetic devices. The first empirical model of SIMT appeared in the literature in 1954. It was developed by Angel [101] and refined by Ludwigson and Berger [102]. It consists of a logarithmic-autocatalytic relationship between martensitic phase fraction $f_{\alpha'}$ and the true strain of the specimen ε to reproduce the sigmoidal shape of experimental SIMT kinetics:

$$\ln\left(\frac{f_{\alpha'}}{1-f_{\alpha'}}\right) = p_s \ln(\varepsilon) + k_s \qquad \text{(I—10)}$$

In Equation (I—10), p_s and k_s are two fitting parameters, linked with austenite mechanical stability. An even simpler model has been developed by Gerberich et al. [103] for metastable austenitic stainless steels, which describes the relationship between $f_{\alpha'}$ and ε_γ^{pl} as being parabolic and dependent of only one parameter. Despite its very simple form, Equation (I—10) reproduces experimental data in the respective papers [101]–[103] and allowed for a first quantification of austenite destabilization kinetics as a function of alloying contents and temperature.

Other empirical laws can be found in the literature for other types of steels, like a linear dependence between the logarithm of austenite phase fraction $\ln(f_\gamma)$ and ε_γ^{pl} in a dual-phase steel with fine retained austenite islands [104]. The one developed by Matsumura et al., derived from Equation (I—10), takes the following form [105]:

$$\frac{1}{f_\gamma} - \frac{1}{f_\gamma^0} = \frac{k_s}{p_s}\varepsilon^p \qquad \text{(I—11)}$$

In the last formula, f_γ and f_γ^0 are the austenite phase fraction and its initial value. The value of p_s does not evolve significantly for a given type of steel. Its value is 3 for austenitic stainless steels, 2 for duplex stainless steels and 1 for TRIP-aided steels such as medium Mn steels [105]. Due to its dependence to one parameter k_s, Equation (I—11) is still used in the literature to quickly quantify austenite mechanical stability in medium Mn steel [106].

Empirical models have proven to be useful to quickly quantify the evolution of austenite mechanical stability. However, in those laws, the dependence of parameters on chemistry and other microstructural parameters are never known a priori, making them unable to be used for predicting the mechanical behaviour of an unknown steel. Angel [101] also highlighted that experimental SIMT kinetics usually saturate below 100% of transformation, while at high strain, all empirical models either reach 100%. Another issue with such empirical laws is that they lack of theoretical basis. Thus, they do not give any clue to understand the underlying phenomena controlling SIMT, contrary to the model presented in the next section.

B. Olson-Cohen seminal model

Olson and Cohen are the first to propose a model with solid physical basis [10], [11] linking the austenite volume fraction $f_{\alpha'}$ and the austenite plastic strain ε_γ^{pl}. Their seminal work remains today the basis of most physically based model of SIMT found in the literature. Their theories rely on the TEM observation that α-martensite nucleates at the intersection of shear bands [10]. Shear bands can consist of ε-martensite, but SIMT can occur even when ε-martensite is not thermodynamically stable with respect to neither austenite nor α-martensite. In the latter case, shear bands can be packets of stacking faults in the FCC structure, or fronts of gliding dislocations.

Olson and Cohen's model is introduced in [11]. They suppose that the shear bands fraction f_{sb} inside an austenite grain increases linearly with the plastic strain ε in the available volume in austenite, until a saturation of this available volume inside the grain. This calculation is analogous to the one explaining the formation of athermal martensite, and naturally is based on the extended volume

theory. Under those hypotheses, a small increase in the plastic strain $d\varepsilon_\gamma^{pl}$ will conduct to a small increase in the shear bands fraction df_{sb} according to the following equation:

$$\frac{\mathrm{d}f_{sb}}{1-f_{sb}} = \alpha \,.\, \mathrm{d}\varepsilon_\gamma^{pl} \qquad \text{(I—12)}$$

where α is the band formation rate, depending on the stacking fault energy and on the level of strain. After integration, the fraction of shear bands follows an exponential law:

$$f_{sb} = 1 - exp\left(-\alpha\varepsilon_\gamma^{pl}\right) \qquad \text{(I—13)}$$

The number of shear bands per unit austenite volume N_{sb} is linked with the fraction f_{sb} by the equation:

$$f_{sb} = V_{sb} \,.\, N_{sb} \qquad \text{(I—14)}$$

where V_{sb} is the shear bands average volume, supposed constant. By geometrical considerations, Olson and Cohen demonstrate the following relationship between N_{sb} and the number of intersections per unit austenite volume N_i.

$$N_i = K \,.\, (N_{sb})^n \qquad \text{(I—15)}$$

In Equation (I—15), K is a geometrical parameter related with the size of austenite grains, and n is a constant higher than 2. Considering the probability p that a shear band intersection gives a martensite embryo, an increment in the number of intersections dN_i produces an increase in the number of martensitic embryos per unit austenite volume $dN_{\alpha'}$:

$$dN_{\alpha'} = p \,.\, dN_i \qquad \text{(I—16)}$$

The martensite volume fraction $f_{\alpha'}$ (the ratio with respect to the initial volume of austenite) can be related with the number of embryos per unit austenite volume $dN_{\alpha'}$ and to the mean volume of a martensite lath $V_{\alpha'}$ forming at the considered level of strain by the formula:

$$\frac{\mathrm{d}f_{\alpha'}}{1-f_{\alpha'}} = V_{\alpha'} \,.\, dN_{\alpha'} \qquad \text{(I—17)}$$

Equation (I—17) explains that the increase in the fraction of martensite depends only the nucleation rate but not on the growth of martensite laths (diffusionless transformation).

Finally, by combining the last five Equations (from (I—12) to (I—17)), and after an integration, the following relationship between $f_{\alpha'}$ and ε_γ^{pl} is proposed by Olson and Cohen [11]:

$$f_{\alpha'} = 1 - exp\left\{-\beta\left[1 - exp\left(-\alpha\varepsilon_\gamma^{pl}\right)\right]^n\right\}$$
$$\beta = \frac{V_{\alpha'}\, K}{{V_{sb}}^n}\, p \qquad \text{(I—18)}$$

From Equation (I—18), it must be stressed that the relationship between $f_{\alpha'}$ and ε_γ^{pl} only depends on three parameters, α, β and n. The exponent n is a geometric constant, usually set equal to 2 [10], [11], [107]. Only α and β are influenced by the temperature. Indeed, the parameter α depends on the stacking fault energy, which is a function of the temperature, and β depends on the probability p of the nucleation of a martensite embryo, which is influenced by the temperature. In Figure 29, data

extracted from the study on stainless steels made by Angel et al. [101] are used to validate the model developed by Olson and Cohen. With the good calibration, it is possible to reproduce the experimental dependence of SIMT with temperature. The higher the temperature of the tensile test is, the slower the SIMT kinetics is. Equation (I—18) enables describing with a good precision the sigmoidal shape of experimental measurements. Moreover, the model also takes into account the saturation of the martensitic transformation below 100%, contrary to the empirical models described in the section I.4.A [11], [101], [103].

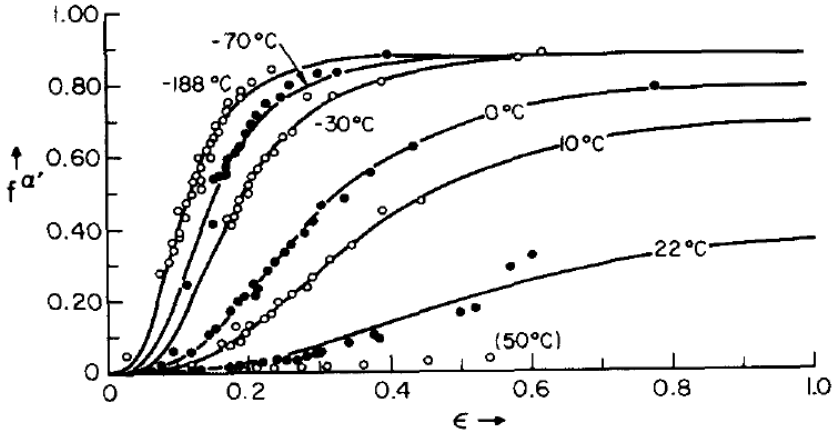

Figure 29: Comparison between the experiments conducted by Angel et al. [101] on a 304 stainless steel (dots) and the simulations using Olson and Cohen equations (reproduced from [11]).

Thanks to its simplicity, the Olson-Cohen law is widely used in the literature to model the martensitic transformation [2], [108] and the strain-induced martensitic transformation [8], [109] [110], [111]. Different improvements have been made to the Olson-Cohen theory, clarifying the relationship between the parameters found in the theory and thermodynamical quantities like temperature, chemistry and stress-state. Samek et al. [107] for instance studied the explicit dependence of chemistry and temperature on α and β parameters of Equation (I—18) (with n=2), postulating that each parameter follow a Boltzmann-type equation. Their results are only suitable for conventional TRIP-steels.

The model developed by Olson and Cohen is the origin of most physically-based models for SIMT found in the literature. Since 1975, Olson and Cohen (OC) model has been improved to consider its direct dependence to driving force $\Delta G^{\gamma \rightarrow \alpha'}$, stress triaxiality or strain rate. While being one-dimensional, OC model has also been extended for 3D simulation, allowing for a better description of triaxiality effects. The next sections are dedicated to the presentation of augmented OC models.

C. Thermodynamical description of SIMT

In the original OC model, the thermodynamical driving force $\Delta G^{\gamma \rightarrow \alpha'}$ for martensitic transformation do not appear explicitly. For martensitic transformation, the driving force $\Delta G^{\gamma \rightarrow \alpha'}$ was first introduced in isothermal condition by Pati and Cohen [112] in 1969. They used an Arrhenius-type law to describe the evolution of the nucleation rate of martensite embryos $dN_{\alpha'}/dt$. The dependence of the activation energy ΔW on $\Delta G^{\gamma \rightarrow \alpha'}$ is not explicitly given by Pati and Cohen. Then, the activation energy ΔW was introduced for stress-assisted martensitic transformation by Olson and Cohen [113] in

1982. In this paper, the authors give the explicit dependence of ΔW on $\Delta G^{\gamma\rightarrow\alpha'}$ as a linear function with two positive parameters A and B:

$$\boldsymbol{\Delta W = A + B\,\Delta G^{\gamma\rightarrow\alpha'}} \qquad \textbf{(I—19)}$$

When ε-martensite appears transiently during SIMT mechanism, $\Delta G^{\gamma\rightarrow\alpha'}$ becomes $\Delta G^{\gamma\rightarrow\varepsilon}$ in equation (I—19). Following those developments, Perlade et al. [8] propose an alternative formulation as a function of the plastic strain :

$$\frac{\mathrm{d}N_{\alpha'}}{\mathrm{d}\varepsilon_{\gamma}^{pl}} = \frac{I_0}{\Lambda_0} exp\left(-\frac{\Delta W}{RT}\right) \qquad \textbf{(I—20)}$$

In Equation (I—20), ΔW is the activation energy (calculated with (I—19)), I_0/Λ_0 is the potent number of nucleation sites per unit volume, which increases when $\varepsilon_{\gamma}^{pl}$ increases assuming a lenticular shape of martensite. The length Λ_0 is the distance between martensite plates. Initially being the austenite grain size, Λ_0 decreases with plastic strain due to austenite fragmentation with SIMT. The fractions of strain-induced martensite $f_{\alpha'}$ is then calculated combining Equations (I—20) and (I—17).

In Perlade's theory, the dependence of martensite nucleation rate on the difference in Gibbs energy $\Delta G^{\gamma\rightarrow\alpha'}$ between austenite and martensite allows to introduce the sensitivity of SIMT kinetics to austenite composition, the stress-state and the temperature. Indeed, Perlade et al. calculate $\Delta G^{\gamma\rightarrow\alpha'}$ as the following sum:

$$\boldsymbol{\Delta G^{\gamma\rightarrow\alpha'} = \Delta G^{\sigma=0,M_s} + \Delta S^{\sigma=0,M_s}(T - M_s) + \frac{\partial \Delta G^{\gamma\rightarrow\alpha'}}{\partial \sigma_{\gamma}}\sigma_{\gamma}} \qquad \textbf{(I—21)}$$

In the last equation, $\Delta S^{\sigma=0,Ms}$ is the entropy difference between austenite and martensite, $\Delta G^{\sigma=0,Ms}$ is a constant equal to -1250 J.mol^{-1}, experimentally found to be independent of austenite carbon content. The mechanical term $\sigma_\gamma \times \partial\Delta G^{\gamma\rightarrow\alpha'}/\partial\sigma_\gamma$ was already described in the section I.3.A.c), and was introduced in Equation (I—1). It can be calculated with Equations (I—2) or (I—7), depending on the local or macroscopic stress triaxiality. M_S is a function of austenite composition, as highlighted by Equations (I—5) and (I—6). The following values are found for the other constants: $\Delta S^{\sigma=0,Ms}$ = 6.8 J.mol^{-1}.K^{-1}; $\partial\Delta G^{\gamma\rightarrow\alpha'}/\partial\sigma_\gamma$ =-0.55 J.mol^{-1}.MPa^{-1} for uniaxial tensile deformation.

Other formalisms exist to introduce thermodynamical quantities in OC type models. The classical homogeneous nucleation theory can be used in OC model [114]–[116]. This kind of models is found in the recent works of Haidemenopoulos et al. [12], [86], [117], [118]. Some other SIMT models can be implemented in full-field schemes. These improvements allow for a detailed description of the SIMT sensitivity to applied 3D stress tensor (not only triaxiality) [87], [88], [119]. Moreover, some strain-rate sensitive models are also developed in the literature [120], [121]. All those models are acknowledged and detailed in the Appendix C of this manuscript.

These models are not presented in the main text of the manuscript since they have the common downfall to rely on the calibration of numerous parameters, which is usually not done on physical basis. While full-field models allow for the description of more subtle physical phenomena, the goal of the PhD thesis is to obtain a microstructure-based description of the thermomechanical stability of austenite. Therefore, it was chosen to use instead a mean-field model in the present PhD, as 3D full-field models cannot be parametrized on microstructure basis. When comparing Perlade's and Haidemenopoulos' approaches, there are fewer and more microstructure-linked parameters in

the former. Thus, the theory employed to model SIMT in the thesis project will be a continuation of Perlade's one, explain why the description of the other models is only found in Appendix C.

This section of the bibliographic report highlighted the numerous models existing for SIMT. The empirical models found in the literature allow for a quick evaluation of austenite mechanical stability, making it a function of one parameter only. However, they lack of the predictive nature necessary to model mechanical behaviour of any given TRIP steel. The seminal work of Olson and Cohen on SIMT has been detailed. One extension of the OC theory developed by Perlade et al., suitable for mean-field scheme, has been detailed. Other mean-field (Haidemenopoulos et al.) and full-field models, inspired or not by OC framework, are acknowledged in Appendix C, alongside the numerous advantages and disadvantages of those models compared to the selected mean-field scheme.

To model SIMT, it is necessary to simulate austenite mechanical behaviour, and thus the load transfer between the constituting phases of the steel. The next sections are dedicated to the different approaches used to model the mechanical behaviour of a composite materials such as the medium Mn steels, based on the behaviour of individual phases, namely ferrite, austenite and martensite in this work. A last part will focus on the modelling of TRIP effect itself with a special attention paid to both Greenwood-Johnson and Magee effects.

5. Mechanical properties of medium Mn steels

Mean-field TRIP micromechanical models found in the literature [8], [12], [117] predict the macroscopic mechanical behaviour of metastable multiphase steels under mechanical loading by calculating first the respective flow stress in each constituting phase in response to an applied deformation. Then, the stress and deformation state of austenite are used to calculate the progress of SIMT. Finally, all the information is gathered to calculate the global response of the steel. This section is dedicated to the explanation of the step-by-step functioning of TRIP models, starting with the possible homogenization schemes based on phase scale mechanical description, and finishing by the TRIP effect. For the modelling of the martensitic transformation, please refer to the previous sections.

A. Homogenization laws for multiphase materials

The prediction of the mechanical behaviour of multiphase materials, knowing the behaviour of constituting phases, is a topic of first importance in materials science, and especially in metallurgy; This is called the problem of homogenisation. Different methods exist to perform such calculations, depending on the level of accuracy needed

The most important distinction to be made is between medium field models (mechanical quantities are averaged to a phase scale, in 1D or 3D) or local field models (mechanical quantities are explicitly calculated at different points in a given phase, generally in 3D). They may or may not take into account particular neighbourhood effects when, for example, working on a representative basic volume of microstructure or considering only an average environment (in the case of self-consistent approaches). In short, there is a wide variety of models. Without being exhaustive, the most common models are:

- Mean field models: This class of model relies on Hill's theory which show that the macroscopic stress and strain is the sum of the individual phase stresses and strains weighted by their respective phase fraction. Additional assumptions are added to described the interactions between phases. The boundaries of the problem are given by the so-called iso-stress and iso-strain assumptions, in which the stress or the strain respectively is supposed to be equal among the phase of the materials. In elasticity, the iso-stress hypothesis is called the Voigt assumption and the iso-strain one is called the Reuss assumption. In plasticity, they are respectively named after Taylor and Sachs. Those approaches are from being realistic except if the microstructure is suitable

- Other possible localization law can be proposed using experimental data [122], using a self-consistent framework [123], or using the Eshelby inclusion model, considering the Mori-Tanaka correction, with local elasto-plastic behaviour [84], [124]. Those methods rely on more complex calculations or arbitrary fitting parameter. A more recent method belonging to this category was developed by Bouaziz and Buessler [125], the iso-work assumption. Under this hypothesis during mechanical loading, each phase is supposed to have the same incremental work. By comparing it to iso-stress, iso-strain and self-consistent, the authors highlight a good agreement between the iso-work and self-consistent approach at a lower calculation cost

- Local Field methods are often based either on FE method or on FFT solving schemes, finite element relies on heavy computation to model the microstructure REV (Representative Elementary Volume) [111], [118], especially when conducted on 3D, but have the advantage of considering the spatial, topological and morphological distribution of the phases and their neighbourhood effects, whereas mean field methods can only account for morphological effects. In this type of calculation, the implementation of metastable phases is also more complex.

Examples of modelling with iso-work assumption (mean field calculation in 1D) are given by authors working on 3rd generation TRIP steels (Perlade et al. [8], Seo et al. [126], Aristeidakis et al. [12]).. In the case of Q&P steels, with four phases taken into account (retained austenite γ, primary martensite α'_p, secondary martensite α'_s and fresh martensite α'_m), Hills' equations and iso-work assumption take the following form:

$$\boldsymbol{\sigma}(\boldsymbol{\varepsilon}) = \boldsymbol{\sigma}_{\gamma}(\boldsymbol{\varepsilon}_{\gamma})\boldsymbol{f}_{\gamma}(\boldsymbol{\varepsilon}_{\gamma}) + \boldsymbol{\sigma}_{\alpha'_p}\left(\boldsymbol{\varepsilon}_{\alpha'_p}\right)\boldsymbol{f}_{\alpha'_p}\left(\boldsymbol{\varepsilon}_{\alpha'_p}\right) + \boldsymbol{\sigma}_{\alpha'_s}(\boldsymbol{\varepsilon}_{\alpha'_s})\boldsymbol{f}_{\alpha'_s}(\boldsymbol{\varepsilon}_{\alpha'_s}) + \boldsymbol{\sigma}_{\alpha'_m}(\boldsymbol{\varepsilon}_{\alpha'_m})\boldsymbol{f}_{\alpha'_m}(\boldsymbol{\varepsilon}_{\alpha'_m}) \qquad \textbf{(I—22)}$$

$$d\boldsymbol{\varepsilon} = \boldsymbol{f}_{\gamma}d\boldsymbol{\varepsilon}_{\gamma} + \boldsymbol{f}_{\alpha'_p}d\boldsymbol{\varepsilon}_{\alpha'_p} + \boldsymbol{f}_{\alpha'_s}d\boldsymbol{\varepsilon}_{\alpha'_s} + \boldsymbol{f}_{\alpha'_m}d\boldsymbol{\varepsilon}_{\alpha'_m} \qquad \textbf{(I—23)}$$

$$\boldsymbol{\sigma}_{\gamma}d\boldsymbol{\varepsilon}_{\gamma} = \boldsymbol{\sigma}_{\alpha'_p}d\boldsymbol{\varepsilon}_{\alpha'_p} = \boldsymbol{\sigma}_{\alpha'_s}d\boldsymbol{\varepsilon}_{\alpha'_s} = \boldsymbol{\sigma}_{\alpha'_m}d\boldsymbol{\varepsilon}_{\alpha'_m} \qquad \textbf{(I—24)}$$

The first equation is the stress mixture rule, with σ and ε the macroscopic stress and strain, σ_i, ε_i and f_i the stress, strain and phase fraction of a given phase i. The second equation is the strain increment mixture rule, with ε the macroscopic strain. The third equation is the iso-work hypothesis. At this step of the simulation, each individual phase stress, the volume fraction of each phase and the macroscopic strain increment are known. Thus, the macroscopic stress is obtained. Also, each individual phase strain can then be calculated by combining previous formulae (i, j, k and h represent each phase):

$$d\varepsilon_i = \frac{d\varepsilon}{f_i + f_j * \frac{\sigma_i}{\sigma_j} + f_k * \frac{\sigma_i}{\sigma_k} + f_h * \frac{\sigma_i}{\sigma_h}} \quad \text{(I—25)}$$

To validate this approach, authors can calculate the hardening parameter n, or the stress-strain partitioning parameter β (for a two-phase composite), and compare them to experimental data:

$$n = \frac{\varepsilon}{\sigma}\frac{d\sigma}{d\varepsilon} \quad and \quad \beta = \left|\frac{\sigma_2 - \sigma_1}{\varepsilon_2 - \varepsilon_1}\right| \quad \text{(I—26)}$$

The parameter n is used to state when necking occurs with the Considère criterion (n=ε). When β is equal to 0, the composite is in iso-stress condition. When β is very huge, the composite starts to be close to iso-strain condition. Perlade et al. compared their model results on β to experimental measurements, as shown in Figure 30. At low macroscopic strain, the β parameter is huge, close to an iso-strain condition, while it becomes very low at higher strain. The good agreement between experiments and simulation shows that the iso-strain condition is relatively realistic. As it is also easy to implement compared to self-consistent/Eshelby methods, this method is ideal to conduct first order calculations or to be implemented in a model controlling an industrial production line [125].

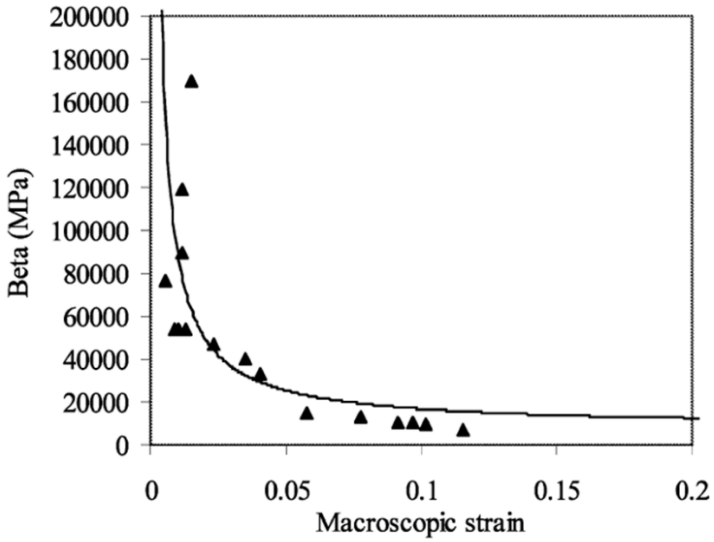

Figure 30: Comparison between the experimental (dots) and theoretical (line) stress-strain partitioning parameter β [8].

B. Transformation induced plasticity (TRIP)

The mechanically induced martensitic transformation has many impacts on the behaviour of the steel undergoing mechanical loading. In the case of steels, SIMT replaces a relatively soft austenite by a hard martensite, and affects mechanically the surrounding phases, inducing a hardening effect. SIMT also has a softening effect linked with the internal stress accommodation due to the volume expansion linked with the martensitic transformation and the variant selections of martensite laths. All these contributions lead to a dynamic work-hardening, which is called the TRIP effect. While the softening effect may become significant in fully austenitic steels, the additional strain remains small when compared to the strain due to applied stress during tensile test [127]–[129], as explained afterwards. Therefore, in the PhD thesis, only the hardening effect of TRIP effect will be accounted for.

A brief explanation of the softening effect linked with SIMT is given in this section. Two mechanisms have been developed in the literature to explain the softening contribution of the TRIP effect: the Greenwood-Johnson (G-J) effect and the Magee effect. These two effects may be considered in a latter version of the model.

In the Greenwood-Johnson approach [128], [130], the TRIP effect origins from the volume change occurring during austenite to martensite transformation. This volume change induces volumetric strain, which is accommodated by the softer mother austenite. If an external tensile load is applied, the plastic deformation will orientate with respect to the loading direction, as illustrated on Figure 31 [35]. The resulting plasticisation is then a superposition of the effect of the applied and internal stresses.

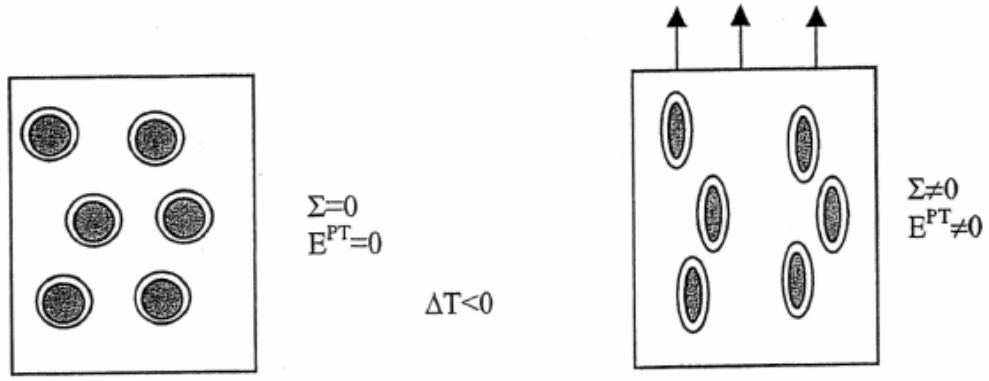

Figure 31: Representation of the Greenwood-Johnson effect, with Σ the macroscopic stress and E^{pt} the plastic strain [35].

Greenwood and Johnson propose to consider the transformation induced plasticity by adding a new term ε_{TRIP} to the macroscopic strain. In the authors' framework, a small uniaxial stress is applied on a steel which undergoes cooling. Considering a rigid perfectly plastic austenite, the authors found the following relationship to calculate the stress-induced strain:

$$\boldsymbol{\varepsilon_{TRIP} = \frac{5}{6}\frac{\Delta V}{V}\frac{\sigma}{\sigma_{\gamma}^{YS}}} \qquad \textbf{(I—27)}$$

where ΔV/V is the volume variation due to the transformation, σ the applied stress and σ_{γ}^{YS} the yield stress of austenite. This model has been proven to be only valid for small applied stresses [35], [131].

Several models have been developed afterwards to better represent the reality. They all take a similar form, based on three functions f, g and h [132]:

$$\boldsymbol{\dot{\varepsilon}_{TRIP} = f\left(\frac{\Delta V}{V}; \sigma_{\gamma}^{YS}\right) . g\left(f_{\alpha'}; \dot{f}_{\alpha'}\right) . h\left(S, \sigma_{\gamma/\alpha'}^{YS}\right)} \qquad \textbf{(I—28)}$$

with S the deviatoric part of applied stress. An example of this kind of law, often cited in the literature, is given in the work of Leblond [133]:

$$\boldsymbol{\dot{\varepsilon}_{TRIP} = \frac{\Delta V}{V}\frac{1}{\sigma_{\gamma}^{YS}\varepsilon_{\gamma}^{eff}} ln(f_{\alpha'})\, \dot{f}_{\alpha'}\, h\left(\frac{\sigma_{Mises}}{\sigma_{\gamma/\alpha'}^{UTS}}\right) S} \qquad \textbf{(I—29)}$$

where S is the deviatoric stress, σ_{Mises} is the macroscopic von Mises stress ($\sigma_{Mises} = (3/2\ S_{ij}S_{ij})^{1/2}$), $\sigma_{\gamma/\alpha'}^{UTS}$ the ultimate tensile stress of the martensite/austenite composite and $h(\sigma_{Mises}/\sigma_{\gamma/\alpha'}^{UTS})$ a correcting factor which highlights the non-linearity of transformation induced plasticity at high stress.

The second approach to explain transformation induced plasticity is proposed by Magee [129]. He emphasized that martensite can only develop under 24 variants. Without external stress, each variant will randomly appear, leading to no macroscopic shear. However, under applied stress, variants favoured by the added mechanical driving force will be selected, as shown in Figure 32. The martensitic needles will orientate with respect to the loading direction. Those microscopic shears will cumulate, inducing a macroscopic shear stress in the austenite, thus "plasticising" the austenite and contributing also to the macroscopic strain.

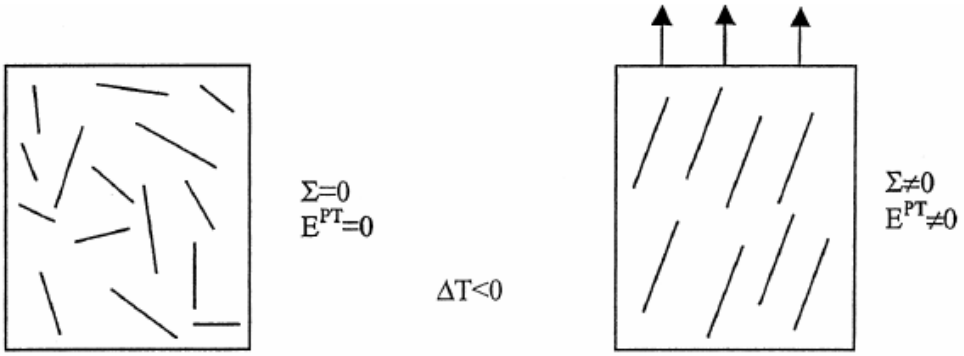

Figure 32: Representation of the Magee effect, with Σ the macroscopic stress and E^{pt} the plastic strain [35].

Magee effect can thus be seen as an orientation effect. Previously exposed Leblond model [133] does not take into account this effect, only modelling the accommodation process linked with Greenwood-Johnson effect.

Fischer et al. implemented a full-field micromechanical model of TRIP-aided steels into a finite element algorithm, calculating the evolution of each phase flow stress and the SIMT kinetics. The laws they used for SIMT are highlighted in Appendix C. They simulate the classical TRIP-test, consisting in a martensitic transformation under constant applied stress (here 80 MPa). The transformation kinetics was taken from experiments and went from 0 to 100%. The purpose of this simulation is to obtain information on TRIP strain ε^{TP}. The TRIP strain rate is calculated as:

$$\dot{\varepsilon}_{ij}^{TP} = \frac{3}{2} K \frac{d\lambda}{df_{\alpha'}} S_{ij} \dot{f}_{\alpha'} \qquad \text{(I—30)}$$

In Equation (I—30), K is the Greenwood-Johnson constant, λ a heuristic function of $f_{\alpha'}$. The direction 3 was chosen equal to the tensile direction. They first highlighted that the TRIP strain was not equal in all directions, even in the 2 and 1 directions, which are initially equivalent. Some shear strains also appear. Figure 33 highlights the decomposition of the strain ε_{33}^{TP} into an elastic straining, a Greenwood-Johnson contribution and a Magee contribution. First, the orientation effect is far more influential than the plasticization effect. Moreover, upon unloading, there is a diminution of the global TRIP strain. While the G-J contribution remains constant, the Magee term decreases. The authors explain this diminution by the apparition of two to three further variants oriented with respect to the internal stress state, leading to a self-accommodating effect. However, the additional strains due to TRIP effect remain small in this example, below 1.5% at 30% of transformation.

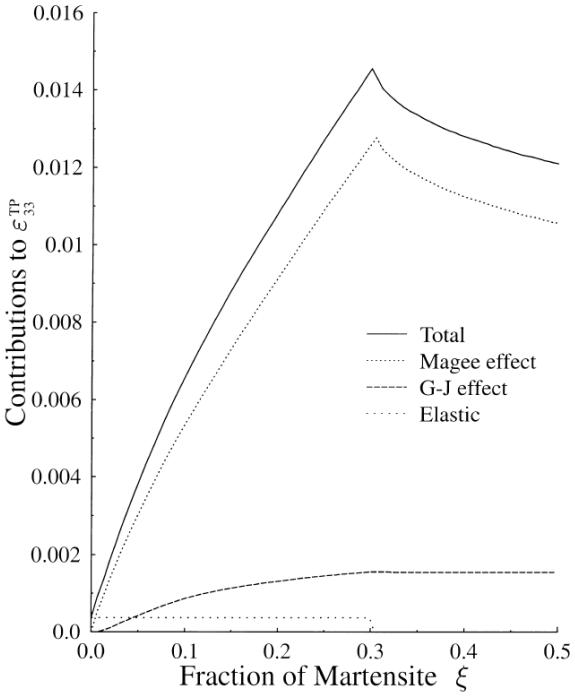

Figure 33: Contributions of the various deformation mechanisms to the TRIP-strain ε_{33}^{TP} in the tensile direction. Total unloading from 80 MPa [134].

Another approach to study the effect of the strain-induced martensitic transformation on mechanical properties of a TRIP steel is given by Dan et al. [127]. They work within an elastoplastic framework, using finite element simulations. The authors highlight the necessity of considering the volumetric strain $d\varepsilon_v$ besides the usual longitudinal true strain $d\varepsilon$ when calculating the necking strain. The criterium becomes:

$$\frac{d\sigma}{\sigma} = d\varepsilon - d\varepsilon_v \qquad \text{(I—31)}$$

Without considering the TRIP effect, the necking strain is 0.23 in the studied steel. Accounting for all those effects, the necking strain becomes 0.25, which is a negligible increase of 8%.

To summarize, two independent mechanical effects of SIMT exist in steels. The first is a hardening effect, due to the high level of martensite flow stress when compared with austenite. The second effect is a softening linked with Greenwood-Johnson and Magee mechanisms. While the softening effect may become significant in fully austenitic steels [128], [129], the additional strain remain small when compared to the strain due to applied stress during tensile test [127]. Therefore, in the PhD thesis, only the hardening effect of TRIP effect will be accounted for.

The final section is dedicated to a last specificity of the steels studied in this PhD, i.e. the mechanical instabilities (Lüders and Portevin-Le Chatelier effects) due to static strain and dynamical strain ageing mechanisms affecting the constituting phases of the steels.

6. Mechanical instabilities in medium Mn steels

The good mechanical performances of Medium Mn steels are undermined by the presence of mechanical instabilities often reported in literature, such as Lüders bands [135]–[137] and Portevin-Le Chatelier effect (PLC) [108], [138]–[140]. Those phenomena reduce the potentials of these steels for the automotive industries, as deformation bands forming during stamping processes of sheets could make the part mechanically unreliable during crash test (local thinning), as shown in Figure 34. The PLC effect is also accompanied by a negative strain rate sensitivity, which lower the crash performance of the steel.

Hence, it is important to understand the underlying mechanisms behind those instabilities, like static strain aging (SSA) and dynamic strain aging (DSA). The effect of both phenomena on a tensile curve is presented in Figure 34. On this single curve, the SSA induces the yield point phenomenon, which is the abrupt drop of stress at the end of elastic domain, permitting to define an upper and lower yield point. The SSA also creates the Lüders plateau (the flow stress does not increase and remains at the level of the lower yield point during a significant deformation step). The DSA explains the PLC effect, which corresponds to the apparition of serrations on the tensile curve during yielding.

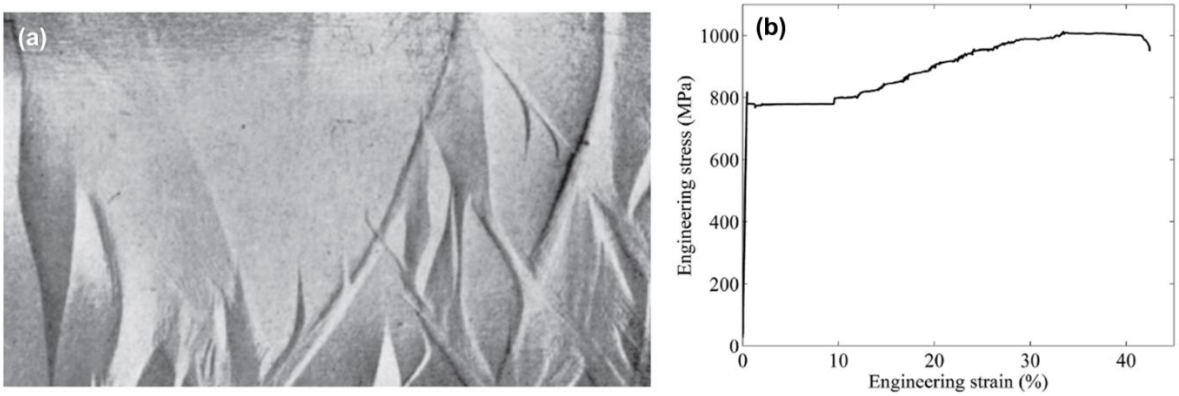

Figure 34 : (a) PLC bands formed in an Al-Cu alloy plate by shape-forming processes [141]. (b) Typical effect of mechanical instabilities on a tensile curve of an UFG medium Mn steel [142]. The SSA leads to the yield point phenomenon and the Lüders plateau, while the DSA causes the serrations observed during plastic deformation.

The SSA and DSA are classically both related to the formation of “Cottrell” atmosphere on dislocations, i.e. the pinning of dislocations by carbon segregation. The first phenomenological explanation of Lüders and PLC bands has been given in 1949 by Cottrell and Bilby [143]. In solid solutions, hydrostatic stresses generated by edge dislocations can be relieved by atoms in substitutional solution. Hence, carbon and nitrogen atoms in steels will thus naturally segregate around dislocations. Cottrell and Bilby [66] have proposed for the first time the explicit form of interaction energy between a solute atom and an edge dislocation. Their model calculates the theoretical resolved shear stress necessary to unpin a dislocation from the carbon segregation, the so-called atmosphere, and then describes the avalanche process explaining the collective unpinning dislocations inducing the yield point phenomenon. They also estimate the formation rate of the atmospheres. This seminal work is the basis to understand phenomenologically SSA and DSA. The discussions will be mainly dedicated to the case of medium Mn steels and their specificities.

A. Static strain aging (SSA) and Lüders plateau

In single phase materials, like ferritic steels or some aluminium alloys, the pinning-unpinning theory of dislocations has been used to explain the Lüders phenomenon, also called discontinuous yielding [143], [144]. SSA leads to a hardening of the materials due to the pinning of dislocations by solute atoms. Discontinuous yielding at the end of elasticity occurs when an unpinning avalanche process takes place in one region of the specimen, leading to a significant local softening (dislocations are freed from their carbon atmospheres) and the nucleation of a strain localization, called the Lüders' band. The band will then propagate by unpinning dislocations in an adjacent area. Usual method that allows tracking Lüders bands consists in full-field strain measurement technique (such as digital image correlation (DIC)), thermographic technique (like IR camera measuring local temperature increase due to plastic strain) and magnetic flux measurement technique [141], [145]–[147]. Those techniques are also used for PLC bands analysis, as detailed in the next section.

From a micromechanical point of view, discontinuous yielding can be observed in a steel only if it presents a low density of mobile dislocations before deformation and if there exists a mechanism for rapid dislocation multiplication [148]. The effect of work-hardenability of materials on Lüders bands has been studied by Ma et al. [149] in the case of a Fe/0.14C/7.14Mn/0.23Si cold-rolled medium Mn steel. They modified the work-hardenability of the steel by increasing the temperature of deformation, which stabilizes retained austenite (f_γ^0=33%). Figure 35 (a) shows the tensile curves of the studied steel at different temperatures. The black curve corresponds to the behaviour at 25°C and shows a typical Lüders plateau followed by PLC serrations during yielding (T_{test}=25°C). The corresponding evolution of the equivalent strain rate distributions across the sample measured in situ by DIC during the tensile test is reported in Figure 35 (b). At 250s, the Lüders band nucleates. It will then propagate across the specimen until 1125s, which is a typical behaviour of steel presenting SSA. Then, between 1250s and 2250s PLC bands nucleate and propagate. At 100°C, the absence of work-hardening, combined with a low density of mobile dislocations, lead to the nucleation of a Lüders band which does not propagate, as shown in Figure 35 (c). This phenomenon induces a premature fracture of the specimen, as shown by the blue tensile curve in Figure 35 (a) (T_{test}=100°C).

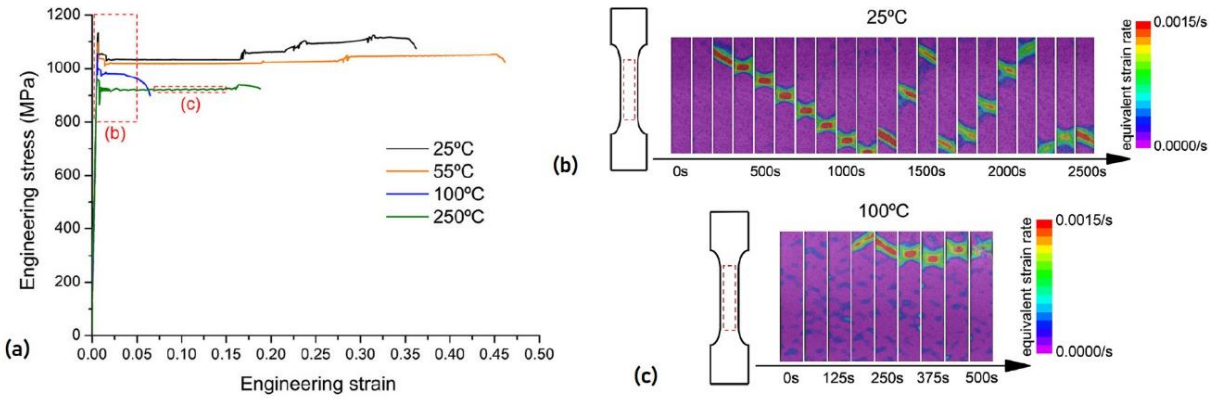

Figure 35: (a) Tensile curves of a Fe/0.14C/7.14Mn/0.23Si cold-rolled medium Mn steel, deformed at different temperatures (between 25°C and 250°C). The local strain rate maps measured in situ by DIC during tensile testing are reported for 25°C (b) and 100°C (c) for different times. Figures are extracted from [149].

Sun et al. [148] studied the discontinuous yielding of a Fe/0.2C/10.2Mn/2.8Al/1Si (wt%) UFG medium Mn steel. In their case, the matrix is austenitic (65%). The authors have controlled the stability of austenite by increasing the intercritical annealing time. In their investigations, they conducted in situ HEXRD experiments during tensile test, using in situ magnetic measurements correlatively with DIC observation, post-mortem EBSD and electron channelling contrast imaging (ECCI). They argued that Cottrell unpinning mechanism cannot be the primary explanation for mechanical instability in such steel, since there is no dependency of the yield drop on the phase fractions. They claimed that α-γ interfaces play a major role in the rapid multiplication of mobile dislocations necessary to nucleate Lüders bands, as highlighted in Figure 36, due to the stress concentration at interfaces and the difficulty to generate dislocations with Frank-Read mechanism in UFG materials [148], [150]. The nucleation of dislocations at interface occurs at a higher stress than dislocation gliding [151]. Combined with a high density of sources, this provides a similar effect to the collective unpinning in regular Cottrell mechanism. The low density of mobile dislocations is explained by the sub-micron size of grains [152], [153]. Moreover, Han and Lee [154] found that the intercritical annealing greatly reduces the density of mobile dislocations in cold-rolled UFG medium Mn steel, contrary to ART processed medium Mn steel which presents a high density of dislocations. This importance of interface between ferrite and austenite can also explain why Lüders instability is not found in steel containing large bands of δ-ferrite, in which the density of interfaces is much lower [40], [155]–[157]. The previous theory remains however controversial and is not accepted by the totality of the scientific community.

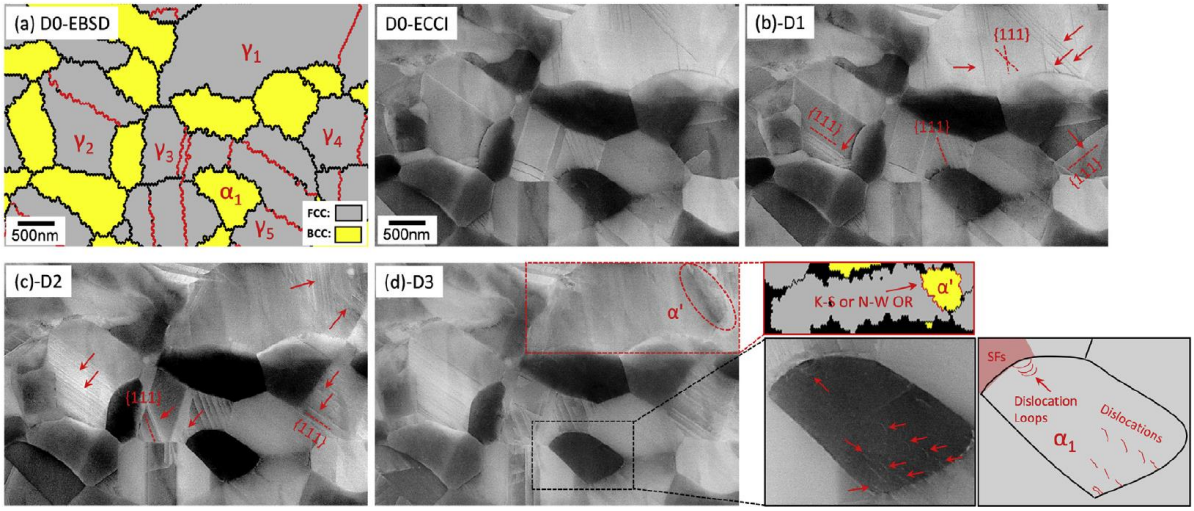

Figure 36: Microstructural evolution of a medium Mn steel during an in-situ three-point bending test. (a) EBSD map (yellow = ferrite, grey = austenite) and ECCI micrograph in the undeformed state. On the EBSD map, red lines correspond to twin boundaries. (b) (c) (d) Evolution of ECCI images of the same area with increasing strain. Red arrows indicate the formation of stacking faults and dislocations [148].

In another article, the same team studied the effect of carbon segregation in α-γ interface on Lüders nucleation [158]. They modified the cooling condition after the intercritical annealing. When samples are water-quenched, carbon is partitioned between ferrite and austenite, but no carbon enrichment of interfaces is found. When samples are air-cooled, the α-γ phase boundaries are greatly enriched in C (C_α = 0.1 at%, C_γ = 0.5 at%, $C_{\alpha\text{-}\gamma}$ = 1.5 at%). This enrichment increases the energy barrier for dislocation nucleation at α-γ interfaces, hence increasing the global yield strength and Lüders elongation of specimens. Overall, the physical origin of instabilities in 3rd generation AHSS remains

unclear in the literature. Even if some theories are under development, the underlying phenomenon is still at the centre of debate.

In medium Mn steels, mechanically induced martensitic transformation can affect discontinuous yielding. According to Sun et al. [148], strain-induced martensitic transformation does not affect directly the nucleation of Lüders bands. However, strain-induced martensite forms inside the bands, providing substantial local work hardening rate (TRIP effect), thus sustaining the band velocity. The necessity of strain-induced martensitic transformation for the propagation of Lüders band is also suggested by Ryu et al. [159]. On the contrary, in a Fe/0.12C/7Mn/0.3Si medium Mn steel, Wang et al. [142] observed that Lüders band formation and propagation can occur without any martensitic transformation. In their case, martensitic transformation increases the strain rate inside the band. Ma et al. [136] analysed the displacement of Lüders band bearing a strain of 16%. In the first step of deformation, between 0% to 10%, significant martensitic transformation occurs, while it becomes negligible between 10% and 16%. Thus, they conclude that martensitic transformation has only an indirect effect on the strain hardening ability that supports the propagation of the band, by increasing the density of geometrically necessary dislocations (GNDs) in the ferritic matrix.

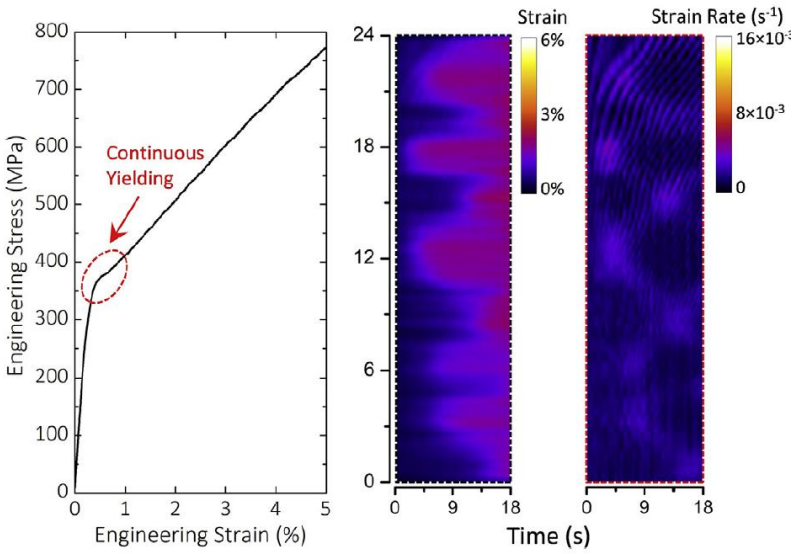

Figure 37: Tensile curve and the corresponding time evolution of the local strain and strain rate all along the specimen obtained by DIC, in a sample presenting a high fraction of stress-induced martensite. Note that even though the yielding seems continuous, there are still some strain rate localizations [148].

For steelmakers, an important topic is to master the appearance of Lüders bands. Sun et al. [148] showed that stress induced martensitic transformation does not occur uniformly across the sample. The part of austenite that transformed during the elastic regime provides potential sites of nucleation for Lüders bands, as the transformation provides fresh mobile dislocations, thus promoting plastic flow. By increasing the duration of the intercritical annealing, thus destabilising the austenite, authors succeed in suppressing discontinuous yielding, as shown in Figure 37. For cold-rolled UFG medium steels, recrystallization occurring during intercritical annealing can also greatly reduce the density of mobile dislocations available in ferrite. By adding Mn in their steel and reducing the duration of the intercritical annealing, Yan et al. [160] have been able to slow down recrystallization processes and suppress the Lüders' plateau. Finally, for cold-rolled UFG and ART medium Mn steels, a crucial parameter is the intercritical annealing temperature T_{IA} of intercritical annealing. Luo et al. [13] have proven that by increasing T_{IA} , it is possible to partially or totally suppress the Lüders instability, as

shown in Figure 38. They worked on two medium Mn steels, a Fe/0.1C/5Mn and a Fe/0.2C/5Mn. For both compositions, they manufactured cold-rolled UFG and fibrous ART steels with different intercritical annealing temperatures T_{IA}. As shown in Figure 38, they succeeded in suppressing Lüders instability in the ART steel by increasing T_{IA}, while reducing it in the UFG steel. This is due to the presence of more fresh martensite in the microstructure after the final cooling [18] (the martensitic transformation causes a plastic deformation in austenite and ferrite and lead to the formation of mobile dislocations). Their study also highlights that the globular UFG steels are more prone to endure mechanical instabilities than ART steels for a given intercritical annealing temperature.

The mechanical behaviours of Luo et al.'s steels [13] are very similar to the ones of the steels studied in this PhD project, which are detailed in Chapter III of this PhD manuscript. Our steels often show PLC banding. This kind of instability is discussed in the next section.

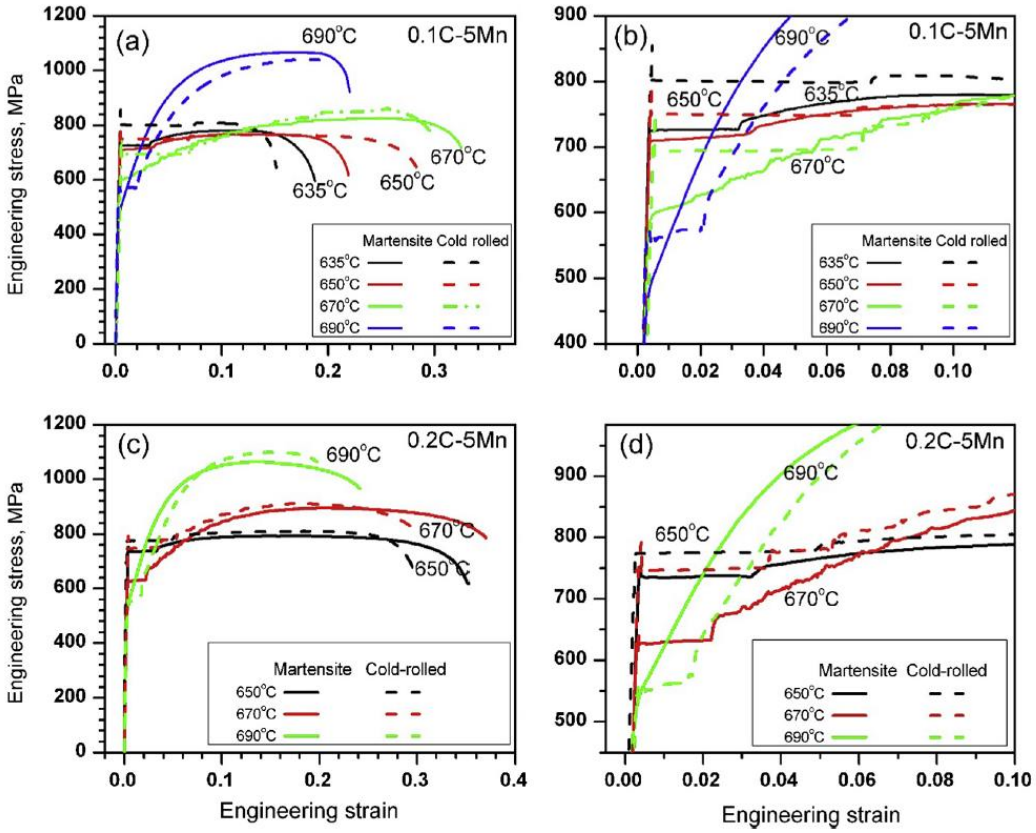

Figure 38: (a) and (c) Tensile curves of medium Mn steels with either a martensitic (continuous line) or a cold-rolled (dotted line) microstructure prior to intercritical annealing (fibrous or UFG morphologies). Two compositions are investigated (Fe/0.1C/5Mn and Fe/0.2C/5Mn). For both compositions, different intercritical annealing temperatures are investigated. (b) and (d) Magnification of the beginning of the curves to put into light the Lüders' plateau [13].

B. Dynamic strain aging (DSA) and Portevin-Le Chatelier effect (PLC)

SSA implies the impingement of dislocations by carbon atoms, DSA corresponds to a dynamic and repeated pinning of mobile dislocations by mobile Cottrell atmospheres. It appears when the velocities of dislocations are of the same order of magnitude as the rate of diffusion of interstitial

atoms (carbon for steels). A competition in fact takes place between carbon diffusion and dislocation mobility [107], [143], [161]. The pinning-unpinning mechanism of dislocations by carbon will locally change the hardening of materials, leading to a non-uniform deformation. Though carbon bulk diffusion is far lower in austenite at room temperature than dislocation velocity, in medium Mn steel, DSA may be sustained by long-range pipe diffusion of carbon, induced by the high density of non-mobile dislocation in both UFG and ART steels [162]. DSA is supposed to explain the negative strain rate sensitivity encountered in most of materials affected by PLC. Nevertheless, there is still debate on the actual phenomenon at the origin of PLC in medium Mn steels [41], [141], [144]. Other mechanisms have been proposed to explain the negative strain-rate sensitivity. Picu [163] proposed for instance that solute clusters could form on forest dislocations, which would modify the strength of junctions between forests and mobile dislocations. In this case, the negative strain rate sensitivity arises from the increased clustering of solute elements when the residence time of the dislocation forests increases. Other authors suggested that PLC appears due to interactions between dislocations and Mn-C clusters [140]. Finally, some authors explained that the negative strain rate sensitivity is directly linked with the effect of adiabatic heat stabilizing the retained austenite and thus reducing the work hardening rate [106].

The PLC effect is namely the apparition of serrations on tensile curve in the plastic domain, which is linked with a localization of strain occurring during yielding. From a macroscopic stance, during tensile testing, strain rate localization domains in the form of inclined bands will appear, grow and move during yielding. By extension, these macro-deformation bands linked with PLC effect are referred as PLC bands. The bands are usually few millimetres wide, inclined at 55° from the tensile direction for thin product and propagate following different patterns [141]. The angle of inclination depends on the specimen geometry. The propagation pattern of mechanical instabilities defines the type of PLC. The type A, type B and type C PLC are represented in Figure 39 taken from [141], alongside their main characteristics (occurrence and behaviour). They are the main types of PLC encountered in metallic alloys, although some exotic other types of PLC have been described in the literature (types D and E PLC for instance [146], [164]). Type A PLC corresponds propagating bands, that move across the tensile specimen. Type B PLC is characterised by non-propagating bands. The propagation of local strain rates is assured by the nucleation of new bands in the region of the specimen adjacent to the fading band. Finally, type C PLC occurs when bands do not propagate and rather nucleate randomly across the tensile sample.

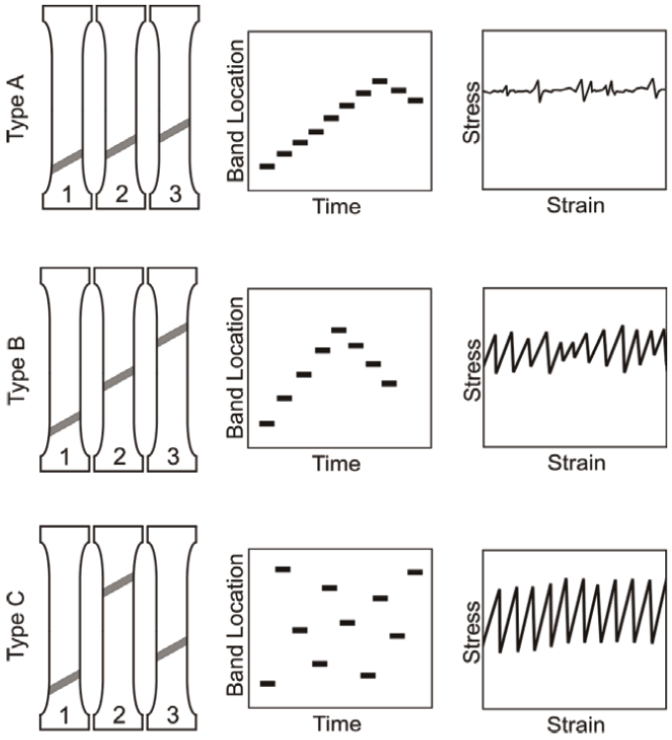

Figure 39: Schematic representation of strain band evolutions across the specimen during tensile test, spatiotemporal organisation and consequences on the tensile curves of type A, type B and type C PLC bands [141].

DIC analysis has been correlated with thermal field measurements by Wang et al. [145] in a Fe/0.14C/7Mn/0.23Si medium Mn steel to obtain an in-situ characterization of PLC band velocity, band width, local strain rates and temperature increments. The strain evolution and heat source evolution maps are shown in Figure 40 (a) and (b). Stage I corresponds to the elastic domain, stage II to a Lüders plateau and stage III to the latter plastic domain. The heat source generation is derived from the measured thermal field, calculated with a discretized heat equation with a source term. From those measurements, they observed that PLC bands width is nearly constant, around a mean value of 1.75 mm. The maximum temperature difference between the sample and the room is 8°C. Considering the axial strain ε, which is the mean value of strain across the sample, they find a linear relationship between ε and the bands velocity V_{PLC}.

Most interestingly, Wang et al. [145] compared the heat Q_P generated by plastic work W_p, assuming a linear relationship between them (assuming a Taylor-Quinney factor of 0.9), and the total heat Q_{tot} determined with IR camera. During stage II, Q_{tot} was 56% superior to Q_p, which can be explained by the exothermic martensitic transformation (austenite fraction f_γ decreases from 29% to 9%). On the contrary, during stage III, both values are very comparable, with only a difference of 2.6%. Experimentally, it is reported that local strain in a given Lüders/PLC band is neither space-dependent nor time-dependent during its propagation, meaning that the strain inside a given band is not a function of time or space [145].

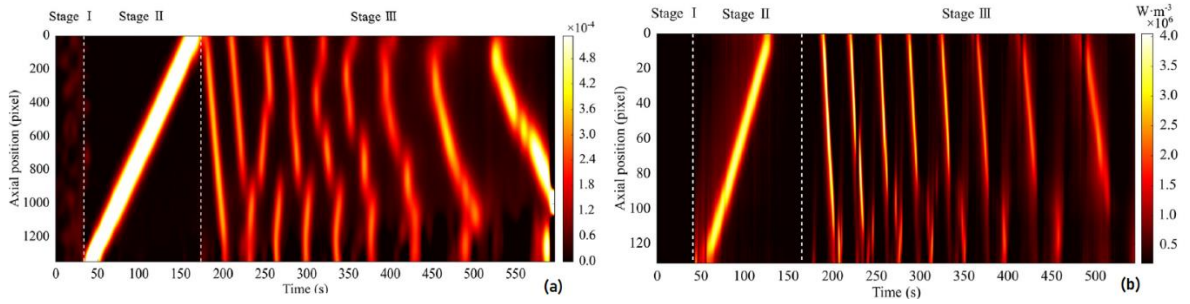

Figure 40: (a) Evolution of the incremental axial strain all along the sample during the tensile test. (b) Evolution of 1D heat source all along the specimen derived from the temperature field measurement during the tensile test [145].

Strain induced martensitic transformation (SIMT) occurs in conjunction with PLC bands [138]. The interaction between both phenomena is still unclear [147]. Callahan et al. [108] quantified by in situ magnetic measurement the evolution of mechanically induced martensite phase fraction during tensile tests. Their results, shown in Figure 41 (a), are representative of the transformation occurring in the analysed area. When the PLC bands come across the analysed part of the specimen, a huge increase in the local martensite phase fraction occurs, explaining the step-like shape of kinetics. Callahan et al. [10], [117] showed that the mean martensite phase fraction all along the specimen can still be obtained by fitting the local phase fraction evolution with theoretical curves like Olson-Cohen as seen in Figure 41 (a) with the dotted curve. Callahan et al. also work on link between SIMT and PLC. They quantified the austenite stability using the empirical law of Matsumura, which is dependent of one parameter k_s (denoted k in their work) as explained in (I—11) from section I.4.A. The higher k_s is, the more unstable austenite is. Concurrently, DIC was used to assess the presence of PLC banding, and the type of the PLC. By testing medium Mn steels intercritically annealed at 3 different temperatures, and strained at 3 strain rates between 10^{-2} s^{-1} and 10^{-4} s^{-1}, they have been able to map the domains of occurrence of PLC as a function of strain rate and austenite stability. They have also specified the type of PLC as a function of the strain-rate and austenite stability. According to them, austenite has to be rather stable (k below 10) for the medium Mn steel to endure PLC effect. The link between SIMT and PLC remains complex and it is still a controversial topic in the literature, with no unifying theory. Some authors suggests that the mean stability of austenite is not the main driver for PLC to occur, but highlights the necessity of inhomogeneity in austenite composition (stability) for the steel to shows serrated flow [71].

For PLC effect to occur, it is necessary that the material presents a negative strain rate sensitivity [144]. The mathematical relationship between negative strain rate sensibility and PLC has been first explained by Penning in 1972 [164] by demonstrating that the negative strain sensitivity creates a range of forbidden strain-rates. If the machine imposes a nominal strain rate in this forbidden range, the material will be forced to deform at two allowed strain rates, one higher and one lower than the nominal strain rate. Due to different work-hardening rates in the different parts of the material, macro-deformation bands will appear and propagate.

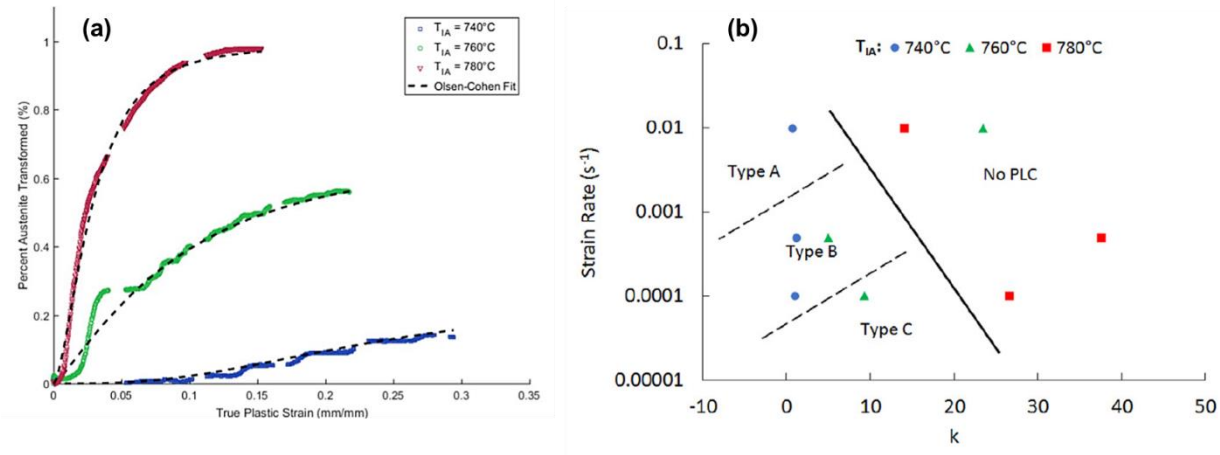

Figure 41: (a) Evolution of strain-induced martensite phase fraction during tensile testing, for UFG Fe/0.2C/5Mn/2.5Al steels annealed at various intercritical temperatures T_i. The Olson-Cohen fits appear in dotted line [108]. (b) Domain map of occurrence of PLC as a function of the strain rate and the austenite stability. The parameter k_s (denoted k in Callahan et al's work) quantifies the mechanical austenite stability.

Since then, to model both Lüders and PLC mechanical instabilities at the scale of SSA and DSA mechanisms (i.e. at dislocation scales), more complex mathematical models were developed, based on the introduction of waiting time and ageing time, which are respectively the times during which dislocation stops moving and being aged due to solute atoms diffusion [165], [166]. While diverse methods are concurrently developed to model at the same time the negative strain rate sensitivity of austenite, the mechanical behaviour of multicomponent materials and the mechanically induced martensitic transformation [110], [147], [167], one recognized theory to model the austenite negative strain rate sensitivity is the KEMC model, named after Kubin, Estrin and MacCormick [165], [166]. While the complete modelling of mechanical instabilities exceeds the scope of the PhD thesis, a simplified version of the KEMC model will be used to model SSA, as detailed in the Chapter IV of this manuscript.

7. Purpose of the thesis in relation with the literature review

The bibliographic report has highlighted the mechanisms of formation of the medium Mn microstructures produced through intercritical annealing. The morphogenesis of both globular UFG and fibrous ART microstructures have been detailed, giving insight into the microstructural, morphological and crystallographic features of the duplex steels studied in the thesis. The conditions of the existence of chemical gradient inside each phase of the medium Mn steels have also been detailed.

An important factor for the study of martensitic transformation is the stability of the mother austenite. This stability has been studied in regards with the contributions of chemistry, residual and applied stresses, size, shape and environment/matrix.

The basic mechanisms concerning martensitic transformation were explained. It was shown how the martensitic transformation can have a thermal or a mechanical origin. The driving force triggering the transformation has a chemical and a mechanical component. This mechanical component highly depends on the stress state of the applied stress, i.e. on the triaxiality of the stress tensor. If the austenite is deformed plastically, new sites of nucleation can also appear at the

intersection of shear bands. The literature review has also been the occasion to highlight the numerous models existing for SIMT. Among them, the seminal work of Olson and Cohen on SIMT has been detailed. One extension of the OC theory suitable for mean-field scheme has been explained, that is the extension developed by Perlade et al. [8].

The different approaches used to model the mechanical behaviour of a composite materials such as the medium Mn steels, based on the behaviour of individual phases, namely ferrite, austenite and martensite in this work, have been reviewed. Different models for TRIP effect have been presented, noticeably highlighting both Greenwood-Johnson and Magee effects.

The mechanical instabilities (Lüders and Portevin-Le Chatelier effects) undermining medium Mn steels have been analysed in regards with the literature. While static strain and dynamical strain ageing mechanisms are commonly used to explain mechanical instabilities in most metallic compounds, the true underlying physical phenomenon provoking them in medium Mn steels is still under debate. The complex link between PLC and SIMT is not elucidated yet.

As said in the introduction, the PhD project aims at understanding the thermomechanical stability of austenite in medium Mn steel and to model it with a microstructure-based model. The materials and methods used in the PhD are explained at the beginnings of Chapters II and III.

To understand the different aspects of austenite stability, a single medium Mn composition of Fe/0.2C/4Mn/1.5Si/0.8Al has been chosen. Both globular and fibrous ART duplex structures are obtained through the intercritical annealing treatment of the steel either from a cold-rolled state or from a fully martensitic state. As shown in this bibliographic review, by varying the annealing temperature T_{IA}, it is thus possible to obtain different austenite states distinguished by their chemical composition, their morphology, their size and internal stresses. The Chapter II will be dedicated to the study of the formation of these microstructures mainly through high-energy X-Ray diffraction (HEXRD) experiments. Correlated with post-mortem SEM characterizations, it is possible to have a good understanding of austenite intrinsic stability before deformation.

Chapter III is dedicated to the experimental determination of austenite destabilization kinetics during deformation. HEXRD experiments during tensile tests have been conducted to measure in situ the strain induced martensitic transformation (SIMT) in different loading conditions. To understand these SIMT kinetics, the mean stress tensors in ferritic, austenitic and martensitic phases are determined in parallel using the $\sin^2\psi$ method and micromechanical calculations.

While giving precious insight on mechanical behaviour of medium Mn steel, true understanding of the relationship between microstructural parameters (alloying content, size, morphology, phase fraction) and austenite mechanical stability is only possible with the micromechanical model developed in Chapter IV. This mean-field model predicts the mechanical response of a medium Mn steel during a tensile test. This approach relied on the modelling of the respective behaviour of each constituting phase and on SIMT kinetics. The model is finally sensitive to the chemical composition of the phases, and their size

Chapter II

II. Formation of medium Mn microstructures

1. Materials and experimental setup

To quantify the underlying effects of morphology, grain size, chemistry and matrix nature on the thermomechanical stability of retained austenite, we have chosen to design model microstructures based on prior thermodynamical calculations. This alloy design will be first presented in this chapter, as well as the thermal treatments used to produce the studied microstructures.

High Energy X-Ray Diffraction (HEXRD) experiments have been conducted on synchrotron beamlines to study in-situ the microstructure formation in the studied steels along with thermal treatments. e.

This is the only technique allowing a real-time monitoring of the complex phase transformations processes. After data processing and sequential Rietveld analysis, such experiments enable determining the evolutions of phase fractions and lattice parameters all along the treatments. These latter parameters can be related to the chemical composition of the phases and their hydrostatic stresses. Eventually, the width and asymmetry of the diffraction peaks could reveal the defect density of the phases and their heterogeneity. The use of this technology in the case of Medium Mn steel is recent and the first publications date from 2019 [168], [169]. In the present work, only the fraction of the phases and their internal stresses will be analysed in detail.

This in situ work by HEXRD must be accompanied by post-mortem analyses by scanning electron microscopy (SEM) and wavelength dispersion spectroscopy (WDS)because HEXRD does not give access, for example, to sizes, micro-textures or even to the local compositions of the phases. These latter microstructural parameters of great importance when evaluating the stability of the residual austenite according to our bibliographic analysis (cf. Chap 1).

A. Design of “model” medium Mn microstructures

a) Choice of intercritical annealing temperatures based on thermodynamical calculations

For this thesis, eight microstructures have been specially designed to investigate the effect of retained austenite stability on the mechanical behaviour of medium Mn TRIP steels. All the steels in this study have the same nominal composition (in wt%): Fe/0.2C/3.94Mn/1.46Si/0.78Al. to ease the comparison and to allow a great versatility in the design.

To analyse the effects of morphology, 4 duplex steels with globular morphology and 4 duplex steels with fibrous morphology have been produced (cf. chap 1 for the definitions).

The medium Mn material used in the thesis was produced in a vacuum induction furnace. Then, ingots were heated at 1100°C for 60 min and hot-rolled a first time. Afterwards, they were cut into blocks and homogenized at 1200°C for 30h to reduce Mn segregation which is common in medium Mn steel. Decarburization was limited during the former thermal treatments by wrapping the blocks in stainless steel foil and placing them in C-steel boxes. The medium Mn plate-sheet was produced by hot-rolling the blocks to 3 mm after another isothermal holding of 30 min at 1200°C. Finally, the cold-rolled steel used in the thesis was obtained by doing a last intermediate annealing at 700°C for 10 min to reduce the hardness of the medium Mn plate-sheet followed by a cold-rolling to 1.5 mm. The cold-rolled microstructure consists of ferrite, cementite and few martensite/austenite films.

The annealing temperatures chosen in this thesis were selected from ortho-equilibrium thermodynamic calculations using the version 18.04 of CEQCSI software (Chemical EQuilibrium Calculation for Steel Industry), an ArcelorMittal in-house-built software (no commercial version available). The austenite and cementite equilibrium phase fractions for a Fe/0.2C/4Mn/1.5Si/0.8Al steel are plotted in Figure 42. According to these calculations, 620°C is the transition temperature between the biphasic α-θ domain to the triphasic α-γ-θ domain; 680°C is the transition temperature from the α-γ-θ domain to the biphasic α-γ domain; 830°C is the transition temperature from the α-γ domain to the monophasic γ domain. For a given composition, the equilibrium transformation temperature A_{e1} is defined as the temperature above which austenite starts to form at equilibrium, while A_{e3} is the lowest temperature at which the single phase austenitic structure is thermodynamically stable [170]. Therefore, the calculated Ae_1 and Ae_3 temperatures are thus respectively 620°C and 830°C. These values are further discussed later in this chapter and compared with the measured experimental phase fractions.

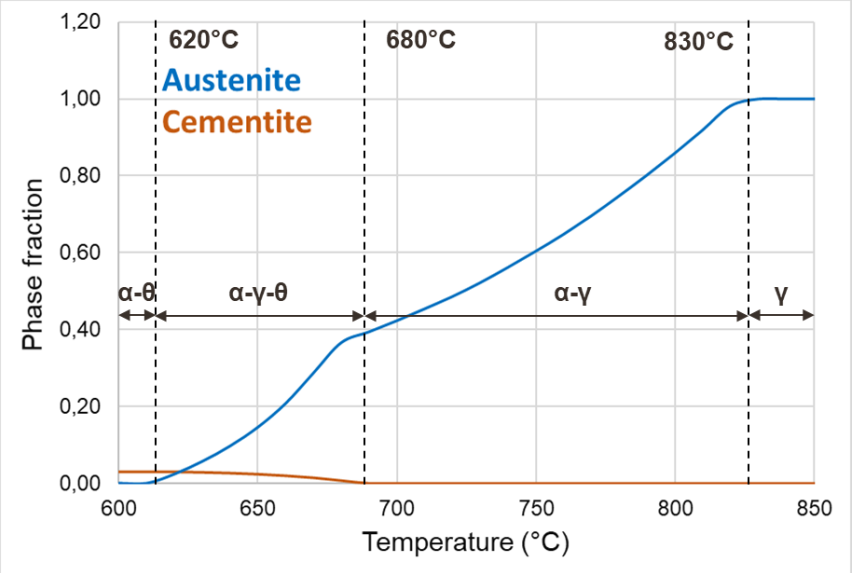

Figure 42: Austenite (blue) and cementite (orange) phase fractions expected at equilibrium as a function of the intercritical annealing temperature. Thermodynamical equilibrium calculations were conducted with CEQCSI software.

Based on the equilibrium calculations, the corresponding thermal treatments are detailed in Figure 43 and Table 2. To obtain fibrous ART microstructures, the cold-rolled steel sheet firstly

undergoes an austenitic annealing at 900°C (above Ae_3) during 5 min followed by a quench to room temperature to form a fully martensitic microstructure. Both initial microstructures are observed by SEM and the results are shown in the next section II.1.A.b). Then the sheet is annealed in the intercritical region and quenched to room temperature. During the intercritical annealing, austenite nucleates at martensite lath boundaries, according to the austenite reversed transformation (ART) mechanism. The newly formed austenite inherits the lath-like shape of its mother martensite, resulting in a fibrous microstructure. This thermal treatment will be referred as the "two-step" annealing. The temperature T_{IA} and time t_{IA} of intercritical annealing were modified to create varied austenite stability before the final quench. For all experiments, the targeted heating rate is 10°C/s, while the cooling rate is about -200°C/s. The higher the T_{IA} is, the more austenite is expected at the end of intercritical annealing. A higher amount of austenite is expected to be less enriched in C and Mn. The enrichment will depend on the expected compositions at equilibrium but also on thermo-kinetics considerations. The less chemical stabilized austenite formed at higher T_{IA} will transform into fresh martensite during final quenching as its M_s is above room temperature. At high annealing temperatures, the microstructures are no more ferrite- austenite duplex, but close to a dual-phase microstructure (ferritic matrix hardened by hard martensite/austenite islands).

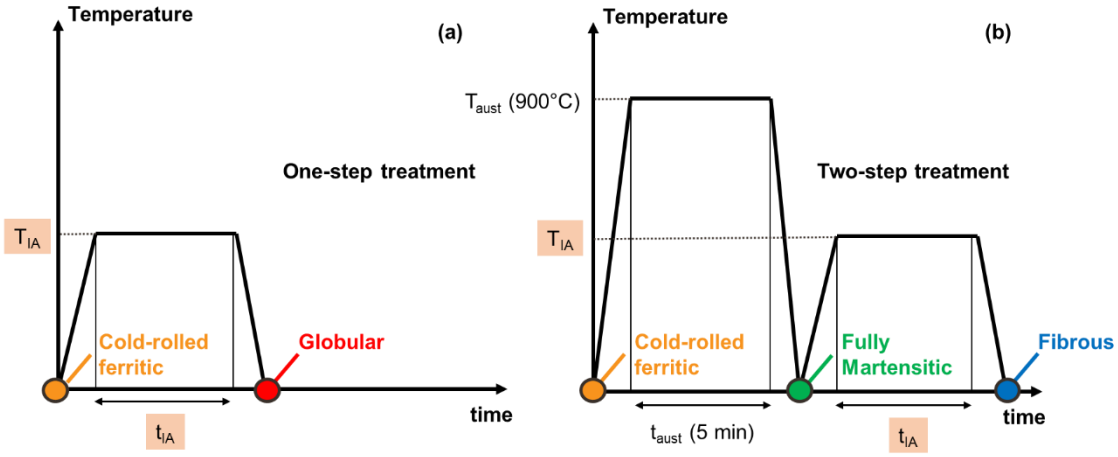

Figure 43: Schematic representations of the thermal treatments applied on the studied steel. (a) One step annealing to obtain globular cold-rolled UFG steels. (b) Two-step annealing to obtain fibrous ART steels. Values of parameters highlighted in orange can be found in Table 2 The initial microstructure state before all thermal treatments is cold-rolled ferrite-cementite-martensite.

The temperatures T_{IA} were chosen considering preliminary SEM analysis and thermodynamical calculations. They are summarized in Table 2, alongside the denomination and the different other parameters of the thermal treatments. The selected T_{IA} ranges between 680°C and 750°C, to obtain varied duplex steels with enough retained austenite. For example. Based on CEQCSI calculations, at T_{IA}=680°C, the calculated fraction f_γ is 36.2%, and at T_{IA}=750°C, f_γ = 60%. The time t_{IA} is adapted for the lowest intercritical temperature, as the kinetics of austenite formation is expected to be very slow at this temperature. Based on CEQCSI calculations presented above, the cementite phase fraction falls to zero above 680°C (included), hence the selected lowest T_{IA}. At 670°C, there is 0.7% of cementite. At 660°C, there is 1,4% of cementite and at 650°C, there is 2% cementite. Thus, the triple α-γ-θ domain is still very close to the lowest chosen T_i=680°C, and f_θ increases rapidly at a few degrees below this T_{IA}.

Microstructure denomination	Type of thermal treatment	T_{aust}	t_{aust}	T_{IA}	t_{IA}
GL680	One-step	n/a	n/a	680°C	30 min
GL700	One-step	n/a	n/a	700°C	15 min
GL720	One-step	n/a	n/a	720°C	15 min
GL750	One-step	n/a	n/a	750°C	15 min
FB680	Two-step	900°C	5 min	680°C	30 min
FB700	Two-step	900°C	5 min	700°C	15 min
FB720	Two-step	900°C	5 min	720°C	15 min
FB750	Two-step	900°C	5 min	750°C	15 min

Table 2: Numerical details on the 8 thermal treatments of the thesis, described in Figure 43.

In the fully austenitic state , the M_s temperature considering only the chemical effect can be calculated with van Bohemen's equation (X_γ represents the weight percent of element X in austenite) [171]:

$$M_s = 565 - 600\left(1 - exp\left(-0.96C_\gamma\right)\right) - 31Mn_\gamma - 13Si_\gamma - 10Cr_\gamma - 18Ni_\gamma - 12Mo_\gamma \qquad (II—1)$$

A value of M_s = 319°C was calculated for the Fe/0.2C/3.94Mn/1.46Si/0.78Al composition. This is a value very close to the experimentally measured one (320°C measured during HEXRD experiments conducted during the preparatory internship, results not shown).

The equilibrium compositions of austenite and ferrite as a function of intercritical annealing temperature, calculated using CEQCSI, are detailed in Table 3 and Table 4 respectively. Carbon and manganese are partitioned in the austenite, while aluminium and silicon partitioned in the ferrite, consistent with the literature review. With increasing T_{IA}, the carbon and manganese concentrations in austenite diminish, which leads to an increase of the M_s temperature of austenite. Hence, large fractions of fresh martensite are expected during the final quenching of samples annealed at 720°C and at 750°C when cooled down to RT (Ms >> RT).

Intercritical annealing temperature	C (wt%)	Mn (wt%)	Al (wt%)	Si (wt%)	M_s
680°C	0,537	7,4	0,619	1,44	45°C
700°C	0,464	6,66	0,631	1,45	95°C
720°C	0,404	6,02	0,650	1,46	140°C
750°C	0,327	5,27	0,682	1,47	195°C

Table 3: Composition at equilibrium in austenite in a Fe/0.2C/4Mn/1.5Si/0.8Al steel. Temperatures M_s calculated with van Bohemen equation [171] are also given.

Intercritical annealing temperature	C (wt%)	Mn (wt%)	Al (wt%)	Si (wt%)
680°C	0,006	2,01	0,904	1,51
700°C	0,006	2,02	0,924	1,52
720°C	0,006	2,06	0,942	1,52
750°C	0,006	2,03	0,980	1,53

Table 4: Composition at equilibrium of ferrite in a Fe/0.2C/4Mn/1.5Si/0.8Al steel.

b) Microstructure prior to intercritical annealing

SEM observations were conducted with a Quanta 650 FEG-SEM at IJL on the initial cold-rolled steel before any thermal treatment, and with a JEOL 7001 FEG-SEM at ArcelorMittal Maizières Research centre on the as-quenched fully martensitic state. In all cases, a solution of 4% Nital was used for etching.

i. Cold-rolled microstructure prior to one-step IA

The SEM observations of the initial microstructure, before intercritical annealing are reported in Figure 44. In (a), the magnification is ×2500, while it is ×5000 in (b). The microstructure is a cold-rolled microstructure containing carbides and a small fraction of austenite-martensite films in a ferritic matrix. The rolling direction is obviously horizontal as deformed phases are aligned in that direction. The dark-grey areas correspond to ferrite grains while the light-grey areas correspond to austenite-martensite γ/α'islands and the bright spots to cementite precipitates θ. A small fraction of austenite is formed during intermediate annealing at 700°C for 10 min of hot rolled sheets before cold rolling, as expected from equilibrium calculations and reported in Figure 42. During cold rolling with 50% reduction, most of austenite transform into martensite to form austenite-martensite films (SIMT). The microstructure is thus close to a highly deformed dual-phase microstructure containing carbides.

As θ and γ/α' appear in lighter contrast than ferrite α, it is possible to obtain an estimation of the fraction of ferrite with a direct thresholding. The method was implemented in python using ndimage library. Four images with a magnification of ×5000 were used. The approximate fraction of ferrite obtained with this method is about 80% to 85%. The ferrite phase fraction at 700°C at equilibrium is 58%. The cold-rolled microstructure is however not at equilibrium, since many cementite precipitates are still present in the steel, and the difference in ferrite phase fraction is surely due to kinematic aspect of the transformation.

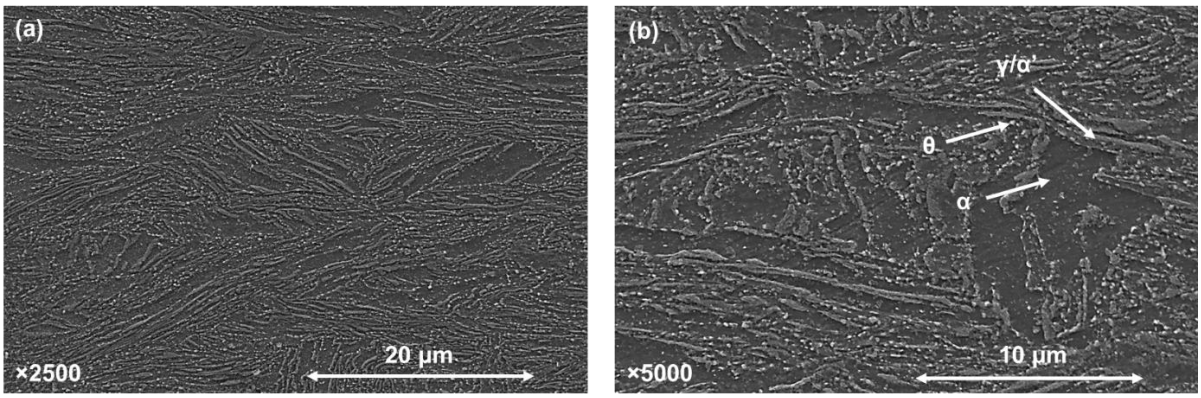

Figure 44: SEM micrographs of the cold-rolled steel (a) at a magnification of x2500 and (b) at a magnification of x5000. The rolling direction is horizontal. The black-grey areas correspond to ferrite, while the light-grey areas correspond to austenite-martensite elongated islands and bright areas to cementite particles.

ii. Martensitic microstructure obtained after the first annealing (two step annealing)

The SEM observations of the martensitic as-quenched microstructure, after the austenitization step and before intercritical annealing are reported in Figure 45. In (a), the magnification is ×2500. In (b), it is ×10000. The microstructure is fully martensitic, consisting of laths, as seen in Figure 45 (b). The literature review highlighted the hierarchical organisation of martensite in packets, blocks and laths (section I.3.A.b)). The different structures can be guessed in the two-secondary electron (SE) micrographs, though electron back-scattering diffraction (EBSD) should be used to really discern them based on their relative misorientations. The prior austenite grain boundaries (PAGB) are highlighted in orange and red for some grains in the two SE maps. The red contoured α' island is the same between maps. The PAGB are the boundaries of austenite grain at the end of the austenitization isothermal holding. While the PAGB are only a guess, they allow for an estimation of the mean grain size of prior austenite. Measuring the mean diameter of 40 martensite islands across 8 images magnified at ×2500, the values of prior austenite grain size range from 25 µm to 3 µm, with a mean value of 13 µm.

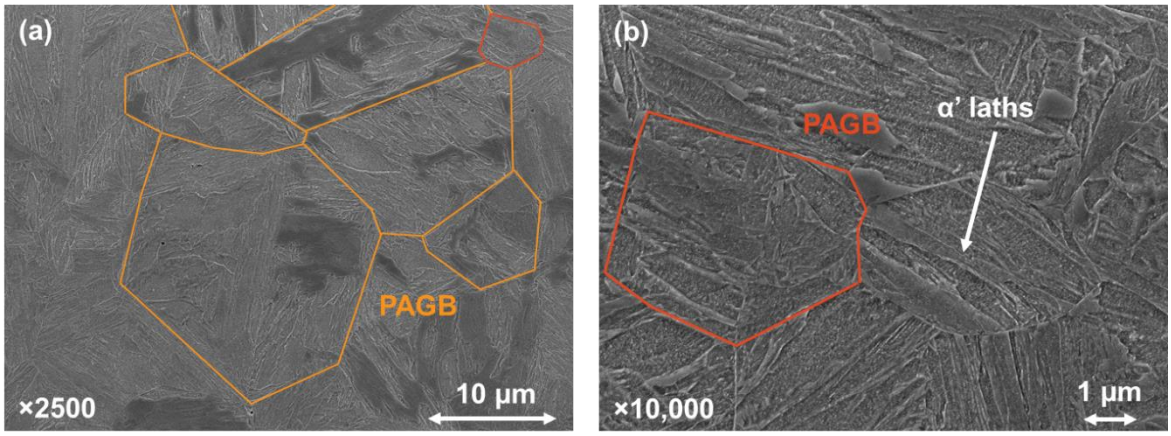

Figure 45: SEM micrographs of the martensitic steel (a) at a magnification of ×2500 and (b) at a magnification of ×10,000. The rolling direction is horizontal. The microstructure consists of martensite laths. PAGB correspond to the prior austenite grain boundaries (in orange and red). The red contoured island is the same between (a) and (b).

In the following, the intercritical annealing treatments designed in this section were performed in a dilatometer during high-energy X-ray diffraction (HEXRD) experiments for the eight model microstructures. The next sections are dedicated to the presentations of these HEXRD experiments and their post-treatments.

B. Setup of in situ HEXRD experiments to study microstructure formation

The experiments consist in performing the designed thermal treatments on a small sample of the studied steel and to follow in situ its phase transformations by simultaneously conducting high energy X-ray diffraction (HEXRD) experiments all along the treatments. In situ analysis refers to the analysis of an experiment that is conducted concurrently with the studied phenomenon (here, the evolution of the microstructures during thermal treatment). A post-mortem analysis is on the contrary a characterization of the final state (i.e. after the thermal treatment).

In situ high energy X-ray diffraction (HEXRD) experiments were performed on the P07 beamline at PETRA III at Deutsches Elektronen-Synchrotron (DESY), Hamburg, Germany in May 2021. A synchrotron X-ray monochromatic beam (500 x 500 μm^2) was used to conduct the powder diffraction measurements in transmission mode. The setup is represented in Figure 46 (a). The high energy (87.1 keV corresponding to a wavelength λ of 0.142344 Å) and a large 2D Perkin Elmer detector allow the collection of Debye–Scherrer diffraction patterns at high rate (up to 10 Hz), which is the key to monitor the metallurgical phenomena during heating and cooling sequences of the heat treatments. These heat treatments were conducted in a modified Bähr DI 805 A/D dilatometer. The temperature was measured with a thermocouple welded just above the diffracting volume to minimize the temperature gradients. The distance between samples and detector is about 1.2m.

The thermal treatments were performed in accordance with Table XX and Figure 43. Eight experiments have been conducted on the medium Mn steel to obtain four globular and four fibrous steels. Only intercritical annealing (IA) were simulated in situ in the dilatometer. The samples were provided by ArcelorMittal in the as-cold rolled state for the one-step treatment. The same samples were used for the two-step treatments, except that the first treatment (austenitization and quench) to obtain a fully martensitic microstructure was performed at ArcelorMittal Maizières research centre by a prior salt bath treatment. The austenitization step was not conducted in situ in the dilatometer to ensure that the time-resolve kinetics of microstructure formation of fibrous duplex steel during IA will be as close as possible to the ones used to conduct tensile tests in Chapter III.

Four diffraction patterns are shown in Figure 46 (b), (c), (d) and (e) obtained respectively for the cold-rolled steel, the as-quenched martensitic steel, the GL720 steel (i.e. at the end of the one-step treatment at T_{IA}=720°C) and the FB720 steel. In these diffraction patterns, each Debye-Scherrer ring corresponds to one diffracting plane family of one given constituting phase. For an X-Ray beam with a wavelength λ to be diffracted by a plane family with an interplanar distance d_{hkl}, it is necessary that the angle θ_B between the incident beam and its projection on any plane of the family (also called the Bragg angle) satisfies the Bragg's law [172]:

$$2\, d_{hkl} \sin(\theta_B) = n\, \lambda \qquad \text{(II—2)}$$

In Equation (II—2), h, k and l are the Miller indices and n is a natural number (other than 0) called the order of interference. Usually, the factor n is omitted in Bragg's law, as the n^{th} order for (hkl) planes is equivalent to the 1^{st} order for (h'k'l') planes, with h'=nh, k'=nk and l'=nl [172]. The randomly polycrystalline nature of the medium Mn steels ensures that for any (hkl) plane, there will be a grain that has the good orientation with regards to the incident X-ray beam for the Bragg's law to be satisfied. Hence, diffraction patterns consist of Debye-Scherrer rings.

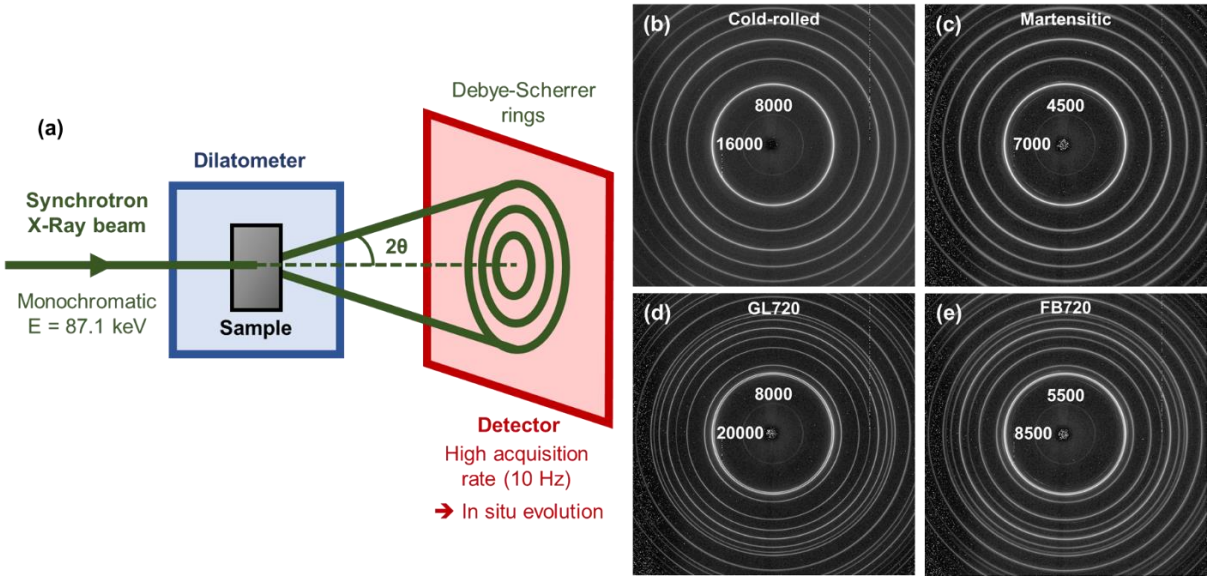

Figure 46: (a) Schematic representation of the experiments conducted at DESY synchrotron. In green is represented the incoming X-Ray beam produced by the synchrotron ring. This X-Ray beam will be diffracted by the sample (in grey) placed in a dilatometer (blue). The diffraction pattern consists of Debye-Scherrer rings and are recorded on a 2D flat detector (red). The actual diffraction patterns obtained for (a) the cold-rolled steel, (b) the as-quench martensitic steel, (d) GL720 steel and (e) FB720 steel.

In Figure 46 (b) and (c), all visible rings are related to the ferritic phase (either ferrite or fresh martensite), while in Figure 46 (d) and (e), twice as many rings are visible, related either to ferrite or to austenite. In both GL720 and FB720, a significant amount of austenite is thus stabilized during IA.

The intensity of the diffracted signal along a given ring is not perfectly uniform. This is highlighted for instance on the $\{110\}_\alpha$ ring (most intense ring), for which the mean values of pixels in the upper and left parts of the ring are given. For example, in the cold-rolled steel, in the upper part of $\{110\}_\alpha$ ring, a pixel has a value of 8000 a.u., while it is 16000 a.u. in the left part of the ring. The ratio of intensity is 2. This varying intensity along a ring is related to the existence of a crystalline texture in the microstructure at macroscopic scale. This is expected for the cold-rolled steel. It appears that the other steels also have a texture. For both as-quenched and FB720 steels, the ratio of intensity is lower (1.5), and higher for GL720 steel (2.5). This ratio should however not be overinterpreted, as it is a function of the varying phase fractions, relaxation of phases during annealing and also the non-uniformity of the synchrotron beam. It can only be used to prove the existence of macroscopic texture in all medium Mn steels studied in this manuscript. The effect of this texture will be reduced anyway by the circular integration of the signal.

The acquisition rate is set to 10 Hz near the heating and cooling steps of the intercritical annealing, while it is set to 1/3 Hz during the isothermal holding. Around 3000 diffraction patterns are obtained per experiment. For FB680 treatment, an error occurred during the cooling step. They were recorded at 1/3 Hz instead of 10 Hz. As the cooling rate was -200°C/s, the diffractograms of FB680 treatment during cooling are not interpretable, as only one result from the superposition of the diffracting volume across multiple hundred degrees Celsius.

Therefore, the FB680 thermal treatment was redone in December 2021. For this FB680 second experiment, the detector was a Pilatus, whose acquisition rate can be as high as 100 Hz. Unfortunately, only the heating and cooling steps have been recorded in this second experiment. Therefore, it has

been decided to show the results of the first FB680 treatment in the “results” sections, and to bring the second FB680 results in the “discussion” section when they are necessary.

The recorded 2D Debye-Scherrer diffraction patterns are then integrated to produce 1D diffractograms (Intensity vs 2θ diffracting angle) using PyFAI software and thanks to a calibration procedure using polycrystalline silicon. A Rietveld analysis is then conducted using FullProf software on each pattern to quantify microstructure parameters (weight fraction & lattice parameters of the constituting phases). The full procedure is detailed in the next section.

2. Post-treatment of the data acquired during in situ experiments

A. Qualitative observation of 1D HEXRD diffractograms

The 1D diffractograms are the summed signal of diffracting plane families and of a background signal (notably due to elastic and inelastic scattering of the incident beam, and instrumental noises [172]). As reminded in the previous section, a plane family (hkl) diffracts when its interplanar distance d_{hkl} and its orientation relative to the diffraction beam fulfils the Bragg’s law. While in transmission powder diffraction setup, a plane family (hkl) creates a ring in the 2D detector space, after the integration, its diffracted ring becomes a peak in the 1D diffractogram. The position of the peak is $2\theta_B$, with θ_B being the Bragg angle. In HEXRD, the energy of incident beam is very high (here E=87.1 keV) when compared to conventional X-ray diffraction (for Cu K_α radiation, E=8 keV [173]). As the wavelength λ is very small in HEXRD, a consequence of Bragg’s law is that most of the photons diffracted by the sample will be situated in small angles ($2\theta_B$ <12°). (see Equation (II—2), Bragg’s law) [173].

In the following, 3 first examples are discussed to show how we identified the possibly involved phases. Phases are distinguished with the position of their respective peaks, which are known thanks to the Rietveld method (explain in the next section).

The diffraction spectrum obtained for the cold-rolled state is given in Figure 47. The scattering angle $2\theta_B$ goes from 3° to 10° to observe all relevant peaks. In this cold-rolled state, the steel contains mainly ferrite and martensite, explaining why only ferrite peaks can be seen without magnification. In the first insert, which is a magnification of the range between $\{110\}_\alpha$ and $\{200\}_\alpha$ peaks, some small peaks are detected. A little peak due to $\{200\}_\gamma$ austenitic plane family can be observed, proving that a small fraction of retained austenite remains in the cold-rolled state (lower than 0.3% however). The other peaks are typical of cementite precipitates. In the second insert, a magnification of the $\{211\}_\alpha$ peak highlights a small asymmetry in the peak shape. Martensite has lattice parameters very close to the those of ferrite, due to similar crystallographic structure. Therefore, this asymmetry is due to the presence of the $\{211\}_{\alpha'}$ martensite peak in the left part of the bottom of $\{211\}_\alpha$ peak. All those observations are consistent with the SEM observations already discussed in section II.1.A.b).

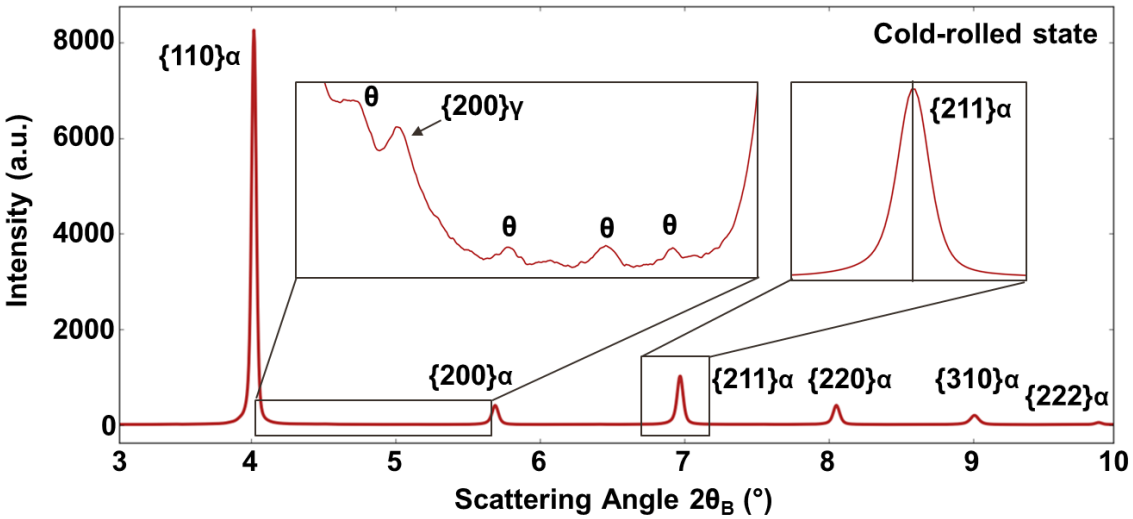

Figure 47: Diffractogram of the medium Mn steel in its cold-rolled state, at the start of one-step experiments. The steel is mainly constituted of ferrite and martensite. In the first magnified area, the highlighted $\{200\}_\gamma$ demonstrates the presence of austenite. Some cementite θ peaks are also present. On the second magnified area, the {211}α peak is slightly asymmetric due to the presence of a mixture of ferrite and martensite (almost the same structure but with slightly different lattice parameters)

Concerning two-step experiments, the initial microstructure is martensitic, and no cementite was found by SEM. The evolution of diffractograms when temperature increases during the heating step of the intercritical annealing of FB720 experiment is shown in Figure 48. It lies in the range 3.5-5.1° between three major diffraction peaks of ferrite and austenite. The temperature at which diffractograms have been taken are indicated by different colours. At RT=30°C (red line), there is indeed no cementite peak in the diffractogram. However, the $\{200\}_\gamma$ peak can be seen, demonstrating the presence of a small fraction retained austenite in the as-quenched martensitic steel.

Few small peaks appear during heating, above 500°C. They are attributed to formation of carbides, i.e., in the case of medium Mn steels, either ε-carbide or cementite [174], [175]. At 550°C (dark blue curve), the visible peak at 4.47° is more probably cementite, since ε-carbide usually appears at far lower temperature (<300°C) [174], [175]. At 720°C (purple curve), the multiple diffraction peaks observed in the studied range are very typical of cementite. Therefore, in both one-step and two-step experiments, cementite precipitates could appear during the thermal treatments.

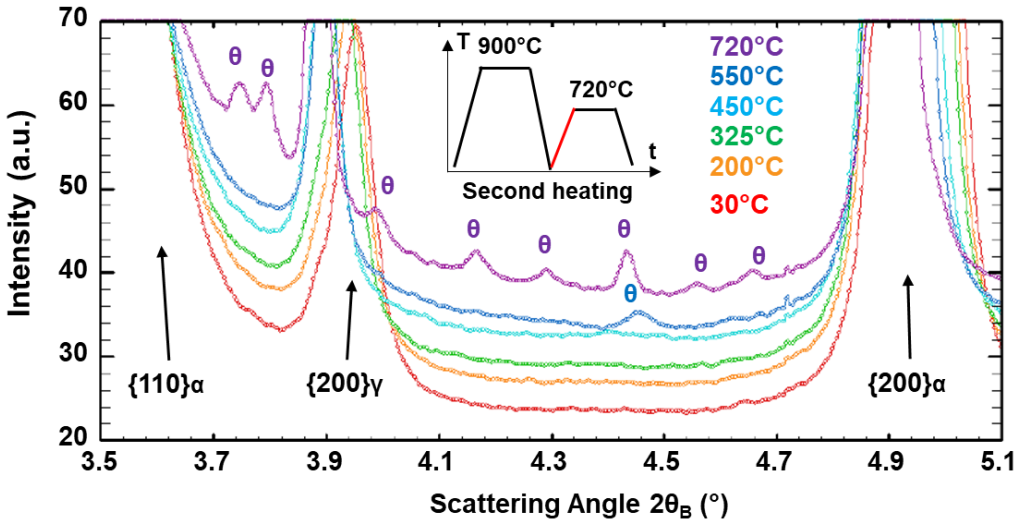

Figure 48: Evolution of diffractograms during the heating step of intercritical annealing of FB720 steel. The main diffraction peaks are generated by austenite and ferrite. The small peaks appearing above 550°C (dark blue and purple diffractograms) are generated by cementite.

As highlighted by the bibliographic chapter, martensite can form during the quench that follows IA. The diffractogram around the $\{211\}_\alpha$ peak is shown at the start of the isothermal holding and after quenching for the GL750 experiment in Figure 49 (a) and (b) respectively. Experimental profile line is indicated in black. Using a least-square approach, ferrite and martensite phases have been modelled by a pseudo-Voigt function (red and green curve respectively). At the start of isothermal holding, one ferrite peak is enough to explain the experimental signal, as both curves are perfectly superimposed. On the contrary, after the quench, the experimental {211} peak is very asymmetric, due to the summations of $\{211\}_\alpha$ and $\{211\}_{\alpha'}$ peaks. Rietveld refinement and metallurgical considerations gives a phase fraction of ferrite of about 60%, and 35% for martensite. It must be emphasized that the fraction of martensite is only obtained indirectly (see the next section) and the sequential deconvolution of ferrite and martensite is impossible in the frame of Rietveld refinement using FullProf software, even with fraction of martensite as high as presented in Figure 49 (b). Therefore, even when a significant fraction of martensite exists, its peaks are far less intense (here the ratio is 1/10) and they remain convolute with ferrite peaks. This is explained by their very similar crystallographic structure.

These three first HEXRD observations demonstrate the presence of four phases in the studied medium Mn steels: ferrite, austenite, martensite and cementite. This is consistent with the literature review. While ferrite and austenite are present in huge quantities, allowing them to be quantified by Rietveld refinement, martensite and cementite are difficult to be directly modelled and quantified. Martensite peaks are indeed too close to ferrite bigger peaks to allow for an independent quantitative modelling. Cementite peaks are too small to be quantified sequentially with Rietveld refinement, hence a ratio intensity reference (RIR) method was used in the PhD to quantify this latter phase. Both methods are detailed in the two next sections, highlighting their respective limits.

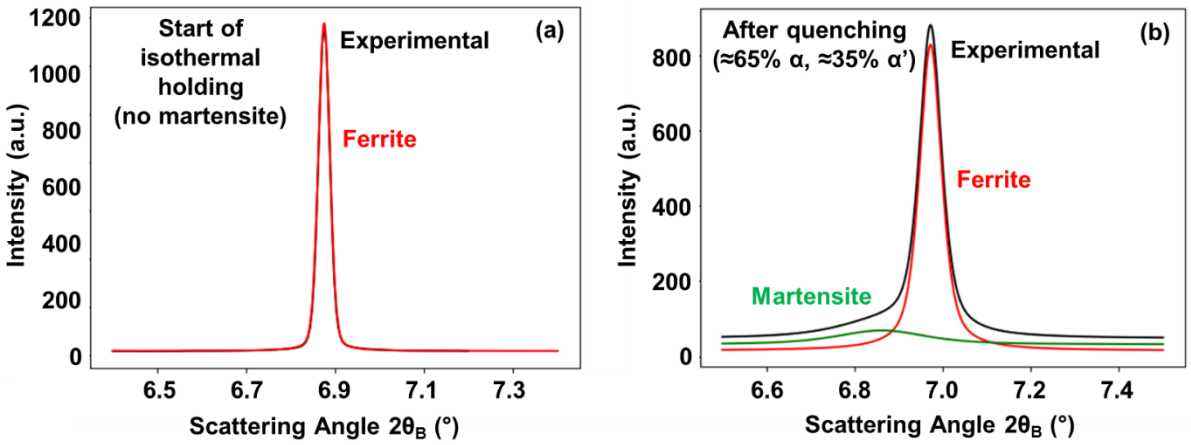

Figure 49: Comparison of area around the {211}α peak at (a) the start of isothermal holding and (b) at the end of one-step experiment at T_{IA} = 750°C (GL750 sample). In black is the experimental profile line, in red is the ferrite peak modelled with a pseudo-Voigt, and in green the modelled martensite peak (only present in (b)).

B. Rietveld refinement

Rietveld refinement is a crystallographic method used for interpreting 1D diffraction line profile based on a simulation of the said profile using experimental diffraction conditions and by calibrating certain crystallographic parameters of the phases in presence. In this method, the phase constituting the materials must be known a priori, alongside an approximative model for their crystallographic structure: space groups, respective lattice parameters and atomic parameters estimated at the first order [172]. This a global technique that uses all peaks in a given $2\theta_B$ range of the diffractograms to determine the phase fractions and other mean physical parameters (lattice parameters of each phase, density of defects, possible heterogeneities, etc). Please note that Rietveld refinement provides the mass fraction of the phases. As austenite and ferrite have the same densities for the studied composition, the different fractions (volume or mass) found in this work will be confounded.

To quantitatively analyse the diffractograms, a Rietveld refinement is conducted using FullProf suite. Rietveld method uses a least squares approach to refine a theoretical line profile until it matches the measured profile. Pseudo-Voigt function was chosen to approximate each peak. This function is a convex combination of a Lorentzian and a Gaussian (respective weights are η and 1-η with η the mixing parameter). Diffractograms were refined with FullProf software in a $2\theta_B$ range from 2.50° to 8.5°, with θ_B the Bragg angle. This range ensures that only peaks derived from fully recorded rings are used in the refinement. This includes the {110}α, {200}α, {211}α, {220}α peaks for BCC phase (space group I_{m3m}) and the {111}γ, {200}γ, {220}γ, {311}γ, {222}γ peaks for FCC phase (space group $F_{m\text{-}3m}$). The fitting parameters considered were a second order polynomial to model the signal background, and for each phase, the scale factor linked with the intensity of peaks, the mixing parameter of pseudo-Voigt function which determines the overall shape of peaks, lattice parameters, overall isotropic temperature factor (Bov) which influences the bottoms of peaks and Caglioti's parameters (denoted U, V and W) which define the full-width at half maximum [172] of peaks. The errors on the phase

fraction measurement and on the lattice parameters are estimated to be around ±1% and ±0.0001 Å respectively with this method.

In total, around 20 parameters were fitted for each diffractogram. During refinements, only a ferritic BCC phase (space group: I_{m3m}) and an austenitic FCC phase (space group: F_{m-3m}) were considered. Indeed, even though martensite is present in the fibrous microstructure (which cannot be strictly BCC), as it is annealed during isothermal holding, it has a very low tetragonality, and the error made on phase fractions is not significant (inferior to the uncertainty of the measurement).

When fresh martensite appears, it shows on the contrary a high tetragonality. A body-centred tetragonal phase (space group: $I_{4/mmm}$) should have been added in the analysis. However, considering this supplementary phase leads to unstable sequential work as the peak is too close to the one of ferrite (see Figure 49). This is the reason why this additional phase has not been considered for sequential analysis, the fraction of BCC phase representing the sum of the ferrite and fresh martensite (the peaks of both phases are too convoluted). This methodology permits to obtain a relevant fraction for austenite and the fraction of martensite should be deduced from a metallurgical reasoning (below Ms, the decrease in austenite fraction corresponds to an increase in the martensite fraction).

In Figure 50, a simulated diffractogram at the end of isothermal holding of the fibrous sample annealed at 720°C is shown as an example. Red points are the experimental diffractogram and the black curve is the theoretical line profile. Each plane family of a specific phase is indicated above the considered peak. Here, the calculated lattice parameter for ferrite is 2.8977 Å and 3.6514 Å for austenite lattice parameter and the phase fraction of austenite is 37%.

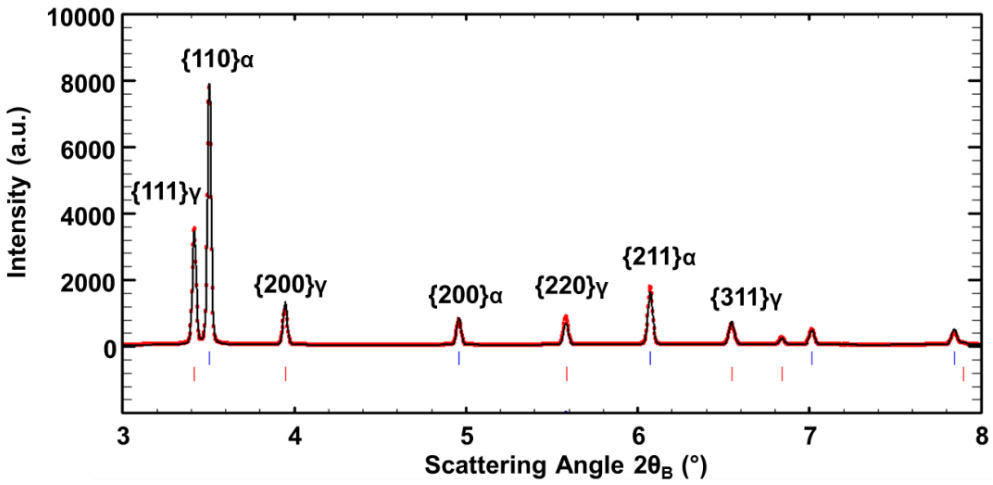

Figure 50: Example of a Rietveld refinement. In red: experimental points of the diffractogram. In black: the theoretical line profile. The plane families are given above the corresponding peaks.

This technique allows for the determination of phase fractions and lattice parameters all along the experiment with a very good precision, especially during thermal treatment experiments. However, for phases with very low phase fractions, like carbides, Rietveld analysis is very user dependent and thus low confidence is found in the results on phase fractions in such case. In the studied medium Mn steels, cementite carbides are found as seen in Figure 47 and in Figure 48. As cementite crystallographic structure is complex (orthorhombic), its peaks are 100 times less intense than the austenite ones and 1000 times than the ferrite ones. It is thus impossible to do sequential Rietveld analysis when accounting for cementite precipitates. Therefore, an alternative method has

been developed to estimate the in situ evolution of cementite phase fraction, based on the ratio-intensity reference (RIR) method, as explained in the next section.

C. Ratio Intensity Reference (RIR) method

With the RIR method, the phase fractions of each material's component are calculated by measuring the ratio of integral breadths, i.e. the area under the peaks of each phase. This ratio is then compared to a reference, allowing for a quantitative analysis of diffractograms. One peak per phase can be used, even though it is better if possible to take multiple peaks, as it reduces the effect of crystallographic texture. In our case, it has been chosen to take the $\{301\}_\theta$ peak for cementite (located at 4.4° in Figure 48), the $\{221\}_\alpha$ peak for ferrite and the $\{311\}_\gamma$ peak for austenite. The advantage of those peaks is that they remain unconvoluted with other peaks during the whole thermal treatments. The areas of peaks are determined by modelling them with a gaussian function. If we call A_α, A_γ, and A_θ the respective phase areas of ferrite, austenite and cementite peaks, and f_α, f_γ, and f_θ the volume phase fractions of the corresponding phases, then the ratios of fractions and areas are both constant during the treatment according to the RIR principle [172]:

$$RIR_\alpha^\theta = \frac{A_\theta}{A_\alpha} = P_\alpha^\theta \frac{f_\theta}{f_\alpha} \qquad \text{(II—3)}$$

$$RIR_\alpha^\gamma = \frac{A_\gamma}{A_\alpha} = P_\alpha^\gamma \frac{f_\gamma}{f_\alpha} \qquad \text{(II—4)}$$

In Equations (II—3) and (II—4), RIR_α^θ and RIR_α^γ are the values of the ratios of areas A_θ/A_α and A_θ/A_α across an experiment, and P_α^θ and P_α^γ are the proportionality factors between the ratios of areas and the ratios of phase fractions. The third equation necessary for the RIR analysis is the sum of the phase fractions which is constant and equal to one. It can be written as:

$$f_\alpha = 1 - f_\gamma - f_\theta \qquad \text{(II—5)}$$

Combining the three previous equations, the two following equations can be obtained, allowing to determine the evolution of phase fractions f_γ, and f_θ during thermal treatments using:

$$f_\theta = \frac{1}{1 + P_\alpha^\theta \frac{A_\alpha}{A_\theta} + P_\alpha^\gamma P_\alpha^\theta \frac{A_\gamma}{A_\theta}} \qquad \text{(II—6)}$$

$$f_\gamma = \frac{1}{1 + P_\alpha^\gamma \frac{A_\alpha}{A_\gamma} + \left(P_\alpha^\gamma\right)^{-1} P_\alpha^\theta \frac{A_\theta}{A_\gamma}} \qquad \text{(II—7)}$$

Knowing f_γ, and f_θ, the phase fraction of ferrite f_α is calculated using Equation (II—5). In previous equations, P_α^θ and P_α^γ (or equivalently RIR_α^θ and RIR_α^γ) are two parameters that must be determined on the diffractogram used as a reference in which the relevant phase fractions are supposed to be exactly known. For P_α^γ, which is only dependent on austenite and ferrite, the reference has been chosen to be the last diffractogram during the isothermal holding. For this image, the fractions of both ferrite and austenite are known with good certainty thanks to Rietveld refinement. The obtained values of P_α^γ are not constant between experiments, and increase as the annealing

temperature decreases, and are higher for fibrous steels than globular ones. The values of P_{α}^{γ} are respectively 1.48 for FB750 and 1.97 for FB680, and 0.88 for GL750 and 1.04 for GL680. This variability of P_{α}^{γ} can be explained by texture differences between experiments, possibly cumulated with different gradients of austenite composition, different crystallite sizes and different dislocations densities. Taking multiple peaks to calculate the integral breaths could alleviate this variability.

The parametrization of P_{α}^{θ} is more complex, as it is more difficult to obtain a reference diffractogram in which the exact fraction of cementite and ferrite is known. For simplicity, it has been decided that P_{α}^{θ} will be constant across samples having the same morphology (either globular or fibrous). In the studied medium Mn steel, which has 0.2C, the maximal fraction of cementite is 3% when all the carbon is trapped in cementite. To obtain a reference containing only ferrite and cementite (therefore respectively 97% and 3% of each phase), multiple thermal treatments were tried. Starting with either a cold-rolled ferritic or a martensitic state: in situ annealing at 600°C during 1h30, and ex situ annealing at 620°C, 630°C or 640°C during 2h. Using an arbitrary value for P_{α}^{θ} in all those experiments, the fraction of cementite was calculated for each available diffractogram. Moreover, using the same arbitrary value for P_{α}^{θ}, the fraction of cementite was also calculated in the eight thermal treatments detailed in section I.A.1. The reference diffractogram for each morphology was chosen to be the one having the maximum fraction of cementite.

At the end, one-step and two-step treatments at 630°C (slightly higher than Ae_1) during 2h were used to parametrized P_{α}^{θ} for both morphologies. For the two selected diffractograms, it was also verified that only cementite and ferrite were present. Then, P_{α}^{θ} was calculated with the hypothesis that f_{α} and f_{θ} are respectively 97% and 3%. Finally, the two obtained values of P_{α}^{θ} are respectively 0.1343 and 0.1030 for globular and fibrous microstructures.

The results of Rietveld and RIR analysis for the eight intercritical annealing are detailed in the next sections.

3. Results

A. Austenite phase fraction

The samples used for the simple annealing experiments have been intercritically annealed at about 700 °C prior to cold rolling. As a consequence, the initial microstructure before heating was made of a mixture of deformed ferrite and martensite and cementite. The estimated initial fraction of cementite is 1.5% according to RIR method (see section II.3.D). The initial retained austenite fraction falls below the resolution limit (0.3%).

The samples used for the double annealing experiments have been annealed at about 900 °C and cooled down rapidly. As a consequence, the initial microstructure before the final intercritical annealing is fully martensitic. The initial fraction of retained austenite is again below the experimental resolution (0.1%).

Figure 51 shows the evolution of the austenite phase fraction as a function of time for one-step (a) and two-steps (b) experiments, for the 4 considered intercritical annealing temperatures.

During the intercritical annealing stages at 720 °C and 750 °C, the fraction of austenite increases rapidly before reaching a kind of plateau, even if the transformations are not finished after 15 min. For both FB700 and GL700 experiments, it can clearly be seen that the slope of the transformation kinetics is not 0 at the end of the isothermal holding. Whatever the initial microstructure, the higher the temperature, the faster are the initial kinetics and the higher the transformed fraction at the end of the stage. At 680 °C, the transformations are not completed yet, even after 30 min. The initial transformation kinetics are faster in the case of one-step (GL), but the fraction reached is higher in the case of two-step (FB) at 700 °C and at 720 °C.

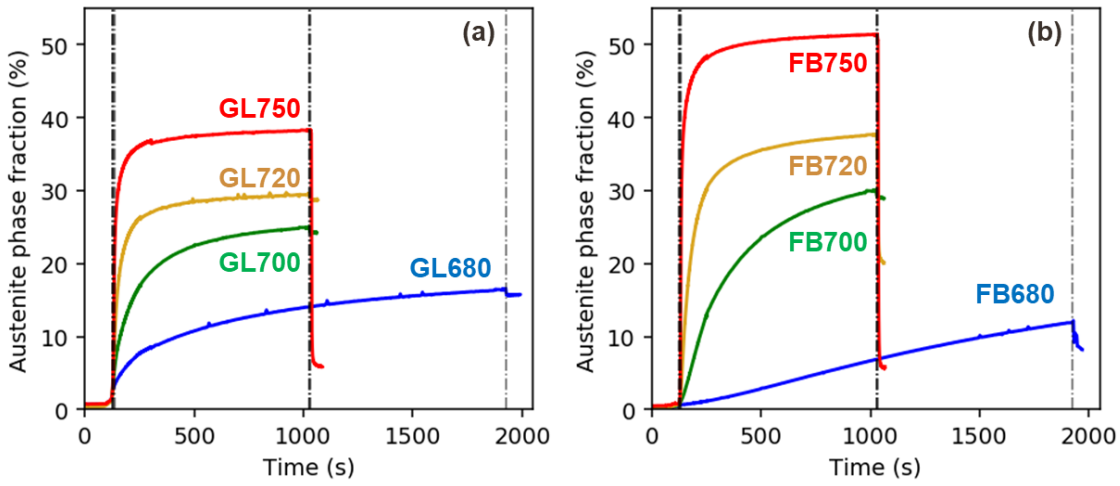

Figure 51: Austenite phase fraction as a function of time for the 4 considered intercritical annealing temperatures. In (a), the initial microstructure is cold-rolled ferritic, while in (b), it is as-quenched martensitic. On (a) and (b), the first vertical line corresponds to heating end (similar values for all treatments). The second vertical line corresponds to the cooling start for 700°C, 720°C and 750°C experiments. The third line corresponds to the cooling start for 680°C experiment.

Figure 52 shows the evolution of the austenite phase fraction as a function of temperature for one-step (a) and two-steps (b) experiments, for the 4 considered intercritical annealing temperatures. In both graphs, the beginning of the annealing is indicated by a black star. During the heating step, for a given initial microstructure, all transformation kinetics are superimposed. For the 750°C experiments, about 10% of austenite is formed during heating. The austenite fraction then increases during the isothermal holding, reaching its highest values. During cooling, for GL680, GL700, GL720, FB680 and FB700 microstructures, the fraction of austenite remains constant, indicating the absence of measurable martensitic transformation. In the FB720, FB750 and GL750 cases, martensite transformation occurs. For example, for FB720, martensite starts at about 100°C (36% of austenite), leaving only 20% of retained austenite at room temperature, which implies a transformed fraction of 16%.

During cooling, there is a slight continuous decrease for all experiments between T_{IA} and RT/M_s. For FB750 steel, at T_{IA}, the austenite phase fraction f_γ is 51.4%, while f_γ is 50.6% at M_S, before the martensitic transformation. For GL700 steel, f_γ decreases from 25% at T_{IA} to 24.3% at RT. For all experiments, this decrease remains in the ±1% uncertainty of the Rietveld method.

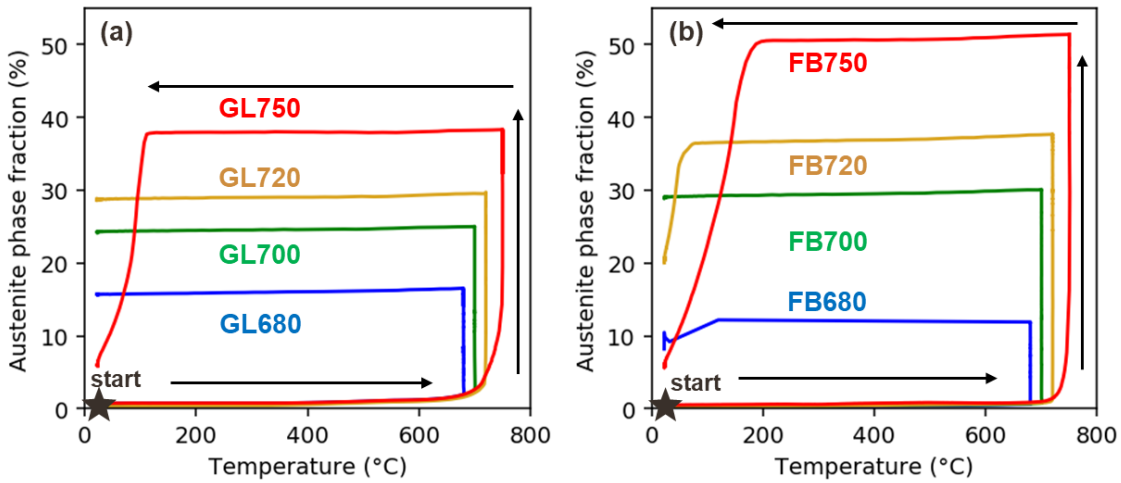

Figure 52: Austenite phase fraction as a function of temperature for the 4 considered intercritical annealing temperatures. In (a), the initial microstructure is cold-rolled ferritic (one-step), while in (b), it is as-quenched martensitic (two-step). The initial state prior to intercritical annealing is indicated by a black star. Arrows indicate the time evolution. The cooling sequence of the FB680 has not been conducted with the relevant acquisition rate, as a consequence, the measurements may not be physically relevant.

Finally, in Figure 53 are compared the phase fractions obtained by RIR method (solid line) and Rietveld refinement (dashed line, reproduced from Figure 51) for the eight thermal treatments. In the presented results, the RIR method was used supposing that there was only ferrite and austenite (A_θ set to 0 in Equation (II—7)), accounting for the true A_θ has a negligible effect on f_γ values determined with RIR method.

As the measurement of austenite phase fractions with RIR method was parametrized on the last diffractogram of the isothermal holding, it is not surprising that the two methods give the exact same values at the end of the isothermal holding. Concerning two-step experiments (Figure 53 (b)), both methods give exactly the same transformation kinetics. Concerning one-step experiments (Figure 53 (a)), the transformation kinetics determined with the RIR methods is slightly slower than the one obtained with Rietveld method. Compared to Rietveld method, RIR method is more sensitive to inaccuracy due to texture. In the cold-rolled state, the steel demonstrates a marked texture due to the mechanical treatment. For one-step experiments, the intercritical annealing does not totally suppress this texture, explaining the slight gap between RIR and Rietveld method. For two-step experiments, the prior austenitization step totally suppresses the texture due to cold-rolling, explaining that both RIR and Rietveld transformation kinetics are so similar.

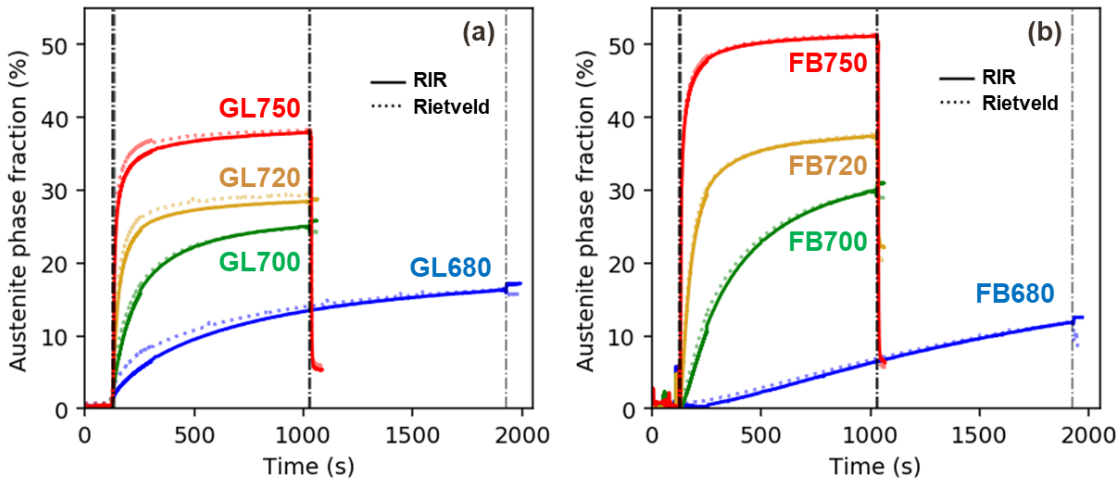

Figure 53: Comparison of the austenite phase fraction evolution determined by RIR method (solid line) and Rietveld refinement (dotted line), as a function of time for the 4 considered intercritical annealing temperatures. In (a), the initial microstructure is cold-rolled ferritic (one-step), while in (b), it is as-quenched martensitic (two-step). In (a) and (b), the first vertical line corresponds to the end of heating stage (similar values for all treatments). The second vertical line corresponds to the cooling start for 700°C, 720°C and 750°C experiments. The third line corresponds to the cooling start for 680°C experiment.

B. Ferrite lattice parameter

Figure 54 shows the corresponding evolution of the ferrite lattice parameters measured during the same experiments as a function of time for (a) one-step and (b) two-step experiments. (c) and (d) are magnifications of the isothermal holding part of Figure 54 (a) and (b) respectively. Figure 55 (a) to (h) shows the same evolution of ferrite lattice parameters as a function of temperature. The lattice parameters in both ferrite and annealed martensite seem to be governed mainly by a thermal expansion, with a "linear" evolution as a function of temperature. The difference in slope also increases with the annealing temperature.

Nevertheless, one can notice that the slope is systematically higher during cooling than during heating. To highlight these differences, the individual curves for all the trials are represented in Figure 55. The observed differences in slope between heating and cooling can be explained by the second order internal stresses due to the difference in the coefficient of thermal expansion (CTE) between ferrite and austenite. This mechanism has already been observed and quantified in the austenite of Q&P steels but never exploited for the ferritic matrix (impossibility related to the martensitic transformation) [25]. The resulting difference in the lattice parameter of the ferritic matrix thus decreases with the annealing temperature and seems more pronounced in the case of fibrous samples. In the analysis conducted in the next section, the main difficulty will be the determination of the stress-free CTE of the ferritic/martensitic matrix to be used as a reference. In the FB720, GL750 and FB750 cases, a deviation from the "linear" trend can be observed at low temperature in conjunction with the martensitic transformation. It must also be mentioned that a systematic decrease in the ferrite lattice parameter is observed during the isothermal holdings in the intercritical range (for all the experiments). This decrease is probably related to the chemical partitioning of C, Mn, Al and Si between ferrite and austenite phases and the recovery and recrystallization phenomenon in the

ferritic matrix, but it is difficult to exploit it as the values are close to the resolution of the experiments. The decrease is relatively more important in fibrous steels than in globular steels.

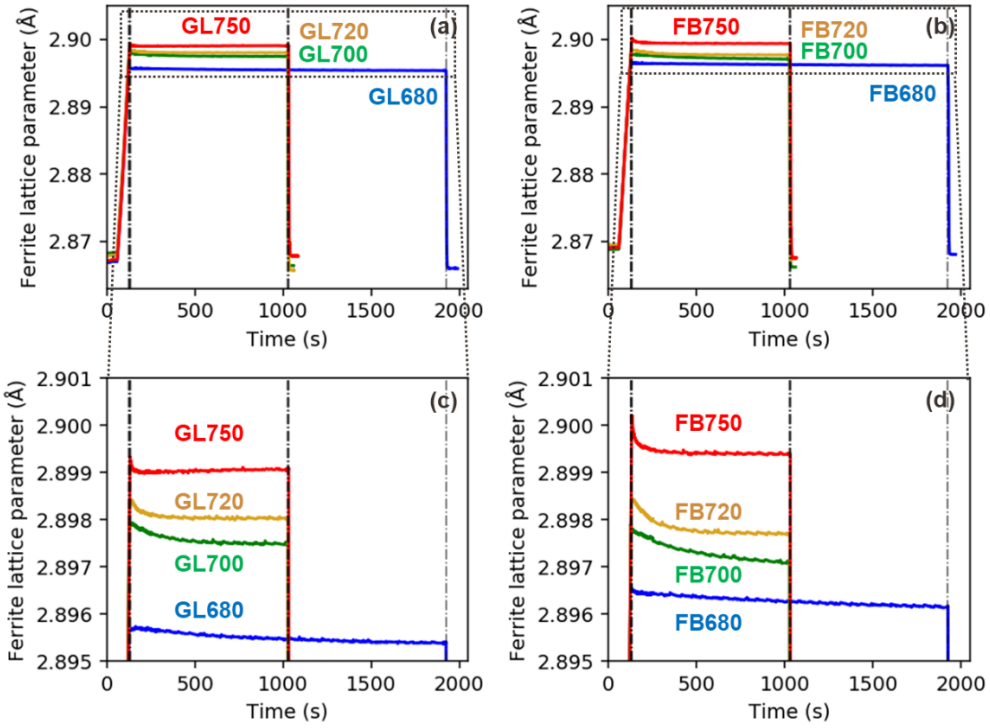

Figure 54: Evolution of ferrite lattice parameters (a) as a function of time for the 4 considered intercritical annealing temperatures. (a) one-step experiments; (b) two-step experiments. Magnification of (a) and (b) during the isothermal holding are shown in (c) and (d) respectively. The first vertical line corresponds to the heating end (similar values for all treatments). The second vertical line corresponds to the cooling start for 700°C, 720°C and 750°C experiments. The third line corresponds to the cooling start for 680°C experiment.

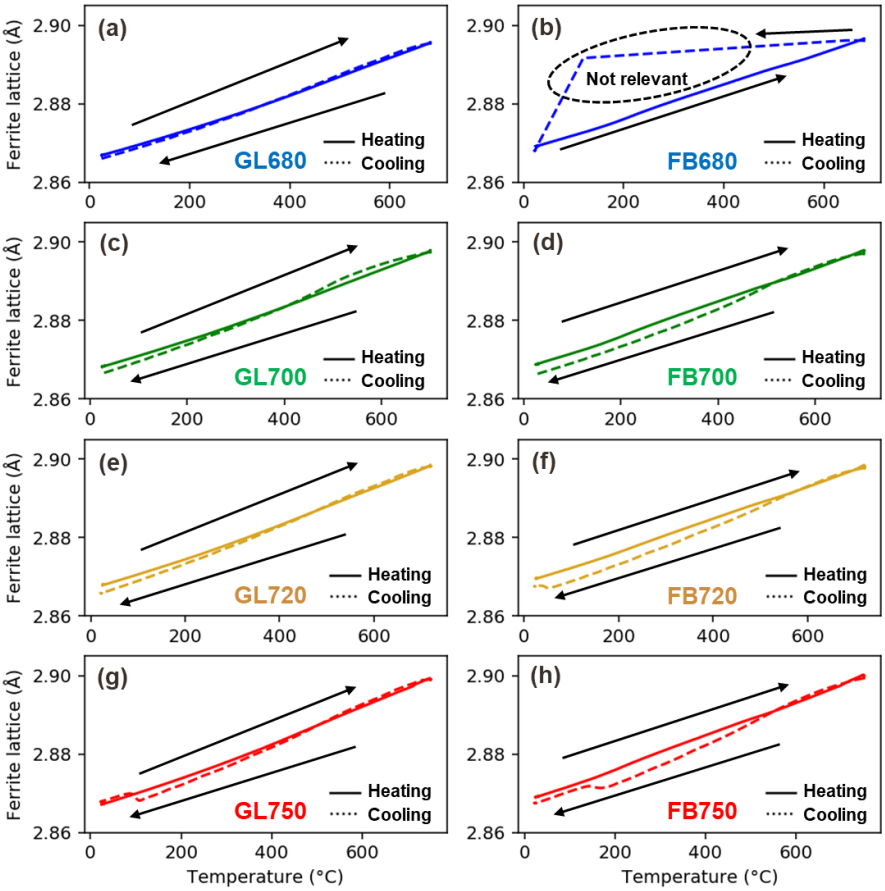

Figure 55: Evolution of the ferrite lattice parameter as a function of temperature for the 8 considered intercritical annealing experiments: (a) GL680, (b) FB680, (c) GL700, (d) FB700, (e) GL720, (f) FB720, (g) GL750 and (h) FB750. Dashed line corresponds to the cooling step, while continuous line corresponds to the soaking and heating steps. The cooling sequence of the FB680 has not been conducted with the relevant acquisition rate, as a consequence, the measurements may not be physically relevant.

C. Austenite lattice parameter

Figure 56 shows the corresponding evolution of the austenite lattice parameters measured during the same experiments as a function of time for (a) one-step and (b) two-step experiments. In (c) and (d) are magnifications of the isothermal holding parts of Figure 56 (a) and (b) respectively. Figure 57 (a) to (h) shows the same evolution of austenite lattice parameters as a function of temperature. The evolution of the austenite lattice parameters is more complex than the ones encountered in the ferritic matrix, as the compositions and the stress states in austenite vary more. As the initial fraction of austenite is very low, it is not possible to track austenite lattice parameter from the start in all experiments with Rietveld refinement.

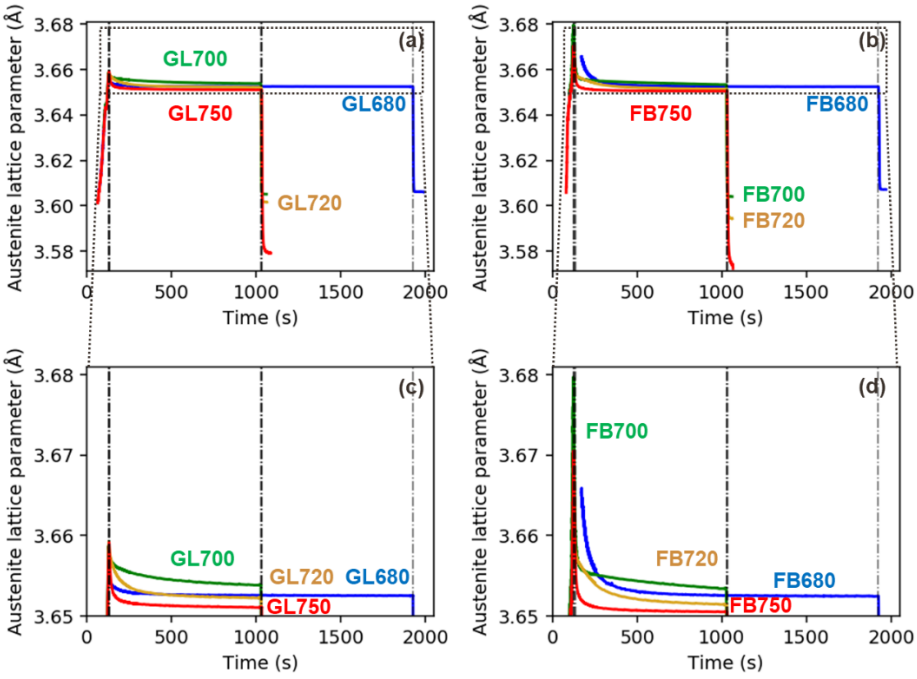

Figure 56: Evolution of austenite lattice parameters (a) as a function of time for the 4 considered intercritical annealing temperatures. (a) one-step experiments; (b) two-step experiments. Magnification of (a) and (b) during the isothermal holding are shown in (c) and (d) respectively. The first vertical line corresponds to the heating end (similar values for all treatments). The second vertical line corresponds to the cooling start for 700°C, 720°C and 750°C experiments. The third line corresponds to the cooling start for 680°C experiment.

During the heating stage, the austenite lattice parameters can only be measured with reliability above 300 °C/400 °C because the fraction of austenite is too low. However, the observed evolutions are similar regardless the experiments. For the GL680 and GL750 treatments, the initial trend looks linear with the expected CTE of an austenitic structure. Then, the curve takes an upward curvature up to 500 °C to reach a local maximum. This increase is attributed to the relaxation of hydrostatic internal stresses inherited from a prior martensitic transformation. Another possible mechanism is carbon partitioning between the austenite and the ferritic matrix (keeping in mind that the fraction of austenite remains lower than 5%). Nevertheless, it is very difficult to be definitive. The observed decrease above 500°C coincides with the massive precipitation of cementite in the microstructure (see section II.3.D). Cementite acts as a carbon trap and it is believed that austenite will be depleted in carbon, which leads to a decrease in its lattice parameter. Above 600 °C, the lattice parameter increases again with a slope higher than expected from the sole CTE. This temperature corresponds approximately to the beginning of cementite dissolution to the benefit of the austenite growth.

During the isothermal holding in the intercritical range, as in ferrite, the lattice parameter of austenite surprisingly decreases drastically. In fact, the expected carbon/manganese partitioning occurring during this stage could have led to an increase in the lattice parameter. However, it must be kept in mind that the fraction of austenite also increases rapidly during this stage. As a consequence, a dilution is in fact observed and it thus leads to a global decrease in the austenite lattice parameter.

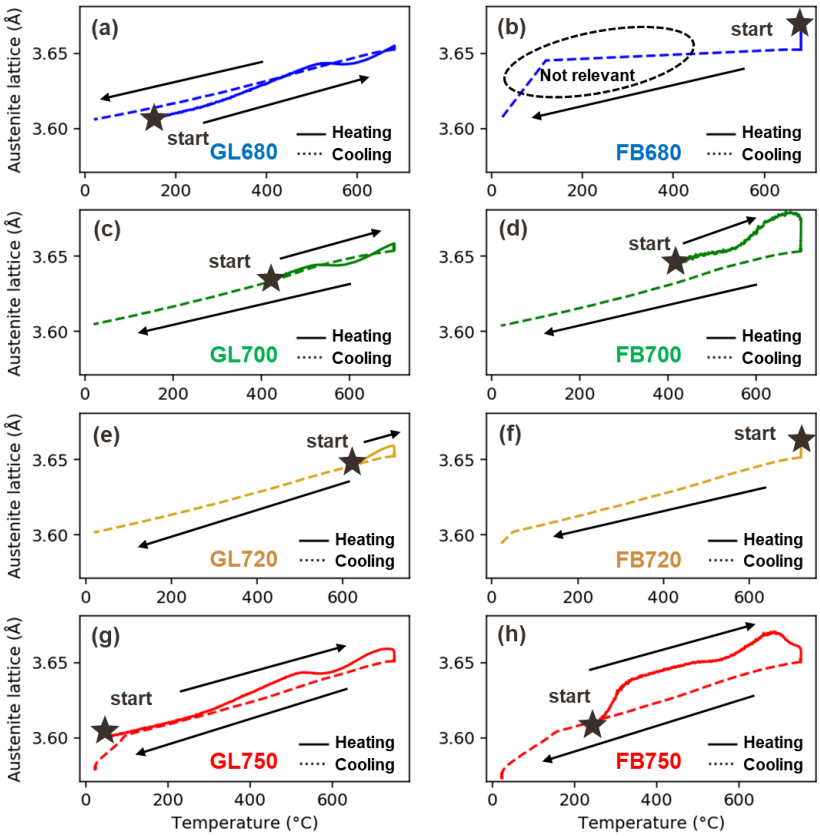

Figure 57: Evolution of the austenite lattice parameter as a function of temperature for the 8 considered intercritical annealing experiments: (a) GL680, (b) FB680, (c) GL700, (d) FB700, (e) GL720, (f) FB720, (g) GL750 and (h) FB750. Dashed line corresponds to the cooling step, while continuous line corresponds to the soaking and heating steps. A black star indicates the start of austenite detection. The cooling sequence of the FB680 has not been conducted with the relevant acquisition rate, as a consequence, the measurements may not be physically relevant.

During cooling, the behaviour looks “linear” (as in the case of the ferritic matrix) as no metallurgical transformations are expected. Nevertheless, the slopes seem to depend on the considered experiments and are lower than expected from a stress-free CTE. As in the ferritic matrix, the hydrostatic internal stresses are progressively built upon cooling in austenite due to the incompatibility of CTE between the phases [25]. In austenite, the final hydrostatic stress is in traction, contrary to the ferritic matrix. In the FB720, FB750 and GL750 cases, a deviation from the “linear” trend can be observed at low temperature in conjunction with the martensitic transformation. This last transformation leads to an additional source of internal stresses of compressive nature.

D. Cementite phase fraction

The evolution of cementite phase fraction as a function of time is shown in Figure 58 for (a) one-step and (b) two-step experiments. (c) and (d) are magnifications of the isothermal holding parts of Figure 56 (a) and (b) respectively. When the cementite phase fraction is zero or very low (<0.5%), like at the end of the intercritical annealing or after the first annealing for the two-step treatment, our mathematical modelling of cementite peak could give absurd results in term of height and full-width at half maximum, making the phase fractions reaching nonsensical values (>5%). To tackle this issue, a

threshold value was imposed on the phase fraction in specific step of the thermal treatment, defined individually for each experiment. They are indicated by horizontal purple dotted line in Figure 58. For a diffractogram, when the fraction of cementite exceeds this threshold, the value determined for the previous diffractogram was used instead.

In Figure 56 (a) and (c), the initial state of the steel is cold-rolled ferritic, with some amount of carbide precipitates. RIR method gives an initial cementite phase fraction of about 2% in the one-step treatments. All the carbon is not precipitated initially in cementite, as its fraction is lower than its maximum possible value (3%). This can be explained by the presence of martensite inherited from previous thermomechanical treatment (about 15% to 20% as seen by SEM), which captures part of the available carbon. During heating, the martensite is tempered and carbide precipitates. The maximum fraction of 3% is reached in all one-step treatments. Then cementite dissolves continuously during isothermal holding.

For two-step treatments (Figure 56 (b) and (d)), the evolution of cementite phase fraction bears the same trends. It first increases, reaching a maximum at the start of the isothermal holding and then decreases continuously until the end. Initially, in the two-step treatments, the steel is as-quenched martensite, and no cementite is present in the microstructure, hence the initial values is close to 0%. During heating, cementite precipitates from fresh martensite (tempering). The value at the start of isothermal holding is about 2.5%, and for FB680, cementite continues to precipitate during the first minutes of the isothermal holding until 250s, reaching 3%. Then, cementite quickly dissolves, the rate depending on the annealing temperature.

For both kinds of morphology, during isothermal holding, cementite dissolution rate increases with increasing annealing temperature T_{IA}. For a given T_{IA}, the rate is higher in the globular microstructure than in the corresponding fibrous one. Except for FB680, whose transformation kinetics is nearly linear, the transformation kinetics are close to a sigmoidal shape. For microstructures annealed at 700°C and above, no more cementite is present at the end of the isothermal holding.

Figure 59 shows the evolution of the cementite phase fraction as a function of temperature for one-step (a) and two-step (b) experiments, for the 4 considered intercritical annealing temperatures. In both graphs, the start of intercritical annealing is indicated by a black star. During the heating step, for a given initial microstructure, all transformation kinetics are superimposed. The precipitation of carbide in one-step treatment starts at 350°C. For globular specimens, for 720°C and 750°C treatments, the cementite starts to dissolve at the end of heating step, before reaching the isothermal holding. A final fraction of f_θ = 0.8% is kept after the GL680 treatment.

For fibrous specimens, the precipitation of cementite carbide starts between 300°C and 400°C. At the end of heating, the fraction is about 2.5%. In Figure 59 (b), it is clearly visible that the fraction of cementite in FB680 experiment first increases to 3% during isothermal holding and then decreases to reach its final value of about 2%. In other one-step and two-step experiments above 700°C, cementite completely dissolves during isothermal holding, as previously stated.

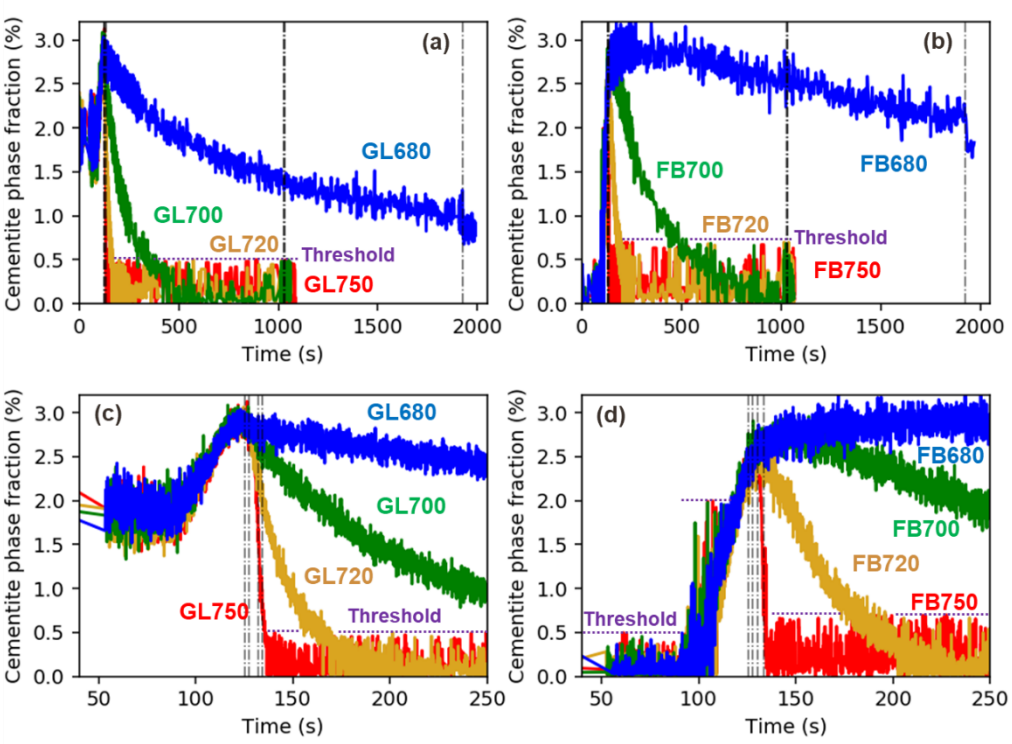

Figure 58: Cementite phase fraction as a function of time for the 4 considered intercritical annealing temperatures. (a) one-step experiments; (b) two-step experiments. The first minutes of the heating and isothermal holding of (a) and (b) are magnified in (c) and (d) respectively. The first vertical lines correspond to the heating end (similar values for all treatments). The second vertical line corresponds to the cooling start for 700°C, 720°C and 750°C experiments. The third line corresponds to the cooling start for 680°C experiment.

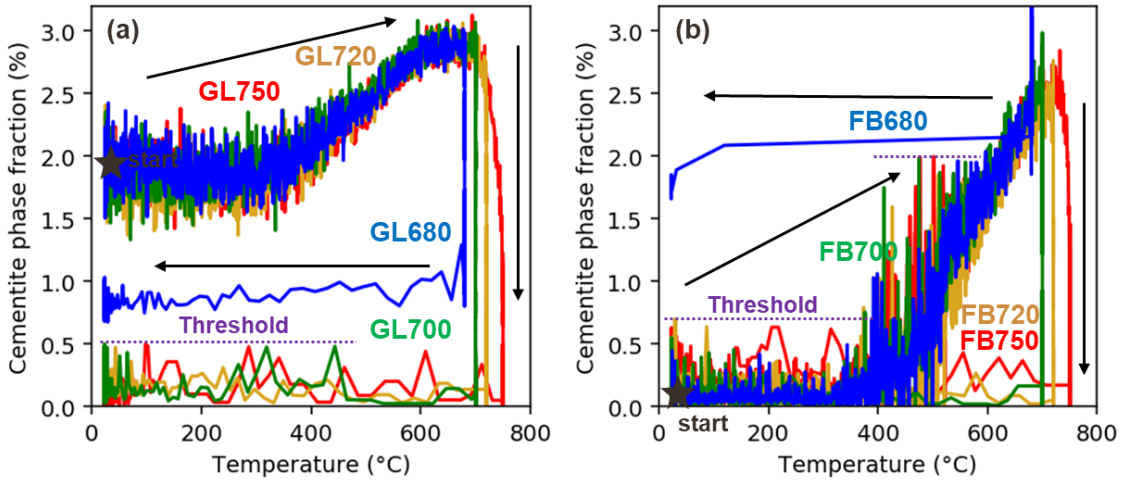

Figure 59: Cementite phase fraction as a function of temperature for the 4 considered intercritical annealing temperatures. (a) one-step experiments;(b) two-step experiments. The initial state prior to intercritical annealing is indicated by a black star. Arrows indicate the time evolution of the thermal treatment.

4. Discussion

The methodology used in this work allows to obtain the effects of C, Mn, Si, Al, and the effect of hydrostatic stresses on the stability of austenite at the end of the thermal treatment. The next sections will be dedicated to quantify each contribution. The following formula will be used for the quantification, which is a combination of the works of van Bohemen [171] and of Allain et al. [25] (C_γ, Mn_γ and Si_γ are the austenite C, Mn and Si contents, σ_γ^h is the residual hydrostatic stress in austenite):

$$M_s = 565 - 600\left(1 - exp(-0.96C_\gamma)\right) - 31Mn_\gamma - 13Si_\gamma + 0.038\,\sigma_\gamma^h \qquad (II—8)$$

A. Carbon partitioning during intercritical annealing

The obtained phase fractions at the end of the studied isothermal holdings in the intercritical range (cf. Figure 52) are gathered in Table 5. These values (two-step: triangles, one-step: circles) have been compared in Figure 60 to the equilibrium value predicted by CEQCSI. The fractions are far below the equilibrium for all the studied cases. It also explains why the transformation rates at the end of the holdings are still significant.

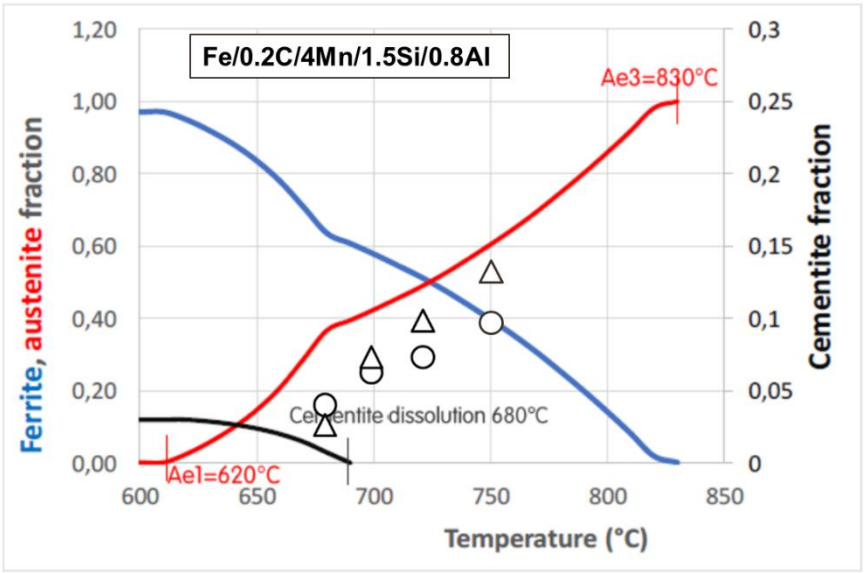

Figure 60: Fractions of ferrite (in blue), austenite (in red) and cementite (black) at the orthoequilibrium of the studied steel as a function of temperature. The experimental values obtained by HEXRD at the end of the isothermal holding have been reported (two-step: triangle, one-step: circle).

As explained above, as the evolution of cementite phase fraction is estimated by the RIR method, a simple mass balance can be used to estimate the carbon content in austenite assuming that the solubility of carbon is negligible in ferrite. The carbon content in austenite is simply given by:

$$C_\gamma = \frac{C_{tot} - f_\theta\, C_\theta}{f_\gamma} \qquad (II—9)$$

	Annealing Temperature:	680 °C	700 °C	720 °C	750°C
Fraction of austenite (vol.%) at the end of the isothermal holding	One-step	16.5	25.0	29.5	39.0
	Two-step	11.9	30.1	37.7	51.3
Fraction of cementite (vol.%) at the end of the isothermal holding	One-step	1.1	0	0	0
	Two-step	2.0	0	0	0
Estimated carbon in austenite (wt%) at the end of the treatment	One-step	0.80	0.79	0.67	0.51
	Two-step	0.52	0.66	0.53	0.38

Table 5: Fractions of austenite and cementite at the end of the isothermal holdings and its estimated carbon content based on a simple mass balance for the 8 studied conditions.

With C_γ the carbon content in austenite, C_θ the carbon content in cementite (6.67 wt%), C_{tot} the nominal carbon content of the alloy (0.2 wt%), f_γ the fraction of austenite and f_θ the fraction of cementite. The in situ evolutions of austenite carbon content calculated with Equation (II—9) are shown in Figure 61 for (a) one-step and (b) two-step experiments during the isothermal holdings for the four intercritical annealing temperatures. The evolutions of carbon content during heating are not calculated since the austenite fraction is too low to obtain reliable values. In Figure 61, the first vertical lines correspond to the end of heating steps while the second and third vertical lines correspond to the start of cooling steps. The evolution of austenite carbon content during the holding is not monotonous. For GL680 sample, the austenite carbon content increases during the whole holding. For microstructures annealed at 720°C and 750°C, the austenite carbon contents reach a maximum after few seconds of the isothermal holding, and then continuously decreases until the end. For GL700 and FB700 specimens, the austenite carbon content first increases until 500s and 700s respectively, then decreases. Those complex and non-monotonous behaviours reflect the competition between two opposite phenomena: (1) the dissolution of cementite precipitates, which is a source of carbon for austenite thus increases the carbon content in austenite; (2) the growth of austenite, which dilutes the total amount of carbon available thus decreases the mean measured value.

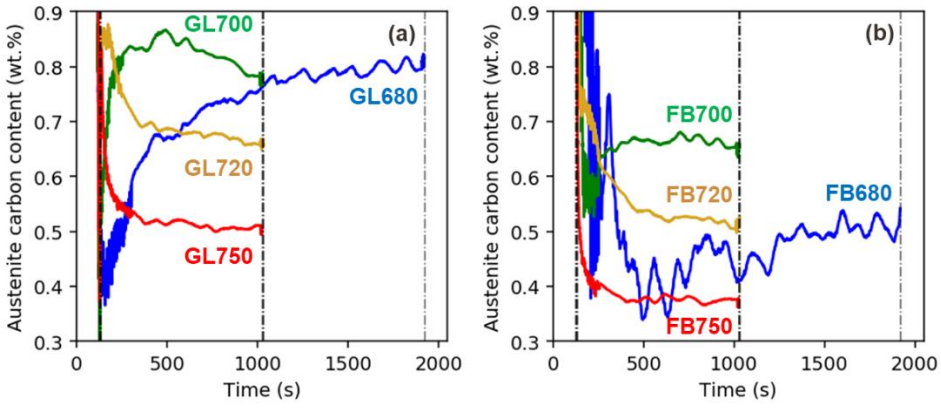

Figure 61: Evolution of austenite carbon content in (a) one-step and (b) two-step experiments during the isothermal holding for the four intercritical annealing temperatures. A moving average filter was used to smooth the curves (10 closest neighbours).

The values at the end of the isothermal holdings calculated with Equation (II—9) are also given in Table 2. At 680 °C, the microstructures contain a significant fraction of cementite at the end of the holding. Thus, the estimation of austenite carbon content is only possible if the cementite phase

fraction is known. Between 700°C and 750°C, the carbon in austenite decreases with the temperature as expected, making the retained austenite less stable. However, for 680°C, the final carbon content is dependent on the dissolution kinetics of cementite. After 30 min, cementite precipitates are still present and capture an important fraction of the available carbon. In GL680, the carbon content of austenite reaches value comparable to the one of austenite in GL700 microstructure. However, for FB680, the carbon content of austenite is similar at the end to the carbon content of FB720 only, as the cementite dissolution is slower in FB680 treatment when compared to GL680.

The evolution of the repartition of carbon between cementite, austenite and ferrite during the intercritical annealing for all one-step and two-step experiments are discussed with more details in appendix D. For all experiments (one-step and two-step), at some point during heating stage, more than 70% of the available carbon is found in cementite.

For globular medium Mn steels, which are produced from the intercritical annealing of cold-rolled sheet, the fact that all carbon is found in the cementite at some point of the thermal treatment is not surprising in regards with the literature review [57]. However, a noticeable implication of the last results is that cementite plays also an essential role for the nucleation of austenite in ART fibrous medium Mn steels. The literature review highlighted the existence of two types of austenite in fibrous ART medium Mn steels, namely an acicular austenite born from ART mechanism, with K-S OR with the matrix, and a globular austenite nucleating at PAGB, with random OR with surrounding grains [7], [65]. The present results show that independently of the intercritical annealing temperature T_{IA}, cementite precipitates play an essential role for the carbon distribution inside the steel, at least transiently.

Finally, during the cooling, as austenite transforms into fresh martensite, Equation (II—9) becomes invalid. As martensitic transformation is diffusionless, the carbon content in austenite will be the same as that in martensite. At the end of the thermal treatment, if we note f_γ^0 and $f_{\alpha'}^0$ the respective fraction of austenite and fresh martensite, and $C_{\alpha'}$ the mean carbon content in martensite, then Equation (II—9) becomes:

$$C_\gamma = C_{\alpha'} = \frac{C_{tot} - f_\theta\, C_\theta}{f_\gamma^0 + f_{\alpha'}^0} \qquad \textbf{(II—10)}$$

This Equation (II—10) is especially useful to calculate the carbon content of austenite after the thermal treatment, when no information on the in situ enrichment during isothermal holding is available. This is the case for the tensile specimens studied in Chapter III, which are annealed in salt-bath furnaces, as discussed below.

Unfortunately, these estimations of the evolution of austenite carbon content are not sufficient to calculate the in situ evolution of M_s temperature as the chemical stability of retained austenite also depends on the partitioning of other alloying elements, in particular its enrichment in Mn, which cannot be deduced unambiguously from the relative evolution or the absolute values of the lattice parameter of austenite and HEXRD data.

It is still possible to assess the effect of carbon using Equation (II—8) [171]. The results of the effect of carbon on M_s, denoted ΔM_S^C, at the end of all experiments are given in Table 6. The austenite most stabilized by carbon is found in GL680 and GL700 microstructures, while the least stabilized by C is found in FB750 (the lower the ΔM_S^C, the higher the stability). There is a gap of 140°C between highest and lowest value of ΔM_S^C. Austenite is more stabilized by carbon in globular microstructures when

compared with the corresponding fibrous microstructures. The effect of carbon on M_S temperature is thus of prime importance to obtain stable austenite at RT.

	Annealing Temperature	680°C	700°C	720°C	750°C
Effect of carbon only on M_s ➔ $\Delta M_S^C = -600 \times (1-\exp(-0.96C_\gamma)$	One-step (GL)	-321°C	-318°C	-284°C	-232°C
	Two-step (FB)	-235°C	-281°C	-239°C	-183°C

Table 6: Effect of carbon content experimentally measured on the M_S temperature. ΔM_s^C is calculated with van Bohemen law, reported in Equation (II—1) [171].

B. Hydrostatic stress inherited from final cooling

As explained above, the slopes of the "linear" decreases of the lattice parameters in both ferrite and austenite do not correspond to the ones expected considering the sole CTE of the respective phases. As no chemical partitioning is expected during cooling, the most plausible explanation for this deviation is the genesis of hydrostatic internal stresses at the phase scale due to the difference of CTE between phases and the related strain incompatibility.

In retained austenite, the slope is lower than the one obtained in a stress-free fully austenitic phase and the inverse situation is observed in ferrite. It means that, at room temperature, the lattice parameter of austenite is higher than expected and the phase is in tensile hydrostatic stress state, whereas compressive stress state appears in ferrite. In such case, identifying the stress-free behaviour of the phases (stress-free CTE) to serve as a reference is the key for a correct evaluation of the internal stresses.

For the ferritic matrix, the difference in the slope is evident when comparing it during heating and cooling for the GL microstructures. The GL microstructures must serve as reference for the fully ferritic matrix (even if containing few cementite) as FB microstructures are initially martensitic, and thus could present significant initial internal stresses which could relax during heating and affect in turn the evolution of the lattice parameter. For the austenite, it is not possible to use the present experiments to observe and quantify the behaviour of a stress-free austenite. Austenitization annealing at 900°C of cold-rolled ferritic steel has been used to create such reference for austenite.

In this study, the stress-free CTE of both austenite (α^γ) and ferrite (α^α) are described with the mathematical description proposed by van Bohemen [176] as a function of the temperature T:

$$\alpha^\gamma(T) = B^\gamma\left(1 - e^{\frac{-T}{\theta^\gamma}}\right) \qquad \text{(II—11)}$$

$$\alpha^\alpha(T) = B^\alpha\left(1 - e^{\frac{-T}{\theta^\alpha}}\right) \qquad \text{(II—12)}$$

With B^i and θ^i (i = γ or α) there are 4 parameters to be calibrated on the reference stress-free behaviours of the austenite and ferrite phases, respectively. The calibration parameters proposed by van Bohemen for a Fe/0.1C/7Mn steel permits to describe, with an excellent agreement, our reference stress-free austenite and ferrite (GL microstructure during heating).

Figure 62 and Figure 63 present in black the measured lattice parameters of austenite and ferrite respectively, for all experiments as a function of temperature, reproduced from Figure 57 and

Figure 55. For FB680 steel, the two experimental lattice parameters are extracted from the second FB680 thermal treatment done in December 2021 and recorded on a Pilatus detector, as discussed in section II.1.B. In the first FB680 treatment, an inappropriate acquisition rate of 1/3 Hz made the measurement of lattices during cooling impossible (see sections II.3.B and II.3.C). The second FB680 thermal treatment gives a microstructure very similar at the end to the first FB680 treatment, with a final fraction of austenite of 13.5% (compared with 12%).

The stress-free thermal expansions of both phases calculated according to Equations (II—11) and (II—12) are represented in blue. The curve was set to coincide with the experimental value at high temperatures for which the internal stresses are supposed to be fully relaxed. When comparing the experimental values (black curves) and the expected stress-free behaviours due to the sole thermal expansion (blue curves) during cooling, a systematic deviation appears, as discussed above. For austenite, the experimental values are higher than the stress-free trend and the contrary is observed for ferrite.

In order to go farther, a mean-field Mori-Tanaka like micromechanical approach has been developed by Allain et al [25]. The apparent CTEs ($\alpha^{\gamma}_{apparent}$ and $\alpha^{\alpha}_{apparent}$) considering the internal stresses are estimated as follows:

$$\boldsymbol{\alpha^{\gamma}_{apparent} = \alpha^{\gamma} + (1 - F^{\gamma})\left(\frac{20\nu^{\alpha} - 10}{15(1 - \nu^{\alpha})}\right)(\alpha^{\gamma} - \alpha^{\alpha})} \qquad \textbf{(II—13)}$$

$$\boldsymbol{\alpha^{\alpha}_{apparent} = \alpha^{\alpha} - F^{\gamma}\left(\frac{20\nu^{\alpha} - 10}{15(1 - \nu^{\alpha})}\right)(\alpha^{\gamma} - \alpha^{\alpha})} \qquad \textbf{(II—14)}$$

With ν^{α} being the Poisson's ratio of ferrite, taken equal to 0.3. This model relies on the assumption that austenite is in inclusion in the ferritic matrix (round shape) and its fraction is low. The constrained behaviours calculated with these apparent CTEs are also represented in Figure 62 and Figure 63 (red curves). For both ferrite and austenite, the model is able to capture globally the observed trends, in particular at low temperatures. For all experiments, for both phases, a systematic deviation is observed in the high temperature range (the experimental values are higher than the predicted ones), without clear explanation so far (the current hypothesis is a possible thermal gradient in the samples due to the gas cooling process at -200°C/s).

When comparing the experimental lattice parameter a^i and the expected stress-free one at room temperature (Δa^i), the hydrostatic pressure in phase i can be calculated using the bulk modulus K^i and the relative lattice volume change ($\Delta V/V$):

$$\boldsymbol{P^i = -K^i\frac{\Delta V}{V} = -3K^i\frac{\Delta a^i}{a^i}} \qquad \textbf{(II—15)}$$

$$\boldsymbol{with \qquad K^i = \frac{E^i}{3(1 - 2\nu^i)}} \qquad \textbf{(II—16)}$$

E^i and ν^i being the Young's modulus and Poison's ratio of the considered phase i. The empirical model of Ghosh and Olson [177] gives E^{γ} = 207 GPa and E^{α} = 201 GPa at room temperature, assuming the nominal composition in substitutional alloying elements and the local composition in carbon (0.67 and 0 wt% respectively). Considering that both ferrite and austenite have the same Poisson's ratio (0.3), K^{γ} and K^{α} are taken equal to 172 GPa and 167 GPa, respectively. For example, for the GL720 experiment, the absolute changes in lattice parameters Δa^i are evaluated to be -4.4×10^{-3} Å and $+1.3 \times 10^{-3}$ Å for austenite and ferrite. The residual hydrostatic stresses are then σ_{γ}^{h} = +634 MPa and

σ_α^h = -227 MPa, respectively. Accounting for the experimental error and the error made on the stress-free reference behaviour, the stresses weighted by the phase fractions are very well equilibrated ($f_\alpha \times \sigma_\alpha^h + f_\gamma \times \sigma_\gamma^h$ = 25 MPa ≈ 0 MPa) and the order of magnitude seems consistent.

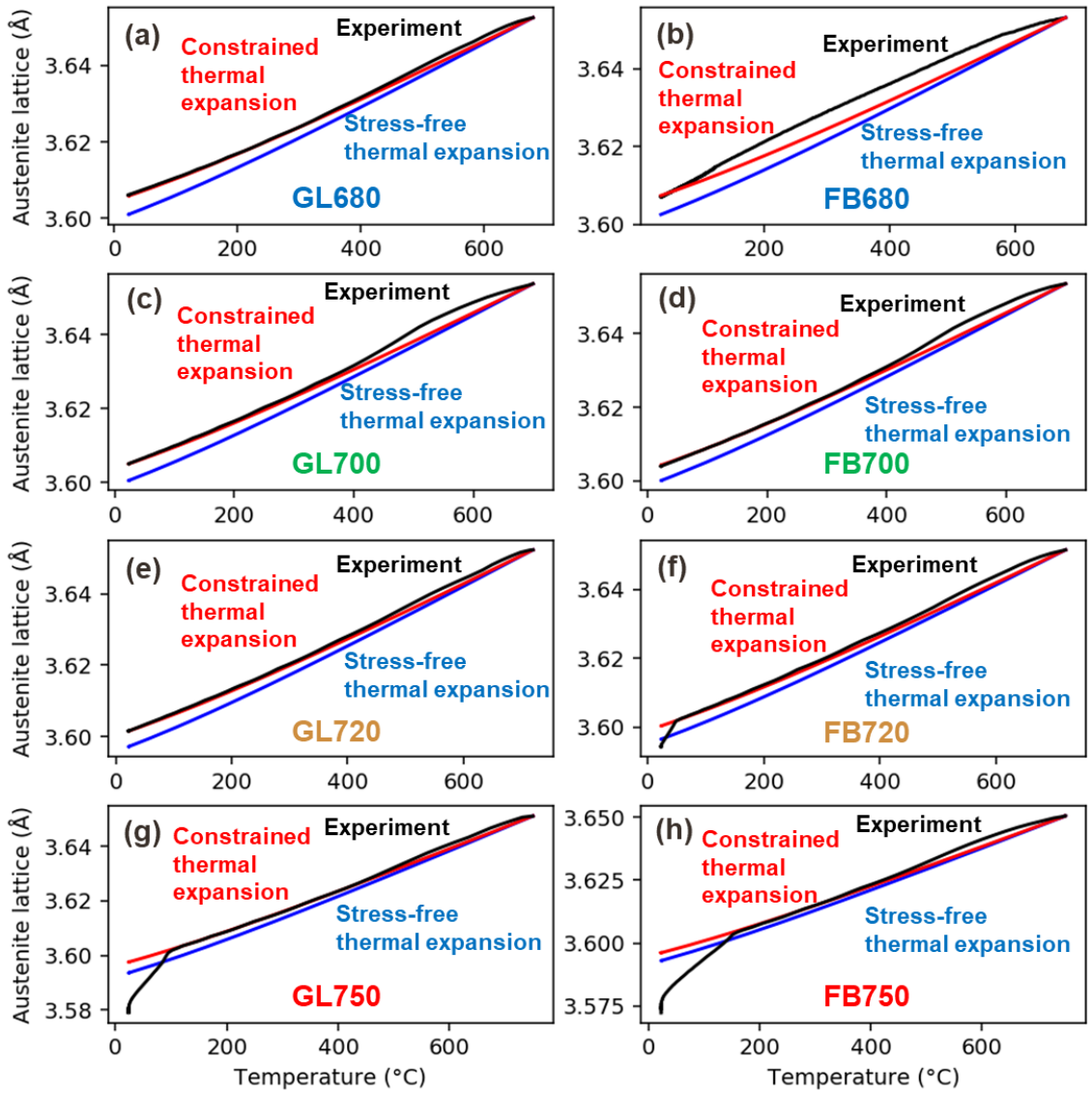

Figure 62: Austenite lattice parameters as a function of the temperature during (a), (c) (e) and (g) one-step treatments and (b), (d), (f) and (h) two-step treatments at different intercritical annealing temperatures. Experimental data in black, reproduced from Figure 57. The stress-free thermal expansions according to Equation (II—11) are represented in blue and the constrained thermal expansions according to Equation (II—13) in red.

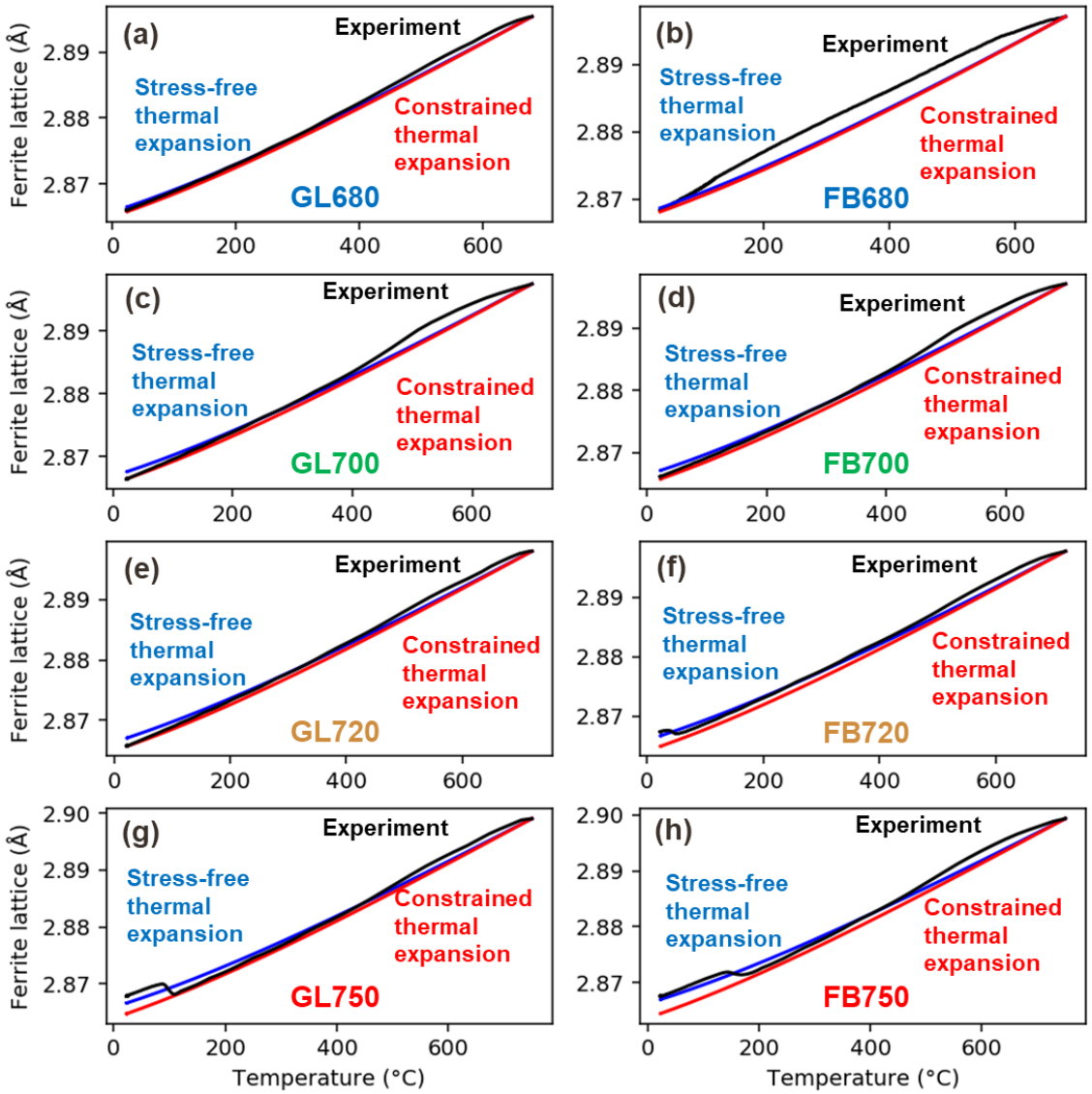

Figure 63: Ferrite lattice parameters as a function of the temperature during (a), (c) (e) and (g) one-step treatments and (b), (d), (f) and (h) two-step treatments at different intercritical annealing temperatures. Experimental data in black, reproduced from Figure 55. The stress-free thermal expansions according to Equation (II—12) are represented in blue and the constrained thermal expansions according to Equation (II—14) in red.

In Table 7, the experimental values obtained with the proposed methodology are summarized for the studied experiments. The methods provide relevant results for all one-step and two-step experiments as the starting microstructure shows already a stress-free behaviour. The results obtained for FB680 and FB700 are consistent with the ones obtained during the GL680 and GL700 experiments. On the contrary, the FB720, FB750 and GL750 show opposite trends. In these latter cases, the final martensitic transformation induces additional compressive stresses in austenite and as a consequence tensile stresses in ferrite. In the absence of the martensitic transformation, values closer to the ones obtained in the GL720 experiment would have been obtained for FB720.

	Annealing Temperature	680°C	700°C	720°C	750°C
Hydrostatic pressure in austenite (MPa)	One-step (GL)	+748	+664	+634	-2066
	Two-step (FB)	+652	+560	-288	-2783
Hydrostatic pressure in ferrite (MPa)	One-step (GL)	-78	-198	-227	+205
	Two-step (FB)	-61	-167	+123	+110

Table 7: Hydrostatic pressures determined in ferrite and austenite at room temperature after the 8 experiments (experimental values). The grey values are affected by the final martensitic transformation.

The micromechanical model can be used to estimate the internal stresses inherited from the difference of CTE (by integrating numerically the previous equations). The results of the calculations depend on the annealing temperature as the higher the temperature the higher the incompatibility of strains. However, the opposite trend is observed experimentally as the fraction of austenite plays a key role in the calculation (even considering that the fraction should remain low in theory). The results of the calculations are reported in Table 8. The order of magnitude and the trends seems well captured by the model in the absence of martensitic transformation. A comparison of the relevant values is proposed in Figure 64 (a). Beyond the direct stress prediction, the interest of the model is to provide values for both ferrite and austenite which satisfy a mechanical equilibrium at room temperature.

	Annealing Temperature	680°C	700°C	720°C	750°C
Hydrostatic pressure in austenite (MPa)	One-step (GL)	+675	+653	+625	+575
	Two-step (FB)	+690	+602	+562	+432
Hydrostatic pressure in ferrite (MPa)	One-step (GL)	-121	-195	-238	-334
	Two-step (FB)	-98	-236	-320	-440

Table 8: Hydrostatic pressures calculated in ferrite and austenite at room temperature after the 8 experiments (in the absence of final martensitic transformation). Theoretical constrained lattices parameters are calculated with Equations (II—13) and (II—14).

Considering that the model is validated by the previous comparison, it can be used to predict the stress state in phases whatever the annealing conditions. Therefore, the tensile hydrostatic stress state in austenite has been plotted in Figure 64 (b) in a map of austenite fraction/annealing temperatures, having in mind that both are correlated indeed. The conditions assessed in Table 7 for the one-step experiments with no martensitic transformation during cooling have been reported (white circles). As discussed above, the decrease in stress in austenite with the temperature is due to the preeminent effect of the fraction compared to the sole effect of the annealing temperature.

To our best knowledge, this is the first work in the scientific community to determine the level of internal stresses building up during the thermal treatment in medium Mn steels. This internal stress impacts linearly the stability of austenite, as proven by the seminal work of Patel and Cohen [83] (see sections I.3.A.c), I.3.A.d) and I.3.B.b) from Chapter I). In their work on Q&P steels, Allain et al. [25] prove that the linear coefficient between the effective M_S and austenite hydrostatic stress σ_γ^h is 0.038°C/MPa. Tensile hydrostatic stress destabilizes austenite (increase of M_S), while compressive hydrostatic stress stabilizes austenite.

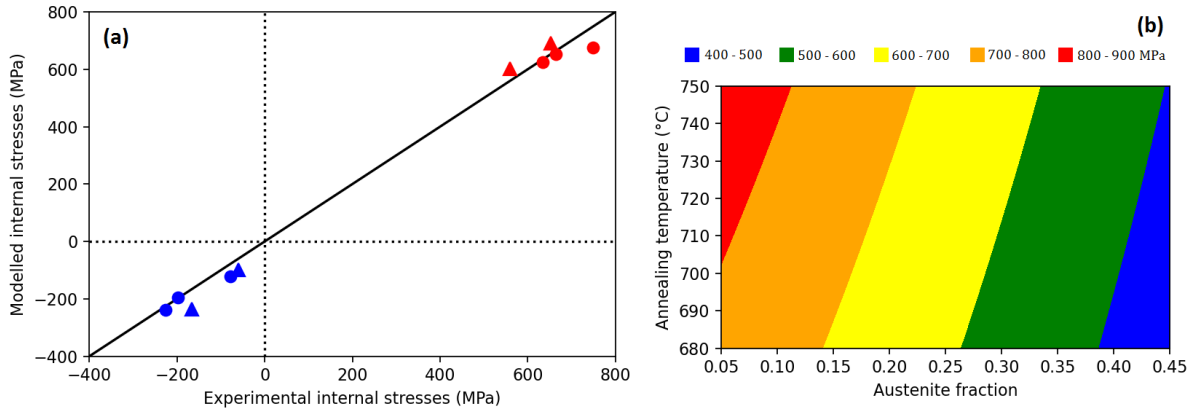

Figure 64: (a) Comparison between the experimental stress states (Table 7) in the absence of martensitic transformation and the modelled stress states (Table 8). The red symbols correspond to austenite and the blue ones to ferrite. The circles represent one-step experiments and the triangles the unique relevant two-step experiments. (b) Hydrostatic pressures predicted in austenite in an austenite fraction/annealing temperature map. The white circles correspond to the one-step experiments below 720°C.

The effect of internal stress on M_S temperature can be calculated with (II—8) [25]. They will be denoted ΔM_s^{σ}. The results are shown in Table 9. The experimental austenite hydrostatic stress σ_{γ}^{h} was used (martensite transformation contribution is thus included). The hydrostatic stress tends to homogenize the M_S temperature between microstructures, as the microstructures which are the most stabilized by C (low T_{IA}) are the ones in which stress destabilizes austenite the most (positive ΔM_s^{σ}). In microstructures with a high T_{IA}, martensitic transformation creates compressive stresses that stabilize austenite (negative ΔM_s^{σ}), decreasing the otherwise very high M_S temperature.

Contrary to chemical effect, which affects austenite at the start of the cooling, internal stress builds up during the cooling. Especially, the stabilizing compressive stress of martensite transformation only occurs after austenite starts to transform into martensite. Therefore, ΔM_s^{σ} must only be interpreted as affecting retained austenite at room temperature, after the thermal treatments (about 5% of retained austenite in the case of GL750 and FB750 microstructures at RT).

	Annealing Temperature	680°C	700°C	720°C	750°C
Effect of internal stress on M_s ➔ $\Delta M_s^{\sigma} = +0.038 \times \sigma_{\gamma}^{h}$	One-step (GL)	+29°C	+26°C	+25°C	-78°C
	Two-step (FB)	+25°C	+20°C	-11°C	-106°C

Table 9: Effect of residual hydrostatic stress experimentally measured on the M_S temperature. ΔM_s^{σ} is calculated with Equation (I—8) [8], [25].

The effect of chemistry cannot be completely determined by HEXRD experiments only. To better understand the effect of substitutional elements, especially Mn, on austenite stability, post-mortem measurements have been done. They are presented in the next sections.

5. Post mortem analysis of plate treated in salt-bath for mechanical testing

Post-mortem analysis of medium Mn microstructures is presented and discussed in this section. Two methods are used: conventional secondary electron (SE) microscopy and wavelength dispersion spectroscopy (WDS). Scanning electron microscopy (SEM) observations were conducted on a Quanta 650 FEG-SEM at IJL for the initial cold-rolled steel before thermal treatment, and on a JEOL 7001 FEG-SEM at ArcelorMittal Maizières Research centre for microstructures after thermal treatments. Eight micrographs were taken for each microstructure, at four different scales, ranging from 80 x 60 µm² to 12 x 9 µm², corresponding to a magnification of x1500 to x10000. In all cases, a solution of 4% Nital was used for etching.

In this section, the analysis is not conducted on the HEXRD specimens. In fact, the purpose of the thesis is to understand the austenite mechanical stability during straining. As tensile specimens cannot be produced in the dilatometer, they were produced through salt-baths annealing. The complete description of in situ tensile tests experiments during HEXRD is given in the next chapter. The temperature schedules for these latter treatments through salt-baths (SB) are exactly the same as the ones described in Table 2. However, the obtained microstructures by SB annealing are not exactly the same as the one obtained in the previous sections after in situ HEXRD experiments . Medium Mn steels are indeed very sensitive to the intercritical annealing temperature and a 5°C error can change significantly the microstructure. The two thermal treatments are compared in Figure 65 for FB680. In red is the thermal treatment in salt-baths (recorded with a single welded thermocouple), while in blue is the thermal treatment conducted in dilatometry and previously analysed (called “HEXRD sample”). The heating rate in model treatment was set at +10°C/s. In salt bath, the heating rate is initially far higher, then decreases exponentially until reaching the intercritical temperature. After that, both thermal treatments are quite similar, with a comparable cooling rate. To characterize the microstructures obtained in salt-baths, post-mortem secondary electron observations were made. A semi-automated algorithm was developed and is presented afterwards to determine the different phase fractions and the distributions of grain sizes for all salt-baths microstructures. The latter size is essential to assess the mechanical stability of austenite. While the same procedure was not intended on dilatometer samples, their SEM images are still presented in Appendix E.

As shown before, the main difference between model thermal treatments in HEXRD dilatometry and treatments in salt-baths is thus in the heating step. To better understand the effect of the heating rate on final microstructure, a second set of dilatometer thermal treatments was analysed in situ in May 2021, alongside the already presented experiment. This second set, called “realistic dilatometer” treatment, is represented in black in Figure 65 for FB680 steel. The purpose of those latter treatments is to reproduce the microstructures obtained in salt-baths more accurately. Compared with model dilatometry treatments, treatments only have a different heating scheme. Until 500°C, the heating rate is set at +50°C/s. Then, between 500°C and T_{IA} - 50°C (i.e. 630°C for FB680), the heating rate is set at 12°C/s. Finally, between T_{IA} - 50°C and T_{IA}, a very low heating rate of +1°C/s was chosen.

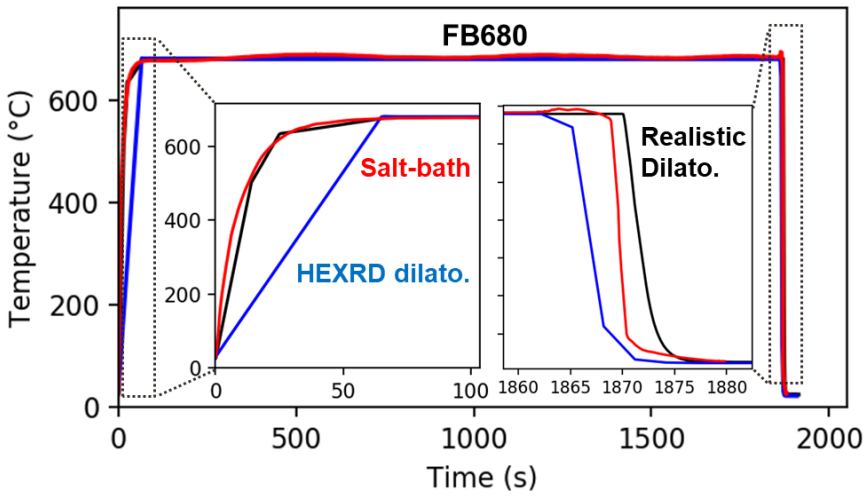

Figure 65: Comparison between the different methods used in the PhD project to produce intercritical annealed medium Mn steels. In red: treatment in salt-bath (used to produce tensile samples – cf. Chap. III). In blue: HEXRD experiments (analysed from section II.1 to II.4). In black: dilatometry treatment trying to reproduce more closely the treatment in salt-bath. The given examples are FB680 thermal treatments. Magnifications of the heating and cooling steps are also given.

The phase fraction of retained austenite obtained by Rietveld refinement at room temperature is compared for all eight microstructures between the three sets of experiments in Table 10. Please note that this fraction may differ from the total fraction of austenite formed during IA, as martensitic transformation can occur during cooling. The austenite fraction is very similar between microstructures obtained by "HEXRD" and "realistic" treatments, which are both done in the same dilatometer. The maximum difference in phase fractions between these two sets is about 4% and is obtained for FB720 and GL680 microstructures. Between microstructures processed through salt-bath and the ones processed through a dilatometer, the difference is more important. At T_{IA} = 680°C and 700°C, more austenite is measured in dilatometry microstructures that in salt-bath treated microstructures. On the contrary, at T_{IA} = 750°C, more retained austenite is found in microstructures obtained in salt-bath. At T_{IA} = 720°C, austenite is found at similar level in globular microstructures, while there is far more austenite in fibrous microstructures produced by dilatometry. Obtaining similar microstructures with salt-bath and dilatometer treatments was one of the major difficulties of the current thesis. The difference between salt-bath and "HEXRD" sets of microstructures are discussed further afterwards.

Microstructure\Austenite fraction	HEXRD	Realistic	Salt-bath
FB680	8.4%	10%	5.5%
FB700	29%	28%	13%
FB720	20%	24%	31%
FB750	5.7%	7.1%	16%
GL680	16%	20%	12%
GL700	24%	26%	18%
GL720	29%	28%	25%
GL750	5.9%	6.2%	18%

Table 10: Austenite phase fraction in each medium Mn microstructure for the three sets of experiments. The denominations of each set are reproduced from Figure 65.

Overall, the obtained microstructures are very similar between “HEXRD” and “Realistic” sets of experiments. Therefore, the transformation kinetics obtained during this third set of experiment (“Realistic”) are not presented in the main body of the manuscript, and are only presented in Appendix F. The latter are still presented here since the dilatometry sample obtained from “realistic treatments” were analysed with wavelength dispersion spectroscopy (WDS), whose results are presented at the end of the chapter. WDS technique allows to measure manganese, aluminium and silicon distributions, which is essential to obtain austenite thermomechanical stability. The obtained results are discussed afterwards as they are considered to be representative to the ones that would have been obtained by analysing microstructures obtained with salt-baths or model HEXRD dilatometry treatments.

A. Methodology of the post-mortem analysis

a) Wavelength dispersion spectroscopy (WDS)

WDS analysis was conducted using the JEOL 7001 FEG-SEM located at ArcelorMittal Maizières Research centre. It is equipped with a field emission gun (FEG), secondary electron (SE) and back-scattered electron (BSE) detectors, an energy dispersive spectrometer (EDS), four wavelength dispersive spectrometers (WDS) and a soft X-Ray emission spectra (SXES) spectrometer.

The electron source emitted by FEG is more stable and narrower than the ones created with tungsten filament or a LaB6 tip. The probe size remains fine at lower accelerating voltages and high probe currents, resulting in good analytical performance. The maximal resolution is 0.1 µm in optimum conditions. This performance is obtained by combining the spatial resolution of the probe with the sensitivity and lateral resolution of WDS detectors. The energy resolution in WDS mode is 8 eV.

The WDS technique is based on the analysis of the X-ray spectrum emitted when an atom is stimulated by incident electrons. These X-Ray spectrums are characteristic of each type of atoms, allowing to discriminate between different elements. In this study, WDS was used to establish composition maps in manganese, aluminium and silicon inside austenite and ferrite grains. While being normally also able to determine the distribution of carbon, there was an external pollution source which made quantitatively inaccurate the WDS analysis of carbon in the presented experiments.

b) Quantification of phase fraction and grain size distribution by SEM analysis

The key microstructure characteristics that can be measured with conventional SE are the phase fractions, the grains size distribution of each phase and their respective shape factor distribution. Indeed, all these parameters are crucial to understand the mechanical behaviour of medium Mn steels, and to further model it. In this work, a semi-automated method was developed to systematically analyse SE images after etching. The image processing has been conducted on Python 3.7.4, using the following libraries: numpy, matplotlib, tkinter, scipy and skimage.

To measure grain size and shape factor distributions, grain contours have to be detected first. To do so, an original algorithm was developed to analyse properly the microstructures, based on the watershed algorithm, which serves to detect grain boundaries. This method is a segmentation algorithm. In Figure 66, the principle of the algorithm is illustrated on a simple 1D example, in which a curve is composed of three valleys having to be detected and contoured separately. To do so, a source is placed at the trough of each valley. Then, "water" appears from those sources, and floods the relief. When two types of water encounter (red and yellow waters at h=90 for example), they do not mix and a vertical barrier appears, which will be considered as the boundary of the domain. At the end of the flood, when h equals the maximum intensity of the curve, all three valleys are separated by clearly defined borders.

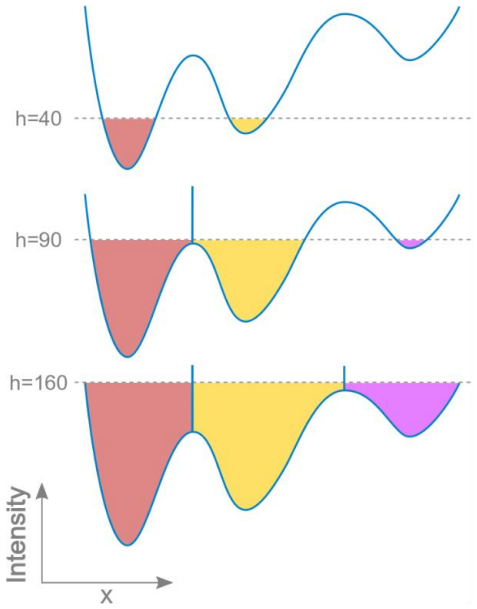

Figure 66: Schematic representation of a watershed algorithm running in 2D. Each colour represents one separated domain, i.e. one grain in our case [178].

In the case of 2D map, a grayscale intensity map has to be extracted from the original map, which will serve for the same purpose as the intensity function shown in Figure 66. In this grayscale intensity map, locally lighter areas should correspond to grain boundaries and darker areas to grain interior. From SEM micrographs, such a grayscale intensity map is easily created by applying a Sobel gradient filter on the image. For instance, when making an 1D slice on the intensity map, the obtained intensity curve is similar to the one shown in Figure 66. The sources are automatically distributed at the local minimums of the intensity map. As the placement of sources is not perfect with an automated algorithm, sources also have to be manually removed and added. The result of the watershed algorithm is a domain map, in which each segmented domain represents a grain. The phase of each grain is determined by calculating the average intensity of the pixels situated in the domain in the original micrograph and comparing this mean intensity with a threshold value. By doing so, the phase identification is not undermined by texture contrast. The grain area A is calculated with the number of pixels contained in the domain. Then, the equivalent grain size D (grain diameter) is calculated considering a spherical grain ($D= 2\sqrt{(A/\pi)}$). A correction of $4/\pi$ is applied on the obtained values since the determination of diameter of three-dimensional objects is made with two-dimensional images [179]. Finally, each grain boundary is fitted by an ellipse that has the same area as the grain, to access their minor axis, major axis and shape factor.

An example of results provided by the algorithm is given in Figure 67. The initial image is a GL680 microstructure (12 x 9 µm²) obtained from model dilatometer treatment (HEXRD). The first result given by the software is the contour map. The algorithm succeeds in separating ferrite grains, austenite grains and cementite precipitates. Contours generate closed areas in the image. Grain boundaries correspondence between the contour map and the initial microstructure is accurate, even between grains of a same phase. The resulting phase map also seems accurate, separating darker ferritic grains from lighter austenite and cementite islands. Although, it must be noted that cementite is accounted as austenite in the algorithm as only 2 phases can be identified with a sole contrast threshold strategy. Thus, the measured austenite phase fraction is overestimated by few percentages in GL680 and FB680. Finally, in Figure 67 (d), the calculated ellipses (green lines) are superimposed on the initial micrography. The ellipse contours match well with the boundaries of the grains situated totally inside image.

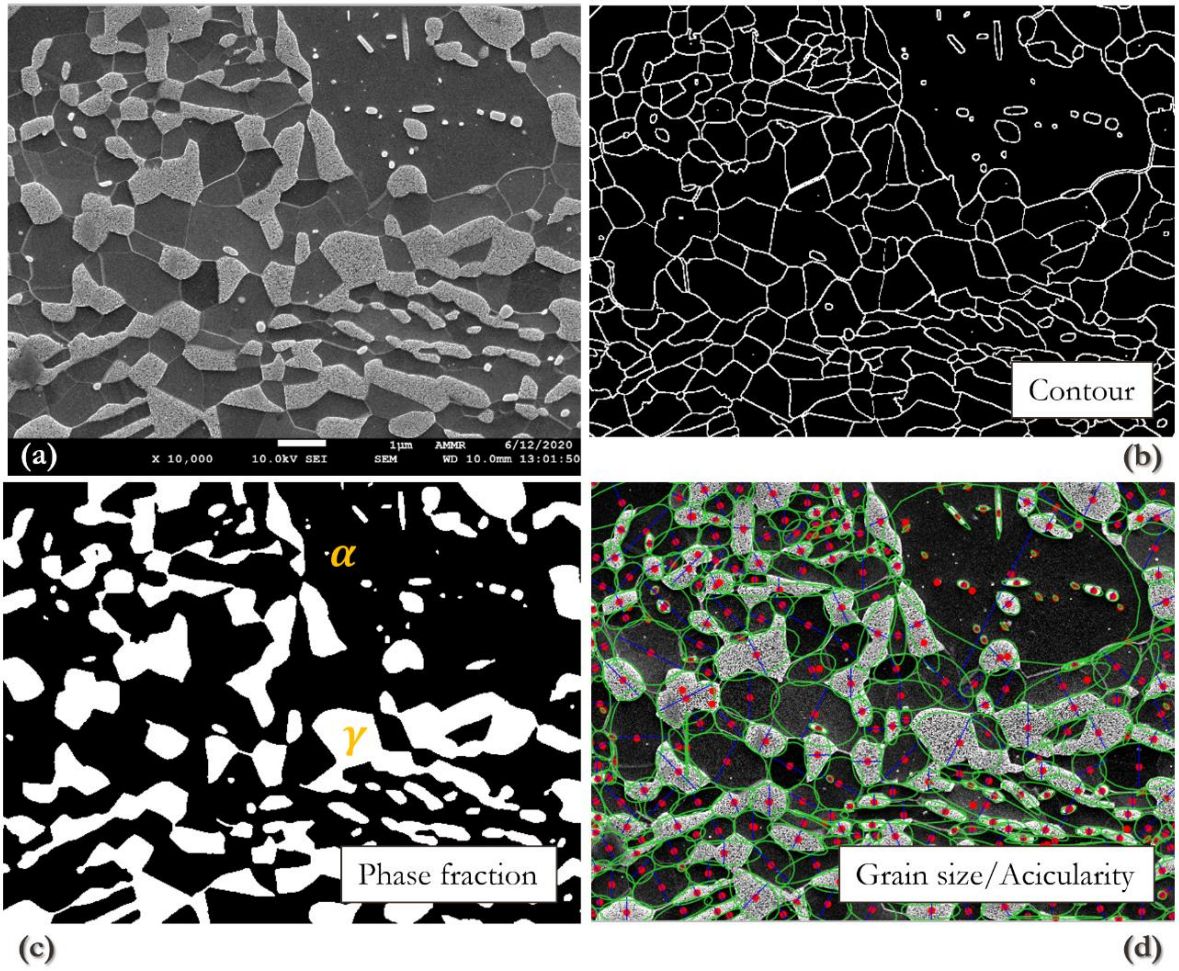

Figure 67: (a) SEM micrograph of the globular microstructure obtained by annealing at T_{IA} = 680°C. (b) The corresponding segmentation of grains calculated with the watershed algorithm. (c) The corresponding phase map (white: austenite and cementite, black: ferrite). (d) Ellipses obtained by the adjustment of grain boundaries, which give access to grain sizes and shape factor distributions. Green lines correspond to ellipse perimeters, red points to ellipse centres and blue line to ellipse minor axes.

A post treatment of data is conducted to eliminate the grains located at the edges of the micrograph from the statistics concerning grain sizes. Also, some portions of few pixels are sometimes detected as a grain by the algorithm due to closely positioned sources. A threshold on the minimum grain size is used to remove them from both ferrite and austenite statistics. Finally, as shown in Figure

67, the ferrite grain boundary is sometimes detected as an individual grain. These grains may be eliminated by using a threshold on the shape factor (as grain boundaries are fitted with an ellipse that has a huge shape factor). As such, these three kinds of grains are excluded from the following statistical analysis of sizes and shape factors, presented in the next sections.

B. Results and discussions

a) Microstructure obtained by salt-baths treatment

i. Duplex microstructures obtained after annealing at 680°C

Figure 68 shows the SEM micrographs for both GL680 (a), (c) and FB680 (b), (d) samples. For each microstructure, both a low and a high magnification are given. The low magnified micrography (×2500) allows to have a global overview of the microstructures, which is especially important in fibrous steels to see the PAG (prior austenite grains, i.e. austenite grains formed during the first austenitic annealing, which have a mean diameter of 13 µm according to section II.1.B.b)). The highly magnified micrography allows to better see the different phases at grain scale. For the globular steel, the most magnified images are at ×10000. Unfortunately, for fibrous steels, they are different and only magnified at ×7500.

Both microstructures are composed of ferrite grains (dark grey), austenite grains (light grey) and cementite precipitates (white). Regions of interest (ROI) are highlighted with coloured circles. In both microstructures, red circles indicate globular austenite and ferrite grains. Blue circles indicate acicular austenite and ferrite grains. Cementite particles in fibrous steel are separated from the ones nucleated on PAGB (prior austenite grain boundaries), and the ones nucleated between martensite laths. They are respectively contoured with green and oranges circles. The colour code developed here is also used in the next sections.

In the GL680 sample, most austenite and ferrite grains are equiaxed, but some areas contain acicular grains. Those latter grains may be remnants of cold-rolled areas from the initial cold-rolled steel (before the intercritical annealing), which may have undergone recovery instead of recrystallization. Equiaxed areas with globular grains may appear due to recrystallization process. Moreover, cementite is non-uniformly present in the globular microstructure. There are some areas with a lot of undissolved cementite, while other areas are devoid of cementite. The absence of austenite in cementite-rich regions is consistent with the austenite nucleation mechanism described in section I.2.A. Overall, GL680 sample presents a very heterogeneous microstructure.

The FB680 microstructure is mainly composed of acicular ferrite grains. The literature review highlighted the existence of two types of austenite in fibrous ART medium Mn steels, namely an acicular austenite born from ART mechanism, with K-S OR with the matrix, and a globular austenite nucleating at PAGB, with random OR with surrounding grains [7], [65]. As expected from literature review (section I.2.B), some globular austenite (red circles) appears also presumably on PAGB, and some fibrous austenite (blue circle) appears between prior martensite laths.

Moreover, it seems that there are more carbides in FB680 than in GL680 samples, in accordance with HEXRD results. Undissolved cementite seems more uniformly distributed in FB680 than in the GL680 microstructure. In fibrous microstructures, PAGB concentrates a lot of cementite (green). However, as the density of martensite laths boundary is higher than PAGB density, most of cementite is still found between martensite laths.

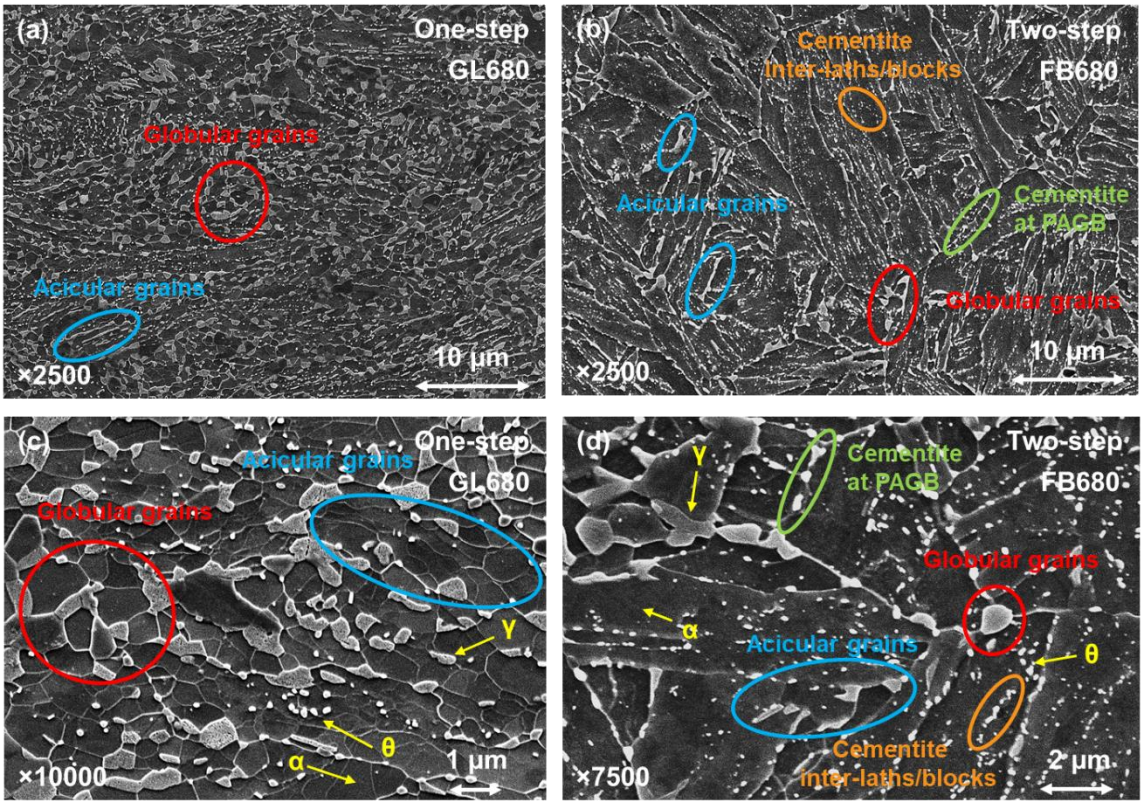

Figure 68: SEM micrographs of globular and fibrous microstructures annealed at 680°C. (a) GL680 magnified at ×2500. (b) FB680 magnified at ×2500. (c) GL680 magnified at ×10000. (d) FB680 magnified at ×7500. Ferrite appears in dark grey, austenite in light grey, cementite in white particles.

ii. Duplex microstructure obtained at 700°C annealing

The GL700 and FB700 microstructures are shown in Figure 69. Both microstructures seem similar to their T_{IA} = 680°C counterpart. They consist mainly of austenite and ferrite grains. Fewer undissolved cementite carbides are present in the microstructure when compared with GL680 and FB680 microstructures. “Austenite” grains in the GL700 look rougher than those annealed at 680°C. This roughness is maybe due to the formation of fresh martensite during final quenching. This would be in accordance with the thermodynamical calculations discussed above.

In FB700, the difference between acicular austenite situated between martensite laths and globular austenite situated at PAGB is clearer than in FB680 microstructure. Most of the austenite seems to be located in the inter-laths regions.

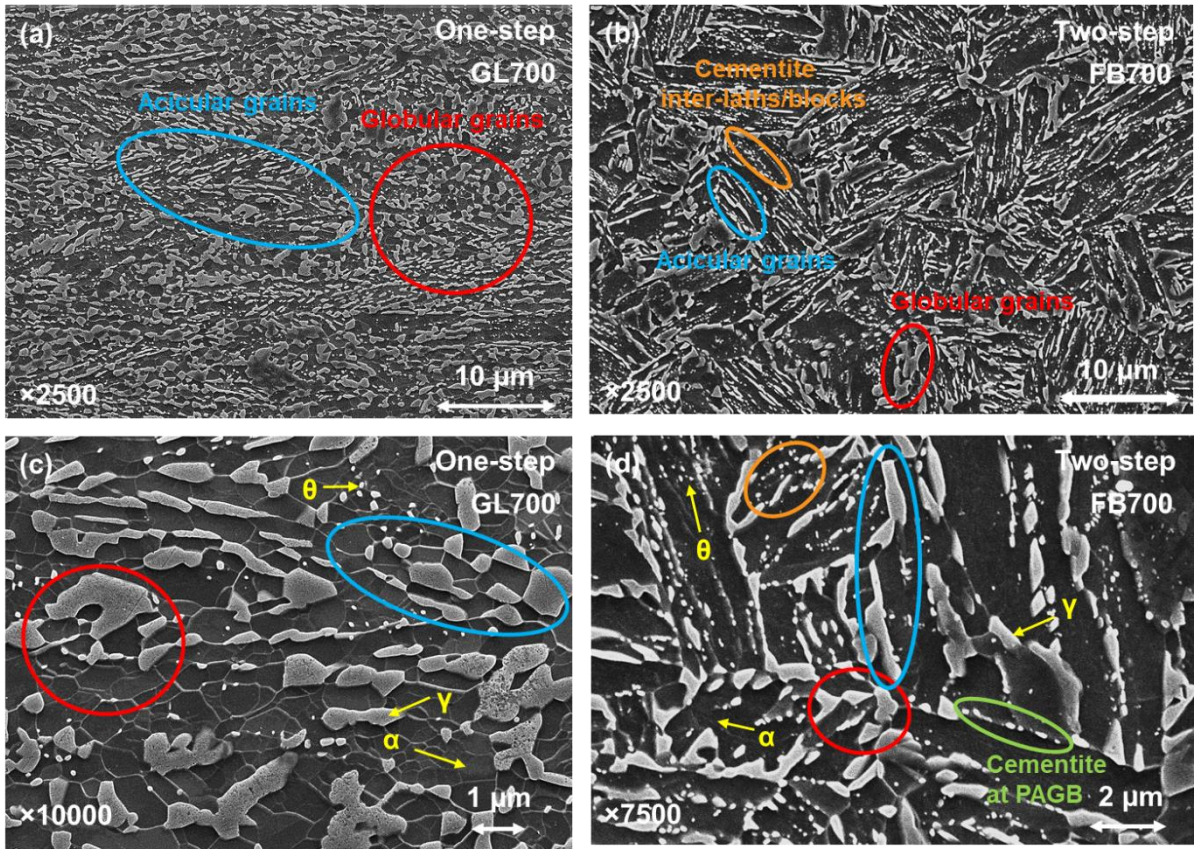

Figure 69: SEM micrographs of globular and fibrous microstructures annealed at 700°C. (a) GL700 magnified at ×2500. (b) FB700 magnified at ×2500. (c) GL700 magnified at ×10000. (d) FB700 magnified at ×7500. Ferrite appears in dark grey, austenite in light grey, cementite in white particles.

iii. Duplex microstructures obtained at 720°C annealing

The globular and fibrous microstructures obtained after annealing at 720°C are presented in Figure 70. They are composed of ferrite grains and martensite/austenite (M/A) islands or films. The M/A islands are far coarser than those in microstructures obtained at lower annealing temperatures, highlighting a higher martensite fraction. Carbide seems totally dissolved during the intercritical annealing in the two microstructures as expected with HEXRD results.

In FB720, the difference between acicular austenite situated between martensite laths and globular austenite situated at PAGB is clearer than in FB680 microstructure. Most of the austenite seems to be located in the inter-laths regions, like for FB700 steel.

The set of austenite grains seems to form a connected space in FB720 steel. On the contrary, austenite grains are generally separated in GL720 steels and only surrounded by the ferritic matrix. This may affect the environmental stability of austenite (due to different repartition of stress between phases, and different resistance to martensite transformation as surrounding phase does not have the same mechanical properties).

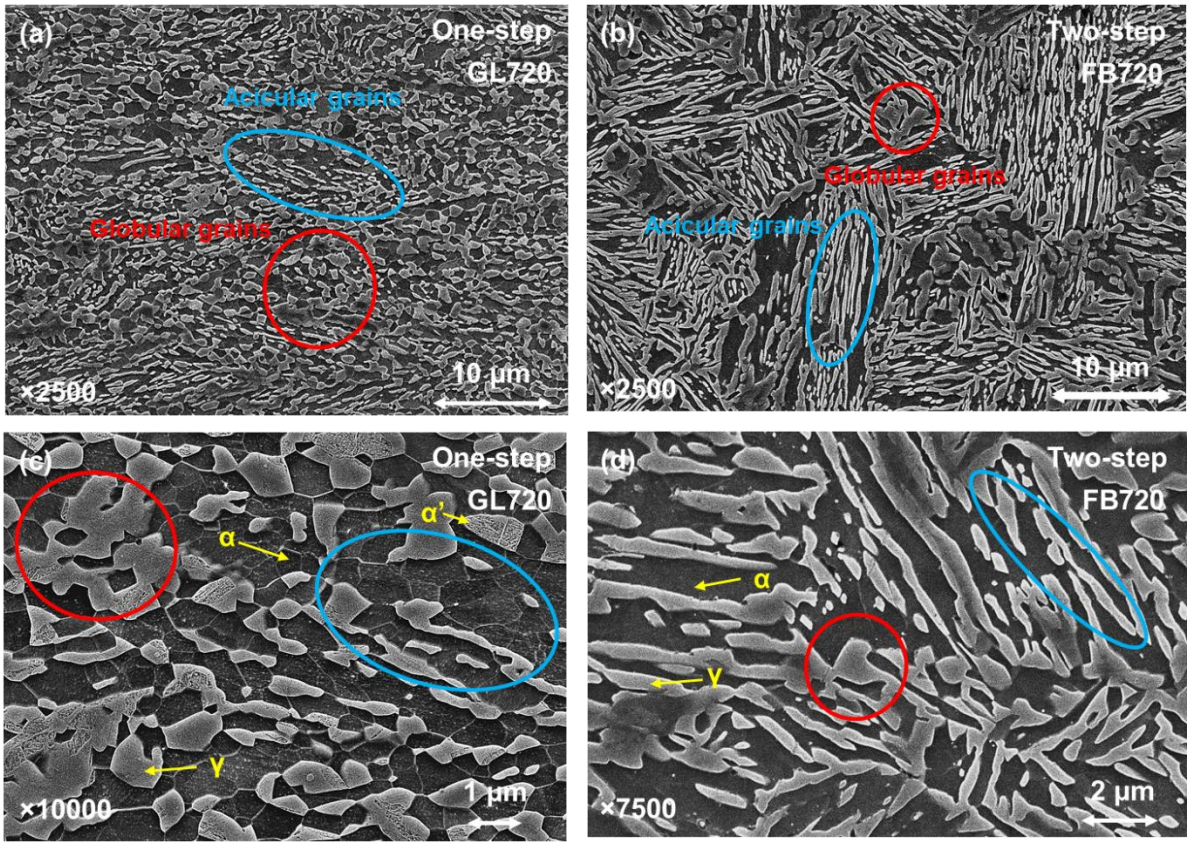

Figure 70: SEM micrographs of globular and fibrous microstructures annealed at 720°C. (a) GL720 magnified at ×2500. (b) FB720 magnified at ×2500. (c) GL720 magnified at ×10000. (d) FB720 magnified at ×7500. Ferrite appears in dark grey, austenite in light grey, cementite in white particles.

iv. Duplex microstructures obtained at 750°C annealing

The microstructures obtained at 750°C can be seen in Figure 71. Both GL750 and FB750 microstructures are composed of ferrite and M/A grains. M/A grains are very rough, and the flat and smooth domains in those M/A grains are rare. a small fraction of austenite is retained in the final microstructure. Thus, most of the austenite produced at 750°C transforms during the final quenching, which is consistent with the very unstable nature of austenite expected at 750°C for the studied steel. When comparing the samples annealed at T_{IA} = 750°C and the ones at T_{IA} = 680°C, it is clear that there is less ferrite in the final microstructure. This is expected also from the thermodynamical calculations presented above.

In FB750 steel, the difference between acicular austenite situated between martensite laths and globular austenite situated at PAGB is less clear than in FB700 and FB720 microstructures. Indeed, acicular austenite follows what seems to be at PAGB, and inside what seems to be at the centre of prior austenite, globular austenite grains are found. This may be due to coalescence of grains at high annealing temperature.

In both GL750 and FB750 microstructures, the set of austenite grains seems to form a connected space. Still, austenite grains are more connected in FB750 than in GL750 steel. Like before, this may affect the environmental stability of remaining austenite.

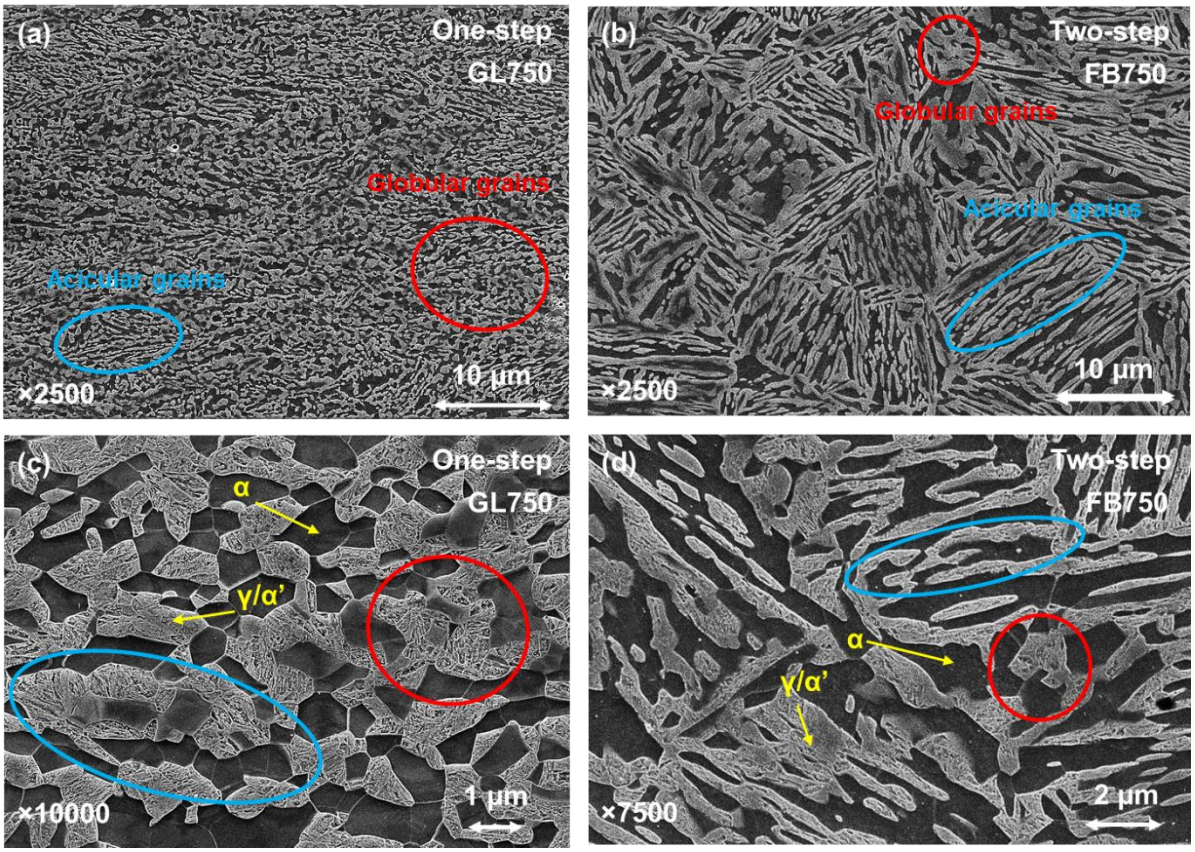

Figure 71: SEM micrographs of globular and fibrous microstructures annealed at 750°C. (a) GL750 magnified at ×2500. (b) FB750 magnified at ×2500. (c) GL750 magnified at ×10000. (d) FB750 magnified at ×7500. Ferrite appears in dark grey, austenite in light grey, cementite in white particles.

In summary, at intercritical annealing temperature T_{IA}=680°C, the studied steels have a microstructure composed of ferrite and austenite grains, M/A islands and contains some small carbides. More cementite carbides are found in fibrous microstructures than in globular ones. Cementite totally dissolves during intercritical annealing above T_{IA} = 720°C. Fresh martensite seems absent from samples annealed at 680°C, but increases with increasing intercritical annealing temperature and becomes the major phase in M/A grains at 750°C. The results are in good agreement with HEXRD results.

A more quantitative microstructural analysis, which is necessary for the micromechanical modelling of such medium Mn steels, is conducted in the next section.

b) Phase fraction

The measured M/A phase fractions for both globular and fibrous microstructures treated in salt-baths are indicated in Figure 72 (red curves in (a) and (b) respectively). The M/A phase fraction is supposed to be close to the austenite phase fraction at the end of the intercritical annealing before quenching. They are compared to the thermodynamic calculation (CEQCSI) in section II.1 (green curve) and the austenite phase fraction obtained in HEXRD samples at the end of the isothermal holding (blue curves).

The experimental values are calculated by averaging the measurements on two images with a field of 12 x 9 µm² images (magnification = ×10000) per microstructure. As the statistical relevance of measurements is low, the uncertainty is estimated to be +/-5%. Overall, the trend for both kinds of morphology as a function of intercritical annealing temperature is similar to that calculated at the equilibrium conditions. There is a constant 10-15% difference between measurements and equilibrium values, which could be attributed to kinetics cause. Indeed, as HEXRD study demonstrates, transformation kinetics are far from being terminated at the end of isothermal holding after 30/15 min.

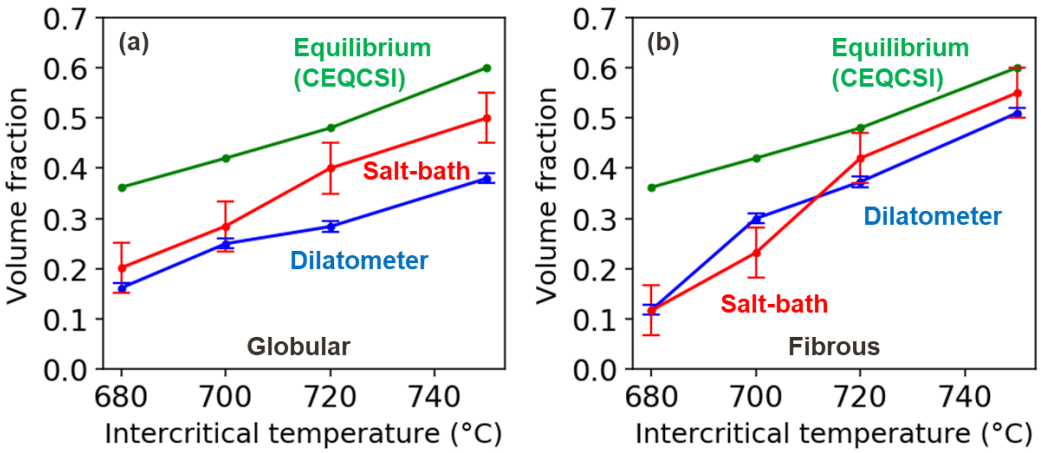

Figure 72: Comparison between the phase fraction of M/A islands calculated at equilibrium by CEQCSI as a function of the IA temperature (green), measured on samples treated in salt-baths by SEM (red) and determined by HEXRD during in situ trials (blue). (a) for one-step and (b) for two-step heat treatments.

When comparing M/A phase fractions between microstructures produced in salt-baths (red) and in HEXRD dilatometer (blue), the phase fractions are very close for fibrous steels, in the margin of error, except for FB700 steel for which the difference is about 8% between the two process conditions. For globular specimens, the difference is negligible at low annealing temperature (T_{IA} < 700°C). At high annealing temperatures (T_{IA} > 720°C), salt-bath treated sample contained 15% more austenite/martensite than the ones produced in dilatometer.

This difference is yet not elucidated, and may be due to difference in heating rate or in uncertainty in temperature control during isothermal holdings. The powers developed by the coil inside the dilatometer to heat the different samples have been verified for all experiments and are consistent with the targeted temperatures. It is also possible that surface decarburization occurred on the dilatometry samples, especially at 720°C and 750°C. Indeed, inside the Bähr dilatometer, the pressure was set below 5×10^{-4} bar. By HEXRD, the obtained phase fractions would be the average of austenite content in the decarburized area and the heart of the sample, diminishing the mean fraction. This aspect should necessitate further investigation as the current data cannot permit to conclude, due to the high sensitivity of duplex medium Mn microstructure to their formation temperature.

Finally, the fraction measured in salt-baths treated specimens are very similar between globular and fibrous steels for a given annealing temperature. At T_{IA} = 680°C, the fraction of austenite is about 20%. At T_{IA} = 750°C, the fraction of austenite is about 50%.

c) Grain size and shape factor

The average grain sizes (equivalent diameter) and shape factors obtained by the algorithm for both phases (M/A islands and ferrite grains) as a function of intercritical annealing temperature for the two microstructural morphologies are reported in Figure 73. The full distributions for all 8 microstructures are given in Appendix G. For each microstructure, the statistics are evaluated over SEM images with a magnification between ×5000 and ×10000, depending on the available data and the finesse of the microstructure. This allow for a sizable statistic of 400 grains for most microstructures.

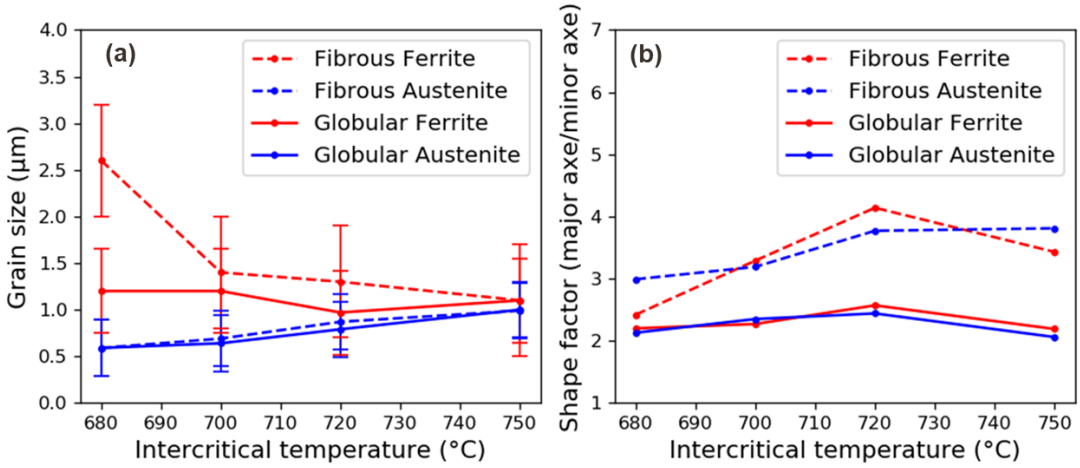

Figure 73: Average grain sizes (a) and shape factors (b) of the two phases as a function of the intercritical annealing temperature for both microstructure morphologies. The bars on (a) are representative of the standard deviation of grain size distributions. They are not represented in (b) for clarity purpose.

Considering the equivalent diameter, the grain size of M/A islands is between 0.5 µm and 1 µm in average. The measured austenite grain size is similar between both morphologies of microstructures. It increases slightly as the intercritical annealing temperature increases.

On the contrary, the ferrite grain size decreases with increasing T_{IA} for fibrous steels. It goes from 2.6 µm to 1.1 µm. For globular steel, the ferrite grain size is overall constant at 1.1 µm, with a minimum of 0.9 µm for GL720. The standard deviation of grain size distributions is about 0.3 µm for austenite grains in both fibrous and globular steels, 0.45 µm for globular ferrite grains and 0.6 µm for fibrous ferrite grains.

These sub-micrometric values are expected for medium Mn steels with ultra-fine grains. Ferrite grain size is higher than the austenite one in both microstructures. Between both microstructures, ferrite is larger in the fibrous microstructures than in the globular ones.

The shape factor is calculated as the ratio between the major axis and the minor axis of the ellipses. As expected, the fibrous microstructure has more acicular grains than globular ones (factor of 5 compared with 2). As previously stated, globular steels are not equiaxed due to the inheritance of cold-rolling. Increasing the intercritical annealing temperature does not increase the shape factor in the case of globular microstructures, while it seems to increase the acicularity of fibrous microstructures. Finally, it is notable that for a given microstructure, ferrite and austenite/martensite have the same shape factor.

The standard deviation of shape factor distributions is about 3 for globular austenite grains, 8 for fibrous austenite grains, 4.5 for globular ferrite grains and 3 for fibrous ferrite grains. The high standard deviation for fibrous austenite shape factor is indicative of the two populations of austenite existing in these steels: acicular austenite between martensite laths and globular austenite at PAGB. Similarly, the high standard deviation for globular ferrite shape factor is indicative of two populations of ferrite in these steels: recovered acicular ferrite and recrystalized globular ferrite.

d) Chemical maps and mean composition of each phase

The chemical maps obtained by WDS provide additional results to assess the chemical stability of austenite at room temperature. It should emphasize that those maps were made on samples processed in dilatometer, after an intercritical annealing with varying heating rates (called realistic dilatometry treatment in section II.5). The results obtained after are however considered to be relevant for all medium Mn microstructures, independently of the method of heat treatment.

For each microstructure, three chemical maps for carbon, for manganese, for aluminium and for silicon were recorded (96 maps in total). Unfortunately, the carbon pollution during the experiments have made impossible any quantitative analysis for carbon. For concision, only four representative maps of GL680 and four representative maps of GL720 microstructures will be presented after.

Four WDS maps are presented in Figure 74 for the GL680 microstructure. (a) is the map for Mn, (b) the map for C, (c) the map for Al, (d) the map for Si. In each map, red and green regions are the ones rich in the considered alloying element, while blue regions are the areas poor in this element. The average value is given alongside each map. From those maps, it can be clearly seen that all alloying elements are partitioned between ferrite and austenite. Austenite grains are the areas rich in carbon and manganese, while ferrite is richer in aluminium and silicon. This follows the trends expected from thermodynamical calculation at equilibrium using CEQCSI software. The maximum Mn content found in austenite grains is about 8.1 wt%.

Four WDS maps are presented in Figure 75 for the GL720 microstructure. Again, (a) is the map for Mn, (b) the map for C, (c) the map for Al and (d) the map for Si. Like before, it can be seen that Mn and C partition inside austenite, while Al and Si partition inside ferrite. There is more austenite in GL720 microstructure than in GL680 one. So, this austenite is less enriched in Mn than the one presented for GL680. Indeed, here, the maximum Mn content of austenite is close to 7.1 wt%. All the other maps, independently of the annealing temperature or the morphology, show the same kind of partitioning behaviour, as expected from the literature review and the equilibrium calculations.

To assess the chemical stability of austenite, it is necessary to know its mean composition in manganese, silicon and aluminium. While the map gives access to the gradient of chemical compositions, it does not give any mean value. To obtain a mean value for each phase, it has been decided to sum the numbers of pixel having an alloying content similar enough to obtain 1D distribution for each map.

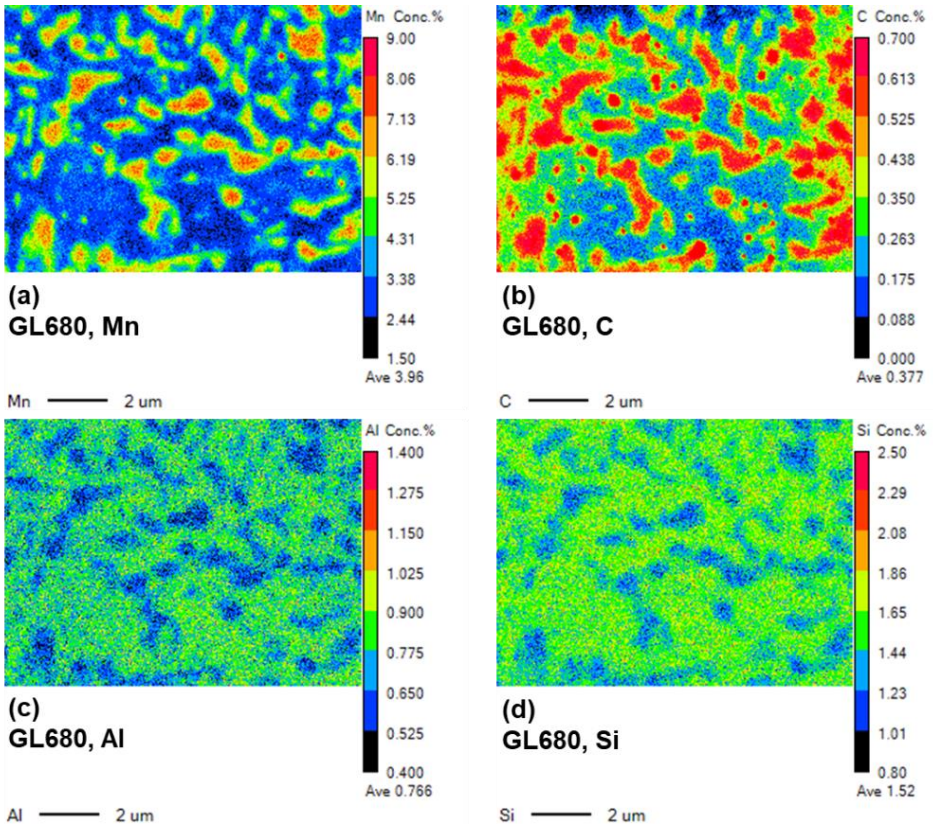

Figure 74: WDS maps of (a) Mn, (b) C, (c) Al and (d) Si distributions for GL680 microstructure.

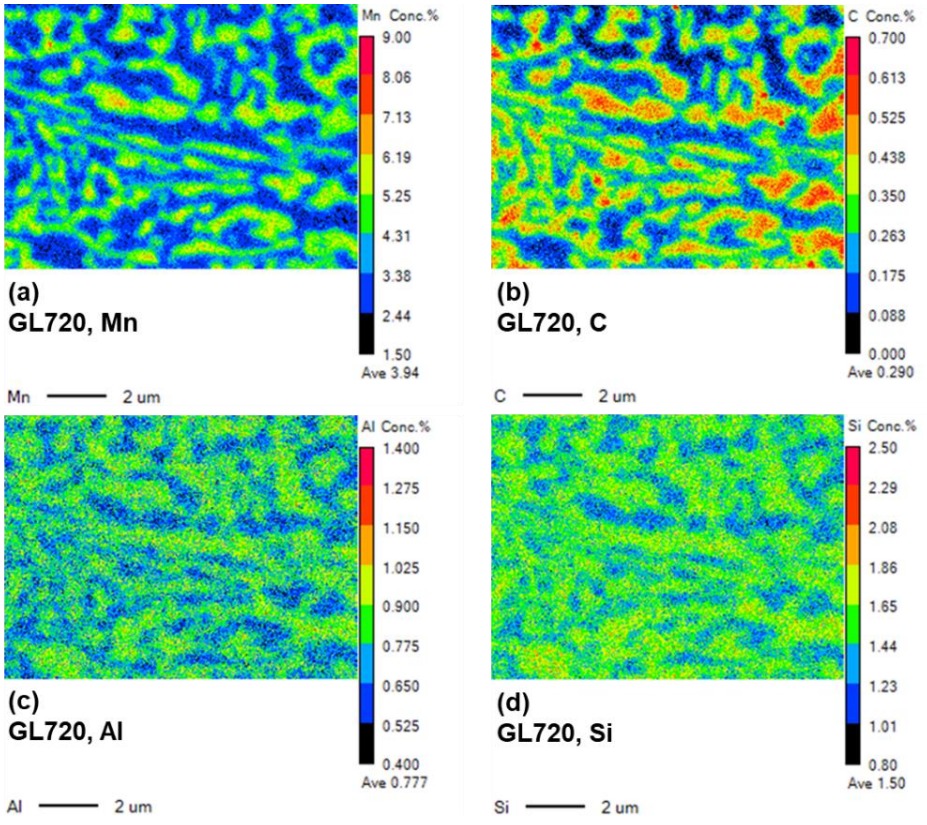

Figure 75: WDS maps of (a) Mn, (b) C, (c) Al and (d) Si distributions for GL720 microstructure.

The 1D diffractograms are then summed between maps belonging to the same sample to obtain a better statistical representativity. Then, the 1D distribution has been fitted with two gaussian functions, one representing ferrite and the other austenite/martensite. The experimental 1D distributions for Mn, Al and Si are shown for FB700 maps in Figure 76 (green dots), alongside the ferrite and austenite contributions (respectively red and blue). The modelled distribution is represented in black. To limit the number of free variables, the areas of the gaussian functions are forced to be linked with the phase fractions of the respective phases (determined by HEXRD). Moreover, the pondered sum of mean alloying content is forced to be equal to the mean value over the three maps of the corresponding alloying content. With this procedure, the mean of gaussian functions can be used to determine the mean value of each substitutional alloying content for each phase. This method is not conventional and was developed in the frame of the PhD work.

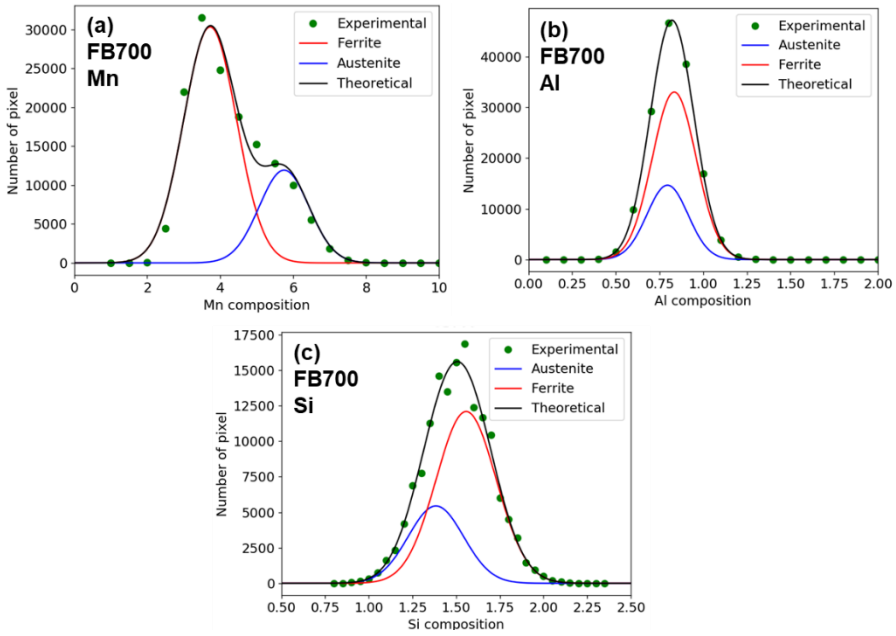

Figure 76: Example of distributions and phase modelling curves obtained in FB700 steel for (a) Mn, (b) Al and (c) Si. The green dots are the experimental number of pixels with a given composition. The blue curve is the austenite distribution. The red curve is the ferrite distribution. The black curve is the total distribution, obtained by the summation of blue and red curves.

Using the previous method, the Mn, Si and Al contents of ferrite and austenite can be estimated for all microstructures. While the carbon content cannot be directly measured, it can still be calculated using a balance equation, supposing that no carbon is situated in ferrite and knowing the fraction of cementite. The formula is given in Equation (II—10). The carbon given here is the one calculated using the phase fractions obtained for salt-baths treated microstructures. The results are given in Table 11.

Please note that the probe size used in the FEG-SEM microscope is 0.2-0.5 µm. The size of our microstructures is about 1 µm for ferritic phase and below 1 µm for austenite. Therefore, the level of partitioned alloying content may be attenuated when compared to the reality. TEM microscopy would be necessary to understand the effect of probe size on measured content. While some measurements have been made in the frame of Dynaustab European project, the results are still under analysis.

Microstructure	C_α	Mn_α	Si_α	Al_α	$C_{\gamma,\alpha'}$	$Mn_{\gamma,\alpha'}$	$Si_{\gamma,\alpha'}$	$Al_{\gamma,\alpha'}$
FB680	neg.	3.76	1.52	0.76	0.6	6.63	1.48	0.75
FB700	neg.	3.50	1.54	0.78	0.69	5.23	1.36	0.75
FB720	neg.	3.36	1.57	0.81	0.51	4.94	1.40	0.70
FB750	neg.	4.02	1.61	0.85	0.33	4.84	1.43	0.69
GL680	neg.	3.29	1.51	0.78	0.68	6.06	1.39	0.71
GL700	neg.	3.47	1.50	0.79	0.60	5.50	1.46	0.70
GL720	neg.	3.40	1.55	0.81	0.51	5.15	1.34	0.70
GL750	neg.	3.52	1.62	0.82	0.40	4.98	1.40	0.68

Table 11: Compositions (wt%) of each phase of the studied medium Mn steels according to our WDS measurements. Austenite and martensite have the same content as martensitic transformation is diffusionless. The carbon content of ferrite is considered negligible compared to other phases.

6. Partial conclusion

Overall, with increasing annealing temperature, the manganese content of ferrite decreases while its aluminium and silicon contents increase very slightly. Concerning austenite and martensite, their carbon and manganese contents decrease significantly while their aluminium and Si contents have no clear tendency with increasing annealing temperature.

In this chapter, the eight microstructures studied in the frame of the thesis were characterized. Their formation during intercritical annealing was followed in situ thanks to HEXRD. Rietveld refinement and RIR methods allow to obtain the time-resolved evolution of ferrite, austenite, cementite and martensite phase fractions. The developed methodology allows to follow the carbon enrichment of austenite during the isothermal holding. The internal stresses building up during cooling in both ferritic matrix and retained austenite have been measured with HEXRD, which is an original result for medium Mn steels.

This work highlights the important role of cementite precipitation and dissolution for the formation of austenite in duplex medium Mn microstructures. While the role of carbide is well known in the literature for globular microstructures, it is a novelty for fibrous microstructures, due to its transient nature difficult to be detected. The obtained results demonstrate that during the heating step of intercritical annealing, at least 70% of the available carbon in the steel is situated inside the cementite precipitates at some point in all the studied microstructures.

A model was proposed to calculate the residual stresses issued from the thermal incompatibility between austenite and ferrite. The model successfully reproduces HEXRD experimental results when no martensitic transformation occurs. The complex mechanical effect of martensitic transformation on austenite and ferrite residual stresses still needs to be understood. This very difficult work far exceeds the scope of this thesis.

Post-mortem analysis was conducted to obtain complementary data to HEXRD. A watershed algorithm has been implemented to perform reliable and systematic measurements. It permits to detect accurately the contours of grains in SEM micrographs. Those contours can then be processed to obtain the fractions of ferrite grains and retained austenite/fresh martensite islands, the number of grains, the distributions of grain size and shape factor.

WDS was used on a FEG-SEM microscope to obtain the alloying contents of Mn, Si and Al in austenite and ferrite. The partitioning of those alloying elements, alongside C, was clearly revealed. Austenite is enriched in C and Mn, while ferrite is slightly enriched in Si and Al, as expected from Chapter I. While the level of partitioning is maybe underestimated with WDS, due to the probe size is in the same order of the grain sizes, it still gives a first order contents for Mn, Si and Al in both ferrite and austenite/martensite phases.

The effects of C, Mn, Si and Al, on M_S temperature alongside the effect of austenite residual hydrostatic stress, are summarized in Table 12. M_s temperature is calculated with Equation (II—8). Accounting for all the effects, the calculated M_S temperatures are close between microstructures, all between 65°C and 145°C. The most stable austenite is found in GL680 steel, while the most unstable is FB720 steel. Overall, austenite in globular microstructures is more stable than that in fibrous corresponding microstructures. The austenite in microstructure annealed at 750°C are greatly stabilized by compressive hydrostatic residual stresses due to the martensitic transformation. Therefore, a surprising result of the current study is that the most unstable austenite at room temperature is found for intermediary annealing temperature, namely at T_{IA} = 720°C.

	Annealing Temperature	680°C	700°C	720°C	750°C
M_S temperature of austenite with C, Mn, Si, Al and internal stress effects	**One-step (GL)**	**67°C**	**84°C**	**129°C**	**82°C**
	Two-step (FB)	**131°C**	**124°C**	**144°C**	**108°C**
Effect of C ➔ $\Delta M_S^C = -600\times(1-\exp(-0.96C_\gamma))$	**One-step (GL)**	**-321°C**	**-318°C**	**-284°C**	**-232°C**
	Two-step (FB)	**-206°C**	**-190°C**	**-177°C**	**-173°C**
Effect of Mn, Si and Al ➔ $\Delta M_S^{Sub} = -31Mn_\gamma -13\ Si_\gamma + 0\ Al_\gamma$	**One-step (GL)**	**-225°C**	**-180°C**	**-284°C**	**-232°C**
	Two-step (FB)	**-225°C**	**-180°C**	**-171°C**	**-169°C**
Effect of residual stress ➔ $\Delta M_S^\sigma = +0.038 \times \sigma_\gamma^h$	**One-step (GL)**	**+29°C**	**+26°C**	**+25°C**	**-78°C**
	Two-step (FB)	**+25°C**	**+20°C**	**-11°C**	**-105°C**

Table 12: Summary of the calculated M_S temperature at the end of one-step and two-step experiments. M_S is calculated with Equation (II—8). Chemical and stress effects on M_s are accounted. The C, Mn, Si and Al contents, and residual stresses change between samples. All different contributions' effect is explicitly given for all microstructures. Chemical M_s is calculated with [171]. The effect of stress is calculated with [25].

One omitted contribution to austenite stabilization highlighted by the literature review was the effect of austenite grain size. Lower grain size tends to stabilize austenite. Formulae found in the literature for conventional TRIP-aided steels were tried (like Equation (I—9)) but gave absurd values. However, while this effect of grain size was not directly accounted for in the current chapter, the effect of austenite grain size on its mechanical stability is still modelled in Chapter IV, during the description of strain-induced martensitic transformation (SIMT).

The Chapter III is dedicated to the mechanical characterization of the different salt-baths microstructures. The results of the Chapter II give precious insight in the microstructures of the PhD thesis. These results will be proved essential for the interpretation of mechanical behaviours during tensile testing.

Chapter III

III. Mechanical stability of austenite

The bibliographic study presented in Chapter I has highlighted the two main plasticity mechanisms encountered in medium Mn steels. Besides the classical gliding of dislocations, the strain induced martensitic transformation (SIMT) with its associated transformation strain is an alternative mechanism. The SIMT induces an additional dynamical hardening called transformation induced plasticity (TRIP).

The factors influencing the SIMT and thus in turn the TRIP effect are the intrinsic properties of the austenite (its chemistry, grain size, morphology and internal stresses, and their respective evolutions during straining), its local neighbourhood (mechanical properties of the ferritic or martensitic surrounding matrix) and the external loading (stress state including stress triaxiality, strain rate or temperature).

The literature review also emphasized that mechanical instabilities could appear in medium Mn steels. Depending on the stability of austenite and the nature of the surrounding phases, fibrous ART steels can undergo a Portevin-Le Chatelier (PLC) effect, while globular specimens tend to present both Lüders and PLC bandings. Therefore, discontinuous yielding is expected to happen during the tensile tests performed in this study.

Chapter II presented the mechanisms of formation of UFG globular and ART microstructures followed in situ with HEXRD. During the intercritical annealing (IA), chemical partitioning occurs between the ferrite and austenite, with an emphasis put on transitory cementite precipitation/dissolution. The chemical composition (C and Mn) of austenite depends on the intercritical annealing temperature. The lower the temperature, the higher the C and Mn contents in austenite is. Another important aspect highlighted by Chapter II is the genesis of internal stresses in both austenite and ferrite during final cooling of the thermal treatments. Austenite inherits a tensile hydrostatic stress state. Post-mortem metallographic observations have also demonstrated that the mean grain size of ferrite and austenite depends on the annealing temperature and processing condition. The lower the temperature, the smaller austenite grain sizes are. All those quantitative observations will be used to understand the evolution of mechanical behaviour between the eight steels of the thesis.

This chapter is dedicated to the determination of the austenite mechanical stability of the studied steels during tensile deformation. This study will be conducted at three levels: the macroscopic mechanical response of the steels (to highlight the TRIP effect), the austenite transformation kinetics (in situ determination) and also the stress partitioning between constituting phases (load transfers). To this end, in situ HEXRD experiments during tensile tests have been performed. These experiments are detailed in the next sections.

1. Materials and experimental setup

A. Reminder: microstructures of the tensile specimens

The tensile specimens were machined from steel plates annealed in salt-baths (SB). Their microstructures were analysed by SEM and the results are presented in Chapter II. A quick reminder of their main characteristics is given in this section. The change of mechanical behaviour in medium Mn steels between tensile trials must be discussed at the light these features.

One important result of the previous chapter is that medium Mn steels are very sensitive to the annealing temperature as well as the heating rate to reach this temperature. It was demonstrated that specimens produced in SB or in a dilatometer have different microstructures even when the targeted thermal treatment was the same. Therefore, in situ experimental results presented in Chapter II cannot be strictly applied to the case of microstructures obtained by salt-bath annealing.

The eight duplex medium Mn steels of the thesis have a nominal composition of 0.2% in C, 3.94% in Mn, 1.46% in Si and 0.78% in Al (all fractions are given in wt%). They are produced through the intercritical annealing of either an as-quenched martensitic steel or a cold-rolled ferritic steel. The annealing temperature T_{IA} is chosen between 680°C and 750°C. At the end of thermal treatments, four phases are possibly found in the microstructures: the ferritic matrix, retained austenite stabilized during IA, undissolved cementite inherited from the heating step of IA or the cold-rolled steel, and fresh martensite forming during the final quench.

Post-mortem SEM analysis of the specimens annealed in SB are detailed in Chapter II. Those analyses allow for the separation of ferrite grains from martensite/austenite (M/A) islands. When present, cementite precipitates are accounted like M/A. A watershed algorithm mixed with thresholding analysis give an access to the phase fractions of ferrite f_α and M/A islands $f_{M/A}$. The mean grain size of ferrite and M/A grains (d_α and $d_{M/A}$) are also assessed. As detailed later in this chapter (in anticipation), the specimens were also characterized by HEXRD. Rietveld refinement has been used to obtain the fraction of austenite f_γ^0 before any deformation. RIR method allows for the determination of the fraction of cementite f_θ (all parameters have been kept in Chapter II). The initial fraction of martensite is then calculated as the difference between the fraction of M/A measured by SEM and the fraction of austenite determined by HEXRD ($f_{\alpha'}^0 = f_{M/A} - f_\gamma^0$). The grain size of austenite d_γ is considered equal to $d_{M/A}$. The fractions and sizes of the different microstructures are summarized in Table 13.

Microstructure	f_α	f_γ^0	$f_{\alpha'}^0$	f_θ	d_α	d_γ^0
FB680	86.1%	5.5%	6%	2.0%	2.6 µm	0.59 µm
FB700	76.2%	13%	9%	1.2%	1.4 µm	0.69 µm
FB720	58.0%	31%	11%	0%	1.3 µm	0.87 µm
FB750	45.0%	16%	39%	0%	1.1 µm	0.99 µm
GL680	79.6%	12%	7%	1.2%	1.2 µm	0.59 µm
GL700	71.5%	18%	10%	0.5%	1.2 µm	0.64 µm
GL720	60.0%	25%	15%	0%	0.97 µm	0.79 µm
GL750	50.0%	18%	32%	0%	1.1 µm	1.0 µm

Table 13: Phase fraction of each phase constituting medium Mn steels and grain sizes of ferrite and austenite. The microstructures were obtained by SB annealing.

During the IA, alloying elements partition between ferrite and austenite. As martensitic transformation is diffusionless, the alloying content in fresh martensite is considered equal to those in austenite. The compositions in Mn, Si and Al in ferrite (denoted Mn_α, Si_α and Al_α) and austenite (denoted Mn_γ, Si_γ and Al_γ) have been determined by WDS analysis on dilatometry sample in Chapter II, section II.5.B.d). The same values are used for microstructures produced by SB to obtain a first order idea of substitutional content of ferrite and austenite in such microstructures.

For simplicity, the carbon content in ferrite C_α was considered equal to 0, as it is negligible in equilibrium calculation compared to other phases (0.006% at most). The carbon content in austenite C_γ is determined with a balance calculation, as stated in Equation (II—10), section II.4.A. Cementite fraction is accounted for in the calculation of C_γ, as it captures a large fraction of the available carbon in 680°C and 700°C microstructures. The estimated compositions of ferrite, austenite and martensite are summarized in Table 14 for the eight steels prepared by SB annealing.

Microstructure	C_α	Mn_α	Si_α	Al_α	$C_{\gamma,\alpha'}$	$Mn_{\gamma,\alpha'}$	$Si_{\gamma,\alpha'}$	$Al_{\gamma,\alpha'}$
FB680	neg.	3.76	1.52	0.76	0.6	6.63	1.48	0.75
FB700	neg.	3.50	1.54	0.78	0.69	5.23	1.36	0.75
FB720	neg.	3.36	1.57	0.81	0.51	4.94	1.40	0.70
FB750	neg.	4.02	1.61	0.85	0.33	4.84	1.43	0.69
GL680	neg.	3.29	1.51	0.78	0.63	6.06	1.39	0.71
GL700	neg.	3.47	1.50	0.79	0.60	5.50	1.46	0.70
GL720	neg.	3.40	1.55	0.81	0.51	5.15	1.34	0.70
GL750	neg.	3.52	1.62	0.82	0.40	4.98	1.40	0.68

Table 14: Estimated alloying contents (wt%) of the constituting phases in the studied medium Mn steels (annealed in SB). Austenite (γ) and martensite (α') have the same content as martensitic transformation is diffusionless (fresh martensite obtained during the final cooling stage). The carbon content of ferrite (α) is considered negligible compared to other phases (neg. = negligible, 0.006wt% at maximum).

B. Setup of in situ HEXRD experiments conducted during tensile tests

In situ HEXRD diffraction experiments during tensile tests have been conducted to follow the SIMT and to quantify the stress partitioning among the three constituting phases, namely ferrite, austenite and martensite (the contribution of cementite is neglected as its fraction is very low). Like for the experiments developed in Chapter II, the trials were performed at the Deutsches Electronen-Synchrotron of Hamburg, on the PETRA III P07 beamline. The monochromatic beam was set at high energy (100 keV for tensile tests) and had a section of 500 x 500 µm². The diffraction patterns (Debye-Scherrer rings) were recorded on a PerkinElmer 2-D plate detector placed at 1.2 m behind the sample (permitting to record about 6 rings per phase of interest). The high acquisition rate (10 Hz) of the detector permits time-resolved investigation of the microstructures during experiments. Si-powder was used as a calibrant. The in-transmission setup allowed for a time-resolved investigation of the microstructures' evolution during trials. Another advantage is that data collected in transmission are statistically relevant, as the analysed volume is large enough (sample width × beam size = 1500 × 500 × 500 µm^3, number of grains in the diffracting volume ≈ 100 millions). Tensile tests were conducted correlatively with HEXRD and digital image correlation (DIC) analysis, as sketched in Figure 77. ARAMIS system (GOM metrology) was installed to conduct stereographic 3D-DIC [145]. The acquisition rate of DIC system was set between 2.5 Hz and 25 Hz, depending on the strain rate of the trial. Figure 78 shows

a picture of the actual experiment. The next two sections will be dedicated to the description of the tensile tests and the DIC setup and method.

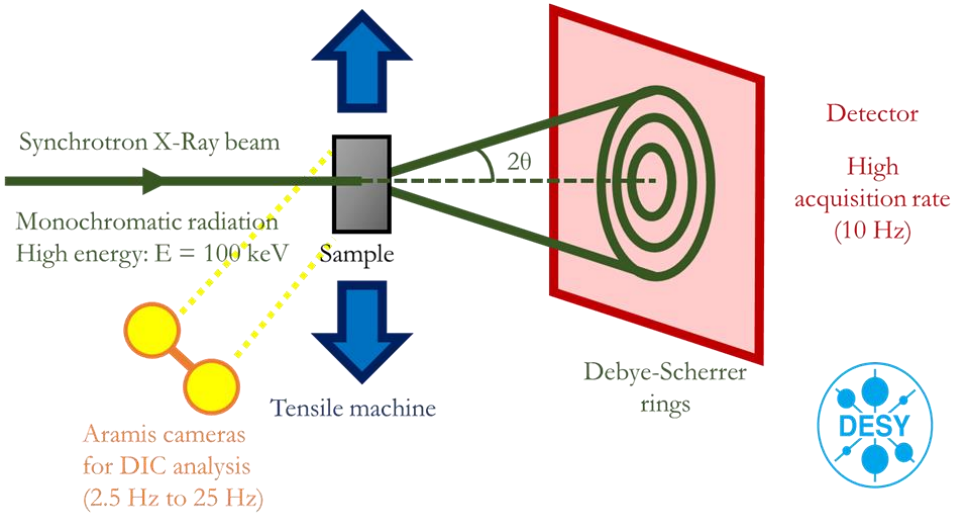

Figure 77: Representation of the experiments conducted at DESY synchrotron. The incoming X-Ray beam produced by the synchrotron ring is represented in green. This X-Ray beam will be diffracted by the sample (grey) placed in a tensile machine (blue). The diffraction pattern consists of Debye-Scherrer rings recorded on a 2D flat detector (red). During the experiments, diffractions patterns are saved with a high acquisition rate (10 Hz). Aramis stereographic cameras are placed 34 cm from the tensile specimen to register videos that will be used for DIC analysis, at an acquisition rate between 2.5Hz and 25Hz.

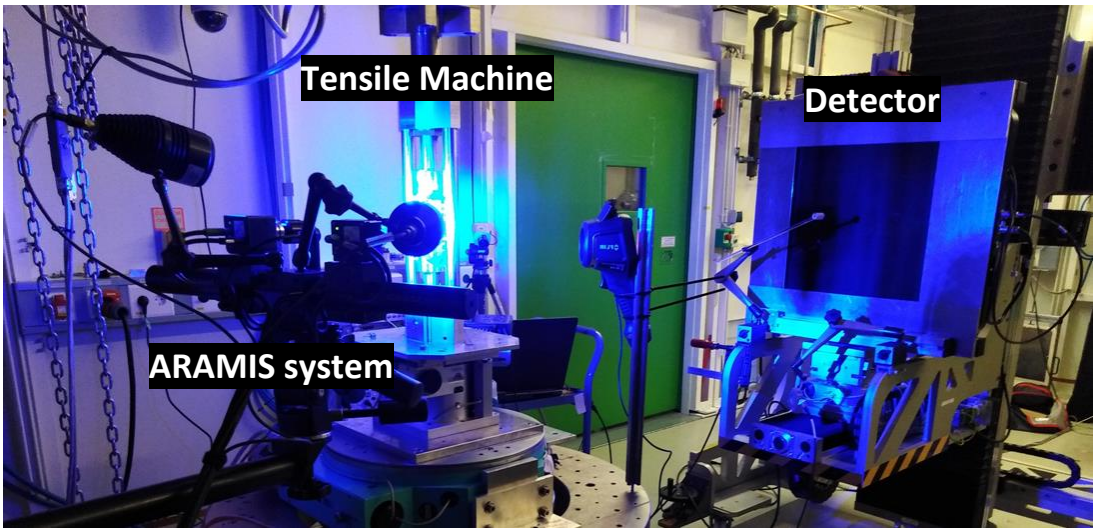

Figure 78: Picture of an experiment conducted at DESY synchrotron on P07 beamline (Nov. 2020). From left to right: the incoming X-Ray beam produced by the synchrotron ring comes from the left side of the photo (not visible). Aramis stereographic system is composed of two cameras and two blue led lamps. Cameras are placed 34 cm from the tensile specimen. The sample placed in a tensile tester is illuminated by the blue led lamps (appears in white/light blue). The Perkin Elmer 2D flat detector which acquires diffraction pattern appears on the right of the image.

C. Tensile machine

To investigate the mechanical stability of retained austenite during loading in the studied steels, tensile tests were conducted in situ using HEXRD at room temperature. The tensile tester had a 20 kN force cell. The tensile specimens have been machined from the annealed cold-rolled sheets. No extensometer was present on the tensile tester. Hence, the regulation of the tensile test was made with the crosshead displacement. Each microstructure (globular and fibrous) has been tested at two different crosshead displacement speeds: 0.01 mm/s and 0.15 mm/s respectively. The speed of 0.01 mm/s corresponds to a quasi-static tensile test condition. The 0.15 mm/s rate was the highest rate accessible on the tensile tester. The globular specimen annealed at 720°C was also deformed at a rate of 0.001 mm/s. The absence of extensometer on the synchrotron tensile tester was compensated by the use of 3D stereographic cameras that allows for an in-situ determination of the strain field all over the gauge length of the tensile specimen. ARAMIS system (GOM metrology) was installed to conduct stereographic 3D-DIC [145] concurrently with HEXRD. It was possible to obtain the mean strain rate over the gauge length for each experiment, as detailed in the next section. The mean strain rates corresponding to 0.01 mm/s and 0.15 mm/s crosshead speeds are respectively 5×10^{-4} s^{-1} and 8×10^{-3} s^{-1}.

Tensile samples have a non-standardized dog-bone shape with large heads. The dimensions of samples are given in Figure 79. Applied strength and crosshead displacement were acquired all along tensile tests at the same time as diffraction patterns. The list of analysed experiments and their respective denominations are given in Table 15.

Experiment denomination	Intercritical temperature T_{IA} (°C)	Morphology of the microstructure	Crosshead displacement rate (mm/s)	Mean strain rate (s^{-1})
FB680-001	680	Fibrous	0.01	5×10^{-4}
FB680-015	680	Fibrous	0.15	8×10^{-3}
FB700-001	700	Fibrous	0.01	5×10^{-4}
FB700-015	700	Fibrous	0.15	8×10^{-3}
FB720-001	720	Fibrous	0.01	5×10^{-4}
FB720-015	720	Fibrous	0.15	8×10^{-3}
FB750-001	750	Fibrous	0.01	5×10^{-4}
FB750-015	750	Fibrous	0.15	8×10^{-3}
GL680-001	680	Globular	0.01	5×10^{-4}
GL680-015	680	Globular	0.15	8×10^{-3}
GL700-001	700	Globular	0.01	5×10^{-4}
GL700-015	700	Globular	0.15	8×10^{-3}
GL720-001	720	Globular	0.01	5×10^{-4}
GL720-015	720	Globular	0.15	8×10^{-3}
GL750-001	750	Globular	0.01	5×10^{-4}
GL750-015	750	Globular	0.15	8×10^{-3}
GL720-0001	720	Globular	0.001	5×10^{-5}

Table 15: Summary of the experiments presented in this work. Mean strain rate is measured by DIC all along gauge length of the tensile specimen. Please note that the IA corresponds to the annealing temperature of the samples. The tests themselves are conducted of course at room temperature.

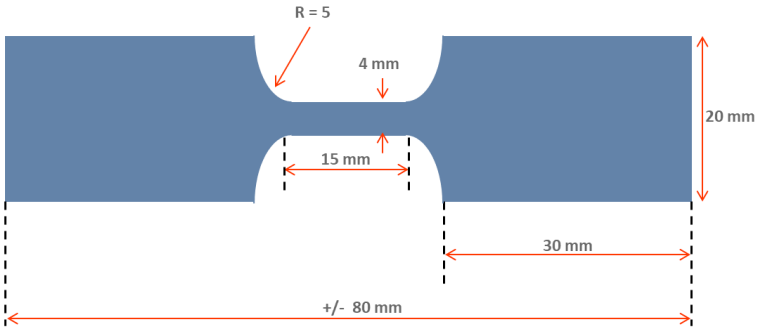

Figure 79: Dimensions of tensile samples (modified Hopkinson geometry according to ArcelorMittal standards). The thickness of the studied specimens is 1.5 mm.

The flat dog-bone specimens were fixed to the tensile machine with two wedge grips. The motor of the tensile machine was placed above the specimen, and only the superior grip is used to apply strain on the specimen, the inferior grip being immobile. The tensile machine is situated above a platform (as seen in Figure 78). During tensile tests, the platform goes down at half the speed of the crosshead. This allows to have always the same diffracting volume during the whole tensile test (no drift of the analysed area).

In the frame of Dynaustab European project, synchrotron experiments on specimens having an optimized geometry were also conducted in October 2022, to test the effect of triaxiality on austenite mechanical stability. Two controlled triaxialities were tested: shear strain and plane strain. The geometrical optimization was proposed by Gent University. Only medium Mn materials annealed at 680°C, 700°C and 720°C were tested with optimized geometry. The same methodology employed on dog-bone tensile specimen and presented in this chapter was used for these shear and plane strain specimens. Unfortunately, as these tests were done late in the schedule of the PhD thesis, the results are not yet fully analysed and thus not presented in the manuscript.

D. Digital image correlation (DIC)

Numerous methods to measure displacement and strain fields on the surface of a deformed part can be found currently in the literature [180]. Compared to more uniaxial approach, such as gauge, extensometer and displacement captors, they have the advantage to determine strain maps and to reveal the strain heterogeneities accompanying Lüders and PLC mechanisms[140], [106], [181].

Different optical measurement techniques exist to obtain displacement and strain fields, such as Moiré shadow techniques, grid methods, holographical interferometry, simple and stereo digital image correlation (DIC) [146], [182]. All those optical methods rely on acquiring pictures (images, interference maps, etc). Those pictures are then used to calculate the displacement field $\underline{u}$ all over the specimen. Those displacement fields are then used to calculate the Green-Lagrange strain tensor $\overline{\overline{F}}$, which is itself used to calculate the symmetric part of the linearized strain tensor $\overline{\overline{\varepsilon}}$. Some of the previously mentioned methods are purely 2D methods, giving access to only the in-plane components (for example: F_{xx}, F_{yy}, F_{xy} and F_{yx} for the xy plane). On the other hand, some of the other methods, like stereo DIC are out-of-plane 2D methods. They give some information on the depth axis, permitting to analyse 6 components of the non-symmetric strain tensor $\overline{\overline{F}}$ (for example F_{xx}, F_{yy}, F_{xy}, F_{yx}, F_{zx} and F_{zy}) [182].

In this work, it was chosen to employ the stereographic DIC method. This method is an out-of-plane 2D method that gives access to displacement field over the 3 axes. It is portable, robust and easy to calibrate. Two cameras acquired images of the surface of the studied specimen at a high acquisition rate. The DIC analysis on the saved videos requires the studied surface of the specimen to be painted with a speckle pattern. In our case, a thin layer of white paint on the specimen surface with a white aerosol spray was first applied on the gauge length of the sample and some black dots on the surface were added using a black aerosol spray. The pattern needs to be random and highly contrasted. The denser the pattern is, the finer the determination of the strain tensor will be possible. An example of painted surface is given in Figure 80. In stereographic DIC, displacement field is reconstructed with the help of a reference image, by following the deformation of the random pattern. Triangulation between two cameras allows obtaining out-of-surface displacements.

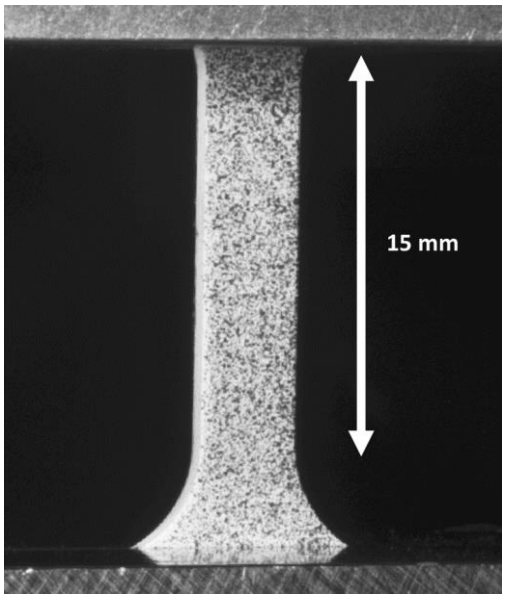

Figure 80: Speckle pattern harboured by the tensile specimen placed on a tensile tester, during the GL720-0001 experiment, just before loading.

The ARAMIS system is used to conduct stereographic 3D-DIC [183]. The system consists of two high precision and high acquisition rate cameras accompanied with two powerful blue led lamps. The cameras are only sensible to blue light radiation (its wavelength is 458 nm with a bandwidth of 10 nm), which prevents any optical interference from other light sources. Moreover, polarizers are placed just before the objectives to diminish pollution from reflexive surfaces. A picture of the system is shown in Figure 81. The maximum acquisition rate is 25 Hz. In the current configuration, the resolution in displacement is 1 µm. The resolution in strain is 0.05%.

Figure 81: ARAMIS system in front of a tensile tester, as exposed on the constructor website [184].

Most of the system functions are controlled with a software called "GOM correlate", GOM being the company selling ARAMIS. The acquisition of the images, as well as the digital image correlation analysis are managed with the software. It is possible to obtain easily the strain field and strain rate field in each direction of space all over the length gauge. In the depth direction, a hypothesis of iso-volume is made by the software. An example of measurement is given in Figure 82 during the FB680-015 experiment. This sample shows a Lüders plateau at yielding onset. The photos have been taken at the middle of the Lüders plateau, when the specimen is partially yielded. In the strain map, the part of the specimen crossed by Lüders deformation bands appears in yellow. In this experiment, two deformation bands have nucleated from both ends of the specimen independently. They appear more clearly on the strain rate map. The strain rate is higher in the band coming from the bottom. Thus, ARAMIS system is sufficient to follow strain rate bands in the case of our medium Mn steels, and allows to gain precious insight into the local evolution of strain all over the length gauge.

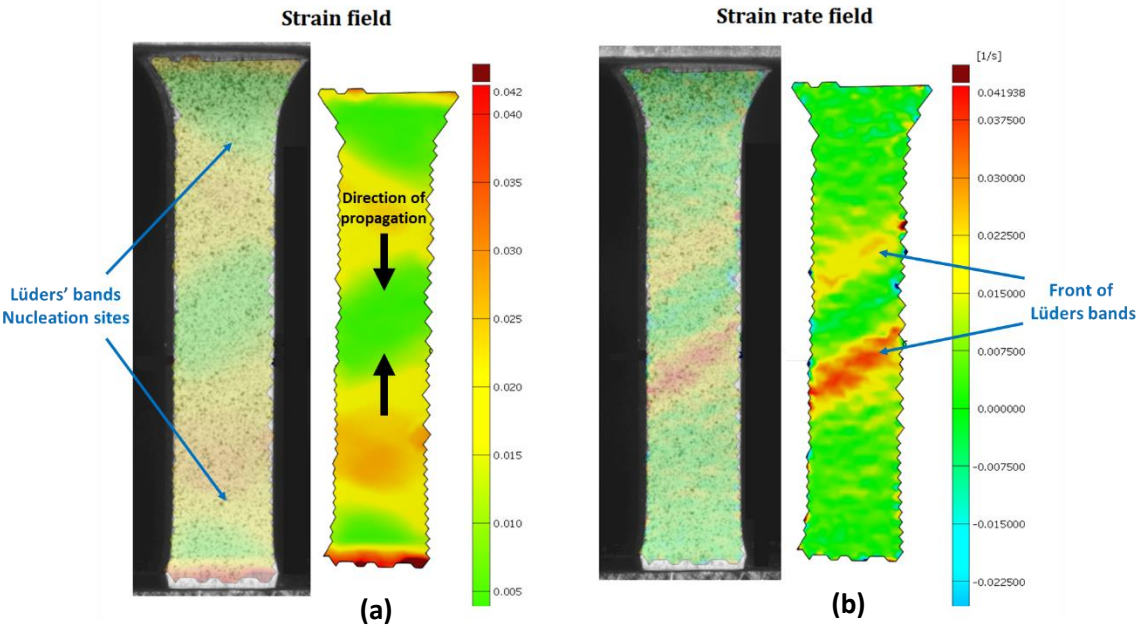

Figure 82: Strain map (a) and strain rate map (b) determined with ARAMIS system at the middle of the Lüders plateau during FB680-015 experiment (colour maps superimposed on the sample in its deformed state). The higher values of strain/strain rate appear in red. In this experiment, two Lüders bands have nucleated at each end of the tensile specimen.

2. Post-treatment of the data acquired during in situ experiments

A. Strains measured by DIC

To compensate for the absence of extensometer, one key value extracted from DIC experiments is the mean strain, i.e. the stain averaged all along the gauge length at a given time. All strains discussed in this section are logarithmic strains. The averaging of the strain is managed by the GOM software, only accounting for the 15×4 mm² gauge surface.

The local strain and strain rate at the position of the diffracting volume can also be obtained by correlating the results of HEXRD and DIC. These three quantities are displayed in Figure 83 for GL720-001 experiment.

As expected, the mean strain (in blue) increases nearly linearly as a function of the time until fracture. The mean value and the value obtained at a given point (in orange) of strain are very close until the appearance of necking (around 700 s). The presence of mechanical instabilities is visible on the strain curve at a given point (orange curve) indicated by the appearance of steps on the evolution of strain. Those instabilities are also visible in Figure 83 (b) and correspond to the peaks on the strain rate curve, since locally the strain rate increases when strain rate bands propagate. The determination of the position of the diffracting volume on the gauge length is not a problem when the specimen is affected by Lüders or PLC banding. In such case, HEXRD data (for example, austenite phase fraction) shows abrupt evolutions. By calculating the time difference between fracture and the visible effect of mechanical instabilities on HEXRD data, it is possible to know the exact time of correspondence when strain rate band crosses the diffracting area and thus its spatial position. For samples not affected by Lüders or PLC effect, it is more difficult to correlate the position of diffracting volume and DIC measurements, but it is less important since strain is homogeneous across the gauge length.

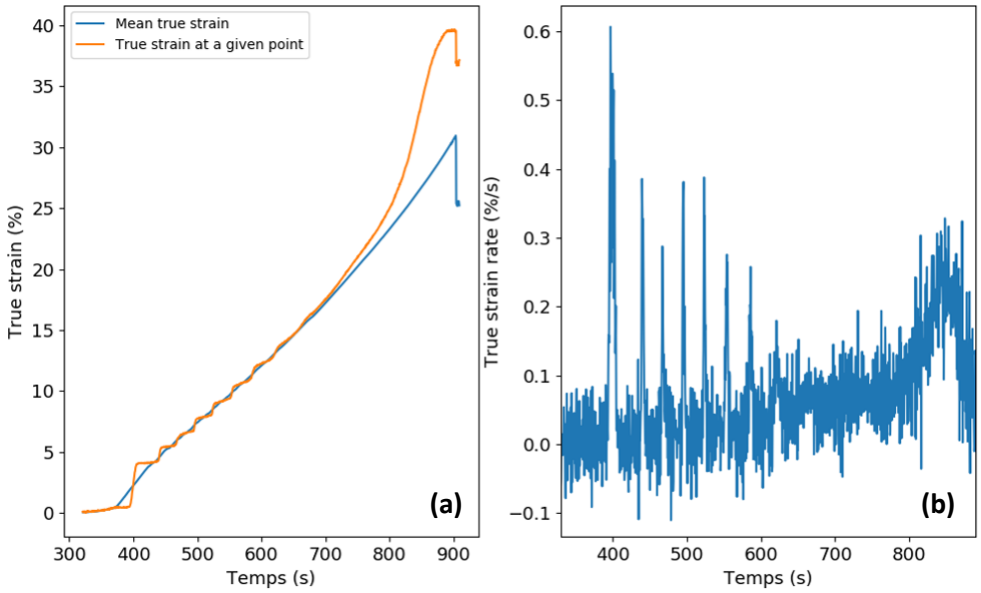

Figure 83: (a) Evolution of mean strain along the gauge length of the specimen (blue curve) and the strain at the diffracting area (orange curve) during the GL720-001 experiment. (b) Evolution of the strain rate at the diffracting area during the GL720-001 experiment.

In what follows, the strain ε_{macro} corresponds to the mean values of true strain. Most of data will be displayed as a function of ε_{macro}, and the curves are represented up to necking. In fact, the deviation between the blue and orange curves in Figure 7 shows that the local deformation at a given point of the sample can be far higher than the mean value as the deformation is localized in the necking area. The mean strain ε_{macro} is thus not representative of the mean behaviour up to this point.

B. Engineering values, true values and necking onset criterion

The tensile tester measures and saves the applied force F used in each experiment, while the DIC analysis gives access to the mean logarithmic strain all along the gauge of the tensile specimen, as explained in section I.3). Hence, to calculate the macroscopic true stress σ_{macro} for each experiment, the following classical formula is used in this work (accounting for an initial cross section S_0 = 1.5×4 mm² for all experiments):

$$\sigma_{macro} = \frac{F}{S_0}\, exp(\varepsilon_{macro}) \qquad \text{(III—1)}$$

However, it can be useful to calculate the equivalent engineering ones, to obtain ultimate tensile strength (UTS) and uniform elongation (UEL) for example. The following formulae are then used:

$$\begin{cases} \varepsilon_{macro}^{eng} = \exp(\varepsilon_{macro}) - 1 \\ \sigma_{macro}^{eng} = \ \sigma_{tot} \exp(-\varepsilon_{macro}) \end{cases} \qquad \text{(III—2)}$$

To determine the onset of necking, the Considère's criterion is employed. This is undoubtedly the most widely used criterion [185]. It assumes that necking occurs when the relative increment in true stress becomes inferior to the relative decrement in cross-sectional area. When necking occurs, the engineering stress vs strain curve reaches its maximum (derivative is zero). This also corresponds to the point when strain-hardening rate becomes equal to stress, and subsequent strain cannot be distributed:

$$\frac{\partial \sigma_{macro}}{\partial \varepsilon_{macro}} = \sigma_{macro} \qquad \text{(III—3)}$$

The formulae (III—1) and (III—2) are only valid before the necking onset. The analysis shown in this chapter is thus limited to mechanical behaviour before necking. All curves are cut at necking (data afterwards are not displayed).

C. Rietveld refinement for SIMT

To estimate the SIMT, the fractions of the different constituting phases have been determined using HEXRD pattern and the same Rietveld refinement procedure as in Chapter II. The method was thoroughly described in section II.2.B. Some quick reminders are given here and the main differences in the approach are highlighted.

Due to the polycrystalline nature of samples and the absence of crystalline texture, recorded 2D diffraction patterns consist of Debye-Scherrer rings. Each ring corresponds to a particular

crystallographic plane family of a phase in the sample. Circular integrations of each 2D diffraction pattern have been conducted with PyFAI library [186], to produce 1D diffractograms. These integrated patterns serve to determine in situ martensitic transformation kinetics during deformation. The evolution of the circularity of the rings due to the applied tensile stress does not affect the measured kinetics by this mean. In fact, if the integration and the refinement are made simultaneously on the different angular sectors of the Debye-Scherrer rings, i.e., considering independently all the texture components, the mean kinetics closely corresponds to the kinetics determined by a complete circular integration (results of the preliminary internship, March-August 2019, shown in Appendix H).

The Rietveld method consists in modelling a theoretical line profile based on radio-crystallographic parameters until it matches the measured experimental profile. The convergence procedure follows a least-squares method. Pseudo-Voigt functions were chosen to approximate the characteristic diffraction peaks of each phase.

During the refinement procedure, one face-centred cubic (FCC) phase was considered for the retained austenite. We have demonstrated in a study published elsewhere [187] that considering two body-centred cubic (BCC) phases, one for ferrite and one for martensite, did not significantly change the austenite phase fraction determined by the Rietveld refinement compared with the scenario considering only one BCC phase for both phases, while it makes significantly harder to do a sequential analysis of diffractograms. As 65000 diffractograms were produced during tensile tests, it was chosen to use one BCC phase to represent both the ferritic matrix and fresh/strain-induced martensite.

Diffractograms were refined with Fullprof software in a $2\theta_B$ range from 2.5° to 8.5°, with θ_B the Bragg angle. As the energy was higher during tensile tests than it was during thermal treatment discussed in Chapter II (100 keV vs 87.1 keV), more rings were fully recorded by the 2D detector. The 2.5° to 8.5° $2\theta_B$ ranges includes the {110}α, {200}α, {211}α, {220}α, {310}α, and {222}α peaks for BCC phase (space group I_{m3m}) and the {111}γ, {200}γ, {220}γ, {311}γ, {222}γ, {400}γ, and {331}γ peaks for FCC phase (space group $F_{m\text{-}3m}$). About 6000 pictures have been indexed for a single tensile trial. Rietveld refinement gives access to phase mass fraction with an uncertainty estimated to be around ±1%.

During deformation, ferrite phase fraction remains constant, contrary to austenite and martensite phase fractions which could vary due to mechanically induced martensitic transformation. In the following, the austenite phase fraction f_γ is directly taken from Rietveld refinement. As stated in section III.1.A, some fresh martensite could be initially present in the microstructure. Its fraction was obtained by correlating HEXRD and SEM data ($f_{\alpha'}^0 = f_{M/A} - f_\gamma^0$). Fresh martensite and strain-induced martensite are considered as a unique phase in the following, in the absence of a reliable way to distinguish them. The martensite fraction $f_{\alpha'}$ is calculated as $f_{\alpha'} = f^0_{M/A} - f_\gamma$ all along the tensile test. The fraction of ferrite is considered constant and is set to the value obtained by SEM (in the absence of other more reliable data). In the microstructures annealed at 680°C and 700°C, some cementite precipitates are also present in the microstructure. However, the stress inside them is not assessed in this work, as cementite crystallographic structure is complex and thus it is more difficult to apply the $\sin^2\psi$ method (difficulty to obtain the radio-crystallographic constants [188]). Therefore, it has been decided to add the fraction of cementite to the fraction of ferrite when doing micromechanical calculations involving phase fractions. The methods used to determine stresses in each constituting phase is explained in the next sections.

D. sin²ψ method

The in situ evolution of mean stress states (3D stress tensor) of the phases has been determined with the sin²ψ method [189]. In this study, this method was mainly developed for ferrite (BCC) and austenite (FCC), as their elastic strains can be determined with good confidence. Concerning martensite (BCT), applying sin²ψ method is more complex. Indeed, the peaks of fresh and strain-induced martensite are convoluted with the shoulders of the ferritic matrix peak. Even for high amount of martensite (>20%), it remains difficult to determine the position of the peaks linked with this phase with a good accuracy (see Figure 8 of section II.2.A). For the latter phase, sin²ψ method was thus compared with micromechanical calculation, as explained afterwards.

a) Application for ferrite and austenite

Applying the sin²ψ method on synchrotron data necessitates multiple numerical steps. In the following, in the sample referential, the normal direction will be denoted ND, the transverse direction will be denoted TD and the rolling direction (concurrently the tensile direction) will be denoted RD, as sketched in Figure 84 (a).

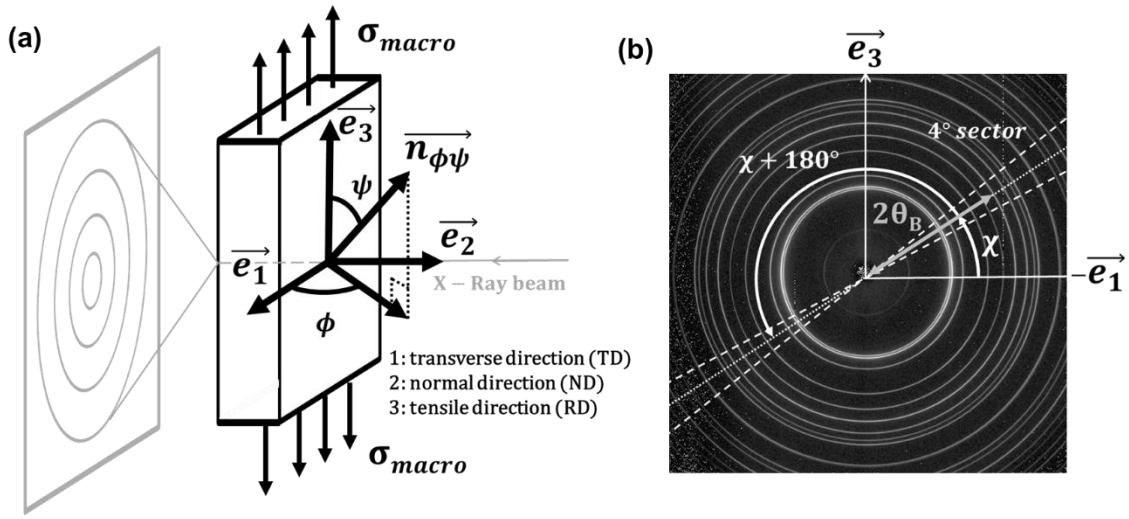

Figure 84: (a) Definition of the angles (ϕ, ψ) used for the sin²ψ method for any plane with a normal vector $\vec{n}_{\phi\psi}$ in the reference system attached to the tensile specimen ($\vec{e}_1$, $\vec{e}_2$, $\vec{e}_3$) = (TD, ND, RD). Tensile direction is denoted RD as it also corresponds to the rolling direction. (b) Definition of the angles ($2\theta_B$, χ) for a random point situated in the 4° sector indicated by dashed lines. They are the polar coordinates linked with ($\vec{e}_3$, $-\vec{e}_1$) reference system on the 2D plane detector surface. Angle χ is defined relative to the bisector (dotted line) of the sector. The sector at χ+180° is also represented.

The normal vector $\vec{n}_{\phi\psi}$ of a crystallographic plane is defined according to two angles ψ and ϕ, ψ being the angle between RD and the normal vector, ϕ being the angle between TD and the projection of the normal vector in the TD and ND planes. To construct a sin²ψ curve, partial integration of a 2D diffraction pattern is done with PyFAI software. The area of integration is composed of a sector centred on an azimuthal angle χ with a small aperture (4° in this study) and another sector centred on χ + 180° (the diametrically opposed sector). Two of those sectors are represented as an example with dashed

lines in Figure 84 (b). Then, for a given plane family, the corresponding peak position θ_B^{peak} is defined by the Bragg angle θ_B of its centre obtained by modelling the peak with a pseudo-Voigt function.

During the empirical modelling of peaks, the local background is modelled by an affine function of $2\theta_B$. For ferrite (BCC phase) and austenite (FCC phase), peak $\{211\}_\alpha$ and peak $\{311\}_\gamma$ were analysed respectively. The plane families associated with those peaks are less anisotropic in their elastic behaviour, which is necessary for the $\sin^2\psi$ method to be representative of the bulk behaviour of the sample [190]. This procedure gives a couple of angles ($2\theta_B^{peak}$, χ). In the case of HEXRD experiments, with a transmission geometry and no tilt between the sample and the incoming x-ray beam, the value of $\sin^2\psi$ and the true strain $\varepsilon_{\phi\psi}$ are linked with the angles θ_B^{peak} and χ by the following formulae [188], [191]:

$$\begin{cases} sin^2\psi = 1 - cos^2\theta_B^{peak}(1 - sin^2\chi) \\ \varepsilon_{\phi\psi} = ln\left(\dfrac{sin\theta_B^0}{sin\theta_B^{peak}}\right) \end{cases} \quad (III—4)$$

where θ_B^0 is the Bragg angle of the considered peak assuming a stress-free state in the phase, ln is the natural logarithm, and θ_B^{peak} its actual position. Doing so for an angle χ gives one point of the ellipse. The $\sin^2\psi$ ellipse linked with a phase of a given diffraction pattern is obtained by varying the azimuthal angle χ from 0° to 180°. When observing all our ellipses, we observe that they were flat (no evidence of the opening). The ellipse is restricted to a line (as shown in Figure 85). This observation is important because it is the proof that in the scenarios studied, the stress tensor of the two phases, austenite and ferrite, do not present on average shear components.

A linear regression is then conducted on the line (flat "ellipse") to obtain its intercept $\varepsilon_{\phi\psi}^0$ and slope $\Delta\varepsilon_{\phi\psi}$. In this study, as we conducted in transmission HEXRD experiments, it was supposed that elastic strains in the transverse and normal directions of the sample are equal during tensile test (i.e., $\varepsilon_{TD} = \varepsilon_{ND}$). Under these transverse isotropy hypotheses, the relationship between the strains in tensile ε_{RD} and transverse directions ε_{TD} and the intercept $\varepsilon_{\phi\psi}^0$ and slope $\Delta\varepsilon_{\phi\psi}$ of the $\sin^2\psi$ curve are given by [188]:

$$\begin{cases} \varepsilon_{RD} = \varepsilon_{\phi\psi}^0 \\ \varepsilon_{TD} = \varepsilon_{\phi\psi}^0 + \Delta\varepsilon_{\phi\psi} \end{cases} \quad (III—5)$$

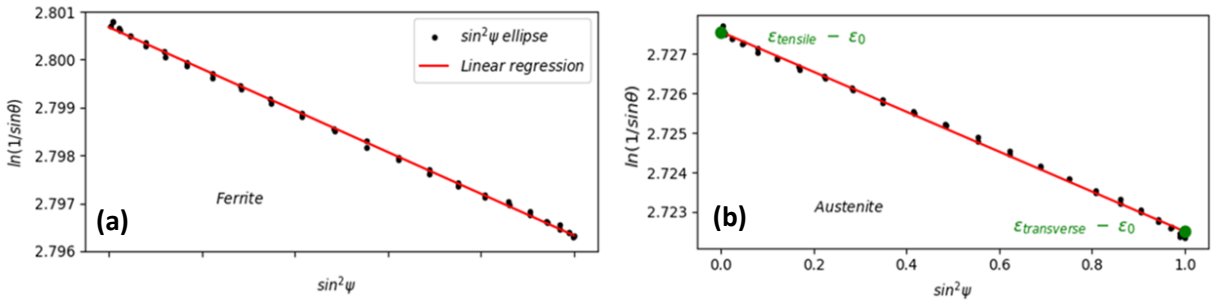

Figure 85: Example of measured strains for the (a) {211}α and (b) {311}γ planes as a function of $\sin^2\psi$ in the elastic regime. Each dot (black) corresponds to a measurement in a 4° sector of the Debye-Scherrer. The Y-axis $\ln(1/\sin\theta_B^{peak})$ is linked to the strain in the ϕ, ψ direction by Equation: (III—4). A linear interpolation (red curve) is represented for the sake of readability. The green dots are linked to the elastic strain measured in the tensile and transverse directions, respectively [187].

Repeating the whole procedure for all diffraction patterns enables determining the evolution of stress state of austenite and ferrite all along the tensile test. Indeed, after determining elastic strains all along the experiments, stresses are calculated using Hooke's law for isotropic materials. The Young's moduli for ferrite and austenite are calculated through Ghosh-Olson formula [192], taking into account the chemical composition of each phase and the temperature. The respective values found are E_α = 207 GPa and E_γ = 201 GPa for GL720 sample. They do not vary significantly between experiments. For all phases, a Poisson's ratio υ of 0.3 is chosen [193]. The bulk elastic constants are used for both ferrite and austenite since we consider the most isotropic family planes ({211}α and {311}γ) for each phase in the stress analysis. The point-to-point $\sin^2\psi$ ellipses calculated using the above procedure in the elastic regime are shown in Figure 85 a and b for ferrite and austenite respectively (extracted from [187]). In those figures, the Y-axis is $\ln(1/\sin\theta_B^{peak})$. The real $\sin^2\psi$ plot (i.e., $\varepsilon_{\phi\psi}$ vs. $\sin^2\psi$) is obtained by adding the unknown value $\ln(\sin\theta_B^0)$ to the Y-axis. This unknown value is related to the initial hydrostatic stress state of the phases before straining. While this addition is not necessary to obtain the von Mises stresses of each phase, it is necessary to obtain the absolute values of the stresses in tensile and transverse directions. The agreement between the experimental values and the linear regression is very good (correlation coefficient ≈ 0.998 for both phases). The flatness of the ellipses means that shear stresses are negligible compared to normal stresses. The same kind of flat ellipses is also found during the plastic regime. Then, with the isotropic hypothesis $\varepsilon_{TD} = \varepsilon_{ND}$, strain and stress tensors have only two independent components $\varepsilon_{11} = \varepsilon_{22}$ and ε_{33} that will be denoted $\varepsilon_{TD} = \varepsilon_{11}$ and $\varepsilon_{RD} = \varepsilon_{33}$ (respectively σ_{TD} and σ_{RD}). In this simple case, von Mises stress σ_{vM} and hydrostatic stress σ_h can be calculated as follows:

$$\begin{cases} \boldsymbol{\sigma_{vM}} = \dfrac{\sqrt{2}}{2}\sqrt{(\boldsymbol{\sigma_{11}}-\boldsymbol{\sigma_{22}})^2+(\boldsymbol{\sigma_{22}}-\boldsymbol{\sigma_{33}})^2+(\boldsymbol{\sigma_{33}}-\boldsymbol{\sigma_{11}})^2} = |\boldsymbol{\sigma_{RD}}-\boldsymbol{\sigma_{TD}}| \\ \boldsymbol{\sigma_h} = (\boldsymbol{\sigma_{11}}+\boldsymbol{\sigma_{22}}+\boldsymbol{\sigma_{33}})/\mathbf{3} = (\boldsymbol{\sigma_{RD}}+\mathbf{2}\boldsymbol{\sigma_{TD}})/\mathbf{3} \end{cases} \quad \textbf{(III—6)}$$

With the current observations and hypothesis, only two values of stress are necessary to describe the whole stress state of a phase. The couple of stress (σ_{RD}, σ_{TD}) can be replaced with (σ_{vM}, σ_h) for example. With stress and strain tensors being diagonal with only two eigen values, von Mises stress is proportional to the slope $\Delta\varepsilon_{\phi\psi}$. By directly applying Hooke's law, it comes:

$$\boldsymbol{\sigma_{vM}} = \frac{\boldsymbol{E}}{\mathbf{1}+\boldsymbol{\nu}}\left|\boldsymbol{\Delta\varepsilon_{\phi\psi}}\right| \quad \textbf{(III—7)}$$

Applying $\sin^2\psi$ method on the Si-calibrant, the uncertainty on stress measurement was determined around 25 MPa.

Due to the overrepresentation of points near $\sin^2\psi$=0 and near $\sin^2\psi$=1 and due to some possible distortion induced by a possible texture, the linear fitting of $\sin^2\psi$ curves is sometimes restricted to central part of the ellipsis ($\sin^2\psi \in [0.2; 0.8]$ for example) in the literature [188]. An analysis of the effect of such restriction has been conducted on our data and is detailed in Appendix I. The overall trends remain similar. Hence, it has been decided in what follows to calculate stresses by fitting the whole $\sin^2\psi$ curves (from $\sin^2\psi$ = 0 to 1) for ferrite and austenite.

The $\sin^2\psi$ method allows to easily obtain the evolution of 3D stress tensors individual component. Obtaining their absolute values is however very complex. The next sections highlight this issue.

b) Treatment of 3D stress tensor

The last section explained the methodology used to apply $\sin^2\psi$ method on ferrite and austenite in transmission HEXRD setup. The ferrite and austenite stress tensors were proven to be diagonal for ferrite and austenite, with no shear stress and only two eigen values in the reference basis of the tensile trial (thus the principal basis).

The von Mises stress is independent from the initial hydrostatic stress imposed by the choice of θ_B^0. However, to calculate σ_h, σ_{RD} and σ_{TD} in both phases, it is necessary to know the initial hydrostatic phase stress state inherited from the manufacturing process in order to choose judiciously the stress-free Bragg angle θ_B^0 of both $\{211\}_\alpha$ and $\{311\}_\gamma$ peaks.

These hydrostatic stress states affect the mean lattice parameter of the phase but cannot be determined with the $\sin^2\psi$ method. As the determination of the lattice parameter is not absolute with our HEXRD set-up, these states cannot be assessed independently with the Rietveld refinement procedure for instance. Hence, the initial hydrostatic stresses in both phases must be imposed at the beginning of the tensile test by another method. We have chosen to base our methodology on the findings of Chapter II.

As a reminder, the hydrostatic stress state in austenite results from two mechanisms: 1) the thermal stresses induced by the difference of coefficients of thermal expansion (CTE) between the ferritic matrix and the retained austenite during cooling after annealing. 2) the thermally induced martensitic transformation leads to compressive hydrostatic stress because of the displacive character of the transformation. The first contribution is well predicted by Allain's model [25], following a Mori-Tanaka micromechanical scheme. This model predicts the hydrostatic stress in ferrite and austenite inherited from intercritical annealing during the final cooling, assuming that each phase is stress-free during the intercritical holding and that no thermal martensitic transformation occurs during cooling. The model depends on the fraction of retained austenite formed during holding, the intercritical annealing temperature and CTE of ferrite and austenite. The austenite and ferrite CTEs are measured through in situ HEXRD during thermal treatment conducted on synchrotron beamline, as detailed in Chapter II. The fraction of austenite formed during intercritical annealing was chosen equal to the fraction of M/A islands measured by SEM.

However, the second contribution to austenite initial hydrostatic stress (i.e. compressive stress inherited from martensitic transformation during quenching) is still not modelled. This makes difficult to evaluate the initial hydrostatic pressure in austenite and ferrite in this work, as there is always a small fraction of martensite formed during final quenching, even for the GL680 and FB680 samples. The error is all the more important as the fraction of fresh martensite becomes higher in the microstructure.

The experiments detailed in Chapter II, section II.4.B demonstrate that even low amount of fresh martensite formed in the cooling generate a significant amount of compressive hydrostatic stress in austenite. For example, in the FB720 steel studied by HEXRD in dilatometry during thermal treatment, the microstructure after treatment consisted of 20% retained austenite and 17% of fresh martensite. The experimental hydrostatic residual stress was -270 MPa, while the theoretical one accounting only for difference in CTE between α and γ was +527 MPa. Therefore, only 17% of fresh martensite induced a compressive hydrostatic stress of nearly -800 MPa in austenite. Absolute value

of hydrostatic stress is thus highly complex to analyse, as a decrease in it can be either due to a decrease in tensile hydrostatic stress or an increase in compressive hydrostatic stress. Their interpretation should be done with caution.

However, the evolution of hydrostatic stresses (i.e. relative values) obtained with $\sin^2\psi$ method in HEXRD is still very precise (uncertainty of 25 MPa), and is still interpretable. In the literature, authors usually neglect the hydrostatic stress inherited from processing in multiphasic materials and choose an initial value of 0 for each hydrostatic stress [99], [194]. In this work, we have chosen another type of normalization of data. The value 0 is set at the onset of yielding. It allows to compare between experiments the effect of strain-induced martensitic transformation (SIMT) on hydrostatic stress of austenite, as SIMT starts with yielding in our experiment.

In what follows, hydrostatic stress refers to the evolution of σ_h obtained by using Allain's model [25] for the initial value of hydrostatic stress. Normalized hydrostatic stress refers to the evolution of σ_h for which the value 0 is set at yielding onset. Same considerations are also made for stress in tensile and transverse directions σ_{RD} and σ_{TD}.

c) Fresh and strain-induced martensite

As stated in the previous part, it is difficult to apply the $\sin^2\psi$ method on martensite due to the closeness between martensite and ferrite crystallographic structures. Some attempts to decorrelate both phases peaks have been made in this work to assess the level of stress in martensitic phase. The $\{211\}_\alpha$ and $\{211\}_{\alpha'}$ families of planes have been chosen due to the representativity of the bulk behaviour of their respective phases. To deconvolute the two peaks, each peak is modelled respectively by a single gaussian function and their parameters are determined by least square method. Pseudo-Voigt functions have also been tried, but the high number of fitting parameters (4 per peak + 2 for background = 10 independent parameters) made the refinement less reliable.

While ferrite has body-centred cubic (BCC) structure and $(211)_\alpha$, $(121)_\alpha$ and $(112)_\alpha$ are equivalent plans, it is not the case for fresh/strain-induced martensite, which has a body-centred tetragonal (BCT) structure. Hence a and c lattice parameters are strictly different, and two gaussian function should be used to model a single "$\{211\}_{\alpha'}$ peak" (which consists in the sum of one $(211)_{\alpha'}$+$(121)_{\alpha'}$ peak and one $(112)_{\alpha'}$ peak). However, this aspect of martensite crystallography has been neglected in what follows, and only one gaussian has been chosen to model "$\{211\}_{\alpha'}$ peak" for numerical instability consideration.

For each diffraction pattern, the deconvolution between $\{211\}_\alpha$ and $\{211\}_{\alpha'}$ has to be made on the 90 sectors. The results of the deconvolution are plotted in Figure 86 at the onset of necking for one sector oriented alongside the tensile direction (Figure 86 (a)), one sector oriented alongside the transverse direction (Figure 86 (b)) and one oriented alongside the diagonal direction (Figure 86 (c), 45° with respect to loading direction). In these figures, the experimental diffractogram appears in black, the simulated $\{211\}_\alpha$ in red, the simulated $\{211\}_{\alpha'}$ in green, and the sum of the two modelled peaks in yellow. The latest sum permits to assess the correctness of the least square refinement in comparison with experimental data. The ferrite and martensite peaks are well separated in the tensile and diagonal directions, but the $2\theta_B$ scattering angle of their centre are really close in transverse direction. This is not surprising as, without external stress field, the $\{211\}_{\alpha'}$ inter-reticular distance $d^{\alpha'}_{211}$

is greater than d^{α}_{211} of ferrite due to martensite being in essence ferrite saturated in carbon. In the transverse direction, both ferrite and martensite undergo compressive stress. However, as martensite is stronger than ferrite, it is expected that compressive stress in transverse sectors will be higher in martensite than in ferrite. The diminution of $d^{\alpha'}_{211}$ will be higher than d^{α}_{211}. Hence, $d^{\alpha'}_{211}$ and d^{α}_{211} will get closer due to compression, and thus the θ_B^{peak} position of {211}α' and {211}α peaks will become confounded (as θ_B^{peak} and d_{211} are linked by the Bragg law: $\sin\theta_B^{peak} = \lambda/2d_{211}$, with λ the wavelength of the synchrotron beam). With the same reasoning, the sector where tensile stress is the highest should be the one where ferrite and martensite peaks are the most uncoupled. This is indeed the case when we compare Figure 86 (a) and Figure 86 (c).

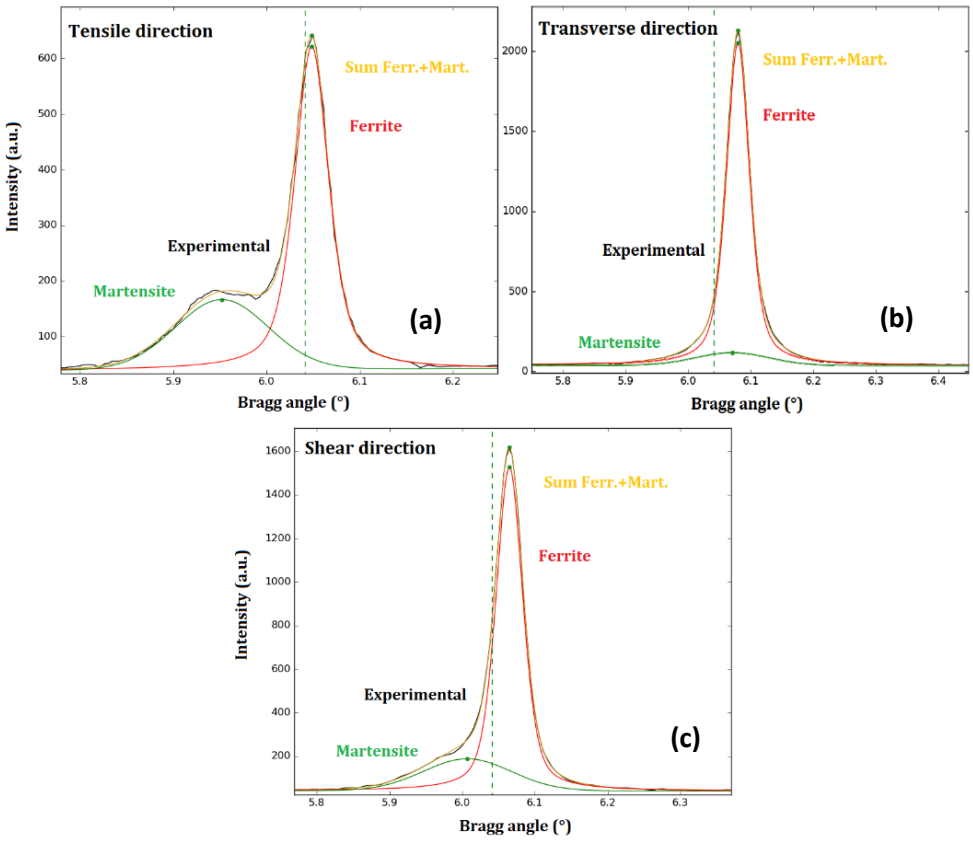

Figure 86: Deconvolution of ferrite (red) and martensite (green) {211} peaks family from the experimental peak (black) obtained after integration of diffraction pattern (a) in the tensile direction (0°), (b) in the transverse direction (90°) and (c) in the diagonal direction (45°) at the onset of necking. The curves in yellow are the sum of martensite and ferrite simulated peaks and must be compared to the experimental curve in black. The results are extracted from GL720-001 experiment.

Once the deconvolution of ferrite and martensite peaks is done over each 90 sectors for each 6000 diffractogram of an experiment, the procedure to obtain martensite ellipse is the same as for austenite and ferrite. The ellipses obtained at three levels of strain are reported in Figure 87 for GL720-001 experiment. During elastic regime (ε=0.4%), only thermally induced martensite is present in the microstructure. The values of stain $\varepsilon_{\phi\psi}$ as a function $\sin^2\psi$ shows an overall linear trend. Some steps can be seen in the experimental points, which are difficult to interpret. They do not arise from numerical discretization, as the value of strain in a given step is not exactly the same between points. At the start of the plastic regime (ε=5%), $\varepsilon_{\phi\psi}$ vs $\sin^2\psi$ curves start to take a shape similar to those of ferrite and austenite ellipses. The points of martensite ellipse remain aligned until the end of tensile test in the $\sin^2\psi$ in the [0; 0.75] range, as seen in Figure 87 (c). During deformation, the highest part of

the ellipse, for $\sin^2\psi$ in the [0.75; 1] range, loses its alignment with the central part of the ellipse. This highest part is linked with planes family whose normal vectors are in the transverse direction. As demonstrated in Figure 86, those martensite peaks are not well decorrelated from ferrite peaks due to internal stresses. These points must be discarded for the linear regression.

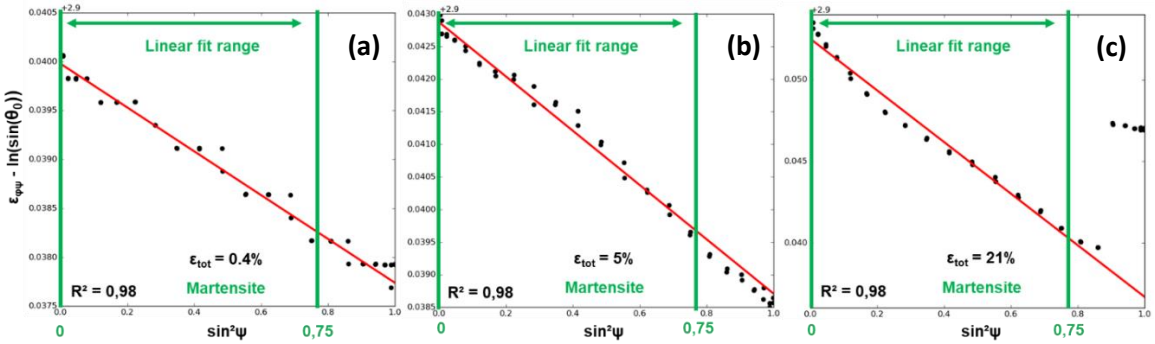

Figure 87: Evolution of martensite $\sin^2\psi$ ellipses (black dots) as a function of strain during GL720-001 experiment. At ε=0.4% (a), the steel is still in elastic regime. At ε=5% (b), the Lüders band has come across all the specimen length. At ε=21% (c), necking starts. The linear regression (red line) was conducted over a $\sin^2\psi$ range of [0; 0.75], indicated by green vertical line. For each regression, the R^2 values is systematically higher than 0.98.

In regards with the preceding observations, martensite von Mises stress will be determined with $\sin^2\psi$ method using a range of [0.0; 0.75] for linear regression (R^2 values is systematically higher than 0.98). The calculations will only be conducted when a significant martensitic phase fraction is present in the microstructure, i.e. for 720°C and 750°C annealed specimens.

The $\sin^2\psi$ method for martensite has a supplementary bias compared to its application on ferrite and austenite. The interplanar distances of the $\{211\}_{\alpha'}$ planes family depend not only on the lattice strain due to stress, but also on its carbon content. The mean carbon content increases during deformation due to SIMT as the less stable austenite, i.e. the less carbon enriched austenite transforms first. If the SIMT is isotropic, the increase in carbon content should lead to a simple increase in the lattice parameter and the von Mises stress measured by $\sin^2\psi$ would still be unaffected. But measurements of SIMT kinetics alongside tensile, transverse and diagonal directions show that the SIMT does not occur at the same rate depending on the angle χ in which it is measured (results shown in Appendix H). Therefore, transformation kinetics subsequent carbon enrichment of martensite is not homogeneous in all sectors of the diffraction patterns, and von Mises stress in martensite represents the evolution of lattice parameter due to both mechanical and chemical origin. This uneven transformation rate can maybe be explained by texture and/or triaxiality considerations.

To confirm the level of stress in martensite obtained for GL720, GL750, FB720 and FB750 experiments, and to have an assessment of stress in martensite for specimens annealed at a lower intercritical annealing temperature T_{IA}, it has been decided to develop a complementary micromechanical approach to determine the stress level in martensite indirectly, using also the knowledge gained at the macroscopic level. This method is developed in the next section.

E. Micromechanical mixture rules

Under the mean field assumption at the phase scale, at each time of the tensile test, the Hill's mixture law was applied [195]. No assumption is made on the level of strain partitioning among phases. The macroscopic true stress of the steel σ_{macro} is the sum of the stress contribution of each phase weighted by their respective fractions:

$$\boldsymbol{\sigma}^{\boldsymbol{i}}_{\boldsymbol{macro}} = \boldsymbol{f}_{\boldsymbol{\alpha}}\boldsymbol{\sigma}^{\boldsymbol{i}}_{\boldsymbol{\alpha}} + \boldsymbol{f}_{\boldsymbol{\gamma}}\boldsymbol{\sigma}^{\boldsymbol{i}}_{\boldsymbol{\gamma}} + \boldsymbol{f}_{\boldsymbol{\alpha'}}\boldsymbol{\sigma}^{\boldsymbol{i}}_{\boldsymbol{\alpha'}} \qquad \textbf{(III—8)}$$

In Equation (III—8), the subscript i may represent RD (rolling direction) or TD (transverse direction). Indeed, Hill's mixture rules is a tensorial equality between macroscopic stress tensor and weighted phase scale stress tensors. The macroscopic stress tensor has only one non-zero component in the tensile direction σ_{macro}^{RD}, which can be denoted σ_{macro} for simplicity (as previously). In transverse direction, $\sigma_{macro}^{TD} = 0$. By summing Equation (III—8) in tensile direction and two times in the transverse direction, and dividing it by 3, it can be proven that Equation (III—8) is valid for hydrostatic stresses. By subtracting the Hill's mixture law in the transverse direction from the one in tensile direction, it can be demonstrated that Equation (III—8) is also valid for von Mises stress if and only if σ_k^{RD} is superior to σ_k^{TD} for each phase $k \in \{\alpha, \gamma, \alpha'\}$. Experimental results show that this is always the case for ferrite and austenite, independently of the value taken for the initial hydrostatic pressure.

In the Hill's mixture rules, σ_{macro} is determined using the values provided by the tensile machine (force) and the DIC (true strain). The fraction of each phase is known by correlating SEM data with Rietveld refinement results. The stresses in ferrite and austenite are known with $\sin^2\psi$ method. The quantity with the most uncertainty is the stress in martensite, as demonstrated in the last section. Therefore, it has been decided in this work to inverse Equation (III—8) to obtain an estimation of the expected level of stress in martensite [195]:

$$\boldsymbol{\sigma}^{\boldsymbol{i}}_{\boldsymbol{\alpha'}} = \frac{\boldsymbol{\sigma}^{\boldsymbol{i}}_{\boldsymbol{macro}} - \left(\boldsymbol{f}_{\boldsymbol{\alpha}}\boldsymbol{\sigma}^{\boldsymbol{i}}_{\boldsymbol{\alpha}} + \boldsymbol{f}_{\boldsymbol{\gamma}}\boldsymbol{\sigma}^{\boldsymbol{i}}_{\boldsymbol{\gamma}}\right)}{\boldsymbol{f}_{\boldsymbol{\alpha'}}} \qquad \textbf{(III—9)}$$

In this inverse mixture rules, it may be indifferently RD, TD, vM (von Mises) or h (hydrostatic). The conditions of validity for this equation are the same as those for Equation (III—8). This equation will be the one used to calculate stress in martensite in the latter part of this PhD manuscript, unless it is told otherwise.

Please note that in certain circumstances, it can happen that the calculated von Mises stress of martensite $\sigma_{\alpha'}^{vM}$ can be negative using this method, because we are working to the limit of resolution. Indeed, if the sum $f_\alpha\sigma_\alpha^{vM}+f_\gamma\sigma_\gamma^{vM}$ is higher than σ_{tot} because of the +25 MPa of uncertainty of the $\sin^2\psi$ method, $\sigma_{\alpha'}^{vM}$ will be lower than 0, as we divide $\sigma_{tot} - f_\alpha\sigma_\alpha^{vM}+f_\gamma\sigma_\gamma^{vM}$ by $f_{\alpha'}$, which is initially small. If $f_{\alpha'}^0 = 10\%$ for example, $\sigma_{\alpha'}^{vM}$ can initially be about -250 MPa. The negativity of $\sigma_{\alpha'}^{vM}$ is an issue which is only linked with uncertainty of stress determination and does not invalidate the use of Equation (III—9) for von Mises stresses. Moreover, this negativity of calculated $\sigma_{\alpha'}^{vM}$ can occur only in the first step of elastic domain, below 400 MPa.

Overall, the five last sections were dedicated to explaining in details the methodology used in this work to obtain time-resolved measurements of strain induced martensitic transformation and stress partitioning between ferrite, austenite and martensite by HEXRD during tensile testing. The

following sections will be dedicated to the presentation of the results for each experiment described in Table 15.

3. Results

As summarized in Table 15, 17 different experiments have been conducted and detailed in this manuscript. For each experiment, a whole set of HEXRD data is generated and analysed in terms of transformation kinetics and stresses at phase scale.

A. Tensile behaviours

The tensile engineering curves measured on specimens with a globular microstructure are shown in Figure 88. In (a), the strain rate is 5×10^{-4} s^{-1} (medium), and in (b), the strain rate is 8×10^{-3} s^{-1} (high).They are determined using Equations (III—1) and (III—2). In the current section, the colour of curves corresponds to the respective IA temperatures T_i (blue for T_i = 680°C, green for Ti = 700°C, yellow for Ti = 720°C and red for Ti = 750°C) used to produce the microstructures. The necking points of all tensile curves are highlighted by a star.

The GL680-001 sample presents a Lüders plateau. Its upper yield stress (UYS) is around 800 MPa and its lower yield stress (LYS) is 740 MPa. The Lüders strain is 4%. Then, the sample deforms with a low work-hardening rate, typical of stable austenite/ferrite duplex steels [90], [108], [196]. Necking occurs at a stress of 840 MPa after a strain of 23%.

For GL700-001 sample, the difference between the upper and lower yield stresses is only about 20 MPa. The presence of less stable austenite induced a higher work-hardening, achieving an ultimate tensile strength (UTS) of 960 MPa. The uniform elongation (UEL) is also higher, at 29%.

The behaviour of GL720-001 sample is similar, with a Lüders plateau of about 4%. However, yielding occurs at a lower stress of 725 MPa. The difference in the upper and lower yielding stresses is 60 MPa, similarly to GL680 sample. The TRIP effect seems very efficient in this microstructure, with a higher work-hardening than GL720 steel to achieve an UTS = 1180 MPa while maintaining a good uniform elongation of 23%.

Finally, GL750-001 sample has a very different mechanical behaviour from the other globular steels. It presents a far lower yield strength (YS) of 500 MPa, with no Lüders plateau. It presents also a large work-hardening rate at low strain (between 0.5 and 6%), with a very high ultimate tensile strength of 1350 MPa but a relatively low uniform elongation of 12%. Overall, the yield point elongation does not significantly change between T_i = 680°C and 720°C, which is contrary to what has been reported in literature [148]. Some serrations can be seen on GL700 and GL720 curves, which are the evidence of a PLC effect.

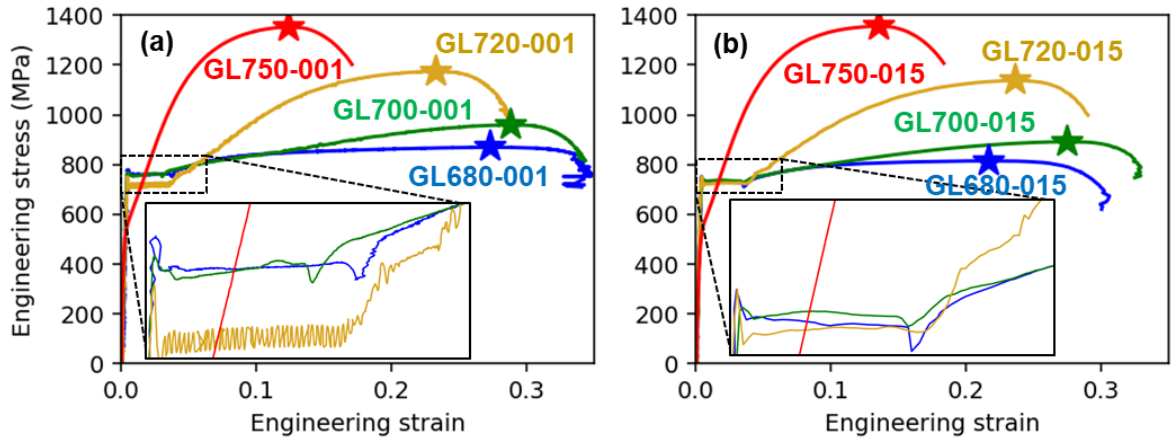

Figure 88: Engineering tensile curves of the samples with globular microstructures at (a) the medium and (b) high strain rates. The stars correspond to the onset of necking.

The tensile curves for globular microstructures obtained at the high strain rate (Figure 88 (b)) are very similar to those obtained at the medium strain rate (Figure 88 (a)). A Lüders plateau is present for the same processing conditions, and the overall evolution of UTS and UEL with IA temperature is identical. The tensile curve of GL720-0001 steel strained at the low strain rate is very similar to that of GL720-001 strained at the medium strain rate, thus not shown here for conciseness.

The evolution of the mechanical behaviour of fibrous ART microstructures as a function of intercritical temperature is very similar to those of globular microstructures, as shown in Figure 89. The curve of FB680-001 steel presents a small Lüders plateau with a length of 1.7%. The yield stress is around 650 MPa. The upper and lower yield points are not present in FB680-001 steel, despite the clear presence of a Lüders instability. The ultimate tensile strength, at around 760 MPa, is lower than that of GL680-001 sample, and the uniform elongation is 14%. The FB700-001 sample exhibits a better ultimate tensile strength and uniform elongation (820 MPa and 22%) than FB680 sample. Nevertheless, these values are inferior to those of GL700 microstructure. Moreover, a very small Lüders plateau, with a length of 0.3% and no lower and upper yield points (UYS=LYS=625 MPa), exists in the curve of FB700-001 steel. The FB720-001 sample has a low yield stress of 490 MPa. The absence or presence of Lüders instabilities is difficult to determine on the tensile curve or by DIC, as PLC effect is affecting FB720-001 microstructure. The efficient TRIP effect gives this steel a good ultimate tensile strength of 1060 MPa and a uniform elongation of 20.0%. These values are once again lower than those of its globular counterpart. Finally, the FB750-001 curve is very similar to that of GL750-001, presenting no mechanical instabilities, a low yield stress of 490 MPa and a very high initial work-hardening. The UTS is 1300 MPa and the UEL is 12%. The values are this time very similar to GL750-001 specimen.

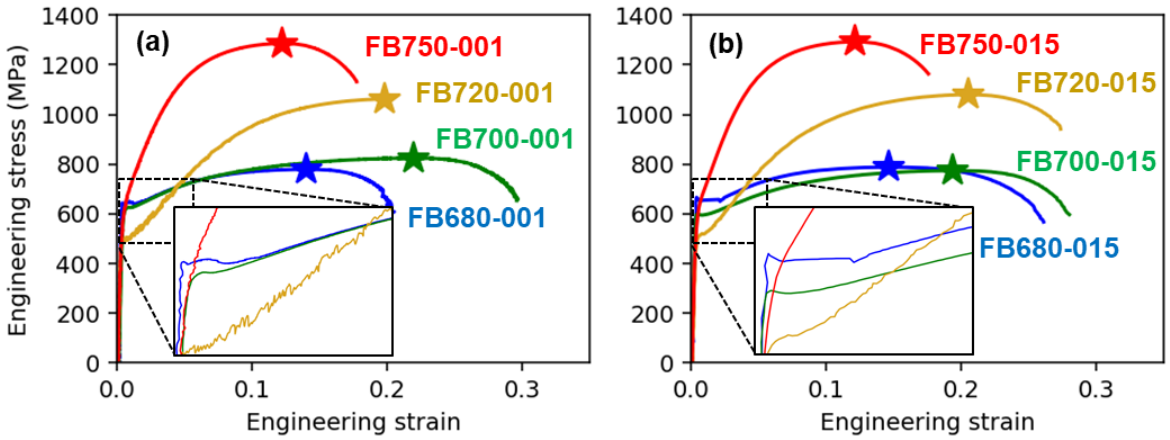

Figure 89: Engineering tensile curves of samples with fibrous microstructures at (a) the medium and (b) high strain rates. The stars correspond to the onset of necking.

Once again, the tensile curves for fibrous microstructures obtained at the high strain rate are very similar to those obtained at the medium strain rate. A Lüders plateau is present for the same processing conditions, and the overall evolution of UTS and UEL with IA temperature is identical.

Overall, the fibrous microstructures, when compared to the globular microstructures with equivalent intercritical annealing temperatures, are less attractive (lower UTS and UEL), especially for the low intercritical temperatures (680°C and 700°C). However, fibrous samples present fewer mechanical instabilities than the globular ones. Lüders plateau are always shorter. Considering Portevin-Le Chatelier effect (PLC), globular samples seem also to be more affected. Indeed, PLC is present on the curves of both GL700 and GL720 steels, but only on the curve of FB720 steel for fibrous microstructures. In GL720 microstructure, PLC even occurs during the Lüders plateau, explaining the oscillation in stress happening during the plateau. In both microstructures, the presence of unstable austenite transforming into martensite during deformation seems necessary for PLC to occur. On the contrary, static strain aging seems independent from the stability of austenite, especially in globular samples.

B. Strain-induced martensitic transformation kinetics

Rietveld refinement allows for in situ tracking of the evolution of austenite phase fractions during tensile tests. Combining it with SEM analysis, it is possible to obtain the phase fraction of ferrite and the evolution of martensite fraction.

For instance, the phase fractions of ferrite (red curve), austenite (blue curve) and martensite (green curve) during tensile test are reported in Figure 90 for the GL720-0001 experiment. The diffracting volume consists initially of 60% of ferrite, 25% of austenite and 15% of martensite. The austenite fraction decreases during the deformation, while the martensite fraction conversely increases, as expected from the strain-induced martensitic transformation. The fraction of ferrite is constant (imposed by our methodology). At necking onset, austenite and martensite fractions are respectively 4% and 36%. Some steps are noticeable on both kinetics curves, associated to PLC mechanical instabilities [187]. The abrupt rises in martensite fraction occurs when the deformation

bands cross the diffracting volume (1.5 × 0.5 × 0.5 mm³). The sudden increase in the local deformation is correlated to a sudden increase in the martensite fraction in the analysed volume.

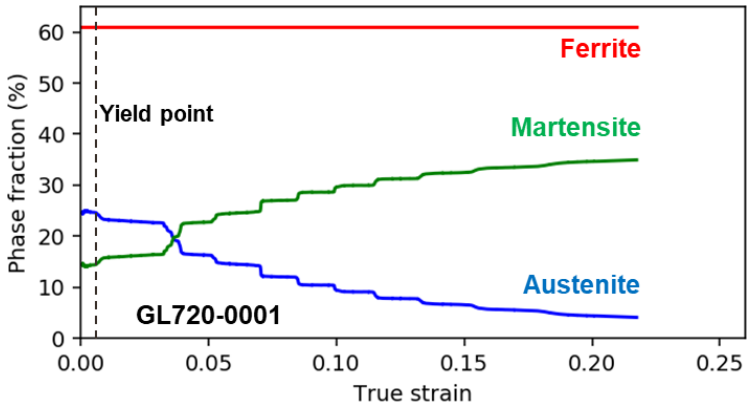

Figure 90: Evolution of ferrite (red), austenite (blue) and martensite (green) phase fractions during the tensile test at 5×10^{-5} s^{-1} of a globular sample annealed at 720°C (GL720-0001). Curves are represented up to necking onset.

The evolution of the other globular microstructures is reported in Figure 91 and those of fibrous microstructures in Figure 92 with the same colour code.

For specimen deformed at the medium strain rate, in all experiments, the same trends are observed as in the last paragraph: ferrite is constant, austenite transforms and martensite appears during deformation due to SIMT. Multiples steps can be observed on the curves of GL700, GL720 and FB720 microstructures, confirming the presence of PLC effect in those specimens, as stated when studying the tensile curves. For GL680, GL700, GL720 and GL750 steels, the initial austenite fractions determined by Rietveld refinement are respectively 12%, 18%, 25% and 18%. The maximum austenite fraction retained at room temperature is thus achieved for an intercritical annealing at 720°C. The same conclusion can be made for fibrous microstructures, for which the initial austenite fractions are respectively 5.5%, 13%, 31% and 16% when annealing temperature T_{IA} increases.

At necking, the corresponding fractions of austenite are respectively 4.7%, 5.5%, 3.8% and 2.5% for globular specimens and 3.8%, 4.3%, 5% and 3.4% for fibrous specimens with increasing T_{IA}. Therefore, the final fractions of austenite are similar between experiments, close to the limits of the method, independently of the morphologies and the annealing temperatures. Concerning martensite, the initial fractions are respectively 7%, 10%, 15% and 32% for globular specimens and 6%, 9%, 11% and 39% for fibrous specimens with increasing T_{IA}. At necking, they are respectively 14%, 23%, 36% and 47% for globular specimens and 8%, 18%, 38% and 52% for fibrous specimens with increasing T_{IA}. Therefore, when T_{IA} increases, more martensite is found initially and at the end in the microstructures, independently of the morphology. Finally, another important result is that there is always martensite in all the studied microstructure, even for those annealed at the lowest temperature.

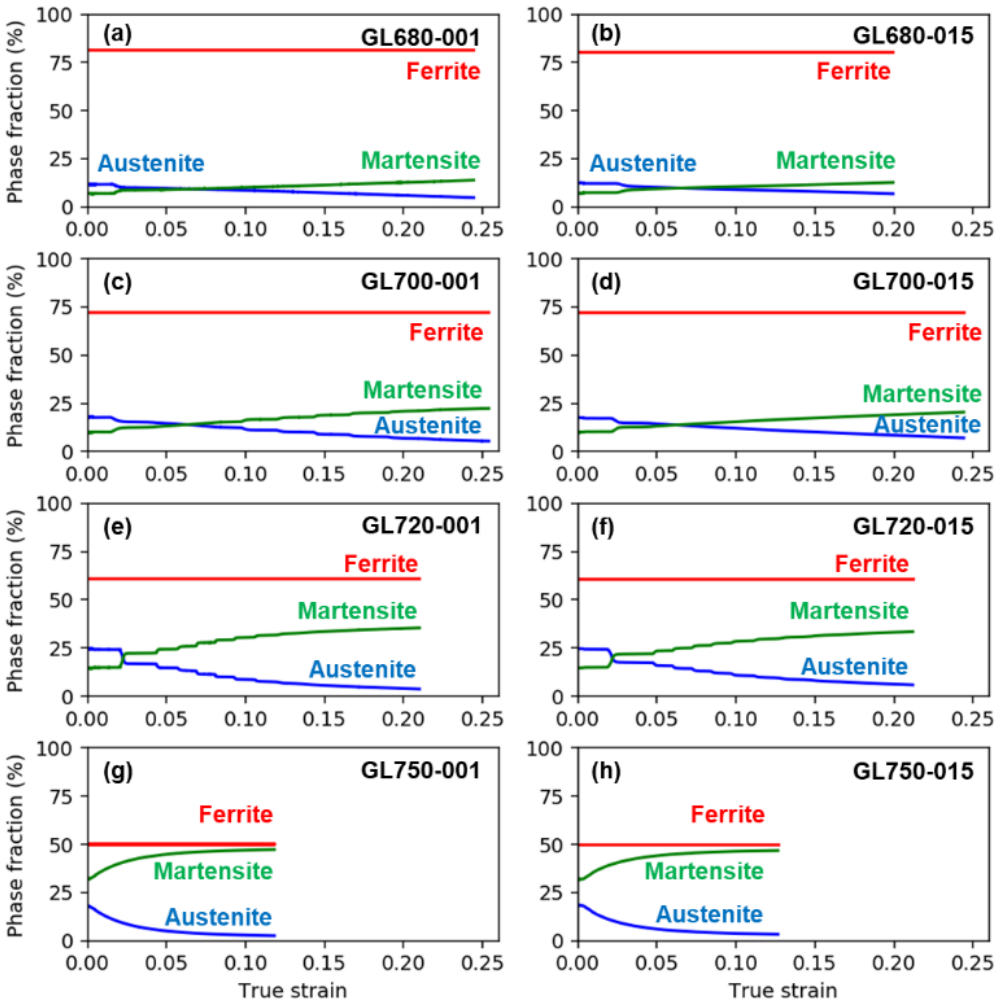

Figure 91: Evolution of ferrite (red), austenite (blue) and martensite (green) phase fractions during the tensile tests of the globular microstructures. (a) GL680-001, (b) GL680-015, (c) GL700-001, (d) GL700-015, (e) GL720-001, (f) GL720-015, (g) GL750-001 and (h) GL750-001. Curves are represented up to necking onset.

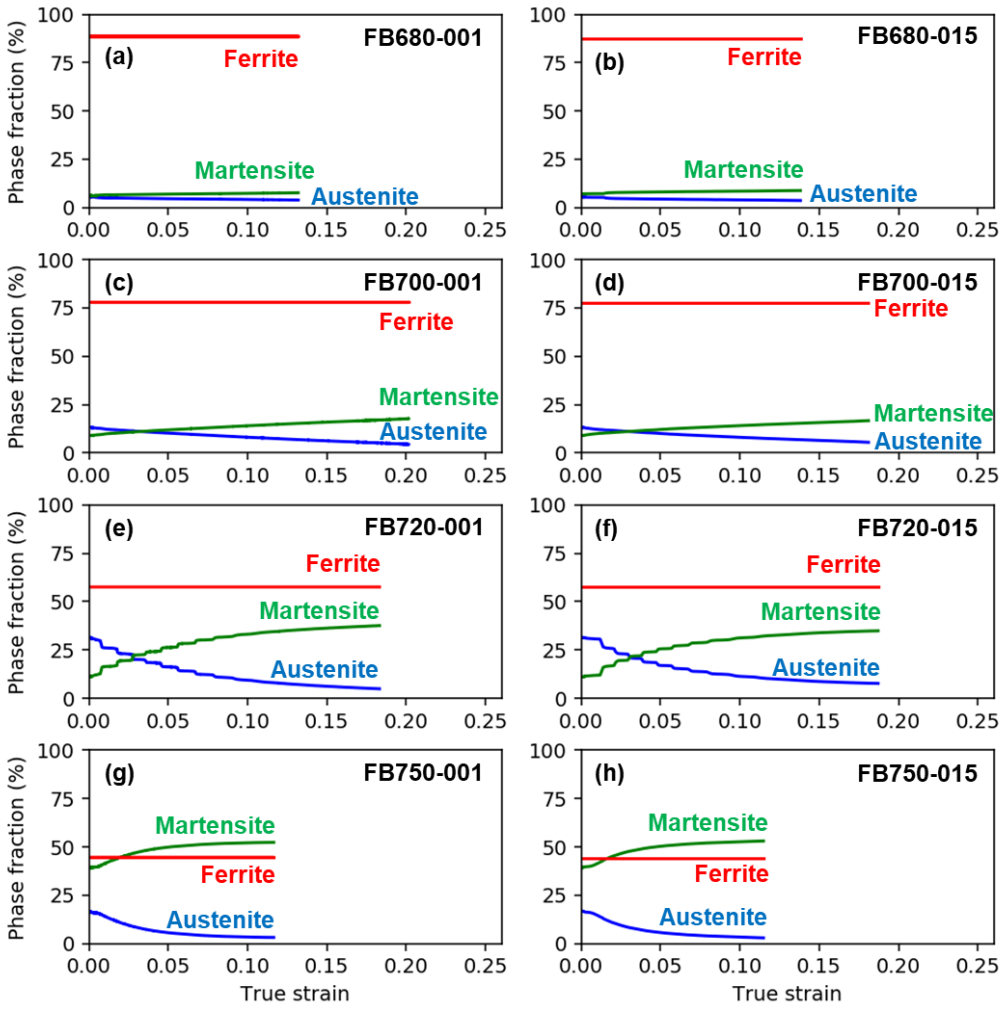

Figure 92: Evolution of ferrite (red), austenite (blue) and martensite (green) phase fractions during the tensile tests of the globular microstructures. (a) FB680-001, (b) FB680-015, (c) FB700-001, (d) FB700-015, (e) FB720-001, (f) FB720-015, (g) FB750-001 and (h) FB750-001. Curves are represented up to necking onset.

At the high strain rates, the transformations kinetics remain very similar for all studied microstructures. All remarks done in the preceding paragraph remain true.

C. Ferrite and austenite 3D stress tensor

The stresses σ_{RD}, σ_{TD}, σ_{vM} and σ_h for ferrite and austenite calculated with $\sin^2\psi$ method are shown in Figure 93 for the GL720-001 experiment as an example of 3D stress tensors typically obtained. In this case, the fraction of fresh martensite inherited from the processing is limited to 15% and the internal stresses induced by the displacive transformation will be neglected, even though they are not negligible. The initial hydrostatic stresses are calculated thanks to the model developed in section II.4.B.

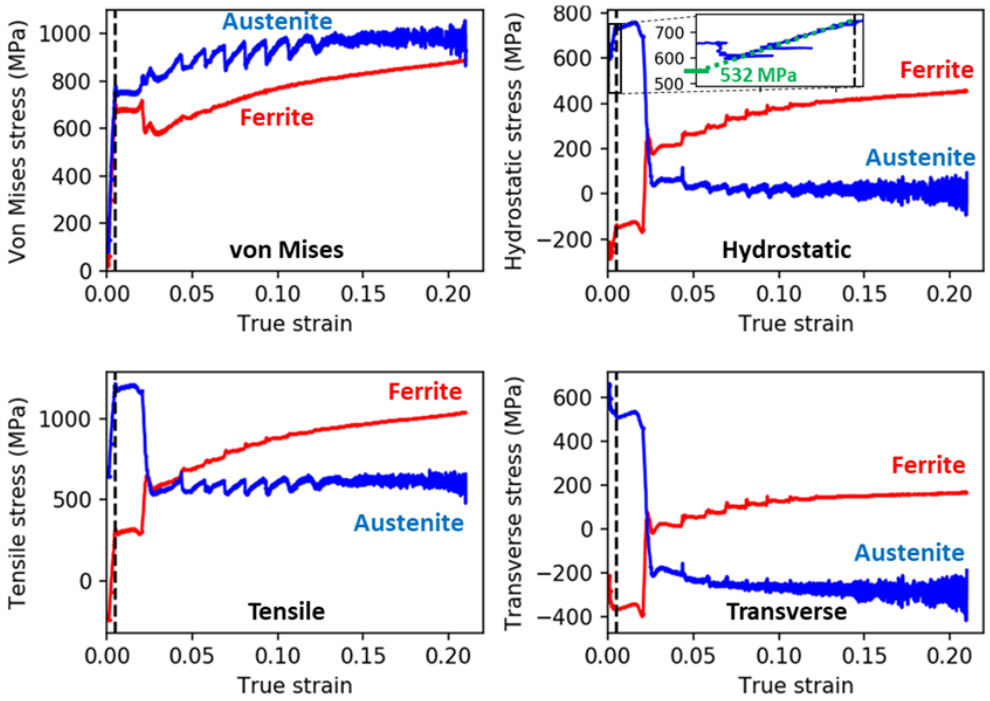

Figure 93: Evolution of stress tensor components in ferrite (red) and austenite (blue) obtained during the GL720-001 experiment: (a) von Mises stress σ_{VM}; (b) hydrostatic pressure σ_h; (c) stress in tensile direction σ_{RD}; (d) stress in transverse direction σ_{TD}. The vertical dotted black line corresponds to the onset of yielding. The curves are cut at the necking onset. The measurement error on stress is around 25 MPa. In (b), a magnification of the austenite hydrostatic stress in the elastic domain highlights how the stresses are calibrated to respect the chosen initial hydrostatic values in both phases.

In the elastic regime, both von Mises stress and tensile stress increase linearly, while the transverse stress decreases for both austenite and ferrite. In comparison, the hydrostatic stress evolves non-monotonously during elastic deformation. As put in evidence in Figure 93 (b) in the magnified box, it first stagnates, then decreases and finally linearly increases. This behaviour is obviously an artefact and can be attributed to a possible gliding of the tensile specimen at the start of the trial. To really consider the initial hydrostatic stress value in σ_{TD}, σ_{vM} and σ_h curves, it is necessary to extend linearly the slope of the stress to lower value of strain, as showcased in green in Figure 93 (b) for austenite.

In the elastic regime, the behaviour of both phases is thus linear modulo the artefact discussed above at the very beginning and highly correlated (same slope, same increase or decrease in stresses) whatever the studied components. Given an elastic strain of 0.35% at yield point, the measured Young's moduli are 190 GPa for von Mises curves and tensile curves. Those "apparent" Young's moduli are close to the theoretical chosen one (≈200 GPa). As both measurements are independent (different rings), it clearly demonstrates that our methodology is valid and robust.

At the yield point, austenite shows a high tensile stress in the longitudinal direction (1210 MPa) and in the transverse direction (520 MPa) due to the high initial tensile hydrostatic stress state (+532MPa). On the other hand, in the ferritic matrix, stresses are lower in the longitudinal direction (320MPa) and in the transverse direction (–375MPa) due to the high initial compressive hydrostatic stress state (-375MPa). As explained in our paper [187], the stresses in the tensile and transverse direction are explained by the sum of initial hydrostatic stress and the external loading – 700 MPa in the tensile direction and 0 MPa in the transverse direction.

At the plastic regime onset, an increase in austenite von Mises stress is observed ($\Delta\sigma_\gamma^{vM}$ = +100 MPa), while a huge drop is seen in all other stresses ($\Delta\sigma_\gamma^{h}$ = -720 MPa, $\Delta\sigma_\gamma^{RD}$ = -650 MPa, $\Delta\sigma_\gamma^{TD}$ = -750 MPa). The contrary is observed for ferrite ($\Delta\sigma_\alpha^{vM}$ = -140 MPa, $\Delta\sigma_\alpha^{h}$ = +430 MPa, $\Delta\sigma_\alpha^{RD}$ = +360 MPa, $\Delta\sigma_\alpha^{TD}$ = +480 MPa). This abrupt behaviour at yielding onset was already experimentally reported by Zhang et al. [100] in their work on a Fe/0.12C/10Mn/1.9Al medium Mn steels during in situ tensile tests on synchrotron beamline, but only for von Mises stress of ferrite and austenite.

During yielding, the austenite von Mises stress increases, while its stress diminishes in the transverse direction. The tensile and hydrostatic stresses do not evolve significantly in comparison. Concerning ferrite, all considered stresses increase during yielding.

If we compare von Mises stresses between ferrite and austenite, no significant difference is observed during the elastic regime as expected. At the beginning of the plastic regime, a difference of 70 MPa is observed during the Lüders plateau between σ_γ^{vM} and σ_α^{vM}. This gap rapidly rises when the Lüders bands goes across the analysed area. The maximal difference in stress between austenite and ferrite is 230 MPa, attained at a global strain of 3%. In this steel, retained austenite is stronger than the ferritic matrix (about +150 MPa at ε=12.5%) all along the deformation, as von Mises stresses reveal the true plastic behaviour of the phases. However, this gap decreases due to a higher work-hardening of ferrite compared with austenite. It must be emphasized that serrations are only observed for austenite, the von Mises curve of ferrite remaining almost smooth. However, the other curves (hydrostatic, tensile and transverse stresses) reveals that ferrite is partially affected by mechanical instabilities. In other experiments, some effects of PLC on ferrite are directly visible on von Mises curves, as explained latter in section III.3.E.

The same results for the GL700-001 experiment are given in Figure 94. The initial value of hydrostatic stress was set with Allain's model. The evolution of von Mises, hydrostatic, tensile and transverse stresses are very similar to those found in the GL720-001 test. In this experiment, the mechanical responses of both phases are purely linear during elasticity. Between the onset of Lüders bands until its arrival in the diffracting volume, all stresses components are constant. Again, at the yielding onset in the analysed volume, ferrite von Mises stress decreases, while austenite von Mises stress increases abruptly. On the contrary, all the other components have the opposite behaviour at yielding onset (σ_γ^{h}, σ_γ^{RD} and σ_γ^{TD} plummet, and σ_α^{h}, σ_α^{RD} and σ_α^{TD} skyrocket). All components of ferrite stress tensor then increase until necking, alongside the von Mises stress in austenite. The austenite transverse, tensile and hydrostatic stress first continue to decrease between 4% to 12%, then increases until necking. In this experiment, serrations can be seen after 10% of deformation, and have the same effect on austenite and ferrite 3D stress tensor previously highlighted during GL720-001 experiment analysis.

For the other experiments, only hydrostatic and von Mises stresses will be shown for brevity, as only two independent components of the stress tensor are necessary to entirely described them in the current study (tensile deformation, see section III.2.D.a)). The von Mises stresses are shown for all experiments in the next section and discussed more deeply as the results as independent of the chosen initial state.

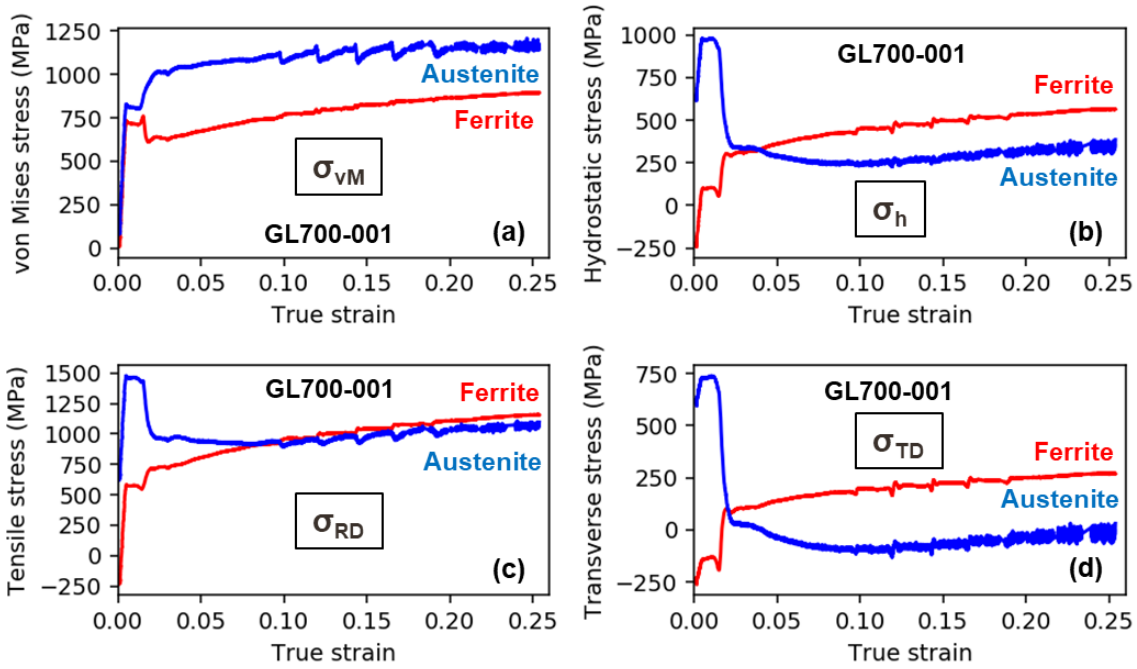

Figure 94: Evolution of stress tensors components in ferrite (red) and austenite (blue) obtained during the GL700-001 experiment: (a) von Mises stress σ_{VM}; (b) hydrostatic pressure σ_h; (c) stress in tensile direction σ_{RD}; (d) stress in transverse direction σ_{TD}. The vertical dotted black line corresponds to the onset of yielding. The curves are cut at the necking onset. The measurement error on stress is around 25 MPa.

Hydrostatic stresses are represented just below for ferrite and austenite in Figure 95 for all tests conducted at the medium strain rate. Again, as a first guess, the initial value of stress is calculated with Allain's model [25] for both ferrite and austenite. With increasing T_{IA}, the initial hydrostatic stress of austenite decreases from 700 MPa to 400 MPa. The one of ferrite also decreases with increasing IA temperature, from -130 MPa to -430 MPa. In all experiments, the trend of hydrostatic stress evolution is always similar. For austenite: increase during elasticity, decreases at first during yielding and then increases until necking. On the contrary, the hydrostatic stress in ferrite is monotonous, always increasing. The effect of mechanical instabilities on hydrostatic stresses are the same as reported before. Accounting for Chapter II results, it must be emphasized that the real initial hydrostatic stress (with martensitic transformation effect) would be lower for austenite and higher for ferrite, but the measured evolution would remain exactly the same. The hydrostatic stresses are not represented here for specimens strained at the high rate for conciseness. They are very similar to those already analysed, and will be shown and discussed in section III.4.C.

The $\sin^2\psi$ method gives access to the hydrostatic, tensile and transverse stresses in ferrite and austenite. However, as the value of initial hydrostatic stress is still difficult to evaluate with certainty (taking into account the presence of initial fresh martensite on hydrostatic stresses), the interpretation of obtained stresses may lead to false idea. As such, only normalised hydrostatic stress will be analysed in the discussion section, as told in the methodology section III.2.D.b).

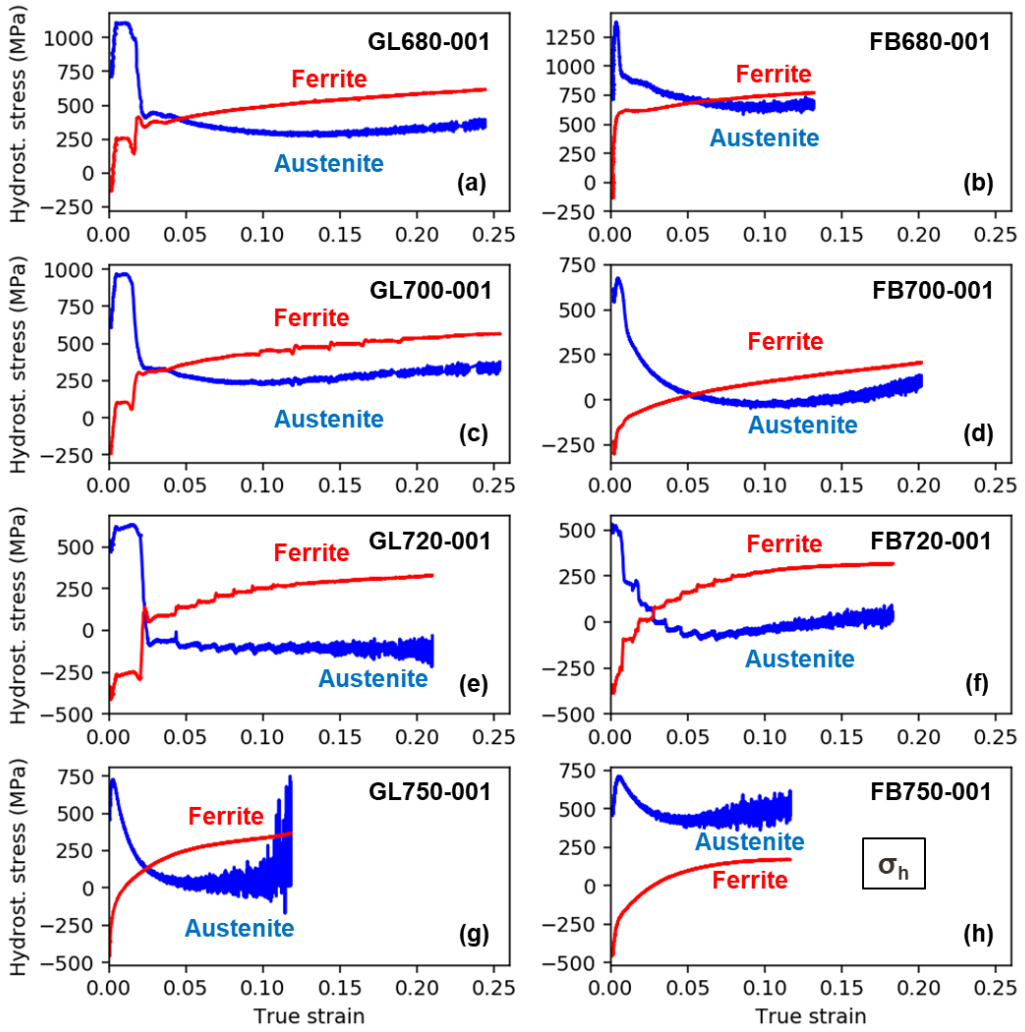

Figure 95: Evolutions of austenite and ferrite hydrostatic stresses as a function of macroscopic true strain for (a) GL680-001; (b) FB680-001; (c) GL700-001; (d) FB700-001; (e) GL720-001; (f) FB720-001; (g) GL750-001; (h) FB750-001 experiments respectively.

It is important to reaffirm here that the determinations of von Mises components do not require to know a priori the starting state of the phases and therefore that the values obtained by the $\sin^2\psi$ methods are directly usable. The next section is dedicated to von Mises stresses, which represents also the flow stress when the phase is yielding.

D. Stress partitioning during quasi-static test

a) Globular microstructures

The comparison between the macroscopic stress σ_{macro} (black), austenite σ_γ^{vM} (blue), ferrite σ_α^{vM} (red) and martensite $\sigma_{\alpha'}^{vM}$ (green) von Mises stresses are shown in Figure 96 for all the experiments conducted on globular microstructures at the medium strain rate. All curves are plotted as a function of the mean macroscopic true strain ε_{macro}. The martensite in Figure 96 stress is calculated with Hill's mixture rules.

The major trends are very similar between experiments. The four curves are confounded during elastic loading. During the Lüders plateau for GL680-001, GL700-001 and GL720-001 specimens, the stress at phase scale remains constant at first. At about half the length of the Lüders macroscopic plateau (visible in the black macroscopic curve), the flow stress abruptly changes in all phases, then stagnate again until the end of the instability. The abrupt change in stress corresponds to the passage of the mechanical instability across the diffracting volume, which is located about at the middle of the gauge length. The flow stress of martensite is always higher than that of austenite, which is itself always higher than that of ferrite.

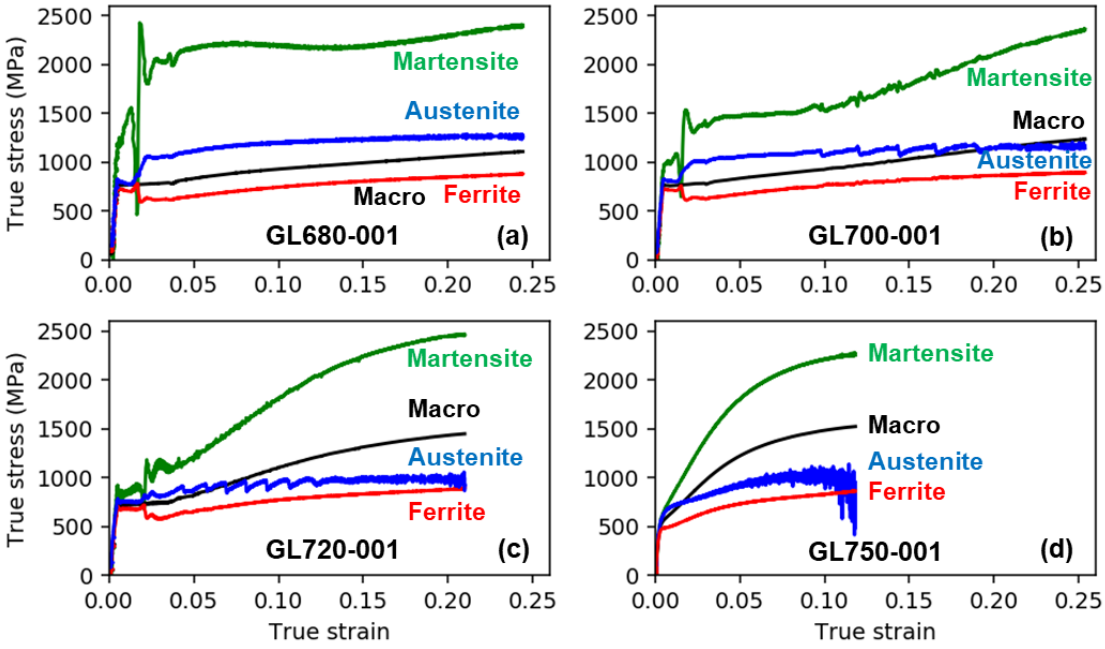

Figure 96: Comparison between the macroscopic stress σ_{tot} (black), the von Mises stresses in ferrite σ_{α}^{vM} (red) and austenite σ_{γ}^{vM} (blue) determined by $\sin^2\psi$ method and the von Mises stress in martensite $\sigma_{\alpha'}^{vM}$ (green) calculated by the mixture rule for the four globular microstructures strained at the medium rate. (a) GL680-001. (b) GL700-001. (c) GL720-001. (d) GL750-001 experiments respectively.

The behaviour of the same steels at higher strain rate is shown in Figure 97. The evolution of stress partitioning during experiments follows the same pattern as before. Phase stresses are close to the macroscopic one before yielding. During work-hardening, martensite is the most loaded phases, followed by austenite and ferrite. The passage of PLC bands across the diffracting volume can be seen on the austenite von Mises stress curve by the presence of serrations. At the medium strain rate, PLC effects is present for the GL700-001 and GL720-001, but at the high strain rate, it is only present for the GL720-015 experiment. Therefore, increasing the strain rate suppresses PLC banding (also confirmed by DIC strain rate map analysis).

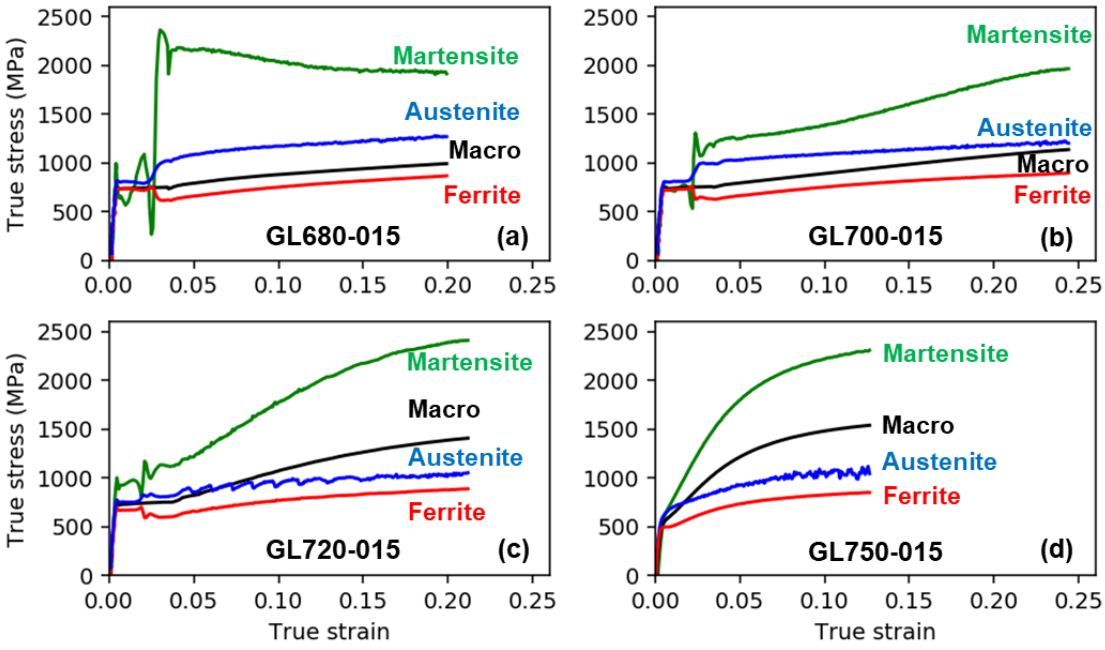

Figure 97: Comparison between the macroscopic stress σ_{tot} (black), the von Mises stresses in ferrite σ_{α}^{vM} (red) and austenite σ_{γ}^{vM} (blue) determined by $\sin^2\psi$ method and the von Mises stress in martensite $\sigma_{\alpha'}^{vM}$ (green) calculated by the mixture rule for the four globular microstructures strained at the high rate. (a) GL680-015. (b) GL700-015. (c) GL720-015. (d) GL750-015 experiments respectively.

At the end of the Lüders plateau, the von Mises stress in ferrite decreases, while the von Mises stress in austenite and martensite increases. This means that only ferrite softens after the passage of Lüders band. If SSA theory is used to understand the Lüders phenomena in medium Mn steels, it could mean that only dislocation present in ferrite are strongly pinned by carbon atoms and are unpinned at the passage of the mechanical instability. Thus, the origin of Lüders instability in medium Mn steels is more likely to be found in ferrite. Please note that this is not evident to use SSA theory to explain Lüders effect in medium Mn steel due to coincident SIMT.

On the other way, as previously stated, only the stress in austenite decreases at the passage of PLC bands. The flow stress in ferrite and martensite either remains constant or increase a bit (like in the GL700-001 experiment) to compensate for the unloading of austenite. This is also visible on hydrostatic stress curve shown in Figure 95. When only a small amount of austenite remains in the microstructure, near necking, the stress curve is highly jerky. This can be explained either by the transition of a A/B type PLC to a C type PLC, or by the low amount of austenite which makes the determination more uncertain. Comparatively, at the macroscopic level, there is no PLC band near necking in the other phases, which also confirms the necessity of having enough austenite in the microstructure to induce macro-deformation banding. Therefore, the other important conclusion is that the dynamical mechanical instabilities in medium Mn steel is more likely to find their origin in austenite.

b) Fibrous specimens

The comparison between the macroscopic true stress σ_{tot} (black), austenite σ_{vM}^{γ} (blue), ferrite σ_{vM}^{α} (red) and martensite $\sigma_{vM}^{\alpha'}$ (green) von Mises stresses are shown in Figure 98 for all samples with a fibrous microstructure strained at the medium rate. The major trends are very similar to those with a globular microstructure. For FB680-001, FB700-001 and FB750-001 experiments, ferrite is softer than austenite, while austenite is softer than martensite. For FB700-001 experiment, austenite flow stress remains higher than the medium Mn global stress, contrary to GL700-001 specimen. Hence, TRIP effect seems more efficient in the case of GL700-001 than for FB700-001. FB720-001 partitioning of stress among phases is similar to other experiments at the necking. However, at the first stage of deformation (ε<0.3%), the stress calculated in martensite is astonishingly low, even lower than in ferrite and austenite. These results cannot really be changed by modifying the value of the initial fraction of martensite, used in Hill's mixture law (Equation (III—9)). This is rather explained by the ±25 MPa uncertainty on $\sin^2\psi$ measurements of ferrite and austenite stress.

Indeed, during the elastic regime, for FB720-001, the macroscopic stress σ_{tot} is initially lower than the sum of the contribution of ferrite and austenite $f_\alpha\sigma_\alpha+f_\gamma\sigma_\gamma$. Therefore, to compensate it, the von Mises stress in martensite is firstly calculated as negative, at -240 MPa. This has no physical meaning and is only explained by the tenfold increase of uncertainty induced by the multiplication by $1/f_{\alpha'}$, the fraction $f_{\alpha'}$ being initially very low. Those errors are reduced during deformation as $1/f_{\alpha'}$ decreases.

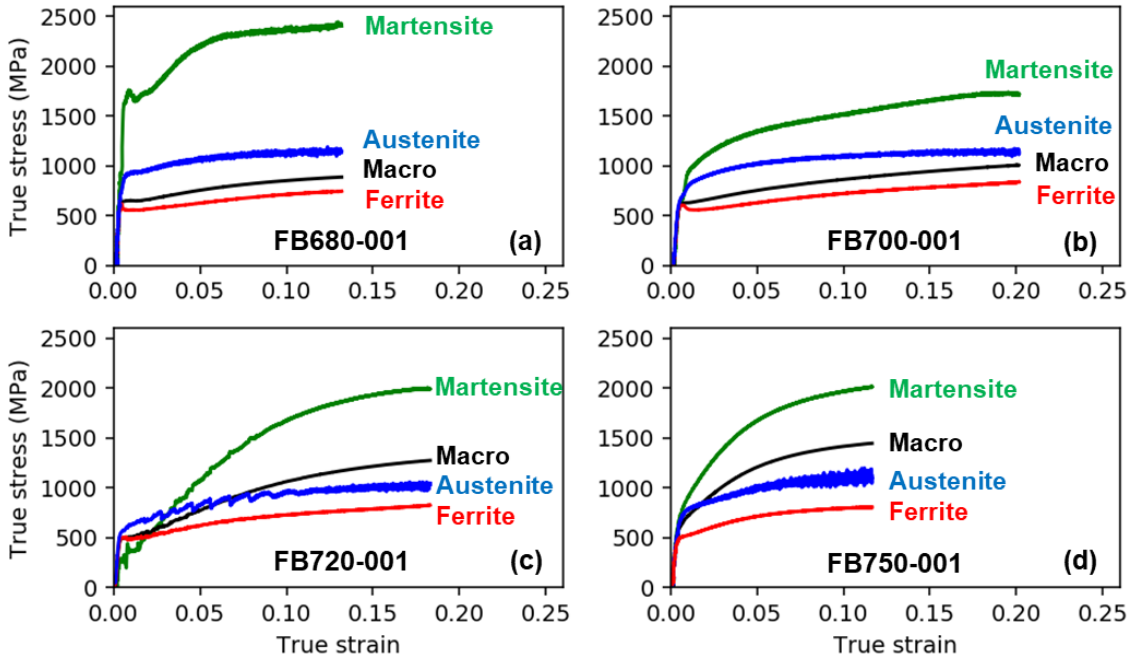

Figure 98: Comparison between the macroscopic stress σ_{tot} (black), the von Mises stresses in ferrite σ_α^{vM} (red) and austenite σ_γ^{vM} (blue) determined by $\sin^2\psi$ method and the von Mises stress in martensite $\sigma_{\alpha'}^{vM}$ (green) calculated by the mixture rule for the four samples with a fibrous microstructure strained at the medium rate. (a) FB680-001. (b) FB700-001. (c) FB720-001. (d) FB750-001 experiments respectively.

The same comparison between the macroscopic true stress σ_{tot} (black), austenite σ_{vM}^{γ} (blue), ferrite σ_{vM}^{α} (red) and martensite $\sigma_{vM}^{\alpha'}$ (green) von Mises stresses are shown in Figure 99 for all samples with a fibrous microstructure strained at the high rate. The major trends are very similar to the previous trends highlighted before. This time, for all steels, ferrite is softer than austenite, while austenite is softer than martensite, even for FB720-015. This last finding supports that the low relative value of martensite von Mises stress in FB720-001 is indeed linked with the amplified measurement uncertainty. For FB700-015 experiment, the von Mises stress seems quite low in comparison to other steels. This was also the case to a lesser degree for FB700-001 steel. While the low initial value of martensite von Mises stress in FB700-015 steel could be attributed to the same reason as that in FB720-001 steel (amplified uncertainty), the fact that the value of $\sigma_{\alpha'}^{vM}$ at the necking onset remains relatively low suggests that there is another explanation. This explanation may be metallurgical or arising from another methodological problem.

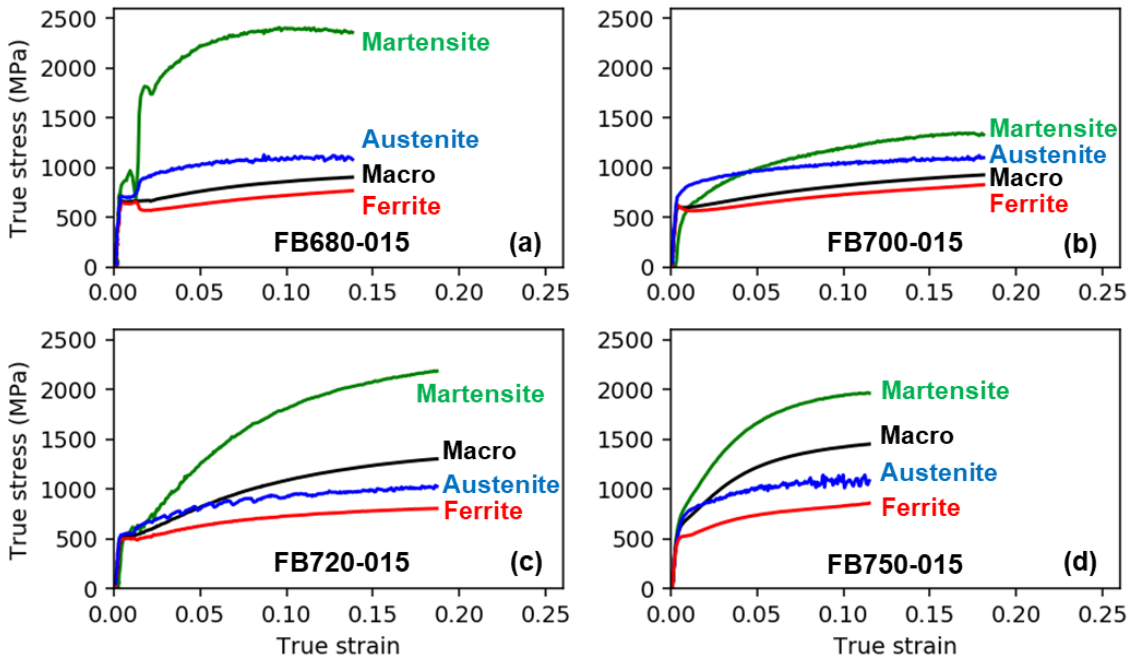

Figure 99: Comparison between the macroscopic stress σ_{tot} (black), the von Mises stresses in ferrite σ_{α}^{vM} (red) and austenite σ_{γ}^{vM} (blue) determined by $\sin^2\psi$ method and the von Mises stress in martensite $\sigma_{\alpha'}^{vM}$ (green) calculated by the mixture rule for the four samples with the fibrous microstructure strained at the high rate. (a) FB680-015. (b) FB700-015. (c) FB720-015. (d) FB750-015.

The remarks concerning static and dynamic strain aging made in the previous section for globular microstructures remain totally valid for fibrous microstructures.

E. Flow stress of martensite

The stress in martensite was calculated using two different methods. As explained in section III.2.D.b), a direct attempt to apply $\sin^2\psi$ method has been made for 720°C and 750°C annealed microstructures, as they have high enough martensite phase fraction. For 680°C and 700°C annealed microstructures, the $\sin^2\psi$ analysis has been tried but it revealed to be fruitless due to numerical deconvolution issues. The second method consists in applying an inverse Hill's mixture rules, as we

know all the other stresses and phase fractions at any deformation. This was detailed in section III.2.E. The main advantage of this last method is that it can be applied even for 680°C and 700°C annealed specimens. Its main drawback is to be highly sensitive to the initial phase fraction of martensite, which induces a huge uncertainty (about 5% in absolute value).

The comparison between the von Mises stresses calculated by both methods are represented in Figure 100 for GL720-001 (a), GL750-001 (b), FB720-001 (c) and FB750-001 (d) experiments. In all experiments with both methods, the stress in martensite evolves linearly in the elastic domain. In the plastic domain, flow stress of martensite continuously increases all along the tensile test. It is however not possible to prove if this increase is linked to a real work-hardening of martensite or explained by an elastic loading of martensite during the plastic deformation of other phases. In fact, the methods grant an access to the stress state but not to the plastic deformation level.

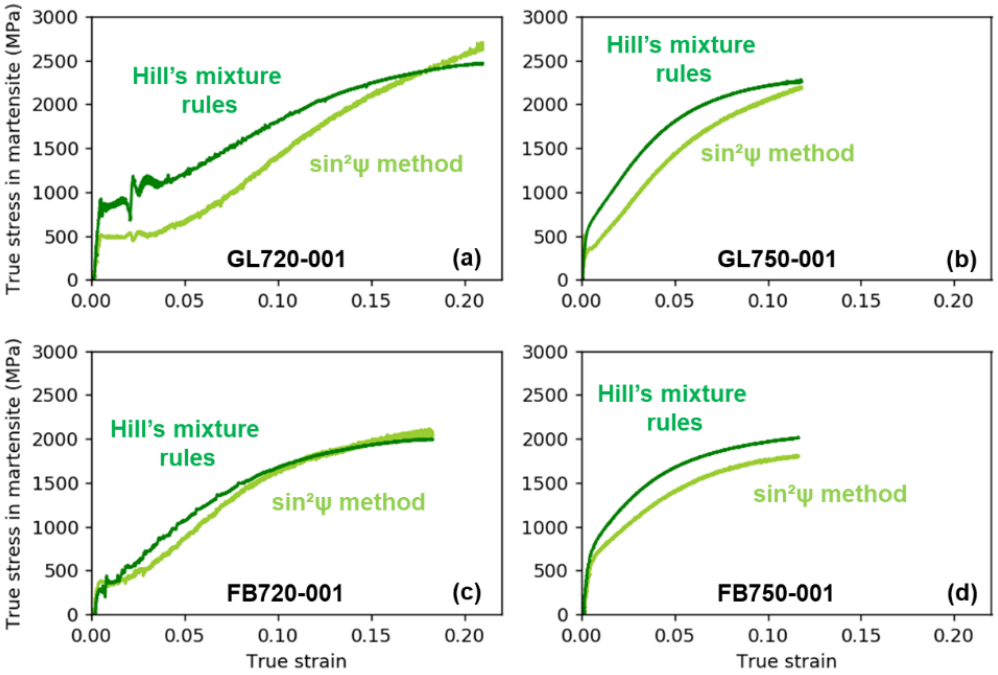

Figure 100: Comparison between the von Mises stress in martensite calculated by Hill's mixture law (dark green) and that calculated using direct $\sin^2\psi$ method (light green) for (a) GL720-001, (b) GL750-001, (c) FB720-001 and (d) FB750-001 experiments. The linear regression during the $\sin^2\psi$ analysis was conducted over the range of [0.2; 0.75].

The martensite stresses predicted by both methods are very similar for all experiments within the expected experimental uncertainties for GL750, FB720 and FB750 experiments. The stresses determined with $\sin^2\psi$ method are slightly lower to those determined with Hill's mixture law, except near necking for FB720 and GL720 specimens.

Using inverse mixture rules, the apparent yield strengths (YS) are respectively 900 MPa, 500 MPa, 350 MPA and 800 MPa for GL720-001, GL750-001, FB720-001 and FB750-001 experiments. Using the $\sin^2\psi$ method, the values are respectively 500 MPa, 350 MPa, 300 MPa and 600 MPa. Both methods give similar trends, even though YS determined with $\sin^2\psi$ method are overall 200 MPa lower than Hill's ones, except for FB720-001 experiments. Using inverse mixture rules, the martensite strengths at necking are respectively 2.4 GPA, 2.3 GPa, 2 GPA and 2 GPa for GL720-001, GL750-001, FB720-001 and FB750-001 experiments. Using the $\sin^2\psi$ method, the values are respectively 2.6 MPa,

2.2 MPa, 2.1 MPa and 1.8 MPa. The strengths at necking are thus very similar between both methods, giving confidence in the measured values.

Furthermore, the levels of stresses reached at the end of the trial (between 2 GPa and 2.4 GPa) are very consistent with the ultimate tensile strength of a 0.5C fully martensitic steel [18]. Fibrous martensites tend to be less loaded at necking than globular ones.

As shown previously, von Mises stress in austenite widely decreases at the passage of PLC bands across the diffracting volume. This is not the case in martensite for GL720 and FB720 specimens, independently of the method used to calculate the flow stress in martensite. Hence, the physical origins of mechanical instabilities in medium Mn steels are surely to be found in austenite, neither in martensite nor in ferrite.

The mechanical instabilities are analysed at a more macroscopic scale in the next section.

F. Strain-rate bands linked with mechanical instabilities

The DIC grants an access to the strain field $\overline{\overline{\varepsilon}}$ all along the gauge of the tensile specimen (3 surface components). The mean strain ε_{macro} over the gauge of the specimen at each step of the trial is determined by averaging the values taken by $\overline{\overline{\varepsilon}}$. As previously explained, Lüders and PLC effect are found in some of the tensile experiments (like GL700-001 and GL720-001), which is expected in medium Mn steels [108], [140]. With DIC, the surface strain field is measured for each time step of the trial. Thus, it is possible to track the appearance and evolution of each Lüders and PLC bands in each experiment. Figure 101 represents the values (colour) of ε_{yy} (diagonal component of strain tensor $\overline{\overline{\varepsilon}}$ in the tensile direction) as a function of the initial position on the sample (Lagrangian approach) and of the time is given for the three experiments. The axial position is normalized from 0 to 1 instead of using the gauge length. In (a), (b), (c) and (d) are represented the map obtained during the FB700-001, GL680-001, GL700-001 and GL720-001 experiments respectively. For reasons of concision, only these maps are given as they are representative of all maps measured during the thesis.

In those maps, vertical lines correspond to the profile of strain along the gauge length at a given time, and horizontal lines correspond to the evolution of the mean strain at a given section of the specimen during the whole tensile test. If the deformation is uniform (no localization bands or before necking), the field must have a continuous gradient as a function of time and uniform as a function of the position. This is the case during most of the FB700-001 test (Figure 101 (a)). In reality, there is a Lüders band starting at 60 s and finishing at 70 s. This is not visible within the current map, as the band's strain is negligible (<0.005). Maps found for FB680-001, FB700-015 experiments and tests done on steels annealed at 750°C are very similar with no visible banding.

The sharp and oblique transitions in the field for GL680-001 experiment (Figure 101 (b)) corresponds to the Lüders band which starts at 50 s at the bottom of the specimen, and reaches the top of the gauge at 130 s. Between 130 s and 400 s, the strain is uniform along the gauge length, confirming the absence of PLC bands in GL680-001. Finally, between 400 s and 780 s, a concentration of strain is visible around the axial position of 0.6, which corresponds to the necking. Maps found for FB680-015 and GL700-015 experiments are very similar, with a visible Lüders band and homogeneous deformation afterwards, until the end of the test.

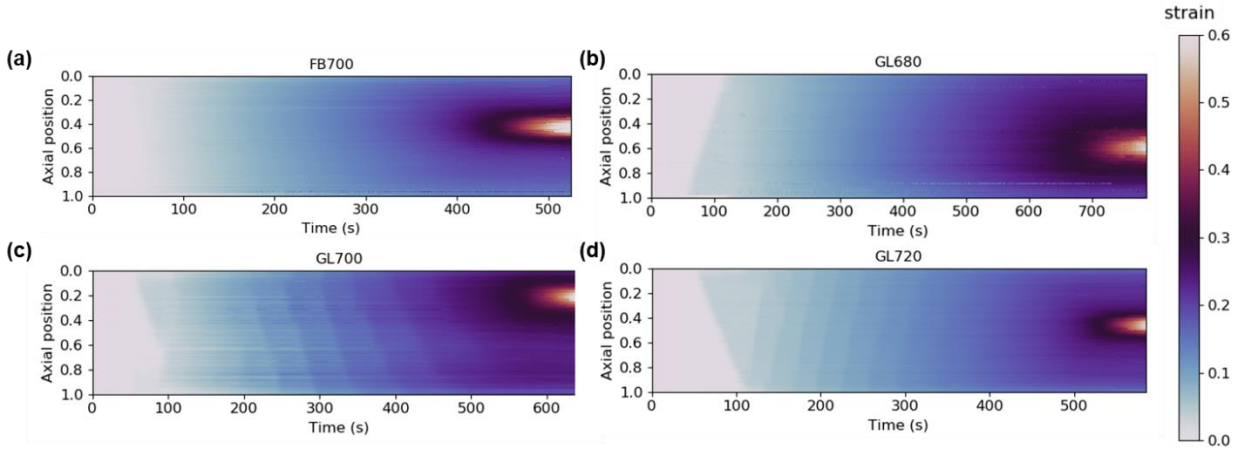

Figure 101: The evolution of the mean axial true strain ε_{yy} determined by DIC as a function of the time and the axial position is represented for (a) FB700-001, (b) GL680-001, (c) GL700-001 and (d) GL720-001 experiments. The values of the strain are represented according to the color code. Last time corresponds to the rupture.

The PLC bands and their associated strain localization correspond in the same way to the oblique sharp transitions between two strain states on the colour maps. Their inclination is linked with the velocity of the bands. During the GL700-001 experiment (Figure 101 (c)), two Lüders bands are initiated at both ends of the gauge and joined at 100 s in the middle of the specimen. Then, between 100 s and 200 s, the deformation looks uniform. Between 200 s and 400 s, rapid strain jumps are observed for a given position corresponding to the crossing of PLC bands. The critical strain to trigger PLC is estimated about 10% in this GL700-001 medium Mn steel. The behaviour observed for GL700-001 (appearance of PLC after a critical strain) was not observed in any other experiment.

For the GL720-001 specimen ((Figure 101 (d)), plastic deformation is only heterogeneous between 0 s and 350 s (Lüders and PLC banding). Between 350 s and until necking, the strain seems homogeneous alongside the gauge, suggesting the existence of a critical strain after which PLC effect ceases in medium Mn steels. In the latter case, the necking begins after 460 s. It is visible with the strong deformation heterogeneity (represented in brown/white, above 0.4). Maps found for FB720-001, GL720-015 and FB720-015 experiments are very similar, with banding occurring from the start to near the end of the test.

The given maps demonstrate that the PLC occurring in the studied medium Mn steels is not a type C PLC. No oblique transition would be distinguished if that was the case. It is however difficult to distinguish from type A to type B PLC from these maps.

The following sections are dedicated to the comparison of global mechanical behaviours, stress partitioning between phases and martensitic transformation kinetics between different experiments to discuss the effect of intercritical temperature T_{IA}, microstructure morphology and strain rate on the medium Mn mechanical behaviour at macroscopic and phase scales. The condition of occurrence of mechanical instabilities (strain rate vs austenite stability) is also discussed in regards with the literature data presented during the literature review.

4. Parameters affecting mechanical response

A. Effect of intercritical annealing temperature

The true tensile curves obtained for the globular and fibrous specimens are compared in Figure 102 for the four intercritical temperatures T_{IA} and two morphologies at two higher strain rates. The ultimate tensile strength increases with increasing T_{IA}, while the uniform elongation is higher for intermediate intercritical annealing temperatures, showing a maximum at T_{IA} = 700°C. Engineering mechanical properties of studied steels strained at medium strain rate are summarized in Table 16 (UEL, UTS, YS/UYS and the presence or absence of mechanical instabilities). As a reminder, in the table are also indicated the initial austenite phase fraction determined with the sole Rietveld refinement and the initial martensite phase fraction calculated by comparing Rietveld refinement results with SEM. Overall, the mechanical performance of the studied steels and their evolution as a function of annealing temperature are in agreements with those already reported about medium Mn steels [13].

In Figure 103 and in Figure 104 are respectively shown the von Mises stress in ferrite and austenite for the 16 experiments strained at the two higher strain rates (5×10^{-4} s^{-1} and 8×10^{-3} s^{-1}). The values have been obtained using $\sin^2\psi$ method. Independently of the strain rate or the morphology, the evolutions of ferrite and austenite von Mises stress are very similar when the annealing temperature T_{IA} is varied.

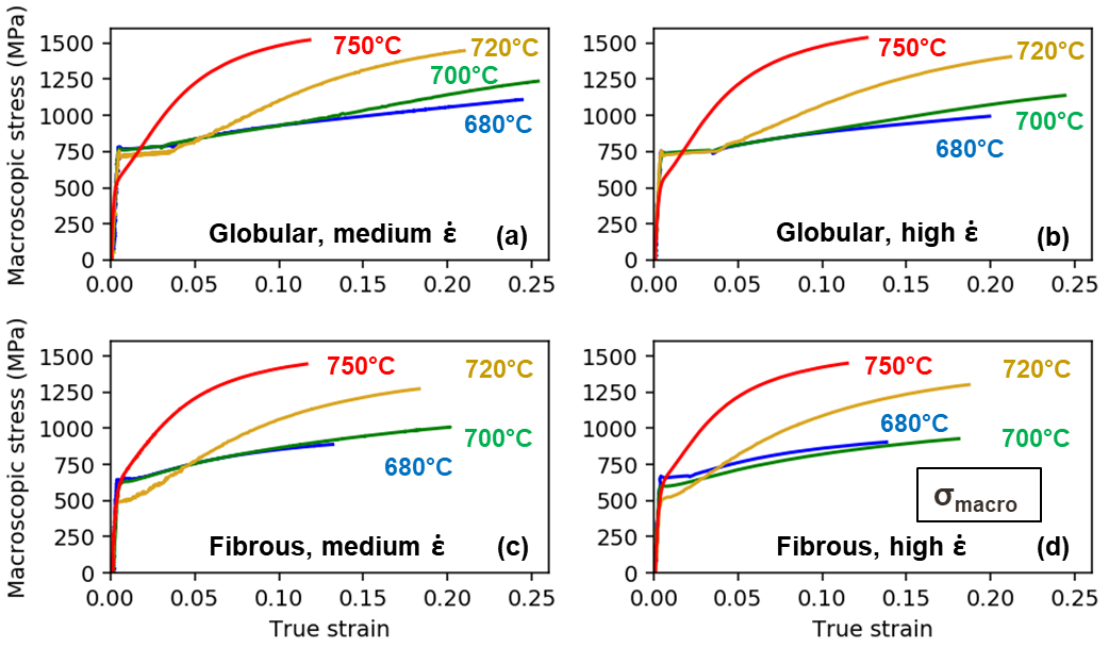

Figure 102: True tensile curves for (a) globular microstructures deformed at the medium $\dot{\varepsilon}$, (b) globular deformed at the high $\dot{\varepsilon}$, (c) fibrous deformed at the medium $\dot{\varepsilon}$ and (d) fibrous deformed at the high $\dot{\varepsilon}$ for the four in IA temperatures. The curves are represented up to necking.

Microstructure	UEL	YS/UYS	UTS	LP/PLC?	f_γ^0	$f_{\alpha'}^0$
GL680-001	23.0%	780 MPa*	840 MPa	LP	12%	7%
GL700-001	29.0 %	760 MPa*	945 MPa	LP/PLC	18%	10%
GL720-001	21.5%	720 MPa*	1095 MPa	LP/PLC	25%	15%
GL750-001	12.5%	435 MPa	1335 MPa	No	18%	32%
FB680-001	14.8%	635 MPa*	800 MPa	LP	5.5%	6%
FB700-001	20.7%	620 MPa*	850 MPa	LP	13%	9%
FB720-001	19.3%	485 MPa	1035 MPa	PLC	31%	11%
FB750-001	12.2%	490 MPa	1250 MPa	No	16%	39%

Table 16: Mean mechanical properties of the studied steels measured during the in-situ experiments at the medium strain rate. The mean uniform elongation and ultimate tensile strength are given for each microstructure. symbol '*' indicates the presence of a Lüders plateau and the upper yield strength is reported. For some steels, the occurrence of a Lüders plateau (LP) and/or Portevin-Le Chatelier (PLC) instabilities can be obviously detected on the tensile curves.

The ferrite flow stress is very similar between the steels annealed between 680°C and 720°C for a given set of tests. On the contrary, the austenite flow stress increases significantly with decreasing T_{IA}. The decrease of austenite flow stress between 680°C and 720°C can be explained by the chemical partitioning during intercritical annealing which makes the austenite more enriched in C and Mn for lower T_{IA}. Moreover, SEM observations show that the austenite grains form at lower T_{IA} have a smaller grain size, thus increasing its flow stress (see Table 13 and Table 14). On the contrary, ferrite chemistry between 680°C and 720°C does not evolve significantly between experiments for a given morphology of microstructure. While there is some variation on the determined ferrite grain size for fibrous steel (2 µm to 1 µm), it does not seem that this difference in size have a significant mechanical impact.

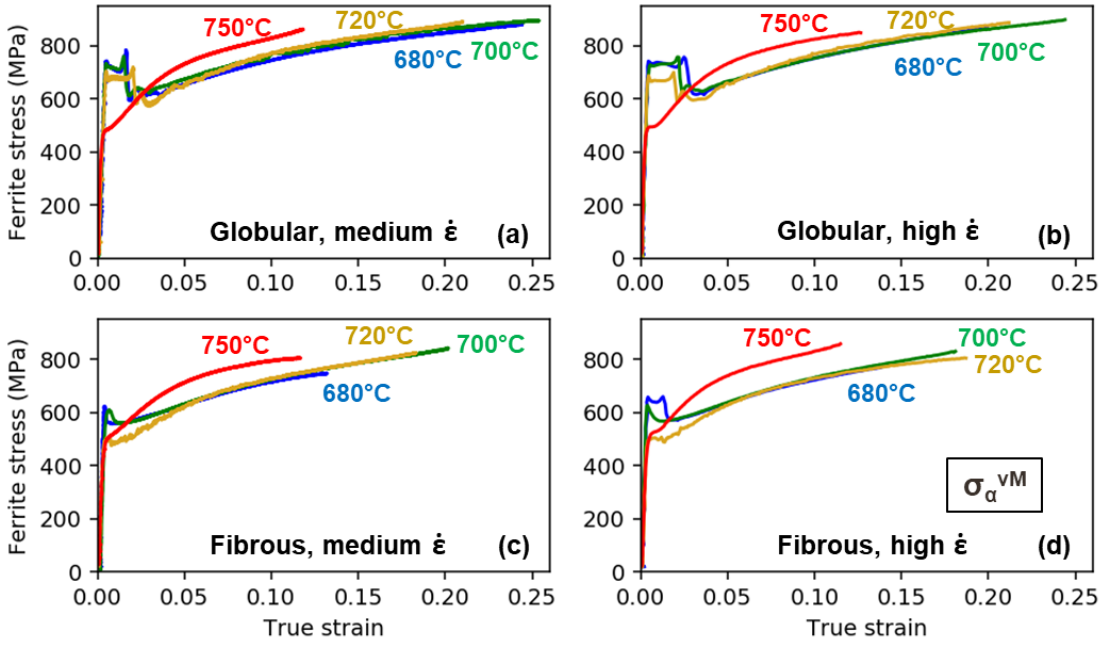

Figure 103: Ferrite von Mises stress as a function of macroscopic true strain for the 16 experiments at the two higher strain rates: (a) globular, medium ε̇; (b) globular, medium ε̇; (c) globular, medium ε̇; (d) fibrous, high ε̇.

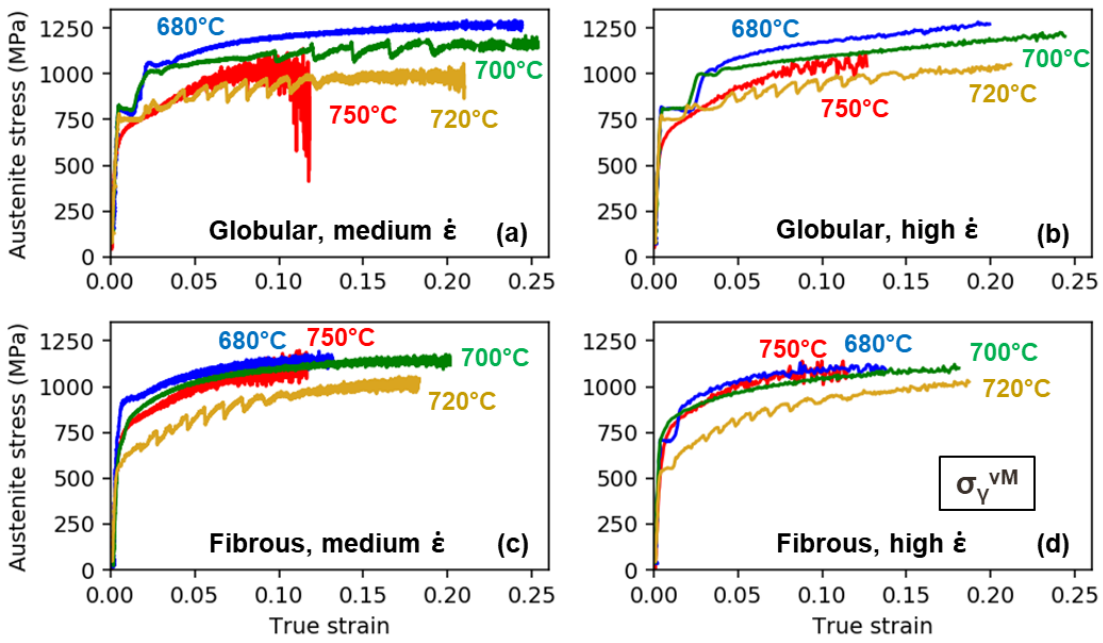

Figure 104: Austenite von Mises stress as a function of macroscopic true strain for the 16 experiments at the two higher strain rates: (a) globular, medium ε̇; (b) globular, medium ε̇; (c) globular, medium ε̇; (d) fibrous, high ε̇.

For T_{IA} = 750°C, both ferrite and austenite seem stronger than after annealing at T_{IA} = 720°C, which is hardly explained by chemical or size considerations, as both remain relatively constant. The high amount of initial fresh martensite ($f_{\alpha'}$>30%) may increase ferrite work-hardening, as it is the case for dual-phase (DP) steel [18]. A similar phenomenon can also be present in austenite, as more martensitic transformation may induce more work-hardening by GNDs (geometrically necessary dislocations).

As seen in Table 16, from T_{IA} = 680°C to T_{IA} = 720°C, the initial austenite phase fraction increases (5% to 31% for fibrous microstructures, 12% to 25% for globular microstructures), then diminishes when T_{IA} = 750°C (16% to 18% for both morphologies). This is observed for both globular and fibrous specimens. To compare the stability of austenite between experiments not having the same initial phase fraction, the phase fraction is normalized by dividing the actual fraction f_γ by the amount of austenite formed during intercritical annealing. As there is fresh martensite before deformation in the microstructures, the latter fraction is equal to the sum of the initial fraction of austenite and martensite $f_\gamma^0 + f_{\alpha'}^0$.

In Figure 105, the evolution of normalized austenite fraction is shown for all the studied experiments. The initial value is not 100%, as fresh martensite is initially present. In globular microstructures (Figure 105 (a) and (b)), the normalized austenite fraction is initially about 63% for GL680, GL700 and GL720 microstructures, and 38% for GL750 microstructure. This is indicative of a far lower stability of austenite formed during the IA in GL750 steel when compared to the others. Independently of the strain rate, the transformation rate increases with T_{IA}, and the normalized fraction of retained austenite at necking increases with decreasing T_{IA}, as expected from thermodynamical calculation. Indeed, at lower T_{IA}, austenite is more enriched in C and Mn, and thus austenite is more stable. Austenite grain size are also smaller at lower T_{IA}, increasing its stability in addition.

For fibrous microstructures (Figure 105 (c) and (d)), the results are more unexpected. The initial normalized phase fractions are 45% for FB680, 60% for FB700 and 75% for FB720 respectively. This means that the austenite formed during IA is more stable in FB720 steel than in FB700 and FB680 steel. This result can be explained by the difficulty to dissolve cementite precipitates at T_{IA}=680°C and T_{IA}=700°C, as demonstrated by in situ HEXRD experiments in Chapter II. SEM micrographs of salt-bath fibrous microstructures also revealed high amount of cementite precipitates. Concerning FB750 steel, the initial value of 30% is consistent with what is found for the GL750 microstructure. Like for globular microstructures, and independently of strain rate, the SIMT rate increases with T_{IA}, and the normalized fraction of retained austenite at necking increases with decreasing T_{IA}. Therefore, even in fibrous steels, the mechanical stability of retained austenite decreases with increasing IA temperature.

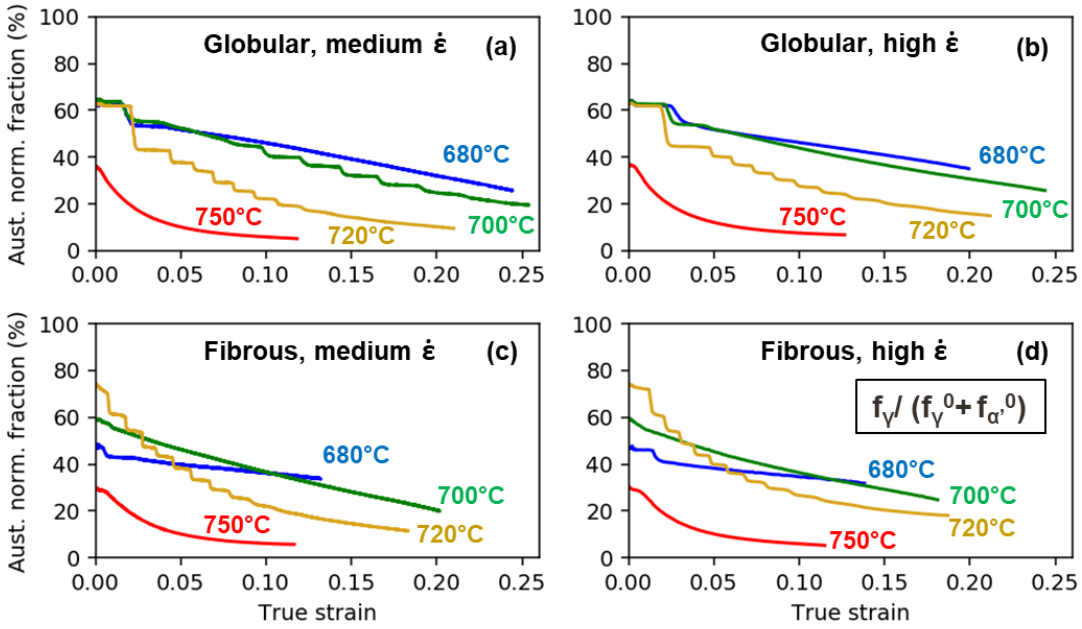

Figure 105: Austenite normalized phase fractions as a function of the macroscopic true strain for the 16 experiments at the two higher strain rates: (a) globular, medium ε̇; (b) globular, medium ε̇; (c) globular, medium ε̇; (d) fibrous, high ε̇.

Martensite von Mises stress can be calculated by inverse mixture law, since the initial martensite phase is known by correlating HEXRD and SEM data in both globular and fibrous specimens. The results for both morphologies at the two higher strain rates are shown in Figure 106. For globular experiments, the calculated stress in martensite at necking is always around 2400 MPa for all T_{IA} at medium strain rates and for GL720-015 and GL750-015 steels at the high strain rate. For GL700-015 and GL680-015 steels, the final stress in martensite is a bit lower at necking, i.e. 2000 MPa. Intercritical annealing temperature does not seem to have an effect on stress in globular martensite at the medium strain rate and the observed difference at higher strain rate is difficult to interpret.

The results for fibrous martensite are more dispersed. The martensite in FB680-001 and FB680-015 is very similar to the globular one, with a strength at necking around 2400 MPa. However, the level of stress in martensite is lower in FB720-001, FB720-015, FB750-001 and FB750-015 specimens, at around 2100 MPa, and even lower in FB700-001 and FB700-015 steels. Independently of the morphology, the apparent work-hardening of martensite is very high initially in 680°C annealed specimens, and is near to zero afterwards. In specimens annealed at 700°C or at 750°C, martensite

work-hardening is either concentrated in the first 10% of deformation or during the last 10%. It is only for GL720-001 and FB720-001 experiments that martensite really strain-hardened during the whole tensile test. This continuous increase in martensite flow stress amplifies the efficiency of TRIP effect in medium Mn steels annealed at 720°C. Indeed, during deformation of these steels, not only the fraction of hard martensite increases, but also their mean flow stress, improving the steels' UTS while maintaining a good UEL compared to other medium Mn duplex steels.

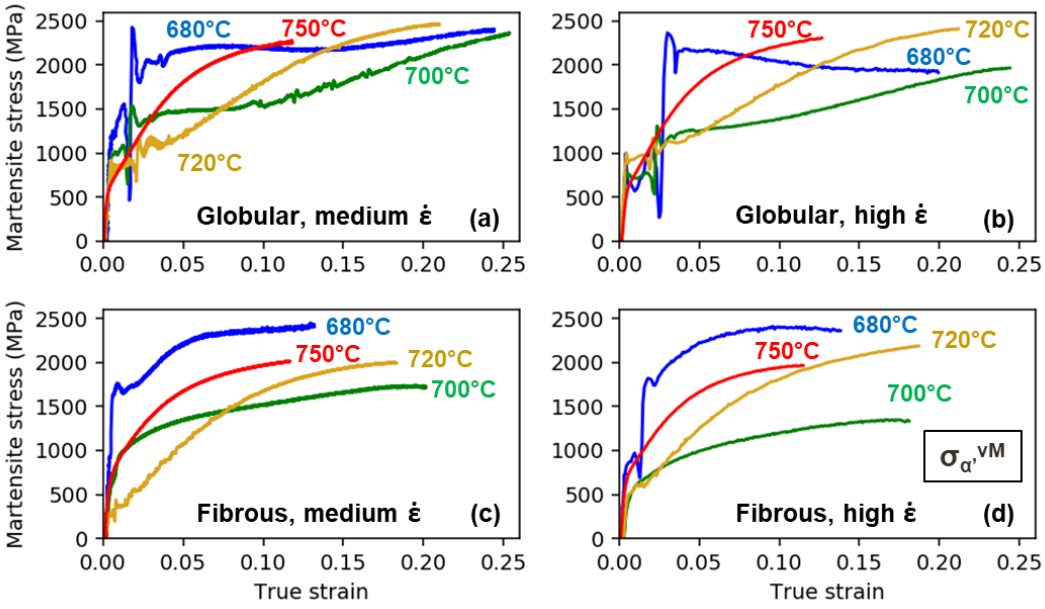

Figure 106: Martensite von Mises stress as a function of macroscopic true strain for the 16 experiments at the two higher strain rates: (a) globular, medium ε̇; (b) globular, medium ε̇; (c) globular, medium ε̇; (d) fibrous, high ε̇.

As emphasized in previous sections, absolute value of hydrostatic stresses must be analysed with caution. However, their variation is undoubtedly quantitative. To better use the $\sin^2\psi$ results and compare the drop in stress at plasticity onset, the hydrostatic stresses have been normalized by setting their value before yielding at 0 MPa. At the onset of yielding, there is a significant drop in hydrostatic stress, and then a more or less linear increase until necking, as seen in Figure 107 for all experiments. The stress drop at the end of elasticity can be linked with multiple phenomena. First, it can be linked to an accommodation by plasticity of hydrostatic stresses inherited from thermal treatments. Secondly, due to SIMT, new martensitic laths can create additional compressive hydrostatic stress in austenite, as they do during athermal martensitic transformation at cooling step in Chapter II, section II.4.B. The two effects are impossible to separate in the current study.

When comparing the four sets of experiments presented in Figure 107, it seems that the higher the annealing temperature, the lower is the drop of austenite hydrostatic stress. For example, in globular microstructures strained at the high strain rate, the normalized hydrostatic stresses drop ranges from -400 MPa to -650 MPa, with intermediate values for intermediate T_{IA}. This effect is less visible but still present for specimens with globular microstructures strained at the medium strain rate, and more visible for specimens with fibrous microstructures. This could be linked with the higher amount of initial martensite in the microstructure, which put already the austenite in hydrostatic compressive stress. It is then more difficult with applied stress and new martensite to create higher level of hydrostatic compressive stress for austenite.

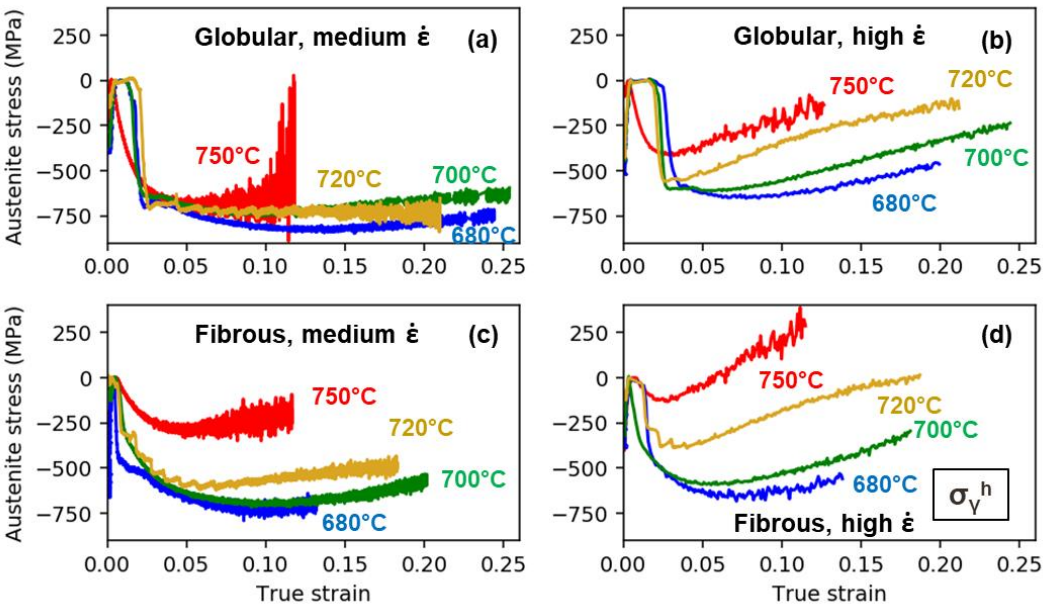

Figure 107: Austenite normalized hydrostatic stress as a function of macroscopic true strain for the 16 experiments at the two higher strain rates: (a) globular, medium ε̇; (b) globular, medium ε̇; (c) globular, medium ε̇; (d) fibrous, high ε̇.

B. Microstructure before annealing

The true tensile curves between specimens with fibrous (blue) and globular (red) microstructures are compared in Figure 108 for all strain rates and annealing temperatures. It is clear that fibrous samples have lower tensile mechanical performance, both in term of ultimate tensile strength and uniform elongation, in all steels annealed below 720°C, independently of $\dot{\varepsilon}$. For T_{IA} = 750°C, the mechanical performance between the two morphologies are closer, but globular steel still performs slightly better.

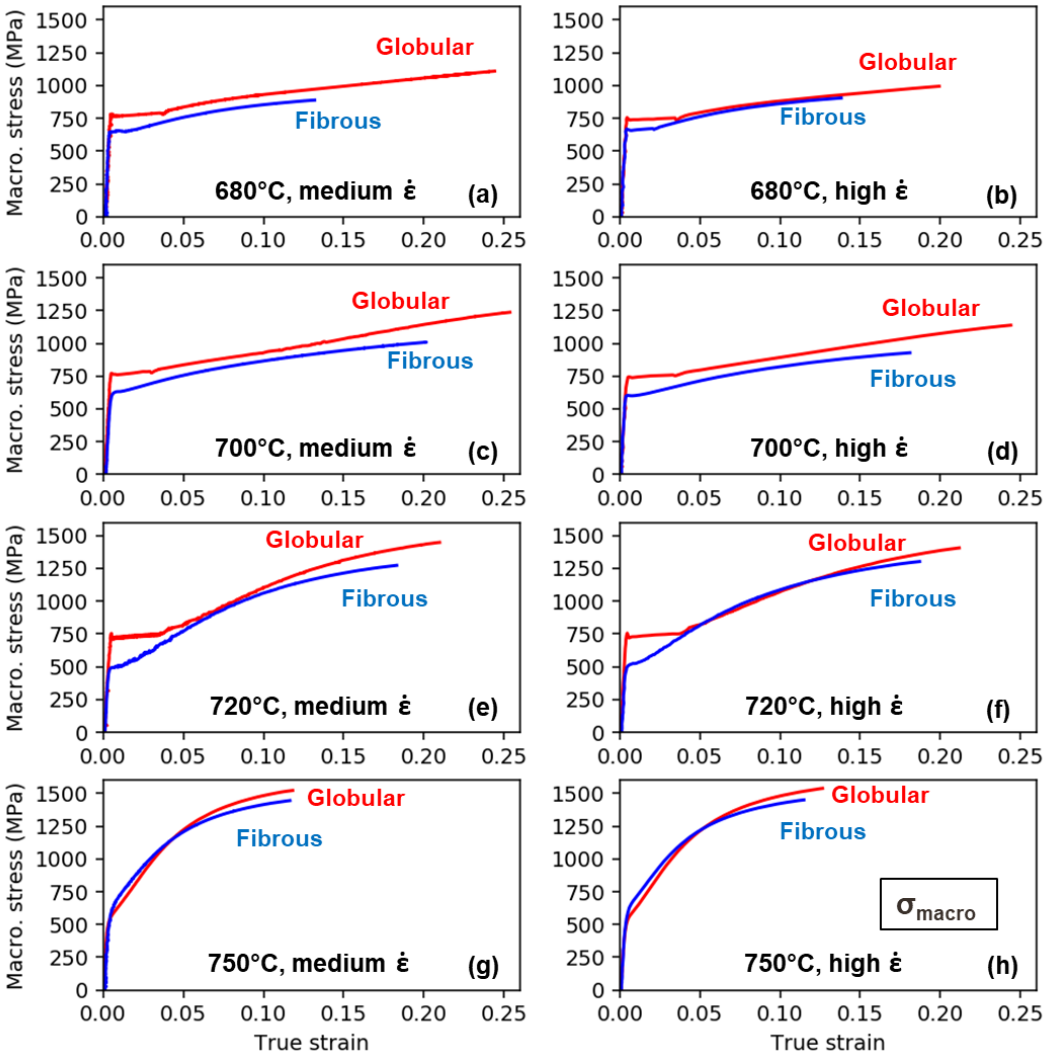

Figure 108: Macroscopic true stress as a function of the macroscopic true strain for the 16 experiments at the two higher strain rates: (a) T_{IA} = 680°C, medium $\dot{\varepsilon}$; (b) T_{IA} = 680°C, high $\dot{\varepsilon}$; (c) T_{IA} = 700°C, medium $\dot{\varepsilon}$; (d) T_{IA} = 700°C, high $\dot{\varepsilon}$; (e) T_{IA} = 720°C, medium $\dot{\varepsilon}$; (f) T_{IA} = 720°C, high $\dot{\varepsilon}$; (g) T_{IA} = 750°C, medium $\dot{\varepsilon}$; (h) T_{IA} = 750°C, high $\dot{\varepsilon}$.

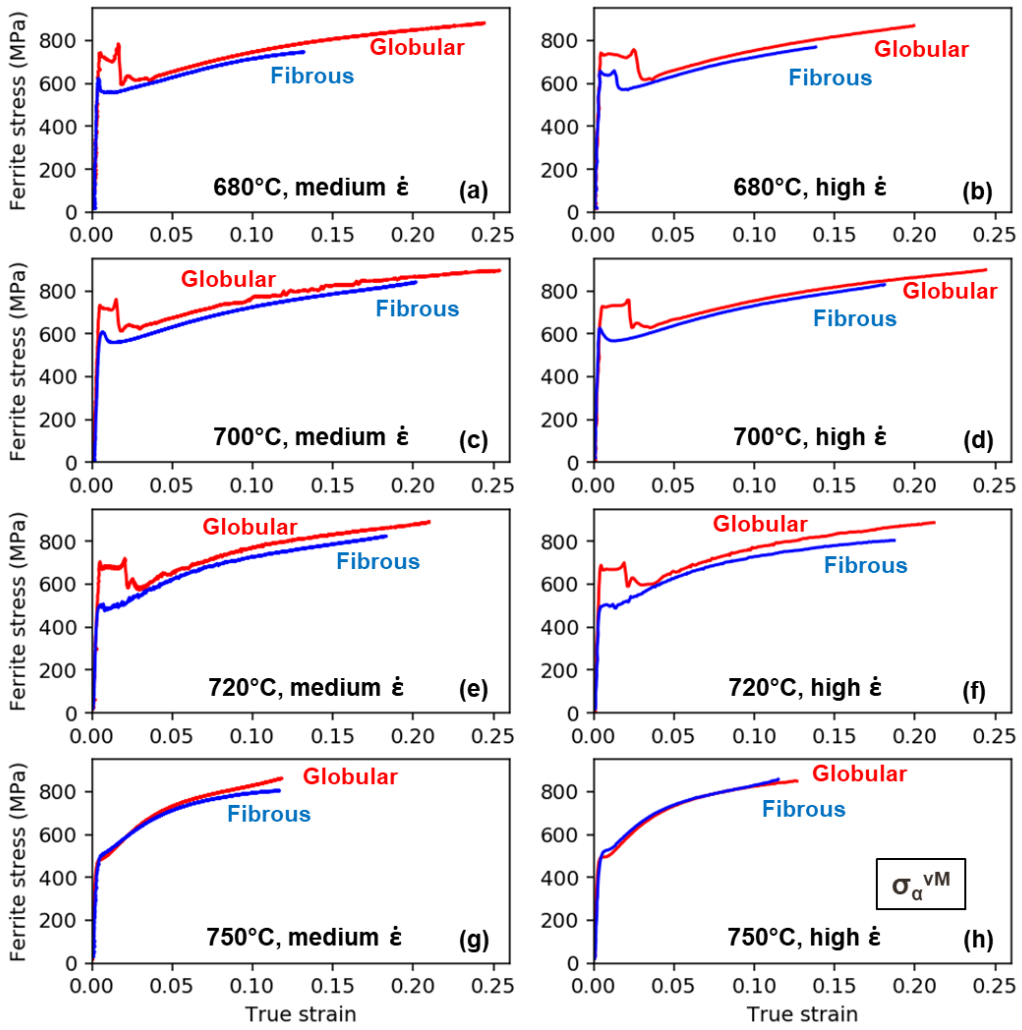

Figure 109: Ferrite von Mises stress as a function of the macroscopic true strain for the 16 experiments at the two higher strain rates: (a) T_{IA} = 680°C, medium $\dot{\varepsilon}$; (b) T_{IA} = 680°C, high $\dot{\varepsilon}$; (c) T_{IA} = 700°C, medium $\dot{\varepsilon}$; (d) T_{IA} = 700°C, high $\dot{\varepsilon}$; (e) T_{IA} = 720°C, medium $\dot{\varepsilon}$; (f) T_{IA} = 720°C, high $\dot{\varepsilon}$; (g) T_{IA} = 750°C, medium $\dot{\varepsilon}$; (h) T_{IA} = 750°C, high $\dot{\varepsilon}$.

HEXRD data gives precious insight into the reason of this outperformance of globular specimens. The flow stresses inside ferrite are compared in Figure 109 between the two morphologies of microstructures for all steels. The von Mises stress is always lower in ferrite in the fibrous microstructures than in the globular ones, except at 750°C where they are more comparable. This observation can be linked to the larger sizes of fibrous ferrite grains compared with the globular ones, except at T_{IA} = 750°C where the grain size was found to be similar (highlighted in Chapter II and in Table 13).

The comparison of flow stress between austenite with different morphologies is less clear (Figure 110). For T_i = 680°C, austenite is stronger in specimens with globular microstructures. For intermediate T_i (700°C and 720°C), the level of flow stress in both austenites is comparable. Finally, for T_i = 750°C, the fibrous austenite is stronger. The trends are similar for higher strain rate. As austenite phase fraction becomes negligible at necking (below 5%), the better mechanical performances of globular microstructures are not to be explained by austenite mechanical behaviour, except maybe at 680°C.

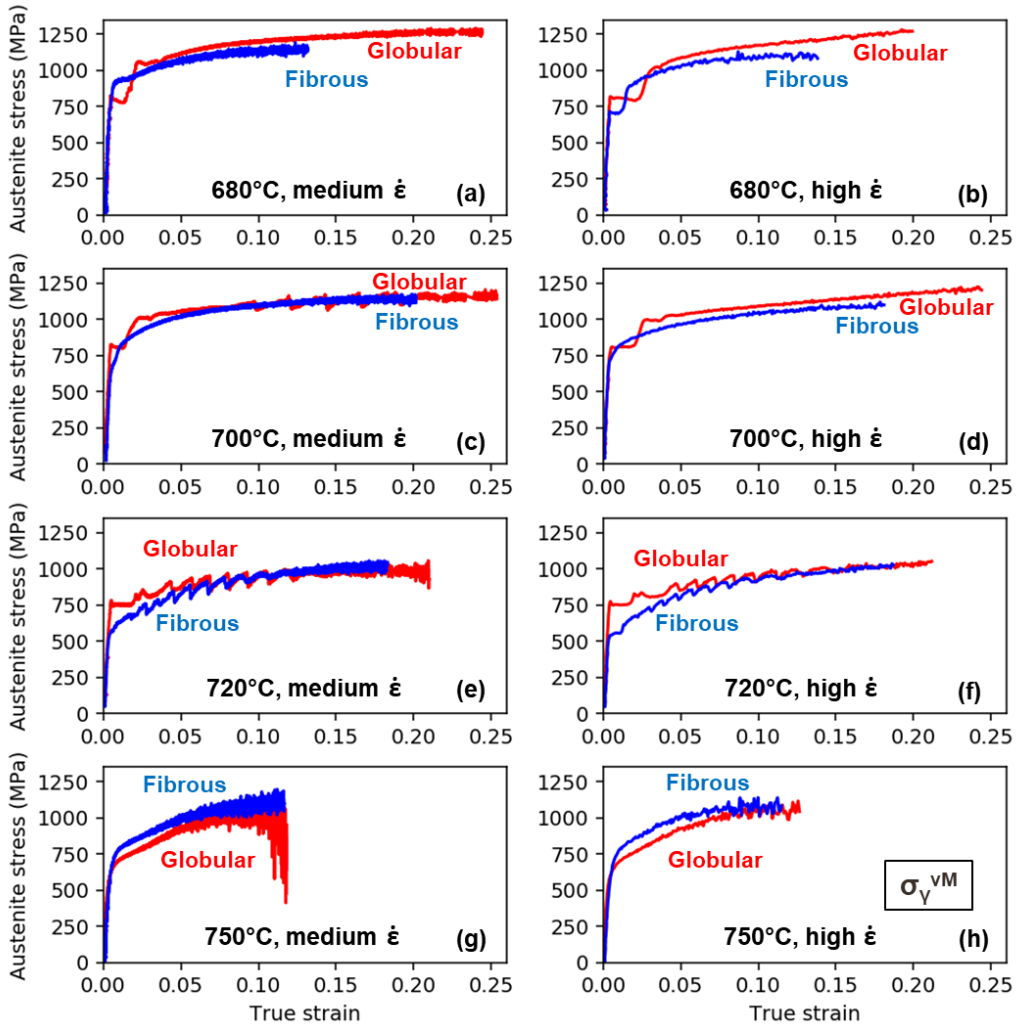

Figure 110: Austenite von Mises stress as a function of macroscopic true strain for the 16 experiments at the two higher strain rates: (a) T_{IA} = 680°C, medium $\dot{\varepsilon}$; (b) T_{IA} = 680°C, high $\dot{\varepsilon}$; (c) T_{IA} = 700°C, medium $\dot{\varepsilon}$; (d) T_{IA} = 700°C, high $\dot{\varepsilon}$; (e) T_{IA} = 720°C, medium $\dot{\varepsilon}$; (f) T_{IA} = 720°C, high $\dot{\varepsilon}$; (g) T_{IA} = 750°C, medium $\dot{\varepsilon}$; (h) T_{IA} = 750°C, high $\dot{\varepsilon}$.

The transformation kinetics are compared in Figure 111 between the two morphologies for all steels. The initial phase fraction of austenite is very low for FB680 (only 6%) compared to 12% for GL680. This gap is still important between GL700 (18%) and FB700 (13%). For higher T_{IA}, the value between specimens with fibrous and globular microstructures are more similar (respectively 25%, 31%, 18% and 16% for GL720, FB720, GL750 and FB750). When looking at transformation kinetics slopes, there is no clear difference between specimens with fibrous and globular microstructures (see Figure 111), except for 680°C due to the very low initial fraction of austenite in fibrous microstructure. Thus, this higher value of initial retained austenite fraction for lower T_{IA} may participate to the better mechanical properties of specimens with globular microstructures, since austenite is stronger than ferrite.

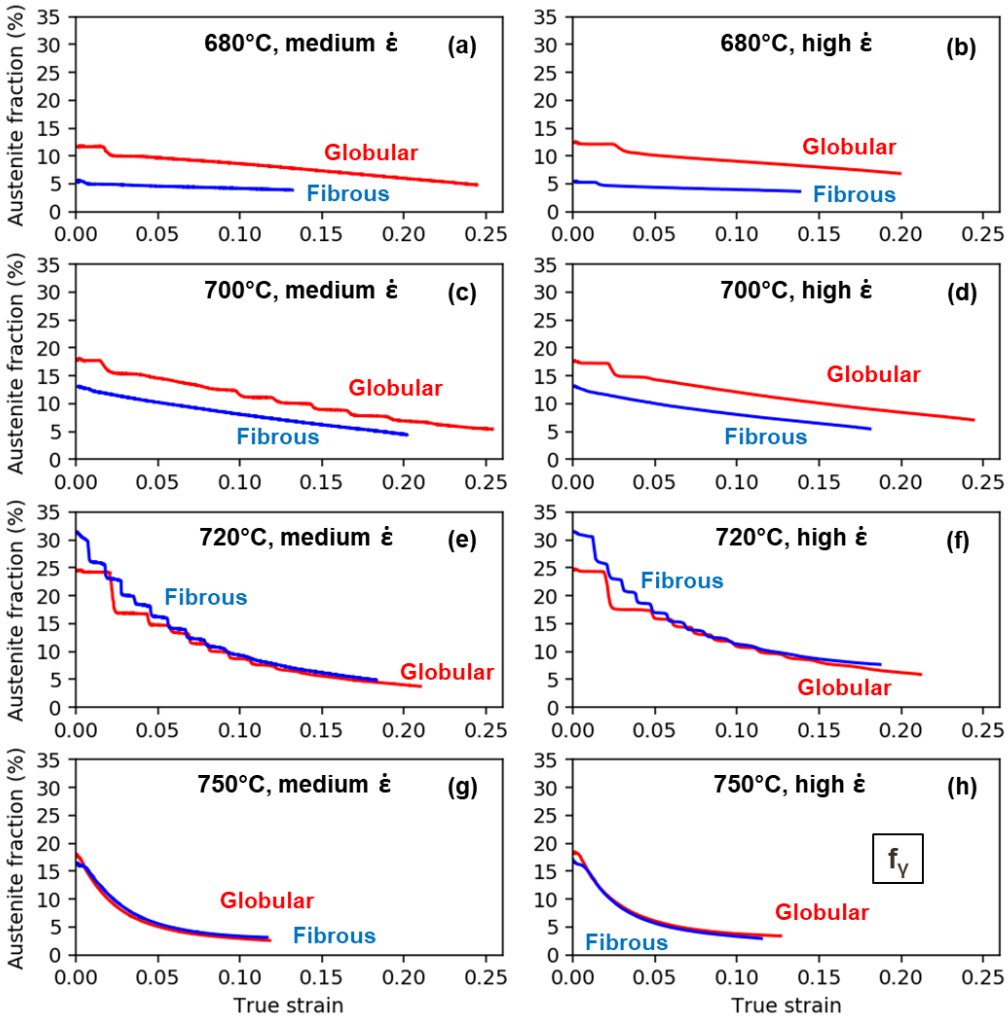

Figure 111: Retained austenite fraction as a function of macroscopic true strain for the 16 experiments at the two higher strain rates: (a) T_{IA} = 680°C, medium $\dot{\varepsilon}$; (b) T_{IA} = 680°C, high $\dot{\varepsilon}$; (c) T_{IA} = 700°C, medium $\dot{\varepsilon}$; (d) T_{IA} = 700°C, high $\dot{\varepsilon}$; (e) T_{IA} = 720°C, medium $\dot{\varepsilon}$; (f) T_{IA} = 720°C, high $\dot{\varepsilon}$; (g) T_{IA} = 750°C, medium $\dot{\varepsilon}$; (h) T_{IA} = 750°C, high $\dot{\varepsilon}$.

The flow stresses of martensite calculated by Hill's mixture rules are shown in Figure 112 between the two morphologies of microstructure for all steels. At T_{IA} = 680°C, the level of stress in martensite is slightly lower in the globular steel than in the fibrous one for both strain rate $\dot{\varepsilon}$. However, between specimens intercritically annealed at 700°C, 720°C and 750°C, the strength of martensite at necking is systematically higher in globular samples, independently of strain rate. Complementary comparisons is made in Figure 112 using $\sin^2\psi$ determined von Mises stress for T_{IA}=720°C and T_{IA}=750°C. The flow stress of martensite is higher during the early strain (ε_{macro}<5%) in fibrous specimens. Afterwards (ε_{macro}>5%), the flow stress is higher in globular martensite for both T_{IA} and independently of the strain rate. The $\sin^2\psi$ method thus confirms the obtained results with the mixture rule. The difference of martensite strength at necking ranges from 300 MPa to 600 MPa at necking for T_{IA}>700°C in favour of globular specimens, which is not negligible. Overall, the martensite in globular microstructures produced at a high enough temperature (700°C in this case) seems stronger than that found in corresponding fibrous microstructure, and participates to the better performance of globular microstructures in these cases.

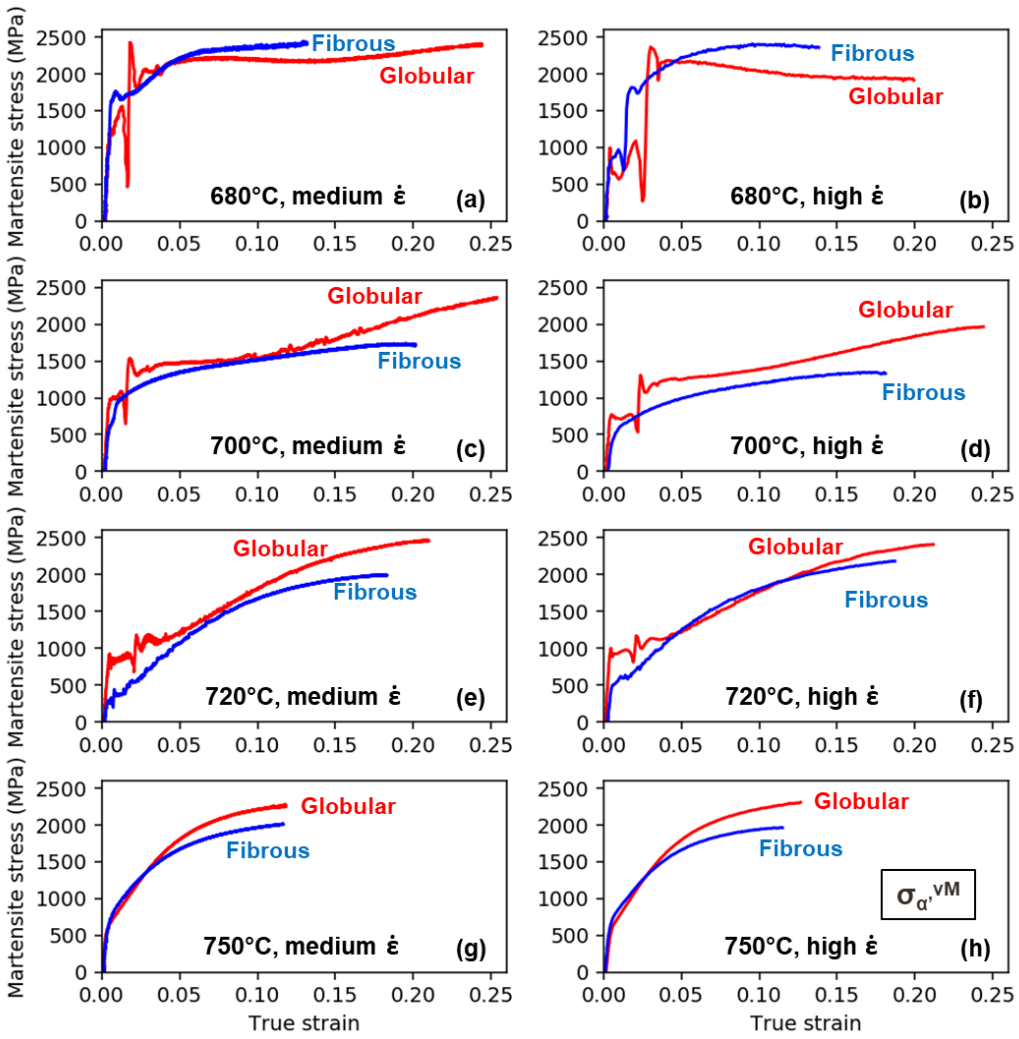

Figure 112: Martensite von Mises stress as a function of macroscopic true strain for the 16 experiments at the two higher strain rates: (a) T_{IA} = 680°C, medium ε̇; (b) T_{IA} = 680°C, high ε̇; (c) T_{IA} = 700°C, medium ε̇; (d) T_{IA} = 700°C, high ε̇; (e) T_{IA} = 720°C, medium ε̇; (f) T_{IA} = 720°C, high ε̇; (g) T_{IA} = 750°C, medium ε̇; (h) T_{IA} = 750°C, high ε̇. The von Mises stresses are calculated with Hill's mixture rules.

Finally, when comparing normalized hydrostatic stress in austenite both microstructure morphologies, the relaxation of hydrostatic stress is slightly higher in globular than in fibrous specimens. The higher the T_{IA} is, the wider the gap is, ranging from 100 MPa to 450 MPa. The same is true for the higher strain rate. In the case of FB750 and GL750 steels, in situ study during thermal treatment by HEXRD (in Chapter II) revealed a higher level of hydrostatic stress in the fibrous microstructure (-2606 MPa) than in the globular microstructure (-1935 MPa). As such, it is more difficult to put fibrous austenite in more compressive state that it is already.

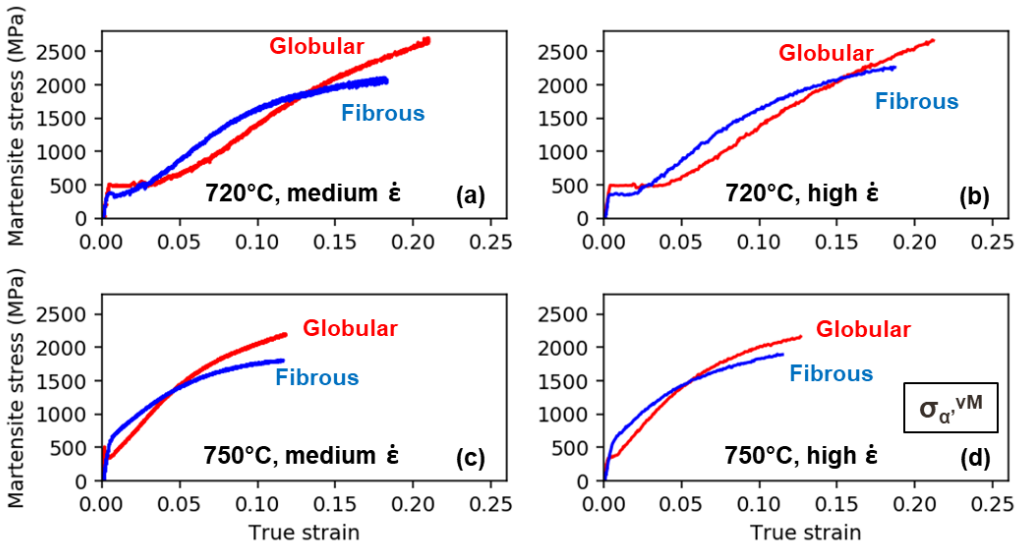

Figure 113: Martensite von Mises stress as a function of macroscopic true strain for 8 experiments: (a) T_{IA} = 720°C, medium $\dot{\varepsilon}$; (b) T_{IA} = 720°C, high $\dot{\varepsilon}$; (c) T_{IA} = 750°C, medium $\dot{\varepsilon}$; (d) T_{IA} = 750°C, high $\dot{\varepsilon}$. The martensite von Mises stresses are determined using $\sin^2\psi$ method.

Another explanation is maybe to be found in terms of orientation between ferrite and austenite grains. In fibrous microstructure, because of the ART mechanism [7], crystallographic orientation relationship exists between austenite and ferrite (which is in reality annealed/recovered martensite). In globular microstructure, no crystallographic orientation relationship is expected (classical nucleation/growth mechanism [57]). Therefore, it is possible that relaxation mechanism differs between microstructures with different morphologies.

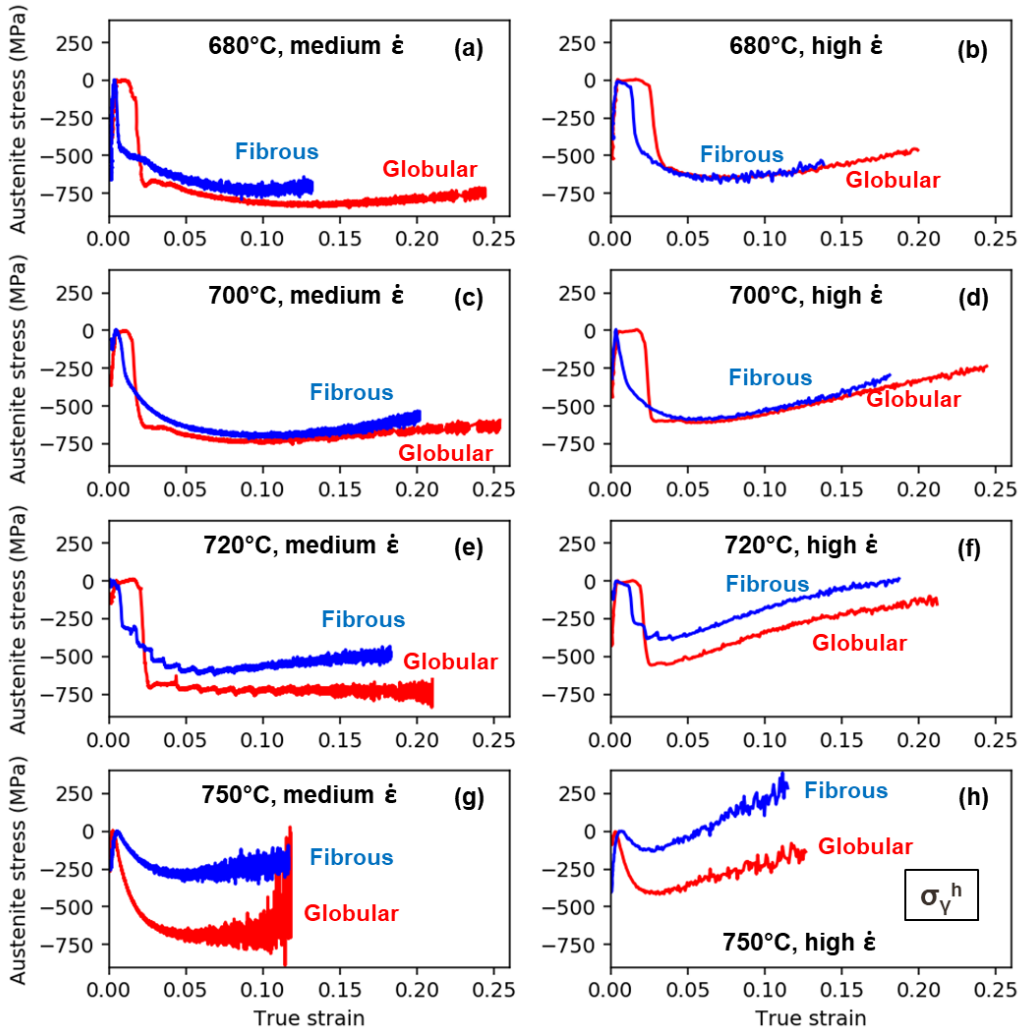

Figure 114: Austenite normalized hydrostatic stress as a function of macroscopic true strain for the 16 experiments at the two higher strain rates: (a) T_{IA} = 680°C, medium $\dot{\varepsilon}$; (b) T_{IA} = 680°C, high $\dot{\varepsilon}$; (c) T_{IA} = 700°C, medium $\dot{\varepsilon}$; (d) T_{IA} = 700°C, high $\dot{\varepsilon}$; (e) T_{IA} = 720°C, medium $\dot{\varepsilon}$; (f) T_{IA} = 720°C, high $\dot{\varepsilon}$; (g) T_{IA} = 750°C, medium $\dot{\varepsilon}$; (h) T_{IA} = 750°C, high $\dot{\varepsilon}$.

C. Strain rate

In this work, one order of magnitude of strain rate change is studied for all microstructures, and two orders of magnitude of strain rate change is studied for the GL720 microstructure. Comparing true tensile curve of the eight studied steels deformed at various strain rates (Figure 115), it seems that GL680, GL700, GL720 and FB700 steels show a negative strain rate sensitivity. For GL720, the difference appears at high strain level (ε_{macro}=13%) between GL720-015 and GL720-001 (Δ^{GL720}UTS = 60 MPa). The stress curve of GL720-001 and GL720-0001 have identical work-hardening. For FB700 samples, the difference in flow stress appears directly at yielding onset (Δ^{FB700}UTS = 70 MPa). HEXRD data can help to explain those negative strain rate sensitivities.

On the contrary, most of fibrous microstructures (FB680, FB720 and FB750), and GL750 steel show no dependence on strain rate in the studied range of $\dot{\varepsilon}$. This is not surprising for FB680, FB750 and GL750 steels, as fresh/strain-induced martensite and ferrite are the main compounds of this grade, and have negligible sensitivity to strain rate in the studied range. For FB720, the absence of apparent strain rate sensitivity is more surprising and maybe due to inhomogeneity of composition or microstructure between specimens strained at the medium and high $\dot{\varepsilon}$.

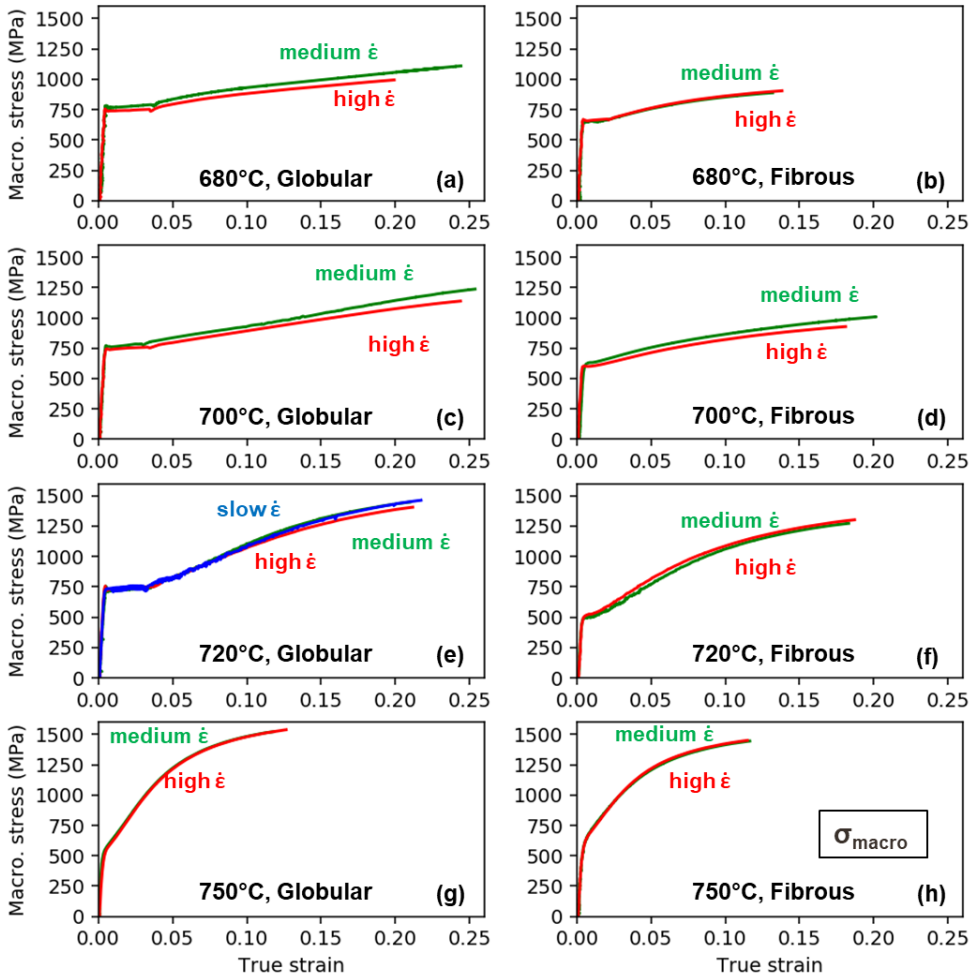

Figure 115: Macroscopic true stress as a function of macroscopic true strain for the 17 experiments at different strain rates: (a) T_{IA} = 680°C, globular; (b) T_{IA} = 680°C, fibrous; (c) T_{IA} = 700°C, globular; (d) T_{IA} = 700°C, fibrous; (e) T_{IA} = 720°C, globular; (f) T_{IA} = 720°C, fibrous; (g) T_{IA} = 750°C, globular; (h) T_{IA} = 750°C, fibrous.

The flow stresses inside ferrite are compared in Figure 116 between all strain rates for all experiments. The strain rate seems to have only a negligible effect on ferrite stress flow in the tested range, as red, green and blue curves are superimposed in Figure 116 for each set of experiments. Thus, ferrite does not participate to macroscopic strain sensitivity in the given studied range of $\dot{\varepsilon}$.

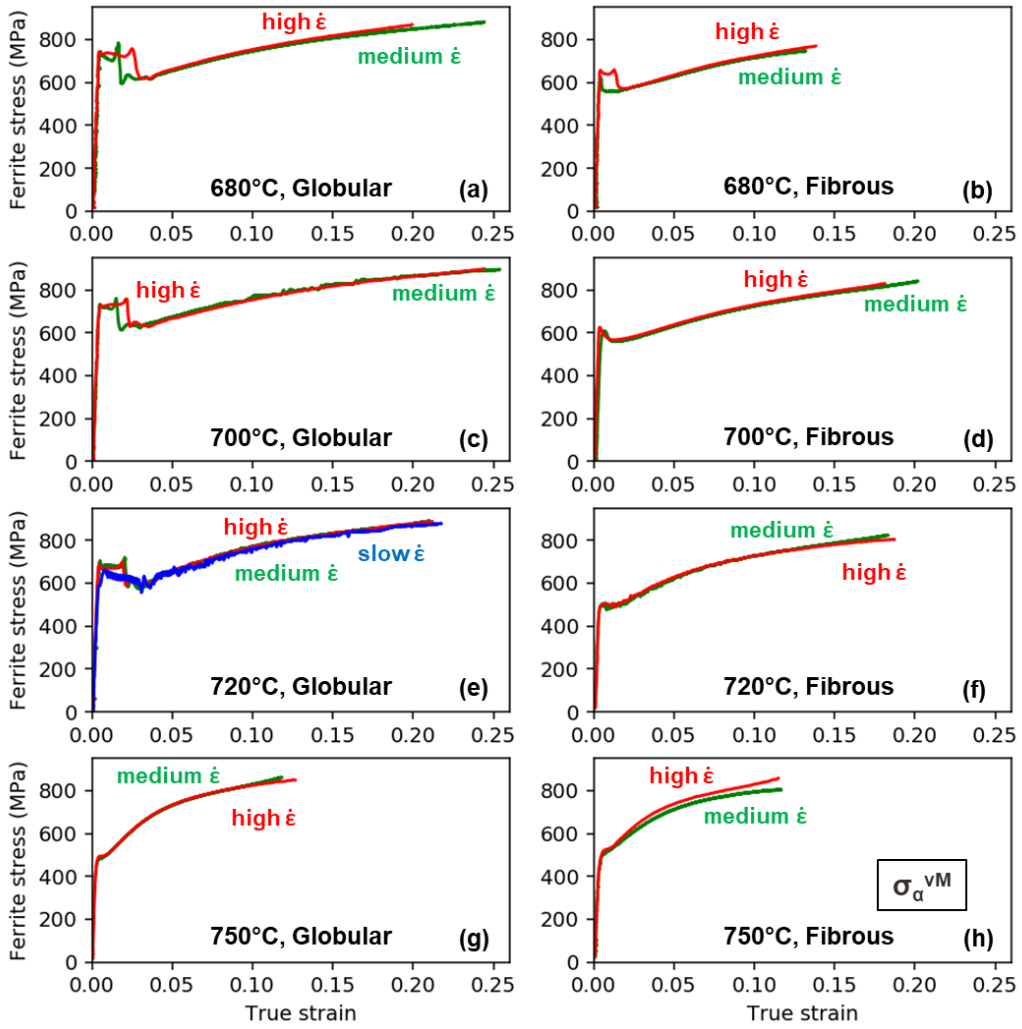

Figure 116: Ferrite von Mises stress as a function of macroscopic true strain for the 17 experiments at different strain rates: (a) T_{IA} = 680°C, globular; (b) T_{IA} = 680°C, fibrous; (c) T_{IA} = 700°C, globular; (d) T_{IA} = 700°C, fibrous; (e) T_{IA} = 720°C, globular; (f) T_{IA} = 720°C, fibrous; (g) T_{IA} = 750°C, globular; (h) T_{IA} = 750°C, fibrous.

The flow stresses of austenite are compared in Figure 117 between all strain rates for all experiments. Contrary to ferrite, austenite which shows a slight negative strain rate sensitivity in FB680, FB700 and GL720 steels. This strength gap of austenite at necking is 150 MPa between GL720-015 and GL720-0001 and 60 MPa between FB700-015 and FB700-001. This negative strain rate sensitivity participates to the global negative strain rate sensitivities of medium Mn steels, but cannot explain it, since less than 5% of austenite usually remains at necking (60MPa × 5% = 3 MPa). One the contrary, for other steels, no strain rate sensitivity is observed for austenite in the studied strain rate range.

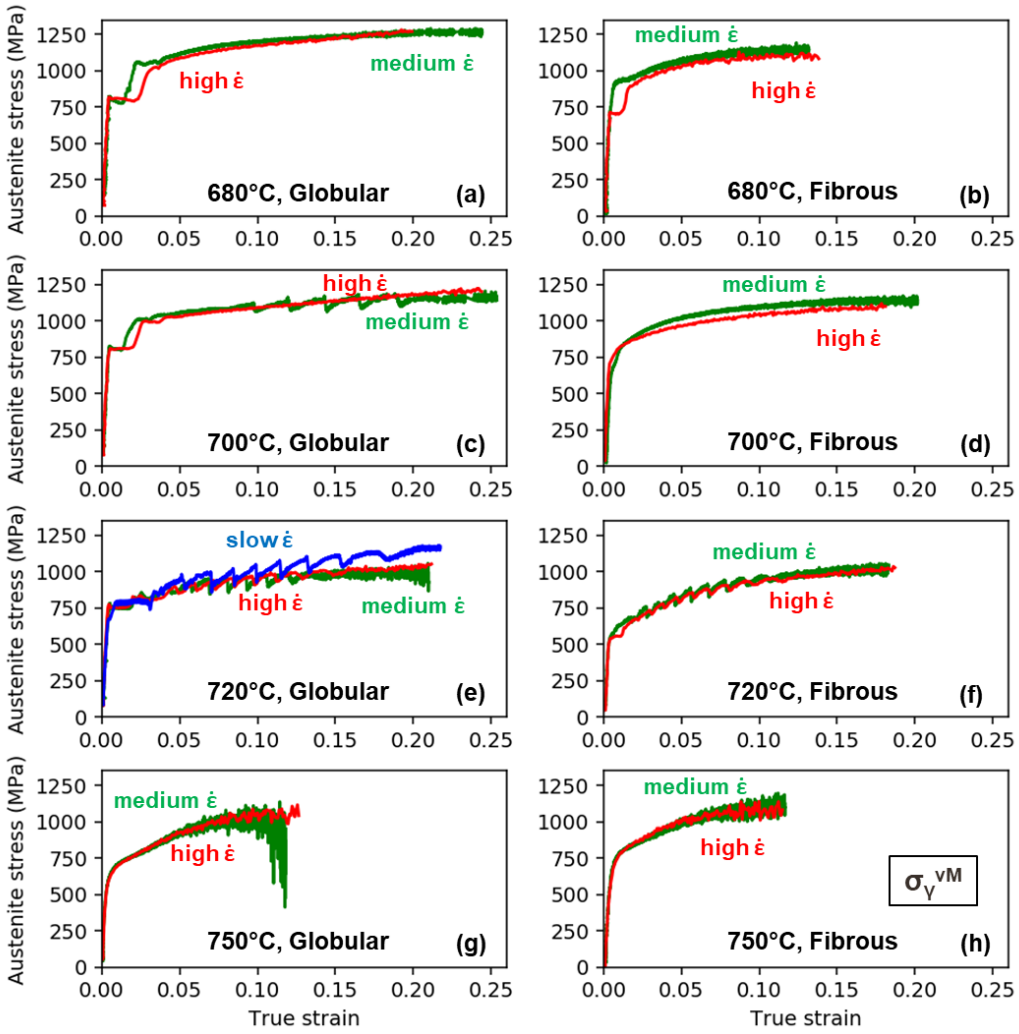

Figure 117: Austenite von Mises stress as a function of the macroscopic true strain for the 17 experiments: (a) T_{IA} = 680°C, globular; (b) T_{IA} = 680°C, fibrous; (c) T_{IA} = 700°C, globular; (d) T_{IA} = 700°C, fibrous; (e) T_{IA} = 720°C, globular; (f) T_{IA} = 720°C, fibrous; (g) T_{IA} = 750°C, globular; (h) T_{IA} = 750°C, fibrous.

The main explanation for medium Mn negative strain rate sensitivity seems to be the slower martensitic transformation kinetics for higher strain rate. In Figure 118, the transformation kinetics are compared between all strain rates for all experiments. The SIMT rates are clearly higher in microstructure strained at lower strain rate for GL680, GL700, GL720, GL750, FB700 and FB720 steels. For both FB700 and FB720, higher fractions of transformed retained austenite are reached at necking onset (final values of the curves) for lower strain rate. The same is true for GL680, GL700, GL720 and GL750 experiments. This phenomenon is known in the literature and is explained by the adiabatic heating [106], [147]. At higher strain rate, heat due to plastic work will dissipate less efficiently, austenite will thus be stabilized by a higher temperature. As such, it will transform less efficiently in martensite.

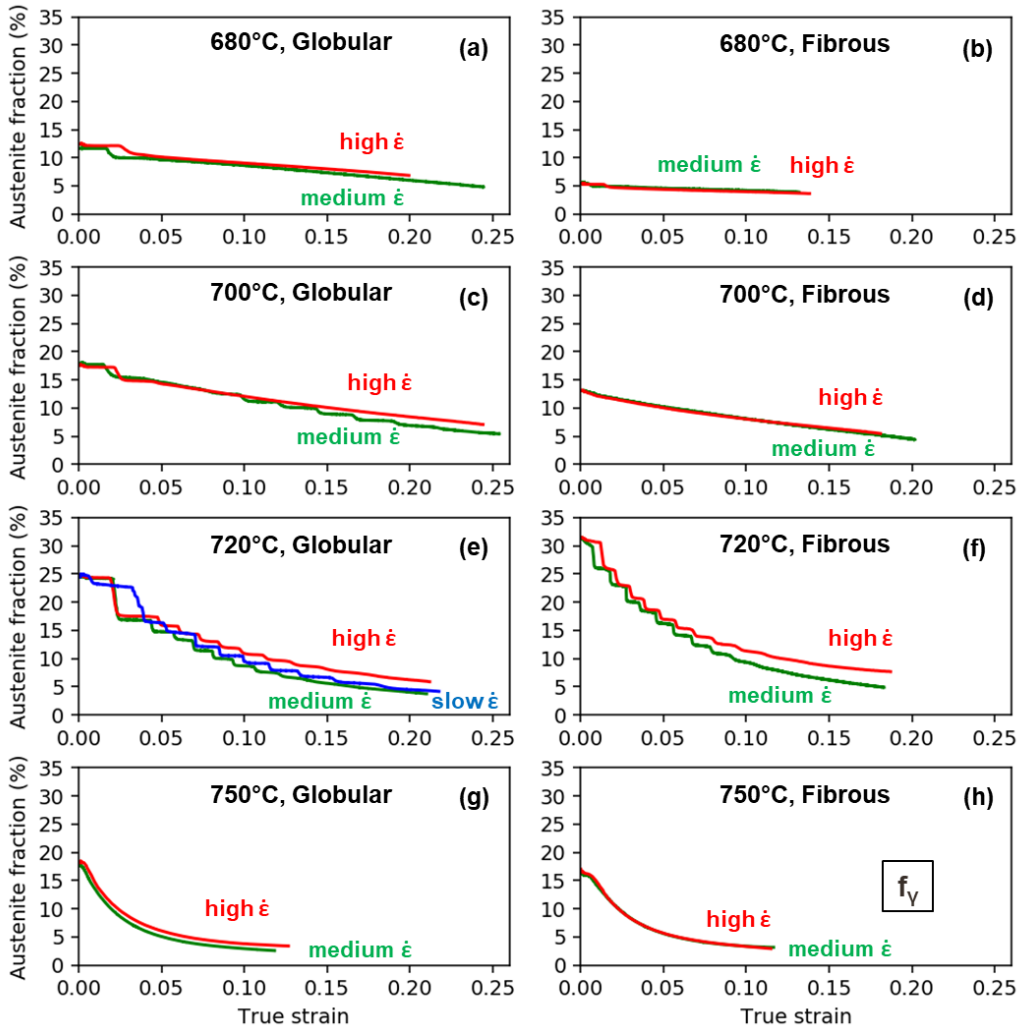

Figure 118: Retained austenite fraction as a function of macroscopic true strain for the 17 experiments: (a) T_{IA} = 680°C, globular; (b) T_{IA} = 680°C, fibrous; (c) T_{IA} = 700°C, globular; (d) T_{IA} = 700°C, fibrous; (e) T_{IA} = 720°C, globular; (f) T_{IA} = 720°C, fibrous; (g) T_{IA} = 750°C, globular; (h) T_{IA} = 750°C, fibrous.

The flow stresses inside martensite calculated by Hill's mixture rules have been compared in Figure 119 between all strain rates for all experiments. The results obtained by $\sin^2\psi$ method are shown in Figure 120 for GL720, FB720, GL750 and FB750 steels. No clear trend appears. For GL720, FB700, FB750, but also GL680 and GL750, the stresses in martensite are clearly not affected by strain rate. This is confirmed with the two determination methods when possible. This mechanical behaviour is similar to as-quenched martensite, which usually show no dependence to strain rate in this range of $\dot{\varepsilon}$.

However, for FB720, martensite apparently shows a positive strain rate sensitivity. As the gap is constant, this might just be an error of uncertainty due to $\sin^2\psi$ measurements on ferrite and austenite, which propagate to martensite stress through the Hill's law, as detailed in section III.3.E.b). The flow stresses calculated directly on martensite with $\sin^2\psi$ method show no dependence on strain rate for FB720 microstructure, until ε_{tot} = 15%. After, a small gap appears and increase linearly, reaching a gap in stress of 200 MPa in favour of FB720-015 experiments. Therefore, it is unclear if there is a positive sensitivity to strain rate for FB720 microstructure, but it is reasonable to consider that this dependence does not exist for the studied range of strain rate. Finally, for both FB700 and GL700

specimens (Figure 119 (e) and (f)), martensite shows a clear negative strain rate sensitivity, like austenite.

The gap in strength at necking is about 300 MPa for both morphologies. This is difficult to interpret, and may be due to complex interactions between stress in strain-induced martensite and SIMT kinetics.

As the transformation kinetics are faster at lower strain-rate, for GL700 steel it could be expected that martensite with high level of carbon and thus higher strength appears sooner in slowly deformed medium Mn steels. Therefore, it is not so surprising to see a negative strain-rate sensitivity. What is surprising is that this negative dependence $\dot{\varepsilon}$ is not systematically observed for other specimens. Nevertheless, as medium Mn microstructures are very sensitive to annealing temperature during processing thermal treatment, it is possible that heterogeneity exist between specimens that should nominally have the same microstructure, thus making interpretation of data difficult in some case.

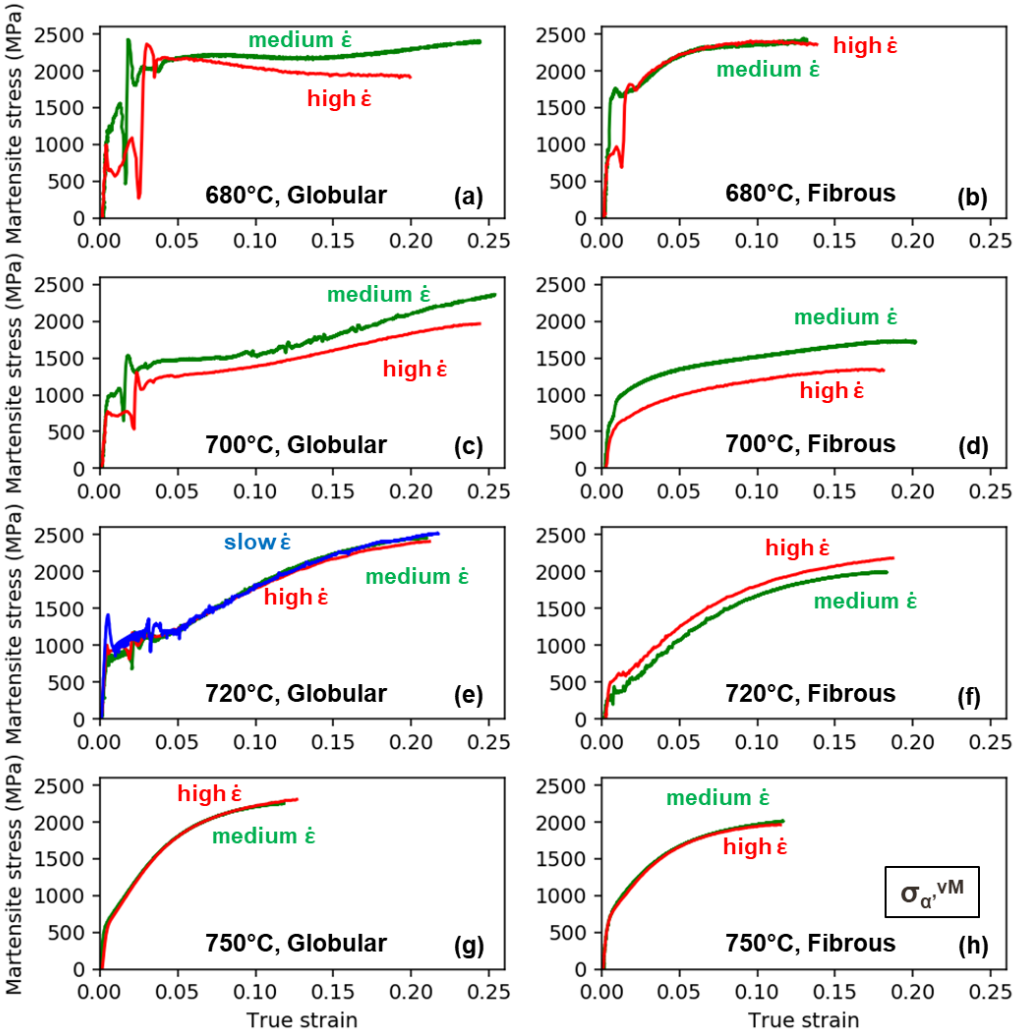

Figure 119: Martensite von Mises stress as a function of macroscopic true strain for the 17 experiments: (a) T_{IA} = 680°C, globular; (b) T_{IA} = 680°C, fibrous; (c) T_{IA} = 700°C, globular; (d) T_{IA} = 700°C, fibrous; (e) T_{IA} = 720°C, globular; (f) T_{IA} = 720°C, fibrous; (g) T_{IA} = 750°C, globular; (h) T_{IA} = 750°C, fibrous. The martensite von Mises stresses are calculated using inverse Hill's mixture rules.

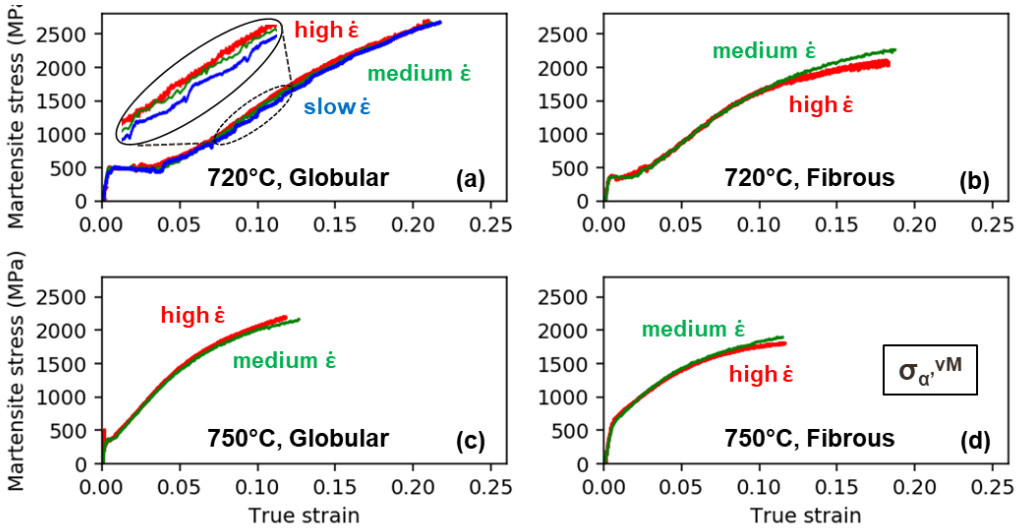

Figure 120: Martensite von Mises stress as a function of macroscopic true strain at different strain rates: (a) T_{IA} = 720°C, globular; (b) T_{IA} = 720°C, fibrous; (c) T_{IA} = 750°C, globular; (d) T_{IA} = 750°C, fibrous. The martensite von Mises stresses are calculated using $\sin^2\psi$ method.

When comparing the normalized hydrostatic strain in austenite (Figure 121), it appears that the faster the tensile test is, the lower the level of relaxation of hydrostatic stress is at the onset of yielding. This result is systematic for all experiments, even for GL720 steel with the 3 tested strain rates. Moreover, for the highest strain rate (8×10^{-3} s^{-1}), the hydrostatic stress in austenite tends to increase linearly with strain, contrary to lower strain rate for which hydrostatic strain in austenite remains close to constant during work-hardening. This systematic observation is not well understood and would need further investigation.

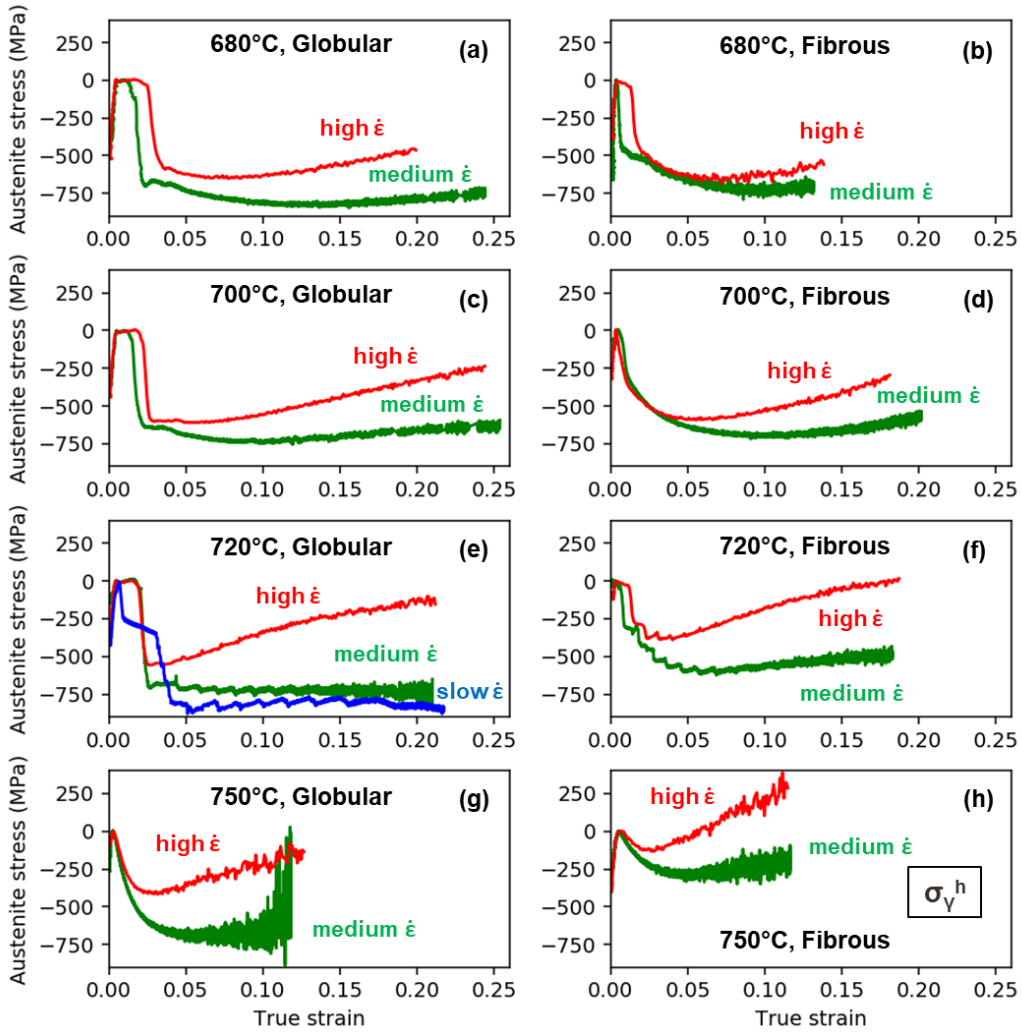

Figure 121: Austenite normalized hydrostatic stress as a function of macroscopic true strain for the 17 experiments: (a) T_{IA} = 680°C, globular; (b) T_{IA} = 680°C, fibrous; (c) T_{IA} = 700°C, globular; (d) T_{IA} = 700°C, fibrous; (e) T_{IA} = 720°C, globular; (f) T_{IA} = 720°C, fibrous; (g) T_{IA} = 750°C, globular; (h) T_{IA} = 750°C, fibrous.

Overall, HEXRD data has proven useful to better understand the dependencies of medium Mn steels' mechanical behaviour on their morphology, intercritical annealing temperature and strain rate. The effect of intercritical annealing temperature on medium Mn macroscopic mechanical behaviour is due to the varied austenite flow stresses with T_{IA} and the different level of austenite/martensite fractions. The origin of the negative strain rate sensitivity is also to be found in austenite and its initial phase fraction. Indeed, both martensite and ferrite have shown to be negligibly affected by $\dot{\varepsilon}$, and by T_{IA} in globular specimens. On the contrary, the difference in mechanical behaviour between globular and fibrous specimens are mainly due to the different levels in flow stress in ferrite and martensite, and initial austenite phase fraction. The evolution of hydrostatic stress in austenite reveals a complex relaxation at the onset of yielding. This relaxation systematically decreases with increasing T_{IA}, increasing $\dot{\varepsilon}$ and is lower in the fibrous samples than in the globular ones.

D. Relationship between SIMT and PLC

The physical origin of PLC effect in medium Mn is still under debate in the scientific community. In such steel, martensitic transformation of retained austenite is often reported to happen inside PLC bands. Callahan et al. have tried to quantify the link between the PLC effect and the mechanical stability of austenite in a Fe/0.2C/5Mn/2.5Al medium Mn steel [106], [147], [181]. Their work was already reported and discussed in section I.6.B.

To quantify the mechanical stability of austenite, they use the Matsumura's law [105], presented in Equation (I—11) from section I.4.A. This law states that the quantity $1/f_\gamma - 1/f_\gamma^0$ is proportional to the plastic strain. The coefficient of proportionality k_s is then used as a measure of austenite mechanical stability. Callahan et al. [106] propose a map linking the condition of appearance of PLC effect and its type (A, B, or C) with the strain rate and the parameter k_s. The map was shown in Figure 41 (b) and is reproduced here in Figure 122 (e).

The procedure used by Callahan et al. was reproduced on the kinetics of the thesis determined by Rietveld refinement and the results (coloured solid lines) are shown in Figure 122 (a), (b), (c) and (d) for the 16 experiments strained at the two higher strain rates (5×10^{-4} s^{-1} and 8×10^{-3} s^{-1}). A linear approximation is then done for each kinetics (black dashed curve). The slopes k_s of the linear approximations were determined by trial and error method, and are indicated with the same colour in Figure 122 as the corresponding kinetics. The value of k_s increases with increasing annealing temperature, which is consistent with the lower mechanical stability of retained austenite determined previously when T_{IA} increases (see Figure 105).

The values of k_s obtained for our globular microstructures at a given $\dot{\varepsilon}$ are reported in Figure 122 (e) alongside the ones found by Callahan et al. [106]. The map presents the area of occurrence of PLC as well as its expected type (A, B or C) as found by Callahan et al. [106]. Only globular microstructures values are reported as the microstructures studied by Callahan were also globular. For the steels studied in thesis, the values have been reported according to the following rules: the colour of the point corresponds to the intercritical annealing temperature; a star corresponds to an experiment in which PLC effect has been detected; an empty circle corresponds to an experiment with no detected PLC

Our experimental data matches partially the original map. For steels annealed at 750°C, no PLC is detected as expected from the map. Both GL720-001 and GL720-015 experiment show type A or B PLC. For GL720-001, its corresponding point is in the PLC domain, near the PLC type B domain. For GL720-015, its corresponding point is very near the PLC domain, in a region where Callahan et al. did not have experimental data. Therefore, considering the chemical difference between our steels and the ones of Callahan, it can be said that the experiments done on GL750 and GL720 steels are in accordance with Callahan's work.

For GL680 microstructure, there is experimentally no PLC effect independently of the strain rate. However, according to Callahan's map, there should be PLC in the steel. This discrepancy is well understood by considering initial austenite phase fraction. In the case of Callahan, the retained austenite fraction before deformation was about 30% for their steels. In our case, there is only 12% of austenite initially. Therefore, our work suggests the necessity of having a minimum phase fraction of austenite initially for the PLC effect to occurs.

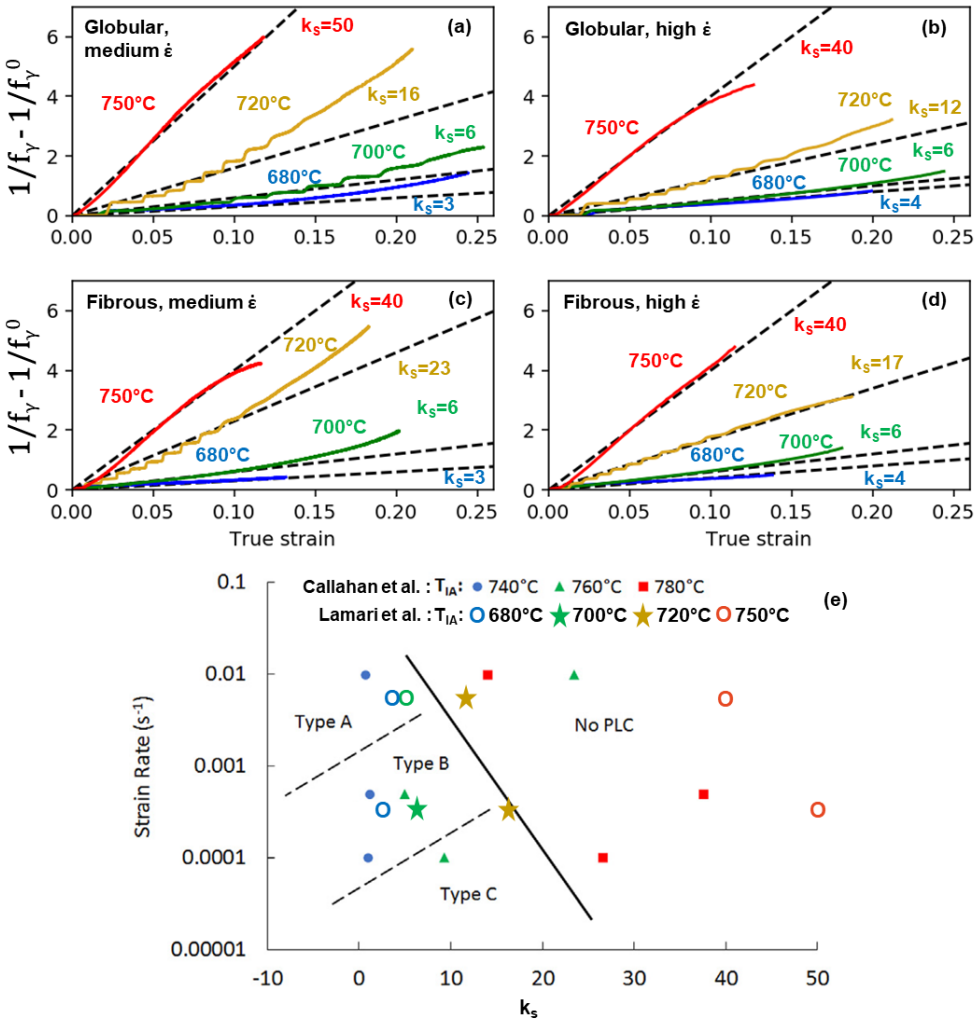

Figure 122: Matsumura's law [105] applied on SIMT kinetics as a function of the macroscopic true strain for the 16 experiments at the two higher strain rates: (a) globular, medium $\dot{\varepsilon}$; (b) globular, medium $\dot{\varepsilon}$; (c) globular, medium $\dot{\varepsilon}$; (d) fibrous, high $\dot{\varepsilon}$. The coloured solid lines correspond to transformed kinetics, and black dashed line corresponds to linear approximation, with k_s being the corresponding slope. (e) Map of the domains where PLC occurs as a function of strain rate and austenite stability (k_s), reproduced from Callahan's work [106]. Our measurements have been added to the map, alongside those of Callahan. For the microstructure studied in this thesis: the colour of the point corresponds to the intercritical annealing temperature; a star corresponds to an experiment in which PLC effect has been detected; an empty circle corresponds to an experiment with no detected PLC.

The GL700 microstructure undergoes PLC effect when strained at medium strain rate but not at high strain rate. However, according to Callahan's map, given the high mechanical stability of its austenite (low k_s), GL700 steel should always show PLC effect in our study. However, GL700 initial amount of austenite is 18%, which is again lower that the one of steel studied by Callahan. What our experiments suggest is that for a given stability of austenite, increasing the strain rate reduces the probability of occurrence of PLC effect. This result was already found by Callahan and is presented on his map. However, the map given by Callahan is only dependent of k_s and $\dot{\varepsilon}$. Our current work suggest that a third axe should be added to this graph, which is the initial austenite phase fraction f_γ^0. The interface between PLC occurrence domain and homogeneous deformation domain would then be a surface. With lower initial phase fraction, the interface between the two domain seems to occur at lower level of stability and strain rate.

5. Intermediate conclusion

Eight microstructures have been designed for the project: 4 globular UFG steels and 4 fibrous ART steels. Tensile tests were carried out on synchrotron beamline at various strain rates, giving necessary information on the mechanical behaviour of all duplex designed steels. The combination of HEXRD with DIC analysis has proven to be very fruitful in this work. The evolution of 3D stress tensors and phase fraction of each phase in the medium Mn steels is possible to be followed. While the stresses in austenite and ferrite are determined by $\sin^2\psi$, the stress in martensite is calculated by an inverse Hill's mixture rules, without assumption on the strain at phase level. The level of stress in martensite calculated by this method was confirmed for specimens annealed at 720°C and 750°C by a direct application of $\sin^2\psi$ method on the deconvoluted martensite peaks. This deconvolution of martensite peaks from those of ferrite is not easy, explaining why it can only be applied on the microstructures having high fraction of martensite. Afterwards in this manuscript, all the stress in martensite will implicitly be those calculated by Hill's mixture rules.

The effect of intercritical annealing temperature on medium Mn macroscopic mechanical behaviour is due to the austenite mechanical stability sensitivity to T_{IA} and different levels of austenite/martensite phase fractions. The origin of the negative strain rate sensitivity in medium Mn steel is also to be found in austenite and its initial phase fraction. Martensite strength evolution with $\dot{\varepsilon}$ is difficult to assess, as its variation does not have a clear trend between experiments. Moreover, its strength is directly linked with the SIMT kinetics. Ferrite has shown to be negligibly affected by both T_{IA} and $\dot{\varepsilon}$. On the contrary, the difference in mechanical behaviour between the globular and fibrous specimens are mainly due to the difference in flow stress of ferrite and martensite and initial austenite phase fraction. The evolution of hydrostatic stress in austenite reveals complex relaxation at the onset of yielding. This relaxation decreases with increasing T_{IA}, increasing $\dot{\varepsilon}$ and is lower in the fibrous samples than in the globular ones.

All gathered data are used to set up and calibrate a mean field micromechanical model that predicts the mechanical behaviour of medium Mn steels and the thermomechanical stability of austenite. This model will be the topic of the next Chapter. One limitation of the current experimental work is that the level of strain in each phase remains unknown. Only stress level can be determined with HEXRD data. The developed mean field micromechanical model remediates this issue, and allows to evaluate the strain partitioning during loading, to better appreciate the evolution of strain inside austenite and thus its mechanical stability. Finally, the model allows for a better understanding of the grain size and alloying content contributions to mechanical behaviour at phase scale, and their respective impact on the TRIP effect and the mechanical response of the whole medium Mn steel.

Chapter IV

IV. Micromechanical modelling of Medium Mn TRIP-aided steels

In Chapter III, the evolutions during deformation of the studied microstructures and the stress partitioning among phases were quantified. These results have raised many questions about the partition of stresses between phases, the size effects or even the assessment of stresses in martensite. In fact, this latter phase appears in part during the processing and induces complex hydrostatic stress state in austenite and in another part during straining. In this chapter, we will see how a micromechanical modelling approach can help answering these questions.

Medium Mn steels are fine structured multiphase aggregate made of ferrite, metastable austenite and as-quenched martensite. Consequently, the interpretation of their mechanical properties requires to know the local mechanical behaviour of each constituent and to understand how they interact with each other, that is, how the stresses and strains are distributed between them.

There are many ways to approach this problem, as outlined in the literature review (Chapter I). In view of the multiple unknowns involved in this study, we wish to give priority to the understanding of the mechanisms in general and of the calculations of order of magnitude. As a result, we have chosen to develop a mean-field approach to describe the phase behaviour limited to a uniaxial monotonous loading (tensile testing) with simplified localization laws (interactions between phases). Iso-work hypothesis appears to be the most suitable in the case of studied steel.

It resembles earlier works as those of P. Jacques, A. Perlade, O. Bouaziz [8], [84], [125], [197]. The emphasis was not deliberately placed on the homogenization scheme which remains very perfectible but rather on the local constitutive laws describing the phases, laws which can be calibrated/validated by our experimental work developed in the preceding chapter.

One of the key issues of this work is the description of the strain induced martensitic transformation (SIMT). It has also been the topic of multiple works in the literature. The different types of approach refer to different physical situation: dispersed austenite in a ferritic matrix like in conventional TRIP-aided steel [86], austenite with low or high SFE like in high Mn steels [12]. For the current work, a physical-based model accounting for autocatalytic transformation is selected as it permits to couple in a proper way the thermodynamics and mechanical aspects of the transformation.

The efficient transformation induced plasticity (TRIP) effect occurring in medium Mn steels is a major factor explaining the very good mechanical performance of these 3rd generation AHSS compared to 1st generation AHSS. TRIP effect is the dynamic work-hardening mechanism linked with SIMT. Its dependence to austenite intrinsic properties (chemistry [48], [93], [95], morphology [26], grain size [49], [50], surrounding matrix [89], [198], internal stresses [25], [83]) was detailed in literature review, alongside its dependence to extrinsic factors related to the loading conditions (triaxiality of stresses [9], [87], strain rate [199], [200], temperature [149], [199]). The work done in

Chapter II and III allows to characterize extensively the initial microstructures in term of chemistry, grain size and phase fractions.

This Chapter is structured in 4 parts. First, the model that predicts the mechanical response of each phase is introduced alongside the SIMT model. Then, the methodology used to calibrate the model is detailed. The results are presented in a third part and compared with experimental data determined in Chapter III. Finally, more subtle implications of the model are discussed.

1. Description of the model

A. General framework of the model

The objective of this model is to be able to predict at last the behaviour of these unstable alloys during a given mechanical loading from a precise knowledge of their microstructures and their mechanism of deformation at the lowest scales (dislocations).

Hence, if the mean stress and strain of the phase i (either α, γ or α') are denoted σ_i and ε_i respectively, the macroscopic flow stress σ_{macro} and strain ε_{macro} of the studied steel are calculated with Hill's mixture rules [195]:

$$\boldsymbol{\sigma_{macro} = f_\alpha \sigma_\alpha + f_\gamma \sigma_\gamma + f_{\alpha'} \sigma_{\alpha'}} \quad \textbf{(IV—1)}$$

$$\boldsymbol{\varepsilon_{macro} = f_\alpha \varepsilon_\alpha + f_\gamma \varepsilon_\gamma + f_{\alpha'} \varepsilon_{\alpha'}} \quad \textbf{(IV—2)}$$

with f_i the volume fraction of phase i, being possibly α (ferrite/annealed martensite), γ (austenite) or α' (fresh and strain-induced martensite).

At each step of the numerical implementation, an applied strain increment $d\varepsilon_{macro}$ is prescribed. The repartition of strain increment among phases is then determined with iso-work hypothesis, widely used for microstructure-based modelling for its good compromise between iso-stress and iso-strain hypotheses and easiness of numerical implementation [8], [12], [18], [125], [126]. It is written as (supposed valid in elasticity and plasticity):

$$\boldsymbol{\sigma_\alpha d\varepsilon_\alpha = \sigma_\gamma d\varepsilon_\gamma = \sigma_{\alpha'} d\varepsilon_{\alpha'}} \quad \textbf{(IV—3)}$$

As the strains ε_α, ε_γ and $\varepsilon_{\alpha'}$ are infinitesimally incremented at each step, they are separated in their elastic and plastic part, respectively ε_i^{el} and ε_i^{pl}, i being α, γ or α'. For a given i, ε_i^{el} is calculated as σ_i/E_i, with E_i the Young's modulus of phase i (calculated with Ghosh-Olson formula [192]). Typical values of Young's moduli are E_α = 207 GPa and E_γ = 201 GPa (for GL720 microstructure). The Young's moduli do not vary very much between experiments. Then, ε_i^{pl} is simply calculated as the difference between ε_i and ε_i^{el}.

For each phase i, the elastic to plastic transition is determined by calculating at each step its flow stress σ_i^{flow} of each phase. If σ_i^{flow} is superior to the phase strain ε_i multiplied by its Young's modulus E_i, then its true stress σ_i is set to $E_i \times \varepsilon_i$. Else, σ_i is set to σ_i^{flow}.

When calculating time-depending quantities (such as phase strain rate), dt was calculated at each step so that the macroscopic strain rate $\dot{\varepsilon}_{macro} = d\varepsilon_{macro}/dt$ is constant at 5×10^{-4} s^{-1} in the considered experimental trial, which is used to calibrate the model.

In the following, for each phase i constituting the medium Mn steels (α, γ or α'), the relationship between the phase flow stress and its plastic strain will be described, i.e. $\sigma_i^{flow}(\varepsilon_i^{pl})$. Moreover, the SIMT will also be modelled, i.e. $f_\gamma(\varepsilon_\gamma^{pl})$.

B. Mechanical behaviour of retained austenite

The model for austenite used in this work was initially developed for fully austenitic TWIP (twinning induced plasticity) steels, using tensile curves to calibrate the different parameters [201]. TWIP steels have the particularity to have two mechanisms that allow plastic accommodation at room temperature: gliding of dislocations and twinning. The two mechanisms are modelled in the model proposed in [201]. In this work, only the equations relative to the gliding of dislocations have been retained.

In the seminal TWIP model for austenite, multiple microstructures were studied, with different austenite grain sizes and different chemistries. Quasi-static tensile tests, but also Bauschinger tests were conducted to obtain independently the parameters of the constitutive equations. In the current work, the flow stress in austenite is calculated accounting for three terms: the friction stress σ_γ^0, the isotropic hardening σ_γ^R and the kinematical hardening σ_γ^X (even if no Bauschinger tests were modelled, this contribution is an important part of the total hardening of TWIP steels):

$$\sigma_\gamma^{flow} = \sigma_\gamma^0 + \sigma_\gamma^R + \sigma_\gamma^X \qquad \text{(IV—4)}$$

The friction stress accounts for the Peierls stress and solid solution strengthening of the austenite. The dependence of σ_γ^0 is given as a function of the element weight fractions by [8], [202]:

$$\sigma_\gamma^0 = 68 + 354C_\gamma + 20Si_\gamma + 20Al_\gamma + 3.7\mathrm{Cr}_\gamma \qquad \text{(IV—5)}$$

In Equation (IV—5), X_γ being the weight fraction in element X of austenite. The Mn content of austenite is not present in Equation (IV—5) as the latter has a negligible effect on the friction stress [201], [202]. As the composition of austenite is different in our eight studied steels because of their specific manufacturing conditions, their friction stresses are also different.

The isotropic stress represents the hardening term due to dislocation forest hardening. The classical Taylor relationship linking σ_γ^R and the dislocations density in austenite ρ_γ (mainly statistically stored dislocations, or SSD) is described by [201]:

$$\sigma_\gamma^R = \alpha_\gamma M_\gamma \mu_\gamma b_\gamma \sqrt{\rho_\gamma} \qquad \text{(IV—6)}$$

In Equation (IV—6), α_γ is a geometrical constant, M_γ is the Taylor factor, μ_γ is the shear modulus and b_γ is the norm of the Burgers vector of perfect dislocations. The kinematic hardening term σ_γ^X represents the back-stress due to geometrically necessary dislocations (GND) and was evaluated with Bauschinger tests on TWIP steels [201]. It follows the simplest relationship proposed by Sinclair et al. [203]:

$$\sigma_\gamma^X = \frac{M_\gamma \mu_\gamma b_\gamma}{d_\gamma^0} n_\gamma \qquad \text{(IV—7)}$$

d_γ^0 is the austenite grain size before deformation. The $1/d_\gamma^0$ dependence of σ_γ^X allows for a better description of grain size effect on austenite flow stress when d_γ^0 is small. In this model, n_γ is the mean number of dislocations piled up at grain boundaries. This number n_γ cannot exceed a maximum value denoted n_γ^0 as dislocation pile-ups at grain boundaries can be relaxed above a certain stress concentration, leading to the saturation of the kinematical hardening term (which is observed experimentally also). Considering λ_γ the mean spacing between slip bands, the number of dislocations arriving at grain boundaries is a function of the plastic strain ε_γ^{pl} and follows the subsequent differential equation [203]:

$$\frac{dn_\gamma}{d\varepsilon_\gamma^{pl}} = \frac{\lambda_\gamma}{b_\gamma}\left(1 - \frac{n_\gamma}{n_\gamma^0}\right) \qquad \text{(IV—8)}$$

The multiplication of SSD follows the classical Kocks-Mecking relationship, which takes into account the accumulation due to the forest of dislocations and boundaries, and annihilation due to dynamic recovery [201]:

$$\frac{d\rho_\gamma}{d\varepsilon_\gamma^{pl}} = M_\gamma\left(\frac{P_\gamma\left(1 - n_\gamma/n_\gamma^0\right)}{b_\gamma d_\gamma^0} + k_\gamma\sqrt{\rho_\gamma} - g_\gamma\rho_\gamma\right) \qquad \text{(IV—9)}$$

In Equation (IV—9), k_γ and g_γ are constants respectively linked with the athermal work hardening and the dynamic recovery. To be consistent with the dislocations piling up at boundaries, the term $(1-n_\gamma/n_\gamma^0)$ is added to impede the efficiency of grain boundaries' contribution to work-hardening. Compared with the formula found in [201], a new term P_γ is introduced to further decrease boundaries efficiency [17]. This term is introduced due to the submicron size of grains (<800 nm for austenite). It arises from a competition between dislocation accumulation and its possible absorption at grain boundary [17], [204]. This probability P_γ can be calculated considering d_γ^0 and a critical grain size d_γ^c with the following formula.

$$P_\gamma = exp\left(-\left(\frac{d_\gamma^c}{d_\gamma^0}\right)^3\right) \qquad \text{(IV—10)}$$

The constant d_γ^c does not depend on austenite composition or grain size. It is set to 600 nm and is determined by a trial and error approach. In the previous studies cited above, austenite grain size ranges from 1 µm to 20 µm. At d_γ^0 = 1 µm, P_γ value is 0.82. At d_γ^0 = 3 µm, P_γ value is 0.99. These values close to 1 explains why it was not necessary to account for P_γ in these previous studies, which is not our case (at d_γ^0 = 0.8 µm, P_γ value is only 0.66).

C. Mechanical behaviour of ferritic matrix

As shown in the previous chapter, ferrite seems to behave as a conventional fine-grained fully ferritic steel whose plasticity is governed by dislocation gliding and interactions. The model for ferrite is thus inspired from the work on fully ferritic steels conducted by Bouaziz et al. [14]. The approach to model ferrite is exactly similar to the one for austenite, accounting for the friction stress σ_α^0, the isotropic contribution σ_α^R and the back-stress σ_α^X, but with relevant calibration parameters of course. In addition to those terms found in previous works, a term σ_α^{SSA} accounting for the SSA mechanism observed experimentally in ferrite (see Figure 96, in section III.3.E from Chapter III) is considered. Hence, the total flow stress of ferrite is written:

$$\boldsymbol{\sigma_\alpha^{flow} = \sigma_\alpha^0 + \sigma_\alpha^R + \sigma_\alpha^X + \sigma_\alpha^{SSA}} \qquad \textbf{(IV—11)}$$

The isotropic and kinematical contributions to hardening follow Equation (IV—6) to (IV—10). Tensile tests and Bauschinger tests were conducted to calibrate the different equations on fully ferritic steels [14]. The parameter P_α of Equation (IV—9) was not present in the initial study [14], as grain sizes ranged from 3 µm to 22 µm. In the current work, ferrite grain size is lower than 1.2 µm, thus adding P_α is a necessity (otherwise predicted stress levels are far too high).

Indeed, the results of Bouaziz's model for ferrite [14] without modification (especially without the addition of P_α term) for our GL720 steel is compared to experimental ferrite von Mises stress in Figure 123 (a). While the experimental stress does not surpass 900 MPa, the modelled stress reaches 1200 MPa. In the literature, Takaki et al [205] have studied the effect of grain refinement on pure ferritic IF (interstitial free) steels. They reduced the ferrite grain size using shoot-peening. Their tensile curves are represented in Figure 123 (b), with the measured grain size for each microstructure. They determined a dependence of the yield strength (YS) and the ultimate tensile strength (UTS) on the grain size. The model proposed by Takaki et al. permits to predict the YS and the UTS using Hall and Petch like law. Using their laws, the value of true stress at yielding onset $\sigma_{0.2}^{true}$ and necking onset σ_{UTS}^{true} obtained for a grain size of 0.97 µm is reported in Figure 123 (a) with blue stars. The latter results confirms the level of stress determined in ferrite using $\sin^2\psi$ method in Chapter III, and demonstrates that the prediction of unmodified Bouaziz model [14] is too high for small grained ferrite.

The dependence of the friction stress σ_α^0 to the alloying elements is given by (X_α is the ferrite weight fraction in element X) [18]:

$$\boldsymbol{\sigma_\alpha^0 = 60 + 33Mn_\alpha + 81Si_\alpha + 48Cr_\alpha + 48Mo_\alpha} \qquad \textbf{(IV—12)}$$

The previous chapter showed that ferrite is certainly affected by a strain-ageing mechanism explaining the Lüders' plateau of the studied steel and the initial drop in its flow stress observed just after the yield point. Even if not completely necessary, this mechanism has been introduced to better describe the very first stage of the plastic deformation of the steels.

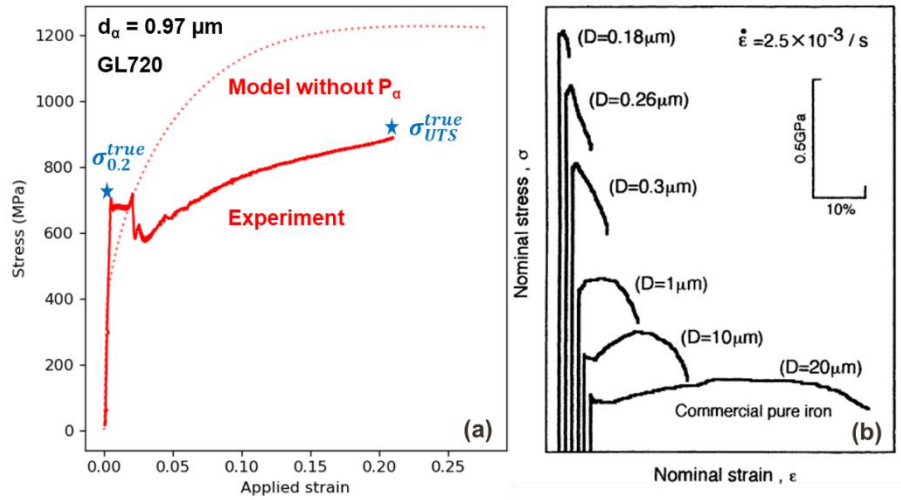

Figure 123: (a) Comparison between the experimental von Mises stress determined in ferrite for GL720 steel, and the predictions of the original model of Bouaziz et al. [14], which does not account for the P_α coefficient. (b) Tensile curves of shoot-pinned IF steels by Takaki et al. [205]. The grain size of ferrite is indicated above the corresponding curve. In (a), the blue star corresponds to value of true stress at yielding and necking onset determined with grain size sensitive equation given by Takaki et al. [205].

For SSA modelling, a simplified version of the Kubin-Estrin-McCormick (KEMC) model is used [16], [206]. It introduces a new internal variable, the ageing time t_a, which corresponds to the effective time that the dislocations have aged (i.e. be pinned by carbon atoms) [207]. Its evolution can be expressed as a function of the plastic strain and the plastic strain rate [16]:

$$t_a = \frac{w}{\dot{\varepsilon}_\alpha^{pl}}\left(1 - exp\left(-\frac{\varepsilon_\alpha^{pl}}{w}\right)\right) + t_a^0\, exp\left(-\frac{\varepsilon_\alpha^{pl}}{w}\right) \qquad (IV—13)$$

In Equation (IV—13), w is the strain increment produced when all mobile dislocations pinned by carbon atoms free themselves and move to their next waiting position, t_a^0 is the initial value of ageing time, and $\dot{\varepsilon}_\alpha^{pl}$ is the derivative of the ferrite plastic strain ε_α^{pl} with respect to time. The contribution of SSA to flow stress is directly a function of t_a [16]:

$$\sigma_\alpha^{SSA} = P^{SSA}\left(1 - exp\left(-\left(\frac{t_a}{t_a^0}\right)^{n^{SSA}}\right)\right) \qquad (IV—14)$$

The parameter P^{SSA} is the difference in stress strengthening comparing the situation in which carbon atoms are in solid solution and the one in which all carbon is dragged by dislocations, and n^{SSA} is a parameter controlling the velocity of the unpinning mechanism. Overall, considering σ_α^{SSA} adds four new parameters and one internal variable. Including σ_α^{SSA} modifies the initial stage of stress and strain partitioning between ferrite and austenite, allowing for a better description of the initial evolution of austenite plastic strain. This is important to describe accurately the first stage of austenite transformation kinetics. However, it does not affect the work-hardening of ferrite as SSA contribution decreases rapidly with plastic strain and remains constant afterwards.

D. Mechanical behaviour of fresh and strain-induced martensite

Among the physically based models for martensite described in Chapter I, three of them have been identified in the literature to possibly describe the behaviour of martensite in medium Mn steels. Theirs resulting predictions are shown in Figure 124 in the case of GL720-001 sample. The chemical and size effects have been taken into consideration when available in the models. The stresses predicted by the models have been plotted as a function of the macroscopic strain ε_{macro}.

Experimentally, ε_{macro} is measured while phase strains ε_{α}, ε_{γ} and $\varepsilon_{\alpha'}$ remain unknown. To enable the proper comparison, the local behaviours of the phases (ferrite/austenite/martensite) have been computed as a function of their local phase strains. The calibration for ferrite and austenite as well as for the SIMT will be shown later. The macroscopic strain is then computed afterward in order to plot Figure 124.

Seo et al. proposed a model for fresh martensite in quenching & partitioning (Q&P) steels [126]. The constitutive equations are similar to Equations (IV—4), (IV—5), (IV—6) and (IV—9). They do not take into account back-stress while it is well established that fully martensitic steel present a huge Bauschinger effect [18], [208], [209]. The probability $P_{\alpha'}$ is set to 1, $k_{\alpha'}$ to 0.015 and $g_{\alpha'}$ to 20. When compared with GL720 experimental determination, the calculated flow stress reaches too high value (3200 MPa) at low strain (4%). The predicted work-hardening is also very low as the density of dislocations is almost at saturation to reach the expected strength of martensite.

Another dislocation-driven model is proposed by Aristeidakis et al. [12]. Their parameters have been chosen to model strain-induced martensite in a Fe/0.3C/10Mn/2Si/3Al medium Mn steel. They set $P_{\alpha'}$ to 0, $k_{\alpha'}$ to 0.09 and $g_{\alpha'}$ to 2.44. The calculated flow stress is closer to the experimental one. However, in Aristeidakis approach, all the parameters are calibrated for each steel, reducing the predicting ability of their model. Moreover, Aristeidakis model fails to reproduce the very high work-hardening rate of GL720 martensite (see Figure 96 (a) in section III.3.D). Both models described above rely on the assumptions that the work-hardening of martensite can be modelled by an increase in the density of dislocations during the deformation. However, it is difficult to sustain this hypothesis because martensite already contains a high density of dislocations [210], [211], which must instead lead to work hardening controlled by recovery, thus low.

The continuum composite approach (CCA) developed by Allain et al. [212] to model as-quenched fully martensitic steels is also considered. In this model, the behaviour of martensite is described as an extended elastic/plastic transition. Martensite is considered as a heterogenous aggregate containing a continuous distribution of phases with different yield strengths. This distribution is inherited from the sequential phase transformation process [210], [211] during quenching. It is thus not adapted to describe the behaviour of the strain induced martensite. As a consequence, the calculated flow stress of martensite by CCA is too high with the wrong apparent work-hardening rate as it has been developed for fully martensitic steels produced by quenching

Overall, to our best knowledge, none of the mean field models based on microstructure features in the literature is suitable to describe the flow stress evolution of mechanically induced martensite.

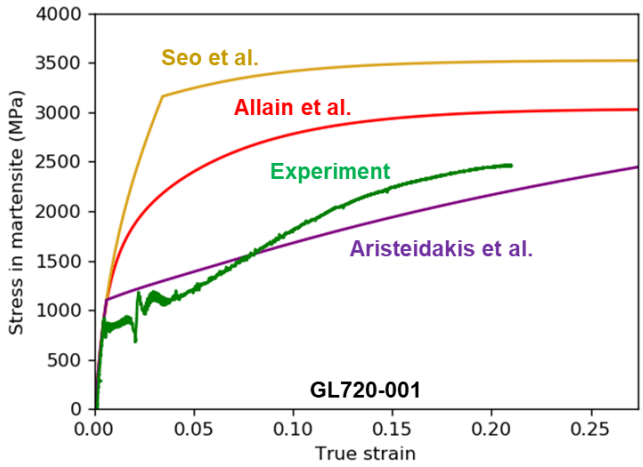

Figure 124: Comparison between the experimental von Mises stress determined in martensite for GL720 steel, and the predictions of the models of Seo et al. [126], Aristeidakis et al , Allain et al. [212] respectively.

One fundamental issue with pre-existing models is that they consider an a priori mechanical behaviour for martensite, i.e. a pre-existing $\sigma_{\alpha'}$ vs $\varepsilon_{\alpha'}$ curve, even though most of the martensite constituting the steel at necking is not initially present in the microstructure. The mean stress of the martensitic phase as a function of its strain $\varepsilon_{\alpha'}$ during tensile trial is expected to vary whether austenite transforms or not, which is something that is not known a priori. The original model presented here, called the MIM model (Mechanically Induced Martensite) in the following, takes into consideration this connection between the mean stress of martensite and the SIMT. For the sake of simplicity, fresh martensite initially present in the microstructure is combined with mechanically induced martensite in the MIM model. In the following, the relative fraction of transformed austenite f_T is calculated as:

$$f_T = \frac{f_{\alpha'}}{f_\gamma^0 + f_{\alpha'}^0} \qquad \text{(IV—15)}$$

In Equation (IV—15), $f_{\alpha'}$ is the fraction of both fresh and strain-induced martensite, f_γ^0 and $f_{\alpha'}^0$ are the fractions of austenite and martensite present in the microstructure before deformation.

The present model is adapted from the CCA model [212]. The martensitic phase is considered as a mixture of elastic perfectly plastic martensite with different yield strengths $\sigma_{\alpha'}^L$. Martensite appearing at a later stage of the tensile test is considered stronger. This is a reasonable assumption since its mother austenite is more stable and thus should have a higher carbon content. Moreover, as later martensite appears in a more deformed and strain-hardened austenite, it could inherit more dislocations from its mother phase during the displacive transformation. The initial fresh martensite obtained during manufacturing is thus considered as softer than martensite obtained during straining as it is obtained at higher temperature during a sequential transformation.

In the MIM model, when martensite appears, it bears a stress equal to its yield strength and this flow stress remains constant until the end of the trial (no work-hardening, no elastic unloading). An a priori probability density function f is defined, such as $f(\sigma_{\alpha'}^L) \times d\sigma_{\alpha'}^L$ is the fraction of martensite having a yield strength between $\sigma_{\alpha'}^L$ and $\sigma_{\alpha'}^L + d\sigma_{\alpha'}^L$ when all austenite is transformed. At a given time of the tensile test, the fraction f_T of austenite that has transformed can be written $F(\sigma_{\alpha'}^L)$, with $\sigma_{\alpha'}^L$ being the flow stress of the most recently formed martensite. Determining the true shape of the distribution would necessitate to measure the distribution of carbon, dislocation densities and lath

sizes of martensites in each sample, which exceeds the scope of this PhD thesis. Similar experimental measurements have been carried out successfully in the case of as-quenched martensite [211], but not for strain-induced martensite. Hence, an Avrami-like law is chosen to model empirically $F(\sigma_{\alpha'}^{L})$ in this work. Therefore, at each time:

$$f_T = F\left(\sigma_{\alpha'}^{L}\right) = \int_0^{\sigma_{\alpha'}^{L}} f(\sigma) d\sigma = 1 - exp\left(-\left(\frac{\sigma_{\alpha'}^{L} - \sigma_{\alpha'}^{0}}{\sigma_{\alpha'}^{\Delta}}\right)^{n_{\alpha'}}\right) \quad \text{(IV—16)}$$

Here, $\sigma_{\alpha'}^{0}$ is the strength of the softest possible martensite islands, $\sigma_{\alpha'}^{\Delta}$ controls the width of the distribution and $n_{\alpha'}$ its shape. These latter three parameters must be calibrated.

Experimentally, $\sigma_{\alpha'}^{L}$ is difficult to determine, contrary to the phase fraction of transformed austenite f_T calculated combining SEM and HEXRD measurements. Numerically, physically based laws exist in the literature and allow to calculate f_T (see next section for the modelling of SIMT), but not $\sigma_{\alpha'}^{L}$. Therefore, it is more convenient to inverse Equation (IV—16) and express $\sigma_{\alpha'}^{L}$ as a function of f_T:

$$\sigma_{\alpha'}^{L} = F^{-1}(f_T) = \sigma_{\alpha'}^{0} + \sigma_{\alpha'}^{\Delta} |ln(1 - f_T)|^{\frac{1}{n_{\alpha'}}} \quad \text{(IV—17)}$$

Finally, as the fraction of transformed austenite f_T is defined relatively to the fraction of martensite/austenite islands $f_{M/A} = (f_\gamma^0 + f_{\alpha'}^0)$, for a given $\sigma \in [0, \sigma_{\alpha'}^{L}]$, the quantity $\sigma f(\sigma) d\sigma$ corresponds the contribution of the martensite having a stress between σ and $\sigma+d\sigma$ to the mean stress of M/A islands. On the other hand, the mean contribution to the whole martensitic phase to M/A mean stress is $f_T \sigma_{\alpha'}$. Therefore, the mean stress of martensite can be calculated by the following continuous summation:

$$f_T \sigma_{\alpha'} = \int_0^{\sigma_{\alpha'}^{L}} \sigma f(\sigma) d\sigma = \int_0^{f_T} F^{-1}(f)\, df \quad \text{(IV—18)}$$

The second form of integral is obtained using reverse chain rules, substituting σ with $F^{-1}(f)$. This form allows for the calculation of the martensite flow stress knowing only from the SIMT kinetics. The latter is modelled in the next section.

E. Mechanically induced martensitic transformation and TRIP effect

As demonstrated in the Chapter III, the SIMT kinetics is very dependent on the microstructure. For microstructure annealed at low temperature, retained austenite is very stable and transformation kinetics is slow. On the contrary, in microstructures produced at high temperatures, the austenite transforms quickly. This is explained qualitatively by the chemical and size considerations. The thermodynamically based model proposed in this work allows for a quantitative understanding of the relationship between mechanical properties and SIMT.

The framework to model SIMT is inspired from Olson and Cohen seminal work, and is the continuation of the model developed by Perlade et al. on more conventional TRIP-aided steels [8], [10], [11], [213]. In this section, the fraction of strain induced martensite is defined by:

$$f_{SIM} = 1 - \frac{f_\gamma}{f_\gamma^0} \quad \text{(IV—19)}$$

In Olson-Cohen's interpretation, SIMT occurs when nucleation sites of martensite are created at the intersection of shear bands by plastic deformation in austenite. At each deformation step, the increment of nucleation sites dN_{SIM} can be written as the product of the initial nucleation site density I_0, an autocatalytic factor λ, a factor depending on the thermodynamic driving force and the increment of plastic strain of austenite [8], [213]:

$$dN_{SIM} = I_0(1 + \lambda f_{SIM})\, exp\left(\frac{A + B\,\Delta G_{\gamma\to\alpha'}}{RT}\right) d\varepsilon_{\gamma}^{pl} \qquad \text{(IV—20)}$$

In Equation (IV—20), R the ideal gas constant, T the temperature and $A+B\Delta G_{\gamma\to\alpha'}$ the activation energy. The activation energy depends linearly on the driving force $\Delta G_{\gamma\to\alpha'}$ for the martensitic transformation [214], [215]. A and B are two positive constants whose values are respectively 4950 J/mol and 1.34 according to [8]. The driving force $\Delta G_{\gamma\to\alpha'}$ can be written as an affine function of austenite carbon content, temperature and stress in austenite [83], [95], [214], [215]:

$$\Delta G_{\gamma\to\alpha'} = \Delta G_{\gamma\to\alpha'}^{T=M_s,\sigma=0} + \Delta S_{\gamma\to\alpha'}^{T=M_s}(T - M_s) + \frac{\partial \Delta G_{\gamma\to\alpha'}}{\partial \sigma}\sigma_{\gamma} \qquad \text{(IV—21)}$$

The chemical driving force $\Delta G_{\gamma\to\alpha'}^{T=Ms,\sigma=0}$ is a linear function of austenite carbon content ranging from -1350 J/mol for GL720 steel to -1500 J/mol for GL680 steel [95]. The difference in entropy between austenite and martensite $\Delta S_{\gamma\to\alpha'}^{T=Ms}$ is constant and set to 6.8 J/mol/K according to [8], [95]. The value of the partial derivative with respect to stress $\partial\Delta G_{\gamma\to\alpha'}/\partial\sigma$ depends on the stress triaxiality [83]. In the case of a tensile test, its value is -0.55 J/mol/MPa [8].

The martensitic start temperature M_S is calculated accorded to van Bohemen relationship (temperature in °C, composition in wt%) [171]:

$$M_S = 565 - 600(1 - e^{-0.96\,C_{\gamma}}) - 31\,Mn_{\gamma} - 13\,Si_{\gamma} + 30Al_{\gamma} \qquad \text{(IV—22)}$$

The autocatalytic factor λ has proven to be proportional to the initial austenite grain size d_{γ}^0 [213]. The proportionality factor is a function of austenite geometrical shape S, the typical length of martensite sub-units u_1 and the fraction of initially-nucleated martensitic sub-units on the austenite grain boundaries ξ [213]:

$$\lambda = \frac{2d_{\gamma}^0}{S\xi u_1} \qquad \text{(IV—23)}$$

Finally, the increment of the fraction of strain-induced martensite df_{SIM} is obtained by multiplying the volume of a martensite lath $V_{\alpha'}$, the remaining fraction of austenite $(1-f_{SIM})$ relative to its initial value f_{γ}^0 and the increment of nucleation sites dN_{SIM} [10], [11]:

$$df_{SIM} = V_{\alpha'}(1 - f_{SIM})\, dN_{SIM} \qquad \text{(IV—24)}$$

In this work, the volume of newly created martensite laths $V_{\alpha'}$ is considered to decrease with decreasing fraction of austenite due to the progressive hindrance of pre-existing martensite laths. Indeed, it is reasonable to consider that the width and thickness of the martensite laths do not evolve much [12]. On the contrary, the lath length is not the same at the beginning of the tensile test when the SIMT occurs in austenite with its initial grain size d_{γ}^0 compared to the end of the trial when austenite is fragmented by SIMT [8], [86], [126]. Therefore, $V_{\alpha'}$ is calculated as the product of its

constant section $S_{\alpha'}$ and the actual austenite grain size d_γ, which is not constant. A simple linear relationship is used to describe the decrease in the austenite grain size with f_{SIM}:

$$d_\gamma = (1 - f_{SIM}) d_\gamma^0 \qquad \text{(IV—25)}$$

Factor (1-f_{SIM}) is not considered in the previous works found in the literature. This factor slows transformation kinetics near the end of the transformation and does not affect the initial slope. It allows for a better description of the end of the transformations kinetics and is necessary to obtain values consistent with experimental observations made in Chapter 3.

2. Calibration of the model

The model parameters have been calibrated to best reproduce the experimental observations discussed in Chapter III. Only von Mises stresses at phase scale and SIMT kinetics are used in the calibration process. The macroscopic stress curves are not used during the parametrization of the model, as the macroscopic stress is only indirectly described through Hill's mixture rule.

The inputs of the model are the initial phase fractions, the grain sizes and the chemistry of ferrite and austenite. Martensite is supposed to have the same concentration in C, Mn, Si and Al as austenite due to the displacive nature of martensitic transformation. The alloying contents of each phase are given in Table 14 in section III.1.A. The initial phase fractions and grain sizes are given in Table 13 in section III.1.A. Cementite was not directly included in the model as its phase fraction is negligible. Its phase fraction was added to the ferrite initial phase fraction to allow a perfect balance.

Six parameters of the model are composition-dependent (σ_γ^0, n_γ^0, σ_α^0, $\sigma_{\alpha'}^0$, $\Delta G_{\gamma\rightarrow\alpha'}^{T=Ms,\sigma=0}$, M_s). Except for $\sigma_{\alpha'}^0$, the dependence of those parameters has not been quantified in the current work but derived from the works on fully ferritic and austenitic alloys (thus independently from the present work). Concerning ferrite, austenite and SIMT constitutive laws, parameters are reused from precedent studies. When compared with austenite model in TWIP steel [201], the only modified parameter is g_γ. As the nominal alloying contents are very different between both steels (22Mn vs 4Mn and 0.8C vs 0.2C), which affect dynamic recovery, its value was adapted from 2.8 to 4.8. The factors P_α et P_γ have been introduced for both austenite and ferrite since grain sizes are submicrometric, contrary to the previous studies. This initial concept developed by Bouaziz et al. [17], is now widely used for medium Mn UFG steel modelling [12], [216]. For SIMT, u_1, which is the typical length of martensite sub-units, has a value of 2 µm in the original article [213]. However, it is also supposed small relative to the austenite grain sizes, which are between 24 µm and 140 µm in [213]. Hence, in our work, as austenite grain size is about 0.7 µm, u_1 has been arbitrarily decreased to 0.15 µm. The initial dislocations densities in ferrite and austenite (ρ_α^0 and ρ_γ^0) are set to 10^{12} m^{-2} [12], [217]. Putting a lower value does not change the simulation.

In the model current form, only one parameter is morphology dependent, meaning its value changes between simulation for fibrous and globular specimens: the ferrite critical grain size d_α^C appearing in Equation (IV—10) to calculate P_α. A value of 1.45 µm is found for all globular specimens, while a value of 1.65 µm is preferable for fibrous specimens. Those values are determined by a trial and error approach. This difference can be understood with crystallographic considerations. Globular

ferrite has no orientation relationship (OR) with other ferrite or austenite grains. On the other hand, fibrous ferrite is actually annealed martensite, and bears a K-S OR with surrounding austenite and ferrite grains. This may increase the probability P_α for a dislocation to be absorbed by grain boundaries of globular microstructures, thus diminishing d_α^C. For austenite, while the same considerations exist, a constant d_γ^C = 0.6 µm has proven to be satisfactory in all experiments.

Concerning SSA and MIM models, no pre-existing data have been found in the literature for medium Mn steels. Parameters of the KEMC model are determined following Marais et al.'s approach [16] developed for a 0.15C-0.7Mn steel. Parameters t_a^0, w, n^{SSA} is found constant when comparing globular experiments with T_{IA} below 720°C. For simplicity, the same parameters are also used for other simulations. Only P^{SSA} parameter is adjusted between microstructures. Between GL680 and GL720 steels, P^{SSA} ranges from 700 MPa to 620 MPa. A simple linear dependence with intercritical annealing temperature is given to P^{SSA} to reflect this evolution in globular steels. For fibrous specimens annealed below 720°C, a constant value of P^{SSA} of 300 MPa is found satisfactory. For specimens intercritically annealed at 750°C, no Lüders plateau exists. Therefore, for such specimens, P^{SSA} is set to 0 MPa.

MIM model introduces 3 parameters which are similar to those found in CCA model [212]. For the sake of the simplicity, the value of $\sigma_{\alpha'}^{\Delta}$ representing the spreading of the yield strength distribution in martensite is considered constant for all the experiments and the value is fixed to the spreading encountered in the CCA model for a 0.6 C martensite. In the same way, the value of $n_{\alpha'}$ is fixed to 1.4 for the 8 studied steels. Only the yield stress of the softest martensite island $\sigma_{\alpha'}^0$ has been calibrated with our experimental data. It is supposed to be proportional to the initial carbon content of martensite, as carbon hardening is the main hardening mechanism for martensite [174]. The value of $\sigma_{\alpha'}^0$ polynomial coefficients has been fixed by trials and error method on experimental martensite stress. The equations for $\sigma_{\alpha'}^0$, alongside the values of all other parameters in the model are summarized in Table 17 and Table 18. Table 17 describes the parameters for austenite and ferrite as the underlying physical behaviour laws are the same. Except 4 parameters which have been revised, all the other parameters are taken from the literature. Table 18 describes the parameters for the SIMT and MIM models.

Physical constants	Ferrite (i=α)	Austenite (i=γ)	Reference
α_i	0,38	0.4	[14]; [201]
M_i	2,77	3.06	[14]; [201]
μ_i	80 GPa	65 GPa	[14]; [201]
b_i	2.5×10^{-10} m	2.5×10^{-10} m	[14]; [201]
k_i	0.007	0.025	[14]; [201]
g_i	1.3	4.8	[14]; calibrated
n_i^0	6.2	$0.02\times\sigma_\gamma^0$	[14]; [201]
λ_i	2.25×10^{-8} m	3.17×10^{-7} m	[14]; [201]
d_i^c	1.65 µm (fibrous) 1.45 µm (globular)	0.6 µm	calibrated
ρ_i^0	10^{-12} m^{-2}	10^{-12} m^{-2}	[217]
w	7×10^{-4}	-	[16]
t_a^0	10^{30} s	-	[16]
n^{SSA}	0.05	-	[16]
P^{SSA}	0 MPa (T_{IA} = 750°C) 300 MPa (fibrous) 2060 – 2T_{IA} MPa (otherwise)	-	calibrated

Table 17: Parameters used for ferrite and austenite constitutive laws. T_{IA} is the intercritical annealing temperature of the steel.

Physical constants	Value	Reference	Physical constants	Value	Reference
$\sigma_{\alpha'}^0$	$2600\times C_{\alpha'}$ -1250 MPa	calibrated	S	6	[213]
$\sigma_{\alpha'}^\Delta$	3193 MPa	[212]	u_1	150 nm	calibrated
$n_{\alpha'}$	1.4	calibrated	ξ	0..4	[213]
$\Delta G_{\gamma\to\alpha'}^{T=M_s,\sigma=0}$	$-757\times C_\gamma$ - 990 J/mol	[8], [95]	$V_{\alpha'}$	1.3×10^{-13} d_γ m³	[8]
I_0	10^{20} m^{-3}	[8]			

Table 18: Parameters used for MIM and SIMT constitutive laws

3. Results of the model

The whole model described above has been applied to reproduce the experimental behaviour of the 8 studied steels measured in Chapter 3. The stresses and strains at phase scale, the SIMT kinetics and the macroscopic behaviour of the steel are not independent. They have been calculated simultaneously but will be presented and discussed separately in the next sections.

When the flow stress in a phase or SIMT is compared between simulations, quantities are plotted as a function of the corresponding local phase strain calculated by the model. When simulations are compared to experimental data, quantities are plotted as a function of the macroscopic strain ε_{macro}. These choices are made since experimentally, ε_{macro} is measured, while phase strains ε_{α}, ε_{γ} and $\varepsilon_{\alpha'}$ have not been determined with our experiments. On the contrary, for model curves, constitutive equations use phase scale strains. The simulated macroscopic strain is only a subsequent result of the homogenization scheme. Experimental data shown in the following sections are obtained during synchrotron tensile test at the medium strain rate 5×10^{-4} s^{-1} in Chapter III. To make the comparison between experimental and simulated data more straightforward, the simulated quantities are displayed until the model macroscopic strain ε_{macro} reaches the experimental value at necking onset. The initial phase fractions of each constituent, alongside their chemical composition and grain sizes are given in Table 14 and Table 13 of section III.1.A.

When relative difference is discussed between experimental data and model predictions, it is calculated as the ratio between the absolute value of the difference of the two values and the experimental value.

A. Ferrite

The flow stress in ferrite σ_{α} is only a function of its plastic strain $\varepsilon_{\alpha}^{pl}$ and its strain rate $\dot{\varepsilon}_{\alpha}$. The dependence of σ_{α} on $\dot{\varepsilon}_{\alpha}$ is only a consequence of the contribution associated with SSA. It is not strictly speaking a strain-rate dependant behaviour law as [218], [219] (i.e. in the studied range of strain rate below 1 s^{-1} at RT). In fact, only the SSA term depends on strain-rate and not the work-hardening. The flow stress in ferrite calculated in the 8 simulations are compared for each morphology in Figure 125.

Concerning globular microstructures (Figure 125 (a)), the yielding point phenomenon is visible for steels annealed below 720°C, while it is absent for GL750 steel. This is consistent with the choice made on P^{SSA} parameter. In GL750 simulation, ferrite flow stress increases continuously during yielding. In the other simulations, the flow stress of ferrite first decreases between ε_{α}=0.003 and ε_{α}=0.03, and then increases until to end. At ε_{α}=0.05, a small gap of 40 MPa exists between the strongest ferrite found in GL700 and the softer one found in GL720. This gap decreases until the end of simulation. Overall, the globular ferrite curves are almost superimposed after ε_{α}=0.07.

In Figure 125 (b) the simulated flow stress evolutions for fibrous microstructures are represented. While there is no yield point phenomenon for any of the simulations of fibrous steels, there are stress plateaus between ε_{α}=0.002 and ε_{α}=0.02 for microstructures with T_{IA} below 720°C. This difference in yield point phenomenon between fibrous and globular simulations is explained by the lower value taken for P^{SSA} in the former case. After ε_{α}=0.05, the calculated flow stress is very close

between experiments, ranging from 570 MPa for FB750 to 610 MPa for FB680. Once again, the gap in stress decreases as work-hardening continues. Therefore, despite some differences in chemistry ($Mn_\alpha \in [3.3\%; 4.2\%]$) and grain size ($d_\alpha \in [1.0\mu m; 2.6\mu m]$) between ferrites of each microstructure, the model reveals that those differences become mechanically negligible after few percent of plastic deformation. This result confirms the trend found experimentally in Chapter III.4.A.

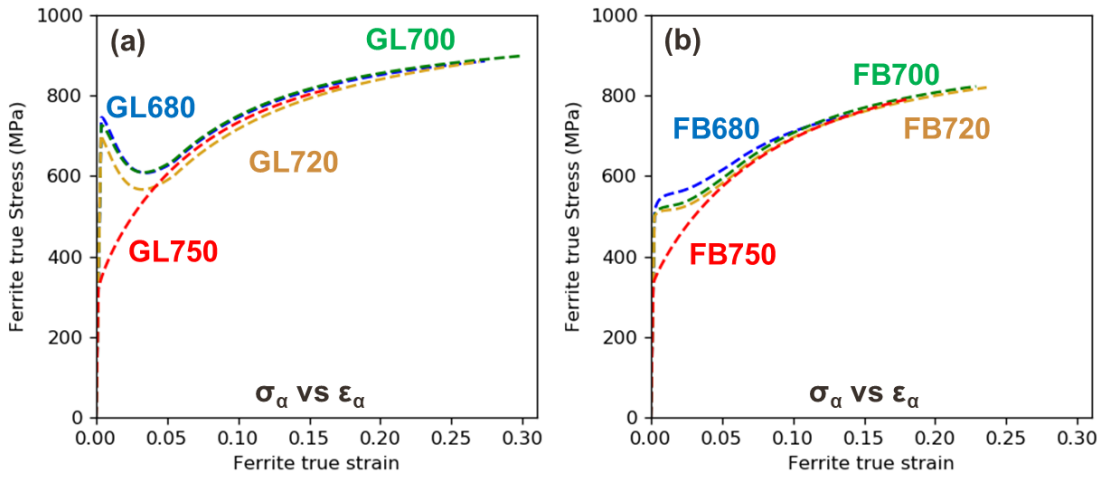

Figure 125: Comparison between the simulated flow stresses in ferrite in globular microstructures (a) and fibrous microstructures (b). The colour code corresponds to the annealing temperatures of the steels. Blue: T_{IA} = 680°C; green: T_{IA} = 680°C; yellow: T_{IA} = 720°C; red: T_{IA} = 750°C.

The average ferrite flow stress in globular steels is 810 MPa at ε_α=0.15. Comparatively, the average ferrite flow stress in fibrous steels is 760 MPa at ε_α=0.15. Experimentally, it was found in Chapter III.4.B that the ferrite in globular steels is 40 MPa stronger than in fibrous steels. Thus, the simulations confirm this result. The model reveals that this difference in strength cannot be attributed to the differences in grain size and chemistry between the two kinds of ferrite, as explained in the previous paragraph. From a numerical point of view, this is solely attributable to the difference in the critical grain size values chosen for both morphologies (d_α^C is set to 1.65 µm for fibrous and 1.45 µm for globular microstructures). This difference in d_α^C is motivated by a difference in crystallographic orientation relationship (OR) between grains for the two morphologies (random OR for globular, K-S OR for fibrous).

P_α term in Equation (IV—9), linked with d_α^C, is very important to capture the size effect in ferrite. Without it, the simulation of ferrite flow stress could reach 1200 MPa, which is not the level expected for 1 µm size ferrite [205].

The simulated evolutions of stress in ferrite are compared with the experimental ones determined in ferrite with $\sin^2\psi$ method for each microstructure in Figure 126. The modelling of ferrite flow stress is especially good for GL680, GL700 and GL720 steels (Figure 126 (a), (c) and (e)), though it must be reminded again that the constitutive laws have mainly be calibrated on independent experiments on fully ferritic steels [14]. Accounting for SSA, the upper yield strength (UYS) is very similar between experiments and model (less than 5 MPa error) for those steels. For FB680, FB700, and FB720 (Figure 126 (b), (d) and (f)), the simulated curves also match the experimental ones very closely, especially after 7% of deformation with a relative error on stress inferior to 1% for the 3 steels. The yielding point phenomenon found experimentally in FB680 and FB700 steels are not reproduced numerically. This is a consequence of the choice made on parameters linked with SSA. Correcting this

mismatch would necessitate to change not only the P^{SSA} parameter, but also w, t_a^0 and n^{SSA}, which is in opposition with the current philosophy of the model to keep SSA modelling in ferrite as simple as possible. Moreover, besides the yield point phenomenon, the Lüders plateau in ferrite is well described by the current set of parameters, with 7% of maximum relative error for FB700 steel.

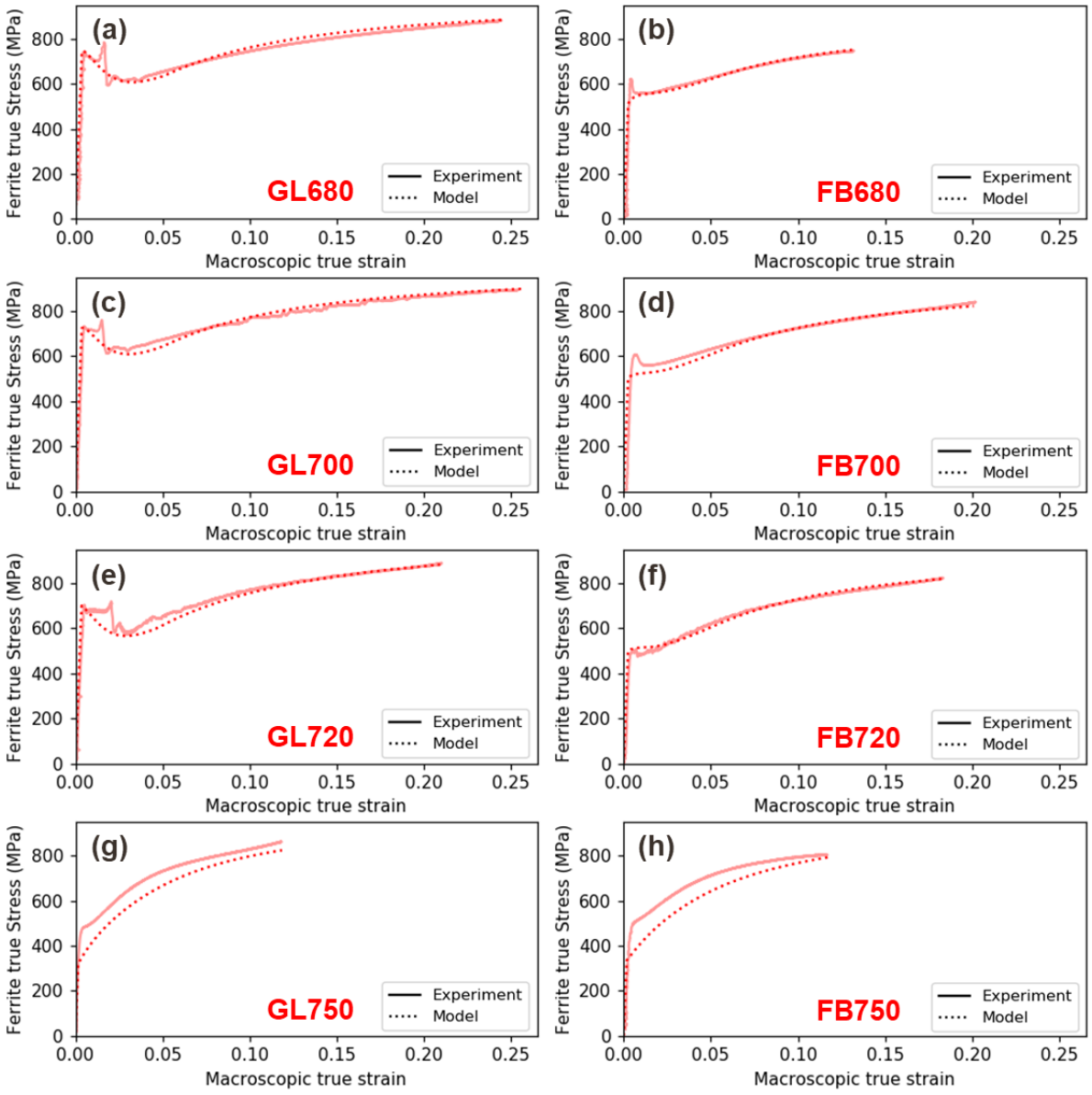

Figure 126: Comparison between the simulated flow stress (dotted line) and the experimental von Mises stress (solid line) in ferrite for (a) GL680, (b) FB680, (c) GL700, (d) FB700, (e) GL720, (f) FB720, (g) GL750, (h) FB750 steels respectively. The stresses in ferrite are plotted as a function of ε_{macro}.

Finally, as seen in Figure 126 (g) and (h), there is a larger discrepancy between simulations and experiments for GL750 and FB750 steels. The simulated yield strength is 160 MPa lower than the experimental one for both simulations. For GL750 steel, the gap decreases to 70 MPa at $\varepsilon_\alpha = 0.02$. Above this strain, the gap remains constant until necking, meaning that while the absolute value of stress is not well described in the current form of the model for GL750 microstructure, work-hardening is on the contrary well described. For FB750 steel, the ferrite stress gap decreases continuously during work-hardening, reaching a value of 10 MPa at necking. This gap can be explained by the low initial dislocation density put in the model. Indeed, if this value of $\rho_\alpha^0 = 10^{12}$ m^{-2} is reasonable for ferrite-

austenite duplex steel [12], [217], it is probably a bit low for steels containing 35% of as-quenched martensite like GL750 and FB750 microstructures. In fact, martensitic transformation (during manufacturing) being displacive with a significant transformation strain induced stresses and thus plasticity (dislocations) in surrounding phases. To circumvent this issue, it is possible to use an improved model which calculates explicitly the GNDs density created in ferrite due to martensite. Such a model inspired from the seminal work of Ashby was developed for instance and used by Allain et al. [18] for dual-phase steels (ferrite-martensite steels). They predict an initial dislocation density of 2.7×10^{13} m^{-2} for a DP570 steel. Another solution consists in using ρ_α^0 as a calibrating parameter. Authors working on medium Mn steels found values of ρ_α^0 higher than 5×10^{13} m^{-2} [12], [126]. To test the validity of the model, complementary simulations have been conducted on GL750 and FB750 microstructures, increasing ρ_α^0 from 10^{12} m^{-2} to 5×10^{13} m^{-3}. The results of the new simulations are compared with experimental results in Figure 127. With this value of ρ_α^0, both yield strength and ultimate tensile strength, as well as work-hardening match between experiments and simulation with a relative error inferior to 3%. Those simulations demonstrate that no fundamental improvements are needed in the model to predict the ferrite mechanical behaviour in medium Mn steels containing a high amount of initial fresh martensite. They also demonstrate that ferrite in 750°C annealed microstructures are indeed stronger than the ones annealed at lower temperatures, as assumed during experimental analysis. Despite this better agreement with synchrotron data, for the sake of consistency and because it is difficult to obtain experimentally a quantitative estimate of the initial dislocation density for any particular microstructure, it is still decided to keep ρ_α^0 as a constant set to 10^{12} m^{-2} in the following sections.

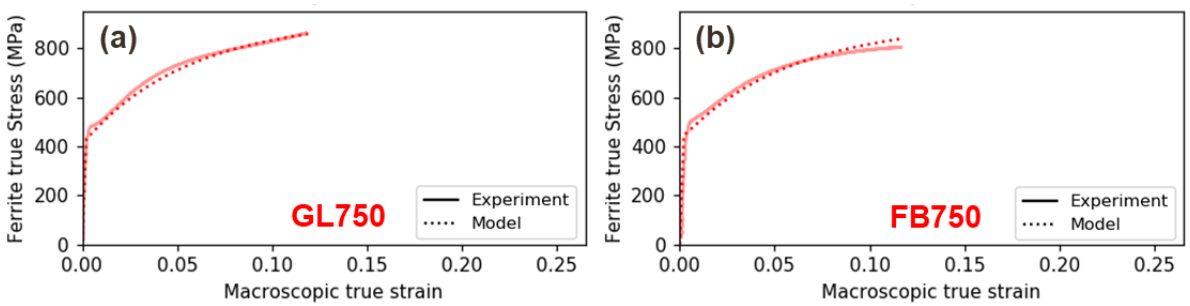

Figure 127: Comparison between the simulated flow stress (dotted line) and the experimental von Mises stress (solid line) in ferrite for (a) GL750 and (b) FB750 steels. The difference with Figure 126 (g) and (h) relies on the choice of the initial dislocation density ρ_α^0 (5×10^{13} m^{-2} in the two simulations). The stresses in ferrite are plotted as a function of ε_{macro}.

Overall, stress evolution in ferrite can be described by the current model for steels intercritically annealed below 720°C. For microstructures produced at 750°C, the model remains satisfactory to describe ferrite work-hardening despite a discrepancy with synchrotron experimental data. The trends experimentally observed concerning the effect of morphologies and annealing temperature are successfully reproduced and explained by the current model. With the same ρ_α^0, simulations demonstrate that the level of stress in ferrite is not significantly affected by the annealing temperature, but is slightly higher in globular ferrite than in fibrous one.

B. Austenite

In the proposed model, the flow stress of austenite σ_γ is a function of its plastic strain ε_γ^{pl} only. The flow stresses in austenite calculated in the 8 simulations are compared for each morphology in Figure 128. The evolution of austenite stress follows the same 3-step pattern independently of microstructure. Firstly, it increases linearly during elastic domain until its yield strength, ranging from 270 MPa to 360 MPa depending on the alloying contents of the austenite. Secondly, the behaviour is characterized by a high work-hardening between ε_γ=0.2% and a strain around ε_γ=2%. This second phase is controlled by a fast increase in the kinematic contribution. Then, thirdly, a slower but steady work-hardening of austenite exists between ε_γ=2% and the end of simulation. This last increase in flow stress is mainly controlled by isotropic work-hardening and is quite similar to that encountered in ferrite. It is noteworthy that the work-hardening is the same for all simulations, independently of austenite size and chemistry. Indeed, when calculating the difference in austenite stress between ε_γ=15% and ε_γ=4%, the results are between 114 MPa and 118 MPa for all simulations.

For both morphologies, simulations demonstrate that austenite flow stress increases with decreasing annealing temperature. This evolution, also found experimentally, is related to the local composition (higher alloying contents -especially carbon) and smaller grain sizes. Both factors are indeed known in the literature to increase the strength of austenite.

When comparing steel intercritically annealed at the same temperatures, it appears that the globular austenite is stronger than the fibrous one. At ε_γ=8%, austenite in GL680 steel is 25 MPa stronger than that in FB680 steel. The difference equals 77 MPa between GL700 and FB700, 53 MPa between GL720 and FB720 and 16 MPa between GL750 and FB750. This trend is explained by the smaller amount of carbon found in the fibrous austenite in comparison with the globular one, alongside a larger grain size d_γ^0 for the fibrous austenite formed at T_{IA} = 700°C and 720°C. Though being systematic, this difference remains small.

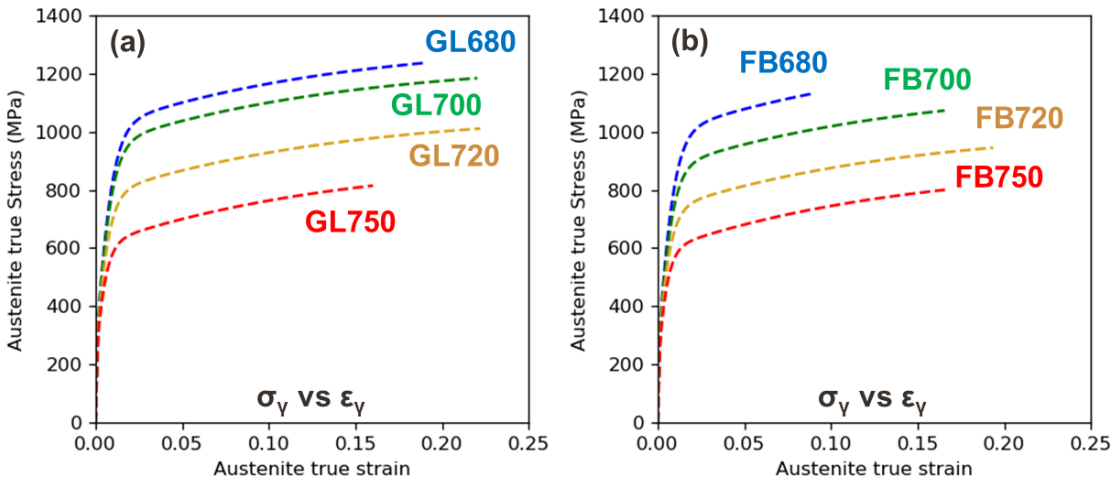

Figure 128: Comparison between the simulated flow stresses in austenite in globular microstructures (a) and in fibrous microstructures (b). The colour code corresponds to the annealing temperatures of the steels. Blue: T_{IA} = 680°C; green: T_{IA} = 680°C; yellow: T_{IA} = 720°C; red: T_{IA} = 750°C.

The simulated evolutions of stress in austenite are compared with the experimental ones determined with $\sin^2\psi$ method for each microstructure in Figure 129 (respectively dotted and solid

curves). The modelling of austenite flow stress matches well the synchrotron data for GL680, FB680, GL700, FB700 and GL720 steels (Figure 129 (a), (b), (c), (d) and (e)), with an accurate evaluation of the work-hardening and level of stress at necking onset. For those five simulations, the maximum relative error with experimental stress at necking strain is 4%. It must be emphasized again that the constitutive laws have mostly be calibrated on independently obtained tensile curves of fully austenitic TWIP steels [201] and the parameters are not changed between simulations. For FB720 microstructure (Figure 129 (f)), the simulation is also very satisfying. At necking, the calculated stress is 960 MPa while the experimental one is superior at 1025 MPa.

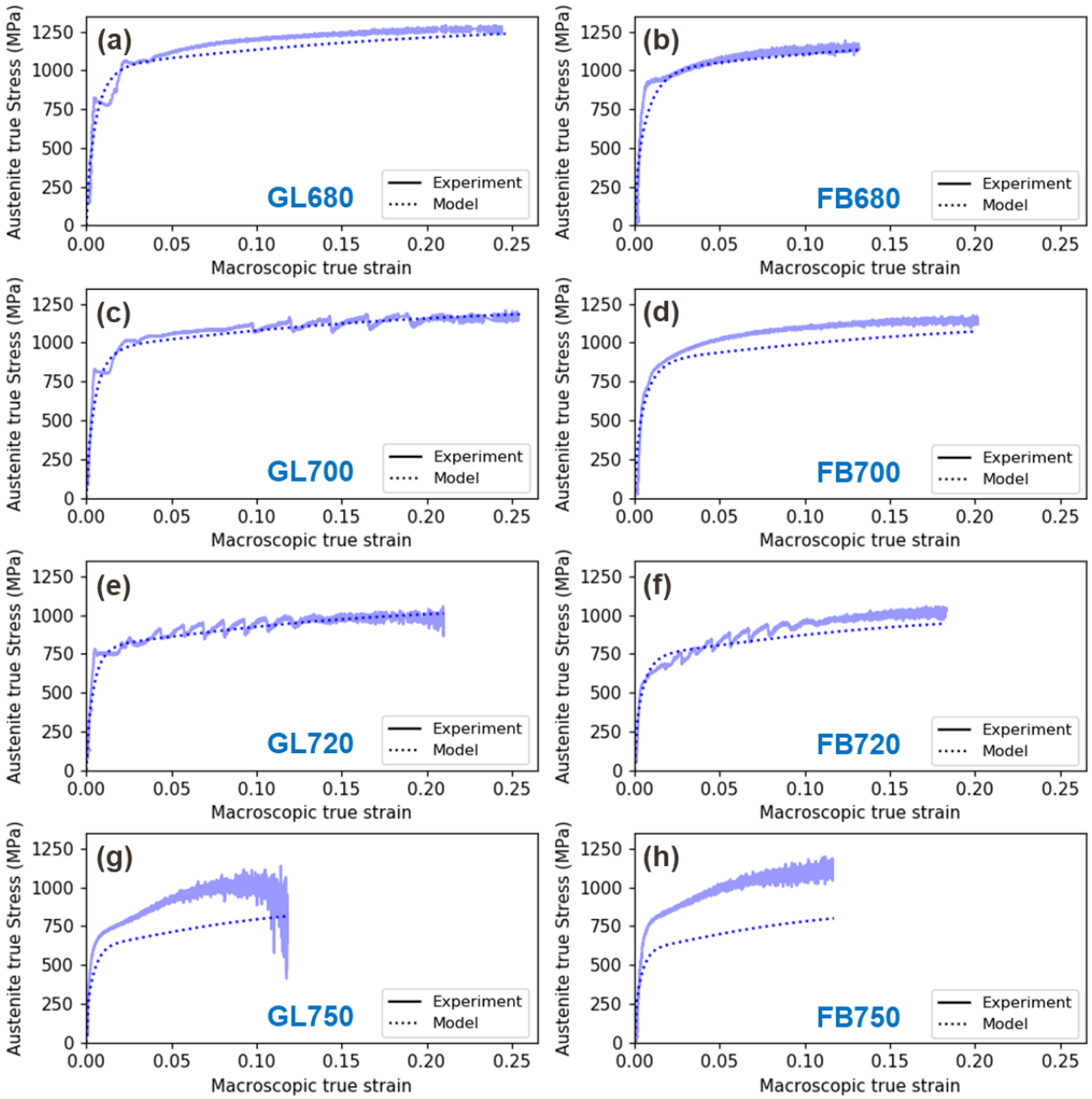

Figure 129: Comparison between the simulated flow stress (dotted line) and the experimental von Mises stress (solid line) in austenite for (a) GL680, (b) FB680, (c) GL700, (d) FB700, (e) GL720, (f) FB720, (g) GL750, (h) FB750 steels respectively. The stresses in austenite are displayed as a function of ε_{macro}.

During the first 2% of strain, experimental von Mises stress evolution can show a plateau. This plateau, also present in ferrite experimental curves, is of course not reproduced numerically in modelled stress since it is a consequence of the propagation of a mechanical instability occurring at macroscopic scale which cannot be simulated in a 0D mean field model. The stagnating experimental

stress is explained by a non-deforming diffracting volume when Lüders band nucleates at the extremity of the specimen.

Like for ferrite, the description of austenite flow stress by the model is not consistent with the experimental data for GL750 and FB750 steels, as highlighted in Figure 129 (g) and (h). Contrary to ferritic phase, not only the absolute value of flow stress mismatches between simulation and tensile trials, but also the work-hardening rate is quite different. The experimental work-hardening is higher than the simulated one.

For ferrite, correcting the initial dislocation density in simulation allowed for an accurate description of experimental behaviour. New simulations are thus conducted for the two steels. For GL750 simulation, ρ_γ^0 is raised to 1×10^{14} m^{-2}. For FB750 simulation, ρ_γ^0 is raised to 2×10^{14} m^{-2}. The results are shown in Figure 130. With the new ρ_γ^0, it is possible to describe accurately the level of stress and work-hardening of austenite until 2.5% of deformation for both steels. However, contrary to ferrite, the work-hardening observed experimentally at higher strain cannot be explained by the model.

Therefore, those simulations suggest that the model lacks an additional work-hardening term that could also explain the higher experimental work-hardening rate of austenite in steels annealed at high temperatures. This term could be linked with the diminution of austenite phase fraction due to SIMT, which could create a dynamic refinement of austenite grain size as done by [8], [126]. This latter mechanism is not accounted for in the current austenite flow stress model. This decrease in grain size would diminish the mean free path of dislocations and thus could increase in turn the isotropic contribution to stress hardening. However, as this supplementary term is only found in GL750, FB750 and maybe FB720, it should be dependent on morphology, austenite chemistry and maybe its surrounding matrix nature (proportion of martensite). On the other hand, it could be argued that the stress determination with $\sin^2\psi$ method bears more uncertainty for GL750 and FB750 steels as austenite is more unstable and transforms more rapidly. For GL750, at ε_γ = 2.5%, the austenite phase fraction f_γ is 8.5%. For ε_γ = 10%, f_γ is 3%. The argument of experimental uncertainty falls short when comparing with other experiments, like FB680, for which the amount of austenite is not significantly higher. Thus, explaining the behaviour of austenite in GL750 and FB750 microstructures would necessitate more investigation. As the current description is accurate enough for all the other steels, the present model will be used, even for GL750 and FB750 simulations. The value of ρ_γ^0 will be kept at 10^{12} m^{-2}, like for ferrite.

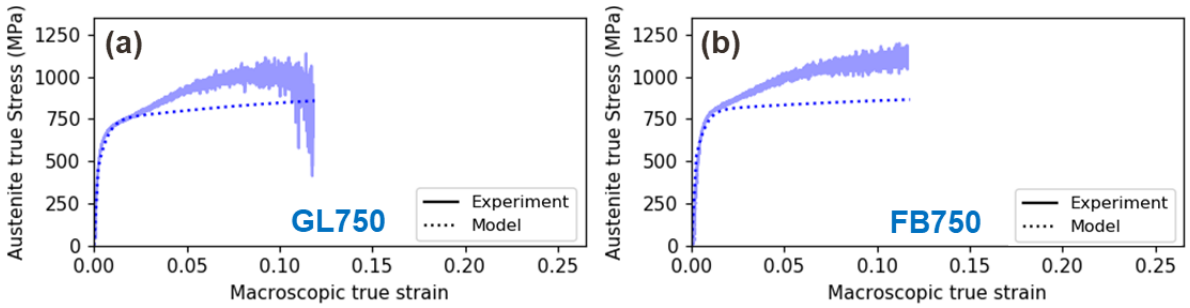

Figure 130: Comparison between the simulated flow stress (dotted line) and the experimental von Mises stress (solid line) in austenite for (a) GL750 and (b) FB750 steels. The difference with Figure 129 (g) and (h) is that the initial density dislocation ρ_γ^0 is increased to 1×10^{14} m^{-2} for GL750 and 2×10^{14} m^{-2} for FB750. The stresses in austenite are displayed as a function of ε_{macro}.

Overall, stress evolution in austenite can be described with very good accuracy by the current model for steels intercritically annealed below 720°C. For microstructures produced at 750°C, the model would need some improvement to describe austenite work-hardening. The trends experimentally observed concerning the effect of annealing temperature are successfully reproduced and explained by the current model. Contrary to experimental data, which are unclear about the effect of morphology on the austenite flow stress, the model suggests that the austenite is stronger in the globular microstructures than in the fibrous ones. This good description of austenite deformation is very important to describe SIMT kinetics, as highlighted in the next section.

C. Strain-induced martensitic transformation (SIMT) kinetics

During the macroscopic deformation, the evolutions of austenite phase fraction and strain-induced martensitic transformation are a function of the austenite plastic strain ε_γ^{pl} only. The SIMT kinetics calculated in the 8 simulations are compared for each morphology in Figure 131. To make the comparison between simulations easier, it is decided to show the fraction of strain-induced martensite f_{SIM} relative to the initial fraction of available austenite, as defined in Equation (IV—19). For example, when f_{SIM} is 50%, half of the austenite present before deformation in the microstructure is transformed.

In all simulations, the fraction of strain-induced martensite increases with strain. The rate of transformation decreases continuously with increasing strain for all microstructures. The higher the annealing temperature is, the higher the rate of transformation of austenite is. The value of f_{SIM} at experimental necking strain never reaches 100%, meaning the transformation is not complete in any of the simulation. The completion of SIMT varies between experiments. For globular microstructures, the final fraction f_{SIM} ranges from 64% for GL680 to 87% for GL750 steel. For fibrous ones, it ranges from 36% for FB680 to 87% for FB750 steel

The comparison between steels with different morphologies annealed at the same T_{IA} reveals no significant difference. At ε_γ = 0.08, f_{SIM} is 33% for GL680 and 32% for FB680. At ε_γ = 0.15, f_{SIM} is 62% for GL700, 68% for FB700, 75% for GL720, 80% for FB720 and 86% for both GL750 and FB750 steels. Thus, for T_{IA} = 680°C and 750°C, no significant difference exists between the rate of transformation of fibrous and globular austenite. For intermediary intercritical annealing temperatures (T_{IA} = 700°C and 720°C), the fibrous austenite seems to transform at a slightly higher rate than globular one. This difference is mainly explained by a grain size effect (Table 13). For steels annealed at T_{IA} = 680°C and 750°C, austenite mean grain size is the same for both morphologies, while they are bigger for fibrous austenite than globular one at intermediary T_{IA}.

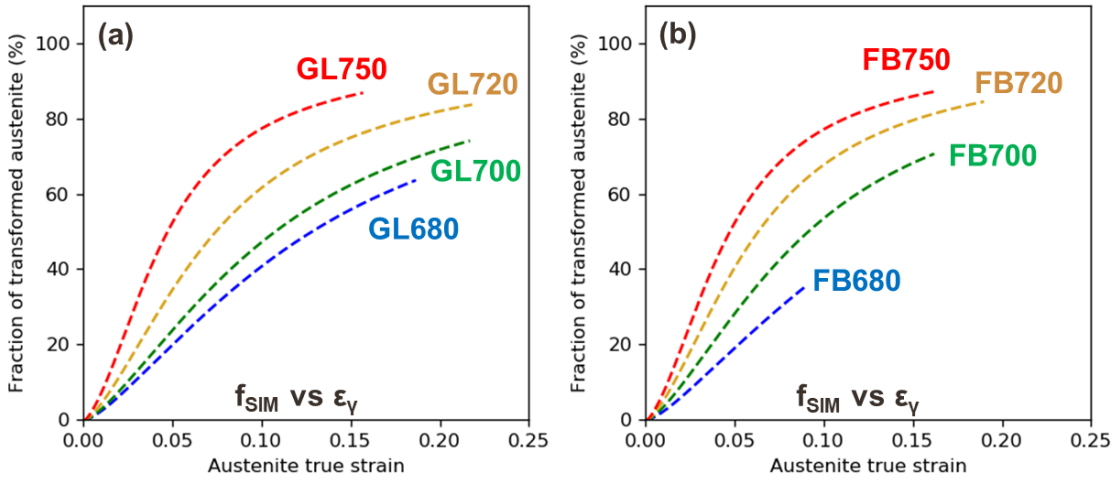

Figure 131: Comparison of the evolution of strain-induced martensite fraction f_{SIM} (relative to the fraction of austenite before deformation) in globular microstructures (a) and in fibrous microstructures (b). The colour code corresponds to the annealing temperatures of the steels. Blue: T_{IA} = 680°C; green: T_{IA} = 680°C; yellow: T_{IA} = 720°C; red: T_{IA} = 750°C.

The simulated evolutions of austenite phase fraction are compared with the experimental ones determined by Rietveld refinement for each microstructure in Figure 132 (respectively dotted and solid curves). The model simulates the evolution of austenite phase fraction, but not its initial value f_γ^0, as it is an input parameter. The initial fractions follow exactly the experimental trends, with the microstructures formed at 680°C bearing the lowest austenite fraction for each morphology and that formed at 720°C containing the highest amount of austenite. The experimental curves contain some steps which are linked with macro-deformation bands propagating along the tensile gauge, and are of course not reproduced by the mean field model.

For all microstructures, the amount of austenite retained at experimental necking strain is very similar between experiments and simulations. The maximal error is obtained for FB750 steel, with an error of 1.1% (f_γ is 3.1% experimentally and 2% numerically). This is a very good result since the absolute uncertainty due to Rietveld refinement method is 1%. For microstructures produced at 680°C and 700°C, the rate of transformation is well modelled all along the tensile test. For microstructures produced at 720°C and 750°C, the rate of transformation is experimentally higher before ε_γ = 0.05. Then, at higher strain, the simulated strain rate is higher, explaining that the final value is overall similar between experiments and simulations.

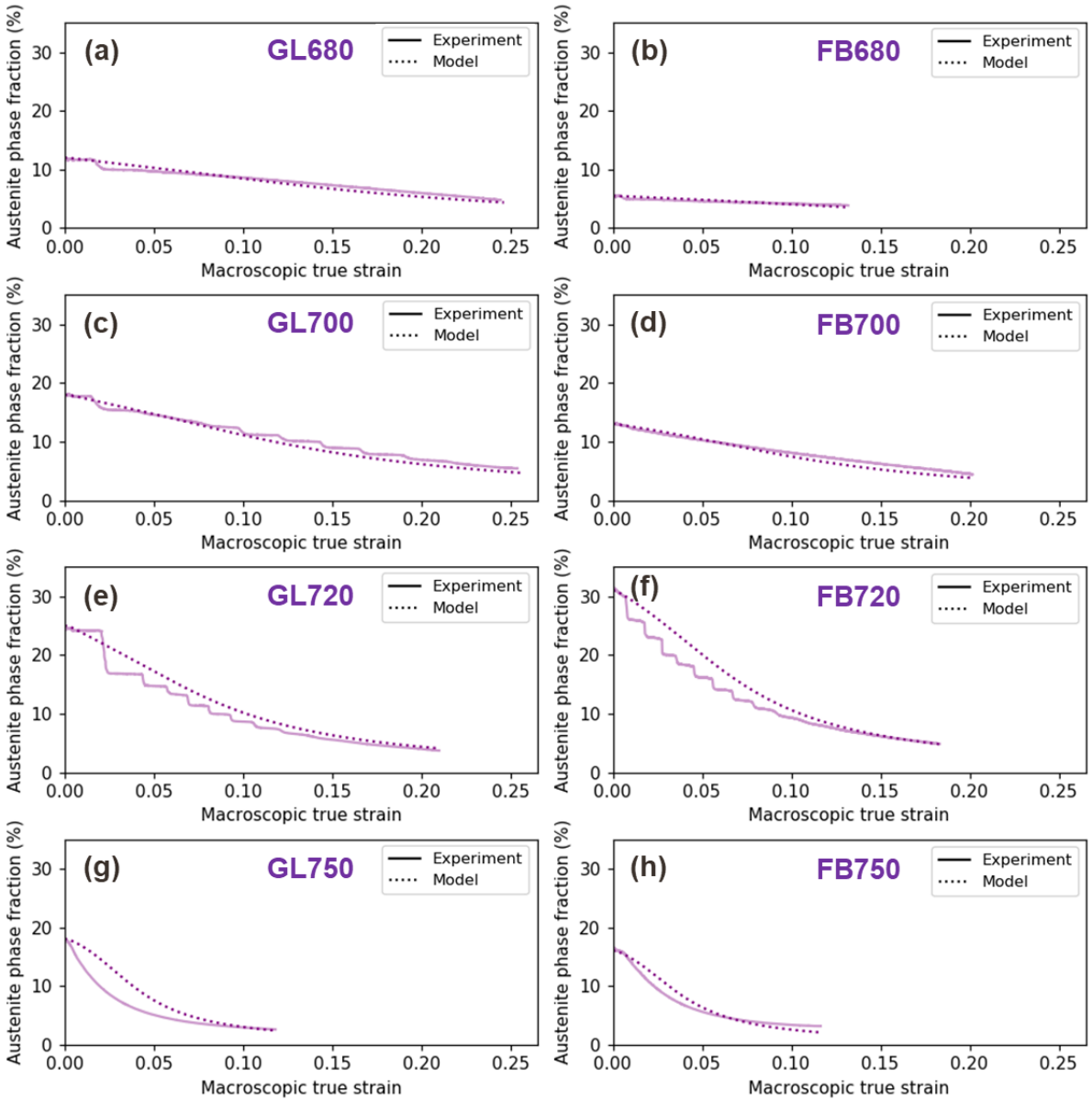

Figure 132: Comparison between the simulated (dotted line) and experimental (solid line) SIMT kinetics for (a) GL680, (b) FB680, (c) GL700, (d) FB700, (e) GL720, (f) FB720, (g) GL750, (h) FB750 steels. The austenite phase fractions are shown as a function of ε_{macro}.

Overall, the model successfully reproduces experimental SIMT kinetics. While the rate of transformation is not perfectly modelled for higher annealing temperatures, the final fraction of austenite is well reproduced. This is of the upmost importance since the stress in martensite is a direct function of austenite phase fraction. As such, any issue encountered with the modelling of martensite flow stress can be interpreted as an issue with MIM model and not of the SIMT model. The results of the MIM model are presented and discussed in the next sections.

D. Martensite

The description of the mechanical behaviour of the martensitic phase is more complex than the one of ferrite and austenite.

It is considered as an aggregate of different martensites, which are individually rigid perfectly plastic. Individual martensites yield strength are described with a density function f, which also serve to calculate the flow stress of the macroscopic martensitic phase, as described in section IV.1.D. This section is divided in two parts. First, the density function is described and analysed for the 8 studied microstructures. Then, the overall mechanical response of martensitic phase is discussed and compared with the experimental data.

a) Martensite yield strength distribution

The density function f as a function of individual martensite yield strength $\sigma_{\alpha'}^{L}$ is shown in Figure 133 (a) for the 4 simulations conducted on the globular steels. Their cumulative counterpart F are shown in Figure 133 (b). Some coloured dots are added to the curves indicative of specific values of f_T (defined in Equation (IV—15)), i.e. at different relative transformed fraction of austenite. At the beginning of the trial, f_T is around 36% for GL680, GL700 and GL720 steels, while it is a bit higher at f_T = 43% for GL750, as indicated by the yellow dots. This high initial value of f_T is due to its definition relative to the total amount of austenite created during intercritical annealing, and only represents the fresh martensite inherited from thermal treatment. For a given f_T, all the martensite phase with a yield strength $\sigma_{\alpha'}^{L}$ lower than the stress $\sigma_{\alpha'}^{L,Max} = F^{-1}(f_T)$ is formed and influences the mean flow stress of the whole martensitic phase $\sigma_{\alpha'}$, while that with a superior $\sigma_{\alpha'}^{L}$ does not exist yet and does not affect $\sigma_{\alpha'}$.

The standard deviation and the shape of all distributions are identical. However, their initial stress threshold $\sigma_{\alpha'}^{0}$ decreases with increasing annealing temperature. Values of $\sigma_{\alpha'}^{0}$ are 388 MPa for GL680 steel, 310 MPa for GL700, 76 MPa for GL720 steel and can even be negative for low-carbon martensite, such as in GL750 for which $\sigma_{\alpha'}^{0}$ = -210 MPa. Those purely numerical values do not represent however the initial flow stress value for the whole martensitic phase at the start of the tensile loading. Indeed, at the start of the tensile test, a large portion of the austenite has been transformed into martensite (f_T > 34%) already. The initial flow stress of martensite is calculated accounting all martensite with a lower $\sigma_{\alpha'}^{L}$ than those indicated with yellow dots in Figure 133, using Equation (IV—18). After calculation, the initial flow stresses of martensite are respectively 1421 MPa for GL680, 1316 MPa for GL700, 1125 MPa for GL720 and 1510 MPa for GL750. Therefore, despite, having a lower $\sigma_{\alpha'}^{0}$, martensite in GL750 steel has a higher initial flow stress due to its higher f_T at the start of simulation.

During the tensile tests, f_T increases due to SIMT, and with it, the mean stress of martensitic phase. The transformed fraction f_T at experimental necking, indicated with purple points decreases when the stability of austenite in the studied steel increases. In GL680 steel, its value is 78%. It is 84% for GL700. In GL720 steel, the relative transformation rate reaches 93% at necking (it remains 2.8% of austenite among the initial 40%). A very close value of f_T = 94% is reached in GL750 steel. For GL720 and GL750 steels, this high value of f_T means that the very last transformed martensite bears a very

high yield strength (about 6400 MPa), corresponding maybe to a nano-twinned martensite. The concerned fraction is however very low.

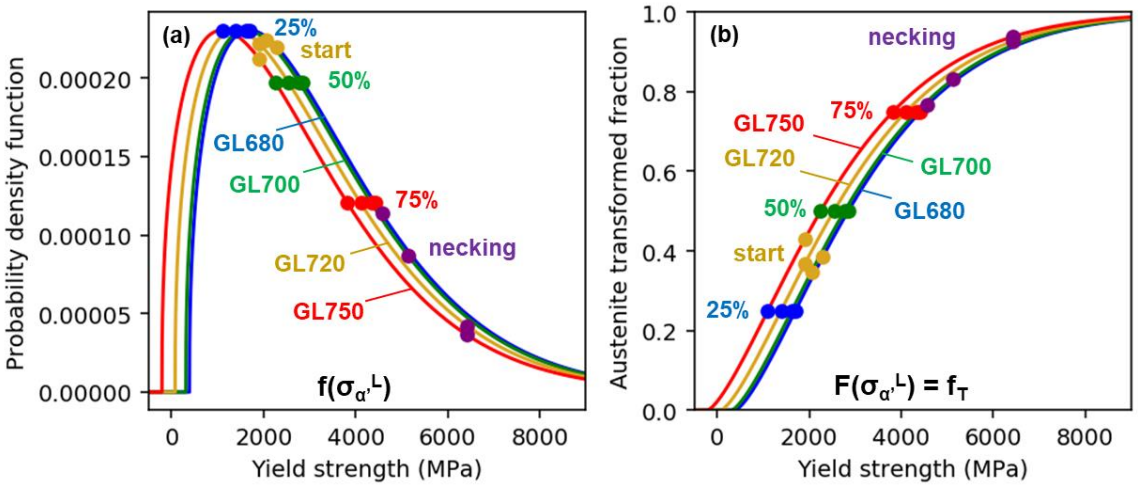

Figure 133: Evolution of the (a) density function and (b) cumulative function for the 4 globular microstructures. Dots have been added at given austenite transformed fraction. (blue: f_T=0.25; green: f_T=0.50; red: f_T=0.75). The yellow and purple points are respectively indicative of the experimental values of f_T at the start of the trial and at the necking onset.

The distributions and the cumulative density functions for the four fibrous microstructures are displayed in Figure 134. Their shapes are identical to the globular ones, though their $\sigma_{\alpha'}^0$ is a little lower for a given T_{IA}. The values of $\sigma_{\alpha'}^0$ are respectively 310 MPa for FB680, 180 MPa for FB700, -2 MPa for FB720 and -314 MPa for FB750. Those lower values compared with the globular equivalent T_{IA} microstructure is due to a lower amount of carbon in austenite. The value of f_T at the start of the simulation is however slightly higher, being around 39% for F680, FB700 and FB720 steels, and 45% for FB750. It is notable that for all 8 microstructures, a quasi-constant value of 35-40% of the austenite formed during intercritical annealing is transformed into fresh martensite upon final cooling during the thermal treatment. The values of f_T at necking (purple dots) are 77%, 84%, 93% and 94% for FB680, FB700, FB720 and FB750 steels respectively, very similar to those reached by their globular counterparts.

The physical origins of the distribution could be attributed to multiple contributions: distributions not only in local carbon contents between different MA islands, blocks sizes, but also in dislocations density and internal stresses [220]–[223]. An improvement to the current work would be to experimentally determine the distribution of each of those contributions using post-mortem techniques such as TEM and atom probe tomography. This work however exceeds the scope of this PhD thesis. Therefore, although being maybe too simple, the JMAK distributions presented in this section will be the one used in the next section to calculate the evolution of flow stress of the whole martensitic phase during deformation.

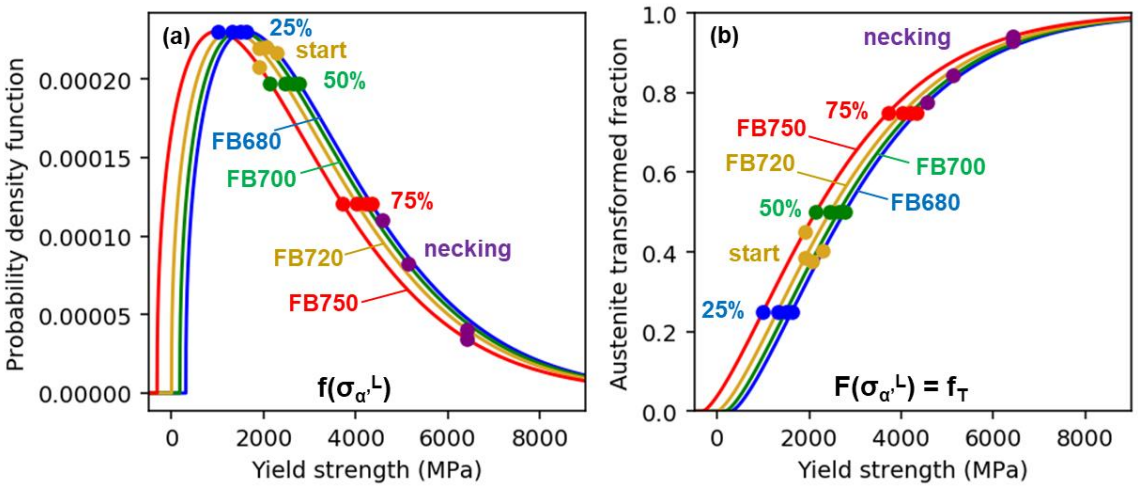

Figure 134: Evolution of the (a) density function and (b) cumulative function for the 4 fibrous microstructures. Dots have been added at given austenite transformed fraction. (blue: f_T=0.25; green: f_T=0.50; red: f_T=0.75). The yellow and purple points are respectively indicative of the experimental values of f_T at the start of the trial and at the necking onset.

b) Overall mechanical behaviour of martensitic phase

In the proposed model, the flow stress of martensite $\sigma_{\alpha'}$ is a function of the fraction of transformed austenite f_T only. As explained in the previous section, when austenite transforms due to SIMT, the newly formed martensite appears at a higher flow stress than the existing martensite in the aggregate. This creates an apparent mean work-hardening for the martensitic phase, as it is calculated by averaging the values of all martensite present in the microstructure. It is noteworthy that, in this model, $\sigma_{\alpha'}$ is independent from $\varepsilon_{\alpha'}$, the latter being calculated with iso-work hypothesis. In the next paragraphs, the martensitic aggregate will be called “martensite” for simplicity.

The flow stresses in martensite calculated in the eight simulations are compared for each morphology in Figure 135. For both morphologies, the apparent yield strength of martensite ($YS_{\alpha'}$) decreases with the increase in T_{IA} between 680°C and 720°C, and rises between 720°C and 750°C. The first diminution can be explained by a decrease of $\sigma_{\alpha'}^0$ while initial value of f_T remains constant. The rise of $YS_{\alpha'}$ between T_{IA} = 720°C and 750°C is explained by the increase of f_T at the start of simulation, and despite a still decreasing value of $\sigma_{\alpha'}^0$ with increasing T_{IA}. While the values of $YS_{\alpha'}$ are relatively close to one another for globular martensite, between 1125 MPa for GL720 to 1510 MPa for GL750, they are more dispersed for fibrous steels, between 785 MPa for FB720 to 1695 MPa for FB680. This diversity can be explained by the conjunction of a lower amount of carbon in austenite in fibrous microstructures compared with globular equivalent and a higher initial value of f_T.

After reaching $YS_{\alpha'}$, martensite flow stress increases for all microstructures. During yielding, the slope of the martensite flow stress curves mirrors the slope of the corresponding austenite phase fraction evolution curves, displayed in Figure 132. For microstructures intercritically annealed below 700°C, the martensite work-hardening rate is constant since the SIMT kinetics is quasi-linear. For microstructures annealed above 720°C, the work-hardening rate decreases when $\varepsilon_{\alpha'}$ increases. For each morphology, the highest work-hardening is observed for the microstructure produced at 720°C.

This is explained by the higher amount of retained austenite present in the microstructure before deformation for those steels. The highest work-hardening is observed for martensite in FB720 steel. Its flow stress increases by 1565 MPa between the beginning and the end of the simulation.

For globular steels, the martensite flow stress at experimental necking onset ranges from 2380 MPa to 2480 MPa. For FB700, FB720 and FB750, the martensite flow stress at necking is 2350 MPa, while that for FB680 martensite is 2070 MPa. This last low value can be explained by an early experimental necking onset for the FB680 steel. Fibrous martensite is always at least 100 MPa lower at necking when compared with the equivalent globular steel. However, it remains notable that for all steels except FB680, the martensite stresses at necking onset are between 2350 MPa and 2480 MPa, despite significant differences in density function parameters and in value of f_T at necking.

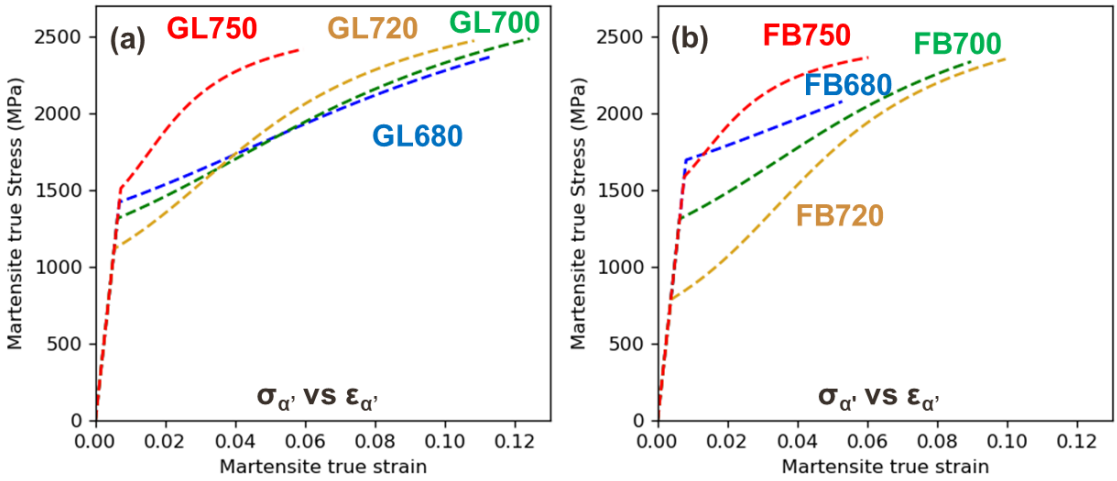

Figure 135: Comparison of the simulated flow stresses in martensite in globular microstructures (a) and in fibrous microstructures (b). The colour code corresponds to the annealing temperatures of the steels. Blue: T_{IA} = 680°C; green: T_{IA} = 680°C; yellow: T_{IA} = 720°C; red: T_{IA} = 750°C.

The simulated flow stress of martensite is compared with the experimental von Mises stress of martensite determined with inverse Hill's mixture rules in Figure 136. The experimental curves exhibit a wide range of mechanical behaviour. For both morphologies, the steels annealed below 700°C show very low or even no work-hardening, while the steels annealed above 720°C display high work-hardening rate. Despite the similar parameters used in the MIM model between the different microstructures, the simulated flow stress of martensite reproduces partially the trends of the experimental data. Indeed, the simulated work-hardening rates of GL680 and FB680 steels are lower than those of GL720 and FB720 steels, as experimentally observed

Concerning globular microstructures, the simulations match quantitatively well with the experimental data. For GL680 steel, the absolute error is initially of 600 MPa for GL680 steel until becoming 0 at necking. Similar observation is made for GL720 steel, for which the initial error is 200 MPa, and then reduces continuously until reaching 0 at necking. For GL700, despite some difference in the overall work-hardening rate, the error on stress is only 100 MPa at necking. It is for GL750 steel that the maximal error is reached for the globular microstructures. The simulation predicts a higher hardening for martensite below $\varepsilon_{\alpha'}$ = 1.2%. It is compensated by a lower hardening rate between $\varepsilon_{\alpha'}$ = 1.2% and 4%. Finally, between $\varepsilon_{\alpha'}$ = 0.4 and 12%, the experimental and simulated work-hardening rates match perfectly. The gap in final stress is 150 MPa for martensite in GL750 steel.

When comparing the simulation and experimental curves for fibrous steels, these differences are more obvious. For FB680, FB720 and FB750, the work-hardening rate is well modelled after few percent of deformation. However, there is a very huge difference in the absolute level of flow stress. The difference at necking is 350 MPa for FB680, FB720 and FB750. For FB700, the error reaches 620 MPa. Except for FB680 steel, the model always predicts better performance than what is experimentally observed for the fibrous martensite.

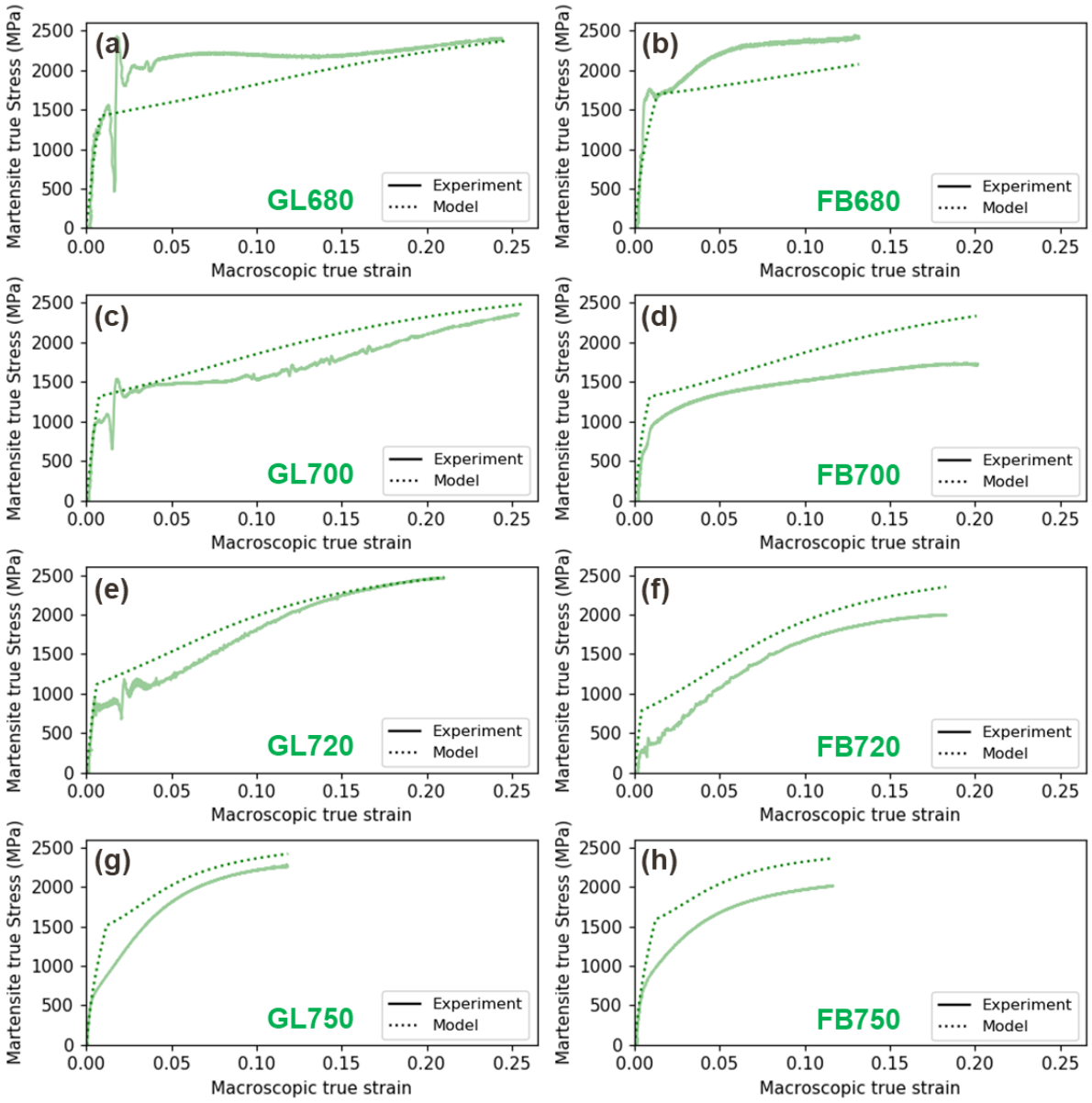

Figure 136: Comparison between the simulated flow stress (dotted line) and the experimental von Mises stress (solid line) in martensite for (a) GL680, (b) FB680, (c) GL700, (d) FB700, (e) GL720, (f) FB720, (g) GL750, (h) FB750 Steels. The stresses in martensite are shown as a function of ε_{macro}.

This apparently huge discrepancy is to be relativized with the mechanical behaviour predicted by other tested mean field models (see Figure 124) found in the literature [12], [18], [100], [126]. Moreover, by optimizing each parameter individually for each microstructure, the MIM model could have reproduced more closely the martensite experimental stress. This is not the choice made in this PhD work, since not enough microstructure related information is known (laths size, dislocation density, presence of carbide, carbon distribution). As explained in Chapter 3, another explanation of

this discrepancy could be found in the experimental precision of the determination of martensite von Mises stress.

Overall, the model can predict the mechanical behaviour of martensite in the globular steels. However, the model overestimates the mechanical performance of fibrous martensite in a non-negligible way. This difference could be alleviated by calibrating the model on each experiment individually, which is not the choice made here. This discrepancy may be indicative of a theoretical lack of understanding of martensite mechanical behaviour in these steels. It is notable that for all simulations, the martensite flow stress at necking is around 2400 MPa, which is consistent with our experimental findings in the globular steels and corresponds to the strength expected in fully martensitic steels with a nominal carbon content of about 0.6 C [51]. The identical value of $\sigma_{\alpha'}$ at necking is the reflection of the staggered values of f_T at necking.

Therefore, quantifying both thermal martensitic transformation and SIMT is very important to understand the mechanical behaviour of martensite.

The satisfactory description of ferrite, austenite and martensite flow stress evolution alongside that of the SIMT kinetics allows to reconstruct the macroscopic stress and strain of medium Mn steels, as presented in the next section.

E. Overall mechanical behaviour of medium Mn steels

The calibration of the model has been done independently of the macroscopic behaviour of medium Mn steels. Only the ferrite, austenite, martensite von Mises stresses, alongside the experimentally determined SIMT curves have been used in the parametrization process, as the macroscopic response of the model is not directly calculated (no equation for σ_{macro} as a function of ε_{macro}).

With the description of evolution of stress and strain in each phase and phase fractions, it is possible with the Hill's mixture law and the iso-work hypothesis to calculate the overall mechanical behaviour of the whole medium Mn steel. The macroscopic stress σ_{macro} calculated are compared for each morphology in Figure 137. For steels annealed below 720°C, an equivalent to the experimental Lüders plateau is obtained by the simulation. This plateau is more pronounced for the globular steels than for the fibrous ones. During yielding, the work-hardening rate, alongside the stress at the end of the simulation increases with increasing annealing temperature. The experimental trend is thus recovered (see Table 13 from section III.4.A).

Comparing level of stress between steels with the same T_{IA}, macroscopic stresses are lower in the fibrous steels than in the globular microstructures below T_{IA} = 700°C. Indeed, between FB680 and GL680 steels, and between FB700 and GL700 steels, there is a quasi-constant gap of 80 MPa after ε_{macro} = 0.04. For microstructures annealed at 720°C, the fibrous steel is initially softer, with a gap of 70 MPa between FB720 and GL720 at ε_{macro} = 0.03. However, this gap reduces continuously during deformation until reaching 10 MPa at ε_{macro} = 0.18. For microstructures annealed at 750°C, the fibrous steel is 90 MPa stronger than the globular one during the whole yielding. Experimentally, it is found in Chapter III that the fibrous steels are always softer than the globular ones, independently of the strain and the intercritical annealing temperature. Therefore, the model partially reproduces experimental findings.

This only partial agreement can be understood by the modelled flow stress in martensite which is not in agreement with the experimental data for the fibrous steels, as discussed in the previous section.

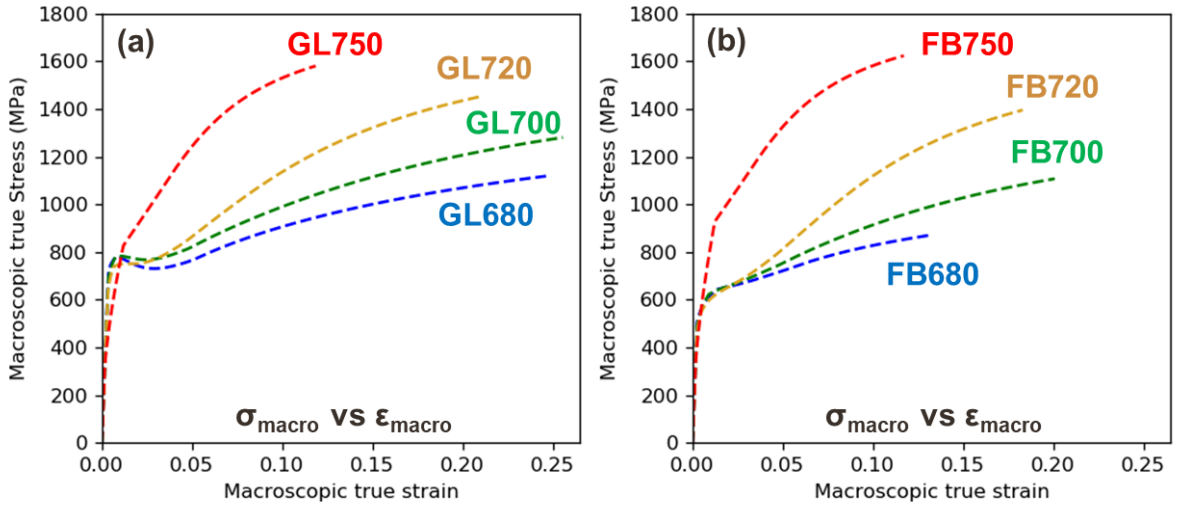

Figure 137: Comparison of the simulated macroscopic true tensile curves in globular microstructures (a) and in fibrous microstructures (b). The colour code corresponds to the annealing temperatures of the steels. Blue: T_{IA} = 680°C; green: T_{IA} = 680°C; yellow: T_{IA} = 720°C; red: T_{IA} = 750°C.

The comparison between the calculated (dotted lines) and experimental (solid lines) tensile curves is shown in Figure 138. For globular steels, the simulations match particularly well with the experimental data. At the experimental necking strain, the relative error on the true stress is inferior to 4% for all globular steels. For GL680, GL700 and GL720 steels, it is expected to have a good prediction since ferrite, austenite and martensite flow stresses are all well estimated at necking, alongside the fractions of austenite and strain-induced martensite. However, for GL750 microstructure, the modelled fractions match the experimental ones at necking, since the simulated flow stress of martensite is overestimated while those of ferrite and austenite are slightly underestimated. Therefore, the good modelling of the mechanical behaviour of GL750 medium Mn steel is due to the conjunction of two deviations. Work-hardening is also very accurately reproduced for those four steels, especially for GL720 steel. For the fibrous microstructures, the results are more mitigated. The relative errors for FB680, FB700, FB720 and FB750 steels are respectively 2%, 10%, 9% and 12%. Even if the work-hardening is well modelled for FB680, it is slightly overestimated for all other fibrous steels.

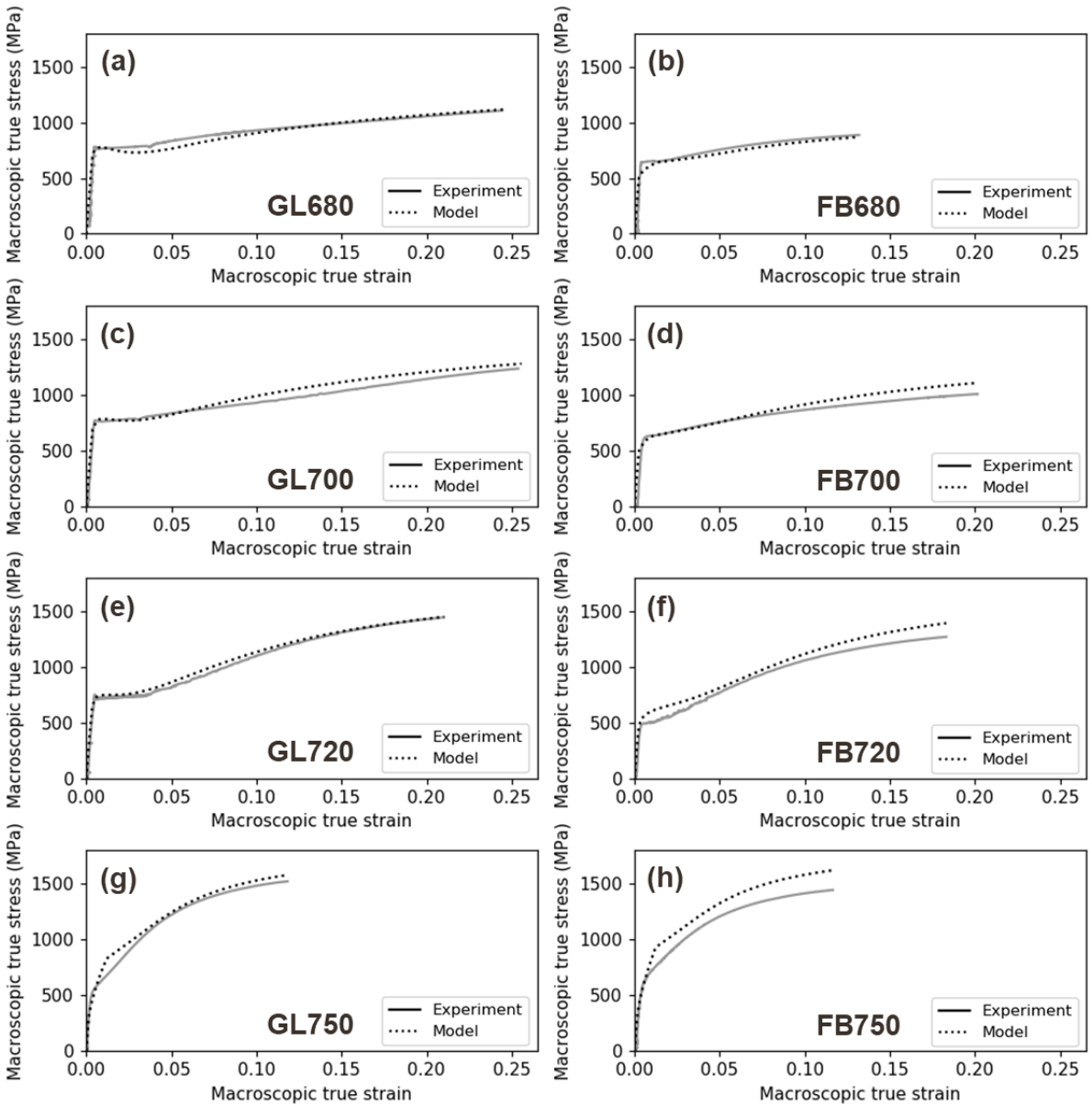

Figure 138: Comparison between the simulated (dotted line) and experimental (solid line) true tensile curves for (a) GL680, (b) FB680, (c) GL700, (d) FB700, (e) GL720, (f) FB720, (g) GL750, (h) FB750 steels respectively.

To know if the current model is able to predict the mechanical behaviour of medium Mn steels at necking, especially their ultimate tensile strength (UTS) and uniform elongation (UEL), it is necessary to use a necking criterion. The Considère's criterion is employed here, as it is the most widely used [185]. It states that necking occurs when the relative increment in true stress becomes inferior to the relative decrement in cross-sectional area. This condition is equivalent to when the work-hardening rate $\Theta_{macro} = d\sigma_{macro}/d\varepsilon_{macro}$ becomes inferior to σ_{macro}.

The simulated work-hardening rate and macroscopic stress are compared in Figure 139 for GL700, GL720 and GL750 steels. The corresponding experimental tensile curves are also reproduced, with their last point being the experimental necking. The other medium Mn steels' work-hardening curves are not given here as they are very similar to those presented in Figure 139. FB680, GL680 and FB700 steels are similar to GL700. FB720 is similar to GL720 and FB750 to GL750. For GL700 and GL720 steels, Θ_{macro} is only plotted after Lüders plateau. The three work-hardening curves show a hill shape,

typical of TRIP-aided steels [12]. TRIP effect is far more efficient in GL720 specimen than in both GL700 and GL750 steels, for which less strain-induced martensite is formed during deformation. Moreover, in GL750 microstructure, there is a high amount of initial fresh martensite, whose high initial work-hardening rate hides the dynamic work-hardening due to TRIP effect.

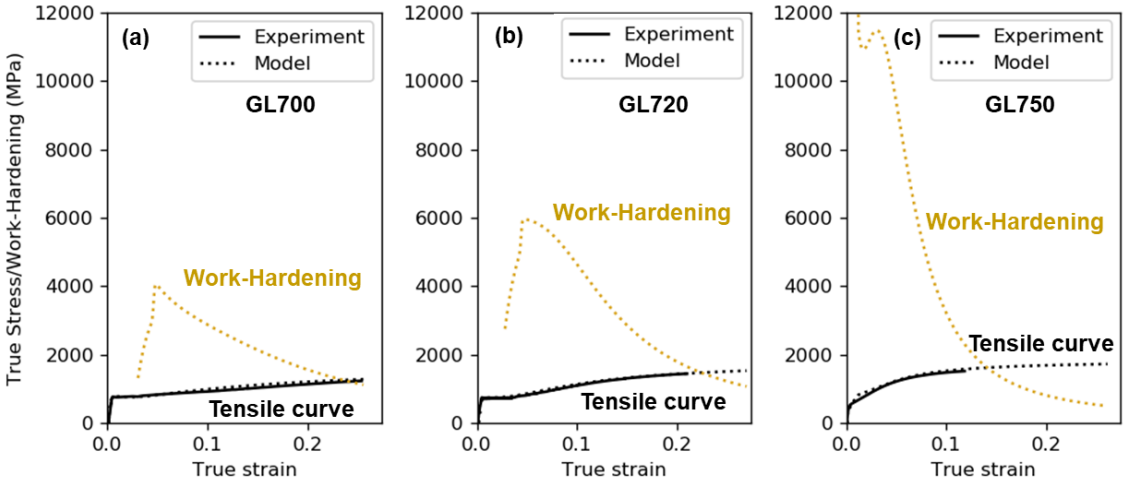

Figure 139: Comparison between the experimental true stress (black solid line), the true stress calculated by the model (black dotted line) and the model work-hardening rate (yellow dotted line).

With Considère's criterion, it is possible to obtain the true stress and true strain at necking onset from the model. These values can serve to calculate conventional quantities such as the UTS and the UEL of the steel using Equation (III—2). The values of UTS and UEL predicted by the model (dotted line) are compared with the experimental ones (solid line) in Figure 140 for the globular and fibrous steels. The modelled trends replicate well the experimental ones. For both morphologies, the UTS increases with increasing T_{IA}, and the UEL curve as a function of T_{IA} presents an inverse U-shape curve with a maximum at T_{IA} = 700°C. The prediction of the macroscopic UTS for the globular steels is especially good, with a relative error of 2.5% in average. The error on the predicted UTS is higher for the fibrous steels, being in average 10%. The prediction of UTS is better than that of UEL. Indeed, the averaged relative error on UEL is 10% for the globular steels and 14% for the fibrous steels. Except for the UEL of GL680 and GL700 steels, all UTS and UEL are overestimated by the model. This overperformance of the model is mainly explained by the flow stress of martensite which is superior in the model for most of the steels in this thesis. Overall, the mean field micromechanical model reproduces very well the macroscopic mechanical behaviour of medium Mn steels, despite the wide variety of encountered microstructures.

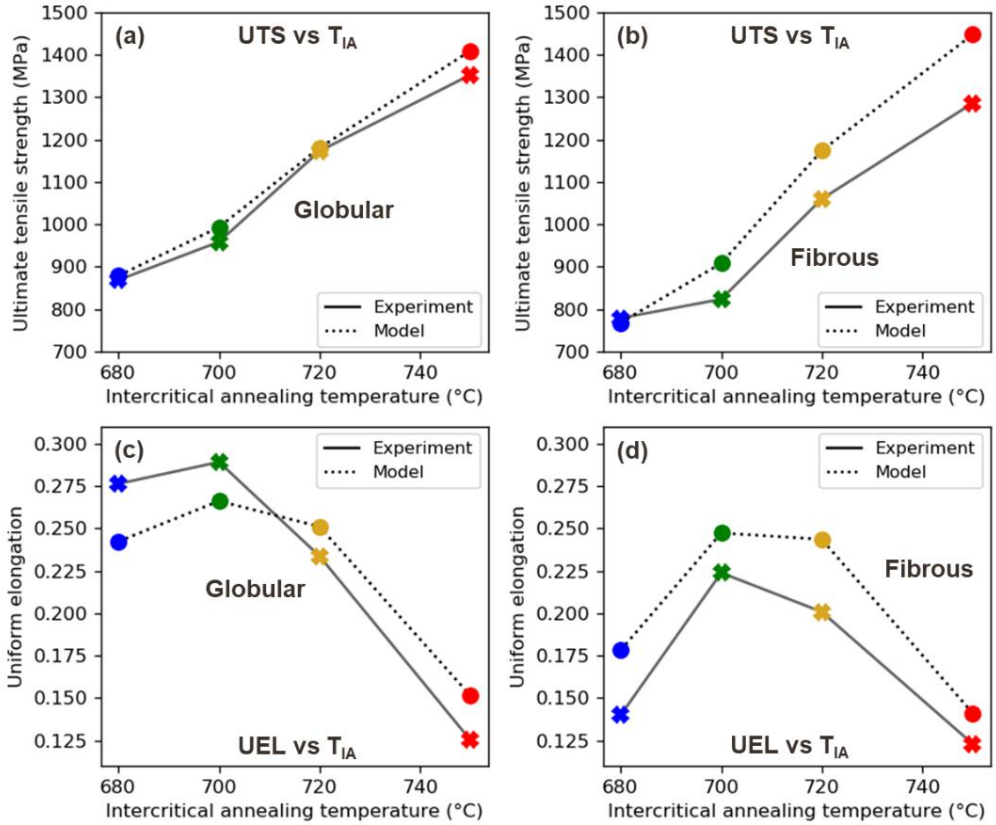

Figure 140: Comparison between the experimental (solid line) and predicted (dotted line) ultimate tensile strength of the globular (a) and fibrous (b) steels. Comparison between the experimental (solid line) and predicted (dotted line) uniform elongation of the globular (c) and fibrous (d) steels. Points indicate the values determined in the steels annealed at T_{IA} = 680°C, 700°C, 720°C and 750°C respectively.

In the last sections, the results of the mean field micromechanical model are presented and discussed for the eight microstructures in the thesis. The studied medium Mn steels are in fact triplex steels, containing ferrite, austenite and martensite. In these steels, the microstructure varies widely, with different phase fractions, grain sizes and phase compositions. Despite having a minimal number of parameters fitted on the experimental data presented in Chapter III, the simulations match well the synchrotron data. The flow stresses of ferrite and austenite, as a function of their alloying contents and mean grain size, are successfully modelled. As classical dislocation-driven models are not appropriate to describe martensite, a new MIM model is proposed, inspired by CCA model used for as-quenched martensite. When compared with the experimental flow stress of martensite, the MIM is adapted to reproduce the observed mechanical behaviour of globular martensite. However, some refinements on the MIM model are still necessary to appropriately simulate the fibrous martensite. The thermodynamic description of strain-induced martensitic transformation proposed in this work allows for an accurate description of SIMT kinetics in medium Mn steels, as a function of austenite intrinsic properties. Using iso-work hypothesis and Hill's mixture rules, the macroscopic mechanical behaviours can be deduced from the micromechanical model. The calculated results are consistent with those obtained with in situ tensile tests, especially for the globular specimens. The model can be used to predict UTS and UEL for medium Mn steels with a relative error inferior to 10% for UTS and 15% for UEL. The next sections will be dedicated to supplementary discussions and analysis allowed by the micromechanical model.

4. Discussions

A. Stress and strain partitioning among phases

With HEXRD experiments, it is possible to determine stress partitioning among phases at each step of the tensile deformation. It is revealed that martensite flow stress is superior to that of austenite, which is superior itself to that of ferrite. The modelled flow stresses follow the same trend for stress partitioning in all experiments. Moreover, with the mean field model, it is possible to obtain information on strain partitioning, which is not possible experimentally.

In Figure 141, the flow stresses of ferrite (red), austenite (blue) and martensite (green) are compared with the simulated macroscopic stresses (black) for (a) GL680, (b) GL700, (c) GL720 and (d) GL750 steels respectively. The flow stress of each phase is displayed as a function of its corresponding phase strain. The macroscopic stress is plotted as a function of the macroscopic strain. The dotted grey lines are iso-work lines at a given macroscopic strain (ε_{macro} = 0.05, 0.10 or 0.15). For a given ε_{macro}, the corresponding ε_{α}, ε_{γ}, and $\varepsilon_{\alpha'}$ are respectively indicated in red, blue and green. For example, in the GL680 simulation, when the macroscopic strain ε_{macro} = 5% is reached, ferrite strain is 5.4%, austenite strain is 4% and martensite is deformed only 2.5%. Usually, in the simulations, iso-work curves are affine lines [18]. However, in the current case, the iso-work curves show some inflexions, which is due to the continuous SIMT occurring all along the simulation.

With iso-work hypothesis, when a phase has a higher level of flow stress, it deforms less. Thus, it is expected that for a given level of macroscopic strain, martensite strain will be lower than that of austenite, the latter being lower than that of ferrite. This is indeed what is observed on every iso-work line. In the globular simulations, ferrite strain is always higher while that of martensite is always lower than the macroscopic strain. For GL680 and GL700 steels, austenite is nearly always stronger than the macroscopic behaviour of the steel. Its strain is thus always lower than the macroscopic strain. The contrary is true in the case of GL750 steel. In GL720 steel, the austenite strain is lower than the macroscopic one until ε_{macro} = 16%. After that value, austenite strain becomes higher than the macroscopic one. For a given ε_{macro}, austenite and ferrite strains at this ε_{macro} increase when the microstructure formation temperature T_{IA} increases.

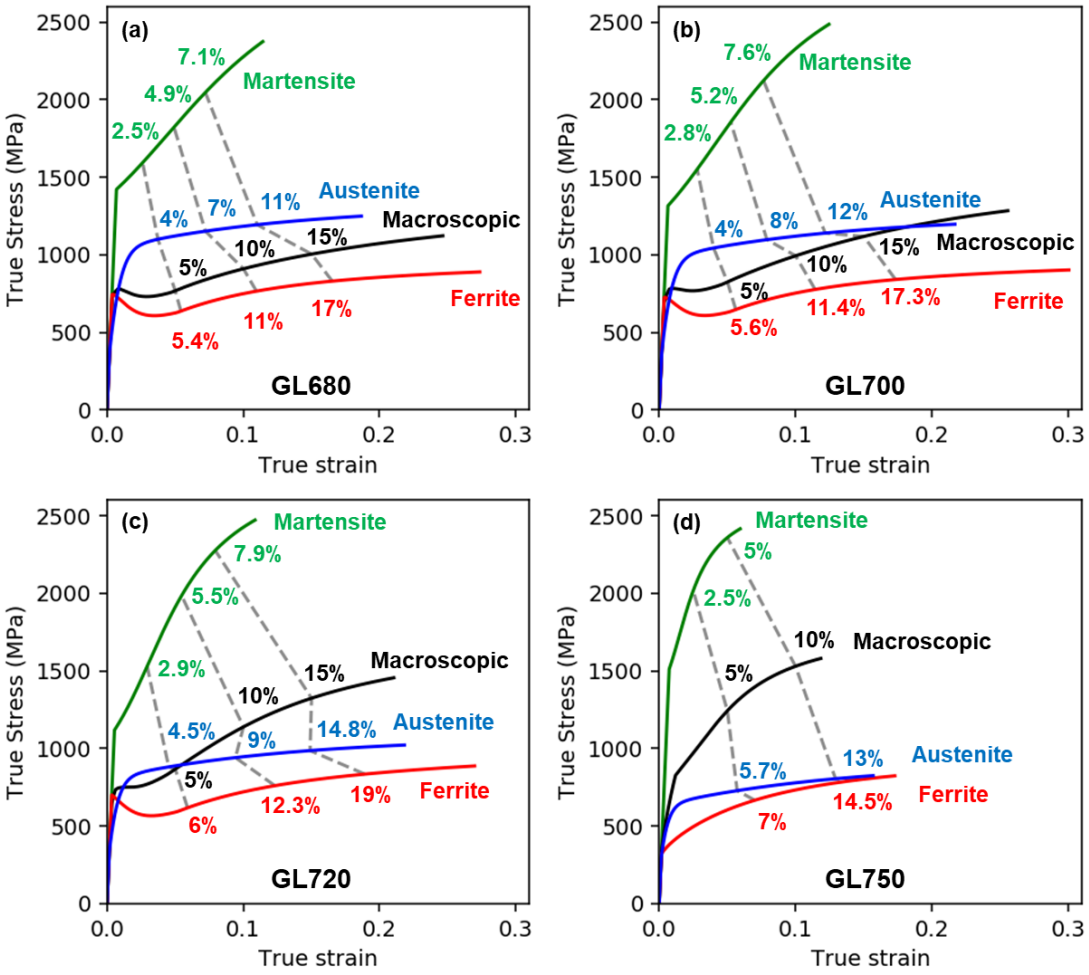

Figure 141: Stress model results (continuous line) for ferrite (red), austenite (blue), martensite (green) and macroscopic stress (black) for (a) GL680, (b) GL700, (c) GL720 and (d) GL750 steels respectively. Simulations end at the experimental necking onset. All the phase stresses are plotted as a function of their respective phase strains. The dotted grey lines indicate strain partitioning among phases at a given macroscopic strain (ε_{macro} = 0.05, 0.10 or 0.15). Values of phase strains for a given ε_{macro} are indicated with the same colour as the flow stress curve.

The flow stresses of ferrite (red), austenite (blue) and martensite (green) are compared with the simulated macroscopic stress (black) for the fibrous steels in Figure 142. Very similar remarks made for the globular steels can be made for the fibrous steels. For a given ε_{macro}, ferrite and austenite strains increase when the annealed temperature T_{IA} increases.

In the current model framework, martensite strain increases between T_{IA} = 680°C and 720°C, and then decreases between steels intercritically annealed at 720°C and at 750°C. The first increase is more pronounced in the case of globular martensite. GL720 deforms 50% more quickly than GL680 martensite. The level of martensite strain at necking is $\varepsilon_{\alpha'}$ = 6% for FB680 and FB750, and is 9% for FB700 and FB720. Therefore, martensite deforms less in the fibrous steels than in the globular ones. This can be attributed to the softer ferrite and softer austenite, which bears more strain in comparison, and the lower amount of austenite in FB680 and FB700 steels when compared with their globular counterparts. However, the interpretation of martensite strain should be done with caution since the level of stress in martensite bears lot of uncertainty.

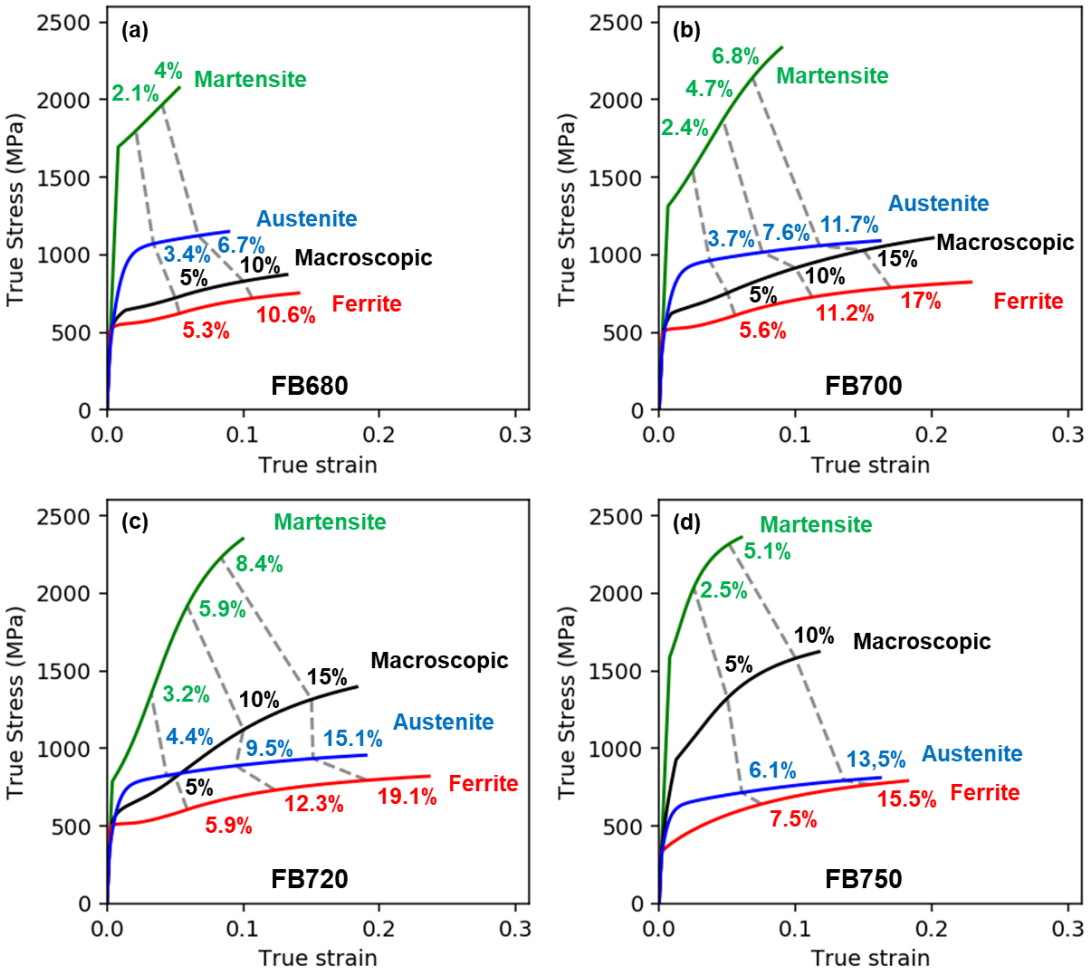

Figure 142: Stress model results (continuous line) for ferrite (red), austenite (blue), martensite (green) and macroscopic stress (black) for (a) FB680, (b) FB700, (c) FB720 and (d) FB750 steels respectively. Simulations end at the experimental necking onset. All the phase stresses are plotted as a function of their respective phase strains. The dotted grey lines indicate strain partitioning among phases at a given macroscopic strain (ε_{macro} = 0.05, 0.10 or 0.15). Values of phase strains for a given ε_{macro} are indicated with the same colour as the flow stress curve.

B. Dependence of austenite mechanical stability on austenite size and alloying contents

In the current modelling of SIMT, two properties of austenite play a role in defining its mechanical stability: its chemical composition and its grain size. To compare both contributions and how they differ in the frame of the current model, it has been decided to simulate alternative scenarios based on the GL720 microstructure. This microstructure is chosen since it has a high amount of retained austenite before deformation and its austenite has a grain size and a carbon content near the mean value when compared with other medium Mn microstructures. Its estimated austenite carbon content is C_γ = 0.51 wt% ant its austenite grain size is d_γ = 0.79 µm. Conserving all other quantities and parameters, in the first set of scenarios, it is decided to test what happens when the carbon content is increased/decreased by 0.2% and 0.4%. In the second set of scenarios, keeping C_γ = 0.51 wt%, it is chosen to increase/decrease austenite grain size d_γ by 0.2 µm and 0.4 µm.

The evolution of austenite phase fraction simulated in the first and second sets of scenarios are respectively reproduced in Figure 143 (a) and Figure 143 (b). For both figures, the reference scenario is indicated by the black solid line. Each simulation ends at the same macroscopic strain of 21%, which is the measured true strain at necking for GL720 steels. The value of ε_γ at the end of the simulation changes between scenarios, since both carbon content and grain size of austenite also affect the flow stress level in austenite and martensite. Please not that in a realistic microstructure, changing the carbon content of austenite would have change the phase fractions, which has not been considered in the simulations. The discussed microstructures are thus not necessarily realistic.

The stabilizing effect of carbon is clearly visible from the simulation results. For a given level of strain in austenite, the fraction of austenite remaining in the microstructure is higher when C_γ is higher than in the reference and conversely when C_γ is lower. In the same way, the stabilization effect of grain size reduction is apparent. For a given ε_γ, the fraction of retained austenite is higher when the grain size is smaller.

The model reveals that for sub-micrometric microstructures such as in medium Mn steels, grain size has more stabilizing effect on austenite than carbon content, in the sense that dividing by two the grain size (from 0.79 µm to 0.39 µm) stabilizes austenite far more than nearly doubling the carbon content (from 0.51%C to 0.91%C). When d_γ is 0.39 µm, the fraction of austenite at the end of the simulation is 14%, while when C_γ is 0.91%, the final fraction is 6.85%. On the other hand, dividing by four the carbon content of austenite (from 0.51%C to 0.11%C) stabilizes less the austenite than multiplying by 1.5 the grain size (from 0.79 µm to 1.19 µm). When d_γ is 1.19 µm, the fraction of austenite at the end of the simulation is 1.47%, while when C_γ is 0.11%, the final fraction is 1.60%. Therefore, in medium Mn steels, according to this alloy design exercise, it is more crucial to control the austenite grain size to obtain mechanically stable austenite than to partition carbon into austenite.

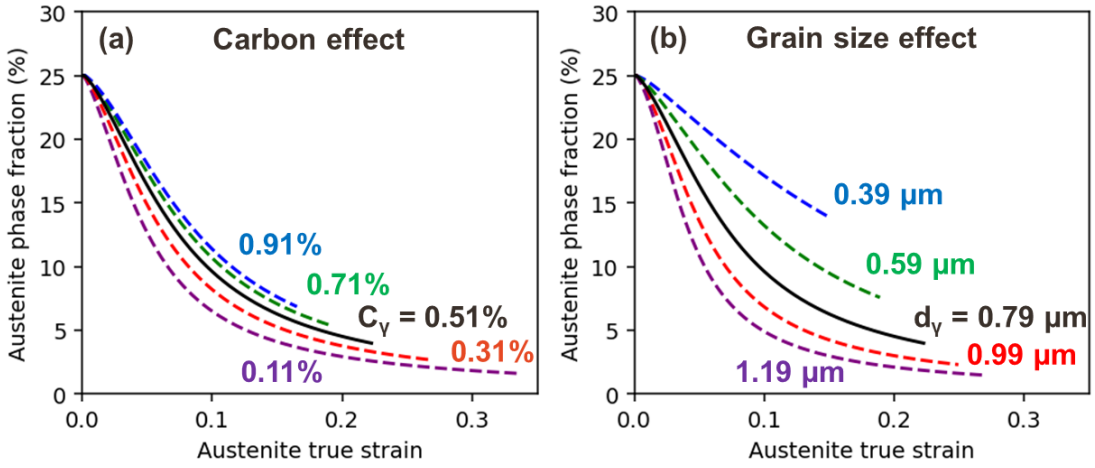

Figure 143: (a) Comparison of the evolution of austenite phase fractions in GL720 steel when the carbon content of austenite C_γ is modified. (b) Comparison of the evolution of austenite phase fractions in GL720 steel when the grain size of austenite d_γ is modified. For (a) and (b), the black solid curve corresponds to the reference simulation, when C_γ and d_γ are at their real values.

The slowing effect of grain size on the SIMT kinetics is due to the specific form of the constitutive SIMT equations. Without the dependence of the martensite lath volume on d_γ, no stabilizing effect of d_γ on austenite would be observed. Three supplementary simulations are conducted to test some hypotheses made on the constitutive laws described in section IV.1.C and the

resulting SIMT kinetics are indicated in Figure 144 and compared with the reference kinetics. The first test is on the autocatalytic nature of the transformation. The autocatalytic factor λ is neglected in the simulation. The corresponding kinetics is displayed in blue and denoted λ = 0. The autocatalytic factor controls mainly the initial slope of the kinetics. Neglecting it makes the SIMT kinetics very slow at the beginning, which is not what is experimentally found. Compensating the absence of autocatalytic transformation by increasing the initial density of nucleation site I_0 makes the slopes better in the beginning but also drastically increases it at higher strains, which conducts to premature consumption of retained austenite. Moreover, despite not being shown here, accounting for the dependence of the autocatalytic factor λ on the austenite initial grain size d_γ^0 is very necessary to obtain the good initial slope for the kinetics of each globular and fibrous steels.

The second tested scenario is not taking the martensite laths volume $V_{\alpha'}$ proportional to $d_\gamma = d_\gamma^0(1-f_{SIM})$, but only to d_γ^0. The resulting kinetics is reproduced in red in Figure 144, and is denoted $V_{\alpha'} = C^{st}$. When compared with the reference kinetics, the slopes are very similar during the first 4% of deformation. After that, the austenite phase fraction plummets to 0. Therefore, taking $V_{\alpha'}$ proportional to d_γ is necessary to slow down the transformation kinetics at higher strain.

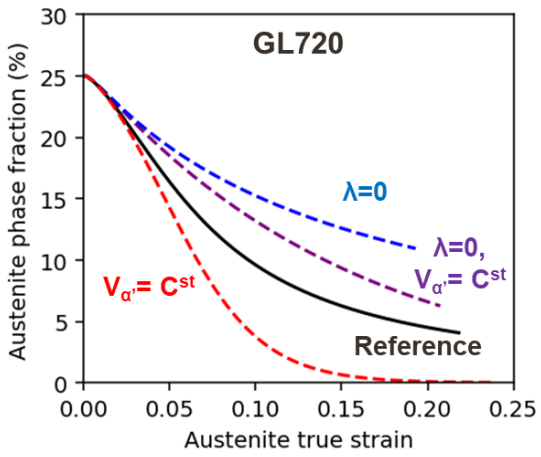

Figure 144: Evolution of the SIMT kinetics for the GL720 steel when the model is modified. The black solid curve is the reference simulation. The blue curve (λ = 0) corresponds to the absence of autocatalytic transformation. The red curve ($V_{\alpha'} = C^{st}$) corresponds to a simulation where the volume of martensite remains constant across the simulation, calculated as $V_{\alpha'} = S_\alpha d_\gamma^0$. The purple curve corresponds to the superposition of the two precedent modifications to SIMT constitutive laws.

The last scenario tested is a combination of the two precedent effects. Its result is shown in purple. In this case, the austenite phase fraction does not converge to 0. However, the transformation kinetics is quasi-linear. This is well understood as there are no retroactive effect of transformation advancement or grain size diminution to alter the slope of the transformation. Therefore, it is important to have λ ≠ 0 to obtain different curvatures for the SIMT kinetics. On the other end, the evolution of $V_{\alpha'}$ as a function of d_γ is thus very important to give the austenite grain size a stabilizing role when it decreases.

C. Isotropic and kinematic contributions to the overall phase behaviour

It is demonstrated in section IV.3.A that ferrite flow stress is constant between steels having the same morphologies, even when the annealing temperature is different. This result is not a priori obvious, since ferrite grain size evolves with T_{IA}. The flow stress of ferrite σ_α is calculated in the model by summing four components: the friction term σ_α^0 which is constant during deformation and only dependent on ferrite composition, the isotropic contribution σ_α^R and kinematic contribution σ_α^X to work-hardening, and the contribution of static strain aging σ_α^{SSA}. The decomposition of ferrite flow stress in these four components is detailed in Figure 145 for GL680 and GL720 steels. The friction term σ_α^0 (blue curve) does not evolve during deformation, and has a similar value between the two simulations, since the alloying contents of ferrite do not change significantly with T_{IA}. The SSA term σ_α^{SSA} (purple curve) is very similar between the two steels and has a high initial value of around 400 MPa. It quickly decreases, and after ε_α = 5%, it stagnates at a value near 0 MPa. Therefore, as previously stated in this chapter, σ_α^{SSA} does not affect work-hardening rate after the Lüders plateau. Finally, the isotropic (red) and kinematics (green) contributions are quite different between simulations. In GL680 steel, the isotropic component σ_α^R is higher than the kinematic component σ_α^X. Moreover, they increase at very similar rate with ferrite deformation. In GL720 steel, the isotropic hardening is lower than the kinematical hardening after ε_α = 5%, σ_α^R increases with a constant slope. The σ_α^X term increases more rapidly and reaches 400 MPa in the GL720 simulation. The difference in the behaviours of σ_α^R and σ_α^X between the two steels is solely explained by the lower ferrite grain size in GL720 steel. It seems however that the decrease of σ_α^R with decreasing grain size is compensated by the increase of the kinematic component σ_α^X, making the overall flow stress σ_α independent from the ferrite grain size in the range observed in the studied medium Mn steels.

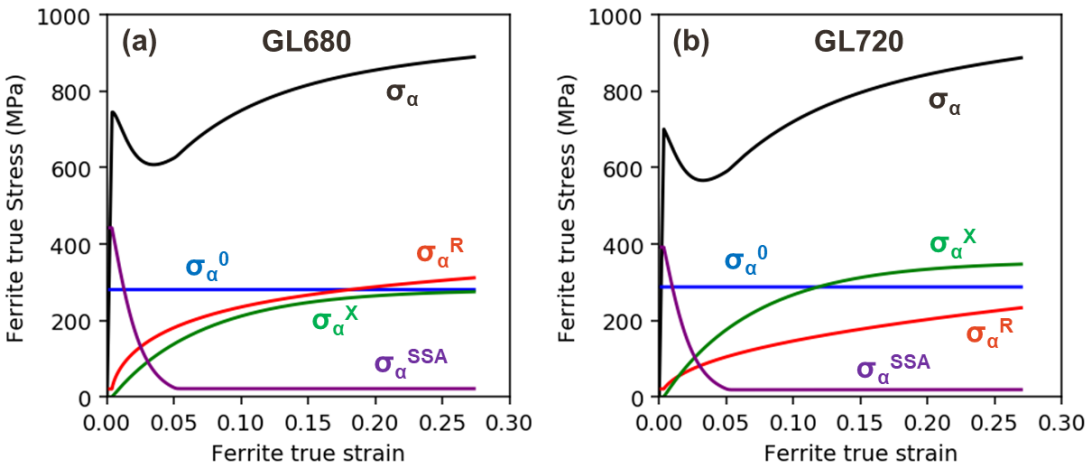

Figure 145: Decomposition of the flow stress of ferrite σ_α (black) into different components: friction term σ_α^0 (blue), isotropic hardening term σ_α^R (red), kinematic hardening term σ_α^X (green) and static strain aging term σ_α^{SSA} (purple), for (a) GL680 steel and (b) GL720 steel.

The flow stress of austenite is also described with dislocation-driven laws. Contrary to ferrite, it is proven in section IV.3.B that the flow stress of austenite decreases when its formation temperature T_{IA} increases. The decomposition of the austenite flow stress σ_γ into the friction stress σ_γ^0, the isotropic contribution σ_γ^R and the kinematic contribution σ_γ^X is detailed in Figure 146 for GL680 and GL720 steels. The friction stress σ_γ^0 is higher in the GL680 simulation, which is expected since austenite has more

carbon in this steel. The austenite isotropic stress σ_γ^R is very similar between the two microstructures and it increases continuously during the whole deformation process. The kinematic term σ_γ^X is very different between the two steels. In the two simulations, it goes from 0 MPa to a saturation value after 3% of austenite deformation. The saturation values are about 600 MPa in the GL680 steel and 400 MPa in the GL720 steel. The difference is explained by the different austenite grain sizes between the two microstructures. The decomposition of σ_γ highlights that the difference in austenite mechanical behaviour between simulations is explained solely by σ_γ^0 and σ_γ^X terms, which are constant after ε_γ = 3%. Afterwards, the austenite work-hardening is only controlled by σ_γ^R. As the isotropic contribution is very similar between different microstructures, it explains that all the studied austenite has a same work-hardening rate, independently from the initial austenite size and chemistry.

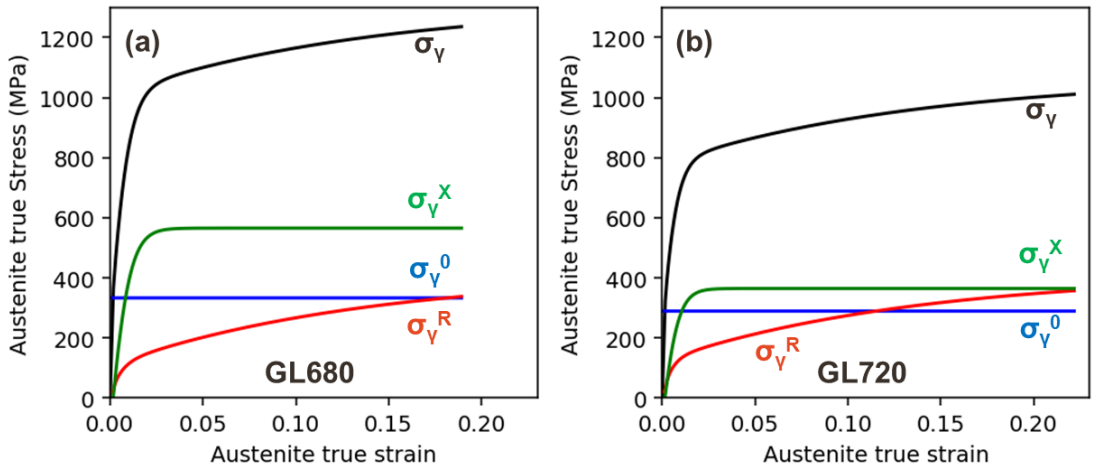

Figure 146: Decomposition of the flow stress of austenite σ_γ (black) into different components: friction term σ_γ^0 (blue), isotropic hardening term σ_γ^R (red) and kinematic hardening term σ_γ^X (green), for (a) GL680 steel and (b) GL720 steel.

D. Relationship between martensite mean stress, mean strain and SIMT

One noticeable implication of the model is that the stress inside martensite is independent from its strain, contrary to what is usually envisioned in mean field micromechanical modelling. It only depends on SIMT kinetics. To better understand this relationship, the simulation has been altered to create two alternative scenarios to correct the simulation of GL720 steel presented before.

In the first alternative scenario, the increment of nucleation sites dN_{SIM} appearing in Equations (IV—20) and (IV—24) has been multiplied by 4 at each step of the simulation. This makes the SIMT kinetics four times faster. This first alternative simulation is denoted “Fast SIMT”. The second alternative scenario is obtained by dividing dN_{SIM} by four, and is denoted “Slow SIMT”. In all scenarios, f_T starts at 36%. For the “Normal SIMT” case, the final fraction f_T = 93% is reached at a strain $\varepsilon_{\alpha'}$ = 0.13. Comparatively, the “Fast SIMT” kinetics reaches this value at $\varepsilon_{\alpha'}$ = 0.03, and reaches f_T = 99% at $\varepsilon_{\alpha'}$ = 0.11. The maximum transformed fraction reached by the “Slow SIMT” kinetics is 65% at $\varepsilon_{\alpha'}$ = 0.16.

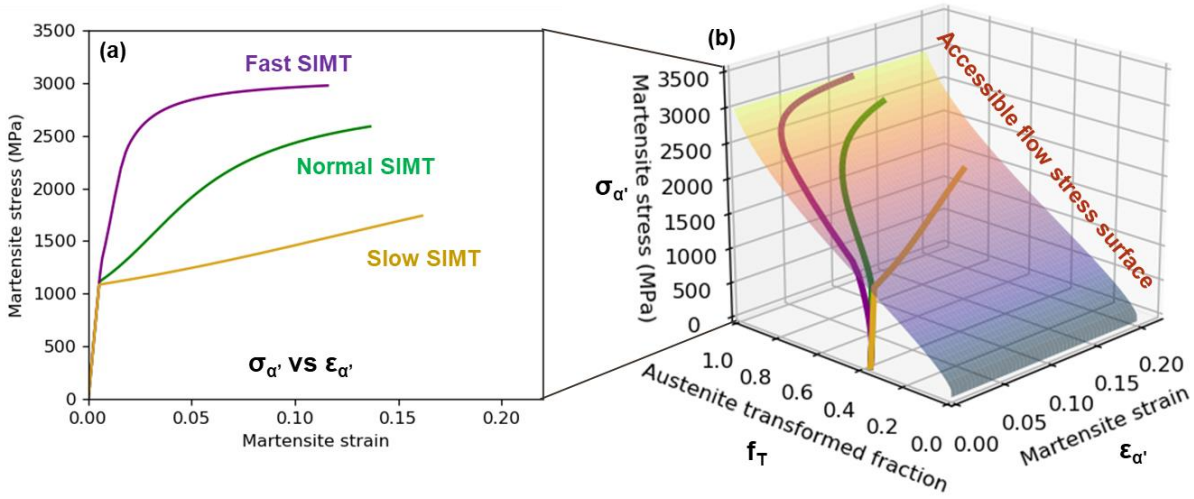

Figure 147: (a) Model $\sigma_{\alpha'}$ vs $\varepsilon_{\alpha'}$ curves for the GL720 microstructure for the three tested SIMT kinetics (Slow: yellow; Correct: green; Fast: purple). (b) 3D surface of accessible flow stress for martensite $\sigma_{\alpha'}$ as a function of its strain $\varepsilon_{\alpha'}$ and the fraction of transformed austenite f_T. The 3 curves from (a) have been plotted in 3D space by adding their dependence on f_T. After elastic domain, the curves are superimposed to the master surface.

The calculated $\sigma_{\alpha'}$ vs $\varepsilon_{\alpha'}$ curves between scenarios are compared in Figure 147 (a). It should be emphasized that the similar curves plotted for ferrite or austenite would only result in superimposed stress. In the "Slow SIMT" scenario, the work-hardening of martensite is lower and it is relatively soft. On the contrary, the "Fast SIMT" martensite has a tensile curve similar to that found for as-quenched martensite [212], with a very high work-hardening rate. In the three simulations, $f(\sigma_{\alpha'}^{L})$, $F(\sigma_{\alpha'}^{L})$ and $F^{-1}(f_T)$, defined in Equations (IV—16) and (IV—17) remain constant. Therefore, for a given fraction of transformed austenite f_T, the stresses in martensite in the three scenarios are the same and is given by Equation (IV—18). The tensile curves shown in Figure 147 (a) have been plotted in ($\varepsilon_{\alpha'}$, f_T, $\sigma_{\alpha'}$) 3D space, in Figure 147 (b). The surface defining the accessible flow stress has also been displayed.

This surface corresponds to the flow stress that martensite can reach for a given fraction f_T. The stress in martensite can be below the master surface only if it is in elastic regime, and its stress is then controlled by classical Hooke's law. When martensite yields, it has to follow the master surface. In Figure 147 (b), the three curves are superimposed with the surface during their plastic regime. The level of strain in martensite is indirectly dependent on the flow stress of martensite, alongside those of ferrite and austenite through the iso-work hypothesis.

Many monotonically increasing $\sigma_{\alpha'}$ vs $\varepsilon_{\alpha'}$ can be imagined with this concept. Zhang et al. [100] have conducted HEXRD and calculated the von Mises stress of strain-induced martensite with the same method used in the current work. The level of stress in martensite is surprisingly low. However, low value of martensitic stress is always correlated with slow transformation kinetics and low final transformed fraction f_T reached in their work. This is consistent with the current framework developed here.

Two improvements could be made over the exposed model. Currently, the master surface is only a function of f_T. However, it could be envisioned that the martensite as a composite phase could be affected by strain-hardening, especially those with low yield strength $\sigma_{\alpha'}^{L}$. This change would make the master surface a function of both f_T and $\varepsilon_{\alpha'}$. Moreover, the austenitic phase is classically described

in the current model by a strain-hardening law. It remains nevertheless a phase whose fraction diminishes with strain. The mean austenite, regarding carbon content, is not the same initially and at necking. Therefore, a similar concept could be applied for austenite with its mechanical behaviour defined by an accessible flow stress surface. This is however less necessary since carbon effect on austenite stress is less significant than that for martensite. Moreover, there is only a low fraction of austenite at the end of the tensile test, meaning that an error on its stress has less effect on the overall medium Mn stress.

5. Conclusion, current limits and future improvements

The studied medium Mn steels are triplex steels, containing ferrite, austenite and martensite. Between steels, the microstructures vary widely, with different phase fractions, grain sizes and alloying contents. Despite having a minimal number of parameters fitted on the experimental data presented in Chapter III, the simulations match well the experimental data obtained with synchrotron analysis. The flow stresses of ferrite and austenite, as a function of their alloying contents and mean grain sizes, are successfully modelled. As classical dislocation-driven models are not appropriate to describe martensite, a new MIM model is proposed, inspired by CCA model used for the as-quenched martensite. When compared with experimental flow stresses of martensite, the MIM model is adapted to reproduce the observed mechanical behaviour of the globular martensite. However, some refinements on the MIM model are necessary to appropriately simulate the fibrous martensite. The thermodynamic description of strain-induced martensitic transformation proposed in this work allows for an accurate description of SIMT kinetics in medium Mn steels, as a function of austenite intrinsic properties. Using iso-work hypothesis and Hill's mixture rules, the macroscopic mechanical behaviours can be deduced from the micromechanical model. Results are congruent with experimental data obtained during in situ tensile tests, especially for the globular specimens. The model can be used to predict UTS and UEL for medium Mn steels with a relative error inferior to 10% for UTS and 15% for UEL.

The most obvious limit of the presented MIM model is in the description of the martensite flow stress distribution. The parameters of the density function are chosen to be simple. They lack however a microstructure-based parametrization. The physical origins of the distribution are clear and can be attributed to multiple contributions: dispersions in local carbon contents between different MA islands, blocks sizes, and possibly density dislocations and internal stresses [220]–[223]. An improvement in the current work would be to experimentally determine the distribution of each of those contributions using post-mortem techniques such as TEM and atom probe tomography.

Currently, the mechanical description of fresh martensite formed during thermal treatment is mixed with the strain-induced martensite. However, it could be envisioned that two separate sets of constitutive equations describe both kinds of martensite. A CCA like model could describe fresh martensite, while MIM model with $f_T = f_{SIM}$ could be adopted for strain-induced martensite. Some attempts have been made in this direction during the PhD project. However, taking directly CCA parameters for fresh martensite leads to very strong fresh martensite (more than 2500 MPa), which is not compatible with synchrotron data. The issue comes from the fact that CCA distribution states for 100% as-quenched martensite. A new idea not explored in the PhD thesis would be to take a CCA

approach, using the same density function, but only considering the 36% softest martensite of the CCA distribution (36% corresponds to the fraction of fresh martensite relative to the fraction of austenite formed during intercritical annealing). This should give softer fresh martensite, as expected from synchrotron measurements.

The model fails to reproduce the behaviour of ferrite and austenite in microstructure annealed at 750°C. This is explained for ferrite by the low initial dislocation densities. Therefore, to improve the model, ρ_α^0 and ρ_γ^0 could be considered as microstructure-based parameters, such as the fractions, the alloying contents of each phase and the grain sizes. Another possibility is to model directly GNDs appearing between martensite and other phases, as it has been done for dual-phase steels [18].

The literature review highlights a difference in orientation relationship (OR) between grains between the globular and fibrous microstructures. The globular grains have random OR, while fibrous ferrite, austenite and martensite should have a K-S OR between them. This is not accounted for in the model and could maybe explain some incomprehensible trend observed for the fibrous steels, especially for the fibrous martensite flow stress.

The current model is not temperature, strain rate and triaxiality dependent. However, the literature review presented in Chapter I highlighted the dependence of austenite mechanical stability on these variables. The lack of available data concerning the effect of those 3 quantities in the studied medium Mn steels explained the incompleteness of the model in this aspect. High temperature tensile tests were conducted at IJL for some of the microstructures, between 200°C and 400°C. Moreover, complementary synchrotron experiments on specimens with an optimized geometry were conducted in November 2022. They allow to study in situ the deformation of medium Mn steels during pure shear and plane strain deformations. However, as those experiments were conducted late in regards to the schedule of the PhD project, the experimental results have not been capitalized yet. Thankfully, the current SIMT model and the description of ferrite and austenite flow stress can be easily adapted to include temperature, strain rate and triaxiality effects, as detailed in Chapter I. The main unknown factor would be the evolution of strain induced martensite flow stress with those variables, as it was not extensively studied in the literature.

Conclusions and Perspectives

1. Summary of key results

The current work aims to set a new stage for the understanding of the retained austenite stability during the formation and the deformation of different steel microstructures. The materials studied in the PhD project are eight model Fe/0.2C/4Mn/1.5Si/0.8Al medium Mn microstructures chosen for their significant fraction of retained austenite at room temperature. Four globular UFG steels and four fibrous ART microstructures were designed on a thermodynamic basis. High energy X-Ray diffractions (HEXRD) experiments on synchrotron beamlines have been extensively used during the thesis to follow in situ the evolution of microstructures during thermal treatments and further mechanical loadings. When necessary, these experiments have been completed with direct post-mortem observations.

The microstructure formation during intercritical annealing was followed in situ thanks to HEXRD. A novel post-treatment methodology has been established, combining Rietveld refinement and RIR methods and allowing to obtain the time-resolved evolution of ferrite, austenite, cementite and martensite phase fractions during the whole thermal cycle. The important role of cementite precipitation and dissolution for the formation of austenite in duplex medium Mn microstructures has been demonstrated. While the role of carbide is well known in the literature for globular microstructures, it is a novelty for fibrous microstructures, due to its transient nature.

The developed methodology allows also to follow the carbon enrichment of austenite during the isothermal holding. The internal stresses building up during cooling in both ferritic matrix and retained austenite have been measured with HEXRD, which is original for medium Mn steels. A model was proposed to calculate the internal stresses due to “thermal” incompatibility between austenite and ferrite. The model successfully reproduces HEXRD experimental results when no martensitic transformation occurs. Post-mortem SEM analysis was also conducted to obtain data complementary to HEXRD. A watershed algorithm has been implemented to perform reliable and systematic measurements of phase fractions and grain sizes with SEM. WDS was used on a FEG-SEM microscope to obtain the alloying contents of Mn, Si and Al in austenite and ferrite. The partitioning of those alloying elements, alongside C, was clearly revealed by the technique. A methodology was thus developed in the thesis that allows to quantitatively determine the effect of austenite alloying contents (both substitutional and interstitial elements) and its internal stresses on austenite stability.

Tensile tests were carried out on synchrotron beamline at various strain rates, giving necessary information on the mechanical behaviour of all designed duplex steels. The combination of HEXRD with DIC analysis has proven to be very fruitful in this work. The evolutions of the 3D stress tensors and phase fractions of each constituting phase in medium Mn steels were followed, thanks to an innovative methodology combining the use of Rietveld refinement, $\sin^2\psi$ method and micromechanical calculations.

The influence of intercritical annealing temperatures on medium Mn mechanical behaviours is proven to be due to austenite mechanical stability sensitivity to the annealing temperatures and different levels of austenite/martensite phase fractions. The origin of the negative strain rate sensitivity in medium Mn steel is also to be found in austenite and its initial phase fraction. Martensite strength evolution with the strain rate is difficult to assess, as its variation did not have a clear trend between experiments. Moreover, its strength is directly linked with the SIMT (strain-induced martensitic transformation) kinetics. Ferrite has shown to be negligibly affected by both annealing temperature and stain rate. On the contrary, the difference in mechanical behaviour between the globular and fibrous specimens are mainly due to different levels in flow stress in ferrite and martensite and the initial austenite phase fraction. The evolution of hydrostatic stress in austenite reveals complex relaxation at the onset of yielding, which depends on the three considered parameters. This relaxation decreases with increasing annealing temperature, increasing strain rate and is lower in the fibrous samples than in the globular ones. Finally, Lüders and PLC effect were extensively studied thanks to the pairing of HEXRD and DIC.

The extensive experimental characterization work was capitalized with the development of a microstructure-based mean-field micromechanical model, which is both size and chemistry dependent. The flow stresses of ferrite and austenite are modelled with a dislocation driven-law whose parameters are mostly extracted from the literature. An improved model for strain-induced martensitic transformation was developed, based on Olson's and Perlade's models. The thermodynamic description of SIMT proposed in this work allows for an accurate description of all experimental SIMT kinetics as a function of austenite intrinsic properties. A new model for martensite has been developed, denoted the MIM (mechanically induced martensite) model, which does not a priori set the mechanical behaviour of martensite. The latter is a function of the SIMT kinetics only.

Using iso-work hypothesis and Hill's mixture rules, the macroscopic mechanical behaviour can be deduced from the micromechanical model. Results are congruent with in situ tensile tests, especially for the globular specimens, at the phase scale and at macroscopic scale. The model can be used to predict UTS and UEL for medium Mn steels with a relative error inferior to 10% for UTS and 15% for UEL.

2. Ongoing works and prospects

The study raised many questions concerning the mechanical behaviour of medium Mn steels and austenite stability inside such steels. Numerous works have been started during the PhD project, but unfortunately not finished due to time constraints:

1) Tensile tests at high temperature (between 100°C to 500°C) were conducted in September 2022 on dog-bone specimens at IJL for GL680, GL700, GL750 and FB700 steels, and are briefly presented in Appendix J. The results showing an outperformance at 300°C raise many questions about the evolution of austenite stability during deformation at high temperature, alongside the evolution of stress and strain partitioning among phases. The proposed micromechanical model could be improved to consider a temperature dependence.

2) HEXRD experiments during tensile tests were conducted in October 2022 on specimens with an optimized geometry to modify the triaxiality of deformation. The optimization was done by Gent University to obtain pure shear and plane strain deformations in the diffracting volume (in the frame of DYNAUSTAB project). These new experiments allow to measure SIMT kinetics as a function of triaxiality. These measurements could be directly compared to the developed model, which is already triaxiality dependent concerning the SIMT model.

3) Lüders and PLC effects have been detected in our medium Mn steels and the bands properties have been measured by DIC. Complementary acoustic experiments have been started at LEM3 in collaboration with Pr. M. Lebedkin on FB720 steels, alongside the supplementary analysis of the HEXRD data presented in Chapter III (spectral analysis, entropy analysis…). These new analyses could be complemented by an upgrade of the current micromechanical model in 1D, with a chain of blocks (as done in [224]), all having the mechanical response described in Chapter IV. The current python code already accounts for this 1D extension. All these developments could allow for a better understanding of the physical origin of mechanical instabilities in medium Mn steels, which is still a puzzling topic in regards with the literature (link with SIMT, occurrence of SSA/DSA…). The subsequent effect of those strain rate bands on SIMT could also be more understood by making the current model strain rate dependent and accounting for the real strain rate of the diffracting volume (which is different from the nominal deformation rate).

4) The current model accounts for one martensitic phase, comprising both fresh and mechanically induced martensites. A direct upgrade could be to account for two populations, one having a mechanical behaviour with laws more similar to as-quenched martensite, the other being described by MIM model. Some first attempts have been made, but directly taking a CCA model [18] for fresh martensite conducted to a too strong martensite. Moreover, the distributions of yield stress, described with a JMAK-like law in the current work, should be experimentally measured by a method like that has been used in J. Macchi thesis for as-quenched and tempered martensite (difficult task combining TEM, EBSD and synchrotron analysis).

5) In November 2020, HEXRD experiments during tensile tests of medium Mn Q&P steels have also been done and analysed. SEM observations of the microstructures were also made. However, the results were not included in the present manuscript (but shared in DYNAUSTAB project). A simple continuation of the current work could consist in extending the developed micromechanical model to these Q&P steels. The extension of the model could be also made on other 3rd generation steels, such as carbide-free bainitic steels (HEXRD experiments during tensile tests have also been conducted).

6) Difference in flow stress of ferrites between the fibrous and globular microstructures is not well understood yet. This could be an effect of the presence of K-S orientation relationship (OR) in the fibrous steels between grains while no specific OR exists in the globular steels. This difference could be better understood in the framework of a full-field crystal plasticity model.

7) Concerning the morphogenesis of medium Mn steels from cold-rolled and fully-martensitic states, the current work sheds a new light on the role of cementite in the austenite formation kinetics. Some simulations, made from a model derived of DICTRA, have been started, with no success. Direct DICTRA simulations of medium Mn microstructures' formation could be done and compared with the experimental data shown in Chapter II, to better understand the mechanism of austenite formation in ART medium Mn steels.

8) A lacking aspect of the current modelling work is the absence of the prediction of hydrostatic stress due to martensitic transformation during the final cooling of the intercritical annealing (IA). A priority of future works would be to understand these effects.

9) One difficulty of the current work was to obtain reproductible medium Mn microstructures. Indeed, between microstructures produced in dilatometer and through salt-bath, martensite phase fractions before deformation are notably different. This is due to the high sensitivity of medium Mn steels to the heating stage of IA. Indeed, depending on the heating rate, cementite size distributions and chemistry will vary, modifying its stability and the subsequent stability of forming austenite. This aspect would also need cautious experimentations, combining metallographic observations and interrupted HEXRD experiments.

10) One aspect of HEXRD analysis that has been put aside in the current methodology is the determination of dislocation densities thank to the full width at half maximum (FWHM) of diffraction peaks. While measurements of FWHM have been made during thermal treatments and tensile tests, the latter is difficult to interpret due to the non-negligible presence of martensite transformation and chemical gradients. However, dislocation density is also known to affect austenite stability. Therefore, its measurement would be an improvement to the current work.

11) Some TEM investigations have been made in the frame of DYNAUSTAB project. The latter reveals the same partitioning of chemical elements as that obtained with the WDS method. However, the full comparison of the two methods, while started, should be finished to assess the effect of probe size (around 0.2-0.5 µm) on WDS measurements of micrometric microstructures such as in medium Mn steels.

References

[1] M. Cherkaoui, M. Berveiller, and X. Lemoine, 'Couplings between plasticity and martensitic phase transformation: overall behavior of polycrystalline TRIP steels', *Int. J. Plast.*, vol. 16, no. 10–11, pp. 1215–1241, Jan. 2000, doi: 10.1016/S0749-6419(00)00008-5.

[2] A. Perlade *et al.*, 'Development of 3rd generation Medium Mn duplex steels for automotive applications', *Mater. Sci. Technol.*, vol. 35, no. 2, pp. 204–219, Jan. 2019, doi: 10.1080/02670836.2018.1549303.

[3] R. Rana and S. B. Singh, 'Automotive Steels', *Woodhead Publ.*, p. 481, 2017.

[4] W. Ding, 'Transformations During Intercritical Annealing and Their Implications for Microstructure and Mechanical Properties of Medium Mn Transformation-Induced Plasticity Steel in Continuous Annealing Line', *J. Mater. Eng. Perform.*, p. 9.

[5] C. L. Wu, C. P. Chang, D. Chen, J. F. Tu, and C. Y. Huang, 'Microstructural characterization of deformation-induced martensite in an ultrafine-grained medium Mn advanced high strength steel', *Mater. Sci. Eng. A*, vol. 721, pp. 145–153, Apr. 2018, doi: 10.1016/j.msea.2018.02.082.

[6] G. Thomas, 'Retained austenite and tempered martensite embrittlement', *Metall. Trans. A*, vol. 9, no. 3, pp. 439–450, Mar. 1978, doi: 10.1007/BF02646396.

[7] X. Zhang, G. Miyamoto, Y. Toji, S. Nambu, T. Koseki, and T. Furuhara, 'Orientation of austenite reverted from martensite in Fe-2Mn-1.5Si-0.3C alloy', *Acta Mater.*, vol. 144, pp. 601–612, Feb. 2018, doi: 10.1016/j.actamat.2017.11.003.

[8] A. Perlade, O. Bouaziz, and Q. Furnémont, 'A physically based model for TRIP-aided carbon steels behaviour', *Mater. Sci. Eng. A*, vol. 356, no. 1–2, pp. 145–152, Sep. 2003, doi: 10.1016/S0921-5093(03)00121-7.

[9] G. Haidemenopoulos, 'Dispersed-phase transformation toughening in ultrahigh-strength steels', *Thesis Ph --Mass. Inst. Technol. Dept Mater. Sci. Eng.*, 1988.

[10] G. B. Olson and M. Cohen, 'A mechanism for the strain-induced nucleation of martensitic transformations', *J. Common Met.*, vol. 28, no. 1, pp. 107–118, Jul. 1972, doi: 10.1016/0022-5088(72)90173-7.

[11] G. B. Olson and M. Cohen, 'Kinetics of strain-induced martensitic nucleation', *Metall. Trans. A*, vol. 6, no. 4, pp. 791–795, Apr. 1975, doi: 10.1007/BF02672301.

[12] J. S. Aristeidakis and G. N. Haidemenopoulos, 'Constitutive and transformation kinetics modeling of ε -, α ' -Martensite and mechanical twinning in steels containing austenite', *Acta Mater.*, vol. 228, p. 117757, Apr. 2022, doi: 10.1016/j.actamat.2022.117757.

[13] H. Luo, H. Dong, and M. Huang, 'Effect of intercritical annealing on the Lüders strains of medium Mn transformation-induced plasticity steels', *Mater. Des.*, vol. 83, pp. 42–48, Oct. 2015, doi: 10.1016/j.matdes.2015.05.085.

[14] O. Bouaziz, A. Aouafi, and S. Allain, 'Effect of Grain Refinement on the Mechanical Behaviour of Ferritic Steels: Evolution of Isotropic Hardening and Kinematic Hardening', *Mater. Sci. Forum*, vol. 584–586, pp. 605–609, Jun. 2008, doi: 10.4028/www.scientific.net/MSF.584-586.605.

[15] O. Bouaziz, H. Zurob, B. Chehab, J. D. Embury, S. Allain, and M. Huang, 'Effect of chemical composition on work hardening of Fe—Mn—C TWIP steels', *Mater. Sci. Technol.*, vol. 27, no. 3, pp. 707–709, Mar. 2011, doi: 10.1179/026708309X12535382371852.

[16] A. Marais, M. Mazière, S. Forest, A. Parrot, and P. Le Delliou, 'Identification of a strain-aging model accounting for Lüders behavior in a C-Mn steel', *Philos. Mag.*, vol. 92, no. 28–30, pp. 3589–3617, Oct. 2012, doi: 10.1080/14786435.2012.699687.

[17] O. Bouaziz, Y. Estrin, Y. Bréchet, and J. D. Embury, 'Critical grain size for dislocation storage and consequences for strain hardening of nanocrystalline materials', *Scr. Mater.*, vol. 63, no. 5, pp. 477–479, Sep. 2010, doi: 10.1016/j.scriptamat.2010.05.006.

[18] S. Y. P. Allain, O. Bouaziz, I. Pushkareva, and C. P. Scott, 'Towards the microstructure design of DP steels: A generic size-sensitive mean-field mechanical model', *Mater. Sci. Eng. A*, vol. 637, pp. 222–234, Jun. 2015, doi: 10.1016/j.msea.2015.04.017.

[19] N. J. Kim and G. Thomas, 'Effects of morphology on the mechanical behavior of a dual phase Fe/2Si/0.1C steel', *Metall. Trans. A*, vol. 12, no. 3, pp. 483–489, Mar. 1981, doi: 10.1007/BF02648546.

[20] K. Sugimoto, A. Kanda, R. Kikuchi, S. Hashimoto, T. Kashima, and S. Ikeda, 'Ductility and Formability of Newly Developed High Strength Low Alloy TRIP-aided Sheet Steels with Annealed Martensite Matrix.', *ISIJ Int.*, vol. 42, no. 8, pp. 910–915, 2002, doi: 10.2355/isijinternational.42.910.

[21] A. Arlazarov, M. Gouné, O. Bouaziz, A. Hazotte, G. Petitgand, and P. Barges, 'Evolution of microstructure and mechanical properties of medium Mn steels during double annealing', *Mater. Sci. Eng. A*, vol. 542, pp. 31–39, Apr. 2012, doi: 10.1016/j.msea.2012.02.024.

[22] H. K. D. H. Bhadeshia and D. V. Edmonds, 'The mechanism of bainite formation in steels', *Acta Metall.*, vol. 28, no. 9, pp. 1265–1273, Sep. 1980, doi: 10.1016/0001-6160(80)90082-6.

[23] J.-C. Hell, M. Dehmas, S. Allain, J. M. Prado, A. Hazotte, and J.-P. Chateau, 'Microstructure – Properties Relationships in Carbide-free Bainitic Steels', *ISIJ Int.*, vol. 51, no. 10, pp. 1724–1732, 2011, doi: 10.2355/isijinternational.51.1724.

[24] F. G. Caballero, S. Allain, J. Cornide, J. D. Puerta Velásquez, C. Garcia-Mateo, and M. K. Miller, 'Design of cold rolled and continuous annealed carbide-free bainitic steels for automotive application', *Mater. Des.*, vol. 49, pp. 667–680, Aug. 2013, doi: 10.1016/j.matdes.2013.02.046.

[25] S. Y. P. Allain *et al.*, 'Internal stresses and carbon enrichment in austenite of Quenching and Partitioning steels from high energy X-ray diffraction experiments', *Mater. Sci. Eng. A*, vol. 710, pp. 245–250, Jan. 2018, doi: 10.1016/j.msea.2017.10.105.

[26] J. Sun and H. Yu, 'Microstructure development and mechanical properties of quenching and partitioning (Q&P) steel and an incorporation of hot-dipping galvanization during Q&P process', *Mater. Sci. Eng. A*, vol. 586, pp. 100–107, Dec. 2013, doi: 10.1016/j.msea.2013.08.021.

[27] J. Speer, D. K. Matlock, B. C. De Cooman, and J. G. Schroth, 'Carbon partitioning into austenite after martensite transformation', *Acta Mater.*, vol. 51, no. 9, pp. 2611–2622, May 2003, doi: 10.1016/S1359-6454(03)00059-4.

[28] D. K. Matlock and J. G. Speer, 'Third Generation of AHSS: Microstructure Design Concepts', in *Microstructure and Texture in Steels*, London, 2009, pp. 185–205. doi: 10.1007/978-1-84882-454-6_11.

[29] 'S-in motion® solutions'. https://automotive.arcelormittal.com/s-in_motion_solutions/overview

[30] S. Zhou *et al.*, 'Nanomechanics of Retained Austenite in Medium-Carbon Low-Temperature Bainitic Steel: A Critical Analysis of a One-Step versus a Two-Step Treatment', *Materials*, vol. 15, no. 17, p. 5996, Aug. 2022, doi: 10.3390/ma15175996.

[31] E. J. Seo, L. Cho, and B. C. De Cooman, 'Kinetics of the partitioning of carbon and substitutional alloying elements during quenching and partitioning (Q&P) processing of medium Mn steel', *Acta Mater.*, vol. 107, pp. 354–365, Apr. 2016, doi: 10.1016/j.actamat.2016.01.059.

[32] P. Jacques, 'On the role of martensitic transformation on damage and cracking resistance in TRIP-assisted multiphase steels', *Acta Mater.*, vol. 49, no. 1, pp. 139–152, Jan. 2001, doi: 10.1016/S1359-6454(00)00215-9.

[33] H. K. D. H. Bhadeshia, 'TRIP-Assisted Steels?', *ISIJ Int.*, vol. 42, no. 9, pp. 1059–1060, 2002, doi: 10.2355/isijinternational.42.1059.

[34] A. Lechartier, 'Influence de la transformation martensitique induite par la déformation sur le comportement mécanique d'aciers inoxydables duplex', *Univ. Grenoble Alpes*, p. 177, Dec. 2015.

[35] M. R. Berrahmoune, 'Transformation martensitique et rupture différée dans l'acier austénitique instable 301LN', *Ecole Natl. Supér. Arts Métiers*, p. 190, Jun. 2006.

[36] T. Iung and J.-H. Schmitt, 'Durcissement des aciers - Austénite et nouvelles microstructures multiphasées', *Étude Propr. Métaux*, Jun. 2017, doi: 10.51257/a-v1-m4342.

[37] H. Schumann, 'Verformungsinduzierte Martensitbildung in metastabilen austenitischen Stählen', *Krist. Tech.*, vol. 10, no. 4, pp. 401–411, 1975, doi: 10.1002/crat.19750100409.

[38] Z. Z. Zhao, J. H. Liang, A. M. Zhao, J. T. Liang, D. Tang, and Y. P. Gao, 'Effects of the austenitizing temperature on the mechanical properties of cold-rolled medium-Mn steel system', *J. Alloys Compd.*, vol. 691, pp. 51–59, Jan. 2017, doi: 10.1016/j.jallcom.2016.08.093.

[39] P. Xia, F. Vercruysse, R. Petrov, I. Sabirov, M. Castillo-Rodríguez, and P. Verleysen, 'High strain rate tensile behavior of a quenching and partitioning (Q&P) Fe-0.25C-1.5Si-3.0Mn steel', *Mater. Sci. Eng. A*, vol. 745, pp. 53–62, Feb. 2019, doi: 10.1016/j.msea.2018.12.064.

[40] Q. Tonizzo, 'Lien microstructure-comportement à rupture d'aciers de troisième génération à structure duplex pour application automobile', *MINES ParisTech*, p. 167, Dec. 2017.

[41] S. Chen, R. Rana, A. Haldar, and R. K. Ray, 'Current state of Fe-Mn-Al-C low density steels', *Prog. Mater. Sci.*, vol. 89, pp. 345–391, Aug. 2017, doi: 10.1016/j.pmatsci.2017.05.002.

[42] A. Chbihi, D. Barbier, L. Germain, A. Hazotte, and M. Gouné, 'Interactions between ferrite recrystallization and austenite formation in high-strength steels', *J. Mater. Sci.*, vol. 49, no. 10, pp. 3608–3621, May 2014, doi: 10.1007/s10853-014-8029-2.

[43] D. Barbier, L. Germain, A. Hazotte, M. Gouné, and A. Chbihi, 'Microstructures resulting from the interaction between ferrite recrystallization and austenite formation in dual-phase steels', *J. Mater. Sci.*, vol. 50, no. 1, pp. 374–381, Jan. 2015, doi: 10.1007/s10853-014-8596-2.

[44] M. Ollat, V. Massardier, D. Fabregue, E. Buscarlet, F. Keovilay, and M. Perez, 'Modeling of the Recrystallization and Austenite Formation Overlapping in Cold-Rolled Dual-Phase Steels During Intercritical Treatments', *Metall. Mater. Trans. A*, vol. 48, no. 10, pp. 4486–4499, Oct. 2017, doi: 10.1007/s11661-017-4231-6.

[45] K. Steineder, D. Krizan, R. Schneider, C. Béal, and C. Sommitsch, 'On the microstructural characteristics influencing the yielding behavior of ultra-fine grained medium-Mn steels', *Acta Mater.*, vol. 139, pp. 39–50, Oct. 2017, doi: 10.1016/j.actamat.2017.07.056.

[46] G. Murry, 'Transformations dans les aciers', *Tech. Ing.*, Sep. 1998.

[47] J. Y. Koo and G. Thomas, 'Thermal cycling treatments and microstructures for improved properties of Fe-0.12% C-0.5% Mn steels', *Mater. Sci. Eng.*, vol. 24, no. 2, pp. 187–198, Aug. 1976, doi: 10.1016/0025-5416(76)90112-9.

[48] A. Arlazarov, O. Bouaziz, J. P. Masse, and F. Kegel, 'Characterization and modeling of mechanical behavior of quenching and partitioning steels', *Mater. Sci. Eng. A*, vol. 620, pp. 293–300, Jan. 2015, doi: 10.1016/j.msea.2014.10.034.

[49] E. Jimenez-Melero *et al.*, 'Martensitic transformation of individual grains in low-alloyed TRIP steels', *Scr. Mater.*, vol. 56, no. 5, pp. 421–424, Mar. 2007, doi: 10.1016/j.scriptamat.2006.10.041.

[50] E. Jimenez-Melero *et al.*, 'Characterization of individual retained austenite grains and their stability in low-alloyed TRIP steels', *Acta Mater.*, vol. 55, no. 20, pp. 6713–6723, Dec. 2007, doi: 10.1016/j.actamat.2007.08.040.

[51] A. Arlazarov, 'Evolution of microstructure and mechanical properties of medium Mn steels and their relationship', *Univ. Lorraine*, p. 213, May 2015.

[52] E. Kozeschnik and H. K. D. H. Bhadeshia, 'Influence of silicon on cementite precipitation in steels', *Mater. Sci. Technol.*, vol. 24, no. 3, pp. 343–347, Mar. 2008, doi: 10.1179/174328408X275973.

[53] M. Amirthalingam, M. Hermans, and I. Richardson, 'Microstructural Development during Welding of Silicon- and Aluminum-Based Transformation-Induced Plasticity Steels—Inclusion and Elemental Partitioning Analysis', *Metall. Mater. Trans. A*, vol. 40, no. 4, pp. 901–909, Apr. 2009, doi: 10.1007/s11661-008-9761-5.

[54] H. Kim, D.-W. Suh, and N. J. Kim, 'Fe–Al–Mn–C lightweight structural alloys: a review on the microstructures and mechanical properties', *Sci. Technol. Adv. Mater.*, vol. 14, no. 1, p. 014205, Mar. 2013, doi: 10.1088/1468-6996/14/1/014205.

[55] Q. Lai *et al.*, 'Mechanism of Austenite Formation from Spheroidized Microstructure in an Intermediate Fe-0.1C-3.5Mn Steel', *Metall. Mater. Trans. A*, vol. 47, no. 7, pp. 3375–3386, Jul. 2016, doi: 10.1007/s11661-016-3547-y.

[56] G. R. Speich, V. A. Demarest, and R. L. Miller, 'Formation of Austenite During Intercritical Annealing of Dual-Phase Steels', *Metall. Mater. Trans. A*, vol. 12, no. 8, pp. 1419–1428, Aug. 1981, doi: 10.1007/BF02643686.

[57] Y. X. Wu *et al.*, 'Austenite formation kinetics from multicomponent cementite-ferrite aggregates', *Acta Mater.*, vol. 196, pp. 470–487, Sep. 2020, doi: 10.1016/j.actamat.2020.07.001.

[58] S. Li, Y. Kang, G. Zhu, and S. Kuang, 'Austenite formation during intercritical annealing in C-Mn cold-rolled dual phase steel', *J. Cent. South Univ.*, vol. 22, no. 4, pp. 1203–1211, Apr. 2015, doi: 10.1007/s11771-015-2634-3.

[59] Z. C. Li, H. Ding, R. D. K. Misra, and Z. H. Cai, 'Microstructure-mechanical property relationship and austenite stability in medium-Mn TRIP steels: The effect of austenite-reverted transformation and quenching-tempering treatments', *Mater. Sci. Eng. A*, vol. 682, pp. 211–219, Jan. 2017, doi: 10.1016/j.msea.2016.11.048.

[60] A. Arlazarov, M. Goune, O. Bouaziz, F. Kegel, and A. Hazotte, 'Time-evolution of microstructure and mechanical behaviour of double annealed medium Mn steel', *Mater. Sci. Technol.*, vol. 35, no. 17, pp. 2076–2083, Nov. 2019, doi: 10.1080/02670836.2019.1585031.

[61] D. P. Yang, D. Wu, and H. L. Yi, 'Reverse transformation from martensite into austenite in a medium-Mn steel', *Scr. Mater.*, vol. 161, pp. 1–5, Mar. 2019, doi: 10.1016/j.scriptamat.2018.09.046.

[62] H. Luo, J. Shi, C. Wang, W. Cao, X. Sun, and H. Dong, 'Experimental and numerical analysis on formation of stable austenite during the intercritical annealing of 5Mn steel', *Acta Mater.*, vol. 59, no. 10, pp. 4002–4014, Jun. 2011, doi: 10.1016/j.actamat.2011.03.025.

[63] N. Nakada, T. Tsuchiyama, S. Takaki, and S. Hashizume, 'Variant Selection of Reversed Austenite in Lath Martensite', *ISIJ Int.*, vol. 47, no. 10, pp. 1527–1532, 2007, doi: 10.2355/isijinternational.47.1527.

[64] N. Nakada, T. Tsuchiyama, S. Takaki, and N. Miyano, 'Temperature Dependence of Austenite Nucleation Behavior from Lath Martensite', *ISIJ Int.*, vol. 51, no. 2, p. 6, 2011.

[65] X. Zhang, G. Miyamoto, T. Kaneshita, Y. Yoshida, Y. Toji, and T. Furuhara, 'Growth mode of austenite during reversion from martensite in Fe-2Mn-1.5Si-0.3C alloy: A transition in kinetics and morphology', *Acta Mater.*, vol. 154, pp. 1–13, Aug. 2018, doi: 10.1016/j.actamat.2018.05.035.

[66] Q. Ye, Y. Yu, H. Zhu, J. Li, L. Qiao, and Y. Yan, 'Formation of core-shell austenite as promoted by alloying solutes in hot-rolled medium Mn steel', *J. Mater. Res. Technol.*, vol. 21, pp. 1053–1060, Nov. 2022, doi: 10.1016/j.jmrt.2022.09.118.

[67] K.-I. Sugimoto, 'Fracture strength and toughness of ultra high strength TRIP aided steels', *Mater. Sci. Technol.*, vol. 25, no. 9, pp. 1108–1117, Sep. 2009, doi: 10.1179/174328409X453307.

[68] B. Hu *et al.*, 'Yielding behavior of triplex medium Mn steel alternated with cooling strategies altering martensite/ferrite interfacial feature', *J. Mater. Sci. Technol.*, vol. 126, pp. 60–70, Nov. 2022, doi: 10.1016/j.jmst.2022.04.003.

[69] W. Wang *et al.*, 'Deformation mechanisms for a new medium-Mn steel with 1.1 GPa yield strength and 50% uniform elongation', *J. Mater. Sci. Technol.*, vol. 132, pp. 110–118, Jan. 2023, doi: 10.1016/j.jmst.2022.05.048.

[70] L. Luo, W. Li, S. Liu, L. Wang, and X. Jin, 'Effect of intermediate temperature annealing on the stability of retained austenite and mechanical properties of medium Mn-TRIP steel', *Mater. Sci. Eng. A*, vol. 742, pp. 69–77, Jan. 2019, doi: 10.1016/j.msea.2018.10.102.

[71] N. Bhowmik, S. Ghosh, S. Mandal, A. Haldar, and P. P. Chattopadhyay, 'Genesis of plasticity-induced serrated metal flow in medium-Mn steel', *Calphad*, vol. 77, p. 102425, Jun. 2022, doi: 10.1016/j.calphad.2022.102425.

[72] Z. J. Xie, C. J. Shang, S. V. Subramanian, X. P. Ma, and R. D. K. Misra, 'Atom probe tomography and numerical study of austenite stabilization in a low carbon low alloy steel processed by two-step intercritical heat treatment', *Scr. Mater.*, vol. 137, pp. 36–40, Aug. 2017, doi: 10.1016/j.scriptamat.2017.05.002.

[73] Q. Guo, H.-W. Yen, H. Luo, and S. P. Ringer, 'On the mechanism of Mn partitioning during intercritical annealing in medium Mn steels', *Acta Mater.*, vol. 225, p. 117601, Feb. 2022, doi: 10.1016/j.actamat.2021.117601.

[74] J. Zhu, R. Ding, J. He, Z. Yang, C. Zhang, and H. Chen, 'A cyclic austenite reversion treatment for stabilizing austenite in the medium manganese steels', *Scr. Mater.*, vol. 136, pp. 6–10, Jul. 2017, doi: 10.1016/j.scriptamat.2017.03.038.

[75] Z. Xu, X. Shen, T. Allam, W. Song, and W. Bleck, 'Austenite reversion and nano-precipitation during a compact two-step heat treatment of medium-Mn steel containing Cu and Ni', *J. Mater. Res. Technol.*, vol. 17, pp. 2601–2613, Mar. 2022, doi: 10.1016/j.jmrt.2022.02.008.

[76] S. Kundu, 'Transformation Strain and Crystallographic Texture in Steels', *Univ. Camb.*, p. 219, Mar. 2007.

[77] H. K. D. H. Bhadeshia, *Bainite in steels: transformations, microstructure and properties*, 2. ed. London: IOM Communications, 2001.

[78] S. Lubin, 'Etude des mécanismes de la transformation de phase bainitique dans les aciers bas carbone', *MINES ParisTech*, p. 239, Jun. 2009.

[79] E. C. Bain and N. Y. Dunkirk, 'The nature of martensite', *Trans AIME*, vol. 70, no. 1, pp. 25–47, 1924.

[80] J. S. Bowles and J. K. Mackenzie, 'The crystallography of martensite transformations I', *Acta Metall.*, vol. 2, no. 1, pp. 129–137, Jan. 1954, doi: 10.1016/0001-6160(54)90102-9.

[81] F. Therrien and V. Stevanović, 'Minimization of atomic displacements as a guiding principle of the martensitic phase transformation', *Phys. Rev. Lett.*, vol. 125, no. 12, p. 125502, Sep. 2020, doi: 10.1103/PhysRevLett.125.125502.

[82] G. Badinier, C. W. Sinclair, S. Allain, F. Danoix, and M. Gouné, 'The Mechanisms of Transformation and Mechanical Behavior of Ferrous Martensite', in *Reference Module in Materials Science and Materials Engineering*, Elsevier, 2017, p. B9780128035818025000. doi: 10.1016/B978-0-12-803581-8.02518-2.

[83] J. R. Patel and M. Cohen, 'Criterion for the action of applied stress in the martensitic transformation', *Acta Metall.*, vol. 1, no. 5, pp. 531–538, Sep. 1953, doi: 10.1016/0001-6160(53)90083-2.

[84] F. Lani, Q. Furnémont, T. Van Rompaey, F. Delannay, P. J. Jacques, and T. Pardoen, 'Multiscale mechanics of TRIP-assisted multiphase steels: II. Micromechanical modelling', *Acta Mater.*, vol. 55, no. 11, pp. 3695–3705, Jun. 2007, doi: 10.1016/j.actamat.2007.02.015.

[85] P. J. Jacques, Q. Furnémont, F. Lani, T. Pardoen, and F. Delannay, 'Multiscale mechanics of TRIP-assisted multiphase steels: I. Characterization and mechanical testing', *Acta Mater.*, vol. 55, no. 11, pp. 3681–3693, Jun. 2007, doi: 10.1016/j.actamat.2007.02.029.

[86] E. Polatidis *et al.*, 'The effect of stress triaxiality on the phase transformation in transformation induced plasticity steels: Experimental investigation and modelling the transformation kinetics', *Mater. Sci. Eng. A*, vol. 800, p. 140321, Jan. 2021, doi: 10.1016/j.msea.2020.140321.

[87] S. Prüger, A. Seupel, and M. Kuna, 'A thermomechanically coupled material model for TRIP-steel', *Int. J. Plast.*, vol. 55, pp. 182–197, Apr. 2014, doi: 10.1016/j.ijplas.2013.10.005.

[88] S. Prüger and M. Kuna, 'A constitutive model for a high alloyed cast CrMnNi TRIP-steel', *PAMM*, vol. 11, no. 1, pp. 425–426, Dec. 2011, doi: 10.1002/pamm.201110204.

[89] D. D. Tjahjanto, A. S. J. Suiker, S. Turteltaub, P. E. J. Rivera Diaz del Castillo, and S. van der Zwaag, 'Micromechanical predictions of TRIP steel behavior as a function of microstructural parameters', *Comput. Mater. Sci.*, vol. 41, no. 1, pp. 107–116, Nov. 2007, doi: 10.1016/j.commatsci.2007.03.005.

[90] Y. F. Shen, L. N. Qiu, X. Sun, L. Zuo, P. K. Liaw, and D. Raabe, 'Effects of retained austenite volume fraction, morphology, and carbon content on strength and ductility of nanostructured TRIP-assisted steels', *Mater. Sci. Eng. A*, vol. 636, pp. 551–564, Jun. 2015, doi: 10.1016/j.msea.2015.04.030.

[91] F. N. Rakotovao, 'Relaxation des contraintes dans les couches de chromine développées sur alliages modèles (NiCr et Fe47Cr). Apport de la diffraction in situ à haute température sur rayonnement Synchrotron à l'étude du comportement viscoplastique. Effets d'éléments réactifs.', *Univ. Rochelle*, p. 236, Nov. 2016.

[92] C. Y. Kung and J. J. Rayment, 'An examination of the validity of existing empirical formulae for the calculation of ms temperature', *Metall. Trans. A*, vol. 13, no. 2, pp. 328–331, Feb. 1982, doi: 10.1007/BF02643327.

[93] K. W. ANDREWS, 'Empirical formulae for the calculation of some transformation temperatures', *J Iron Steel Inst*, pp. 721–727, 1965.

[94] R. Blondé *et al.*, 'High-energy X-ray diffraction study on the temperature-dependent mechanical stability of retained austenite in low-alloyed TRIP steels', *Acta Mater.*, vol. 60, no. 2, pp. 565–577, Jan. 2012, doi: 10.1016/j.actamat.2011.10.019.

[95] J. Wang and S. Van Der Zwaag, 'Stabilization mechanisms of retained austenite in transformation-induced plasticity steel', *Metall. Mater. Trans. A*, vol. 32, no. 6, pp. 1527–1539, Jun. 2001, doi: 10.1007/s11661-001-0240-5.

[96] S. Denis, P. Archambault, E. Gautier, A. Simon, and G. Beck, 'Prediction of residual stress and distortion of ferrous and non-ferrous metals: Current status and future developments', *J. Mater. Eng. Perform.*, p. 11, 2000.

[97] R. J. Arsenault' and M. Taya', 'THERMAL RESIDUAL STRESS IN METAL MATRIX COMPOSTTE~', *Acta Metall.*, vol. 35, no. 3, pp. 651–659, Jun. 1986.

[98] X. C. Xiong, 'The effect of morphology on the stability of retained austenite in a quenched and partitioned steel', *Scr. Mater.*, p. 4, 2013.

[99] M. Zhang *et al.*, 'In situ high-energy X-ray diffraction investigation of the micromechanical behavior of Fe-0.1C-10Mn-0/2Al steel at room and elevated temperatures', *Mater. Sci. Eng. A*, vol. 729, pp. 444–451, Jun. 2018, doi: 10.1016/j.msea.2018.05.102.

[100] M. Zhang *et al.*, 'Deformation-induced martensitic transformation kinetics and correlative micromechanical behavior of medium-Mn transformation-induced plasticity steel', *J. Mater. Sci. Technol.*, vol. 35, no. 8, pp. 1779–1786, Aug. 2019, doi: 10.1016/j.jmst.2019.04.007.

[101] T. Angel, 'Formation of Martensite in Austenitic Stainless Steels Effects of Deformation, Temperature, and Composition', *J Iron Steel Inst*, vol. 177, pp. 165–174, 1954.

[102] D. C. Ludwigson and J. A. Berger, 'Plastic behaviour of metastable austenitic stainless steels', *J Iron Steel Inst*, vol. 207, no. 1, pp. 63–69, 1969.

[103] W. W. Gerberich, G. Thomas, E. R. Parker, and V. F. Zackay, 'Metastable Austenites: Decomposition and Strength.', *Other Information: From 2nd International Conference on the Strength of Metals and Alloys, Pacific Grove, California. UNCL. Orig. Receipt Date: 31-DEC-70*, Jan. 01, 1970. https://digital.library.unt.edu/ark:/67531/metadc871173/ (accessed Nov. 29, 2022).

[104] K.-I. Sugimoto, M. Kobayashi, and S.-I. Hashimoto, 'Ductility and strain-induced transformation in a high-strength transformation-induced plasticity-aided dual-phase steel', *Metall. Trans. A*, vol. 23, no. 11, pp. 3085–3091, Nov. 1992, doi: 10.1007/BF02646127.

[105] O. Matsumura, Y. Sakuma, and H. Takechi, 'TRIP AND ITS KINETIC ASPECTS IN AUSTEMPERED 0.4C-I.SSi-0.8Mn STEEL', *Scr. Metall.*, p. 6, 1987.

[106] M. Callahan, 'Interactions of negative strain rate sensitivity, martensite transformation, and dynamic strain aging in 3rd generation advanced high-strength steels', *Mater. Sci.*, p. 12, 2019.

[107] L. Samek, E. De Moor, J. Penning, and B. C. De Cooman, 'Influence of alloying elements on the kinetics of strain-induced martensitic nucleation in low-alloy, multiphase high-strength steels', *Metall. Mater. Trans. A*, vol. 37, no. 1, pp. 109–124, Jan. 2006, doi: 10.1007/s11661-006-0157-0.

[108] M. Callahan, O. Hubert, F. Hild, A. Perlade, and J.-H. Schmitt, 'Coincidence of strain-induced TRIP and propagative PLC bands in Medium Mn steels', *Mater. Sci. Eng. A*, vol. 704, pp. 391–400, Sep. 2017, doi: 10.1016/j.msea.2017.08.042.

[109] J. Bouquerel, K. Verbeken, and B. Decooman, 'Microstructure-based model for the static mechanical behaviour of multiphase steels', *Acta Mater.*, vol. 54, no. 6, pp. 1443–1456, Apr. 2006, doi: 10.1016/j.actamat.2005.10.059.

[110] J. T. Benzing *et al.*, 'Experimental and numerical study of mechanical properties of multi-phase medium-Mn TWIP-TRIP steel: Influences of strain rate and phase constituents', *Acta Mater.*, vol. 177, pp. 250–265, Sep. 2019, doi: 10.1016/j.actamat.2019.07.036.

[111] M. I. Latypov, S. Shin, B. C. De Cooman, and H. S. Kim, 'Micromechanical finite element analysis of strain partitioning in multiphase medium manganese TWIP+TRIP steel', *Acta Mater.*, vol. 108, pp. 219–228, Apr. 2016, doi: 10.1016/j.actamat.2016.02.001.

[112] S. R. Pati and M. Cohen, 'Nucleation of the isothermal martensitic transformation', *Acta Metall.*, vol. 17, no. 3, pp. 189–199, Mar. 1969, doi: 10.1016/0001-6160(69)90058-3.

[113] G. B. Olson and M. Cohen, 'Stress-assisted isothermal martensitic transformation: Application to TRIP steels', *Metall. Trans. A*, vol. 13, no. 11, pp. 1907–1914, Nov. 1982, doi: 10.1007/BF02645934.

[114] G. B. Olson and M. Cohen, 'A General Mechanism of Martensitic Nucleation= Part I. General Concepts and the FCC HCP Transformation', *Metall. Trans. A*, p. 8, 1976.

[115] G. B. Olson and M. Cohen, 'A General Mechanism of Martensitic Nucleation: Part II. FCC - , - B C C and Other Martensitic Transformations', *Metall. Trans. A*, p. 10, 1976.

[116] G. B. Olson and M. Cohen, 'A general mechanism of martensitic nucleation: Part III. Kinetics of martensitic nucleation', *Metall. Trans. A*, p. 9, 1976.

[117] G. N. Haidemenopoulos, N. Aravas, and I. Bellas, 'Kinetics of strain-induced transformation of dispersed austenite in low-alloy TRIP steels', *Mater. Sci. Eng. A*, vol. 615, pp. 416–423, Oct. 2014, doi: 10.1016/j.msea.2014.07.099.

[118] I. Papatriantafillou, M. Agoras, N. Aravas, and G. Haidemenopoulos, 'Constitutive modeling and finite element methods for TRIP steels', *Comput. Methods Appl. Mech. Eng.*, vol. 195, no. 37–40, pp. 5094–5114, Jul. 2006, doi: 10.1016/j.cma.2005.09.026.

[119] R. G. Stringfellow, D. M. Parks, and G. B. Olson, 'A constitutive model for transformation plasticity accompanying strain-induced martensitic transformations in metastable austenitic steels', *Acta Metall. Mater.*, vol. 40, no. 7, pp. 1703–1716, Jul. 1992, doi: 10.1016/0956-7151(92)90114-T.

[120] Y. Tomita and T. Iwamoto, 'Constitutive modeling of trip steel and its application to the improvement of mechanical properties', *Int. J. Mech. Sci.*, vol. 37, no. 12, pp. 1295–1305, Dec. 1995, doi: 10.1016/0020-7403(95)00039-Z.

[121] T. Iwamoto, T. Tsuta, and Y. Tomita, 'Investigation on deformation mode dependence of strain-induced martensitic transformation in trip steels and modelling of transformation kinetics', *Int. J. Mech. Sci.*, vol. 40, no. 2–3, pp. 173–182, Feb. 1998, doi: 10.1016/S0020-7403(97)00047-7.

[122] J. Lian, Z. Jiang, and J. Liu, 'Theoretical model for the tensile work hardening behaviour of dual-phase steel', *Mater. Sci. Eng. A*, vol. 147, no. 1, pp. 55–65, Oct. 1991, doi: 10.1016/0921-5093(91)90804-V.

[123] S. Berbenni, V. Favier, X. Lemoine, and M. Berveiller, 'Micromechanical modeling of the elastic-viscoplastic behavior of polycrystalline steels having different microstructures', *Mater. Sci. Eng. A*, vol. 372, no. 1–2, pp. 128–136, May 2004, doi: 10.1016/j.msea.2003.11.010.

[124] M. Delincé, Y. Bréchet, J. D. Embury, M. G. D. Geers, P. J. Jacques, and T. Pardoen, 'Structure–property optimization of ultrafine-grained dual-phase steels using a microstructure-based strain hardening model', *Acta Mater.*, vol. 55, no. 7, pp. 2337–2350, Apr. 2007, doi: 10.1016/j.actamat.2006.11.029.

[125] O. Bouaziz and P. Buessler, 'Mechanical behaviour of multiphase materials : an intermediate mixture law without fitting parameter', *Rev. Métallurgie*, vol. 99, no. 1, pp. 71–77, Jan. 2002, doi: 10.1051/metal:2002182.

[126] E. J. Seo, L. Cho, Y. Estrin, and B. C. De Cooman, 'Microstructure-mechanical properties relationships for quenching and partitioning (Q&P) processed steel', *Acta Mater.*, vol. 113, pp. 124–139, Jul. 2016, doi: 10.1016/j.actamat.2016.04.048.

[127] W. J. Dan, S. H. Li, W. G. Zhang, and Z. Q. Lin, 'The effect of strain-induced martensitic transformation on mechanical properties of TRIP steel', *Mater. Des.*, vol. 29, no. 3, pp. 604–612, Jan. 2008, doi: 10.1016/j.matdes.2007.02.019.

[128] G. W. Greenwood and R. H. Johnson, 'The deformation of metals under small stresses during phase transformations', *Proc. R. Soc. Lond. Ser. Math. Phys. Sci.*, vol. 283, no. 1394, pp. 403–422, Jan. 1965, doi: 10.1098/rspa.1965.0029.

[129] C. L. Magee, 'Phase transformations', *ASM Met. Park Ohio 1*, pp. 15–156, 1970.

[130] M. De Jong and G. W. Rathenau, 'Mechanical properties of an Iron-Carbon alloy during allotropic transformation', *Acta Metall.*, vol. 9, 1961.

[131] R. A. Kot and V. Weiss, 'Transformation plasticity in iron-nickel alloys', *Metall. Trans.*, vol. 1, p. 9, Oct. 1970.

[132] S. Meftah, 'Modélisation de la plasticité due à une transformation martensitique dans les aciers', *Inst. Natl. Sci. Appliquées INSA Rouen*, p. 144, Oct. 2007.

[133] J. B. Leblond, 'MATHEMATICAL MODELLING OF TRANSFORMATION PLASTICITY IN STEELS II: COUPLING WITH STRAIN HARDENING PHENOMENA', *Int. J. Plast.*, vol. 5, pp. 573–591, 1989.

[134] G. Reisner, E. A. Werner, and F. D. Fischer, 'Micromechanical modeling of martensitic transformation in random microstructures', *Int. J. Solids Struct.*, vol. 35, no. 19, pp. 2457–2473, Jul. 1998, doi: 10.1016/S0020-7683(97)00149-2.

[135] J. F. Hallai and S. Kyriakides, 'On the effect of Lüders bands on the bending of steel tubes. Part II: Analysis', *Int. J. Solids Struct.*, vol. 48, no. 24, pp. 3285–3298, Dec. 2011, doi: 10.1016/j.ijsolstr.2011.07.012.

[136] J. Ma, H. Liu, Q. Lu, Y. Zhong, L. Wang, and Y. Shen, 'Transformation kinetics of retained austenite in the tensile Lüders strain range in medium Mn steel', *Scr. Mater.*, vol. 169, pp. 1–5, Aug. 2019, doi: 10.1016/j.scriptamat.2019.04.044.

[137] S. Wang, W. Chen, Z. Zhao, X. Zhao, X. Luo, and Q. Wang, 'Effect of microstructure evolution on Lüders strain and tensile properties in an intercritical annealing medium-Mn steel', *J. Iron Steel Res. Int.*, Oct. 2020, doi: 10.1007/s42243-020-00498-7.

[138] B. Sun *et al.*, 'Discontinuous strain-induced martensite transformation related to the Portevin-Le Chatelier effect in a medium manganese steel', *Scr. Mater.*, vol. 133, pp. 9–13, May 2017, doi: 10.1016/j.scriptamat.2017.01.022.

[139] Y. Wang, Z. Ma, R. Song, S. Zhao, Z. Zhang, and W. Huo, 'Correlation between cementite precipitation and Portevin-Le Chatelier effect in a hot-rolled medium Mn steel', *Mater. Lett.*, vol. 258, p. 126796, Jan. 2020, doi: 10.1016/j.matlet.2019.126796.

[140] A. Kozłowska, B. Grzegorczyk, M. Morawiec, and A. Grajcar, 'Explanation of the PLC Effect in Advanced High-Strength Medium-Mn Steels. A Review', *Materials*, vol. 12, no. 24, p. 4175, Dec. 2019, doi: 10.3390/ma12244175.

[141] A. Yilmaz, 'The Portevin–Le Chatelier effect: a review of experimental findings', *Sci. Technol. Adv. Mater.*, vol. 12, no. 6, p. 063001, Dec. 2011, doi: 10.1088/1468-6996/12/6/063001.

[142] X. G. Wang, B. B. He, C. H. Liu, C. Jiang, and M. X. Huang, 'Extraordinary Lüders-strain-rate in medium Mn steels', *Materialia*, vol. 6, p. 100288, Jun. 2019, doi: 10.1016/j.mtla.2019.100288.

[143] A. H. Cottrell and B. A. Bilby, 'Dislocation Theory of Yielding and Strain Ageing of Iron', *Proc. Phys. Soc. Sect. A*, vol. 62, no. 1, pp. 49–62, Jan. 1949, doi: 10.1088/0370-1298/62/1/308.

[144] M. Mazière, 'Modelling the Portevin-Le Chatelier effect in metallic alloys', *Habilit. À Dir. Rech. Univ. Pierre Marie Curie*, Jun. 2016.

[145] X. G. Wang, L. Wang, and M. X. Huang, 'Kinematic and thermal characteristics of Lüders and Portevin-Le Châtelier bands in a medium Mn transformation-induced plasticity steel', *Acta Mater.*, vol. 124, pp. 17–29, Feb. 2017, doi: 10.1016/j.actamat.2016.10.069.

[146] D. Zhemchuzhnikova, 'Influence of the extreme grain size reduction on plastic deformation instability in an AlMg and AlMgScZr alloys', p. 154, 2018.

[147] M. Callahan, 'Analyse de la cinétique de transformation et des instabilités de déformation dans des aciers TRIP "'Moyen Manganèse'" de 3ème génération', p. 190.

[148] B. Sun *et al.*, 'Macroscopic to nanoscopic in situ investigation on yielding mechanisms in ultrafine grained medium Mn steels: Role of the austenite-ferrite interface', *Acta Mater.*, vol. 178, pp. 10–25, Oct. 2019, doi: 10.1016/j.actamat.2019.07.043.

[149] J. Ma, H. Liu, Q. Lu, Y. Zhong, L. Wang, and Y. Shen, 'Temperature-Dependent Macroscopic Mechanical Behaviors and Their Microscopic Explanations in a Medium Mn Steel', *Metall. Mater. Trans. A*, vol. 51, no. 10, pp. 5180–5186, Oct. 2020, doi: 10.1007/s11661-020-05958-z.

[150] L. E. Murr, 'Dislocation Ledge Sources: Dispelling the Myth of Frank–Read Source Importance', *Metall. Mater. Trans. A*, p. 16, 2016.

[151] L. Capolungo, D. E. Spearot, M. Cherkaoui, D. L. McDowell, J. Qu, and K. I. Jacob, 'Dislocation nucleation from bicrystal interfaces and grain boundary ledges: Relationship to nanocrystalline deformation', *J. Mech. Phys. Solids*, vol. 55, no. 11, pp. 2300–2327, Nov. 2007, doi: 10.1016/j.jmps.2007.04.001.

[152] F. K. Yan, 'Strength and ductility of 316L austenitic stainless steel strengthened by nano-scale twin bundles', *Acta Mater.*, p. 13, 2012.

[153] O. Bouaziz, Y. Estrin, Y. Bréchet, and J. D. Embury, 'Critical grain size for dislocation storage and consequences for strain hardening of nanocrystalline materials', *Scr. Mater.*, vol. 63, no. 5, pp. 477–479, Sep. 2010, doi: 10.1016/j.scriptamat.2010.05.006.

[154] J. Han and Y.-K. Lee, 'The effects of the heating rate on the reverse transformation mechanism and the phase stability of reverted austenite in medium Mn steels', *Acta Mater.*, vol. 67, pp. 354–361, Apr. 2014, doi: 10.1016/j.actamat.2013.12.038.

[155] A. Müller, C. Segel, M. Linderov, A. Vinogradov, A. Weidner, and H. Biermann, 'The Portevin–Le Châtelier Effect in a Metastable Austenitic Stainless Steel', *Metall. Mater. Trans. A*, vol. 47, no. 1, pp. 59–74, Jan. 2016, doi: 10.1007/s11661-015-2953-x.

[156] Z. H. Cai, H. Ding, R. D. K. Misra, and Z. Y. Ying, 'Austenite stability and deformation behavior in a cold-rolled transformation-induced plasticity steel with medium manganese content', *Acta Mater.*, vol. 84, pp. 229–236, Feb. 2015, doi: 10.1016/j.actamat.2014.10.052.

[157] S. Lee, S. Shin, M. Kwon, K. Lee, and B. C. De Cooman, 'Tensile Properties of Medium Mn Steel with a Bimodal UFG α + γ and Coarse δ-Ferrite Microstructure', *Metall. Mater. Trans. A*, vol. 48, no. 4, pp. 1678–1700, Apr. 2017, doi: 10.1007/s11661-017-3979-z.

[158] Y. Ma, 'Phase boundary segregation-induced strengthening and discontinuous yielding in ultrafine-grained duplex medium-Mn steels', *Acta Mater.*, p. 15, 2020.

[159] J. H. Ryu, 'Austenite stability and heterogeneous deformation in fine-grained transformation-induced plasticity-assisted steel', *Scr. Mater.*, p. 4, 2013.

[160] S. Yan, T. Li, T. Liang, J. Chen, Y. Zhao, and X. Liu, 'By controlling recrystallization degree: A plain medium Mn steel overcoming Lüders deformation and low yield-to-tensile ratio simultaneously', *Mater. Sci. Eng. A*, vol. 758, pp. 79–85, Jun. 2019, doi: 10.1016/j.msea.2019.05.012.

[161] Y. Estrin' and L. P. Kubin, 'LOCAL STRAIN HARDENING AND NONUNIFORMITY OF PLASTIC DEFORMATION', *Acta Metall.*, vol. 34, no. 12, p. 10, Feb. 1986.

[162] J.-H. Nam, S.-K. Oh, M. Park, and Y.-K. Lee, 'The mechanism of dynamic strain aging for type A serrations in tensile curves of a medium-Mn steel', *Acta Mater.*, vol. 206, p. 116613, Mar. 2021, doi: 10.1016/j.actamat.2020.116613.

[163] R. C. Picu, 'A mechanism for the negative strain-rate sensitivity of dilute solid solutions', *Acta Mater.*, vol. 52, no. 12, pp. 3447–3458, Jul. 2004, doi: 10.1016/j.actamat.2004.03.042.

[164] P. Penning, 'Mathematics of the Portevin-Le Chatelier effect', *Acta Metall.*, vol. 20, 1972.

[165] M. Mazière, 'Investigations on the Portevin Le Chatelier critical strain in an aluminum alloy', *Comput. Mater. Sci.*, p. 5, 2012.

[166] M. Mazière, C. Luis, A. Marais, S. Forest, and M. Gaspérini, 'Experimental and numerical analysis of the Lüders phenomenon in simple shear', *Int. J. Solids Struct.*, vol. 106–107, pp. 305–314, Feb. 2017, doi: 10.1016/j.ijsolstr.2016.07.026.

[167] A. S. Khan, M. Baig, S.-H. Choi, H.-S. Yang, and X. Sun, 'Quasi-static and dynamic responses of advanced high strength steels: Experiments and modeling', *Int. J. Plast.*, vol. 30–31, pp. 1–17, Mar. 2012, doi: 10.1016/j.ijplas.2011.08.004.

[168] X. Hu *et al.*, 'The In Situ Observation of Phase Transformations During Intercritical Annealing of a Medium Manganese Advanced High Strength Steel by High Energy X-Ray Diffraction', *Front. Mater.*, vol. 8, p. 32, Mar. 2021, doi: 10.3389/FMATS.2021.621784/BIBTEX.

[169] J. J. Mueller *et al.*, 'Austenite formation and cementite dissolution during intercritical annealing of a medium-manganese steel from a martensitic condition', *Mater. Des.*, vol. 203, p. 109598, May 2021, doi: 10.1016/J.MATDES.2021.109598.

[170] F. Equihua and A. Salinas, 'Determination of equilibrium transformation temperatures Ae_3 and Ae_1 for low-carbon steels using the *in situ* high-temperature X-ray diffraction technique', *Powder Diffr.*, vol. 25, no. 1, pp. 31–37, Mar. 2010, doi: 10.1154/1.3308411.

[171] S. M. C. van Bohemen, 'Bainite and martensite start temperature calculated with exponential carbon dependence', *Mater. Sci. Technol.*, vol. 28, no. 4, pp. 487–495, Apr. 2012, doi: 10.1179/1743284711Y.0000000097.

[172] P. Gravereau, 'LA DIFFRACTION DES RAYONS X PAR LES POUDRES', *Inst. Chim. Matière Condens. Bordx. ICMCB-CNRS*, p. 209, 2012.

[173] Y. Ren, 'High-Energy Synchrotron X-Ray Diffraction and Its Application to In Situ Structural Phase-Transition Studies in Complex Sample Environments', *JOM*, vol. 64, no. 1, pp. 140–149, Jan. 2012, doi: 10.1007/s11837-011-0218-8.

[174] G. Krauss, 'Martensite in steel: strength and structure', *Mater. Sci. Eng. A*, vol. 273–275, pp. 40–57, Dec. 1999, doi: 10.1016/S0921-5093(99)00288-9.

[175] H.-S. Park, J.-B. Seol, N.-S. Lim, S.-I. Kim, and C.-G. Park, 'Study of the decomposition behavior of retained austenite and the partitioning of alloying elements during tempering in CMnSiAl TRIP steels', *Mater. Des.*, vol. 82, pp. 173–180, Oct. 2015, doi: 10.1016/j.matdes.2015.05.059.

[176] S. M. C. Van Bohemen, 'The nonlinear lattice expansion of iron alloys in the range 100-1600 K', *Scr. Mater.*, vol. 69, no. 4, pp. 315–318, Aug. 2013, doi: 10.1016/j.scriptamat.2013.05.009.

[177] G. Ghosh and G. B. Olson, 'The isotropic shear modulus of multicomponent Fe-base solid solutions', *Acta Mater.*, vol. 50, no. 10, pp. 2655–2675, Jun. 2002, doi: 10.1016/S1359-6454(02)00096-4.

[178] 'Watershed-flooding-graph.png', *ImageJ*. https://imagej.net/File:Watershed-flooding-graph.png.html

[179] M. Kong, R. N. Bhattacharya, C. James, and A. Basu, 'A statistical approach to estimate the 3D size distribution of spheres from 2D size distributions', *Geol. Soc. Am. Bull.*, vol. 117, no. 1, p. 244, 2005, doi: 10.1130/B25000.1.

[180] A. Kumar, A. Dutta, S. K. Makineni, M. Herbig, R. H. Petrov, and J. Sietsma, 'In-situ observation of strain partitioning and damage development in continuously cooled carbide-free bainitic steels using micro digital image correlation', *Mater. Sci. Eng. A*, vol. 757, pp. 107–116, May 2019, doi: 10.1016/j.msea.2019.04.098.

[181] M. Callahan, 'Coincidence of strain-induced TRIP and propagative PLC bands in Medium Mn steels', *Mater. Sci.*, p. 10, 2017.

[182] M. Fazzini, 'DÉVELOPPEMENT DE MÉTHODES D'INTÉGRATION DES MESURES DE CHAMPS', *Univ. Toulouse*, p. 160, Dec. 2009.

[183] X. G. Wang, L. Wang, and M. X. Huang, 'Kinematic and thermal characteristics of Lüders and Portevin-Le Châtelier bands in a medium Mn transformation-induced plasticity steel', *Acta Mater.*, vol. 124, pp. 17–29, Feb. 2017, doi: 10.1016/j.actamat.2016.10.069.

[184] 'ARAMIS | GOM'. https://www.gom.com/fr/systemes-de-mesure/aramis.html

[185] I. S. Yasnikov, A. Vinogradov, and Y. Estrin, 'Revisiting the Considère criterion from the viewpoint of dislocation theory fundamentals', *Scr. Mater.*, vol. 76, pp. 37–40, Apr. 2014, doi: 10.1016/j.scriptamat.2013.12.009.

[186] J. Kieffer and G. Ashiotis, 'PyFAI: a Python library for high performance azimuthal integration on GPU', *ArXiv14126367 Astro-Ph*, Dec. 2014, Accessed: May 11, 2020. [Online]. Available: http://arxiv.org/abs/1412.6367

[187] M. Lamari, S. Y. P. Allain, G. Geandier, J.-C. Hell, A. Perlade, and K. Zhu, 'In Situ Determination of Phase Stress States in an Unstable Medium Manganese Duplex Steel Studied by High-Energy X-ray Diffraction', *Metals*, vol. 10, no. 10, p. 1335, Oct. 2020, doi: 10.3390/met10101335.

[188] G. Geandier, L. Vautrot, B. Denand, and S. Denis, 'In Situ Stress Tensor Determination during Phase Transformation of a Metal Matrix Composite by High-Energy X-ray Diffraction', *Materials*, vol. 11, no. 8, p. 1415, Aug. 2018, doi: 10.3390/ma11081415.

[189] V. Hauk, *Structural and Residual Stress Analysis by Nondestructive Methods: Evaluation - Application - Assessment*. Elsevier, 1997.

[190] L. Castex, J.-L. Lebrun, G. Maeder, and J.-M. Sprauel, *Détermination des contraintes résiduelles par diffraction des rayons X*. Paris, France: ENSAM, 1981.

[191] F. Heidelbach, C. Riekel, and H.-R. Wenk, 'Quantitative texture analysis of small domains with synchrotron radiation X-rays', *J. Appl. Crystallogr.*, vol. 32, no. 5, pp. 841–849, Oct. 1999, doi: 10.1107/S0021889899004999.

[192] G. Ghosh and G. B. Olson, 'The isotropic shear modulus of multicomponent Fe-base solid solutions', *Acta Mater.*, vol. 50, no. 10, pp. 2655–2675, Jun. 2002, doi: 10.1016/S1359-6454(02)00096-4.

[193] B. B. He, Z. Y. Liang, and M. X. Huang, 'Nanoindentation investigation on the initiation of yield point phenomenon in a medium Mn steel', *Scr. Mater.*, vol. 150, pp. 134–138, Jun. 2018, doi: 10.1016/j.scriptamat.2018.03.015.

[194] K. Yan, K.-D. Liss, I. B. Timokhina, and E. V. Pereloma, 'In situ synchrotron X-ray diffraction studies of the effect of microstructure on tensile behavior and retained austenite stability of thermo-mechanically processed transformation induced plasticity steel', *Mater. Sci. Eng. A*, vol. 662, pp. 185–197, Apr. 2016, doi: 10.1016/j.msea.2016.03.048.

[195] R. Hill, 'Elastic properties of reinforced solids: Some theoretical principles', *J. Mech. Phys. Solids*, vol. 11, no. 5, pp. 357–372, Sep. 1963, doi: 10.1016/0022-5096(63)90036-X.

[196] M. N. Shiekhelsouk, V. Favier, K. Inal, S. Allain, O. Bouaziz, and M. Cherkaoui, 'Residual and internal stress states in duplex steel with TWIP effect', p. 6.

[197] O. Bouaziz, T. Lung, M. Kandel, and C. Lecomte, 'Physical modelling of microstructure and mechanical properties of dual-phase steel', *J. Phys. IV*, vol. 11, no. PR4, pp. Pr4-223-Pr4-231, Sep. 2001, doi: 10.1051/jp4:2001428.

[198] P. J. Jacques, F. Delannay, and J. Ladrière, 'On the influence of interactions between phases on the mechanical stability of retained austenite in transformation-induced plasticity multiphase steels', *Metall. Mater. Trans. A*, vol. 32, no. 11, pp. 2759–2768, Nov. 2001, doi: 10.1007/s11661-001-1027-4.

[199] D. Q. Zou, S. H. Li, and J. He, 'Temperature and strain rate dependent deformation induced martensitic transformation and flow behavior of quenching and partitioning steels', *Mater. Sci. Eng. A*, vol. 680, pp. 54–63, Jan. 2017, doi: 10.1016/j.msea.2016.10.083.

[200] N. I. Vázquez-Fernández, T. Nyyssönen, M. Isakov, M. Hokka, and V.-T. Kuokkala, 'Uncoupling the effects of strain rate and adiabatic heating on strain induced martensitic phase transformations in a metastable austenitic steel', *Acta Mater.*, vol. 176, pp. 134–144, Sep. 2019, doi: 10.1016/j.actamat.2019.06.053.

[201] O. Bouaziz, S. Allain, C. P. Scott, P. Cugy, and D. Barbier, 'High manganese austenitic twinning induced plasticity steels: A review of the microstructure properties relationships', *Curr. Opin. Solid State Mater. Sci.*, vol. 15, no. 4, pp. 141–168, Aug. 2011, doi: 10.1016/j.cossms.2011.04.002.

[202] I.-C. Jung and B. C. De Cooman, 'Temperature dependence of the flow stress of Fe–18Mn–0.6C–xAl twinning-induced plasticity steel', *Acta Mater.*, vol. 61, no. 18, pp. 6724–6735, Oct. 2013, doi: 10.1016/j.actamat.2013.07.042.

[203] C. W. Sinclair, W. J. Poole, and Y. Bréchet, 'A model for the grain size dependent work hardening of copper', *Scr. Mater.*, vol. 55, no. 8, pp. 739–742, Oct. 2006, doi: 10.1016/j.scriptamat.2006.05.018.

[204] K. S. Kumar, H. Van Swygenhoven, and S. Suresh, 'Mechanical behavior of nanocrystalline metals and alloys11The Golden Jubilee Issue—Selected topics in Materials Science and Engineering: Past, Present and Future, edited by S. Suresh', *Acta Mater.*, vol. 51, no. 19, pp. 5743–5774, Nov. 2003, doi: 10.1016/j.actamat.2003.08.032.

[205] S. Takaki, K. Kawasaki, and Y. Kimura, 'Mechanical properties of ultra ®ne grained steels', *J. Mater. Process. Technol.*, p. 5, 2001.

[206] S. Ren, M. Mazière, S. Forest, T. F. Morgeneyer, and G. Rousselier, 'A constitutive model accounting for strain ageing effects on work-hardening. Application to a C–Mn steel', *Comptes Rendus Mécanique*, vol. 345, no. 12, pp. 908–921, Dec. 2017, doi: 10.1016/j.crme.2017.09.005.

[207] P. G. McCormick, 'Theory of flow localisation due to dynamic strain ageing', *Acta Metall.*, vol. 36, no. 12, pp. 3061–3067, Dec. 1988, doi: 10.1016/0001-6160(88)90043-0.

[208] M. Erdogan and R. Priestner, 'Effect of martensite content, its dispersion, and epitaxial ferrite content on Bauschinger behaviour of dual phase steel', *Mater. Sci. Technol.*, vol. 18, no. 4, pp. 369–376, Apr. 2002, doi: 10.1179/026708302225001679.

[209] R. V. Milligan, W. H. Koo, and T. E. Davidson, 'The Bauschinger Effect in a High-Strength Steel', *J. Basic Eng.*, vol. 88, no. 2, pp. 480–488, Jun. 1966, doi: 10.1115/1.3645883.

[210] J. Macchi *et al.*, 'Dislocation densities in a low-carbon steel during martensite transformation determined by in situ high energy X-Ray diffraction', *Mater. Sci. Eng. A*, vol. 800, p. 140249, Jan. 2021, doi: 10.1016/j.msea.2020.140249.

[211] J. Macchi, G. Geandier, J. Teixeira, S. Denis, F. Bonnet, and S. Y. P. Allain, 'Time-resolved in-situ dislocation density evolution during martensitic transformation by high-energy-XRD experiments: A study of C content and cooling rate effects', *Materialia*, vol. 26, p. 101577, Dec. 2022, doi: 10.1016/j.mtla.2022.101577.

[212] S. Allain, O. Bouaziz, and M. Takahashi, 'Toward a New Interpretation of the Mechanical Behaviour of As-quenched Low Alloyed Martensitic Steels', *ISIJ Int.*, vol. 52, no. 4, pp. 717–722, 2012, doi: 10.2355/isijinternational.52.717.

[213] S. M. C. van Bohemen and J. Sietsma, 'Modeling of isothermal bainite formation based on the nucleation kinetics', *Int. J. Mater. Res.*, vol. 99, no. 7, pp. 739–747, Jul. 2008, doi: 10.3139/146.101695.

[214] L. Kaufman and M. Cohen, 'Thermodynamics and kinetics of martensitic transformations', *Prog. Met. Phys.*, vol. 7, pp. 165–246, Jan. 1958, doi: 10.1016/0502-8205(58)90005-4.

[215] G. B. Olson and M. Cohen, 'A General Mechanism of Martensitic Nucleation: Part II. FCC - , - B C C and Other Martensitic Transformations', *Metall. Trans. A*, p. 10, 1976.

[216] S. Lee, Y. Estrin, and B. C. De Cooman, 'Constitutive Modeling of the Mechanical Properties of V-added Medium Manganese TRIP Steel', *Metall. Mater. Trans. A*, vol. 44, no. 7, pp. 3136–3146, Jul. 2013, doi: 10.1007/s11661-013-1648-4.

[217] S. Lee and B. C. De Cooman, 'Tensile Behavior of Intercritically Annealed 10 pct Mn Multi-phase Steel', *Metall. Mater. Trans. A*, vol. 45, no. 2, pp. 709–716, Feb. 2014, doi: 10.1007/s11661-013-2047-6.

[218] J.-M. Pipard, T. Balan, F. Abed-Meraim, and X. Lemoine, 'Elasto-visco-plastic modeling of mild steels for sheet forming applications over a large range of strain rates', *Int. J. Solids Struct.*, vol. 50, no. 16–17, pp. 2691–2700, Aug. 2013, doi: 10.1016/j.ijsolstr.2013.04.022.

[219] S. Allain, O. Bouaziz, and J. P. Chateau, 'Thermally activated dislocation dynamics in austenitic FeMnC steels at low homologous temperature', *Scr. Mater.*, vol. 62, no. 7, pp. 500–503, Apr. 2010, doi: 10.1016/j.scriptamat.2009.12.026.

[220] J. Han, S.-J. Lee, C.-Y. Lee, S. Lee, S. Y. Jo, and Y.-K. Lee, 'The size effect of initial martensite constituents on the microstructure and tensile properties of intercritically annealed Fe–9Mn–0.05C steel', *Mater. Sci. Eng. A*, vol. 633, pp. 9–16, May 2015, doi: 10.1016/j.msea.2015.02.075.

[221] H. Luo, Y. Li, W. Li, S. Zhong, C. Xu, and X. Jia, 'Interactions of nanoprecipitates, metastable austenite, and Lüders banding in an ultra-low carbon medium Mn steel with abnormal strength dependence of hydrogen embrittlement', *Materialia*, vol. 22, p. 101380, May 2022, doi: 10.1016/j.mtla.2022.101380.

[222] L. Liu *et al.*, 'Effect of different matrix structure in medium-Mn quenching and partitioning steel on austenite stability and work hardening behavior', *Mater. Today Commun.*, vol. 32, p. 103851, Aug. 2022, doi: 10.1016/j.mtcomm.2022.103851.

[223] P. Kantanen *et al.*, 'Microstructures and mechanical properties of three medium-Mn steels processed via quenching and partitioning as well as austenite reversion heat treatments', *Mater. Sci. Eng. A*, vol. 847, p. 143341, Jul. 2022, doi: 10.1016/j.msea.2022.143341.

[224] M. A. Lebedkin and L. R. Dunin-Barkovski, 'Dynamic mechanism of the temperature dependence of the Portevin–Le Chaˆ telier effect', *Phys Solid State*, p. 6, 1998.

[225] T. Maki, K. Kobayashi, and I. Tamura, 'EFFECT OF AUSAGING ON THE MORPHOLOGY OF MARTENSITE IN Fe-Ni-Ti-Co ALLOYS', *J. Phys. Colloq.*, vol. 43, no. C4, pp. C4-541-C4-546, Dec. 1982, doi: 10.1051/jphyscol:1982484.

[226] L. Malet, 'The formation of plate martensite in a Fe-High Ni alloy: Crystallography and Variant Selection', May 2015, Accessed: Jun. 28, 2020. [Online]. Available: http://hdl.handle.net/2013/

[227] D. T. Han, Y. B. Xu, F. Peng, Y. Zou, and R. D. K. Misra, 'The determining role of pre-annealing on Mn partitioning behavior in medium-Mn-TRIP steel: experimental and numerical simulation', *J. Mater. Sci.*, vol. 55, no. 10, pp. 4437–4452, Apr. 2020, doi: 10.1007/s10853-019-04256-3.

[228] A. M. Sherman, G. T. Eldis, and M. Cohen, 'The aging and tempering of iron-nickel-carbon martensites', *Metall. Trans. A*, p. 11.

[229] F. D. Fischer, G. Reisner, E. Werner, K. Tanaka, G. Cailletaud, and T. Antretter, 'A new view on transformation induced plasticity (TRIP)', *Int. J. Plast.*, vol. 16, no. 7–8, pp. 723–748, Jun. 2000, doi: 10.1016/S0749-6419(99)00078-9.

[230] F. D. Fischer and G. Reisner, 'A criterion for the martensitic transformation of a microregion in an elastic–plastic material', *Acta Mater.*, vol. 46, no. 6, pp. 2095–2102, Mar. 1998, doi: 10.1016/S1359-6454(97)00374-1.

[231] J. Serri, M. Martiny, and G. Ferron, 'Finite element analysis of the effects of martensitic phase transformation in TRIP steel sheet forming', *Int. J. Mech. Sci.*, vol. 47, pp. 884–901, Jun. 2005, doi: 10.1016/j.ijmecsci.2005.02.001.

[232] H. N. Han, C. G. Lee, C.-S. Oh, T.-H. Lee, and S.-J. Kim, 'A model for deformation behavior and mechanically induced martensitic transformation of metastable austenitic steel', *Acta Mater.*, vol. 52, no. 17, pp. 5203–5214, Oct. 2004, doi: 10.1016/j.actamat.2004.07.031.

[233] C. Deleuze, 'Méthodologie d'analyse des contraintes résiduelles par diffraction des rayons X sur des pièces d'alliage de titane de nuance Ti-10V-2Fe-3Al', *Arts Métiers ParisTech*, p. 176, Oct. 2010.

[234] D. Faurie, G. Geandier, P.-O. Renault, E. Le Bourhis, and D. Thiaudière, 'Sin2 ψ analysis in thin films using 2D detectors: Non-linearity due to set-up, stress state and microstructure', *Thin Solid Films*, vol. 530, pp. 25–29, Mar. 2013, doi: 10.1016/j.tsf.2012.02.031.

[235] S. Roy, J. Gibmeier, and A. Wanner, 'In situ Study of Internal Load Transfer in a Novel Metal/Ceramic Composite Exhibiting Lamellar Microstructure Using Energy Dispersive Synchrotron X-ray Diffraction', *Adv. Eng. Mater.*, vol. 11, no. 6, pp. 471–477, Jun. 2009, doi: 10.1002/adem.200800352.

Appendix A: Martensitic transformation phenomenology

Several mechanisms have been theorised to describe how austenite can become martensite from a crystallographic point of view, i.e. what the displacement of each atom is during the transformation. The first description was made by Bain and Dunkirk in 1924 [79]. In this paper, the authors highlight that austenite, usually described with an FCC structure (Figure 148 (a)) can also be described with an BCT structure (red unit cell in Figure 148 (b)) with a c/a ratio of √2. The strain describing the martensitic transformation, called the Bain strain ε_{Bain}, is then reduced to a compression in the long direction and a dilatation in the other directions, as shown in Figure 148 c, b. The Bain strain matrix in the (b_1, b_2, b_3) basis (as seen in Figure 148) is thus:

$$\varepsilon_{Bain} = \begin{bmatrix} \frac{\sqrt{2}\, a_{\alpha'}}{a_\gamma} & 0 & 0 \\ 0 & \frac{\sqrt{2}\, a_{\alpha'}}{a_\gamma} & 0 \\ 0 & 0 & \frac{c_{\alpha'}}{a_\gamma} \end{bmatrix}_{(b_1,b_2,b_3)} \quad (0\text{—}1)$$

with a_γ the austenite lattice parameter with an FCC structure, $a_{\alpha'}$ and $c_{\alpha'}$ the martensite lattice parameters.

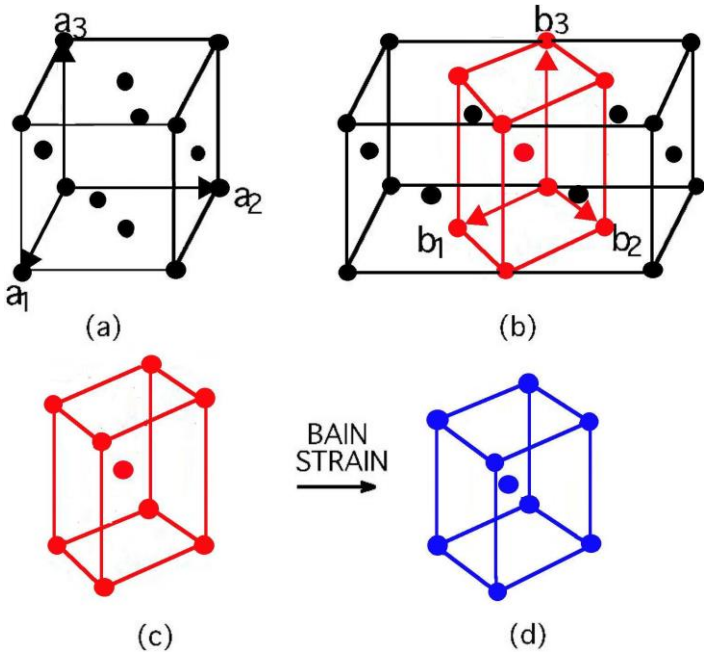

Figure 148: (a) Austenite lattice with an FCC structure. (b) Austenite lattice described as a BCT structure (in red), inscribed in the classical FCC structure (in black). The Bain strain is then described as the strain transforming the red austenite cell (c) into the blue martensite cell (d) [76].

By itself, the Bain strain cannot fully describe martensitic transformation. Indeed, as the γ/α' interface is glissile [77], the strain at the origin of the deformation must contain an invariant line, which is not the case of ε_{Bain}. However, composing the Bain strain ε_{Bain} with a rigid body rotation ω_{Rot} can solve

this incompatibility. Nevertheless, the resulting strain $\varepsilon_{Bain} \times \omega_{Rot}$ is still inconsistent from the empirically measured strain ε_{emp} discussed before and fail to explain the observed habit planes. Several developments exist in the literature to explain this apparent anomaly, like the Phenomenological Theory of Martensite Crystallography (PTMC) [76], [80], or more recently the Minimization of atomic Displacement (MD) theory [81]. The Figure 149, extracted from the MD theory [81], highlights the steps to obtain a deformation that is macroscopically similar to the invariant-plane strain ε_{emp} but microscopically similar to the Bain strain ε_{Bain}. In grey dotted-line is the original austenite habit plane before transformation, and in black is the same plane after the martensitic transformation. The two first steps show the successive application of ε_{Bain} and ω_{Rot}. Then, the two last steps highlight the effect of a slipping process.

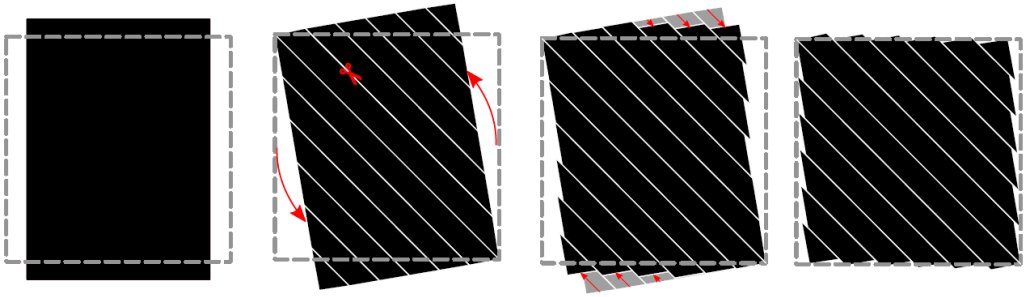

Figure 149 : Illustration of the effect of the slipping process. The dashed squares show the undistorted plane and the black rectangle on the left shows that same plane to which the Bain strains of -18,4% and 15,5% are applied. The steps to obtain a shape that is macroscopically similar to the undistorted plane but microscopically similar to the Bain-strained plane are shown from left to right [81].

The strain accompanying the martensitic transformation is the origin of high elastic energy. This will lead to an accommodation of elastic strain by several inelastic mechanism, such as the apparition of auto-accommodating variants, the morphological adaption of martensite (plate, lath…) and the plastic deformation by twinning and slipping [35]. Contrary to PTMC model, the observed habit plane or the shear deformations are not an entry of the model but are deduced from the simulation. [81].

Appendix B: Plate and lath martensite

At a mesoscopic scale, martensite can reveal varied morphologies, depending on its mother phase composition and deformation and the transformation temperature. Even though numerous nomenclatures exist to describe the possible morphologies of the martensite, authors in literature mainly describe two forms of martensite: plate and lath [82]. For plate martensite one dimension of martensite "grain" is negligible compared with the others two while for lath martensite, two dimensions are negligible to the last one.

In the plate-like shape, also referred as lenticular or feather-like shape, martensite consists of coarse neighbouring plates. Some authors still distinguish lenticule from plate, considering that lenticular martensite is thicker than thin-plate martensite [82], [225]. Figure 150 is an electron backscatter diffraction (EBSD) map. The yellow dotted-line corresponds to the prior austenite boundary. At the centre of lenses, there are midribs, which consist of closely spaced transformation twins [174]. Plate martensite contains both fine mechanical twins and dislocation tangles. In this case, the mother austenite has a low M_s temperature, below 100°C.

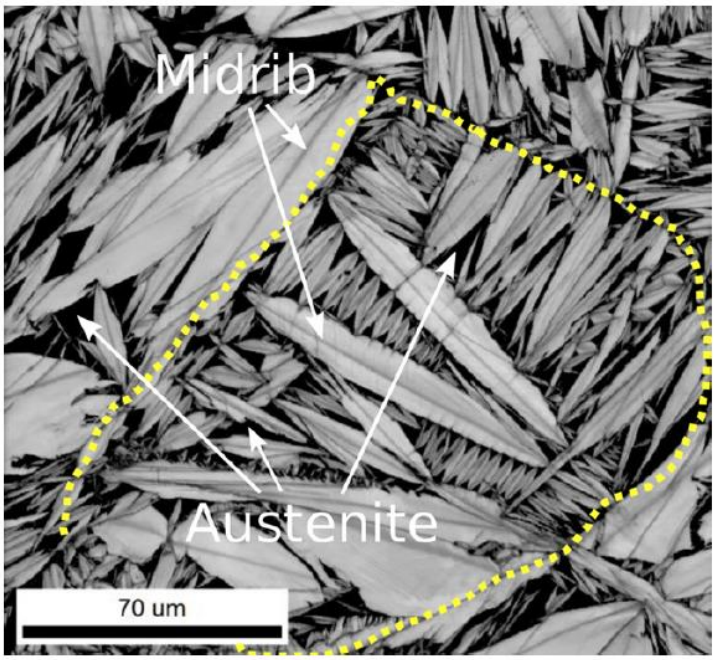

Figure 150: Lenticular martensite (grey) in a Fe-31Ni-0.155C observed by EBSD. Midrib corresponds to the twinned region at the centre of the plate. Black areas correspond to residual austenite [82], [226].

In contrast, lath-like martensite is formed in an austenite having a higher M_s, thus formed at higher temperature, typically above 300°C [82]. In medium Mn steels, austenite M_S temperature after IA is around room temperature. Therefore, the martensite should be plate-like. However, in the literature, martensite is reported to have a lath morphology [5], [65], [74], [227].

Martensite laths are structured in sets named blocks and packets. Such microstructure is shown in Figure 151 [7]. The studied steel is a medium Mn steel (Fe/0.3C/2Mn/1.5Si) in its as-quenched state from an austenitic annealing. Blocks consist of laths sharing the same orientation relationship with the mother austenite, while packets consist of blocks that share the same habit plane. The prior

austenite grain boundary (PAGB) is indicated by a dotted-white line in Figure 151 (a) and (b), while a packet boundary (PB) is indicated in black. At a higher magnification, in Figure 151 (c), blocks boundaries are indicated in black, while the white lines (low angle misorientation) reveal boundaries between laths. The X-ray diffractogram (Figure 25 (d)) highlights a very small amount of retained austenite in this steel, estimated to be around 2% by Zhang et al. [7].

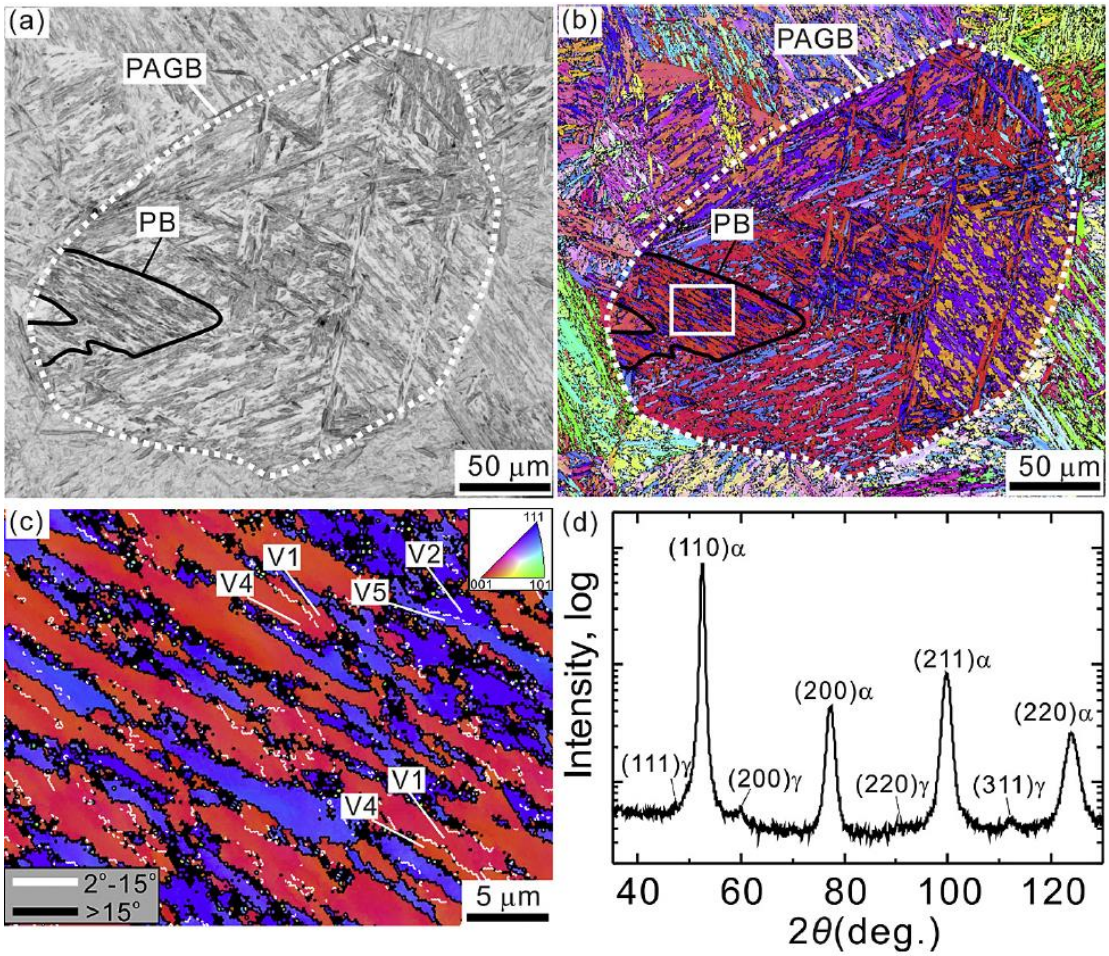

Figure 151: Martensite laths found in an as-quenched steel (Fe-2Mn-1.5SI-0.3C) observed in (a) an OM image and (b) a α orientation map. PAGB corresponds to the prior austenite grain boundary, PB corresponds to the packet boundary. (c) is a zoom from the white rectangle in the (b) map, where low and high angle boundaries are indicated. (d) is the X-ray diffraction profile of the specimen [7].

As explained before, the morphology of martensite is often linked with the M_s temperature of the austenite because of chemical considerations. Sherman et al. have detailed the complex relationship between the austenite alloying content and the morphology of martensite [228]. As depicted in Figure 152, in Fe-Ni-C steels, linear relationships between their content in nickel and carbon delimitate domains in which the martensite will be lath-like or plate-like [228]. A grey area exists between those two ideal morphologies, in which martensite will have mixed morphologies. In this graph, isopleths of M_s temperature are indicated by dashed-lines. Their non-linear shape demonstrates that knowing the M_s temperature of austenite is however not sufficient to predict the martensite morphology.

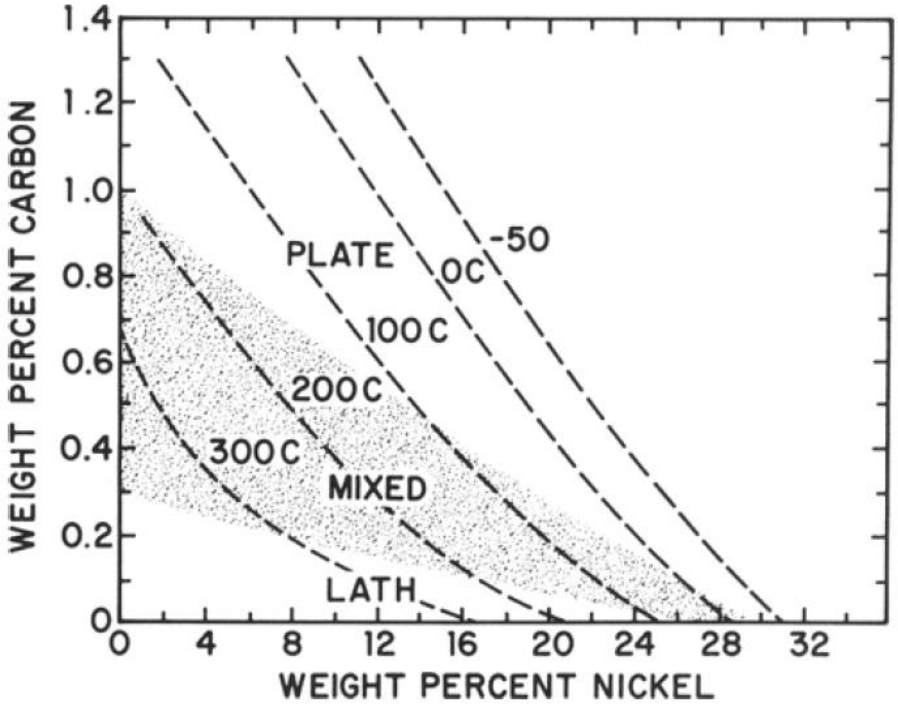

Figure 152: The morphology of martensite as a function of the composition in Ni and C of the former austenite. The dashed-line correspond to isopleths of M_s temperature [228].

The dependence of the martensite morphology on the carbon content in Fe-C alloys is reported in Figure 153 from Krauss et al.'s work [174]. The results differs slightly from the results of Sherman et al. [228] detailed in the last paragraph. Under 0.6% of C, under normal water or oil quench conditions, lath martensite is expected. Above 1.0% of C, martensite will be plate-like. Usually, twinning is reported in high-carbon plate martensite, while plasticity by dislocation motion is reported in low-carbon lath martensite. However, Krauss et al. [174] have reported that twinned martensite can also be found in low-carbon steel, when the cooling rate is high enough, as illustrated in Figure 153. Indeed, in such ultra-fast cooling case, dislocation motion is suppressed, hence replaced by mechanical twinning. The "normal" cooling rate martensite are reported with black dots, while the fast cooling rate martensite is reported with crosses. It can also be observed from this graph that very high cooling rate decreases the M_s temperature for a given chemical composition.

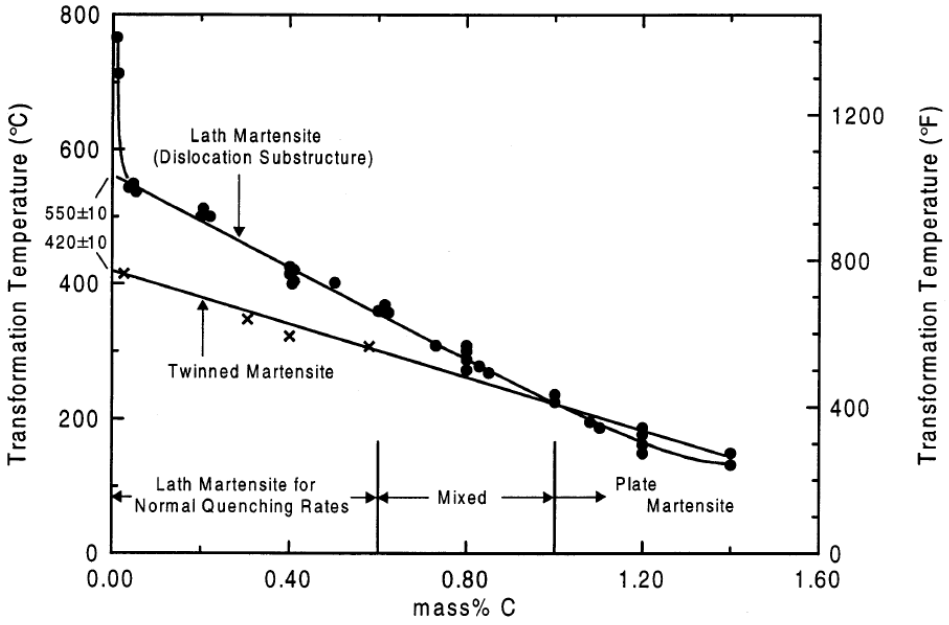

Figure 153: Morphology of martensite and M_s temperature as a function of the carbon content in Fe-C alloys. Two cooling rates are represented (water quench cooling rate martensite is reported with black dots, ultra-fast cooling rate martensite is reported with crosses) [174].

Appendix C: Improvements of Olson-Cohen model

1. Homogeneous germination theory extension to OC model

Perlade's approach on OC model was used in the thesis for its reliance on very few non-physically measurable parameters. However, other models exist and are acknowledged in this section. The developments which allow to account for 3D, triaxiality and strain rate effect are also detailed in this appendix.

Another way to incorporate thermodynamical quantities in OC model is to use the classical homogeneous germination theory. Introduced for SIMT by Olson and Cohen in 1976 [114]–[116], the germination of embryos is controlled by a competition between volumetric driving force and the surface energy of martensite/austenite interface. Firstly proven for γ⟶ε SIMT [114], the justification of germination theory was quickly extended to γ⟶α' SIMT [115], [116]. In this theory, the SIMT kinetics is controlled by the critical embryo thickness n*. Haidemenopoulos et al. recently adapted it for the case of dispersed austenite in medium Mn steel [117]. In their work, they calculate the critical embryo thickness as:

$$\boldsymbol{n^* = \frac{2\,\gamma_s}{\rho_{fe}\left[\Delta G_{ch} + \Delta G_{\sigma} + E_{str} + W_f\right]}} \qquad \textbf{(0—1)}$$

In the previous equation, γ_s is the interfacial energy, ρ_{fe} is the number of moles per unit area in a close packed plane, ΔG_{ch} is the chemical driving force for the martensitic transformation, ΔG_{σ} is the mechanical contribution to driving force, E_{str} is the coherency strain energy and W_f is the frictional work of the interfacial motion. The different previous terms are either constant or dependent of austenite chemistry and stress state. The ΔG_{σ} term is equal to $\sigma_{\gamma} \times \partial \Delta G^{\gamma \rightarrow \alpha'} / \partial \sigma_{\gamma}$ from Perlade's model. Thus, the size n* varies with the austenite stress. In Haidemenopoulos et al's model, the number of martensitic embryos $N_{\alpha'}$ is divided in two: $N_{\alpha'}^{\sigma}$ are the additional embryos produced by stress; $N_{\alpha'}^{\varepsilon}$ are the additional embryos produced by strain. Both $N_{\alpha'}^{\sigma}$ and $N_{\alpha'}^{\varepsilon}$ are exponential function of the critical embryo size n*:

$$\boldsymbol{N_{\alpha'}^{\sigma} = N_{\alpha'}^{\sigma,0} \exp(-\alpha_{\sigma} n^*)} \qquad \textbf{(0—2)}$$

$$\boldsymbol{N_{\alpha'}^{\varepsilon} = N_{\alpha'}^{\varepsilon,max}\left(1 - exp\left(-k\left(\varepsilon_{\gamma}^{pl}\right)^{m}\right)\right) exp(-\alpha_{\varepsilon} n^*)} \qquad \textbf{(0—3)}$$

The number of stress-assisted embryos $N_{\alpha'}^{\sigma}$ is dependent of the initial number of pre-existing nucleation sites $N_{\alpha'}^{\sigma,0}$, the shape factor constant for the stress-modified potency distribution α_{σ} and n*. The number of strain-induced embryos $N_{\alpha'}^{\varepsilon}$ is dependent of the maximum number of nucleation sites that can be created by plastic deformation $N_{\alpha'}^{\varepsilon,max}$, two positive constants k and m, the shape factor constant for the strain-modified potency distribution α_{ε} and n*. While $N_{\alpha'}^{\sigma}$ is only a function of stress, $N_{\alpha'}^{\varepsilon}$ is both a function of the plastic strain and stress. The increasing fraction of martensite $f_{\alpha'}$ due to mechanically induced transformation is then expressed as a function of $N_{\alpha'}^{\sigma}$, $N_{\alpha'}^{\varepsilon}$ and the mean volume of austenite particles:

$$\alpha' = 1 - \exp\left(-V_\gamma\left(N_v^\sigma + N_v^\varepsilon\right)\right) \quad (0—4)$$

Equation (0—4) is in reality an alternative expression of Equation (I—18) from OC model. The model developed by Haidemenopoulos et al. [117] allows to describe the evolution of SIMT kinetics as a function of chemistry, austenite grain size and stress state. Polatidis et al. [86] recently used the same model to replicate experimental SIMT kinetics measured in Q&P steels by neutron diffraction during uniaxial tension, equibiaxial tension and biaxial tension/compression. They successfully captured the effect of size and triaxiality.

Finally, to learn more about the modelling of γ⟶ε⟶α' mechanically induced transformation, the reader should refer to Aristeidakis and Haidemenopoulos' recent paper [12], which summarizes the scientific development on this topic. They describe a mean-field micromechanical model to predict the behaviour of diverse TRIP-TWIP steels, based on the prediction of stress and strain at phase scale and an augmented OC model. Their SIMT model accounts for $\Delta G^{\gamma\rightarrow\varepsilon}$ via the stacking fault energy (SFE) and then uses it to predict the evolution of stress-assisted and strain-induced nucleation rate of twins, ε and α' embryos. They also model the growth in length, width and thickness of each kind of embryos using SFE. As ε-martensite does not appear in low-alloyed medium Mn steel, the modelling of γ⟶ε⟶α' will not be further detailed.

The previous sections highlighted that some improvement can be made on the original Olson-Cohen model to integrate thermodynamic quantities, allowing more easily to account for the effects of chemistry, temperature and the stress state sensitivity on SIMT kinetics. The presented models were all mean field models. However, full-field models also exist in the literature, also derived from the OC theory. They are most suitable to capture triaxiality and strain rate effect, as discussed in the next sections.

2. Full-field description of SIMT

The effect of stress triaxiality on SIMT was discussed in section I.3.A.c) and compared to experimental data. The mean field micromechanical model previously presented are sensitive to triaxiality thanks to the $\partial\Delta G^{\gamma\rightarrow\alpha'}/\partial\sigma_\gamma$ term used in Perlade's model and in Haidemenopoulos' model (respectively Equations (I—21) and (0—1)). However, the section I.3.A.c) revealed that the slope of the SIMT kinetics does not evolve monotonically with triaxiality index T^{3D} defined as the ratio between the volumetric and deviatoric stress invariants. However, the value of $\partial\Delta G^{\gamma\rightarrow\alpha'}/\partial\sigma_\gamma$ is linearly dependent on T^{3D} in the previous models, hence the previous models cannot reproduce all experimental trends. Therefore, full-field modelling is necessary to obtain 3D stress tensor evolution during mechanical loading and capture the effect of triaxiality on SIMT at grain scale.

Stringfellow et al. propose an alternative description of the mean-field OC model to make it suitable for tensorial calculus [119]. They express the OC model in a generalized rate form and include in the expression of martensite nucleation the effect of the stress state. After mathematical developments, the rate of increase in martensite volume fraction $df_{\alpha'}/dt$ is stated to be equal to under isothermal condition:

$$\frac{f_{\alpha'}}{dt} = (1 - f_m)\left(A\dot{\gamma}_\gamma + B\dot{T}^{3D}\right) \quad (0—5)$$

with γ_γ the plastic shear strain in the austenite, T^{3D} the triaxiality parameter. The A and B parameters are not constant and have a complex expression, rapidly explain here. For more details, please refer to original paper. The A coefficient is expressed as:

$$A = \alpha\,\beta_0\,r\,(1 - f_{sb})(f_{sb})^{r-1}\,P \quad (0—6)$$

with P the probability that a shear band intersection act as a nucleation site, f_{sb} the shear bands volume fraction, α, β_0 and r three parameters of the model. The probability P is calculated with the hypothesis that there is a gaussian distribution of shear band intersection potencies:

$$P = \frac{1}{\sqrt{2\pi}}\int_{-\infty}^{g} exp\left(-\frac{1}{2}\left[\frac{g' - \mu_P}{\sigma_P}\right]^2\right) dg' \quad (0—7)$$

In the last equation, μ_p and σ_p are the mean value and the standard deviation of the distribution (both determined experimentally), and g is a normalized thermodynamic driving force, defined as a linear function of T^{3D} and the normalized temperature Θ:

$$g = g_0 - g_1\Theta + g_2 T^{3D} \quad (0—8)$$

Coefficient B in the expression of $df_{\alpha'}/dt$ is then calculated as:

$$B = \frac{g_2}{\sqrt{2\pi}}\,\beta_0\,(f_{sb})^r\,exp\left(-\frac{1}{2}\left[\frac{g' - \mu_P}{\sigma_P}\right]^2\right) H\left(\dot{T}^{3D}\right) \quad (0—9)$$

where H is the Heaviside function, reflecting the irreversibility of the transformation. Stringfellow et al. then incorporate this model for SIMT in a self-consistent scheme to predict with finite element (FE) simulation the mechanical behaviour of conventional four phase TRIP-aided steels.

Prüger et al. [87], [88] improved the made by Stringfellow et al. by incorporating more thermodynamic quantities in the expression of $f_{\alpha'}$. In Equation (0—5), they replace the triaxiality parameter T^{3D} by the difference between the driving force $\Delta G^{\gamma\rightarrow\alpha}$ and an energy barrier $\Delta G_{barrier}$. The driving force $\Delta G^{\gamma\rightarrow\alpha}$ is the sum of chemical, temperature and triaxiality contributions. Following the work of Lani et al. [84], the energy barrier $\Delta G_{barrier}$ is described as a linear function of the austenite viscoplastic strain, based on the observation that dislocation density increase with strain facilitates martensitic transformation.

The last model presented in this section is not derived from the original Olson and Cohen theory. Developed by Fischer and Reisner [134], [229], [230], the SIMT occurs when a local transformation criterion (LTC) is satisfied. The LTC is based on the equations of conversation of mass, momentum and energy, the second law of thermodynamics and kinematic relations. The martensitic transformation occurs when thermodynamic force F overcomes a transformation barrier F_c, i.e. when $F > F_c$. Authors proposed the following expression for the thermodynamic force F acting on an interface point between austenite and martensite [134], [229]:

$$F = \left(\rho_\gamma\phi_\gamma - \rho_{\alpha'}\phi_{\alpha'}\right) - \left(\frac{\sigma_\gamma + \sigma_{\alpha'}}{2}\right) : \varepsilon^* \quad (0—10)$$

In this relationship, ρ_i is the density of each phase, ϕ_i is the chemical Helmholtz free energy, σ_i the local stress tensor of each phase and ε^* is the local transformation tensor. The inertia effect, the difference in martensite and austenite elastic constants and the discontinuity of the plastic strain at the interface point in a grain are neglected. The authors emphasize that the formula above does not include any term that explicitly depends on the elastic-plastic behaviour, even though σ_i depends on each phase plasticization. The value of energy barrier F_c has been reported to be between 150 and 200 MPa for steels. This point condition for the triggering of the transformation is extended to a microregion V_μ, which begins as a nucleus to become a lath or lens [134]:

$$\int_{V_\mu} \boldsymbol{\sigma}|_{ts}\, \boldsymbol{\varepsilon}^* \boldsymbol{dV} + \boldsymbol{V}_\mu\left(\boldsymbol{\rho}_\gamma \boldsymbol{\phi}_\gamma - \boldsymbol{\rho}_{\alpha'} \boldsymbol{\phi}_{\alpha'}\right) \geq \boldsymbol{V}_\mu \boldsymbol{F_c} + \boldsymbol{\Delta\Gamma} + \boldsymbol{W}^{\boldsymbol{\tau}}_{\boldsymbol{pl}} + \boldsymbol{W}^{\boldsymbol{\tau}}_{\boldsymbol{el}} \qquad \textbf{(0—11)}$$

where $\sigma|_{ts}$ is the stress state at the start of the transformation process, $\Delta\Gamma$ is the interfacial energy, W^{τ}_{pl} and W^{τ}_{el} are the plastic and elastic work due to the stress state fluctuation during the deformation. Those two last terms highly depend on the chosen variant of martensite, allowing for a good description of orientation relationship and crystallographic effects.

The full-field models presented in the previous sections can be implemented into finite element (FE) algorithms. They potentially allow to describe with more precision than mean-field model the effect of temperature, strain and stress partitioning among phases, chemistry, grain sizes and stress state on SIMT. They also give information on morphological and crystallographic aspect the SIMT, which is impossible with mean-field modelling. Several other models are found in the literature [118], [231], [232], but are not presented here for concision. One last important aspect of SIMT is its dependence on strain rate, which is reviewed in the next section.

3. Effect of strain rate on SIMT kinetics

Some basis to model strain-rate effect in TRIP aided steel is given in this section. Since no dynamic deformation test is envisioned for the PhD project, only a quick review is done.

Inspired by the work of Stringfellow et al. [119], Tomita and Iwamoto proposed a generalized law to predict the martensitic transformation kinetics, adding the strain rate sensibility in the model [120], [121]. The rate of increase in martensite volume fraction is expressed by the following equations, similar to the one obtained by Stringfellow:

$$\begin{aligned} \dot{\boldsymbol{f}}_{\boldsymbol{m}} &= (\mathbf{1} - \boldsymbol{f}_{\boldsymbol{m}})\, \boldsymbol{A}\dot{\boldsymbol{\gamma}}_{\boldsymbol{a}} \\ \boldsymbol{A} &= \boldsymbol{\alpha}\, \boldsymbol{\beta}_{\mathbf{0}}\, \boldsymbol{r}\, (\mathbf{1} - \boldsymbol{f}_{\boldsymbol{sb}})(\boldsymbol{f}_{\boldsymbol{sb}})^{\boldsymbol{r}-\mathbf{1}}\, \boldsymbol{P} \end{aligned} \qquad \textbf{(0—12)}$$

The different quantities are defined in the last section. The effect of strain rate is incorporated in the bands formation rate α, which is calculated as:

$$\boldsymbol{\alpha} = (\boldsymbol{\alpha}_1 \boldsymbol{T}^2 + \boldsymbol{\alpha}_2 \boldsymbol{T} + \boldsymbol{\alpha}_3)\left(\frac{\dot{\boldsymbol{\gamma}}_\gamma}{\dot{\boldsymbol{\gamma}}_{\boldsymbol{ref}}}\right)^{\boldsymbol{M}} \qquad \textbf{(0—13)}$$

with M a coefficient describing the sensibility to the strain rate and $\dot{\gamma}_{ref}$ the reference strain rate at which α_1, α_2 and α_3 have been measured. The effect of temperature and strain rate on the normalized driving force for SIMT $\tilde{g}$ is given in Figure 154 [120]. Four temperatures and two strain rates are

simulated. The low strain rate 5×10^{-4} s^{-1} corresponds to quasi-static tensile test (solid line). The high strain rate 5×10^{2} s^{-1} corresponds to dynamic tensile test (dashed line). The higher the driving force is, the more rapid the SIMT kinetics will be. The model demonstrates that austenite mechanical destabilization is quicker when temperature decreases and when the strain rate decrease (g̃ is higher). Another example of a 3D elastoplastic model using the same equations is given by Dan et al. [127]. The full understanding of strain rate effect on SIMT kinetics is still difficult in the literature, since the purely strain rate effect is always experimentally correlated with adiabatic heating and thus temperature effect.

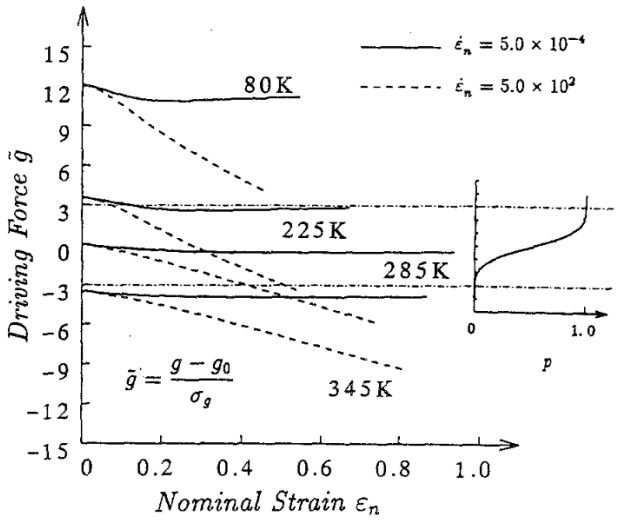

Figure 154: Normalized driving force g̃ for the martensitic transformation as a function of the strain. Its evolution is given for 4 temperatures and 2 strain rates. In solid line are the evolution of $\Delta G^{\gamma\rightarrow\alpha}$ at low strain rate (5×10^{-4} s^{-1}). In dashed line are the evolution of $\Delta G^{\gamma\rightarrow\alpha}$ at high strain rate (5×10^{2} s^{-1}) [120].

This Appendix C highlighted the numerous models existing for SIMT. The empirical models found in the literature allow for a quick evaluation of austenite mechanical stability, making it a function of one parameter only. However, they lack the predictive nature necessary to model mechanical behaviour of any given TRIP steel. The seminal work of Olson and Cohen on SIMT has been detailed. Two extensions of the OC theory suitable for mean-field scheme have been detailed, respectively the extension developed by Perlade et al. and the one developed by Haidemenopoulos et al. respectively. Other full-field models, inspired or not by OC framework, have been highlighted, alongside the numerous advantages of those models compared to mean-field scheme. While they allow for the description of more subtle physical phenomena, one downfall of full-field models is that they necessitate the calibration of numerous parameters, which is usually not done on physical basis. The goal of the PhD thesis is to obtain a microstructure-based description of the thermomechanical stability of austenite. Therefore, it was chosen to use a mean-field model in the PhD, as 3D models cannot be parametrized on microstructure basis. When comparing Perlade's and Haidemenopoulos' approaches, there is fewer and more microstructure-linked parameters in the former. Thus, the theory employed to model SIMT in the thesis project is a continuation of Perlade's one.

Appendix D: In situ carbon partitioning during intercritical annealing

To better understand the evolution of the repartition of carbon between the phases during intercritical annealing, the evolution of their respective contributions $f_i \times Ci$ (i = α, γ or θ) are shown for the four globular steels in Figure 155 and compared to the nominal carbon content of the steel (0.2 wt%, black line). In globular steel, the ferritic phase is truly ferrite, containing a negligible amount of carbon (red line). In the cold-rolled ferritic state, 70% of the global carbon is contained in the cementite (green line). The remaining carbon is situated in the small fraction of martensite-austenite films (blue) inherited from the intermediate annealing at 620°C between hot-rolling and cold-rolling. During heating stage, for the four thermal treatments, all carbon migrates to the cementite phase, while martensite-austenite films disappear. During IA, austenite nucleates while cementite dissolves. At this point, the blue curves in Figure 155 represent only the carbon contained in newly formed austenite. For high annealing temperatures (<720°C), the carbon quickly migrates from cementite to austenite. At 700°C, the complete dissolution of cementite only occurs at the middle of the intercritical holding (500 s), explaining the inverse U-shape curve observed for austenite carbon enrichment in GL700 experiment in Figure 61 (b). At the end of the annealing at 680°C, 40% of the total carbon is still captured by cementite.

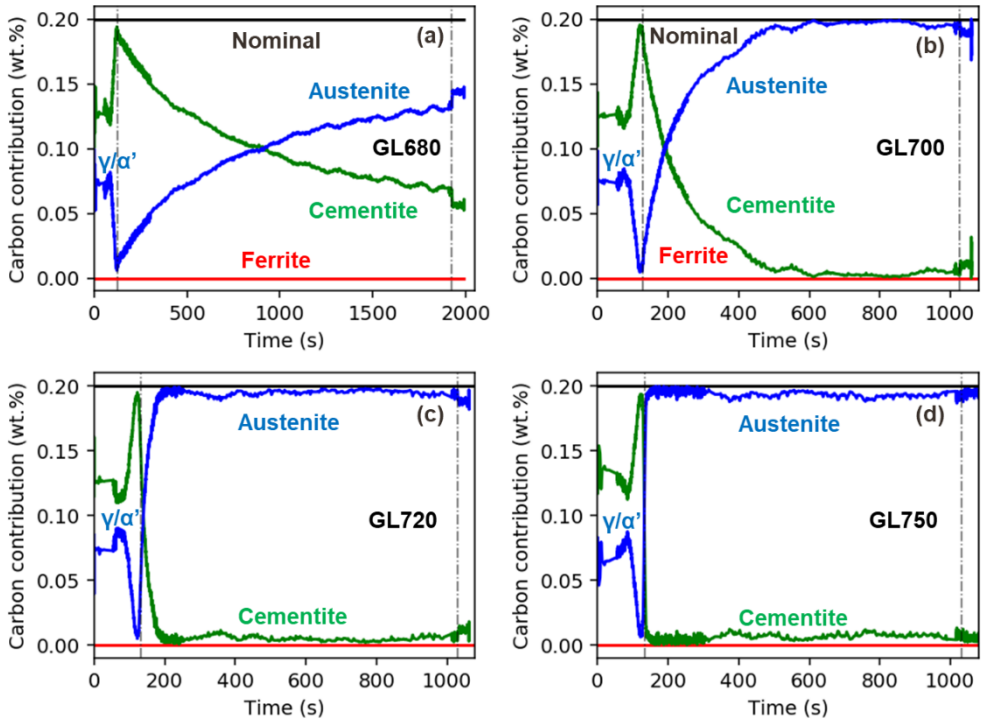

Figure 155: Repartition of the carbon between each phase of the globular steels: ferrite (red), austenite (blue), cementite (green). The nominal carbon content is indicated by the black line. (a) For GL680, (b) for GL700, (c) for GL720 and (d) for GL750 experiments. The first vertical line corresponds to heating end. The second vertical line corresponds to cooling start. A moving average filter was used to smooth the curves (10 closest neighbours).

Concerning fibrous steels, HEXRD techniques do not allow to distinguish the carbon contained in austenite from the one contained in the "ferritic" matrix (firstly as-quenched martensite, then annealed and highly recovered martensite). The evolutions of the total carbon contained in cementite $f_\theta \times C_\theta$ (green curves) during intercritical annealing is compared to the carbon contained in "ferrite" and austenite $f_\alpha \times C_\alpha + f_\gamma \times C_\gamma$ (purple curve) and to the nominal carbon content (black) in Figure 156 for the four two-step treatments. The sum $f_\alpha \times C_\alpha + f_\gamma \times C_\gamma$ is calculated as being $C_{tot} - f_\theta \times C_\theta$.

Contrary to globular steel, no carbon is initially situated in cementite. During the heating step and early isothermal holding, the available carbon migrates from as-quenched martensite to cementite. Except for FB680 microstructure, never all the carbon of the steel is situated in the cementite phase. At maximum, 90% of the carbon is situated in the cementite for FB700, and 80% for both FB720 and FB750 steels. Then, at annealing temperature higher than 720°C, the cementite quickly dissolves and all carbon goes to austenite/ferrite. For FB700, this process is slower, and only at the end of the isothermal holding that all cementite dissolves. In FB680 treatment, even after 30 min annealing, most of the available carbon is still contained in cementite (70%), explaining the low value of austenite carbon content found in Figure 61 for FB680 steel during the whole treatment.

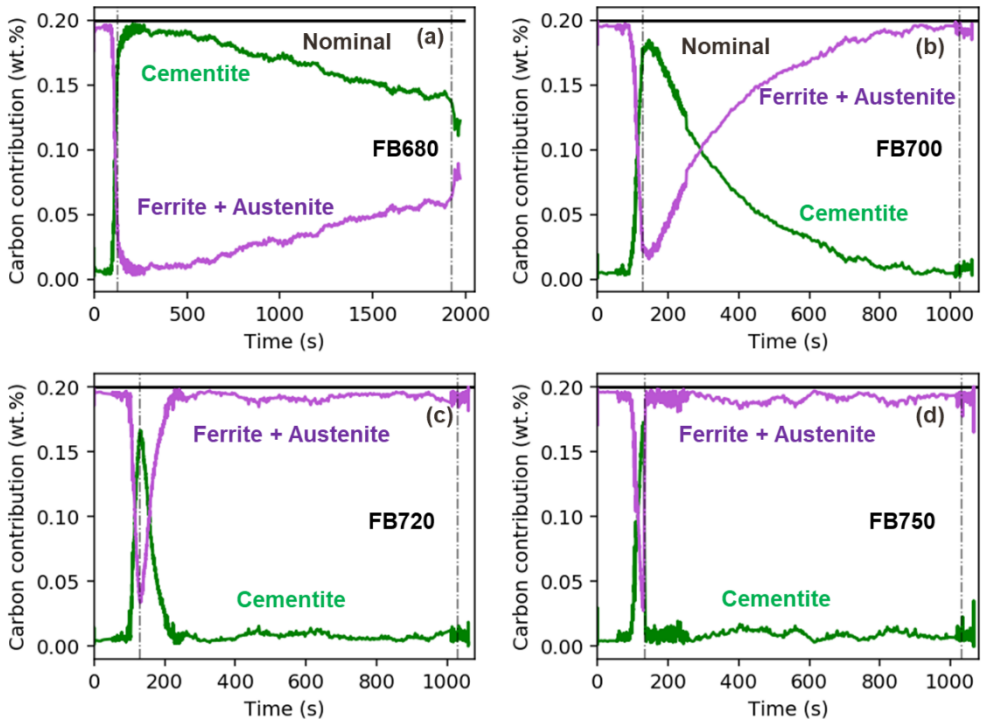

Figure 156: Repartition of the carbon between each phase of the fibrous steels: ferrite + austenite (purple), cementite (green). The nominal carbon content is indicated by the black line. (a) For FB680, (b) for FB700, (c) for FB 720 and (d) for FB 750 experiments. The first vertical line corresponds to heating end. The second vertical line corresponds to cooling start. A moving average filter was used to smooth the curves (10 closest neighbours).

Appendix E: SEM observations of HEXRD samples

SEM micrograph images of HEXRD samples are shown in Figure 157, Figure 158, Figure 159 and Figure 160 for GL680, GL700, GL720 and GL750 microstructures respectively. The images were made on a Zeiss Gemini 500 SEM microscope. Unfortunately, only the images for the globular specimens are available. The microstructures shown here are exactly those studied in situ in Chapter II from section II.1 to section II.4. The observations are made at ¼ of the thickness of the sample, near the thermocouple. The microstructures are similar to those obtained with in salt-bath (SEM observations in section II.5.B). With increasing annealing temperature, the amount of martensite/austenite (M/A) islands increase. Like for salt-bath treated specimens, the inheritance of cold-rolling is visible globular microstructures, with areas of acicular grains (highlighted in blue). In GL680 and GL700 specimens, cementite precipitates can be seen. For GL680, it is in accordance with the results of the RIR method presented in section II.3.D. For GL700 sample, all cementite carbides disappear before the end of the experiment with the RIR method. While a small amount of retained cementite is present and seems very small in GL700 microstructure according to SEM observation. The M/A islands in GL750 microstructure seems essentially composed of martensite, in accordance with the Rietveld results. Their appearance and morphology are different from that observed for GL750 microstructure produced in salt-bath, which contains more austenite.

When using a direct threshold on ×2500 images to obtain the amount of M/A islands, the following fractions are obtained: 21% for GL680, 29% for GL700 and 40% for GL720. These values are higher than those obtained in situ by the Rietveld method (respectively 16% for GL680, 25% for GL700 and 29% for GL720). While for GL680 and GL700 steels, the difference remains low, the 11% difference for GL720 between the two measurements is quite high and would need further investigation.

A direct threshold is not applicable for GL750 microstructure which contain too much martensite. The method used for salt-bath microstructure could be applied, necessitating a grain segmentation with watershed algorithm. This method takes however too much time to apply in the frame of the current appendix.

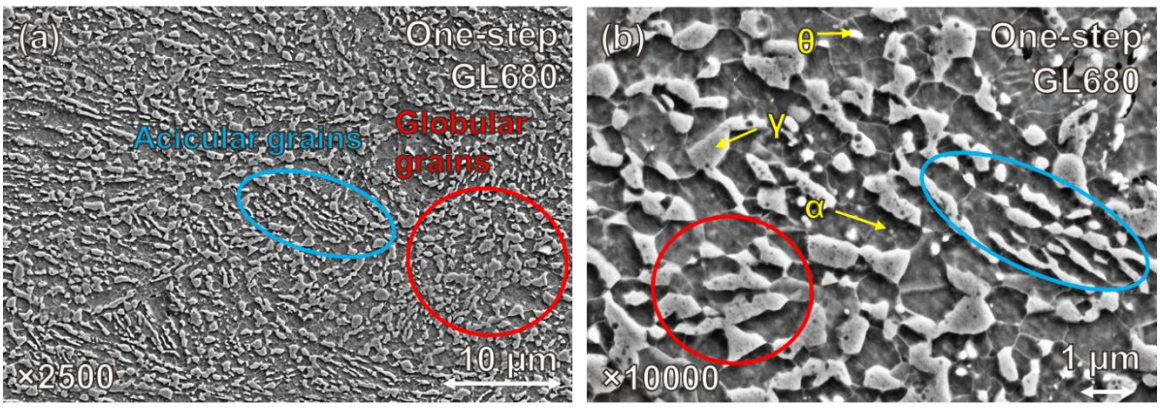

Figure 157: SEM micrographs of globular microstructures produced at 680°C in HEXRD dilatometry (microstructure formation described in Chapter II). (a) GL680 magnified at ×2500. (b) GL680 magnified at ×10000. Ferrite appears in dark grey, austenite in light grey, cementite in white particles.

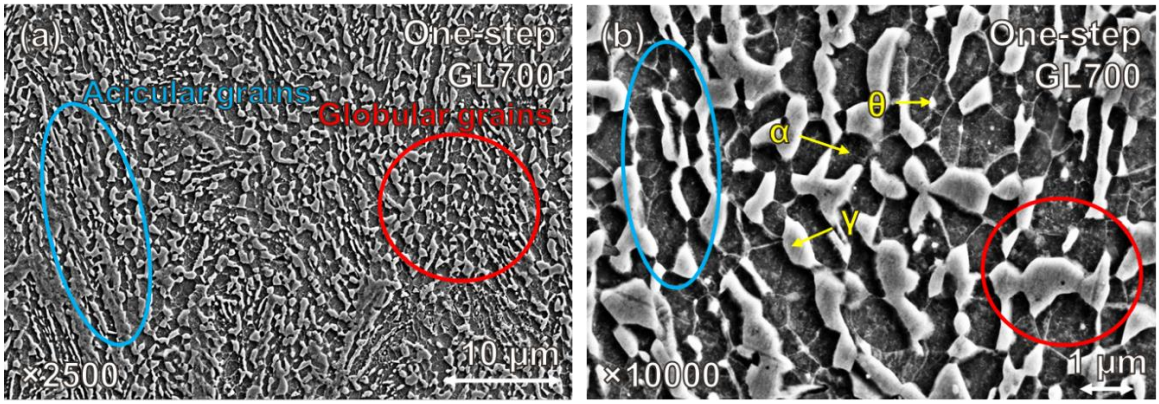

Figure 158: SEM micrographs of globular microstructures produced at 700°C in HEXRD dilatometry (microstructure formation described in Chapter II). (a) GL700 magnified at ×2500. (b) GL700 magnified at ×10000. Ferrite appears in dark grey, austenite in light grey, cementite in white particles.

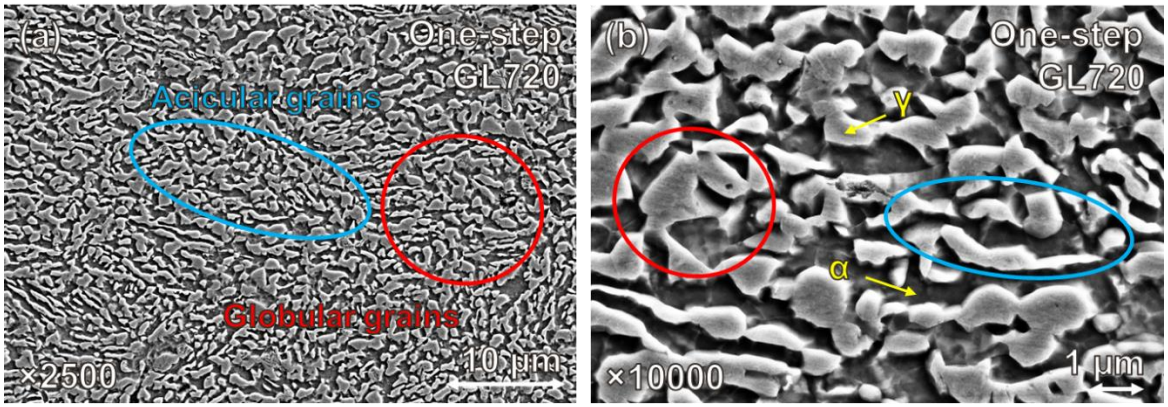

Figure 159: SEM micrographs of globular microstructures produced at 720°C in HEXRD dilatometry (microstructure formation described in Chapter II). (a) GL720 magnified at ×2500. (b) GL720 magnified at ×10000. Ferrite appears in dark grey, austenite in light grey, cementite in white particles.

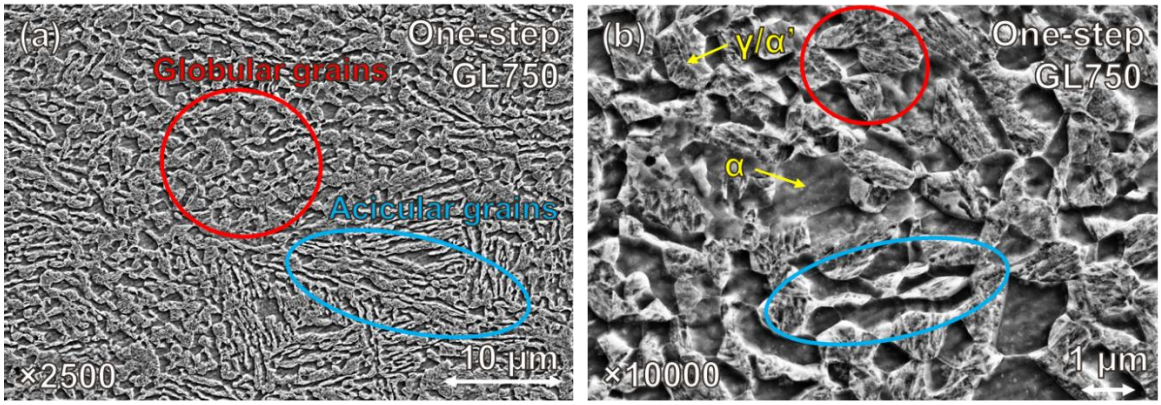

Figure 160: SEM micrographs of globular microstructures produced at 750°C in HEXRD dilatometry (microstructure formation described in Chapter II). (a) GL750 magnified at ×2500. (b) GL750 magnified at ×10000. Ferrite appears in dark grey, austenite in light grey, cementite in white particles.

Appendix F: Effect of the heating rate on medium Mn microstructure formation

In the PhD manuscript, three sets of microstructures were presented. One set of microstructures was produced by salt-bath and the results are presented in Chapter III during tensile tests. The second set was produced in a dilatometer and studied extensively in Chapter II, from section II.1 to II.4. This second set was called “HEXRD dilatometer” set. The main difference between salt-bath treatment and HEXRD dilatometer sets is the heating rate of intercritical annealing. In the latter, the heating rate is set at + 10°C/s, which is unrealistic. A third set of microstructures was thus produced in situ in dilatometry, denoted “realistic dilatometer”. The purpose of those latter treatments is to reproduce the microstructures obtained in salt-baths more accurately. Compared with model dilatometry treatments, treatments only have a different heating scheme. Until 500°C, the heating rate is set at +50°C/s. Then, between 500°C and T_{IA} - 50°C (i.e. 630°C for FB680), the heating rate is set at 12°C/s. Finally, between T_{IA} - 50°C and T_{IA}, a very low heating rate of +1°C/s was chosen. Overall, the obtained microstructures are very similar to those obtained with HEXRD dilatometry treatments. It was these “realistic dilatometer” microstructures that were studied by WDS in section II.5.B.d). The three thermal treatments are compared in Figure 161 for FB680. In red is the thermal treatment in salt-baths (recorded with a single welded thermocouple), while in blue and black are the “HEXRD” and “realistic” thermal treatment conducted in dilatometry.

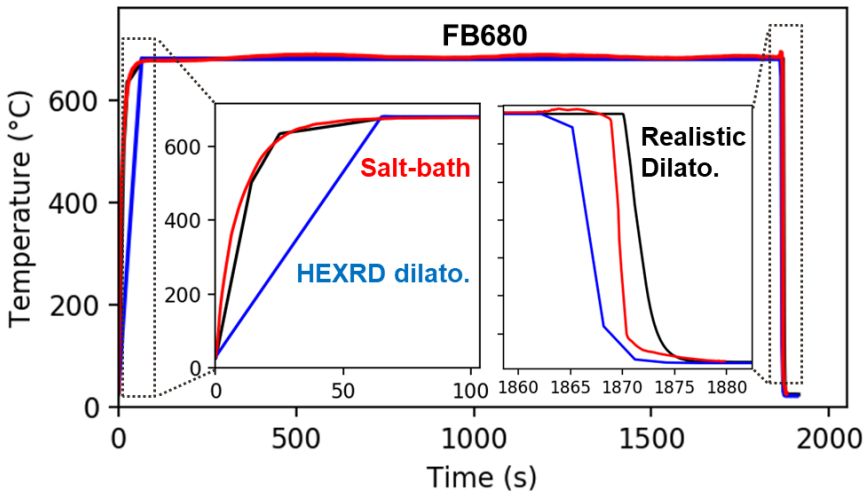

Figure 161: Comparison between the different methods used in the PhD project to produce intercritical annealed medium Mn steels. In red: treatment in salt-bath (used to produce tensile samples – cf. Chap. III). In blue: HEXRD experiments (analysed from section II.1 to II.4). In black: dilatometry treatment trying to reproduce more closely the treatment in salt-bath. The given examples are FB680 thermal treatments. Magnifications of the heating and cooling steps are also given.

The kinetics of austenite formation during realistic experiments are shown in Figure 162 and Figure 163 as a function of time and temperature respectively. They are calculated using Rietveld refinement. In comparison are reproduced from Chapter II the kinetics obtained during “HEXRD dilatometry” experiments (black dashed curve). The evolution as a function of the annealing temperature is similar between the two sets of experiments. The evolution of austenite phase fraction during the formation of GL720, GL750, FB680, FB700 and FB720 microstructures are very similar

between the two sets of experiments. There is more difference for GL680, GL700 and FB750 experiments, for which the fractions of austenite/martensite are significantly different in the final microstructure.

For FB720 and GL750, the formed phase fraction during intercritical annealing is similar and the experimental M_S temperatures are also really close. On the contrary, during the treatment of FB750 microstructure, more austenite is formed in the "HEXRD" experiment than in the "realistic" one. On the contrary, the austenite formed in the FB750 HEXRD treatment is less stable than that formed during the realistic treatment, as, the M_S temperature is higher in HEXRD FB750 experiment than in the FB750 realistic experiment. This is consistent with the chemical partitioning mechanism of carbon.

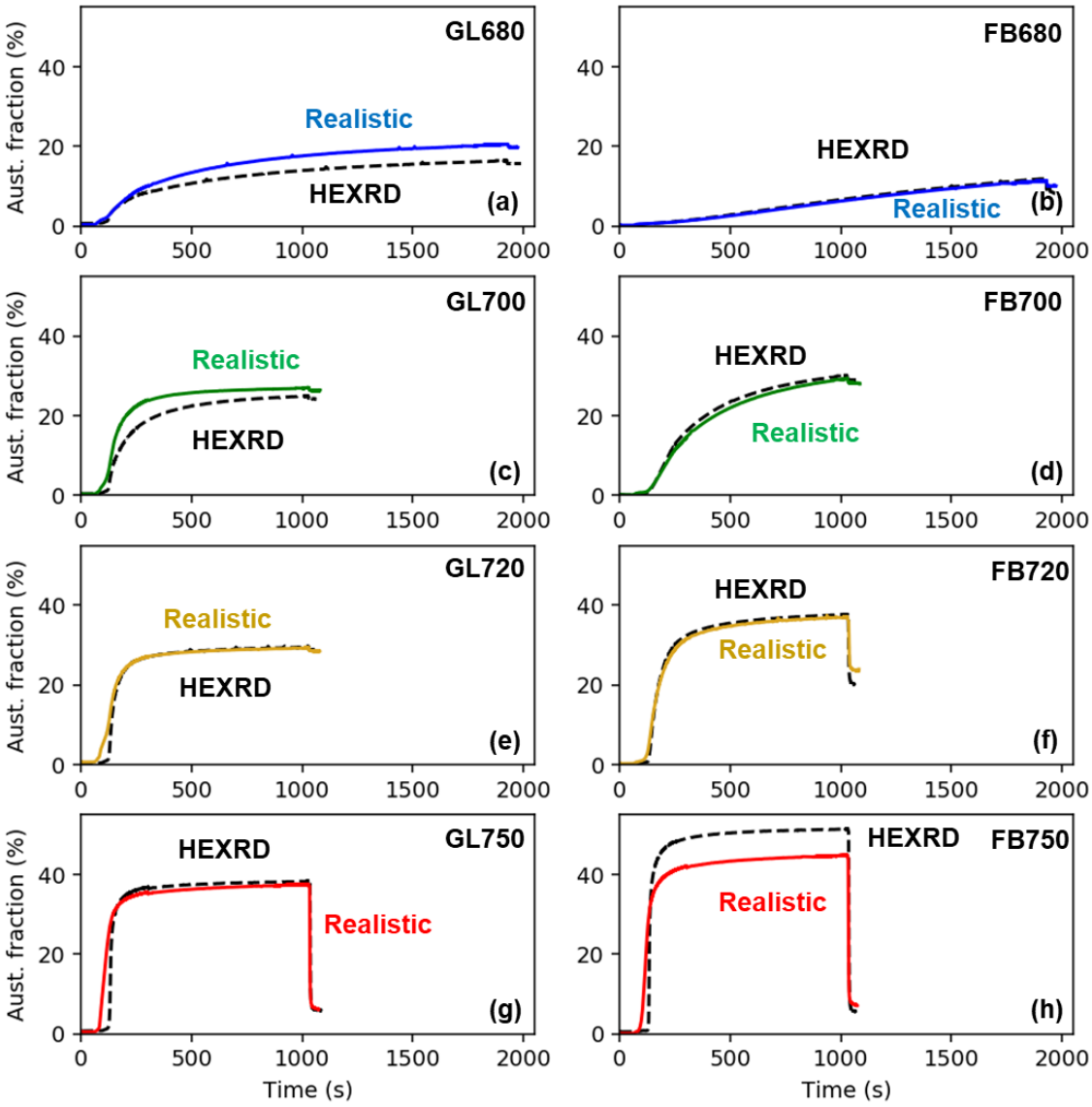

Figure 162: Austenite phase fraction as a function of time for the eight realistic experiments (coloured curves): (a) GL680, (b) FB680, (c) GL700, (d) FB700, (e) GL720, (f) FB720, (g) GL750 and (h) FB750. The kinetics obtained during "HEXRD dilatometry" experiments are reproduced from Chapter II (black dashed curve).

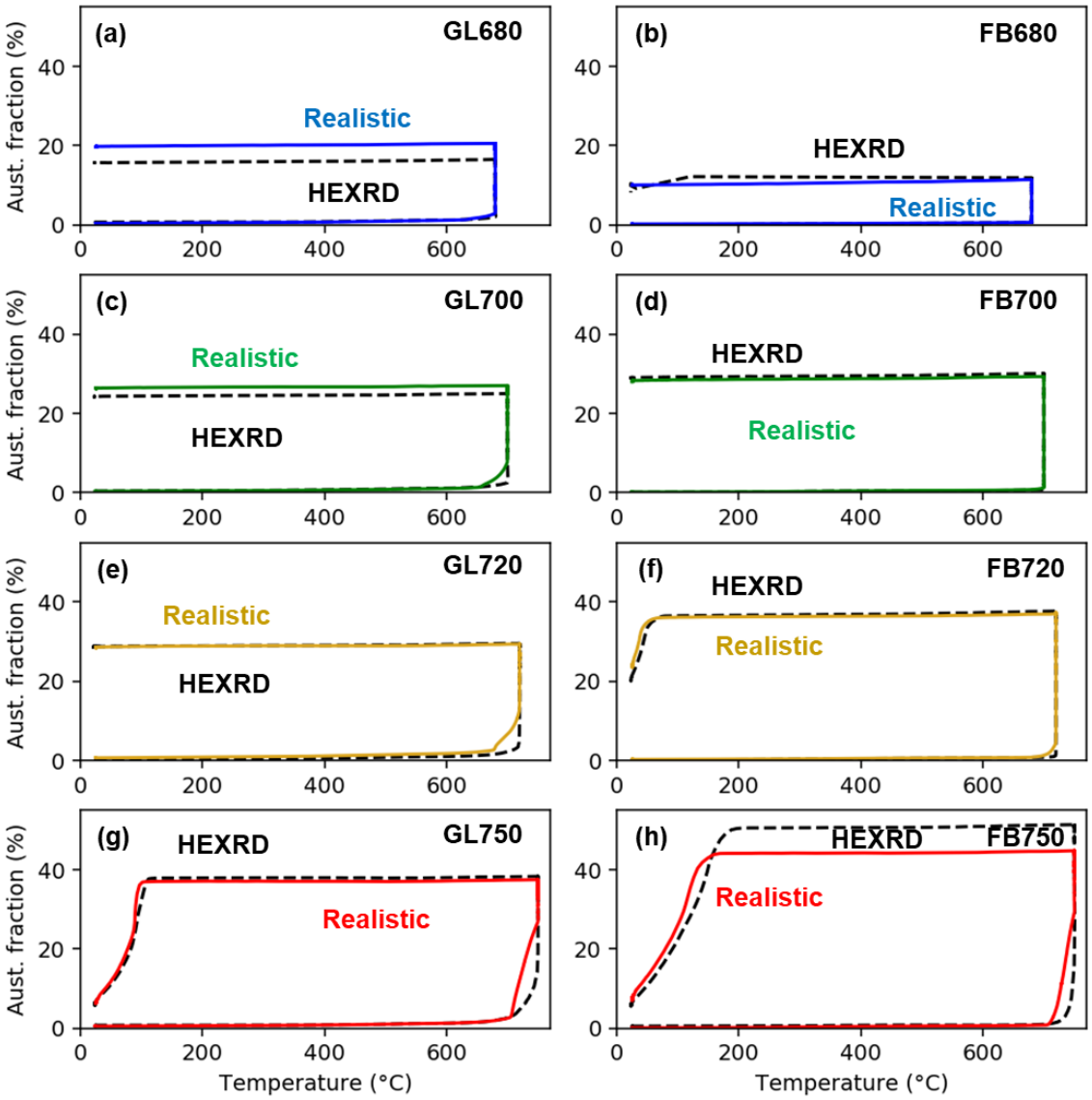

Figure 163: Austenite phase fraction as a function of temperature for the eight realistic experiments (coloured curves): (a) GL680, (b) FB680, (c) GL700, (d) FB700, (e) GL720, (f) FB720, (g) GL750 and (h) FB750. The kinetics obtained during "HEXRD dilatometry" experiments are reproduced from Chapter II (black dashed curve).

Appendix G: Distributions of grain size and shape

Mean values of grain sizes and shape factor of each duplex microstructure were given and discussed in Chapter II, section II.5.B.c). They are extracted from distributions calculated by the algorithm created for this project (detailed in section II.5.A). The grains are modelled with ellipsis, and the major and minor axis are also determined by the algorithm. The different distributions are given in the figure below. They are calculated by analysing SEM images with a magnification between ×5000 and ×10000, depending on the available data and the finesse of the microstructure. Alongside each distribution are given the mean and standard deviation calculated with the fitted log-normal distribution, the median, mean and standard deviation calculated directly on the data and the number of grains used for each distribution.

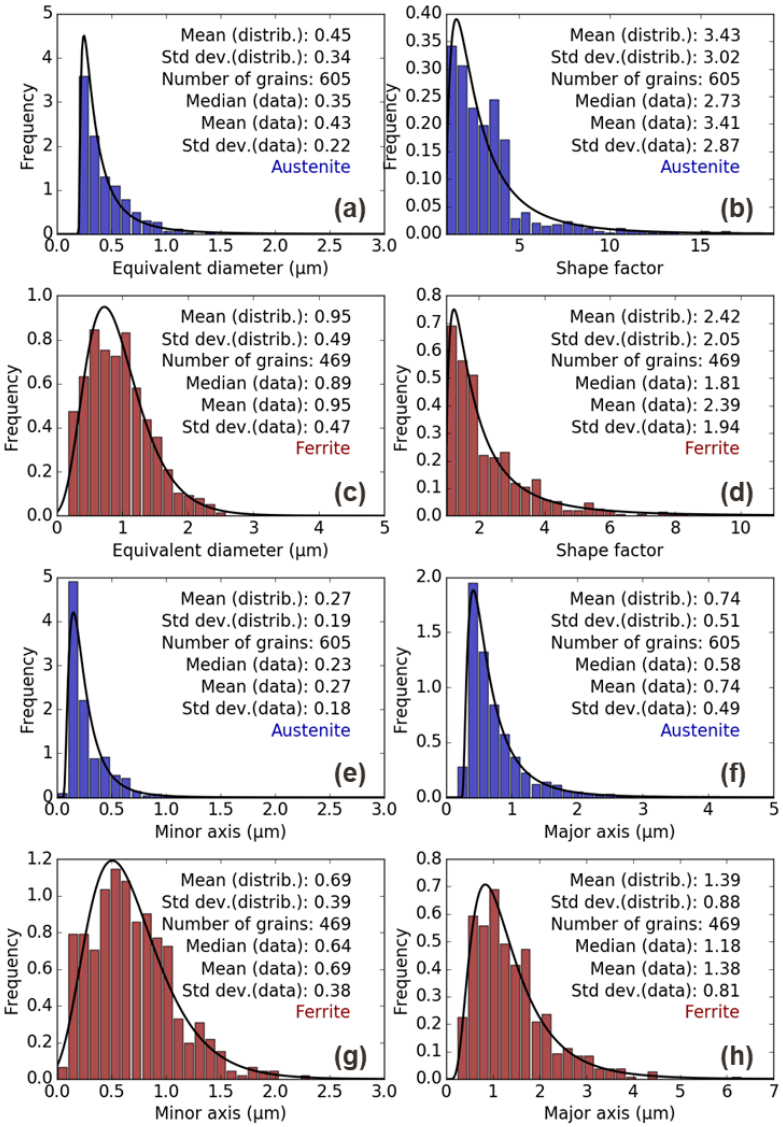

Figure 164: Distributions of (a) and (c) equivalent diameter, (b) and (d) shape factor, (e) and (g) minor axis and (f) and (h) major axis for both (c), (d), (g) and (h) ferrite grains, and (a), (b), (e) and (f) austenite/martensite islands, in the globular microstructure annealed at T_{IA} = 680°C.

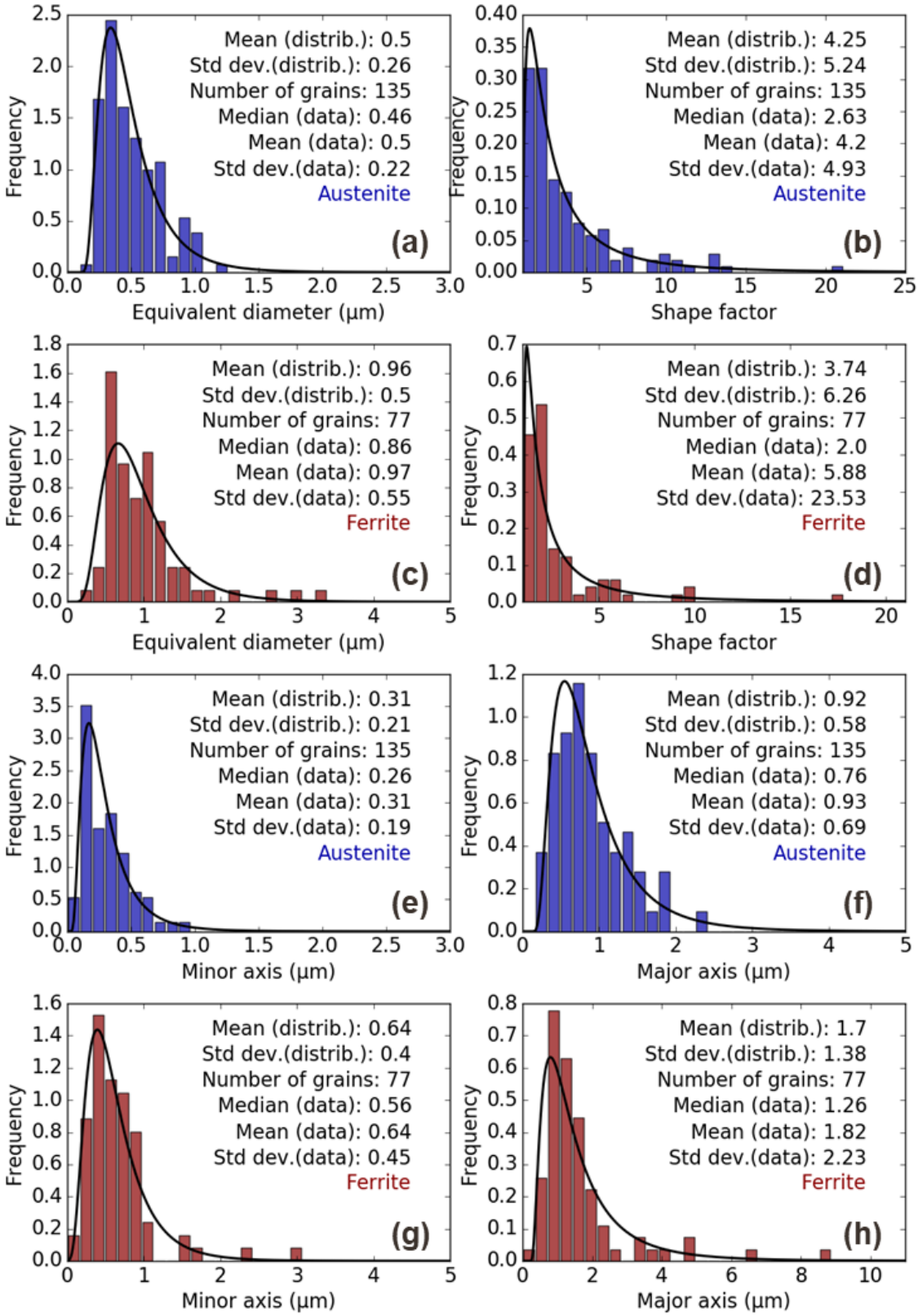

Figure 165: Distributions of (a) and (c) equivalent diameter, (b) and (d) shape factor, (e) and (g) minor axis and (f) and (h) major axis for both (c), (d), (g) and (h) ferrite grains, and (a), (b), (e) and (f) austenite/martensite islands, in the globular microstructure annealed at T_{IA} = 700°C.

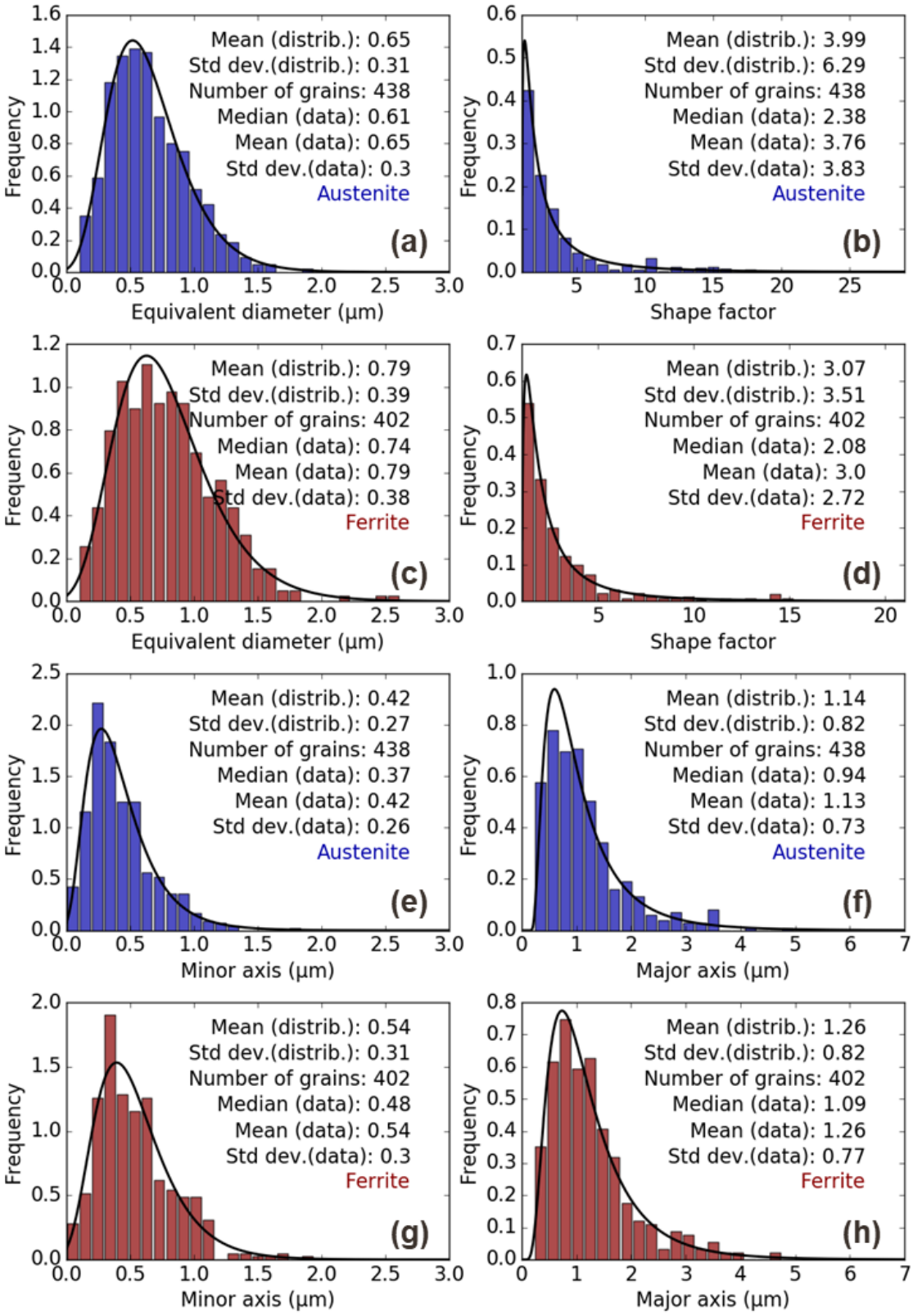

Figure 166: Distributions of (a) and (c) equivalent diameter, (b) and (d) shape factor, (e) and (g) minor axis and (f) and (h) major axis for both (c), (d), (g) and (h) ferrite grains, and (a), (b), (e) and (f) austenite/martensite islands, in the globular microstructure annealed at T_{IA} = 720°C.

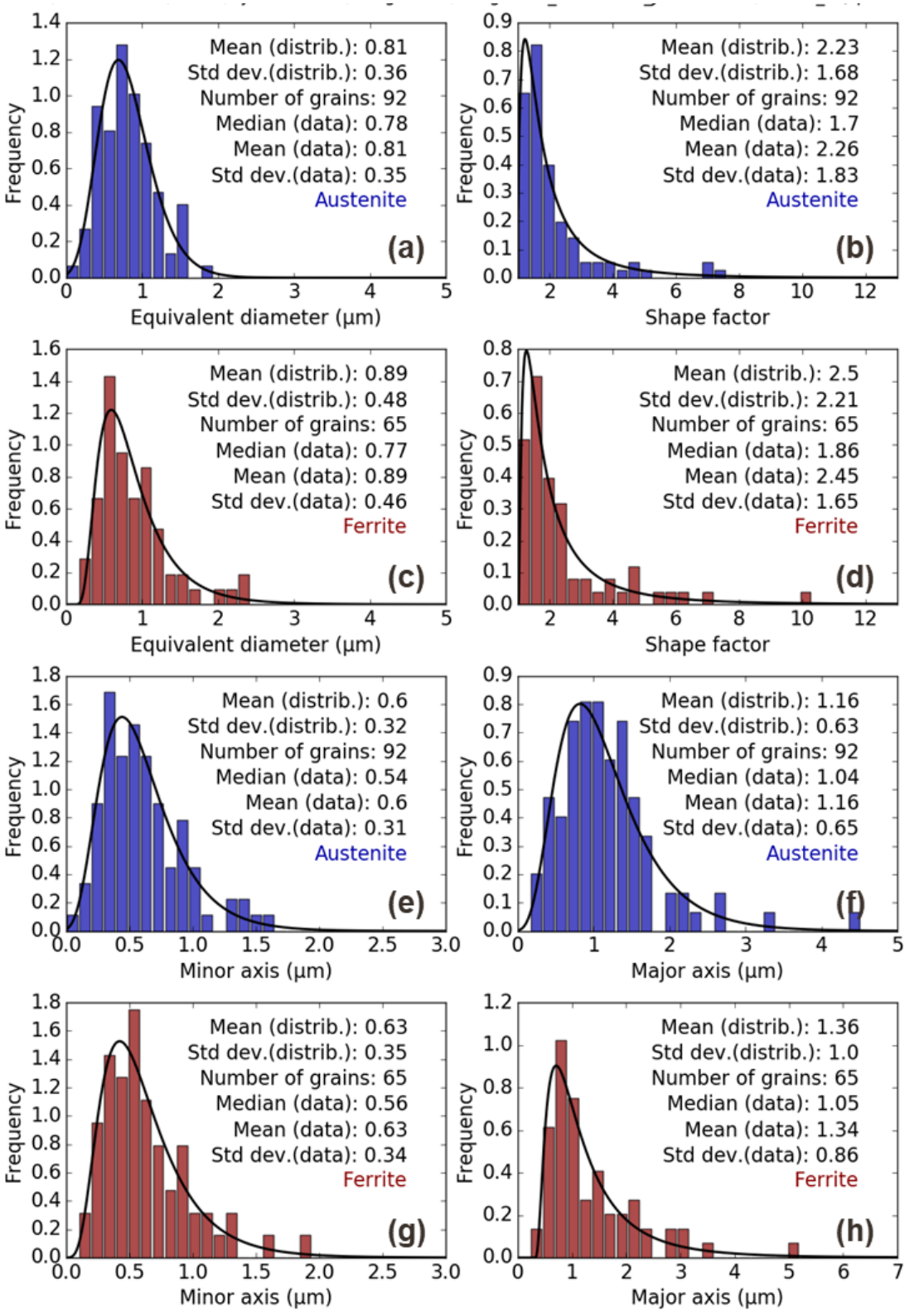

Figure 167: Distributions of (a) and (c) equivalent diameter, (b) and (d) shape factor, (e) and (g) minor axis and (f) and (h) major axis for both (c), (d), (g) and (h) ferrite grains, and (a), (b), (e) and (f) austenite/martensite islands, in the globular microstructure annealed at T_{IA} = 750°C.

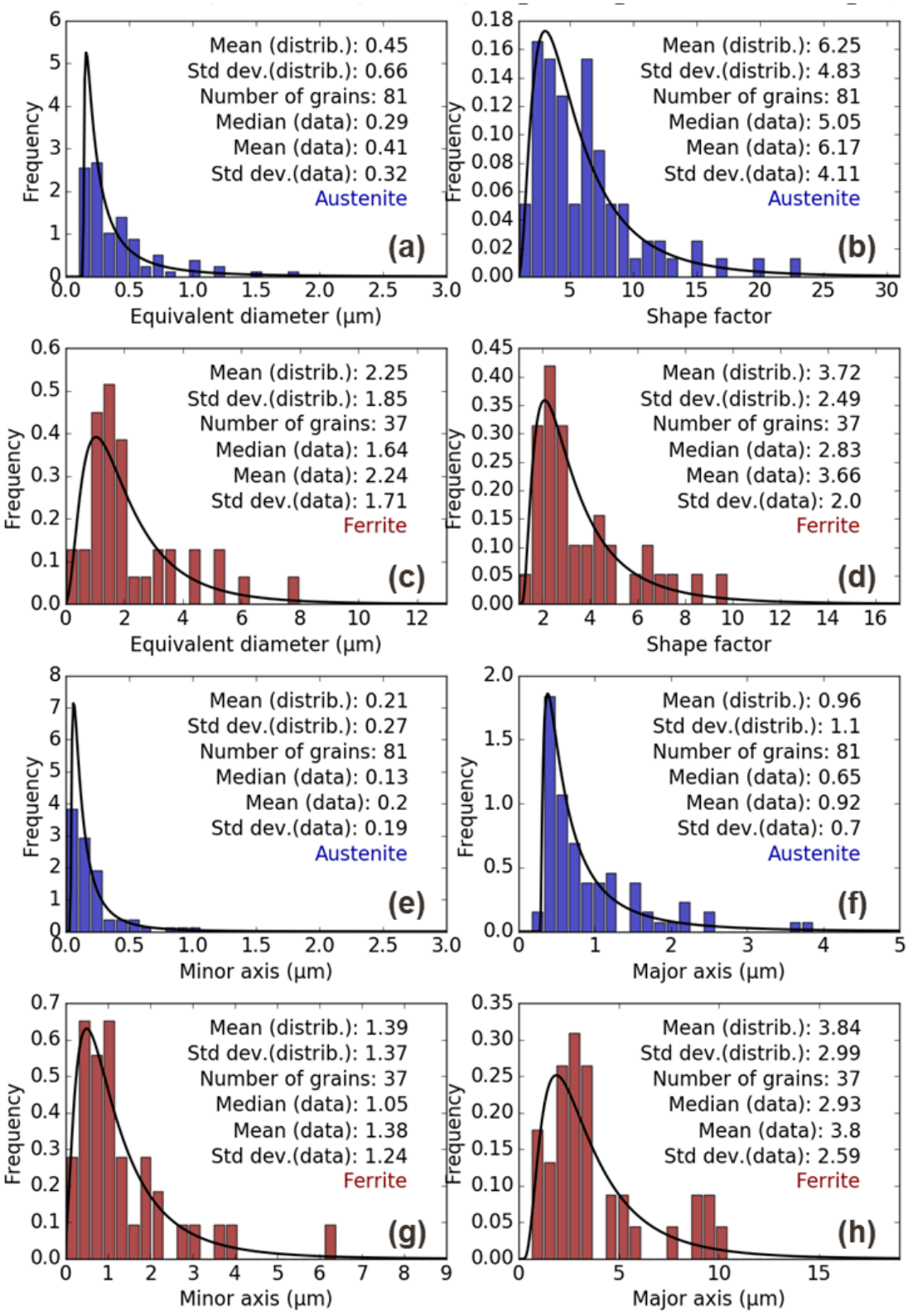

Figure 168: Distributions of (a) and (c) equivalent diameter, (b) and (d) shape factor, (e) and (g) minor axis and (f) and (h) major axis for both (c), (d), (g) and (h) ferrite grains, and (a), (b), (e) and (f) austenite/martensite islands, in the fibrous microstructure annealed at T_{IA} = 680°C.

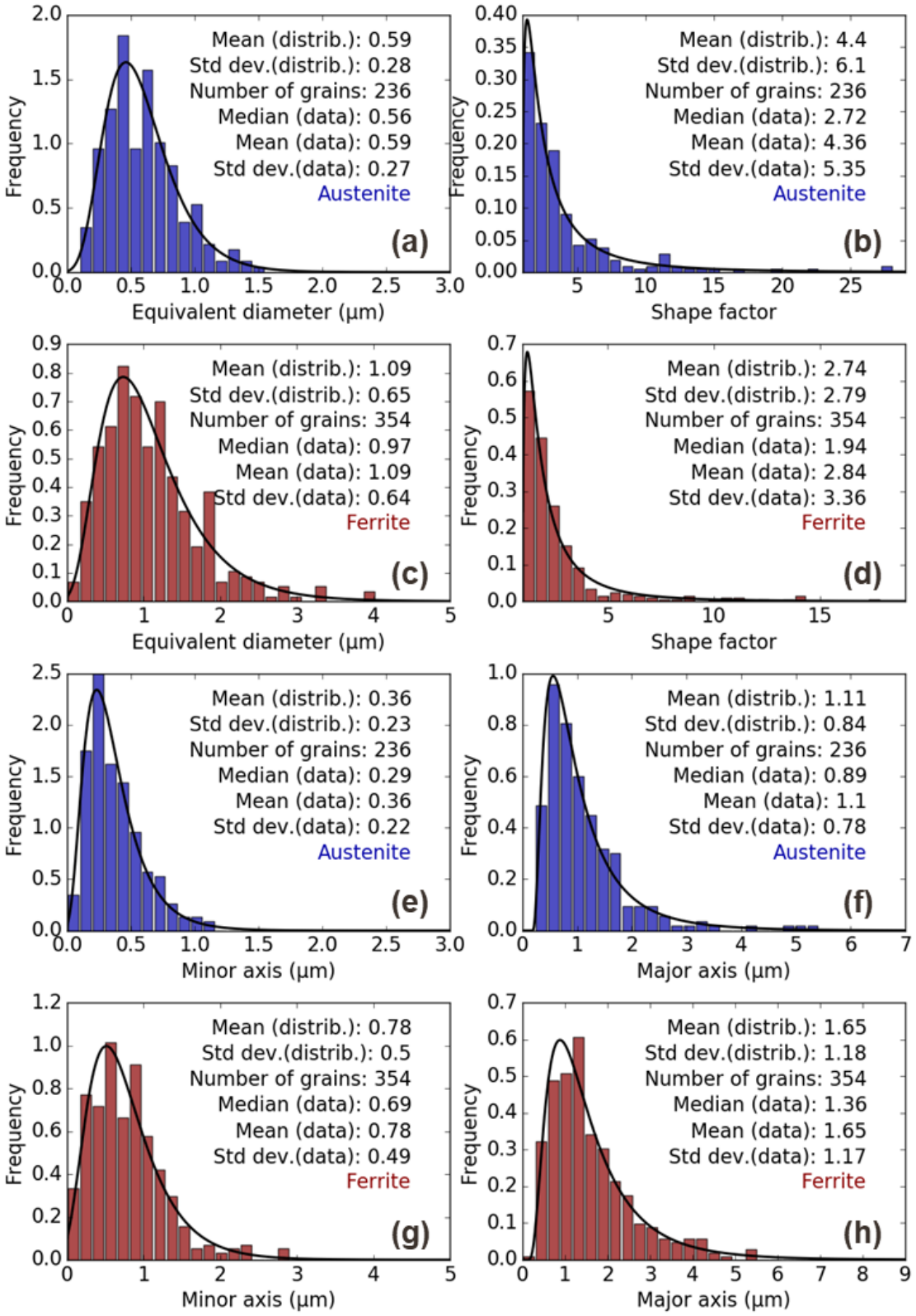

Figure 169: Distributions of (a) and (c) equivalent diameter, (b) and (d) shape factor, (e) and (g) minor axis and (f) and (h) major axis for both (c), (d), (g) and (h) ferrite grains, and (a), (b), (e) and (f) austenite/martensite islands, in the fibrous microstructure annealed at T_{IA} = 700°C.

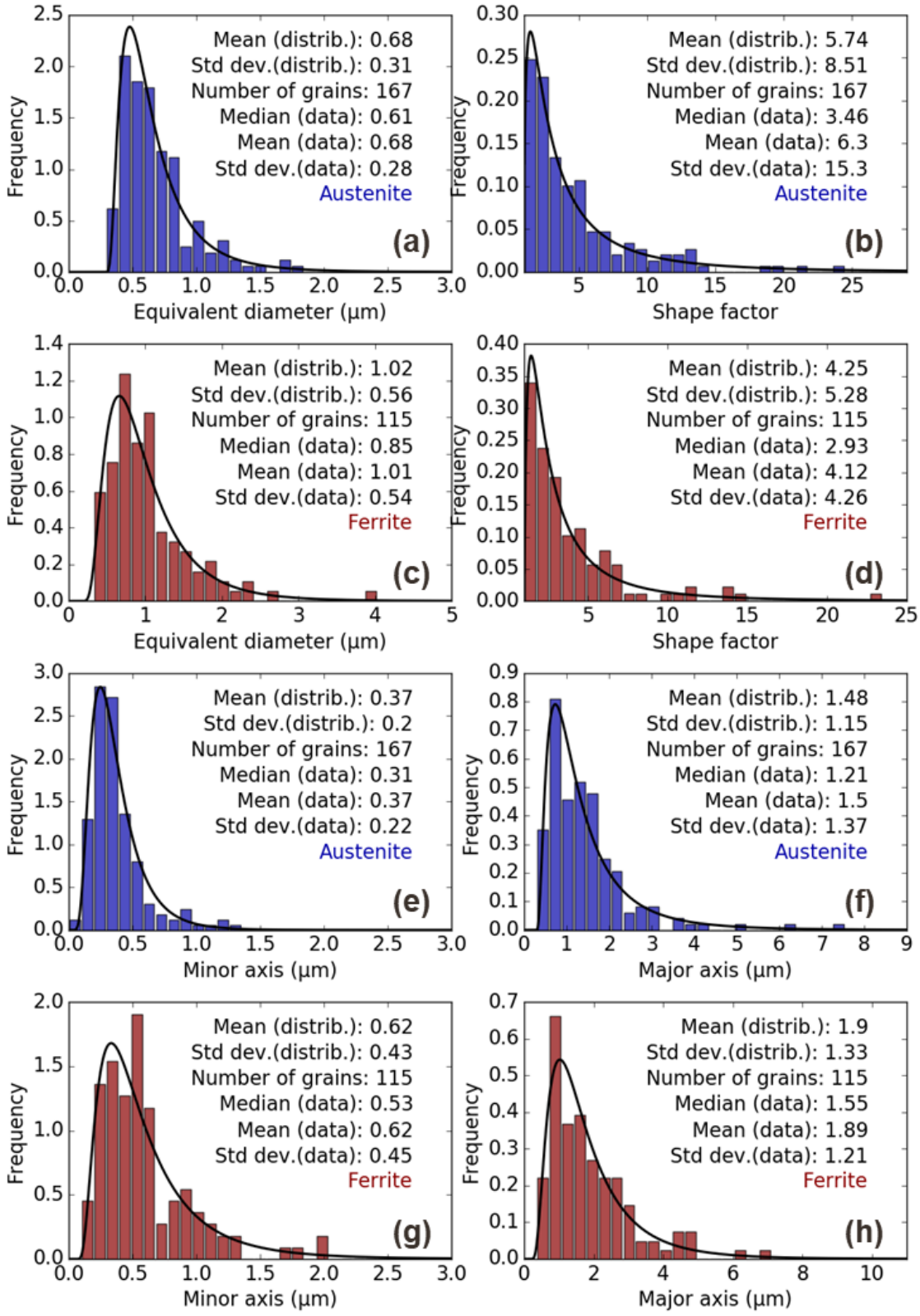

Figure 170: Distributions of (a) and (c) equivalent diameter, (b) and (d) shape factor, (e) and (g) minor axis and (f) and (h) major axis for both (c), (d), (g) and (h) ferrite grains, and (a), (b), (e) and (f) austenite/martensite islands, in the fibrous microstructure annealed at T_{IA} = 720°C.

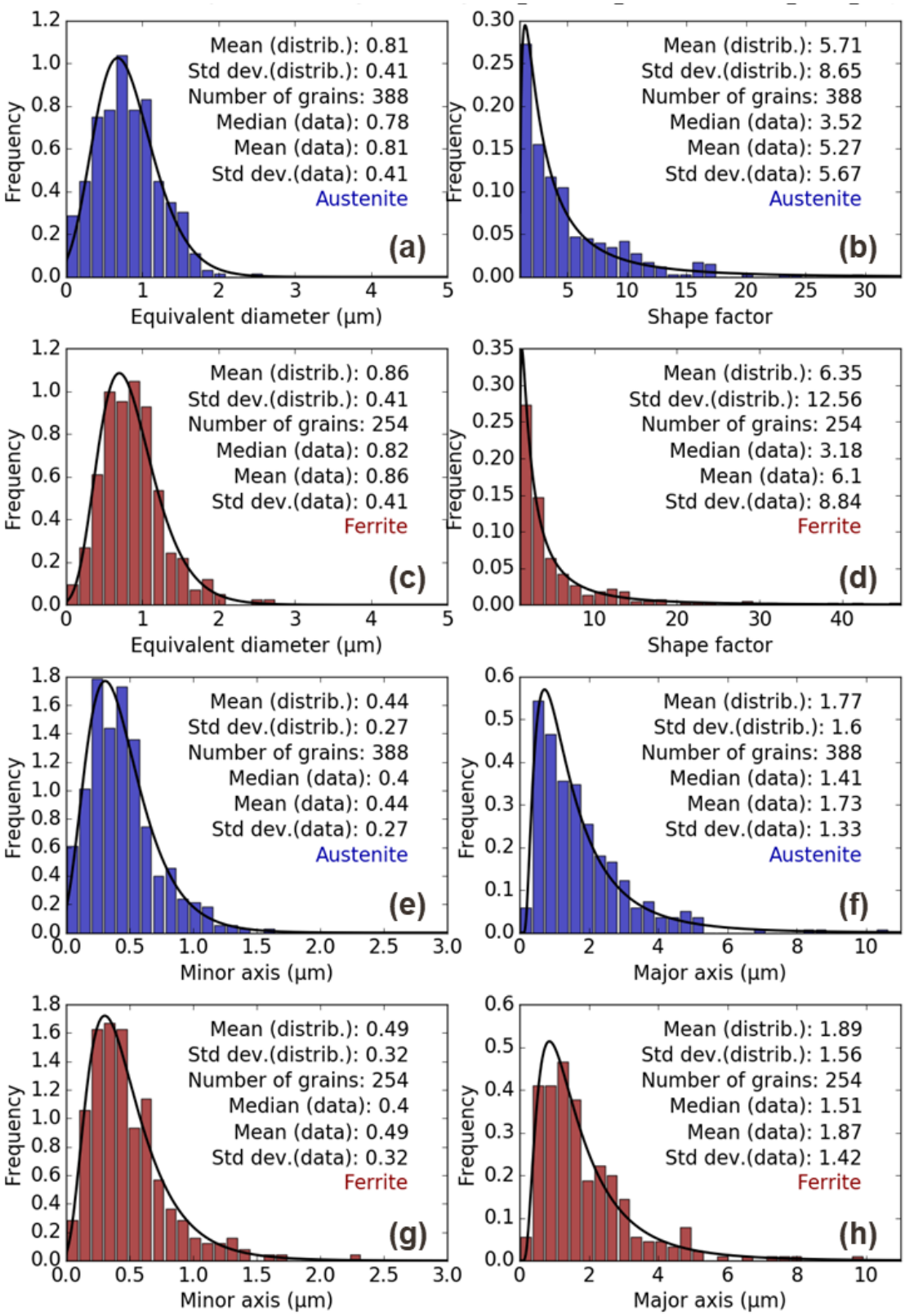

Figure 171: Distributions of (a) and (c) equivalent diameter, (b) and (d) shape factor, (e) and (g) minor axis and (f) and (h) major axis for both (c), (d), (g) and (h) ferrite grains, and (a), (b), (e) and (f) austenite/martensite islands, in the fibrous microstructure annealed at T_{IA} = 750°C.

Appendix H: Effect of plane orientation on SIMT

During the internship preceding the PhD thesis, two globular and fibrous steels were studied during tensile test by HEXRD. They were produced through one-step and two-step thermal treatments at 715°C during 15 min as described in Chapter II. The crosshead displacement rate was 0.01 mm/s.

To determine the transformation kinetics during the tensile tests, two methods have been conducted. The results for all experiments are shown in Figure 48. The first method consists in the Rietveld refinement of the diffractogram calculated with the whole diffraction pattern. The obtained kinetics (blue curve) will be called the “full integration” kinetics.

For the second method, the partial integration of diffraction patterns has been conducted in 15° sectors along the tensile direction (orange), the transverse direction (green) and the two diagonal/shear directions (red and purple), giving 4 new sets of diffractograms per experiments. All of them were refined to obtain four new transformation kinetics, one per direction. Those kinetics were averaged to obtain a kinetics (black curve), called the averaged kinetics, assumed to be representative of the global behaviour of austenite in the steel.

At the start of all experiments, there is a gap of + 5% between the transverse kinetics and the full integration kinetics, and a gap of -5% between the two shear kinetics and the full integration kinetics. The serrations are present at the same moment in all kinetics. For both experiments at the highest strain rate, the stress induced martensitic transformation seems more intense in the tensile direction than in other directions.

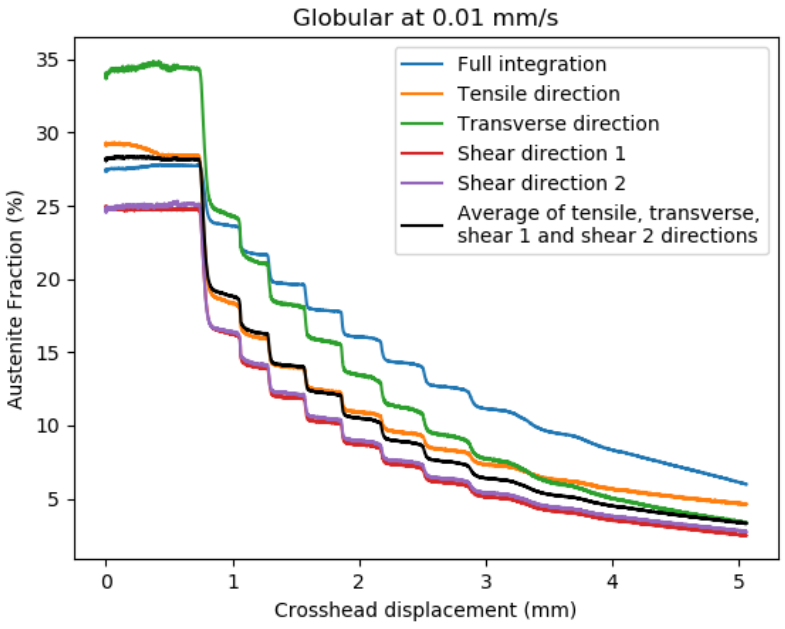

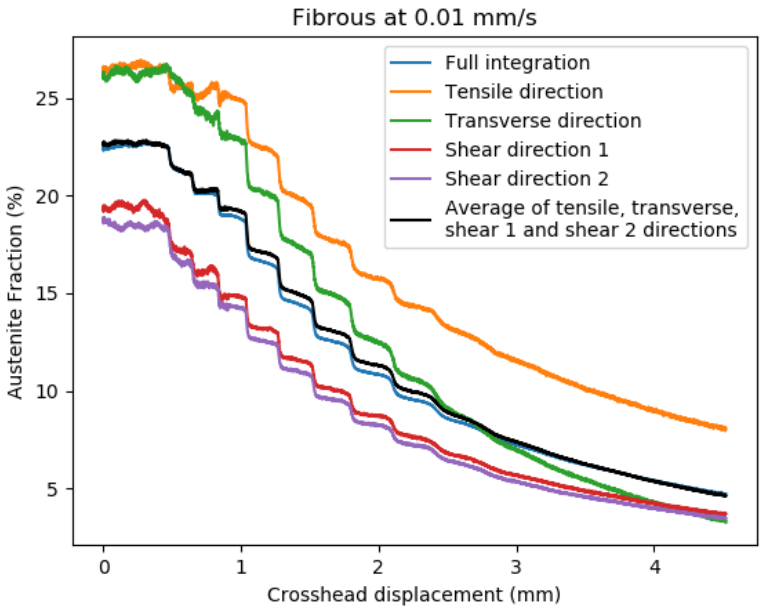

Figure 48: Transformation kinetics obtained the two methods for different microstructures, and the kinetics found after partial integration.

Overall, the averaged kinetics and the full integration kinetics are really similar. Between both kinetics, the initial austenite fraction is always the same in all experiments. The main difference between the two methods is seen in the experiment on the globular microstructure. The first serration in the averaged kinetics is far higher than in the full integration kinetics. From a theoretical point of view, the averaged kinetics is certainly more accurate than the full integration one. However, those calculations also show that the error made by taking the full integration kinetics, which is simpler to calculate, is in most cases not significant.

Appendix I: Discussion about the validity of the sin²ψ method

The approach to obtain stress inside each phase using HEXRD was defined in the precedent section. Ellipses linked with elastic deformation are obtained through sin²ψ method. However, the sin²ψ method is theoretically fully validated if the diffracting material is homogeneous (i.e. consisting of one phase), isotropic, not textured and without gradient of any nature (stress or composition) [233]–[235]. For medium Mn steels, these hypotheses are almost all violated. The material is biphasic/triphasic. It is initially textured due to an inheritance from cold-rolling for globular samples and to the ART mechanism for fibrous samples. This texture increases during deformation due to grain rotation induced by tensile strain. Finally, chemical gradient exists in both ferrite and austenite due to the partitioning of C, Mn, Si and Al during intercritical holding. The general effect of gradient on sin²ψ ellipse is to create a deviation to linearity for extremal value of sin²ψ, while texture gives rather a "snake-like" appearance to sin²ψ curves [233].

The ferrite and austenite ellipse (black dots) obtained for the GL720-001 specimen at the onset on necking are reported in Figure 172. The onset of necking was chosen because it is where sin²ψ curves deviate the most from linearity, due to more textured phase and, concerning austenite, a lower fraction. Ellipse openings are negligible, confirming the absence of shear stress in both ferrite and austenite. Linear regressions appear in Figure 172 as red straight lines. For perfectly isotropic and homogeneous materials, the choice of sin²ψ range for fitting the ellipse does not impact neither the intercept nor the slope of the linear regression, since the ellipse is perfectly linear. In the current case, two linear regression ranges have been investigated, indicated in green in Figure 172: $\sin^2\psi \in [0; 1]$ (whole ellipse; Figure 172 a and b) and $\sin^2\psi \in [0.2; 0.8]$ (Figure 172 c and d). The linear fit in this case is affected by the choice of sin²ψ interval. The effect of diminishing the range for linear regression is similar for both austenite and ferrite. It decreases the slope and intercept of the linear fit. This leads to the decrease in tensile strain and the increase in transverse strain. As the ellipse slope $\Delta\varepsilon$ is proportional to the von Mises stress σ_{vM} ($\Delta\varepsilon = E/(1+\nu)\times\sigma_{vM}$), flow stress in each phase is expected to diminish with decreasing sin²ψ range.

Austenite and ferrite von Mises stresses all along the tensile test were calculated for three different sin²ψ intervals: [0.2; 0.8], [0.1; 0.9] and [0; 1]. The von Mises stress in martensite was calculated following Hill's mixture rules in all cases, as explained in the preceding section. Results are reported in Figure 173. In the elastic regime, no significant influence of sin²ψ interval is observed. However, at the onset of yielding, as expected from ellipse observations, the von Mises stresses for both austenite and ferrite are higher when the sin²ψ range for linear regression is larger. There is no significant difference between choosing [0.2; 0.8] and [0.1; 0.9] for the calculation. Comparing [0; 1] and [0.2; 0.8] von Mises stresses, the difference is maximal at necking onset for both ferrite ($\Delta\sigma$ = 90 MPa) and austenite ($\Delta\sigma$ = 150 MPa). The repercussion on martensite von Mises stress is that the smaller the sin²ψ interval is, the larger the value of flow stress is. The maximal gap is 200 MPa. However, the conclusions made are independent from linear regression interval: martensite is stronger than austenite which is stronger than ferrite, and only austenite von Mises stress is affected by mechanical instabilities after the Lüders plateau. The linear regression interval only affects the local values and shows the relevance of the method stability.

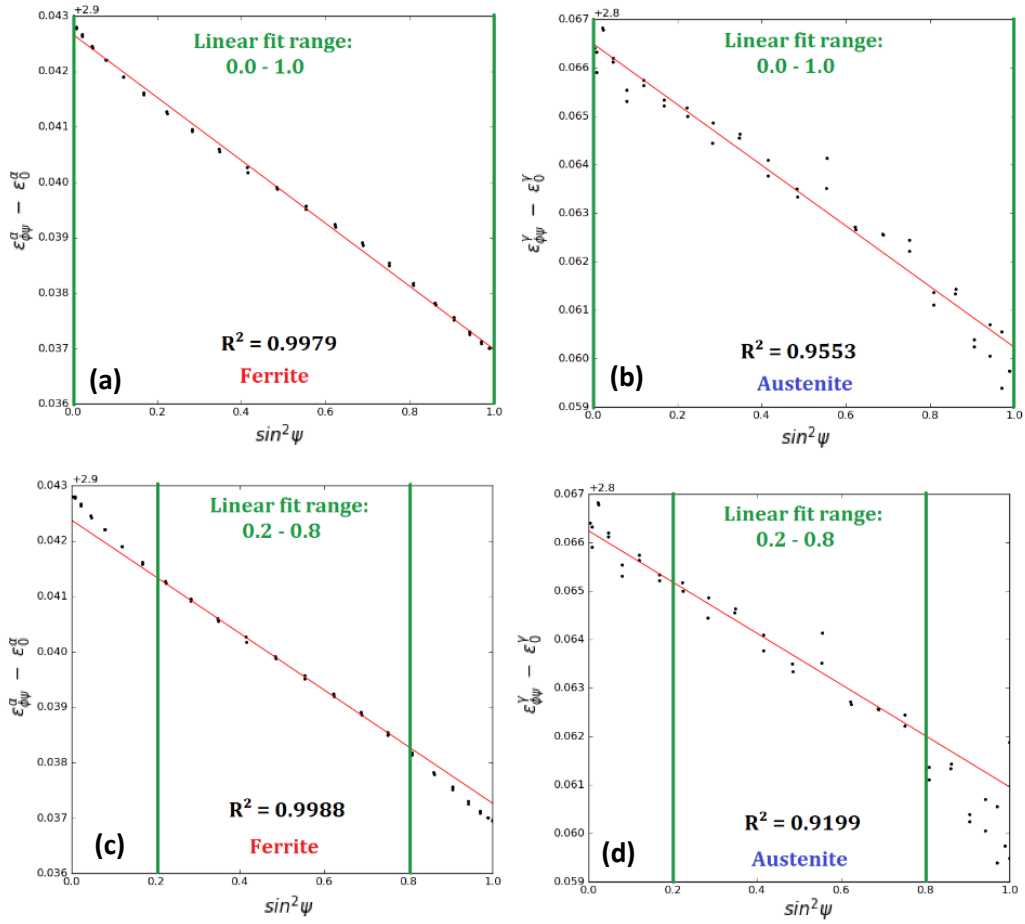

Figure 172: sin²ψ ellipse (black dots) obtained on the GL720-001 experiment at the onset of necking (diffraction image n°4734) for ferrite (a and c) and austenite (b and d). The red line in each subplot corresponds to the results of the linear regression over the sin²ψ range indicated in green. The coefficient of determination R² of each linear regression is indicated.

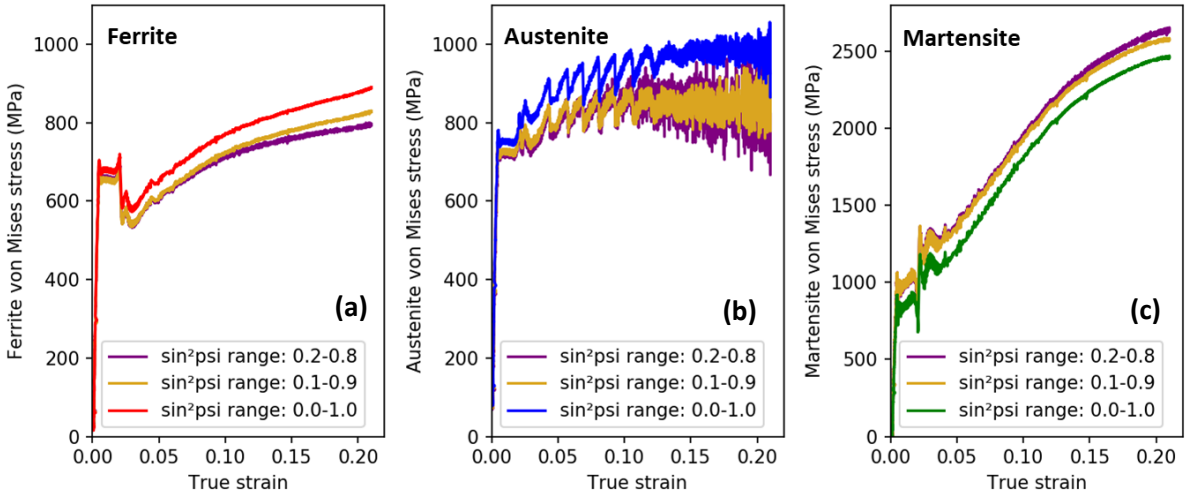

Figure 173: Effect of the sin²ψ range used for linear fit on the von Mises stresses in ferrite (a), austenite (b) and martensite (c) for the GL720-001 experiment. The stress in red, blue and green represents the stress obtained after linear fitting over the whole sin²ψ range. In gold are the curves obtained after a linear fit over 0.1-0.9 sin²ψ range, and in purple the ones obtained over 0.2-0.8 sin²ψ range.

There is no clear physical reason to choose [0; 1] interval compared with other intervals [233]. The correctness of a linear regression being linked with its coefficient of determination R^2, the latter are plotted for both ferrite and austenite for all $\sin^2\psi$ range in Figure 174. For ferrite, in all cases, the R^2 value is really close to 1 for all chosen intervals during plasticity. The R^2 value is slightly higher during the first stage of plasticity for [0; 1] interval, up to ε=15%. Concerning austenite however, the higher the strain is, the more the R^2 value deviates from 1. This general behaviour is linked with the decrease in austenite phase fraction as strain-induced martensitic transformation progresses, reducing the accurateness of peak position fitting. The effect is accentuated by decreasing the $\sin^2\psi$ range. At necking, the R^2 value for austenite is 0.96 for [0; 1], 0.89 for [0.1; 0.9] and 0.80 for [0.2; 0.8]. Hence, for the following sections of the report, the $\sin^2\psi$ range for linear regression of austenite and ferrite ellipse is always set to [0; 1].

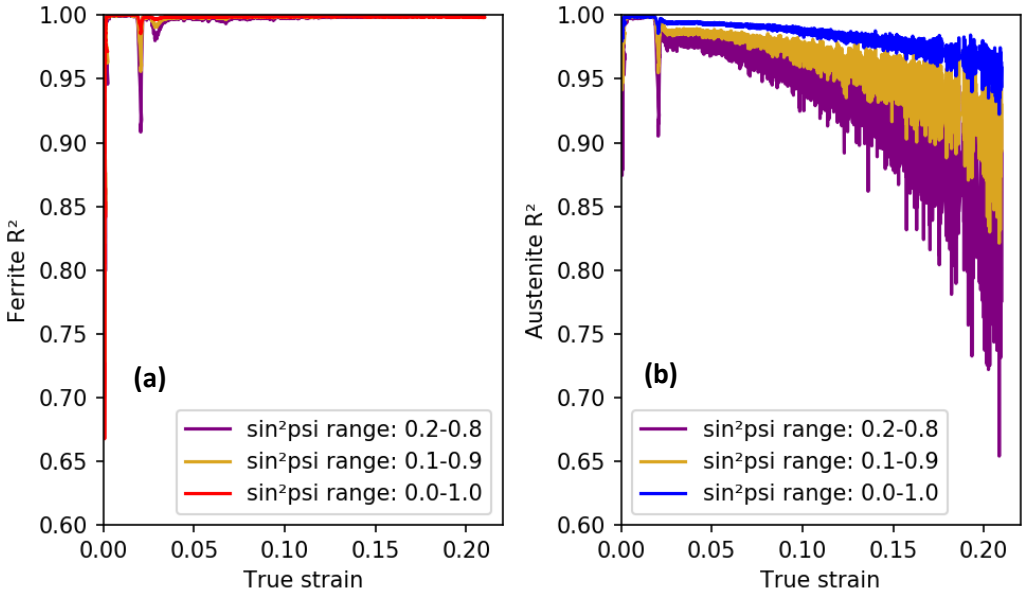

Figure 174: Effect of the $\sin^2\psi$ range used for linear fit on the coefficient of determination R^2 in ferrite (a) and austenite (b) of the GL720-001 experiment. The R^2 curves in red in (a) and blue in (b) are R^2 values obtained after linear fitting over the whole $\sin^2\psi$ range. In gold are the curves obtained after a linear fit over 0.1-0.9 $\sin^2\psi$ range, and in purple the ones obtained over 0.2-0.8 $\sin^2\psi$ range.

Appendix J: Preliminary tensile tests at high temperatures

In September 2022, tensile tests were conducted at IJL at high temperature, ranging from 100°C to 500°C. The dog-bone specimens used were leftovers from synchrotron experiments presented in Chapter III. As such, there were not enough specimens remaining to do all experiments. Only GL680, GL700, GL750 and FB700 microstructures have been tested. The extensometer present on the tensile machine was not fully calibrated at the time of tests. Therefore, the tensile curves are plotted as a function of the crosshead displacement for all experiments in Figure 175. Regulation was made with the crosshead displacement, except for the GL680 test at 400°C, which was regulated with strain. The ultimate tensile strength at room temperature (RT) is also represented as a horizontal line.

Overall, the steels' UTS decreases with increasing testing temperature, except at 300°C (green curve), where the steels mechanical behaviour improves, both in term of UTS and uniform elongation (UEL). This outperformance at 300°C is surprising and not expected from literature review. Another surprising fact is the presence of PLC effect in most tensile curves. For GL750 steel, PLC effect is not present at RT. However, it is present from 100°C to 400°C. Among the presented curves, the only curve with no presence of PLC effect is the GL750 test at 500°C.

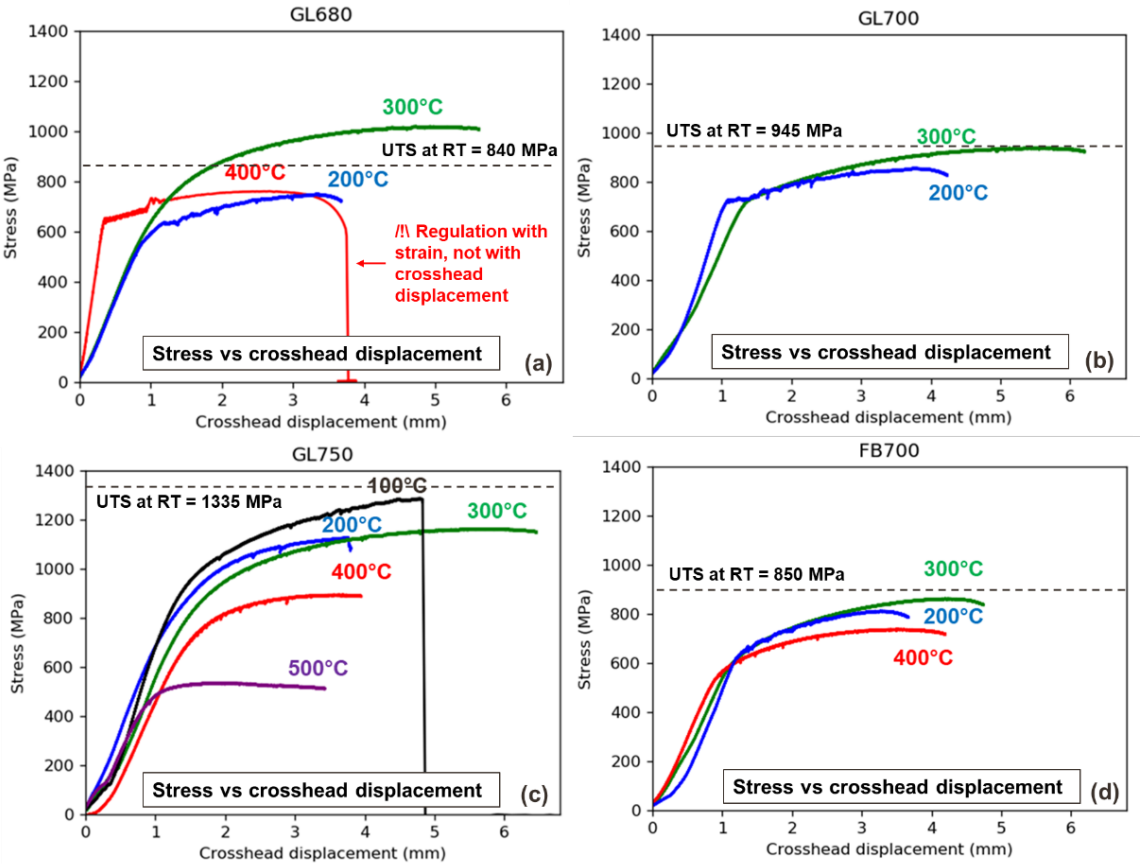

Figure 175: Engineering stress vs crosshead displacements obtained from tensile tests at high temperature for (a) GL680, (b) GL700, (c) GL750 and FB700 microstructures. The value of ultimate tensile strength determined at room temperature (RT) is displayed as a horizontal dashed line.

List of intermediate reports and publications

Several reports and one article have been written in the frame of the PhD thesis. Complementary results to those shown in the manuscript can be found in these works. Most of them have been published internally at ArcelorMittal Maizières research centre They are listed here:

Intermediate report:

- Internship bibliographic report, "Transformation martensitiques induites dans les aciers THR de 3ème génération : modélisation et expérience", March 2019, 22 pages
- End of internship report, "Retained austenite mechanical stability in TRIP-aided steels studied by in situ High-Energy X-Ray Diffraction", August 2019, 43 pages

- 1st year bibliographic report, *"Mechanically induced martensitic transformations in 3rd generation Advanced High Strength Steels: Phenomenology and Modelling*", July 2020, 70 pages
- 1st year progress report on microstructure design, *"Medium Mn steels: Phenomenology of microstructure genesis and macroscopic mechanical response*", April 2021, 64 pages
- 2nd year progress report on synchrotron tensile tests, "*In situ study of mechanical stability of retained austenite in medium Mn steel by high-energy X-Ray diffraction experiments*" March 2022, 58 pages

- Dynaustab report on synchrotron tensile tests, February 2022, 20 pages
- Dynaustab report on synchrotron thermal treatment, February 2022, 17 pages

- TMS2020 conference report, March 2020, 4 pages
- HMnS2022 conference report, June 2022, 8 pages

- 1st year report for "Comité de suivi individuel de thèse", August 2020, 15 pages
- 2nd year report for "Comité de suivi individuel de thèse", June 2021, 18 pages
- 3rd year report for "Comité de suivi individuel de thèse", September 2022, 19 pages

Article:

- M. Lamari, S. Y. P. Allain, G. Geandier, J.-C. Hell, A. Perlade, et K. Zhu, « *In Situ Determination of Phase Stress States in an Unstable Medium Manganese Duplex Steel Studied by High-Energy X-ray Diffraction* », *Metals*, vol. 10, nº 10, p. 1335, oct. 2020, doi: 10.3390/met10101335.

Résumé

Les aciers moyen manganèse appartiennent à la famille des aciers à très haute résistance mécanique (THR) de 3ème génération. Leurs propriétés exceptionnelles sont dues à leurs microstructures duplex particulières, qui contiennent une matrice "ferritique" de taille micrométrique et une quantité importante d'austénite résiduelle. Cette nouvelle génération d'aciers est considérée comme l'une des meilleures possibilités par les constructeurs automobiles pour continuer à améliorer la sécurité des véhicules légers tout en réduisant leur consommation d'énergie et donc leur empreinte environnementale. La bonne formabilité et la résistance élevée de ces aciers sont expliquées par la transformation martensitique induite par la déformation (SIMT) de l'austénite résiduelle pendant un chargement mécanique. La transformation progressive de l'austénite ductile en martensite dure provoque une augmentation rapide de l'écrouissage macroscopique de l'acier, mécanisme connu sous le nom d'effet de plasticité induite par la transformation (TRIP). La compréhension et la modélisation de la stabilité de l'austénite résiduelle et de la réponse mécanique associée de ces aciers sont donc d'un grand intérêt à la fois scientifique et industriel.

Huit microstructures différentes ont été conçues sur la base de calculs thermodynamiques afin d'évaluer l'effet respectif de la morphologie, de la composition et de la taille des grains sur la stabilité de l'austénite. La formation des microstructures duplex lors du recuit intercritique a été caractérisée in situ par des expériences de diffractions des rayons X haute énergie (DRXHE) sur la ligne de lumière synchrotron. En plus de mesurer les cinétiques d'austénitisation en utilisant la méthode d'affinements Rietveld, ces expériences révèlent les mécanismes de précipitation/dissolution des carbures lors du chauffage et les grandes contraintes hydrostatiques résiduelles à l'échelle des phases obtenues après le refroidissement final. L'origine de ces contraintes hydrostatiques a été expliquée et quantifiée à travers un modèle. Un travail exhaustif de microscopie électronique à balayage (SEM) et de microsonde de Castaing a également été effectué pour mesurer les tailles et les compositions chimiques des différentes phases de la microstructure.

Le comportement mécanique en traction des aciers étudiés a été mesuré en combinaison avec des expériences HEXRD et des mesures de corrélation d'images numériques (DIC). Ces expériences in situ uniques permettent de mesurer simultanément les cinétiques SIMT, la répartition des contraintes en 3D entre les phases (à savoir la ferrite, l'austénite et la martensite) en utilisant les méthodes des $\sin^2\psi$ et les déformations locales le long des éprouvettes. Ceux-ci servent en particulier à caractériser les bandes de Lüders et de Portevin-Le Chatelier (PLC) qui affectent les aciers moyen Mn étudiés.

Toutes ces données expérimentales ont servi à développer un modèle micromécanique à champ moyen innovant pour prédire le comportement en traction des aciers moyen Mn avec des microstructures austénite-ferrite-martensite. Il repose sur la description des comportements locaux de chaque phase et de la SIMT, tous deux étalonnés sur nos expériences HEXRD. Les écrouissages de l'austénite et de la ferrite sont modélisés grâce à un modèle sensible à la taille basées sur les densités de dislocations. Le comportement de la martensite fraîche et induite par la déformation est considéré, au contraire, comme une transition élastique/plastique étendue. Les cinétiques SIMT sont basées sur une évaluation thermodynamique de la stabilité de l'austénite résiduelle inspirée par le travail pionnier d'Olson et Cohen. Le modèle montre une excellente concordance avec les observations expérimentales.

Abstract

Medium manganese steels belong to the so-called 3rd generation of Advanced High Strength Steel (AHSS). Their ground-breaking properties are due to their particular duplex microstructures, which contain a micrometric “ferritic” matrix and a large amount of retained austenite. This new generation of steels is seen as one of the best possibilities for carmakers to continue improving the safety of light-duty vehicles and reduce their energy consumptions[2] and thus their environmental footprints. The good formability and the high resistance of those steels are explained by the strain-induced martensitic transformation (SIMT) of residual austenite during a mechanical loading. The gradual transformation of ductile austenite into high strength martensite causes a rapid increase in the macroscopic work-hardening of the steel, mechanism known as Transformation Induced Plasticity effect (TRIP). Understanding and modelling the stability of retained austenite and the related mechanical response of these steels are thus of great interest both from a scientific and industrial point of view.

For this purpose, eight different microstructures have been designed based on thermodynamical calculations in order to evaluate the respective effect of the morphology, the composition and the grains size on austenite stability. The formation of the duplex microstructures during intercritical annealing have been characterized in situ by high-energy X-ray diffractions (HEXRD) experiments on synchrotron beamline. In addition to measuring austenitization kinetics using Rietveld refinements, these experiments reveal in an original way the mechanisms of primary precipitation/dissolution of carbides during heating and the large residual hydrostatic stresses at the scale of the phases obtained after final cooling. The origin of these latter has been explained and quantified through a model. An extensive scanning electron microscopy (SEM) and Castaing microprobe work was also conducted to measure the sizes and chemical compositions of the different microstructure components.

The tensile mechanical behaviour of the studied steels has been measured in combination with HEXRD experiments and Digital Image Correlation (DIC) measurements. These unique in situ experiments permit to measure simultaneously the SIMT kinetics, the 3D stress partitioning between phases (namely ferrite, austenite and martensite) using $\sin^2\psi$ methods and the local strains all along the tensile specimens. These latter serve in particular to characterize Lüders and Portevin-Le Chatelier (PLC) bands which affect the studied medium Mn steels.

All those experimental inputs have served to develop an innovative mean field micromechanical framework to predict the tensile behaviour of medium Mn steels with austenite-ferrite-martensite microstructures. It relies on the description of the local behaviours of each constituting phase and of the SIMT of retained austenite, both calibrated on our HEXRD experiments. The work-hardening of austenite and ferrite are modelled thanks to a size-sensitive model based on dislocation densities. The behaviour of fresh and strain induced martensite is considered on the contrary as an extended elastic/plastic transition. The SIMT kinetics is based on a thermodynamical assessment of the stability of retained austenite inspired by Olson and Cohen pioneering work. The model is thus finally sensitive to the size of the microstructure components, to their local composition and to their respective stability and it shows an excellent agreement with the experimental observations.